



HAL
open science

Relativistic phases in condensed matter

Eric Brillaux

► **To cite this version:**

Eric Brillaux. Relativistic phases in condensed matter. Condensed Matter [cond-mat]. Université de Lyon, 2021. English. NNT: 2021LYSEN018 . tel-03375226

HAL Id: tel-03375226

<https://theses.hal.science/tel-03375226>

Submitted on 12 Oct 2021

HAL is a multi-disciplinary open access archive for the deposit and dissemination of scientific research documents, whether they are published or not. The documents may come from teaching and research institutions in France or abroad, or from public or private research centers.

L'archive ouverte pluridisciplinaire **HAL**, est destinée au dépôt et à la diffusion de documents scientifiques de niveau recherche, publiés ou non, émanant des établissements d'enseignement et de recherche français ou étrangers, des laboratoires publics ou privés.



Numéro National de Thèse : 2021LYSEN018

THÈSE DE DOCTORAT DE L'UNIVERSITÉ DE LYON

opérée par

l'École Normale Supérieure de Lyon

**École Doctorale N°52
Physique et Astrophysique de Lyon**

Discipline : Physique

Soutenu publiquement le 12/07/2021 par :
Éric BRILLAUX

Relativistic Phases in Condensed Matter

Phases relativistes en matière condensée

Devant le jury composé de :

MEYER, Julia	<i>Professeure</i>	<i>CEA Grenoble</i>	Rapporteure
LE DOUSSAL, Pierre	<i>Directeur de Recherche</i>	<i>LP ENS</i>	Rapporteur
VOZMEDIANO, María	<i>Professeure</i>	<i>ICMM</i>	Examinatrice
GURARIE, Victor	<i>Professeur</i>	<i>University of Colorado</i>	Examinateur
CARPENTIER, David	<i>Directeur de Recherche</i>	<i>LP ENS de Lyon</i>	Directeur
FEDORENKO Andrey	<i>Chargé de Recherche</i>	<i>LP ENS de Lyon</i>	Co-encadrant

Abstract — This thesis focuses on the electronic properties of crystalline materials known as relativistic semimetals, where the energy bands touch linearly at discrete points of the Brillouin zone. A historical example of such material is graphene, whose elementary excitations behave as two-dimensional massless Dirac fermions, even though they propagate at sublight speed. Massless relativistic fermions also appear in the spectrum of three-dimensional materials: Weyl and Dirac semimetals. In this thesis, we analyse the stability of the band crossing points with respect to perturbations, either disorder or interactions. The first part addresses the disorder-driven continuous phase transition of a Weyl semimetal to a metallic phase. In this semimetal-metal transition, which differs from Anderson’s localisation, the disorder-averaged density of states acts as an order parameter. As an alternative way to characterise the transition, we study a continuous set of exponents, the multifractal spectrum, which encodes the geometrical properties of the critical wave functions. These multifractality exponents, which we determine within a renormalisation group approach, govern the scaling law of the typical density of states. We also investigate the fate of surface states in disordered Weyl and Dirac semimetals using a self-consistent approximation, and show that the Dirac surface states undergo a similar disorder-induced transition. The second part addresses twisted bilayer graphene, a system where the interplay between interlayer tunnelling and the moiré geometry of the bilayer leads to an unusual ‘magic’ angle physics. The Fermi velocity vanishes at a discrete set of so-called magic angles, which enable many-body effects to dominate the electronic properties. We classify all contact interactions allowed by symmetry, and develop a renormalisation group approach to study the competition between the relevant instabilities. We explain the emergence of a gapped phase at charge neutrality that breaks the three-fold rotational symmetry, which we call a nematic insulator.

Résumé — Cette thèse traite des propriétés électroniques de cristaux où les bandes d’énergie se croisent linéairement : les semimétaux relativistes. Un exemple historique en est le graphène, dont les excitations élémentaires se comportent comme des fermions de Dirac sans masse. Les fermions relativistes se rencontrent aussi dans les semimétaux de Weyl et de Dirac. Nous étudions ici la stabilité du point de croisement vis-à-vis de perturbations (désordre ou interactions). Dans une première partie, nous caractérisons la transition de phase continue induite par le désordre (différente d’Anderson) entre un semimétal de Weyl et un métal, dont la densité d’états moyenne sert de paramètre d’ordre. Comme signature alternative, nous étudions un ensemble d’exposants, le spectre multifractal, qui décrit les propriétés géométriques des fonctions d’ondes critiques, et dicte la loi d’échelle de la densité d’états typique. Nous déterminons ces exposants à partir d’une approche de groupe de renormalisation. Nous étudions aussi les états de surface des semimétaux de Weyl et de Dirac désordonnés par une approximation auto-cohérente, et montrons que les états de surface de Dirac deviennent également métalliques. Dans une seconde partie, nous discutons des bicouches de graphène dont les axes cristallins sont décalés d’un léger angle. Suite aux sauts des électrons entre couches, la vitesse de Fermi s’annule à certains angles « magiques », ou l’énergie cinétique devient comparable à l’énergie d’interaction. Nous identifions toutes les interactions autorisées par les symétries, et étudions leur compétition à partir d’une méthode de groupe de renormalisation. Nous expliquons l’émergence au point de neutralité d’une phase isolante dont la densité d’états locale brise la symétrie de rotation, que nous appelons isolant nématique.

List of publications

- BRILLAUX, E. and A. A. FEDORENKO (2021a). “The semi-infinite Gross-Neveu model”. *In preparation*.
- BRILLAUX, E., D. CARPENTIER, and A. A. FEDORENKO (Oct. 2019). “[Multifractality at the Weyl-semimetal – diffusive-metal transition for generic disorder](#)”. *Physical Review B* 100.13, p. 134204.
- BRILLAUX, E., D. CARPENTIER, A. A. FEDORENKO, and L. SAVARY (Aug. 2020). “[Nematic insulator at charge neutrality in twisted bilayer graphene](#)”. *arXiv:2008.05041*.
- BRILLAUX, E. and A. A. FEDORENKO (Feb. 2021b). “[Fermi arcs and surface criticality in dirty Dirac materials](#)”. *Physical Review B* 103.8, p. L081405.

Acknowledgments

Part of this PhD project originates from the four-month long placement I undertook at the Laboratoire de Physique for my master's degree. At the beginning of the master's year, Andrei was managing the exercise sessions of a course on phase transitions and the renormalisation group. I really enjoyed this course, and was very interested in Andrei's research, which is the reason why I contacted him to discuss the possibility of a placement under his supervision. He then proposed a collaboration with David, my future PhD director. I got acquainted with the disorder-induced transition in Weyl semimetals during these last months of my academic studies, and continued to explore these subjects as a PhD student at the Laboratoire de Physique, under the direction of David and co-direction of Andrei. I feel privileged to have benefited from the expertise of two supervisors. David guided me and helped me in interpreting many of my results. Andrei was always available to discuss technical details, and we worked the two of us on a separate project on surface effects in Weyl and Dirac semimetals.

I wish to thank another crucial actor in my PhD, who is Lucile Savary. Lucile proposed an ambitious and stimulating project on a very hot topic : twisted bilayer graphene. Although this project differs sensibly from the other part of my PhD, I managed to leverage my knowledge in statistical field theory to tackle this difficult topic with a different perspective from most previous works on the subject. I thank Lucile for her help, especially in understanding the linear representation theory of groups.

Of course, I thank warmly the two rapporteurs of my manuscript, Julia Meyer and Pierre Le Doussal, along with the two other members of my PhD committee, María Vozmediano and Victor Gurarie. I enjoyed the stimulating scientific discussion we had together during my defense, and I thank them for the corrections they proposed to improve my manuscript.

One cannot have good working conditions in a laboratory without the people that help it running. I thus would like to thank the technicians and secretaries, especially Laurence Mauduit, who manages the missions for the theoretical physics team, along with the two successive directors of the laboratory, Thierry Dauxois and Jean-Christophe G eminard.

My family played a key role in my well-being during my PhD, all the more that I spent the entire duration of the first lockdown of the pandemic at my parents' house. I thus thank my mother H el ene, my father Olivier and my sisters Lucie and Camille. I also have a thought for my grand-mother Marguerite, who passed away at the end of my third year, and who often expressed how proud she was of the academic progress of her grand-children.

Finally, I wish to thank many of my friends. I kept a strong contact with the friends with whom I prepared the agregation examination, since we have written a textbook on experimental physics together during my PhD: Benjamin G. and C., Louis, Th eo, J er emy, David, Camille, Alexandre, Antoine, Louisiane and Christopher. I was glad to find so many people fond of sport in the laboratory, and I would like to thank J er emy, David, Thierry, Aliz ee, Marc, Philippe, Facundo and Wilbert for our cycling rides together, along with Stephane, Bastien and Marcello for our fitness and running sessions. I would like to thank my co-workers in the office, and especially Salamb o and Stephane, with whom I have done many activities (movies, parties, volleyball and so on). I also thank my friends from high school, Pierre, Jean-Baptiste, Quentin and Manon.

Contents

List of Figures	ix
List of Tables	xi
Introduction	1
1 Relativistic condensed matter	5
1.1 Relativistic quantum physics	6
1.1.1 The Dirac equation	6
1.1.2 Special cases of the Dirac equation	8
1.2 Relativistic semimetals	10
1.2.1 Electronic band theory	11
1.2.2 From metals to relativistic semimetals	14
1.2.3 Graphene	16
1.2.4 Weyl and Dirac semimetals	19
1.3 Hallmark of relativistic semimetals	23
1.3.1 Topology	23
1.3.2 Surface states	27
1.3.3 Transport	32
1.4 What this thesis is about	37
1.4.1 Disorder	37
1.4.2 Interactions	39
1.5 The renormalisation group	40
1.5.1 Renormalisation in spirit	41
1.5.2 Perturbative expansion	50
I Disorder in three-dimensional relativistic semimetals	57
2 The disorder-driven semimetal-metal transition	59
2.1 Quantum phase transitions in disordered electronic systems	60
2.1.1 A historical example: Anderson's localisation	60
2.1.2 Modelling disorder in relativistic semimetals	63
2.1.3 Relevance of weak disorder	65

2.2	Phenomenology of the semimetal-metal transition	67
2.2.1	Phase diagram	67
2.2.2	Conventional scaling laws	70
2.2.3	Effect of various types of disorder	74
2.3	The self-consistent Born approximation	75
2.3.1	Approximation schemes of the self-energy	76
2.3.2	Solution to the self-consistent equation	78
2.4	Wave function statistics	80
2.4.1	Multifractality	81
2.4.2	Typical versus average densities of states	86
	Conclusion	88
3	Field-theoretical description of the semimetal-metal transition	89
3.1	Effective field theory	90
3.1.1	From clean to dirty Weyl semimetals	90
3.1.2	Replicated action	93
3.2	Renormalisation group in presence of correlated disorder	95
3.2.1	Renormalisation group procedure	95
3.2.2	Beta functions and flow diagram	97
3.2.3	Time-reversal- and valley-symmetry breaking disorder	100
3.3	Multifractality within the replicated field theory	103
3.3.1	Multifractal spectrum to two-loop order	103
3.3.2	Comparison with other transitions	106
	Conclusion	108
4	Surface criticality in disordered semimetals	109
4.1	Surface states in clean semimetals	110
4.1.1	Boundary conditions	110
4.1.2	Surface states	114
4.2	Spatially resolved properties with disorder	119
4.2.1	Qualitative effect of disorder	119
4.2.2	Self-consistent approach	121
4.2.3	Profile of the local density of states	123
4.2.4	Beyond the local self-consistent approximation	125
4.3	Surface states of disordered semimetals	127
4.3.1	Criticality of Dirac surface states	127
4.3.2	Robustness of Fermi arcs	129
	Conclusion	131
II	Electronic interactions in twisted bilayer graphene	133
5	Overview of magic angle twisted bilayer graphene	135
5.1	Bilayer graphene systems	136
5.1.1	Commensurate stacking arrangements	136
5.1.2	Twisted bilayer graphene	139
5.2	Band structure	143

5.2.1	Effect of interlayer hopping	143
5.2.2	The magic angle physics	144
5.3	Experimental findings	147
5.3.1	Experimental setup	147
5.3.2	Global phase diagram	149
5.3.3	Nematic phases	151
	Conclusion	154
6	Low-energy theory near charge neutrality	155
6.1	Single-particle description	156
6.1.1	The single-valley continuum model	156
6.1.2	Hopping strength expansion	159
6.2	Algebraic classification of interaction channels	163
6.2.1	Symmetry analysis of the model	164
6.2.2	Symmetry-preserving contact interactions	167
	Conclusion	172
7	Nematic insulator at charge neutrality	173
7.1	Mean-field approach	174
7.1.1	Nature of the correlated phases	174
7.1.2	Solutions of the self-consistent equations	176
7.2	Renormalisation group approach	179
7.2.1	Renormalisation procedure	179
7.2.2	Loopwise and hopping strength expansions	184
7.2.3	Flow diagram	185
7.3	Perspective	187
7.3.1	Twist angle disorder	187
7.3.2	Coulomb interaction	188
7.3.3	Valley and spin degrees of freedom	189
	Conclusion	191
	General conclusion	193
A	Standard field-theoretic tools	197
A.I	Grassmann algebra	197
A.II	Dimensional regularisation	198
A.II.1	Basic properties	198
A.II.2	Explicit calculation	199
A.II.3	Feynman integrals with long-range correlation	201
B	Feynman graphs of the replicated theory	205
B.I	Four-point vertex functions	205
B.II	Two-loop multifractal vertex	208

C	Surface properties of disordered relativistic semimetals	213
C.I	Solution to the self-consistent equation	213
C.I.1	Bulk contribution	213
C.I.2	Chirality-preserving boundary condition	214
C.I.3	Chirality-breaking boundary condition	214
C.II	The semi-infinite Ising ferromagnet	215
C.II.1	Mean-field approach	215
C.II.2	Phase diagram	216
D	Linear representation of point groups	219
D.I	Representations and group actions	219
D.I.1	Definitions	219
D.I.2	Characters	220
D.II	Key properties of irreducible representations	223
D.II.1	Direct product	223
D.II.2	Reality	224
D.II.3	Magnetic point groups	225
D.II.4	Induction	228
D.III	Symmetry-preserving interactions in twisted bilayer graphene	229
E	Diagrammatic expansion in twisted bilayer graphene	233
E.I	Free theory	233
E.I.1	Correction of the Fermi velocity by interlayer hopping	233
E.I.2	Correction of the order parameters by interlayer hopping	234
E.I.3	Mean-field self-consistent equations	235
E.II	Renormalisation group analysis of the interacting theory	236
E.II.1	Polarisation	237
E.II.2	Yukawa vertex	238
	References	241
	Introduction	241
	Relativistic condensed matter	241
	Disorder in three-dimensional relativistic semimetals	246
	Electronic interactions in twisted bilayer graphene	253
	Appendices	259

List of Figures

1.1	Dispersion relation in a one-dimensional periodic lattice	12
1.2	Band structures of copper and diamond	14
1.3	Lattice and band structures of Weyl semimetal TaP	15
1.4	Lattice structure of graphene	17
1.5	Band structure of graphene	18
1.6	Classification of three-dimensional relativistic semimetals	21
1.7	Pseudospin winding of chiral fermions and Chern number	25
1.8	Edge modes in zigzag graphene ribbons	28
1.9	Surface states in Weyl and Dirac semimetals	29
1.10	Observation of Fermi arcs in Weyl semimetal TaP	30
1.11	Quantum transport in graphene	33
1.12	Magneto-transport properties of relativistic semimetals	35
1.13	Lattice defects in three-dimensional crystals	38
1.14	Flow diagram of the Ising model	44
1.15	Beta function of the Gross-Neveu model	50
2.1	Critical behaviour of Anderson's localisation	61
2.2	Critical behaviour of the semimetal-metal transition	68
2.3	Flow diagrams with different types of disorder	74
2.4	The Schwinger-Dyson equation for disordered systems	77
2.5	Approximation schemes for the self-energy	78
2.6	Mean density of states within the self-consistent approximation	79
2.7	Multifractality wave function density at Anderson's localisation	81
2.8	Order parameters at Anderson versus semimetal-metal transitions	85
3.1	Two-point vertex function of the replicated theory at two-loop order	98
3.2	Stability regions of the fixed points	98
3.3	Flow diagram in presence of short- and long-range correlated disorder	99
3.4	Flow diagram in presence of scalar and vectorial random potentials	103
3.5	One-loop diagrams for the multifractal operator	105
4.1	Model of a semi-infinite binodal Weyl semimetal	111
4.2	Surface states in Weyl and Dirac semimetals	116
4.3	Spectral density map of Fermi arcs	118

LIST OF FIGURES

4.4	Spectral density map of general surface states	119
4.5	Energy dependence of the surface self-energy	123
4.6	Density profile of disordered Fermi arcs and Dirac surface states	124
4.7	Shooting method solution of the self-consistent equation	126
4.8	Density of states and group velocity of Dirac surface states	128
4.9	Phase diagram of dirty semi-infinite Dirac semimetals	129
4.10	Density of states and group velocity of Fermi arcs	130
5.1	Atomic and band structures of Bernal-stacked bilayer graphene	138
5.2	Moiré pattern in twisted bilayer graphene	140
5.3	Number of atoms per commensurate supercell	141
5.4	Mini Brillouin zone of the moiré pattern	142
5.5	Effect of interlayer hopping on the moiré band structure	144
5.6	Band structure at the first magic angle	145
5.7	Wave function density at the first magic angle	146
5.8	Experimental setup for twisted bilayer graphene	148
5.9	Phase diagram of twisted bilayer graphene	150
5.10	Charge-ordered stripes at charge neutrality	152
5.11	Nematic superconductivity at half-hole filling	153
6.1	Diagrammatic expansion of the self-energy of the free theory	162
6.2	Fermi velocity corrected by interlayer hopping	162
6.3	Summary the of symmetry-preserving interaction channels	170
7.1	Mean-field band structure of the dominant correlated phases	175
7.2	Theoretical density map of the nematic phase	176
7.3	Interlayer hopping corrections to the four dominant order paratemers	177
7.4	Mean-field order parameters of the four dominant instabilities	178
7.5	One-loop polarisation and Yukawa vertex of the interacting theory	183
7.6	Flow diagram for the two leading gapping and nematic instabilities	187
B.1	One-loop four-point vertices of the replicated theory	205
B.2	Two-loop four-point vertices of the replicated theory (I)	206
B.3	Two-loop four-point vertices of the replicated theory (II)	207
B.4	Two-loop four-point vertices of the replicated theory (III)	207
B.5	Two-loop diagrams for the multifractal operator	210
C.1	Surface effects in Ising ferromagnets	217
E.1	Diagrammatic expansion of the self-energy of the free theory	234
E.2	One-loop polarisation and Yukawa vertex of the interacting theory	237

List of Tables

2.1	Conventional critical exponents at the semimetal-metal transition	72
3.1	Channels of random perturbations in binodal Weyl and Dirac semimetals .	102
4.1	Symmetries of semi-infinite binodal Weyl and Dirac semimetals	113
6.1	Characters table of the unitary symmetry group of twisted bilayer graphene	166
6.2	One-dimensional channels at charge neutrality	168
6.3	Two-dimensional channels at charge neutrality	169
7.1	One-loop beta functions for the gapping and nematic channels	185
B.1	Poles of the two-loop diagrams for the multifractal operator	211
D.1	Classes of conjugation of the unitary symmetry group	230
D.2	Characters table of the unitary group	231

Introduction

Condensed matter physics aims at explaining the macroscopic properties of solids and liquids from the collective behaviour of the microscopic constituents. Among the most studied phases, crystalline solids, which consist of a periodic assembly of atoms, have played a pivotal role in the development of condensed matter physics. One reason for this success may be that the prospect of their applications has driven the activity of the scientific community and oriented the research direction towards the understanding of crystalline matter. At any rate, these materials have greatly interested physicists because of the relative simplicity to describe them, in contrast to amorphous solids and liquids, which lack positional order. Crystalline solids offered a wonderful playground for the new-born quantum mechanics during the 1930's, and have arguably represented one of its greater successes (KITTEL 1971).

With the electronic band theory in their toolbox, condensed matter physicists have managed to classify crystalline solids according to their electronic properties. Metals, in particular, have the ability to carry electrical currents with limited power loss, because the electrons within move almost freely. The study of metals led to major discoveries on electricity and magnetism, and enabled a formidable industrial and technological progress during the XIXth century. Other materials were discovered around the same period, whose electrical conduction properties are dramatically enhanced by temperature or the presence of impurities. These so-called semiconductors have spurred numerous applications, especially since the design of the first transistor from gold-semiconductor contacts at the end of the 1940's (BARDEEN 1948). By acting as amplifiers and switches, transistors now constitute the building block of computer-based devices, which have shaped the modern technological landscape. While these 'conventional' semiconductors present a window of energy forbidden to electrons – a gap –, some exotic materials with a vanishing energy gap have recently spurred a renewed interest. In these particular semimetals, intermediate between semiconductors and metals, the electron dynamics mimics the behaviour of massless relativistic particles. For this reason, these materials are also called relativistic semimetals. The first isolated material of this kind was graphene in 2004, a monoatomic layer of carbon peeled from graphite (NOVOSELOV 2004). Three-dimensional analogues of graphene closely followed, in the form of Dirac (LIU 2014) and Weyl (LV 2015) semimetals.

Relativistic semimetals enjoy extraordinary properties. For example, the high mobility of its electrons endows graphene with an excellent electrical and thermal conductivity, which foretells promising applications; the fastest field-effect transistor designed by IBM are already based on graphene technology, and operates at frequencies larger than 100 GHz,

where silicon-based transistors hardly reach 1 GHz (WU 2011). The most exotic features of graphene, though, arise from the relativistic nature of its elementary excitations. To cite only one, the Hall effect of massless particles differs from their massive counterparts; under a large perpendicular magnetic field, the transverse conductivity of graphene varies in steps with an unusual half-integer quantisation rule. Weyl and Dirac semimetals also display exotic phenomena. These materials host surface states at zero energy, which therefore require no doping to transport charge carriers, and which can refocus electronic wave packets through negative refraction (CHEN 2020). In Weyl semimetals, the elementary excitations possess a degree of freedom related to the so-called chiral symmetry. Remarkably, a subtle property of the theory of chiral fermions, the chiral anomaly, leaves unique signatures in magneto-transport measurements. The low-energy physics of relativistic semimetals thus offers interesting parallels with the high-energy physics of elementary particles. Through these exotic materials, some theoretical predictions of quantum field theory finally bear experimental consequences in condensed matter physics.

Yet, perturbations of the electron dynamics can dramatically affect the properties of relativistic semimetals. A strong enough disorder, for example, can destroy the linear band crossing points of pristine three-dimensional materials. Disordered Weyl and Dirac semimetals thus transit to a metallic phase through a quantum critical point, near which some observables (such as the density of states) obey universal scaling laws. This phase transition differs from other disorder-driven quantum phase transitions such as Anderson’s localisation. Similarly, many-body effects alter the electron dynamics when the kinetic and electron-electron interaction energies are comparable. For example, interactions play a crucial role when the tunnelling between crystalline membranes overlaid with a relative twist quenches the electron kinetics. In twisted bilayer graphene, notably, interlayer tunnelling entirely suppresses the quasi-particles velocity and flattens the energy bands at specific ‘magic’ values of the twist angle. Electron-electron interactions then prevail and lead to an extraordinarily rich phase diagram, where diverse correlated orders – superconducting, insulating, nematic, etc. – emerge, and combine or compete.

In this thesis, we investigate some aspects of relativistic phases in presence of perturbations. We resort to a field-theoretical formalism to describe the effective low-energy physics of these perturbed phases, either of Weyl fermions moving in the background of random defects (in disordered Weyl semimetals) or two-dimensional Dirac fermions experiencing many-body correlations (in twisted bilayer graphene). We rely heavily on renormalisation group methods to study the large-scale behaviour. The manuscript is organised as follows.

- In Chapter 1, we define and characterise relativistic semimetals. After presenting the Dirac equation, we recall the basics of electronic band theory, propose a simple atomistic model for graphene, and review the topological, surface and transport properties of relativistic semimetals. We also present the renormalisation group approach, which we will use extensively in the rest of this thesis.
- In Chapter 2, we focus on the phenomenological aspects of the new non-Anderson transition found in disordered three-dimensional relativistic semimetals. We recall the key features of the well-known Anderson transition, and discuss how to treat disorder in relativistic semimetals. We then present the scaling laws of some critical observables, and prove the existence of this semimetal-metal transition within a self-consistent approximation. Finally, we analyse the multifractal nature of the

critical wave functions, which leads in particular to different scaling laws for the typical and average observables.

- In Chapter 3, we analyse the semimetal-metal transition in presence of both short-range and long-range correlated disorder through the lens of the renormalisation group. We build an effective theory for disordered Weyl semimetals, determine the renormalisation flow of the disorder strengths, and compute the multifractal exponents of the critical wave function and the scaling exponent of the typical density of states. We compare our results to similar non-Anderson transitions and to Anderson's localisation.
- In Chapter 4, we study the surface properties of disordered Weyl and Dirac semimetals. We design a self-consistent approximation to determine the local density of states, and investigate the fate of surface states in presence of disorder. In particular, we show that criticality manifests itself in Dirac surface states, while Fermi arcs avoid this surface critical point.
- From Chapter 5 onwards, we address twisted bilayer graphene. We study the emergence of large moiré patterns in twisted bilayer graphene, and explain phenomenologically how interlayer tunnelling flattens the energy bands at specific 'magic' angles. We also present the experimental phase diagram of magic angle twisted bilayer graphene, which acquires a superconducting, insulating or nematic character upon doping.
- In Chapter 6, we build a low-energy theory of twisted bilayer graphene near charge neutrality; first at the single-particle level (including the interlayer tunnelling), where we diagonalise the Hamiltonian perturbatively in the tunnelling strength; then in presence of all electronic interactions allowed by symmetry, which we classify using the theory of group representations.
- In Chapter 7, we study the non-standard theory developed in the previous chapter within a mean-field and a renormalisation group approach to the model, where we expand perturbatively in both the tunnelling and interaction strengths. From the renormalisation flow, we analyse the competition between different instabilities, and show that the proximity to the magic angle favours the emergence of a gapped phase with a broken three-fold rotational symmetry at charge neutrality, which is compatible with experiments.

Relativistic condensed matter

Condensed matter offers a wonderful playground for quantum mechanics, where the geometry and nature of the atomic lattice, the interplay between internal degrees of freedom, and many-body effects can lead to exotic electronic phases. New phases of matter recently attracted attention, where emergent excitations mimic the behaviour of the fundamental particles near light speed, which is governed by relativistic quantum physics. The birth of this research area – *relativistic* condensed matter – dates to the first experiments on graphene, a single layer of carbon atoms, which hosts two-dimensional Dirac fermions as elementary excitations; the later realisation of three-dimensional analogues of graphene, the Weyl and Dirac semimetals, rekindled interest in this domain.

In this introductory chapter, we review the famous Dirac equation, which we apply to the case of two spatial dimension, and from which we derive the Weyl equation for massless fermions. We then recall the basics of electronic band theory to define relativistic semimetals, namely graphene and Weyl and Dirac semimetals. We also review their topological, surface and transport properties. The stage will then be set to define the goal of this thesis, which consists in studying the stability of the semimetallic phase under disorder or interactions. To do so, we will need to introduce the renormalisation group approach for effective interacting theories.

1.1 Relativistic quantum physics	6
1.1.1 The Dirac equation	6
1.1.2 Special cases of the Dirac equation	8
1.2 Relativistic semimetals	10
1.2.1 Electronic band theory	11
1.2.2 From metals to relativistic semimetals	14
1.2.3 Graphene	16
1.2.4 Weyl and Dirac semimetals	19
1.3 Hallmark of relativistic semimetals	23
1.3.1 Topology	23
1.3.2 Surface states	27

1.3.3	Transport	32
1.4	What this thesis is about	37
1.4.1	Disorder	37
1.4.2	Interactions	39
1.5	The renormalisation group	40
1.5.1	Renormalisation in spirit	41
1.5.2	Perturbative expansion	50

1.1 Relativistic quantum physics

1.1.1 The Dirac equation

Introduction — Quantum mechanics matured dramatically during the 1920s. The principles of the quantum world – the wave-particle duality, the probabilistic interpretation of the wave function, the uncertainty principle, the effect of measurement – were all set at that time. Despite its many successes in explaining experimental data, such as the photoelectric effect or the atomic spectra, quantum mechanics did not incorporate the notion of relativistic invariance developed earlier by A. Einstein. Its relativistic extension came soon after, at the end of the same decade. In 1928, British physicist P. Dirac proposed the eponymous relativistic equation for quantum particles (DIRAC 1928):

$$(i\hbar\gamma^\mu\partial_\mu - mc)\Psi = 0. \quad (1.1)$$

Not only did P. Dirac unite quantum mechanics (through Planck’s constant \hbar) and special relativity (through the speed of light c) in a most elegant fashion; he also included naturally the intrinsic angular momentum of particles – the spin – recently discovered by G. Uhlenbeck and S. Goudsmit (GOUDSMIT 1926). The Dirac equation describes all spin one-half particles, which comprises all fermions encountered in particle physics, such as electrons, protons and neutrons. It marks the birth of relativistic quantum mechanics, which later shaped into a powerful theory of the interaction of light and matter: quantum electrodynamics.

From Schrödinger to Dirac — Textbooks do not usually follow the historical path that led P. Dirac to postulate Eq. (1.1) from the Schrödinger equation (PESKIN 1995). The reason is that the dynamical variable of quantum mechanics (the wave function ψ) and its relativistic counterpart (the Dirac field Ψ) are essentially different objects. But because we deem Dirac’s thread of thought of high pedagogical interest, we will present its historical derivation (BJORKEN 2013; SREDNICKI 2007).

The Schrödinger equation rests on the non-relativistic expression $E = \mathbf{p}^2/2m$ for the energy E of a free massive particle of mass m and momentum \mathbf{p} . Quantum mechanics describes particles as a scalar field $\psi(\mathbf{r}, t)$ function of space \mathbf{r} and time t , the so-called wave function. By promoting the energy E and momentum \mathbf{p} to their equivalent quantum operators $i\hbar\partial_t$ and $-i\hbar\boldsymbol{\partial}$ respectively, E. Schrödinger found the differential equation

$$\left(i\hbar\partial_t + \frac{\hbar^2\boldsymbol{\partial}^2}{2m^2}\right)\psi = 0. \quad (1.2)$$

Clearly, Eq. (1.2) breaks relativistic invariance, since time and space derivatives appear at different orders (first order for time, second order for space). To treat time and space on an equal footing, we should start instead from Einstein's formula

$$E = c\sqrt{\mathbf{p}^2 + m^2c^2}. \quad (1.3)$$

But how to make sense of the square root once we substitute the momentum for its quantum operator? To circumvent this problem, we may consider squaring Eq. (1.3) to lift the root, and *then* make quantum replacement. This leads to the Klein-Gordon equation,

$$\left(\hbar^2\partial^\mu\partial_\mu + m^2c^2\right)\psi = 0, \quad (1.4)$$

where repeated indices are contracted according to Einstein's sum rule, $\partial^\mu\partial_\mu = \sum_{\mu=0}^3\partial^\mu\partial_\mu = \partial_{ct}^2 - \boldsymbol{\partial}^2$. P. Dirac originally discarded Eq. (1.4) because of the impossibility to build a positive probability density, but the Klein-Gordon equation was later resurrected as a relativistic equation for scalar quantum fields, which describe spinless particles.

In the hope of preserving a positive density, P. Dirac built a first-order equation out of the second-order Eq. (1.4), so as to somehow restore the initial square root. The most general form for a first-order equation of the Dirac field Ψ reads

$$(i\hbar\partial_{ct} + i\hbar\boldsymbol{\alpha}\cdot\boldsymbol{\partial} - mc)\Psi = 0, \quad (1.5)$$

where the coefficients $\boldsymbol{\alpha} = (\alpha_1, \alpha_2, \alpha_3)$ and β must be compatible with the relativistic energy-momentum relation (1.3). Taking the square of Eq. (1.5), we see immediately that these coefficients cannot be simple scalars, but must satisfy the algebra

$$\{\alpha_i, \alpha_j\} = 2\delta_{ij}, \quad \{\alpha_i, \beta\} = 0, \quad (1.6)$$

where the curly brackets $\{A, B\}$ stand for the anticommutator $AB + BA$. This entails that $(\alpha_1, \alpha_2, \alpha_3)$ and β are hermitian traceless matrices: the field Ψ no longer represents a scalar, but a vector constrained by the transformation laws of special relativity. Such an object is called a *spinor*. As for the Schrödinger equation, Eq. (1.5) admits a Hamiltonian formulation. Indeed, it can be written as $i\hbar\partial_t\Psi = \mathcal{H}\Psi$, where the Hamiltonian reads

$$\mathcal{H} = -i\hbar c\boldsymbol{\alpha}\cdot\boldsymbol{\partial} + \beta mc^2 \quad (1.7)$$

The Hamiltonian formulation of Eq. (1.7) will be of utmost importance in Sec. 1.2, where it will enable us to make contact with the standard quantum mechanics of crystalline materials.

The Dirac matrices — The above matrices satisfy further constraints. In particular, they square to the identity: $\alpha_i^2 = \beta^2 = \mathbb{1}$. Their eigenvalues are thus ± 1 , and since the matrices have zero trace, they possess equally many positive and negative eigenvalues. Hence, $(\alpha_1, \alpha_2, \alpha_3)$ and β must be even-dimensional. In three spatial dimensions, this enforces the spinor to be made of at least four components, thus defining a four-dimensional linear representation of the Lorentz group. Now, to make the relativistic invariance of Eq. (1.5) more explicit, one usually defines the Dirac matrices $\gamma^0 = \beta$ and $\gamma^i = \beta\alpha_i$, such that multiplying Eq. (1.5) by γ^0 finally gives Eq. (1.1). Relativistic invariance becomes clear from the properties of the Dirac matrices, which satisfy the Clifford algebra

$$\{\gamma^\mu, \gamma^\nu\} = 2\eta^{\mu\nu}. \quad (1.8)$$

The Minkowski metric $\eta^{\mu\nu}$, with signature $(+, -, -, -)$, together with the speed of light c , constitute indeed the two fundamental characteristics of space-time.

Particles and antiparticles — In building Eq. (1.5), we glossed over a detail of high importance. Indeed, by squaring the energy-momentum relation of Eq. (1.3) to find the Klein-Gordon equation, we allowed for positive energy states, for which

$$E = +c\sqrt{\mathbf{p}^2 + m^2c^2}, \quad (1.9)$$

but also for unintended negative energy states, for which

$$E = -c\sqrt{\mathbf{p}^2 + m^2c^2}. \quad (1.10)$$

This doubling in the number of eigenstates also transpires in the size of the Dirac spinor, which bears four components, while we expect spin one-half particles to be in only two states, spin up or spin down. This seriously threatens the theory, since in absence of any lower energy bound, there is no ground state. Unless, as P. Dirac suggested, unobservable particles occupy all negative energy states, and excitations of this ground state, known as the Dirac sea, appear as pairs of a particle and an *antiparticle* (both with positive energy). The total charge being conserved, an antiparticle carries the same mass and spin, but the opposite charge as its particle counterpart. The positron (the antiparticle of the electron) was indeed observed a few years later (1932), and lent strong credence to Dirac's theory. Antiparticles became a key concept in condensed matter physics beyond the context of relativity, where they are known as *holes*. Electrons and holes alike contribute to the electrical, optical, and thermal properties of certain solids, especially the semiconductors.

1.1.2 Special cases of the Dirac equation

The Dirac equation accurately describes the massive fermions which live and move in the real three-dimensional world. But some theorists, among which features H. Weyl, drawn by sheer curiosity, searched for more exotic particles that would also meet the requirements of relativistic quantum mechanics. Their discoveries turned out to be of high interest in condensed matter physics, where emergent phenomena sometimes exhibit the same behaviour as those exotic particles. We review below two special cases of the Dirac equation: the two-dimensional Dirac equation and the Weyl equation.

The Dirac equation in two space dimensions — In Sec. 1.1.1, we derived the Dirac equation in three space dimensions, putting the total count to four space-time dimensions. We found it impossible to define a set of four matrices satisfying the Clifford algebra (1.8) if they are less than four-by-four. Yet, it is possible to find a set of only *three* anticommuting two-by-two hermitian matrices. Thus, if particles are ascribed to move in two spatial dimensions, the Dirac spinor need only have two components instead of four. We know that the Pauli matrices ($\sigma_1, \sigma_2, \sigma_3$) generate the space of two-by-two hermitian matrices; they also satisfy the anticommuting relation $\{\sigma_i, \sigma_j\} = 2\delta_{ij}$, like the matrices α_i and β of Eq. (1.5). Guided by this similarity, we try to build realisations of the Dirac matrices from the Pauli matrices. We start by setting $\gamma^0 = \beta = \sigma_3$. From then, two equally convenient choices for (γ^1, γ^2) are

$$\left\{ \begin{array}{l} \gamma^1 = \gamma^0\sigma_1 = +i\sigma_2 \\ \gamma^2 = \gamma^0\sigma_2 = -i\sigma_1 \end{array} \right\}, \quad \text{or} \quad \left\{ \begin{array}{l} \gamma^1 = -\gamma^0\sigma_1 = -i\sigma_2 \\ \gamma^2 = +\gamma^0\sigma_2 = -i\sigma_1 \end{array} \right\}. \quad (1.11)$$

A quick check shows that Eq. (1.11) is indeed consistent with the anticommutation rules $\{\gamma^\mu, \gamma^\nu\} = 2\eta^{\mu\nu}$, for $\mu, \nu = 0, 1, 2$. The Dirac Hamiltonian stems from the Pauli matrices as

$$\mathcal{H} = c\boldsymbol{\sigma} \cdot \mathbf{p} + mc^2\sigma_3, \quad \text{or} \quad \mathcal{H} = -c\boldsymbol{\sigma}^* \cdot \mathbf{p} + mc^2\sigma_3, \quad (1.12)$$

depending on the chosen representation, and where the two-dimensional Pauli vector $\boldsymbol{\sigma} = (\sigma_1, \sigma_2)$ represents the spin. Importantly, the third Pauli matrix σ_3 plays a different role than σ_1 and σ_2 in two space dimensions, since it does not couple to a kinetic variable, but to the particle mass.

The helicity operator — Both Hamiltonians of Eq. (1.12) involve the projection of the momentum \mathbf{p} along the spin operator $\boldsymbol{\sigma}$. In particular, in the limit of massless Dirac fermions, the first Hamiltonian reduces (up to some factor) to the *helicity* operator

$$h = \boldsymbol{\sigma} \cdot \mathbf{n}, \quad (1.13)$$

where $\mathbf{n} = \mathbf{p}/p$ is the direction of momentum. The second Hamiltonian of Eq. (1.12) follows from the first one by applying the antiunitary time reversal operation \mathcal{T} , which reverses \mathbf{p} and complex conjugates $\boldsymbol{\sigma}$. Helicity thus provides a good quantum number for massless fermions, and its two eigenvalues ± 1 label the positive and negative energy states. These results hold in any dimension; we will use the notion of helicity again in the next paragraph on the massless Dirac equation in three spatial dimensions, known as the Weyl equation.

The Weyl equation — Let us go back to the three-dimensional case. The Dirac matrices are primarily defined by the Clifford algebra of Eq. (1.8), and so many possible ways exist to represent the Dirac matrices. These representations are all related by a unitary transformation. Among the most natural choices, the Dirac matrices admit a compact relativistic representation in the so-called Weyl basis, where

$$\gamma^\mu = \begin{pmatrix} 0 & \sigma^\mu \\ \bar{\sigma}^\mu & 0 \end{pmatrix}, \quad (1.14)$$

where $\sigma^\mu = (\sigma_0, +\boldsymbol{\sigma})$, $\bar{\sigma}^\mu = (\sigma_0, -\boldsymbol{\sigma})$, σ_0 is the two-by-two identity matrix, and $\boldsymbol{\sigma} = (\sigma_1, \sigma_2, \sigma_3)$ the three-dimensional Pauli vector. The Dirac equation then reads

$$\begin{pmatrix} -mc & i\hbar(\partial_{ct} + \boldsymbol{\sigma} \cdot \boldsymbol{\partial}) \\ i\hbar(\partial_{ct} - \boldsymbol{\sigma} \cdot \boldsymbol{\partial}) & -mc \end{pmatrix} \Psi = 0. \quad (1.15)$$

The convenience of the Weyl basis becomes clear in the context of massless Dirac fermions. By setting $m = 0$ in Eq. (1.15), the Dirac equation decouples into two separate blocks. If one splits the Dirac spinor Ψ into left- and right-handed parts (Ψ_R, Ψ_L) , each subspinor satisfies its own equation of motion

$$(\partial_{ct} \pm \boldsymbol{\sigma} \cdot \boldsymbol{\partial})\Psi_{R,L} = 0, \quad (1.16)$$

where the plus and minus signs apply to Ψ_R and Ψ_L , respectively. Eq. (1.16) is known as the Weyl equation, in tribute to German theorist H. Weyl, which first introduced the

left- and right-handed subspinors (WEYL 1929). The block decomposition of the massless Dirac equation (1.15), though more obvious in the Weyl basis of Eq. (1.14), holds in any representation. The possibility of such decomposition stems from the reducibility of the Dirac spinor as a four-dimensional representation of the Lorentz group, which breaks down into a direct sum of two conjugate irreducible representations (SREDNICKI 2007). To cast the Dirac equation into this block-diagonal form in a systematic way, we introduce the chiral matrix

$$\gamma^5 = i\gamma^0\gamma^1\gamma^2\gamma^3 = \begin{pmatrix} \sigma_0 & 0 \\ 0 & -\sigma_0 \end{pmatrix}. \quad (1.17)$$

It is hermitian, squares to identity, and anticommutes with the Dirac matrices: $\{\gamma^5, \gamma^\mu\} = 0$. Thanks to these properties, we can build chiral projectors $P_{R,L} = \frac{1}{2}(1 \pm \gamma^5)$, whose eigenvectors $P_R\Psi = \Psi_R$ and $P_L\Psi = \Psi_L$ are nothing more than the left- and right-handed Weyl spinors, and which satisfy, for a zero mass, the evolution equations $i\hbar\partial_t\Psi_{R,L} = \mathcal{H}_{R,L}\Psi_{R,L}$, with Hamiltonian $\mathcal{H}_{R,L} = \mp c\boldsymbol{\sigma} \cdot \mathbf{p}$. This notion of *chirality*, i.e. the possibility to break down a Dirac spinor into two elementary constituents, each belonging to an irreducible representation of the Lorentz group, applies to massive fermions as well, but provides a good quantum number for massless fermions only.

Note that for massless fermions with a fixed energy (either positive or negative), the chiral eigenvectors $\Psi_{R,L}$ coincide with the eigenvectors of the helicity operator, as a result of Eq. (1.16). This should not blur the distinction between those two concepts: chirality refers to a distinct representation of the Lorentz group: chiral eigenvectors are thus invariant under a Lorentz boost; helicity refers to the projection of the spin on the direction of motion, which for massive particles can always be reversed through a well-chosen change of reference frame. We will see that in condensed matter the notion of chirality extends to spinors with more than two components thanks to topological considerations.

1.2 Relativistic semimetals

Neutrinos were once promising candidates for Weyl fermions, until the observation of oscillations in the flavour of solar neutrinos definitely proved that they possess a small but non-zero mass (FUKUDA 1998). At present, the standard model of particle physics excludes exotic fermions (Weyl and, for obvious reasons, two-dimensional Dirac) from the list of elementary particles. Yet, these particles do emerge in condensed matter physics as effective low-energy excitations (*quasi-particles*) in crystalline solids, as we will see in Sec. 1.2.1 and Sec. 1.2.2. The sighting of relativistic quasi-particles dates back to the study of Luttinger liquids (GIAMARCHI 2004). In these one-dimensional electronic phases, particles move at the Fermi velocity v_F , which, as in all electronic phases, is more than two orders of magnitude smaller than the speed of light c , and depends on the details of the material. However, all metals in one dimension follow the Luttinger physics, which means that Luttinger liquids are rather trivial realisations of relativistic quasi-particles.

Relativistic condensed matter really came under the spotlight in 2004 when K. S. Novoselov and A. Geim isolated graphene, a atomically thick layer of graphite (NOVOSELOV 2004). As we will see in Sec. 1.2.3, graphitic layers had been studied theoretically for a long time (WALLACE 1947), but the works of Novoselov and Geim mark the first experimental discovery of Dirac fermions in two dimensions. It was later predicted numerically that three-dimensional alloys known as pyrochlore iridates should host massless Weyl excitations

due to strong electron-electron interactions (WAN 2011). Weyl quasi-particles were indeed observed in 2015 by several teams in tantalum-based compounds (LV 2015; XU 2015b). Around the same period, massless Dirac excitations were spotted in sodium bismuthide (LIU 2014b). Subsequent efforts revealed many other examples of such three-dimensional materials, which we will present in Sec. 1.2.4. Those phases that host either two- or three-dimensional relativistic excitations, which includes graphene, Weyl and Dirac semimetals, are commonly known as *relativistic semimetals*.

1.2.1 Electronic band theory

Introduction — Condensed matter physics describes dense macroscopic phases and especially crystalline solids, through their mechanical, thermal, magnetic or electrical properties. Although the term *crystal* originally referred to ice or gems, its meaning extended after the XVII^e century to all solid chunks that present a regular aspect (KITTEL 1971). During the XIX^e century, mineralogists understood that this regularity originates from the periodic arrangements of elementary constituents at the microscopic scale. In 1912, M. Von Laue proposed to probe this microscopic arrangement using X-rays. By diffracting on the atomic lattice, a light with a wave length of the order of the lattice spacing should form specific intensity patterns that reveal the underlying crystalline structure. One year later, W. L. Bragg experimentally determined the structure of the ionic crystals KCl, NaCl, KBr and KI, thereby validating Von Laue’s theory.

Crystals exhibit rich electrical properties. The electrical conductivity, which measures how easily a material transports electrical charges when subject to a potential difference, covers an incredibly large range – it varies of thirty orders of magnitude from the best conductors (noble metals, such as copper, silver, gold) to the strongest insulators (diamond). In metals, a sufficient number of electrons are able to carry an electrical current through the periodic lattice formed by the residual cations. Those are the *conduction* electrons, as opposed to the *valence* electrons, which are firmly bound to the cations. The classical Drude theory predicts that conduction electrons should frequently collide with the cations over distances of the order of the lattice spacing. This is not the case: measurements show that the average distance of free motion – the so-called mean free path – extends to hundreds of atomic distances. This suggests that electrons scatter on defects or thermal excitations of the lattice (phonons), rather than on the ions themselves. In fact, they should propagate freely in a perfectly periodic potential! Electronic band theory explains this paradoxical result. To do so, we solve the quantum mechanical problem of a single electron in a periodic potential, under some approximation scheme.

Bloch waves — Free electrons are described as static plane waves $\psi(\mathbf{r}) \propto e^{i\mathbf{k}\cdot\mathbf{r}}$ with wave vector \mathbf{k} . Thanks to the continuous translational invariance, \mathbf{k} is a good quantum number and can be used to label the energy eigenstates. When the electrons are enclosed in a box of size L , periodic boundary conditions quantise the components of the wave vector in units of $2\pi/L$, as shown in Fig. 1.1(a). In a perfect crystal, a gas of conduction electrons feels the periodic potential $U(\mathbf{r})$ of the cations, which demote the continuous to a discrete translational invariance. As a result, the single-particle, or Bloch Hamiltonian

$$\mathcal{H}(\mathbf{r}) = -\frac{\hbar^2 \partial^2}{2m} + U(\mathbf{r}) \quad (1.18)$$

is invariant under translations by a lattice vector \mathbf{T} , namely $\mathcal{H}(\mathbf{r} + \mathbf{T}) = \mathcal{H}(\mathbf{r})$. Since lattice translations commute with one another and with the Hamiltonian, these operators are all co-diagonalisable. In analogy with the free case, let us write as $e^{i\mathbf{k}\cdot\mathbf{T}}$ the eigenvalues of the translation operators, and let $\psi_{\mathbf{k}}(\mathbf{r})$ be the corresponding energy eigenstate. We see that the wave functions deviate from a plane wave only by an envelope that shares the lattice periodicity,

$$\psi_{\mathbf{k}}(\mathbf{r}) = e^{i\mathbf{k}\cdot\mathbf{r}} u_{\mathbf{k}}(\mathbf{r}), \quad (1.19)$$

where $u_{\mathbf{k}}(\mathbf{r} + \mathbf{T}) = u_{\mathbf{k}}(\mathbf{r})$ for all \mathbf{T} . This theorem, due to F. Bloch, constitutes the central result of electronic band theory (BLOCH 1929). A wave function of the form (1.19) is called a Bloch wave. As for plane waves, Bloch waves are indexed by a vector \mathbf{k} , which reduces to a wave vector in the limit of zero lattice potential, and satisfies the same boundary conditions. It also enters conservation laws in electron-phonon scatterings; for this reason, the quantity $\hbar\mathbf{k}$ (or abusively, \mathbf{k} itself) is known as the *crystal momentum*. However, the crystal momentum differs from the conjugate momentum $\mathbf{p} = i\hbar\boldsymbol{\partial}$, since the envelope of the Bloch wave $u_{\mathbf{k}}(\mathbf{r})$ also carries spatial variations.

The first Brillouin zone — We have already shown that the wave vector and the crystal momentum admit a lower bound due to periodic boundary conditions, of order $2\pi/L$, with L the system size. On the microscopic scale, the lattice spacing a also constrains crystal momentum by setting an upper bound π/a , as shown in Fig. 1.1(a). This upper

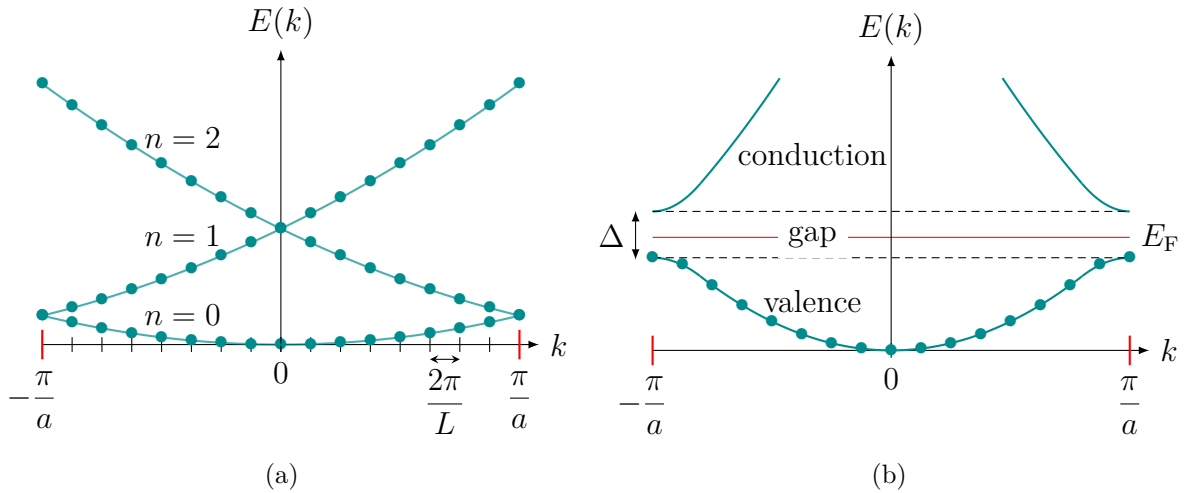


Figure 1.1 | (a) The energy-momentum relation of free electrons is quadratic: $E = \hbar^2 k^2 / 2m$, with E the energy and k the wave vector. On a one-dimensional lattice of constant a , it is convenient to systematically choose the crystal momentum k inside the first Brillouin zone $[-\pi/a, \pi/a]$. The folding of the energy-momentum relation to the first Brillouin zone leads to an infinite number of energy bands $E_n(k)$ with band index n . Periodic boundary conditions quantify the wave vector in units of $2\pi/L$, where L denotes the system size. (b) A weak periodic potential favours the formation of stationary waves near the corners of the Brillouin zone, thus bending the bands outwards and creating an energy gap Δ . The highest occupied band (valence band) can carry electrical charges if it is partially filled, i.e. if the Fermi level E_F lies below the gap, in which case the material is metallic, or semi-metallic. Otherwise, the material is an insulator because electrons cannot reach the upper band (conduction band) at zero temperature (case shown here).

bound has the following interpretation. Any one-dimensional plane wave whose wave vector k' exceeds π/a coincides on all lattice sites with another plane wave of wave vector $k < \pi/a$. Thus, k and k' carry the same information, and we can conventionally assign to any Bloch wave a crystal momentum in the range $[-\pi/a, \pi/a]$. In higher dimensions, the set of the differences $\mathbf{k}' - \mathbf{k} = \mathbf{G}$ of all such vectors organises into a periodic lattice: the reciprocal lattice. And the locus of all crystal momenta closer to the origin than any other point of the reciprocal lattice delimits a primitive cell, called the (*first*) Brillouin zone. While the Brillouin zone reduces to the interval $[-\pi/a, \pi/a]$ in one dimension, it takes more complex and diverse shapes in three-dimensional crystals. For instance, Fig. 1.2(a) and 1.3(b) show the Brillouin zones for the face-centred cubic and body-centred tetragonal lattices, respectively. When representing Bloch waves, we will always choose the crystal momentum within the Brillouin zone.

Energy bands in the weak potential limit — The energy $E(\mathbf{k})$ depends on crystal momentum for arbitrary large values of \mathbf{k} , including outside the Brillouin zone, so that physically equivalent Bloch waves $\psi_{\mathbf{k}}$, whose crystal momenta differ by a vector of the reciprocal lattice, have different energies. To represent all energies associated with a given crystal momentum, we fold the graph of the function $E(\mathbf{k})$ onto the Brillouin zone. This leads to an infinite set of energy bands $E_n(\mathbf{k})$ labelled by a band index n . Free electrons only possess a kinetic energy

$$E_{\text{K}}(\mathbf{k}) = \frac{\hbar^2 \mathbf{k}^2}{2m}, \quad (1.20)$$

which is a continuous function of crystal momentum, so that the energy bands touch at the corners of the Brillouin zone, as in Fig. 1.1(a). The energy spectrum is connected.

In the background of the lattice potential, conduction electrons prefer instead to form stationary waves near the corners of the Brillouin zone because of Bragg reflections. This opens forbidden regions, or *gaps*, in the energy spectrum, as in Fig. 1.1(b). To show this, let us consider a one-dimensional lattice, and keep only the first Fourier components of the lattice potential $U(x) = 2U_1 \cos(G_1 x)$. Let $u_k(x) = \sum_G C(k - G)e^{-iGx}$ be the envelope of the Bloch wave, where the sum extends over all reciprocal lattice vectors G , and $2G_1 = 2\pi/a$ is the smallest non-trivial reciprocal vector. The eigenvalue equation $\mathcal{H}\psi_k = E\psi_k$ can be massaged into

$$\begin{pmatrix} E_{\text{K}}(k) - E & U_1 \\ U_1 & E_{\text{K}}(k - 2G_1) - E \end{pmatrix} \begin{pmatrix} C(+G_1) \\ C(-G_1) \end{pmatrix} = \begin{pmatrix} 0 \\ 0 \end{pmatrix}. \quad (1.21)$$

The system (1.21) admits a non-trivial solution if the determinant of the left matrix vanishes. Close to a corner of the Brillouin zone, $\delta k = k - G_1 \ll k$, and for a weak potential $U_1 \ll E_{\text{K}}(G_1)$, the roots of the determinant equation lead to two energy bands (KITTEL 1971)

$$E_{\pm}(k) \simeq E_{\text{K}}(G_1) \pm U_1 + E_{\text{K}}(\delta k) \left(1 \pm \frac{2E_{\text{K}}(G_1)}{U_1} \right) \quad (1.22)$$

The presence of the potential U_1 opens an energy gap $\Delta = 2U_1$ at the corners $k = \pm G_1$ of the Brillouin zone. In Fig. 1.1(b), we represent schematically the two energy bands $E_{\pm}(k)$ within the weak potential approximation.

Since electrons are fermions, they fill the energy bands from bottom to top, according to the Fermi-Dirac distribution, characterised entirely by the temperature T and the chemical

potential $\mu(T)$. The chemical potential is typically fixed by the valence of the atoms, the presence of impurities, or external voltage doping. Throughout this work, we will focus on properties at zero temperature, for which the Fermi-Dirac distribution reduces to a step function. In this case, the highest occupied state has a fixed energy $\mu(T = 0) = E_F$, called the Fermi energy. Much of the electrical properties of solids are entirely determined by the position of E_F in the energy landscape, and in particular whether the Fermi level lies inside the energy gap, as in Fig. 1.1(b), or outside the energy gap. In the following section, we distinguish the band structures of metals, insulators, semimetals, and finally relativistic semimetals.

1.2.2 From metals to relativistic semimetals

The shape, filling and symmetry of the band structure dictate the response of a material to an electric field. In general, the position of the Fermi level cannot be predicted beforehand, and is found numerically from calculated band structures, as in Fig. 1.2(b) and Fig. 1.2(c). In simple cases, however, the filling of the energy bands depends only on the total number of conduction electrons per unit cell (KITTEL 1971). As per the Pauli exclusion rule, an eigenstate with a definite energy E and crystal momentum \mathbf{k} can host at most two electrons with opposite spins. Let us see how these constraints determine the metallic, insulating, semimetallic, or relativistic semimetallic nature of the material.

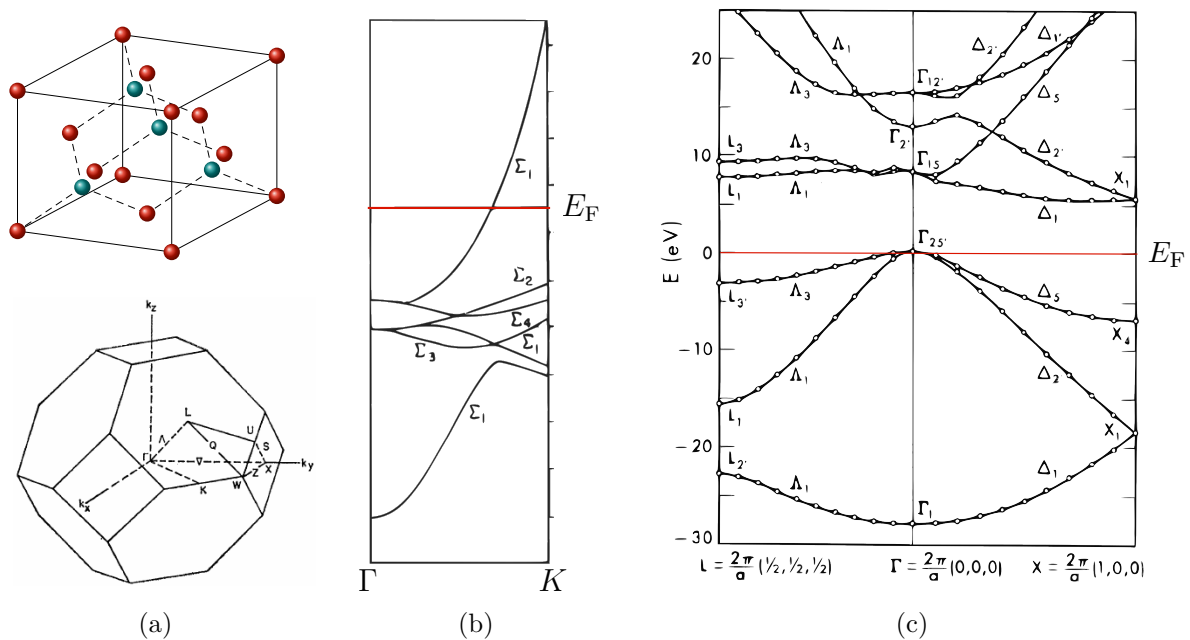


Figure 1.2 | (a) Face-centred cubic structure of copper (red sites) with the associated first Brillouin zone. The structure of diamond differs by the filling of half of the tetrahedral interstices (in blue). (b) Calculated band structure of the metal copper along the high symmetry line Γ -K of the first Brillouin zone (a). The Fermi level cuts the middle of a band, where the electronic density of states is high and any gain of energy, however small, can excite electrons and induce a current. Extracted from (BURDICK 1963). (c) Calculated band structure of the insulator diamond along the high symmetry lines L- Γ -X of the first Brillouin zone (a). The Fermi level lies within an energy gap. Extracted from (SASLOW 1966).

- If the unit cell cedes an odd number of conduction electrons, for instance when it encloses an odd number of atoms of valence one or one atom with an odd valence, the electrons fill only partially the valence band, and the Fermi level lies in the middle of the band. Due to the high density of states near the Fermi level, a large number of conduction electrons partake in charge carriage, and the material easily conducts electricity: it is a *metal*. This is the case of noble metals such as copper (Fig. 1.2(b)) and alkaline elements, for which each unit cell gives one conduction electron.
- If the unit cell cedes an even number of conduction electrons, for instance when it encloses an even number of atoms of valence one, or atoms with an even valence, the electrons fill entirely the valence band. Unless the bands overlap in some region of the Brillouin zone, the Fermi level lies within an energy gap, so that no electron from the valence band can be promoted to the conduction band to carry electricity: the material is an *insulator*, or a *semiconductor*. The difference between these two materials is purely practical: in semiconductors, the density of charge carriers at room temperature can reach values as high as 10^{13} cm^{-3} , leading to a sizeable conductivity (KITTEL 1971). The larger the energy gap with respect to the ambient thermal energy $k_B T \simeq 25 \text{ meV}$, the smaller the conductivity. Diamond, with an energy gap of 5.4 eV , is an insulator (Fig. 1.2(c)), while germanium, with an energy gap of 0.74 eV , is a semiconductor widely used in diodes and solar cells. Yet, both diamond and germanium possess eight conduction electrons per unit cell.
- Other band structures exist. In our one-dimensional band structure of Fig. 1.1(b), the lattice potential generates a gap on both sides of the Brillouin zones. In some instances, the minimum of the conduction band and maximum of the valence band do not face each other at the corners of the Brillouin zone, but overlap in energy without touching. If the Fermi level lies within this overlap, the material conducts electricity, but less efficiently than metals. Like in semiconductors, both holes and

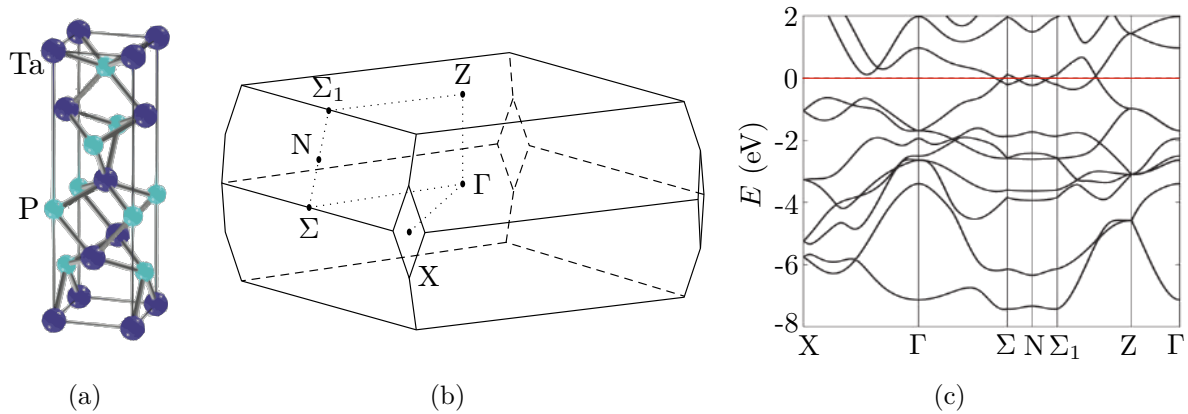


Figure 1.3 | (a) Body-centred tetragonal lattice of the Weyl semimetal TaP (tantalum phosphide). Adapted from (Lv 2015). (b) First Brillouin zone associated to the body-centred tetragonal lattice in real space. (c) Calculated band structure of TaP along high symmetry lines in absence of spin-orbit coupling (XU 2015a). The Fermi level $E_F = 0$ cuts the band structure close to linear crossing points of the valence and the conduction bands (only 40 meV above the W_1 nodes near the points Σ , N and Σ_1 , and 24 meV below the W_2 nodes between Σ_1 and Z). The low-energy excitations of the Fermi sea mimic massless relativistic particles.

electrons contribute to charge carriage. Such materials correspond to *semimetals*, among which feature alkaline earth elements (Be, Mg, Ca, etc.).

- The energy difference between the valence and conduction bands generically depends on crystal momentum, and may even vanish at some special points of high symmetry. At these band crossing points, the energy-momentum (or dispersion) relation is generically linear; if the Fermi level lies close to the node, the elementary excitations of the Fermi sea behave as massless relativistic particles. The band structure of tantalum phosphoride (TaP) shown in Fig. 1.3(c) hosts such crossing points. These materials are dubbed *relativistic semimetals*. Though this terminology suggests some strong similarity between relativistic and non-relativistic semimetals, the transport properties of these materials differ completely.

We now study the first observed relativistic semimetal: graphene.

1.2.3 Graphene

K. Novoselov and A. Geim proved the existence of two-dimensional massless Dirac fermions for the first time in condensed matter with the first experiments on graphene (NOVOSELOV 2004). They confirmed the anomalous character of the Hall effect in graphene – relativistic particles behave differently under a magnetic field than non-relativistic particles – and were awarded the Nobel Prize in 2010 for their discovery. This was a great achievement per se. Yet, the authors also proved at the same time that crystals can be stable, in low dimensions, even though thermal fluctuations prevent atoms from ordering on long distances. Graphene sheets work around this problem by rippling, thus deforming from a planar shape. The theory of graphene dates back to the works of P. R. Wallace (WALLACE 1947), which did not attract much attention at the time, when graphene appeared merely as an intermediate step towards understanding the electronic properties of graphite. Other exotic graphitic allotropes were known before graphene, such as carbon nanotubes and fullerenes, but none of them display relativistic properties.

Tight-binding approach — Graphene consists in a hexagonal arrangement of carbon atoms linked by sp^2 covalent bonds, originating from the hybridisation of $2s$ and $2p_{x,y}$ orbitals. This honeycomb lattice is not of Bravais type: the repeated translations of a single atom by two independent vectors \mathbf{a}_1 and \mathbf{a}_2 cannot generate the whole lattice. To apply Bloch theorem, we decompose the honeycomb lattice into one triangular lattice with two atoms A and B per unit cell. In the (x, y) basis of Fig. 1.4(a), the unit vectors of the triangular lattice are

$$\mathbf{a}_1 = \frac{a_0}{2} (3, \sqrt{3}), \quad \mathbf{a}_2 = \frac{a_0}{2} (3, -\sqrt{3}), \quad (1.23)$$

where $a_0 = 1.42 \text{ \AA}$ is the carbon-carbon distance (CASTRO NETO 2009). We conventionally place atom A at the origin of the unit cell; atom B is then located at $\boldsymbol{\delta} = a_0(1, 0)$. The low-energy properties of graphene result from the one electron of the $2p_z$ orbital, which we denote as $\phi(\mathbf{r})$. Let \mathcal{H} be the real-space Hamiltonian of a conduction electron moving on the honeycomb lattice. In a tight-binding approach, the conduction electrons strongly attach to the atoms and have a small probability amplitude (WALLACE 1947)

$$t = \int d^3r \phi(\mathbf{r})^* \mathcal{H} \phi(\mathbf{r} + \boldsymbol{\delta}) \simeq -2.7 \text{ eV} \quad (1.24)$$

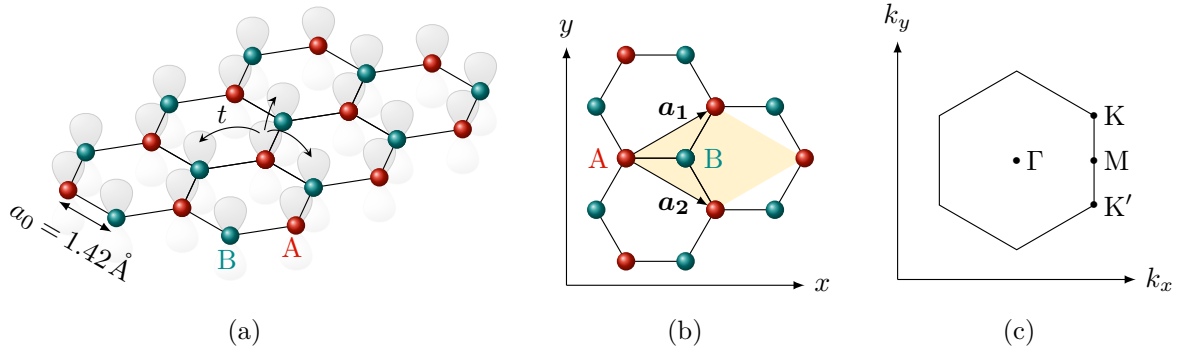


Figure 1.4 | (a) Graphene consists in a sheet of carbon atoms arranged in a honeycomb lattice. In a tight-binding description, electrons from $2p_z$ orbitals take part in π bonds, and tunnel from an atom of sublattice A (respectively B) to a neighbour B atom (respectively A) with a probability amplitude t . (b) The honeycomb lattice of graphene splits into a triangular Bravais lattice generated by the vectors \mathbf{a}_1 and \mathbf{a}_2 , where each unit cell (in yellow) encloses two atoms A and B. (c) The Brillouin zone associated to a triangular lattice is a hexagon rotated by 30° with respect to the real-space lattice. Among the special points of the Brillouin zone feature the totally symmetric Γ point at the origin, the mirror symmetric M points, and the three-fold symmetric K and K' points.

to hop from an atom A to any of the three neighbour B atoms (rotational symmetry ensures the hopping amplitude to be the same for the three atoms). We will neglect hopping processes between further away atoms. We now build a basis of two Bloch waves, one for each sublattice A or B, as superpositions of plane waves of wave vector \mathbf{k} modulated by the localised $2p_z$ orbitals,

$$\psi_A(\mathbf{r}) = \sum_{\mathbf{r}_A} e^{i\mathbf{k}\cdot\mathbf{r}_A} \phi(\mathbf{r} - \mathbf{r}_A), \quad \psi_B(\mathbf{r}) = \sum_{\mathbf{r}_B} e^{i\mathbf{k}\cdot\mathbf{r}_B} \phi(\mathbf{r} - \mathbf{r}_B). \quad (1.25)$$

These two wave functions are not orthogonal, but their small overlap only renormalises next-to-nearest neighbour hopping, which we already neglected. Ignoring this overlap, the real-space Hamiltonian projects in the basis of the Bloch waves to a two-by-two matrix with components $\mathcal{H}_{ij} = \int d^3r \psi_i(\mathbf{r})^* \mathcal{H} \psi_j(\mathbf{r})$. Since the on-site energies $\mathcal{H}_{AA} = \mathcal{H}_{BB}$ are equal, they merely shift the band structure, and we may omit them. We then find the Bloch Hamiltonian

$$\mathcal{H} = \begin{pmatrix} 0 & tf(\mathbf{k}) \\ tf(\mathbf{k})^* & 0 \end{pmatrix}, \quad (1.26)$$

where the function $f(\mathbf{k}) = 1 + e^{i\mathbf{k}\cdot(\mathbf{a}_1-\delta)} + e^{i\mathbf{k}\cdot(\mathbf{a}_2-\delta)}$ accounts for the three-fold spatial modulation of the hopping amplitude.

Dirac cones — The eigenvalues of Hamiltonian (1.26) are $E_{\pm}(\mathbf{k}) = \pm|tf(\mathbf{k})|$, and give one valence band (minus sign) and one conduction band (plus sign), shown in Fig. 1.5. The bands satisfy the three-fold rotational symmetry of the triangular lattice, and a fragile particle-hole symmetry, which breaks down when one includes next-to-nearest neighbour hopping. We also see that the two bands touch at the six corners of the hexagonal Brillouin

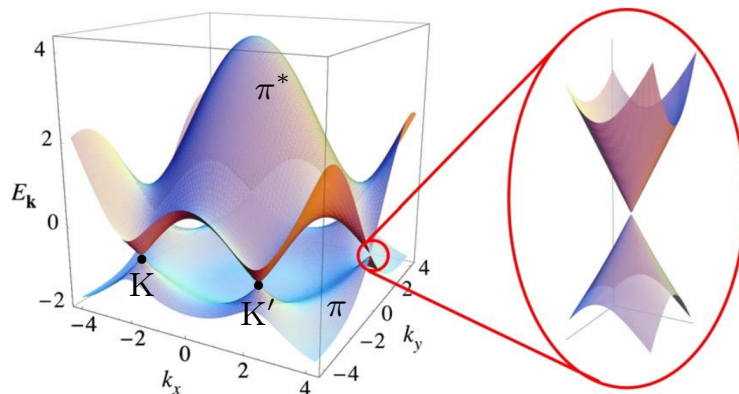


Figure 1.5 | The band structure of graphene hosts time-reversed partner Dirac cones located at the corners of the Brillouin zone (K and K' points). The valence (π) and conduction (π^*) bands touch linearly at the Dirac nodes, which coincides with the Fermi level in undoped graphene, leading to relativistic low-energy excitations. In this plot, next-to-nearest neighbour hopping breaks the particle-hole symmetry. Adapted from (CASTRO NETO 2009).

zone, where $f(\mathbf{k}) = 0$, i.e. at the two non-equivalent crystal momenta

$$\mathbf{K} = \frac{2\pi}{3a_0} \left(1, \frac{1}{\sqrt{3}} \right), \quad \mathbf{K}' = \frac{2\pi}{3a_0} \left(1, -\frac{1}{\sqrt{3}} \right), \quad (1.27)$$

and their images under three-fold rotations. For crystal momenta close to the touching points at \mathbf{K} and \mathbf{K}' , Hamiltonian (1.26) simplifies to

$$\mathcal{H}(\mathbf{K} + \mathbf{q}) \simeq \hbar v_F \boldsymbol{\sigma} \cdot \mathbf{q}, \quad \mathcal{H}(\mathbf{K}' + \mathbf{q}) \simeq -\hbar v_F \boldsymbol{\sigma}^* \cdot \mathbf{q}, \quad (1.28)$$

at first order¹ in effective momentum \mathbf{q} , and where $v_F = -3ta/2\hbar \simeq 8.7 \times 10^5 \text{ m} \cdot \text{s}^{-1}$ is the so-called Fermi velocity. Eq. (1.28) match the two copies of the Dirac Hamiltonian of Eq. (1.12), and describe two-dimensional massless Dirac fermions with momentum $\mathbf{p} = \hbar\mathbf{q}$ and velocity v_F instead of the speed of light c . The band structure of graphene thus hosts two non-equivalent *Dirac cones* at the points K and K', which are related by time reversal.

To ensure that the low-energy physics is relativistic, we must finally check that the Fermi level of clean graphene coincides with the nodal level $E = 0$, i.e. lies at the crossing points. This is indeed the case since each carbon atom gives one electron, so that the valence band is full and the conduction band empty. In experiments, however, and particularly with epitaxial graphene, the presence of impurities and the proximity to the substrate, which affects the charge distribution, tend to shift the Fermi level away from the crossing point (FUCHS 2008).

A key difference between quasi-particles in graphene and genuine Dirac fermions comes from what the Pauli matrices stand for: in high-energy physics, they represent the actual spin; in graphene, they represent the sublattice, which is an effective degree of freedom that emerges in a crystal when the unit cell hosts several atoms. In the context of condensed matter, this effective degree of freedom is called *pseudospin*. Of course, conduction electrons also possess an actual spin, on which the energy may depend when processes like spin-orbit

¹Higher order corrections in crystal momentum lead to a trigonal warping of the band structure: the energy contours stretch along the three crystallographic axes, thus deforming the dispersion relation from perfect cones.

coupling come into play; but in graphene, spin-orbit coupling is weak because carbon atoms are light (the energy split is less than 20 neV) (CASTRO NETO 2009). The presence of two non-equivalent Dirac cones leads to yet another *valley* degree of freedom. Though the dispersion relations of the non-equivalent cones look identical, the behaviour of the wave function differs when circling around one or the other node in a closed loop: the two valleys have different topologies, as we will see in Sec. 1.3.1.

Density of states — The density of states (DoS) $\rho(E)$ is an equilibrium quantity, function of the energy E , which measures the number of eigenstates per unit of energy. It enters the expression of thermodynamic properties of electronic phases (total internal energy, specific heat, etc.), and depends directly on the electronic band structure. Let us determine the DoS in graphene near the Fermi level. To later generalise to three-dimensional phases, we will consider a system of linear size L with a relativistic dispersion relation in arbitrary dimension d . The low-energy relation dispersion $E = \hbar v_F q$ is isotropic: it depends only the norm q of the quasi-particle momentum \mathbf{q} , but not on its direction. Let the integer $s = 4$ accounts for the spin and valley degeneracy in graphene. By definition, the quantity

$$\rho(E)dE = \frac{s\Omega_d q^{d-1}}{(2\pi)^d} dq \quad (1.29)$$

represents the number of states per sample ‘volume’ L^d in a shell of thickness dE centred at the energy E . The 2π factor comes from the quantisation of crystal momentum under periodic boundary conditions, while the angular factor $\Omega_d = 2\pi^{d/2}/\Gamma_E(d/2)$ is the surface of the d -sphere, with $\Gamma_E(x)$ Euler’s Gamma function. For a relativistic dispersion relation, we easily find (CASTRO NETO 2009; SYZРАНOV 2018)

$$\rho(E) = \frac{s\Omega_d}{(2\pi\hbar v_F)^d} E^{d-1}. \quad (1.30)$$

Graphene, for which $d = 2$, thus exhibits a linear DoS near the Dirac nodes. More generally, in two- and three-dimensional relativistic phases, the DoS vanishes at the nodal level. Therefore, the conductivity due to propagating modes vanishes in relativistic semimetals at zero temperature. We will discuss several consequences of the relativistic nature of the dispersion relation in the transport properties of relativistic semimetals in Sec. 1.3.3.

1.2.4 Weyl and Dirac semimetals

Graphene provides a special example of a relativistic phase, being two-dimensional. All other relativistic semimetals known at present have three dimensions. Most of the three-dimensional relativistic semimetals fall into two categories: Weyl semimetals, where two bands cross linearly; and Dirac semimetals, where four bands cross linearly. The first class was observed in alloys of the tantalum (TaP and TaAs) and niobium (NbAs and NbP) families in 2015, while the second class was observed a year before in sodium bismuthide (Na₃Bi) and similar compounds.

Weyl semimetals — Tantalum phosphoride (TaP) is an example of a three-dimensional relativistic semimetal where only two non-degenerate bands touch (see Fig. 1.3). Assuming the Fermi level coincides with the nodal level, the low-energy excitations behave as two-component massless relativistic particles, i.e Weyl fermions. The low-energy band structure

forms a so-called Weyl cone, as depicted in Fig. 1.6(a). The quasi-particle dynamics follows from the Hamiltonian (1.15) with the mass m set to zero,

$$\mathcal{H} = \chi \hbar v_F \boldsymbol{\sigma} \cdot \mathbf{q}, \quad (1.31)$$

where by convention we assign a chirality index $\chi = +1$ for left-handed and $\chi = -1$ for right-handed fermions, and $\boldsymbol{\sigma} = (\sigma_1, \sigma_2, \sigma_3)$ are the three Pauli matrices, and typically $v_F \simeq 10^6 \text{ m} \cdot \text{s}^{-1}$. Real materials always host more than one Weyl node, and in analogy with graphene, we will often use the term *valley* to refer to the corresponding degree of freedom. Similarly, the pseudospin $\boldsymbol{\sigma}$ represented by the Pauli matrices in Eq. (1.31) corresponds to sublattice, orbital or spin degrees of freedom, or mixtures of them. In TaP, the pseudospin emerges from spin-orbit doublets in the 3d orbitals of Ta and the 4f orbitals of P (XU 2015a).

It would seem that forcing the valence and conduction bands to meet as in Eq. (1.31) requires to fine-tune physical parameters, as in graphene where a mass term can gap the Dirac nodes in absence of any protective symmetry. But this is not the case in three dimensions. In a Weyl semimetal, the Hamiltonian projected onto a set of two proximate bands is of the form

$$\mathcal{H} = \sum_{\mu=0}^3 \sigma_{\mu} f_{\mu}(\mathbf{k}) = \sigma_0 f_0(\mathbf{k}) + \boldsymbol{\sigma} \cdot \mathbf{f}(\mathbf{k}), \quad (1.32)$$

where f_0 and $\mathbf{f} = (f_1, f_2, f_3)$ are arbitrary functions. First, the equal number of components of \mathbf{k} (which is the dimension of real space) and \mathbf{f} (which is the dimension of the Pauli algebra) guarantees that if there exists a crystal momentum \mathbf{b} such that $\mathbf{f}(\mathbf{b}) = \mathbf{0}$, nothing can get rid of the crossing point: tuning \mathbf{b} or $f_0(\mathbf{b})$ only moves the node in the energy landscape (BURKOV 2015).

Second, the two bands must be non-degenerate away from the crossing point, i.e. we wish that only a few crystal momenta \mathbf{b} satisfy $\mathbf{f}(\mathbf{b}) = \mathbf{0}$. Unfortunately, the symmetries of spatial inversion \mathcal{I} and time reversal \mathcal{T} , when both present, force the band degeneracy. Indeed, these symmetries act on time, space and crystal momentum in the following way:

$$\mathcal{T} : \begin{cases} t \mapsto -t \\ \mathbf{r} \mapsto \mathbf{r} \\ \mathbf{k} \mapsto -\mathbf{k} \end{cases}, \quad \mathcal{I} : \begin{cases} t \mapsto t \\ \mathbf{r} \mapsto -\mathbf{r} \\ \mathbf{k} \mapsto -\mathbf{k} \end{cases}, \quad (1.33)$$

with the caveat that \mathcal{T} is antiunitary (it complex conjugates objects on which it acts). Let then $\Theta = \mathcal{I}\mathcal{T}$ be the product of inversion and time reversal. Both symmetries reverse \mathbf{k} , which implies that the Bloch waves $\psi_{\mathbf{k}}$ and $\Theta\psi_{\mathbf{k}}$ have the same energy $E(\mathbf{k})$. Since $\Theta^2 = -1$ for spinful fermions, the energy eigenstates $\psi_{\mathbf{k}}$ and $\Theta\psi_{\mathbf{k}}$ cannot be equal, but belong instead to two orthogonal eigenspaces of Θ , which means that the energy band $E(\mathbf{k})$ is two-fold degenerate everywhere. To ensure the non-degeneracy except at high symmetry points, at least one of these symmetries must be broken.

- *Non-centrosymmetric* Weyl semimetals break inversion while preserving time reversal. Time reversal reverses the crystal momentum, i.e. the node's position \mathbf{b} and the wave vector \mathbf{q} of the low-energy excitations, but also conjugates the pseudospin. Yet, the operators $\boldsymbol{\sigma} \cdot \mathbf{q}$ and $-\boldsymbol{\sigma}^* \cdot \mathbf{q}$ describe two copies of the same chiral fermion. Weyl nodes thus pair with time-reversal partners of the *same* chirality: a left-handed node

at $-\mathbf{b}$ accompanies a left-handed node at $+\mathbf{b}$, and similarly for right-handed nodes. Topology also constrains left- and right-handed nodes to come in equal number, which forces \mathcal{T} -breaking Weyl semimetals to host at least four Weyl nodes. The first Weyl semimetals observed in 2015, TaAs (LV 2015) and TaP (XU 2015b), crystallise in a body-centred tetragonal structure and belong to this non-centrosymmetric class.

- *Magnetic* Weyl semimetals break time reversal while preserving inversion.

Inversion reverses the crystal momentum. Weyl nodes thus pair with inversion partners of *opposite* chiralities: a left-handed node at $-\mathbf{b}$ accompanies a right-handed node at $+\mathbf{b}$. Though several candidates were proposed, such as $\text{Y}_2\text{Ir}_2\text{O}_7$ (WAN 2011), HgCr_2Se_4 (XU 2011) and $\text{Co}_3\text{Sn}_2\text{S}_2$ (XU 2018), observing magnetic Weyl semimetals poses a great challenge because of the need to enhance the magnetic order through chemical doping. Experiments recently identified a magnetic Weyl semimetallic phase in $\text{Co}_3\text{Sn}_2\text{S}_2$ (LIU 2019).

Dirac semimetals — Sometimes, extra spatial symmetries pin two Weyl nodes of opposite chiralities at the same point, provided the pseudospins represent independent degrees of freedom. This requires their position \mathbf{b} to be time-reversal invariant, i.e. that there exists a vector \mathbf{G} of the reciprocal lattice such that $\mathcal{T}\mathbf{b} = -\mathbf{b} = \mathbf{b} + \mathbf{G}$. The resulting crossing point is linear with a four-fold degeneracy,

$$\mathcal{H} = \hbar v_F \boldsymbol{\alpha} \cdot \mathbf{q} = \hbar v_F \begin{pmatrix} \boldsymbol{\sigma} \cdot \mathbf{q} & 0 \\ 0 & -\boldsymbol{\sigma} \cdot \mathbf{q} \end{pmatrix}. \quad (1.34)$$

Eq. (1.34) is precisely the Hamiltonian for massless Dirac fermions in three dimensions; the corresponding low-energy band structure forms a Dirac cone, as shown in Fig. 1.6(b). Interestingly, a Dirac semimetal can be viewed as an intermediate massless phase between a topological insulator and a trivial insulator, with masses (gaps) $m > 0$ and $m < 0$,

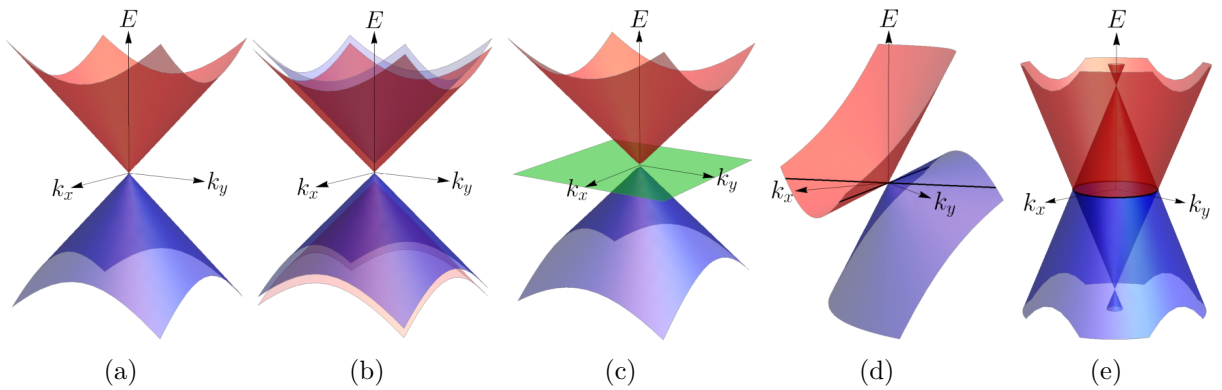


Figure 1.6 | (a) In a type-I Weyl node, two bands cross linearly. (b) A type-I Dirac node hosts two Weyl nodes of opposite chiralities pinned at the same crystal momentum, leading to a four-band linear crossing. (c) A pseudospin-one node hosts an additional flat band. (d) A type-II Weyl cone tilts sufficiently in one direction to produce electron and hole pockets. (e) When the valence and conduction bands merge over some energy region, they cross over a nodal circular line.

respectively. We expect Dirac semimetals to be less robust than their Weyl counterparts, to the extent that Dirac nodes are protected by symmetry but not by topology. The observation of Dirac semimetals actually predates that of Weyl semimetals: sodium bismuthide (Na_3Bi) (LIU 2014b) and cadmium arsenide (Cd_3As_2) (BORISENKO 2014; LIU 2014a) were identified as Dirac semimetals in 2014. The Dirac cones of these materials are protected by three-fold and four-fold rotational symmetries, respectively (CHIU 2016).

Higher order semimetals and the likes — The zoology of relativistic semimetals would be incomplete without mentioning the following exotic phases.

- *Higher-order* semimetals.

The low-energy excitations of a Weyl cone mimic massless spin one-half relativistic particles. A natural extension would consist of relativistic excitations with higher spin, e.g. spin one. A spin one fermion belongs to a three-dimensional representation of the Lorentz group; the corresponding massless Hamiltonian

$$\mathcal{H} = \hbar v_F \mathbf{J} \cdot \mathbf{q} \quad (1.35)$$

looks similar to a Weyl Hamiltonian, except that the pseudospin $\mathbf{J} = (J_x, J_y, J_z)$ represents three-times-three generalisations of the Pauli matrices, which satisfy the algebra of the angular momentum $[J_i, J_j] = 2i\epsilon_{ijk}J_k$. The three-fold degenerate crossing point involves an extra flat band $E_0 = 0$ besides the valence and conduction bands $E_{\pm} = \pm\hbar v_F q$, as seen in Fig. 1.6(c). The Hamiltonian (1.35) can incorporate a mass term at the cost of doubling the degeneracy of each band, and ruining the algebra of angular momentum. The corresponding particles, which do not belong to any conventional spin representation, are known as Kane fermions; they appear in $\text{Hg}_{1-x}\text{Cd}_x\text{Te}$ alloys, where they induce a topological phase transition upon tuning the gap near a critical cadmium concentration x and temperature T (TEPPE 2016).

- *Type-II* semimetals.

The Weyl semimetals we have considered up to now satisfy Lorentz invariance at low energies; they are said to be of type I. The Weyl Hamiltonian (1.31) originates from the generic two-by-two Hamiltonian (1.32) assuming that $\mathbf{f}(\mathbf{k})$ is isotropic and linear near the crystal momentum \mathbf{b} , and that $f_0(\mathbf{k})$ is constant up to possible quadratic corrections. But Lorentz invariance is not a fundamental requirement in condensed matter, and materials could break one of the previous conditions. When relaxing the condition of isotropy, the dispersion relation can become quadratic in one particular direction, while remaining linear in other directions, in which case the material is a semi-Dirac phase. When relaxing the second condition, e.g. assuming that $f_0(\mathbf{k}) = \hbar v_0 q_x$ varies linearly with momentum along a given direction x , the Weyl cone tilts in that same direction. If $v_0 > v_F$, the Fermi level crosses no longer a single point but a two-dimensional section of the (three-dimensional) Weyl cone: the band structure forms electron and hole pockets, as shown in Fig. 1.6(d). Among these so-called type-II semimetals features WTe_2 (SOLUYANOV 2015).

- *Nodal line* semimetals.

Nodal line semimetals, like type-II semimetals, host extended Fermi surfaces. A nodal line semimetals arise when the Dirac Hamiltonian acquires an off-diagonal element of the form

$$\mathcal{H} = \mu\beta\sigma^{yz} + \hbar v_F \boldsymbol{\alpha} \cdot \mathbf{q} = \begin{pmatrix} \hbar v_F \boldsymbol{\sigma} \cdot \mathbf{q} & \mu\sigma_1 \\ \mu\sigma_1 & -\hbar v_F \boldsymbol{\sigma} \cdot \mathbf{q} \end{pmatrix}, \quad (1.36)$$

where $\sigma^{\mu\nu} = \frac{i}{2}[\gamma^\mu, \gamma^\nu]$ is the spin tensor. The conduction and valence bands then shift towards one another so as to merge over some energy μ around the Fermi level, and the Fermi surface forms a circle of radius $\mu/\hbar v_F$, as in Fig. 1.6(e).

1.3 Hallmark of relativistic semimetals

The properties of relativistic semimetals differ from that of conventional phases of matter in many respects. We pointed out in Sec. 1.2.3 that the DoS vanishes at the Fermi level. In this section, we exemplify the most exotic features of relativistic semimetals regarding their surface and transport measurements. Though transport offers the richest signatures of the relativistic physics – from the scaling of the optical conductivity to the chiral anomaly –, surface properties, to which we dedicate a chapter of this thesis, will be our primary concern. Most of these experimental signatures originate not only from relativistic nature of the low-energy excitations, but also from the topology of the Weyl cones. Although this thesis needs few prerequisites in topology, we will thus devote a subsection to topological aspects, and define three important concepts: the Berry phase, the winding number, and the Chern number.

1.3.1 Topology

The discovery of topological insulators around the same period as graphene launched a novel area of research: topological condensed matter (BERNEVIG 2013; CHIU 2016). *Topology* refers to the robustness of some mathematical objects against smooth deformations. It disregards the specific geometry and focuses instead on invariant features, which enables to classify topological objects by integer numbers. In relativistic semimetals, chirality – which is yet a relativistic concept – serves this purpose of classification. Far from being some barren curiosity, topology has become a powerful tool to explain and predict the exotic surface and transport properties of relativistic phases.

The Berry phase — Because of the probabilistic interpretation of quantum mechanics, a quantum state $|\psi\rangle$ must be normalised. However, $|\psi\rangle$ and $e^{i\phi}|\psi\rangle$ represent the same state for all real ϕ . This freedom in the choice of the overall phase endows quantum mechanics with a U(1) gauge invariance, as in electromagnetism.

Consider some Hamiltonian $\mathcal{H}(\lambda)$, which depends on a set of parameters $\lambda = \{\lambda_1, \lambda_2, \dots\}$. For each value of λ , we make an arbitrary choice of phase and assign a basis $\{|m(\lambda)\rangle\}$ to the Hamiltonian. We now wish to know how an energy eigenvector $|\psi(t)\rangle$, which originally coincides with one vector of the basis, say $|n(\lambda)\rangle$, evolves when λ traces out a closed path in parameter space under time evolution, governed by the Schrödinger equation

$\mathcal{H}|\psi\rangle = i\hbar\partial_t|\psi\rangle$. An energy eigenvector always acquires a dynamical phase

$$\varphi = -\frac{i}{\hbar} \int E_n(\lambda(t)) dt, \quad (1.37)$$

which contains no essential information about the Hamiltonian's structure. We absorb it into a redefinition of the eigenvector $|\Psi\rangle = e^{-i\varphi}|\psi\rangle$, which still differs from $|n\rangle$ by some phase factor $e^{i\theta(\lambda)}$. To keep track of the eigenvector throughout the time evolution, we must tune λ slowly enough not to mix $|\Psi\rangle$ with another eigenvector at a nearby level crossing. This *adiabatic* condition ensures parallel transport² (WITTEN 2016):

$$\langle\Psi|\partial_\lambda|\Psi\rangle = i\partial_\lambda\theta + \langle n|\partial_\lambda|n\rangle = 0. \quad (1.38)$$

Over a closed path \mathcal{C} , the state $|\Psi\rangle$ thus acquires a *Berry* phase

$$\gamma_n = \oint_{\mathcal{C}} \partial_\lambda\theta d\lambda = \oint_{\mathcal{C}} \mathcal{A}_n, \quad (1.39)$$

where $\mathcal{A}_n = i\langle n|d|n\rangle$ is the Berry connection. The Berry connection depends on the choice of phase for the basis of eigenvectors $|n\rangle$, as opposed to the Berry phase, which no change of basis can absorb. This property illustrates the gauge dependence of the former, and gauge invariance of the latter up to a phase of 2π . The Berry phase is also insensitive to the precise parametrisation $\lambda(t)$ of the closed path \mathcal{C} , so that nothing requires t to represent actual time.

As an example, let us compute the Berry phases for both positive and negative energy states in graphene. The low-energy Hamiltonians near the valleys K (of the form $\boldsymbol{\sigma}\cdot\mathbf{q}$) and K' (of the form $-\boldsymbol{\sigma}^*\cdot\mathbf{q}$) are naturally parametrised by the momentum $\mathbf{q} = q(\cos\theta, \sin\theta)$. The eigenvectors are (CASTRO NETO 2009)

$$|\psi_\pm\rangle = \frac{1}{\sqrt{2}} \begin{pmatrix} e^{-i\theta} \\ \pm 1 \end{pmatrix}, \quad |\psi'_\pm\rangle = \frac{1}{\sqrt{2}} \begin{pmatrix} e^{i\theta} \\ \mp 1 \end{pmatrix}, \quad (1.40)$$

where the plus (minus) sign refers to electrons (holes). Clearly, the Berry phase around any closed loop that does not enclose the Dirac nodes vanishes. But when the path \mathcal{C} circles counter-clockwise around one node at a fixed radius q , the Berry phase reads, irrespective of the band index,

$$\gamma = i \int_0^{2\pi} \langle\psi_\pm|\partial_\theta\psi_\pm\rangle d\theta = \pi \quad (1.41)$$

for the valley K, and $\gamma' = -\pi$ for the valley K'. Though the Berry phase equals exactly $\pm\pi$ for massless Dirac fermions, it is not quantised in general and may take all values between (modulo 2π). For instance, the Berry phase of massive Dirac fermions depends continuously on \mathbf{q} , and in the Aharonov-Bohm effect, the Berry phase $\gamma = e\Phi/\hbar c$ varies continuously with the magnetic flux Φ . Experiments can measure the Berry phase of elementary excitations in graphene using angle-resolved photoemission spectroscopy (ARPES) and by comparing the response to linearly and circularly polarised lights (LIU 2011).

²Actually, adiabaticity is superfluous, and this hypothesis was later removed by Berry.

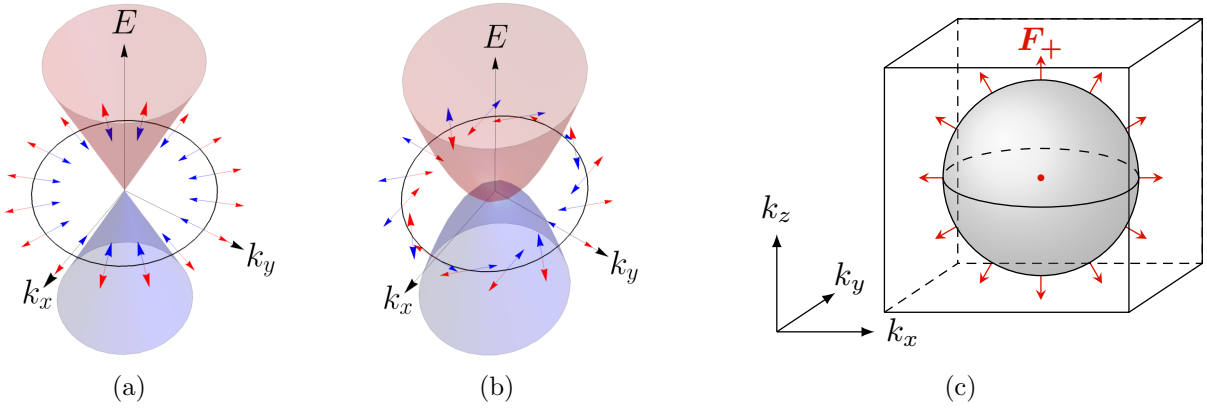


Figure 1.7 | Winding number and topological charge. (a) In graphene, the pseudospins of both electrons (red) and holes (blue) wind once around the Dirac node, clockwise for the valley K and counter-clockwise for the valley K'. (b) In Bernal-stacked bilayer graphene, the dispersion relation near the nodes becomes quadratic. The pseudospin winds twice. (c) A Weyl node (red dot) acts as a Berry monopole. The Berry field strength in the conduction band points outwards or inwards depending on the chirality, and its flux over a sphere (in gray) that surrounds the node is quantised in units of 2π . The corresponding integer is the Chern number; it generalises the notion of chirality to larger topological charges. In a Weyl node of positive chirality $\chi = +1$, the Berry field strength in the conduction band \mathbf{F}_+ points outwards.

The winding number — The 2π ambiguity of the Berry phase sometimes poses a problem to identify whether a given Hamiltonian describes a trivial or a topological phase. This is not the case in graphene, where $\gamma = \pm\pi$, but some topological phases present Berry phases multiple of 2π . For two-dimensional systems with a chiral symmetry³, we can define a (less general) invariant that solves this ambiguity, while enabling to extend the notion of chirality to higher-order band crossings: the winding number (CHIU 2016).

The winding number counts how many times the pseudospin rotates around a topological point in the Brillouin zone, like a Weyl node, when the crystal momentum spans a closed loop. A two-by-two Hamiltonian with no σ_3 mass term is proportional to a unitary matrix of the form $\boldsymbol{\sigma} \cdot \mathbf{n}$ where $\mathbf{n} = (\cos \phi, \sin \phi)$ depends on crystal momentum. Because the pseudospin of energy eigenstates, which are also helicity eigenstates, is locked in the direction of \mathbf{n} , we may as well use the vector \mathbf{n} to count the winding of the pseudospin. The winding number is then defined by

$$\nu = \frac{1}{2\pi} \int_0^{2\pi} \partial_\theta \phi \, d\theta. \quad (1.42)$$

This definition extends to chirally symmetric Hamiltonians defined on Hilbert spaces of any dimension. For simplicity, we chose in Eq. (1.42) the same circular path as for the Berry phase in Eq. (1.41). And indeed in graphene $\phi = \pm\theta$ near the valleys K and K' respectively, so that the winding number $\nu = \pm 1$ coincide, up to a factor of π , with the Berry phase, as we can see in Fig. 1.7(a). In graphene, the pseudospin is locked in

³Here, chirality is understood in the sense of condensed matter, not in the sense of special relativity. In condensed matter, a chiral ‘symmetry’ refers to a unitary antisymmetry of the Hamiltonian, i.e. an operator C which anticommutes with \mathcal{H} : $\{C, \mathcal{H}\} = 0$. If ψ denotes an eigenstate of energy E , then $C\psi$ is an eigenstate of opposite energy $-E$. The sublattice polarisation operator σ_3 implements a chiral symmetry in graphene (in absence of any mass term).

the direction of the crystal momentum and winds only once, either clockwise ($\nu = +1$) or counter-clockwise ($\nu = -1$). In Bernal-stacked bilayer graphene, which harbours a quadratic dispersion relation, the pseudospin winds twice as fast, and $\nu = \pm 2$, as shown in Fig. 1.7(b) (McCANN 2013).

The Chern number — In three dimensions, the analogy with electromagnetism suggests to express the Berry phase of Eq. (1.39) as a flux over a surface \mathcal{S} that borders the closed path \mathcal{C} , using Stokes' theorem. The two-form associated to the Berry connection is the Berry curvature $\mathcal{F}_n = d\mathcal{A}_n$. It is gauge invariant. In the same way as the Berry connection $\mathcal{A} = \mathbf{A} \cdot d\mathbf{k}$ can be viewed as a gauge vector potential \mathbf{A} , the Berry curvature can be viewed as a curl, or Berry field strength $\mathbf{F} = \nabla \times \mathbf{A}$ (which reduces trivially to a scalar in two dimensions, up to a Hodge transformation). Expressed in terms of curvature instead of connection, the Berry phase reads

$$\gamma_n = \int_{\mathcal{S}} \mathcal{F}_n = \int_{\mathcal{S}} \mathbf{F}_n \cdot d\mathbf{S}, \quad (1.43)$$

where $\mathcal{C} = \partial\mathcal{S}$ and the orientation of the infinitesimal transverse vector $d\mathbf{S}$ follows from the orientation of \mathcal{C} .

As an example, consider the Weyl Hamiltonian with positive chirality. The energy eigenstates are eigenvectors of the helicity $\boldsymbol{\sigma} \cdot \mathbf{q}$. A possible basis consists of the following vectors, expressed in polar coordinates,

$$|\psi_+\rangle = \begin{pmatrix} e^{-i\phi} \cos(\theta/2) \\ \sin(\theta/2) \end{pmatrix}, \quad |\psi_-\rangle = \begin{pmatrix} e^{-i\phi} \sin(\theta/2) \\ -\cos(\theta/2) \end{pmatrix}, \quad (1.44)$$

where the sign \pm refers to the sign of the energy. The corresponding Berry connections are $A_+ = \cos^2(\frac{\theta}{2}) d\phi$ and $A_- = \sin^2(\frac{\theta}{2}) d\phi$. Taking a path that circles around the Weyl node along the equator, we find that contrary to graphene, the energy eigenstates of a Weyl Hamiltonian have opposite Berry phases $\gamma_{\pm} = \pm\pi$, where the plus (minus) sign applies to electrons (holes). As a result, the Berry curvatures also have opposite signs $\mathcal{F}_{\pm} = \pm \frac{1}{2} \sin \theta d\theta \wedge d\phi$. The corresponding Berry field strength

$$\mathbf{F}_{\pm} = \pm \frac{\mathbf{q}}{2q^3} \quad (1.45)$$

has the same expression as the electric field created by an electric charge $Q = 2\pi$ located at the Weyl node.

Guided by the analogy with Gauss's theorem, we propose to integrate over a closed sphere around the node, instead of an open surface that borders a Berry path, as shown in Fig. 1.7(c). This defines a topological charge, the Chern number (BERNEVIG 2013)

$$C_n = \frac{1}{2\pi} \oint_{\mathcal{S}} \mathbf{F}_n \cdot d\mathbf{S}, \quad (1.46)$$

where n denotes the band index. In the conduction band, the Chern number is $C_+^R = 1$ for right-handed fermions, and $C_+^L = -1$ for left-handed fermions. Weyl nodes thus carry Berry monopoles, whose topological charge in the conduction band coincides with the chirality index $\chi = \pm 1$. Unlike chirality, the Chern number depends on the band index,

but without further indication, we will conventionally consider the conduction band, so as to ensure a one-to-one correspondence between the former (which is a relativistic notion) and the latter (which is a topological notion). The Chern number applies not only to three-dimensional relativistic semimetals, where the closed surface can be taken as a sphere around the band crossing point, but also to two-dimensional systems with an isolated band, in which case the Brillouin zone serves as a closed surface. The latter situation corresponds to topological insulators, which we will discuss briefly in Sec. 1.3.2. Physically, a non-zero topological charge reflects an obstruction to smoothly define wave functions over the whole Brillouin zone.

The no-go theorem — An immediate consequence of topology is that it constrains the nature and number of the Weyl (or higher order) nodes a material can host (WITTEN 2016). By virtue of the Bianchi identity, the second differential of the Berry connection (which is a one-form) vanishes, which entails that $d\mathcal{F} = 0$ wherever the Berry curvature is well defined; this corresponds to the whole Brillouin zone for isolated bands, but precludes Weyl and Dirac nodes in relativistic semimetals. Let us denote by \mathcal{B} the Brillouin zone from which we exclude all the bad points by removing small open balls centred at the nodes. Due to periodic boundary conditions, the Brillouin zone is a closed manifold, and thus the boundary of \mathcal{B} reduces to the spheres \mathcal{S}_α centred at the nodes $\alpha = 1, \dots, N$. Applying Stokes' theorem, we find that the sum of all Chern numbers vanishes,

$$0 = \frac{1}{2\pi} \int_{\mathcal{B}} d\mathcal{F} = \sum_{\alpha=1}^N \frac{1}{2\pi} \int_{\mathcal{S}_\alpha} \mathcal{F} = \sum_{\alpha=1}^N C_\alpha. \quad (1.47)$$

This result is known as the Nielsen-Ninomiya or no-go theorem (NIELSEN 1981). In particular, Weyl semimetals must host pairs of nodes of opposite chiralities. Topology imposes no constraints on the number of Dirac nodes in three-dimensional materials, which have zero Chern numbers, though there are usually symmetry constraints.

1.3.2 Surface states

Chern insulators — A well-known consequence of topology is the bulk-boundary correspondence (BERNEVIG 2013). In the simplest topological insulators, the Chern insulators, the two bands closest to the Fermi level and separated by an energy gap have non-zero Chern numbers. To realise a trivial to topological phase transition, let us consider the massive Dirac Hamiltonian in two dimensions

$$\mathcal{H} = \hbar v_F \boldsymbol{\sigma} \cdot \mathbf{q} + \Delta \sigma_3. \quad (1.48)$$

This Hamiltonian describes Dirac fermions of mass Δ and energy $E = \pm \sqrt{(\hbar v_F q)^2 + \Delta^2}$. The energy bands are insensitive to the sign of the mass, but the conduction band acquires a non-zero Chern number $C = +1$ when $\Delta < 0$, while having a zero Chern number for $\Delta > 0$. Decreasing the energy gap Δ induces a phase transition from a gapped trivial phase (trivial insulator) to a gapped topological phase (Chern insulator). The intermediate gapless phase is precisely a Dirac semimetal. Chern insulators host gapless states which are exponentially localised near the edge, and topologically protected against disorder, even when the gap closes (MEYER 2013). These edge states allow for ballistic transport, which makes Chern insulators conducting at the boundary while insulating in the bulk. In this

regard, three-dimensional Dirac semimetals can be seen as the surface of four-dimensional Chern insulators. As we will see below, gapless phases host surface states themselves, though of different nature, in the form either of edge modes (graphene), Fermi arcs (Weyl semimetals) or Dirac surface states (Dirac semimetals).

Edge modes in graphene — In Sec. 1.2.3, our interest lay on the bulk properties of graphene. The relativistic and topological physics also manifests themselves on the boundary in the form of exponentially localised states (BERNEVIG 2013; CASTRO NETO 2009). Because of electron-electron interactions, edge modes in graphene nanoribbons behave as Luttinger liquids, and ensure charge and spin transport in the presence of a magnetic field. The spectrum of these edge modes depends strongly on the geometry of the edges, whether zigzag, armchair, or more complicated shapes, but in all instances, the edge modes exist over a large region of the Brillouin zone at nearly zero energy. We will discuss only the zigzag geometry.

In an infinite graphene ribbon oriented in the x direction, periodic boundary conditions apply along x while open boundary conditions apply at the two edges at positions $y = 0$ and $y = L_y$, where L_y denotes width of the ribbon. The longitudinal wave vector k_x is a good quantum number, unlike the transverse wave vector. Because of the different orientations of the bonds A-B and B-A within a transverse chain of atoms, neighbour sites see different hopping amplitudes t and $t_{k_x} = t(1 + e^{ik_x a})$, where $a = a_0\sqrt{3}$ is the lattice constant of graphene. This dispersion leads to exponentially localised states near the edges with a penetration length $\xi = 1/\ln|2\cos(k_x a/2)|$. For $k_x L_y \gg 1$, we can safely neglect the overlap between the surface states of the two opposite edges, and the edge energy band becomes flat with zero energy, except near the Dirac nodes. The location of this band depends on the relative weight of the zero-energy modes over the sites A and B, and thus on the microscopic details of the chains. If the chains comprise an even number of sites, edge modes develop over either one of two complementary ranges of k_x , depending

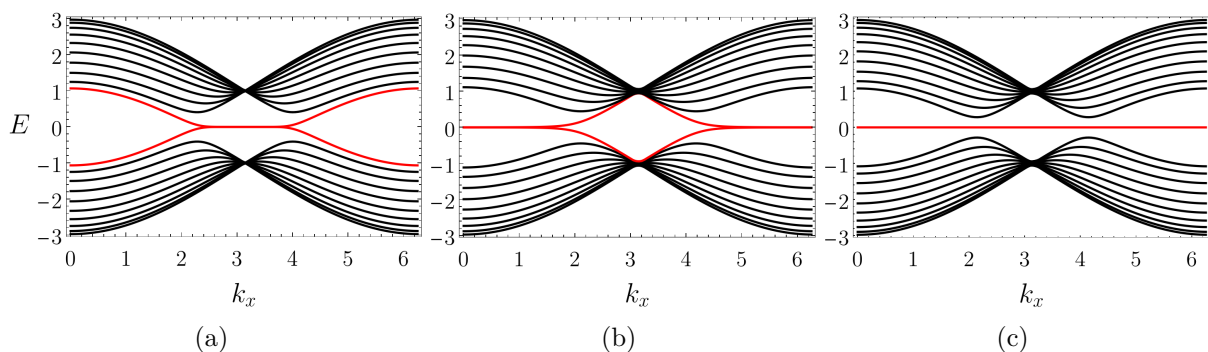


Figure 1.8 | Band structure in infinite graphene ribbons along the x direction with zigzag geometry, within a tight-binding approach. The energy E is plotted against the longitudinal wave vector k_x . When the transverse chains of atoms, which are roughly oriented along the transverse y direction, contain an even number of sites (here 20), two edge modes of almost zero energy (a portion of the red bands) develop between the Dirac nodes. (a) For A and B terminations at $y = 0$ and $y = L_y$ respectively, the edge modes exist only in the range $[2\pi/3, 4\pi/3]$ of k_x . (b) For B and A terminations, they exist only in the complementary range $[0, 2\pi/3] \cup [4\pi/3, 2\pi]$. (c) When transverse chains of atoms contain an odd number of sites (here 21), the two edge modes are pinned at exactly zero energy over the full longitudinal Brillouin zone.

on whether the two terminal sites are A at $y = 0$ and B at $y = L_y$ (Fig. 1.8(a)), or B at $y = 0$ and A at $y = L_y$ (Fig. 1.8(b)). If the chains comprise an odd number of sites, the edge modes exist for all k_x at exactly zero energy and the surface energy band disconnects completely from the bulk bands (Fig. 1.8(c)).

Fermi arcs — Topological surface states also appear in three-dimensional relativistic semimetals (WAN 2011; HASHIMOTO 2008). They lead to richer band structures, being localised on a two-dimensional instead of a one-dimensional boundary. These surface states, namely the Fermi arcs, Dirac surface states, and Fermi rays, constitute the topic of Chapter 4.

Let us consider first the surface states of Weyl semimetals. The constant energy contours on the surface Brillouin zone form crescent-shaped lines which connect the projections of two Weyl cones with opposite chiralities, as shown in Fig. 1.9(a). Precisely at the nodal level, the line terminates on the nodes, thus forming a *Fermi arc*. Weyl semimetals usually host many nodes for symmetry reasons. For instance, the Weyl semimetal TaP harbours no less than twenty-four Weyl nodes, because the body-centred tetragonal lattice associate nodes of opposite chiralities by four-fold rotations and reflections (Lv 2015). Weyl nodes thus have high chances of overlapping when projected to the surface Brillouin zone of a material cleaved along high symmetry surfaces. The (001) surface of TaP comprises eight nodes with Chern number ± 1 and eight nodes with Chern number ± 2 . A pair of surface nodes can thus host more than one Fermi arc; in fact, the same number as the absolute topological charge. Fig 1.10 shows a surface spectral density map obtained by ARPES in TaP. One of the Fermi arcs which join two proximate nodes of topological charges ± 2 is clearly visible. Besides, this pair of nodes also host trivial surface states, whose constant energy contours avoid the nodes and close in large loops. These additional states are probably associated with deeper layers below the boundary (XU 2015b).

Unfortunately, transport signatures of surface states are difficult to isolate because of the conducting bulk. Some promising techniques to evidence surface transport rely on the

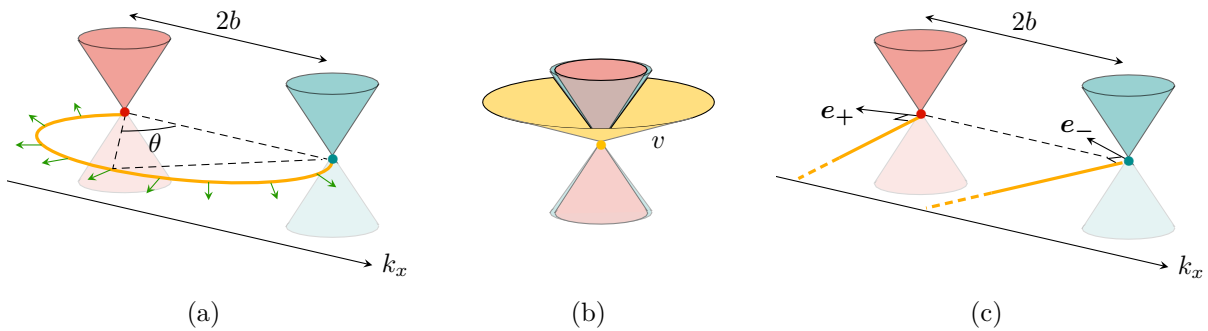


Figure 1.9 | (a) Pairs of Weyl nodes of opposite chiralities host Fermi arcs at the nodal level (in orange), parametrised by an aperture angle θ . The group velocity of the surface states (in green) is locally normal to the arc. (b) The same chiral-breaking boundary condition leads to Dirac surface states in Dirac nodes, which disperse along a semi-cone of positive energy on one surface (in orange) and negative energy on the other. The slope $\hbar v$ of the single-branch cone corresponds to a reduced Fermi velocity $v = v_F \cos \theta$, where v_F stands for the Fermi velocity of the bulk excitations. (c) Pseudospin-breaking boundary conditions lead to one disconnected Fermi ray at each node (in orange), parametrised by a normal surface vector e_{\pm} .

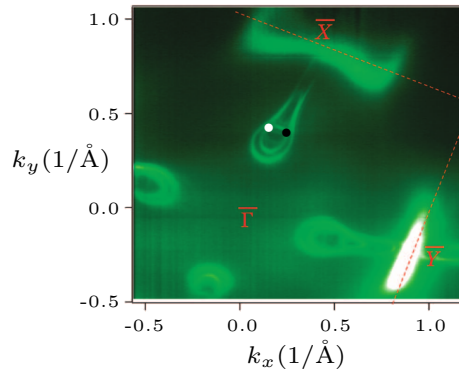


Figure 1.10 | Spectral density map at the Fermi energy of the (001) surface of the Weyl semimetal TaP, from angle-resolved photoemission spectroscopy (XU 2015b). The black and white dots along the $\bar{\Gamma}$ - \bar{X} line indicate two projected Weyl nodes of topological charges ± 2 . The green ‘tadpole’ feature that surrounds these two nodes comes from six surface states, among which four are trivial (they avoid the nodes and form closed loops) and two are Fermi arcs. The outermost green line is trivial, while the inner crescent is a Fermi arc.

hybridisation of surface and bulk states (ARMITAGE 2018). Another transport signature of surface states is negative refraction (CHEN 2020). Indeed, the edges of two adjacent boundaries refract surface states with a perfect -1 refraction index, provided the Fermi arcs are properly oriented. This enables to refocus electronic wave packets, so that the spatially resolved conductance peaks at the image of the point source.

One can predict the existence of Fermi arcs using a correspondence with topological insulators (WAN 2011). At any fixed transverse momentum k_{\perp} between a pair of Weyl nodes, the effective Hamiltonian $\mathcal{H}(k_{\parallel}, \mathbf{k}_{\perp} = \text{cte})$ is gapped and thus describes a two-dimensional Chern insulator, which hosts chiral edge states at zero energy. Integrating over k_{\perp} , we see that a Fermi line stretches continuously from one node and necessarily terminates to a node of opposite chirality. Physically, Fermi arcs arise from scattering processes on the boundary that reverse the chirality of Weyl fermions. The requirement that the cross current vanishes at the surface (particles cannot exit the material) leads to the boundary condition (WITTEN 2016)

$$M\Psi_s = \Psi_s \quad (1.49)$$

for the surface Dirac spinor Ψ_s , where the unitary matrix M satisfies $\{M, \tau_z \sigma_z\} = 0$. The index z denotes the direction normal to the surface and σ, τ the Pauli matrices in the pseudospin and chiral sectors, respectively. The boundary matrix M should depend on crystal momentum in general, but reduces to a constant in the low-energy limit, which is enough to explain all qualitative properties of Fermi arcs. A realisation of such chirality-mixing but pseudospin-preserving boundary matrix which is also compatible with the alignment of nodes along, say, the x direction, is

$$M = \tau_x \sigma_z \sin \theta - \tau_y \sigma_0 \cos \theta. \quad (1.50)$$

This boundary matrix of Eq. (1.50) breaks the surface rotational symmetry, along with the transverse mirror symmetry $y \mapsto -y$ for non-zero θ , which allows Fermi arcs to bend from a straight line. It is possible to determine the Green’s function compatible with Eq. (1.49), from which we can find the surface dispersion relation (FARAEI 2018). With the boundary

matrix of Eq. (1.50), the Fermi contour forms a circular arc with aperture angle θ , as defined in the schematic of Fig. 1.9(a). In real materials, however, Fermi arcs deviate from a circular shape due to quadratic corrections to the energy bands. In addition, no theoretical argument constrains the value of the aperture angle, which should then be fixed by microscopic details: termination of the boundary, presence of adatoms, etc.

Dirac semimetals also host Fermi arcs. Since one Dirac node consists of two overlapping Weyl nodes, the Fermi arcs appear in pairs and join Dirac nodes on either end. But unlike in Weyl semimetals, double Fermi arcs are not topologically protected, and can deform into closed Fermi loops (KARGARIAN 2016). Experiments later confirmed this fragility, since Fermi loops were observed in cubic PtBi₂ (WU 2019).

Dirac surface states — Besides Fermi arcs, Dirac semimetals can host another type of surface states confined around a single Dirac node in reciprocal space (SHTANKO 2018). Since a Dirac cone consists of two Weyl cones of opposite chiralities superimposed at the same crystal momentum, any Fermi arc joining the overlapping Weyl nodes formally reduces to a point. The boundary matrix (1.50) then leads to a linear surface dispersion relation $E = s\hbar v(\theta)q$ with a diminished velocity $v(\theta) = v_F \cos \theta$, and where $s = \pm 1$ according to which side of the material the surface faces (Fig. 1.9(b)). These *Dirac surface states* leak exponentially in the bulk over a penetration depth $\xi = 1/q \sin \theta$. For $\theta = 0$, all surface states dissolve into the bulk.

A striking feature of these surface states is that the boundary hosts only one band, either of conduction or valence: particle-hole symmetry is utterly broken. In practice, particle-hole symmetry is restored at the scale of the material, because a finite sample has two opposite surfaces along each direction, each hosting one type of surface carriers.

Fermi rays — Dirac fermions could also retain the same chirality under scattering from the boundary, but exchange instead their pseudospin. In this case, spinors with a definite handedness are eigenvectors of the boundary matrix. The most general boundary matrix of this type reads

$$M = \hat{\tau}_+ \boldsymbol{\sigma} \cdot \mathbf{e}_+ + \hat{\tau}_- \boldsymbol{\sigma} \cdot \mathbf{e}_-, \quad (1.51)$$

where $\hat{\tau}_\pm$ denote the valley projectors, and $\mathbf{e}_\pm = (\cos \theta_\pm, \sin \theta_\pm)$ are two unit vectors parallel to the surface. The emerging surface states at the nodal level disperse along two independent *Fermi rays* pointing in the directions orthogonal to \mathbf{e}_\pm , and stemming from the nodes of chiralities $\chi = \pm 1$ respectively, as illustrated in Fig. 1.9(c). The separation between the nodes has no influence on the Fermi rays, so that Fermi rays could appear in Weyl and Dirac semimetals alike. Similarly to the boundary matrix (1.50), the boundary matrix (1.51) breaks the O(2) rotational symmetry in the surface plane, along with all mirror symmetries in general. The rays' orientations should be determined by microscopic details of the boundary, and thus should be extremely sensitive to surface roughness (WITTEN 2016). This boundary condition also mixes neighbouring Landau levels in a background magnetic field, making Landau quantisation ill-defined (FARAEI 2018). Keeping in mind that Weyl excitations only emerge at low energies, and that we discarded much information about the complete band structure, seemingly infinite Fermi rays may not extend to the whole Brillouin zone but terminate at another remote pair of nodes, thus leading to large Fermi arcs (HASHIMOTO 2017).

1.3.3 Transport

The relativistic dispersion relation yields unusual scaling laws, notably in the DoS, as we have seen in Sec. 1.2.3, but also in several transport properties, such as the optical conductivity. Relativistic particles also tunnel more easily than non-relativistic particles, a phenomenon known as Klein tunnelling. Quantum transport leads to a minimal non-zero conductivity in graphene in absence of propagative modes. But it is topology which certainly leads to the most intriguing transport phenomena: the presence of a zeroth Landau level in graphene, which results in a half-integer quantum Hall effect, the anomalous Hall effect in Weyl and Dirac semimetals, and the chiral anomaly.

Optical conductivity — Let us consider a d -dimensional material where the Fermi level lies at a band touching point (it could be a relativistic semimetal or any degenerate semiconductor). Except for pathological cases, the bands touch with a power-law dispersion $E \propto q^\alpha$, with α a real positive number. Various theoretical approaches (Boltzmann transport, Kubo formalism) show that the optical conductivity $\sigma(\omega)$ scales with frequency ω as $\omega^{(d-2)/\alpha}$ at low temperature (ARMITAGE 2018). In three-dimensional relativistic semimetals, where $\alpha = 1$ and $d = 3$, this induces a linear dependence,

$$\sigma(\omega) = N \frac{e^2}{12h} \frac{\omega}{v_F}, \quad (1.52)$$

with N the number of nodes. Several experiments confirmed Eq. (1.52) over some window of energy, even though quantitative agreement is difficult to reach because of the many non-idealities in the band structure: higher-order corrections to the dispersion, anisotropy, the presence of additional flat bands. In the Dirac semimetal ZrTe₅, the optical conductivity follows Eq. (1.52) up to 150 meV, but with a slope thirty times larger than expected from ARPES measurements of the Fermi velocity (CHEN 2015).

Klein tunnelling — A peculiarity of Weyl fermions is the absence of backscattering when crossing a potential barrier, or Klein tunnelling (KLEIN 1929). Klein tunnelling simply refers to the counterpart of the tunnelling effect for relativistic particles, but the two effects differ so strongly that the former is often considered paradoxical. Whereas the probability for a non-relativistic particle to transmit through a potential barrier decays exponentially with its width, the barrier is absolutely transparent to relativistic particles at normal incidence (DUPLANTIER 1991). One interpretation of this counter-intuitive behaviour is that a barrier of height V_0 can reflect an incoming particle, of positive energy $E < V_0$, but also transmit it as a hole of negative energy $V_0 - E$. Klein tunnelling occurs in relativistic semimetals, provided the scattering decouple the valleys, and thus preserve chirality. The absence of backscattering has deep consequences for disordered relativistic semimetals, since it prevents electrons from localising. We will see in Sec. 1.4.1 that under strong enough disorder, these materials undergo a phase transition quite different from localisation. Klein tunnelling promises several applications of graphene, notably in p - n junctions and quantum dots (CASTRO NETO 2009).

Minimal conductivity of graphene — Though the DoS vanishes at the Fermi level of a Dirac node, graphene presents a small but non-zero universal conductivity at charge neutrality (CASTRO NETO 2009; PERES 2010; DAS SARMA 2011). In two dimensions, the

conductivity at charge neutrality equates the unit of quantum conductance up to some numerical factor,

$$\sigma_0 = \frac{s e^2}{\pi h}. \quad (1.53)$$

For a clean infinitely wide strip of graphene, the integer $s = 4$ accounts for the spin and valley degeneracy (TWORZYDŁO 2006). No propagating states engage in conduction at the Fermi level, so that only the contribution of evanescent modes can explain the non-vanishing of σ_0 . This is surprising, since the transmission probability of an evanescent mode decays exponentially with the system size in the thermodynamic limit. But for two-dimensional massless fermions specifically, the summation of all these exponentially small transmission probabilities yields a conductance G proportional to the aspect ratio $W/L \gg 1$ in the limit of infinite width W and fixed length L , which justifies the expression (1.53) for the conductivity $\sigma_0 = GL/W$. Although experimental data spread significantly because of the various probe geometries and sample heterogeneity, most measurements fall closer to $4e^2/h$, in disagreement with Eq. (1.53) (GEIM 2007). The quantitative discrepancy may originate from the presence of charged impurities or electron-electron interactions.

In addition, the ratio of noise power and mean current, measured by the Fano factor, takes the same value $F = 1/3$ as for disordered metals, even though clean graphene exhibits ballistic, not diffusive transport. Both the conductivity and the Fano factor display quantum oscillations upon doping, as more and more propagating modes contribute to charge carriage across the strip. This shot noise is sensitive to the boundary condition. The transverse momentum of mode n reads indeed $q_n = (2n + 1)\pi/2W$ for a smooth edge, but $q_n = n\pi/W$ for a metallic armchair edge, which leads to a phase difference $\pi L/2W$ in the quantum oscillations. Fig. 1.11(a) and 1.11(b) show respectively the conductivity and Fano factor as a function of the chemical potential, for those two boundary conditions.

Interestingly, Louvet et al. have recently shown using a low-energy model of three-band semimetals that the existence of a minimal conductivity also originates from topological

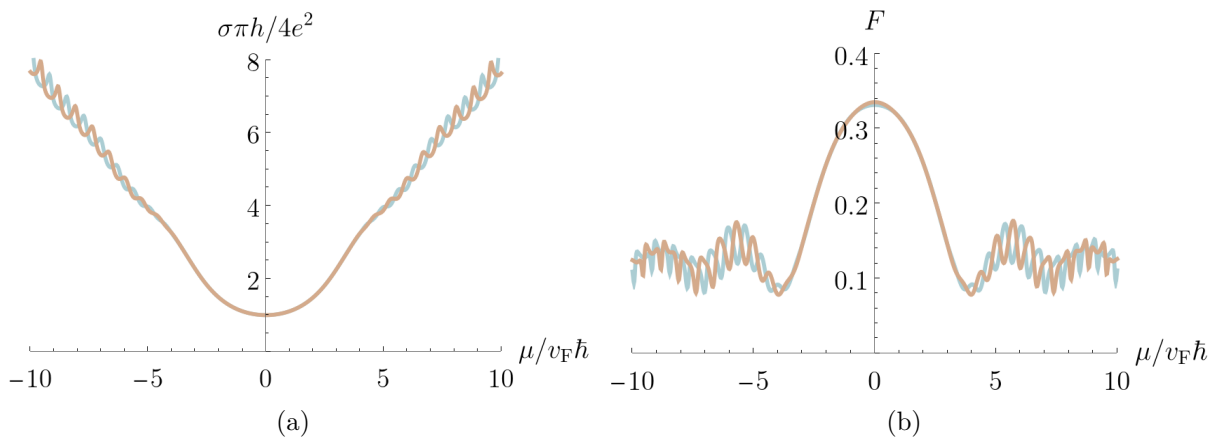


Figure 1.11 | The conductivity σ and Fano factor F of clean graphene show shot noise oscillations as a function of the chemical potential μ . The phase of the: smooth edge (in blue) or armchair edge (in brown). Here we set the aspect ratio to $W/L = 4$ (a) The conductivity tends to the universal value $4e^2/\pi h$ at charge neutrality $\mu = 0$, and increases roughly in a linear fashion at high μ . (b) The Fano factor tends to $1/3$ at charge neutrality for an infinitely wide strip, the same value as for disordered metals.

considerations (LOUVET 2015). Because of topological constraints, the transverse conductivity obeys an unusual half-integer quantisation rule in graphene under a magnetic field, a phenomenon known as the half-integer quantum Hall effect. Weyl semimetals also experience a Hall effect even in absence of a magnetic field, which can be termed as anomalous. Though these effects will not be the focus of this thesis, we will briefly discuss them for the sake of completeness. In addition, in presence of both an electric and a magnetic field, Weyl semimetals manifest a positive magneto-conductivity as a result of the chiral anomaly. By presenting the chiral anomaly, we will make contact with field theories, which constitute the framework of this thesis.

The half-integer quantum Hall effect — The quantum Hall effect also differs between relativistic and non-relativistic particles. Quantum Hall effects refer to the quantisation of the transverse conductivity that occurs in some materials under specific conditions. In two-dimensional gapless phases like graphene, the Hall effect appears under strong out-of-plane magnetic fields. The conductivity plateaus arise at half-integer fillings instead of integer fillings because of the relativistic nature of massless Dirac fermions. In two-dimensional Chern insulators and three dimensional relativistic semimetals, a distinct effect occurs in absence of any magnetic field: the anomalous Hall effect.

In two-dimensional gapless phases, whether relativistic or not, the transverse conductivity per Landau level

$$\sigma_{xy} = \frac{e^2}{h} \nu \quad (1.54)$$

is quantised through some yet-unspecified parameter ν . The existence of such quantisation is remarkable, because quantum mechanics usually leads to the quantisation of microscopic, not macroscopic observables, and Eq. (1.54) persists in presence of electron-electron interactions and disorder (TONG 2016) – in fact, the quantum Hall effect requires disorder for large conductivity plateaus to be visible!

The plateaus first observed in non-relativistic phases follow Eq. (1.54) with integer values of ν (KLITZING 1980). Physically, the plateaus appear when charge carriers completely fill a number ν of Landau levels, i.e. for an electron density $n = \nu B / \Phi_0$, where B is the magnetic field and $\Phi_0 = h/e$ is the flux quantum. In relativistic materials, the Landau levels can have both positive and negative energies, and each valley hosts an extra chiral Landau level, which is half-filled at charge neutrality. This leads to an odd quantisation of the transverse conductivity, with half-integer values $\nu = \pm 1/2, \pm 3/2$, etc., as K. Novoselov and A. Geim showed in 2006 (Fig. 1.12(a)).

The anomalous quantum Hall effect — In Weyl semimetals, the transverse conductivity remains non-zero in absence of a magnetic field. To show this, we invoke the same argument we used to prove the existence of Fermi arcs in Sec. 1.3.2. Let us consider one pair of nodes of opposite chiralities located at the momenta $\pm \mathbf{b}$, with $\mathbf{b} = b \mathbf{e}_z$ aligned along the z -axis. For a fixed component k_z of the longitudinal momentum in the range $[-b, b]$, the low-energy Hamiltonian $H(k_x, k_y, k_z = \text{cte})$ describes a two-dimensional Chern insulator, whose chiral edge mode contributes a term e^2/h to the transverse conductivity (YANG 2011). Integrating over the range $[-b, b]$, we find

$$\sigma_{xy} = \frac{e^2}{\pi h} b. \quad (1.55)$$

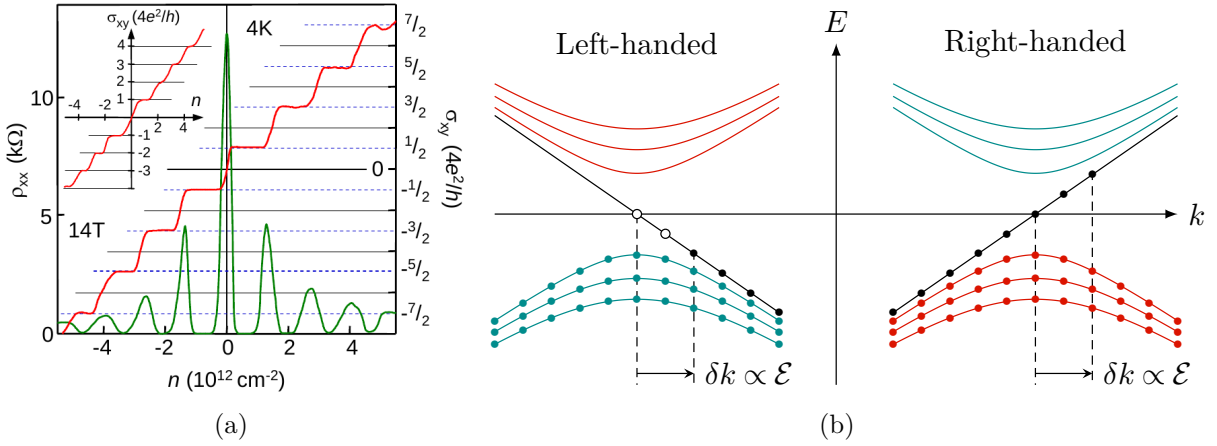


Figure 1.12 | Transport in relativistic semimetals under a magnetic field. (a) In disordered graphene the Hall effect leads to the plateaus of the Hall conductivity σ_{xy} appear at half-integer fillings (NOVOSELOV 2004). Concomitantly, the longitudinal resistivity ρ_{xx} vanishes. Inset: Hall conductivity in the integer Hall effect, characteristic of non-relativistic phases. (b) The zeroth Landau levels of relativistic fermions are chiral: the sign of the slope in momentum space depends on the fermions' handedness (BURKOV 2015). In three-dimensional semimetals, an additional parallel electric field \mathcal{E} pumps particles from one node to the node of opposite chirality, thus giving rise to a chiral current.

Real materials host many pairs of Weyl nodes, whose positions \mathbf{k}_i and chiralities χ_i are constrained by lattice symmetries. To generalise Eq. (1.55), the node separation $2b$ must be replaced by the ‘chiral charge centre’ $\sum_i \chi_i \mathbf{k}_i$. Unfortunately, lattice symmetries (such as the cubic symmetry in pyrochlore iridates) often pin the chiral charge centre at the origin, so that the transverse conductivity vanishes unless some uniaxial strain favours a special direction. Weyl semimetals thus exhibit a pressure-induced anomalous Hall effect, with a linear pressure dependence of the transverse conductivity (YANG 2011).

The chiral anomaly — Striking properties emerge in presence of both a magnetic and an electric field. One is the chiral anomaly, which appears only in odd dimensions (ARMITAGE 2018). In a Weyl semimetal subject to a magnetic field \mathbf{B} , applying an electric field \mathcal{E} pumps electrons between nodes of opposite chirality at a rate (NIELSEN 1981; SON 2013)

$$\frac{dn_\chi}{dt} = \chi \frac{e^2}{h^2} \mathcal{E} \cdot \mathbf{B}, \quad (1.56)$$

where n_χ denotes the population of the node with chirality $\chi = \pm 1$. Thus, even uniform and constant fields generate a valley imbalance. The origin of this pumping lies in the chiral nature of the zeroth Landau level, as sketched in Fig. 1.12(b): Weyl particles near charge neutrality propagate either along or opposite to the field direction according to their chirality (ARMITAGE 2018). An electric field that points in the same direction as the magnetic field pushes away the particles along the chiral Landau level, thus depopulating one node to the benefit of the other. In practice, a steady state settles when intervalley scattering, with a characteristic time τ_τ , compensates the pumping current.

The resulting DC chiral current is proportional to the magnetic field B and the driving force $\mathcal{E} \cdot \mathbf{B}$. Hence, the conductivity acquires an anisotropic contribution which

is quadratic in the magnetic field, and whose value is maximal along the magnetic field direction (BURKOV 2015; SON 2013):

$$\sigma(B) = \sigma_0 + \frac{e^4 B^2 \tau_F}{4\pi^4 \rho_F}, \quad (1.57)$$

where ρ_F is the DoS at the Fermi level. This enhancement of conduction, known as the positive magneto-conductivity, contrasts strongly with metals and conventional semiconductors, which usually present a small negative magneto-conductivity insensitive to the magnetic field's direction (ARMITAGE 2018). The positive magneto-conductivity also manifests itself in Dirac semimetals, because a magnetic field can lift the valley degeneracy of a Dirac node and pull the resulting Weyl cones apart. It thus represents one of most compelling signatures of relativistic physics. Experiments confirmed the positive magneto-conductivity in both Weyl (TaAs, TaP, NbAs, NbP) and Dirac (Na₃Bi, Cd₃As₂, ZrTe₅) semimetals.

The chiral anomaly originally referred to discrepancies in the decay rate of the neutral pion π^0 . The observed rate of the process $\pi^0 \rightarrow \gamma + \gamma$, in which a neutral pion decays into two photons, was much smaller than the one first computed within quantum electrodynamics. Quantum field theorists later understood that one-loop processes which were thought to vanish on symmetry grounds actually contribute (ADLER 1969; BELL 1969). Indeed, the conservation of the axial current $J_5^\mu = \bar{\Psi} \gamma^\mu \gamma_5 \Psi$, which follows from Noether's theorem in classical electrodynamics, does not survive quantum corrections.

To see this, let us consider the path integral formalism of quantum electrodynamics. The partition function \mathcal{Z} lies at the heart of field theories, since it enables to generate expectation values of all kinds of operators (including current operators and their derivatives, where lies our interest). Within the path integral formalism, it can be written as an integral over the Dirac fields of the Feynman weight, namely

$$\mathcal{Z} = \int D\Psi D\bar{\Psi} e^{iS/\hbar}, \quad (1.58)$$

where S is the action of the theory (here quantum electrodynamics). Assuming that the theory satisfies the local U(1) axial symmetry, the gauge transformation of the fields

$$\Psi \mapsto e^{-i\alpha\gamma_5} \Psi, \quad \bar{\Psi} \mapsto \bar{\Psi} e^{-i\alpha\gamma_5}, \quad (1.59)$$

where $\alpha(x)$ depends on the space-time variable x , leaves the path integral \mathcal{Z} invariant. Usually, the invariance of the path integral implies the invariance of the action; and under the transformation of Eq. (1.59), the action acquires the additional part

$$S_5 = - \int d^4x \alpha(x) \partial_\mu J_5^\mu(x). \quad (1.60)$$

This would suggest that $\partial_\mu J_5^\mu = 0$ in order to ensure the axial symmetry, yielding the conservation of the axial current. But unexpectedly, the path integral gets an extra contribution from the measure $D\Psi D\bar{\Psi}$. After some algebra, one can show that transforming the measure as per Eq. (1.59) amounts to add an additional term to the action,

$$S_{\text{meas}} = - \frac{e^2}{16\pi^2 \hbar^2 c} \epsilon^{\mu\nu\rho\sigma} \int d^4x F_{\mu\nu}(x) F_{\rho\sigma}(x), \quad (1.61)$$

where $F_{\mu\nu}$ denotes the electromagnetic field tensor. Since the sum $S_{\text{meas}} + S_5$ must vanish, the divergence of the axial current actually reads (SREDNICKI 2007)

$$\partial_\mu J_5^\mu = -\frac{e^2}{16\pi^2\hbar^2 c} \epsilon^{\mu\nu\rho\sigma} F_{\mu\nu} F_{\rho\sigma}, \quad (1.62)$$

a result known as the Adler-Bardeen theorem. For homogeneous and stationary magnetic and electric fields, Eq. (1.62) reduces indeed to the chiral pumping formula of Eq. (1.56).

1.4 What this thesis is about

The electronic properties discussed in Sec. 1.3.2 and Sec. 1.3.3 originate from the relativistic behaviour of the low-energy excitations in perfectly clean materials. We have seen that topology ensures a certain robustness of the Weyl nodes, to the extent that linear crossing points cannot disappear without merging, because they carry a topological charge. A natural question then arises, as to whether this topological protection preserves the relativistic behaviour under perturbations, beyond electronic band theory. Our works cover two main types of perturbation.

One is disorder, which when strong enough affects both bulk and surface properties of relativistic semimetals. In three-dimensional phases (Weyl and Dirac semimetals), disorder induces a quantum phase transition towards a diffusive metallic phase in the bulk, which possesses a non-zero DoS (Chapter 2 and Chapter 3 of Part I). The surface states of relativistic semimetals also bear signatures of this semimetal-metal transition (Chapter 4 of Part I). We discuss the types of defects encountered in relativistic semimetals and the stability of the crossing point under disorder in Sec. 1.4.1.

Another is electron-electron interactions, which can generate correlated phases when the kinetic energy becomes comparable to the interaction energy, for instance in the presence of flat bands. A seminal example of such phases is twisted bilayer graphene (TBG) (Part II). In Sec. 1.4.2, we show that electron-electron interactions play a minor role in Weyl or Dirac semimetals and graphene, unlike in TBG.

1.4.1 Disorder

In physics, the term *disorder* denotes the state of a system which possess fewer symmetries than other states of the same system often viewed as ‘ideal’. In condensed matter physics, disorder typically takes the form of crystalline defects. These imperfections often smear the electronic properties of relativistic semimetals, leading to quantitative changes, but can sometimes affect their qualitative properties. Disorder usually modifies the transport phenomena discussed in Sec. 1.3.3, but we will focus on equilibrium properties in the rest of this thesis – especially the DoS.

Crystalline defects — Electronic band theory rests on the assumption that conduction electrons move in the background potential of a perfectly periodic lattice of cations. This pristine crystalline state is often frustrated, though. Real solids contain some amount of impurities, and even with a pure chemical composition, atoms do not perfectly arrange on lattice sites, because, for instance, the material keeps some memory of the solidification. Any discrepancy to the crystalline arrangement is called a *defect*; the presence of a

macroscopic number of defects induces disorder. According to the dimensionality of a defect, one distinguishes between point defects on one hand, and extended (line and plane) defects on the other hand (KITTEL 1971).

- Point defects spoil the crystalline arrangement only near one or few sites. These can be vacancies (empty sites where an atom should be), insertion atoms (atoms in excess that fit in small interstices), or chemical impurities (unexpected chemical elements), as shown in Fig. 1.13(a).

Vacancies appear when the thermal motion excites atoms out of some lattice sites. The ejected atoms either deposit on the surface (Schottky defects), or jump to an interstitial site (Frenkel defects), thus leading to an insertion atom. A metal has a typical activation energy $E_a \simeq 1$ eV: just below the fusion temperature (roughly $T \simeq 10^3$ K), the fraction of vacancies reaches values of $e^{-E_a/k_B T} \simeq 10^{-5}$.

Chemical impurities are not thermally activated. Although they sometimes affect the sample quality, they are often beneficial; in fact, they are widely used to enhance the electrical conductivity – a process known as doping – in semiconductors, which enter the fabrication of all our modern electronic devices. They can also improve the mechanical resistance of building materials. Steel, for example, is crafted by adding carbon impurities to iron.

- Extended defects affect lines or planes of atoms. Linear defects induce either positional (dislocation) or orientational (disclination) disorder. Examples include edges dislocations, where an abrupt change in the in-plane atomic arrangement introduces irregularities in the crystalline structure, as shown in Fig. 1.13(b). Planar defects consist of stacking faults, i.e. disruptions of the stacking sequence over a few layers. All these extended defects settle at random lattice sites and orient themselves randomly. They can be thermally activated.

Let us mention another type of defect specific to two-dimensional crystals: ripples. These defects echo with a thorny debate surrounding graphene before its experimental discovery, as to whether such planar crystals could exist. Wielding the Mermin-Wagner

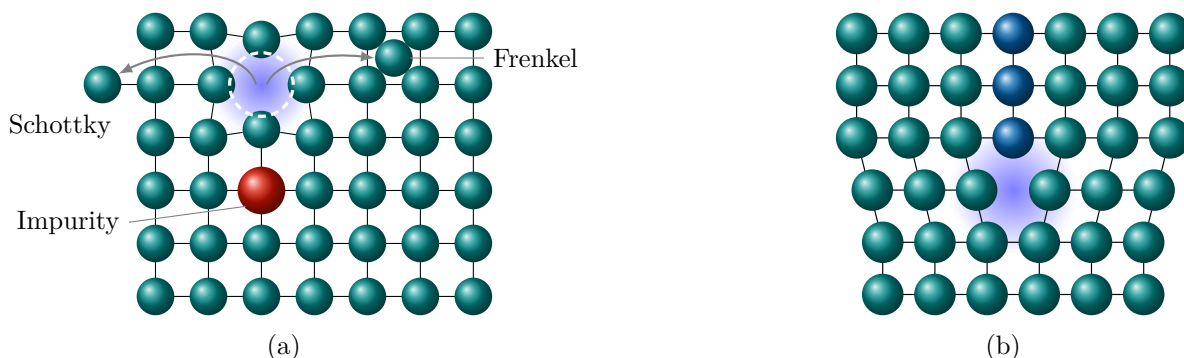


Figure 1.13 | Lattice defects in three-dimensional crystals. (a) Point defects consist of: vacancies (blueish region), left when an atom either exits a lattice site and deposits on the surface (Schottky defect), or jumps to an interstitial site (Frenkel defect); and chemical impurities, when an unexpected chemical element substitute some atoms of the lattice. (b) Crystals can also host linear defects, such as edge dislocations (represented here).

theorem as proof, which states that thermal fluctuations destroy long-range order in two dimensions and below, many thought graphene sheets to be unstable, and that they would fold into fullerene molecules or carbon nanotubes. This argument breaks down because two-dimensional crystals are not perfectly planar; they tend to bend out of the plane to form rippled membranes. Quasi-particles in graphene thus propagate in a curved space, which brings interesting parallels with quantum gravity (VOZMEDIANO 2008). The rippling of graphene sheets allows for the propagation of out-of-plane vibrations of the honeycomb lattice (flexural modes). Due to random fluctuations of the bending rigidity, out-of-plane phonons scatter effectively on electrons (GORNYI 2015).

Stability of the crossing point — Disorder usually smears the properties of crystals, leading to quantitative differences at the very least, or transitions towards new phases of matter in the most dramatic cases. A natural tool to probe the stability of the relativistic semimetal phase is the DoS, which vanishes at the nodal level, unlike metals where a large number of states populate the Fermi level. Since no propagating modes engage in electrical conduction at zero temperature, three-dimensional relativistic semimetals are insulating. But what about dirty semimetals? Can a new phase of matter set in for sufficiently strong disorder? Quantum phase transitions are common in electronic phases. A remarkable example of how disorder can alter the properties of pristine materials is Anderson’s localisation.

P. W. Anderson showed indeed that destructive quantum interferences of particles which propagate in a random potential can localise them for strong enough disorder (ANDERSON 1958). Anderson’s original approach rests upon a tight-binding formalism with nearest neighbour hopping and random on-site energies. The term ‘Anderson transition’ now applies to a larger variety of metal-insulator transitions where electrons become localised in some region of the energy landscape, such as in quantum Hall plateaus (HUCKESTEIN 1995).

Later, E. Fradkin established that disorder induces a transition in relativistic semimetals towards a metallic phase (FRADKIN 1986). Similar non-Anderson transitions occur in all materials which host a power-law dispersion relation $E \propto q^\alpha$ near a band edge or touching point, provided the dimension d exceeds 2α (SYZRANOV 2018). This includes, besides three-dimensional relativistic semimetals, high-dimensional gapless semiconductors, quantum kicked rotors, and arrays of trapped ions.

This thesis brings relativistic semimetals in the spotlight. We will thus restrict the terminology and refer to the ‘semimetal-metal’ transition for Weyl and Dirac semimetals, and to ‘non-Anderson’ transitions when mentioning other high-dimensional materials as a side note. Yet, these two transitions share similar features, and some qualitative results that we will present for the semimetal-metal transition extend to non-Anderson transitions.

1.4.2 Interactions

Interactions in graphene, Weyl and Dirac semimetals — Electronic band theory deals with the single-particle physics, but in real materials, electrons interact with each other, either through direct Coulomb repulsion or through indirect lattice-mediated interactions. Due to the point-like nature of the Fermi surface, electrons interact differently in relativistic semimetals than in Fermi liquids, which possess an extended Fermi surface. Electron-electron interactions lead to two kinds of excitations of the Fermi sea: electron-hole

pairs and collective modes known as plasmons (CASTRO NETO 2009).

In undoped relativistic semimetals, plasmons do not exist because their dispersion relation merges with the electron-hole continuum. In addition, the formation of electron-hole pairs costs a lot of energy, so that we expect interaction effects to be small. On the other hand, the absence of eigenstates at the Fermi level prevents screening and may protect the long-ranged nature of the Coulomb repulsion. Besides, the effective fine structure constant of graphene is much larger than in quantum electrodynamics, about $\alpha_f \simeq 1$. These arguments suggest that on the contrary, electron-electron interaction is strong in relativistic semimetals. Yet, renormalisation group analyses show that Coulomb repulsion is marginally irrelevant in graphene and irrelevant in Weyl and Dirac semimetals, so that quantum corrections highly suppress the strength of Coulomb repulsion (GONZÁLEZ 1994; VOZMEDIANO 2011). Therefore, many-body effects have only quantitative effects in relativistic semimetals.

Twisted bilayer graphene — To find interesting physics, one has to look for electronic systems where the kinetic energy is quenched. A prominent example is TBG, which has become very fashionable since the discovery in 2018 of Mott insulating and unconventional superconducting phases at some special ‘magic’ angles (CAO 2018a; CAO 2018b).

TBG consists in the overlay of two graphene sheets with a relative twist of the crystalline axes. Unlike commensurate stacking arrangements, bilayers with a twist form incommensurate packings. Yet, the interference between the two mismatched lattices give rise to a so-called moiré pattern, which defines a new structural length scale hundreds of times larger than the inter-atomic distance. Interlayer tunnelling, which is spatially modulated by the moiré pattern, tends to suppress the Fermi velocity of the Dirac fermions and flatten the energy bands. At special values of the twist angle, dubbed ‘magic’ angles, the kinetic energy is quenched so much so that interactions dominate the electron dynamics. The quenching of the kinetic energy is specific to the moiré physics, and arises only in few-layer systems bound together by weak Van der Waals interactions. Although the electronic properties of TBG differ from that of relativistic semimetals, the Dirac physics serves as the starting point of the low-energy description. The difficult task then consists in including interlayer hopping and many-body effects in the effective theory, which we can treat with a renormalisation group approach.

1.5 The renormalisation group

Throughout this thesis, we will extensively use the renormalisation group technique to investigate the large-scale behaviour of low-energy effective theories in presence of either disorder or interactions. The concept of renormalisation emerged in the early developments of quantum electrodynamics, as an attempt to make sense of the short-distance divergences that arise in correlation functions. We will first present the basic ideas of renormalisation, starting from its development in quantum field theory and going on to its later use in critical phenomena. We will briefly discuss the real-space renormalisation group in spin systems, and then exemplify its momentum-space representation on a theory of interacting fermions known as the Gross-Neveu model. We will then implement the renormalisation group using a perturbative expansion near the lower critical dimension.

1.5.1 Renormalisation in spirit

The problem of infinities — The theory of quantum electrodynamics aims at describing the interaction of light and charged matter. The nascent quantum electrodynamics of the early 1930s developed along two research directions (SCHWEBER 2020). In the first research tradition, Dirac’s hole theory, individual particles constitute the fundamental objects of quantum mechanics. The sentient particles which physicists produce and detect originate from excitations of a vacuum where all negative-energy states are filled: the Dirac sea. The promotion to a positive-energy state creates a particle, e.g. an electron, and leaves a vacancy in the Dirac sea known as a hole, which physicists perceive as an antiparticle, e.g. a positron. This viewpoint progressively lost support after the 1940s, although the concept of holes made its way into condensed matter physics. In the other research tradition, developed by W. Pauli and W. Heisenberg, the fundamental objects consist in quantum fields instead of individual particles, which result from elementary excitations of the fields.

Both descriptions – Dirac’s hole theory and quantum field theory – describe the quantised electromagnetic field and its coupling to fermions. The electromagnetic field couples to electrons, of charge e , with a relative strength

$$\alpha_f = \frac{e^2}{4\pi\hbar c}, \quad (1.63)$$

known for historical reasons as the fine structure constant. The hole and field theories predicted with equally reasonable accuracy the cross-sections of electron-positron pair creation, Compton scattering, and other elementary processes, at the lowest order in the coupling strength. Yet, both theories faced huge troubles when trying to incorporate higher-order corrections, in the form of divergences, which appear when particles scatter on virtual photons of arbitrarily large momenta. These infinities seemed to have a profound meaning and seriously impeded the progress of quantum field theory until the first half of the 1940s. The solution came between 1943 and 1950 under the pen of F. Dyson, J. Schwinger, S. Tomonaga, and R. Feynman, among others. By reparametrising the mass m and charge e of the electron, they managed to absorb the divergences to extract sensible, quantitative predictions – a procedure called *renormalisation* (TOMONAGA 1946; SCHWINGER 1948; DYSON 1949). In this procedure, the actual electron mass m , i.e. the one which enters in all physical processes, differs from the mass parameter m_0 of the free theory. The evaluation of the discrepancy $\delta m = m - m_0$ can be organised in a perturbative expansion in the coupling strength. In particular, the first order leads to a logarithmic divergence

$$\delta m = \frac{3\alpha_f m}{2\pi} \ln\left(\frac{\hbar\Lambda}{mc}\right). \quad (1.64)$$

The ultraviolet cut-off Λ represents the maximal momentum of virtual photons; it acts as an ancillary variable to regularise the divergent theory and subtract infinities. The electron charge e had to be similarly reparametrised. Thanks to his original insight, R. Feynman then endowed renormalisation with a powerful diagrammatic scheme to effectively compute the corrections to the mass and charge order by order in the coupling strength (FEYNMAN 1949a; FEYNMAN 1949b; FEYNMAN 1950). All subsequent observations – the hyperfine structure of hydrogen, the Lamb shift, the magnetic moment of the electron – agreed beautifully with the predictions of the renormalised theory of quantum electrodynamics.

Renormalisation in critical phenomena — The idea of renormalisation progressively made its way to the study of continuous phase transitions (ZINN-JUSTIN 2012; CARDY 1996; GOLDENFELD 2018). First proposed by L. Kadanoff and later developed by K. Wilson, the *renormalisation group* extends the recipe of renormalisation in quantum electrodynamics to the scaling theory of critical phenomena. By adapting the renormalisation procedure to critical phenomena, it became clear that renormalised quantum field theories, much like the statistical field theories used to model phase transitions, intrinsically depend on an energy scale. In addition, field theories have to include a maximum energy scale to be well-defined. In quantum field theories, this scale is given by the ultraviolet cut-off Λ of Eq. (1.64). Effective theories of critical systems, on the other hand, naturally include a momentum cut-off; this is the inverse of the lattice constant a , or any microscopic length scale. Yet, nothing forbids to define such effective theories at an *arbitrary* length scale, intermediate between the microscopic limit $a = \Lambda^{-1}$ and the macroscopic limit set by the system size L . Similarly, the quantum field theories of the now-celebrated standard model could well be approximations of a more fundamental theory at the energies accessible to experiments and usual observations (WEINBERG 1995).

Before explaining what the renormalisation group is, we should say a few words about what it is *not*, and stress how unfortunate this terminology now seems. First, the renormalisation group refers to a set of transformations which act on the parameters of the theory (coupling strength α , mass m , etc.) upon rescaling the length. In critical phenomena, the multiplication of two such transformations also belongs to this set, but only up to a certain maximum length (the size of the system, or any large scale that cuts the renormalisation flow). Besides, these transformations do not admit an inverse, because much information about the microscopic degrees of freedom is lost under coarse graining, and the lattice structure defines a minimal length scale to the problem anyway. Hence, the mathematical structure of the renormalisation procedure is that of a *semi-group*, rather than a group. Second, critical phenomena face no infinity issues as quantum field theory, since they incorporate a physical cut-off from the beginning through the lattice constant or the limit of validity of the low-energy theory. ‘Renormalisation’ in critical phenomena denotes the way certain parameters behave under rescaling, regardless of any perturbative scheme. The renormalisation group does not require any field theory either; it can apply to any Hamiltonian that describes a phase transition in a thermodynamic system. Finally, there is not *one*, but many renormalisation group procedures. The same ideas can indeed be implemented in several ways, according to the nature of the degrees of freedom (discrete lattice variables or continuous fields), the treatment of the couplings (perturbative or exact) and the technical details (regularisation and subtraction).

Real-space renormalisation — Kadanoff’s motivation for devising the renormalisation group was to understand the origin of scaling laws near critical points and the universality of critical exponents (KADANOFF 1966). The mean-field approximation, which was the standard approach at the time, was indeed powerless to predict the critical exponents correctly. A canonical example of critical phenomena is the famous Ising model. The Ising model describes a ferromagnetic-paramagnetic second-order phase transition in a system of classical spins one-half $s_i = \pm 1$ placed on a lattice. The spins couple with nearest neighbours with a homogeneous strength J , and interact with an external magnetic field B ;

the corresponding Hamiltonian is of the form

$$H(\{s_i\}; B) = -J \sum_{\langle i, j \rangle} s_i s_j - B \sum_i s_i, \quad (1.65)$$

where $\langle i, j \rangle$ represents a sum over distinct pairs of nearest neighbours.

The Hamiltonian (1.65) describes the system at the microscopic level, i.e. at a length scale about the lattice constant a . The macroscopic properties are encoded in the free energy $W(B) = -\log \mathcal{Z}(B)$, where the partition function \mathcal{Z} follows from a sum over all spin configurations

$$\mathcal{Z}(B) = \sum_{\{s_i\}} e^{-H(\{s_i\}; B)}, \quad (1.66)$$

in natural units where $k_B T = 1$. The free energy describes the collection of spins under a constant external field. To describe the same system at constant magnetisation, the appropriate thermodynamic potential follows from the free energy through a Legendre transformation, which gives the macroscopic effective Hamiltonian

$$\Gamma(\{S_i\}) = -W(B) - B \sum_i S_i, \quad (1.67)$$

where $S_i = \langle s_i \rangle$ denotes the average spin (LE BELLAC 2002). In the mean-field approximation, the macroscopic effective Hamiltonian Γ assumes the same functional form as the microscopic Hamiltonian (1.65), with the same exact couplings J and B . The mean-field approach treats indeed all spins as independent magnetic moments coupled to the background magnetic field created by all other spins, so that the correlation length ξ essentially reduces to the lattice constant a . In vicinity of the critical point, fluctuations prevail, the correlation length diverges, and Γ deviates radically from Eq. (1.65). The goal of the renormalisation procedure is to keep track of the effective Hamiltonian Γ as we increase the correlation length ξ , or equivalently as we vary the intermediate length scale at which we define the effective theory.

The early formulation of the renormalisation group proposed by L. Kadanoff relies on a coarse-graining procedure in real space. Let $\ell > 1$ be the corresponding scaling factor. Since the spins correlate over a large distance near the critical point, one can see blocks of spins of size $\ell a \ll \xi$ as giant spins S_i^ℓ with a well-defined up or down direction (the one favoured by most individual spins within the blocks). Neighbour block spins couple with a new strength J_ℓ and perceive a new external field B_ℓ , both of which function of the scaling factor ℓ . If there were no other coupling terms, the effective Hamiltonian $\Gamma_\ell(\{S_i^\ell\}; J_\ell, B_\ell)$ would describe an Ising system with a new correlation length $\xi_\ell = \xi/\ell$ (measured in units of the new lattice spacing). In reality, the coarse-graining procedure generates coupling terms which were absent in the microscopic Hamiltonian of Eq. (1.65), and which must sometimes be included to correctly describe the system; fortunately, the procedure generates only irrelevant operators in the Ising model, in the sense that the corresponding coupling strengths vanish in the limit $\ell \rightarrow \infty$.

Since the new correlation length ξ_ℓ is smaller than ξ , the coarse-graining procedure pushes the system further away from criticality, except exactly at the phase transition where $\xi = \infty$. It formally defines a transformation R_ℓ on the set of coupling constants,

$$R_\ell : K = (J, B, \dots) \mapsto K_\ell = (J_\ell, B_\ell, \dots). \quad (1.68)$$

By iterating transformation (1.68), which amounts to tune ℓ to larger and larger values, K_ℓ traces out a trajectory in the space of coupling constants, which depends on the initial set of coupling constants K . Such trajectory is known as a renormalisation group *flow*. In the thermodynamic limit, the infinite repetition of transformation (1.68) leads to non-analytic behaviours in the free energy and its derivatives: there lies the very origin of phase transitions. The coupling constants then reach a fixed point of Eq. (1.68), denoted as $K^* = R_\infty(K)$, meaning that $K^* = R_\ell(K^*)$ for any scaling factor ℓ . Similarly, the correlation length satisfies $\xi^*/\ell = \xi^*$ at the fixed point for any ℓ , which leads to the two following possibilities.

- When $\xi^* = \infty$, the fixed point is *critical* (C), as sketched in Fig. 1.14. Within linear theory, at least one eigendirection of the flow is associated to a positive eigenvalue, which means that the coupling constants flows away from the critical point along this direction. This eigenvalue, which dictates the critical scaling laws, is insensitive to the microscopic values and nature of the coupling constants; this robustness is at the origin of universality.
- When $\xi^* = 0$, the fixed point is *trivial*. If all eigendirections of the flow are associated to a negative eigenvalue, except the one associated to an external field, the fixed point is stable. Its basin of attraction delineates a phase in the space of coupling constants. The Ising model possesses two stable points, one for the paramagnetic phase (P), the other for the ferromagnetic phase (F), as sketched in Fig. 1.14. In presence of a magnetic field, the coupling constants of the Ising model flow towards sinks (S) at infinite B , which describe a magnetised spin system. It may happen that all eigendirections are associated to a negative eigenvalue, in which case the fixed point is a source. Source points typically appear at the crossing of several critical lines.

Although Kadanoff's block-spin approach to renormalisation is correct in spirit, it does not provide a systematic way to compute the critical exponents, and miss the strong

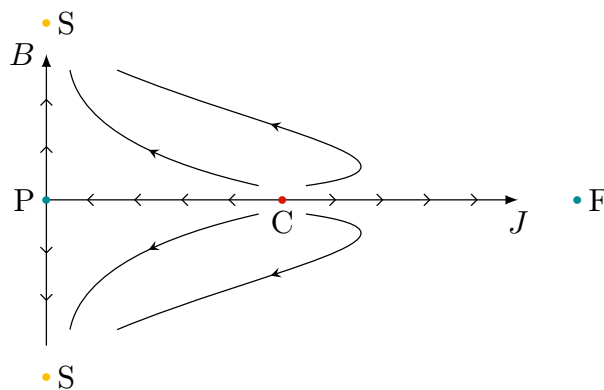


Figure 1.14 | Flow diagram of the Ising model in the (J, B) plane, with J coupling strength and B the magnetic field, in units of $k_B T$. The arrows indicate renormalisation flows (J_ℓ, B_ℓ) with increasing scaling factor $\ell \rightarrow \infty$ from particular microscopic values of the coupling constants. The critical fixed point $C = (J^*, 0)$ controls the ferromagnet-paramagnet transition. The stable fixed point $P = (0, 0)$ characterises the high-temperature paramagnetic phase, while $F = (\infty, 0)$ characterises the low-temperature ferromagnetic phase. The sinks $S(0, \pm\infty)$ describe the spin system magnetised by an external field.

analogy with the renormalisation recipe of quantum field theory. In the following, we review the current understanding of the renormalisation group developed in the seminal works of K. Wilson (WILSON 1971b; WILSON 1971a; WILSON 1972; WILSON 1974), using as a guiding thread a fermionic field theory with quartic interaction known as the Gross-Neveu model.

The Gross-Neveu model — The similarity with the renormalisation procedure in quantum field theory becomes clearer when the Hamiltonian depends on field variables instead of spins on a lattice. This often occurs in condensed matter, either when continuum space can replace the lattice structure under a sufficiently large coarse graining, or when the variables themselves depend continuously on position, such as electronic wave functions. In the Ising model, the coarse-grained spins can be described by a scalar field φ which self-interacts through a quartic potential. Hence, the Ising model maps to the φ^4 model with $O(N)$ symmetry in the special case $N = 1$. Like in any classical transition, thermal fluctuations trigger the ferromagnetic order in the Ising model. On the contrary, quantum fluctuations spontaneously break the symmetry of the zero-temperature ground state in quantum phase transitions. An example of a quantum field theory with symmetry breaking is the Gross-Neveu model.

The Gross-Neveu model describes N flavours of massless Dirac fermions, encoded by two fields $\psi = \{\psi_a, a = 1, \dots, N\}$ and its adjoint $\bar{\psi} = \{\bar{\psi}_a, a = 1, \dots, N\}$, which interact via a quartic scalar potential (GROSS 1974; ZINN-JUSTIN 2002). In the path integral formulation of quantum field theory – which we will use extensively –, these fermionic fields obey a complex Grassmann algebra, whose properties are recalled in Appendix A. The action of the Gross-Neveu model reads

$$S = \int d^d x \left[\bar{\psi} (-i\gamma^\mu \partial_\mu) \psi + \frac{g}{2} (\bar{\psi} \psi)^2 \right] \quad (1.69)$$

in d space-time dimensions, where for brevity the field dependence on the space-time variable $x = (\mathbf{r}, t)$ is implicit. The parameter $g > 0$ stands for the coupling strength of the quartic interaction. From Eq. (1.69), we see that the N flavours behave as independent copies of the same Dirac fermion. The decoupling of all flavours endows the Gross-Neveu model with a global $U(N)$ symmetry. Indeed, for any unitary matrix $R \in U(N)$, the transformation

$$\psi_a \mapsto (R\psi)_a = \sum_b R_{ab} \psi_b, \quad \bar{\psi}_a \mapsto (\bar{\psi} R^{-1})_a = \sum_b (R^{-1})_{ab} \bar{\psi}_b \quad (1.70)$$

leaves Eq. (1.69) invariant. The Gross-Neveu, which is renormalisable near $d = 2$ dimensions, originally served as $(1 + 1)$ -dimensional toy model for quantum chromodynamics, given the similar properties of these two theories. In particular, the Gross-Neveu model features asymptotic freedom and dynamical mass generation – a phenomenon at the basis of the electroweak unification (ROSENSTEIN 1991) –, while being simpler to treat than quantum chromodynamics. Indeed, the absence of any mass term in action (1.69) ensures its invariance under either the discrete chiral symmetry⁴

$$\psi \mapsto \gamma_5 \psi, \quad \bar{\psi} \mapsto -\bar{\psi} \gamma_5, \quad (1.71)$$

⁴In $(3 + 1)$ dimensions, the chiral symmetry becomes a continuous $U(1)$ symmetry; the dynamical mass generation is then associated with a Goldstone boson, identified as the idealised pion of quantum electrodynamics.

in even dimension, or inversion $\mathbf{r} \mapsto -\mathbf{r}$ in odd dimensions. For a positive coupling strength g the quartic potential describes an attractive interaction; if moreover the interaction is strong enough, the fermions form bound states, thereby breaking the chiral symmetry. The formation of bound states requires some energy, though, which explains why fermions acquire an effective mass.

Mean-field analysis — We propose here to show the spontaneous mass generation at the mean-field level. The emergence of a fermion mass is already clear in the mean-field approximation, where the action becomes Gaussian,

$$S_{\text{MF}} = \int d^d x \bar{\psi} (-i\gamma^\mu \partial_\mu + m) \psi, \quad (1.72)$$

and acquire an extra mass term $m = g\langle\bar{\psi}\psi\rangle$. As is standard in mean-field approximations, we estimate the ensemble average $\langle\dots\rangle$ using the Gaussian action itself, given by Eq. (1.72), which leads to a self-consistent equation for m . The existence of a solution enforces a condition on g . To ease the computation, we first diagonalise the action by switching to Fourier space. With \mathbf{k} the space-time momentum, and $\{\bar{\psi}_{\mathbf{k}}, \psi_{\mathbf{k}}\}$ the Fourier-transformed fields⁵, the action becomes

$$S_{\text{MF}} = \int_{\mathbf{k}} \bar{\psi}_{\mathbf{k}} (\gamma^\mu k_\mu + m) \psi_{\mathbf{k}}, \quad (1.73)$$

where we use the notation shorthand

$$\int_{\mathbf{k}} = \int \frac{d^d k}{(2\pi)^d}. \quad (1.74)$$

We now express the mean-field expectation value

$$\langle\bar{\psi}\psi\rangle = \frac{1}{\mathcal{Z}} \int D\bar{\psi} D\psi (\bar{\psi}\psi) e^{-S_{\text{MF}}} = \frac{\partial}{\partial m} \log \int D\bar{\psi} D\psi \exp \left[- \int_{\mathbf{k}} \bar{\psi}_{\mathbf{k}} (\gamma^\mu k_\mu + m) \psi_{\mathbf{k}} \right], \quad (1.75)$$

and evaluate the Gaussian integral, which gives

$$\langle\bar{\psi}\psi\rangle = \frac{\partial}{\partial m} \log \det(\gamma^\mu k_\mu + m) = \int_{\mathbf{k}} G(\mathbf{k}), \quad (1.76)$$

where $G(\mathbf{k}) = (\gamma^\mu k_\mu + m)^{-1}$ denotes the Fourier-transformed propagator (or Green's function) of the Gaussian theory. By plugging Eq. (1.76) into the expression $m = g\langle\bar{\psi}\psi\rangle$ for the mass, and simplifying by $m \neq 0$ on both sides, we get the implicit relation between the coupling strength and the mass in the phase with broken symmetry

$$1 = g \int \frac{d^d k}{(2\pi)^d} \frac{1}{k^2 + m^2}. \quad (1.77)$$

⁵Different conventions exist for the Fourier transform; in compliance with the tradition of high-energy theorists, we choose the one with the 2π factors in the inverse transform with the wave vector as Fourier parameter,

$$\hat{f}(\mathbf{k}) = \int d^3 r e^{-i\mathbf{k}\cdot\mathbf{r}} f(\mathbf{r}), \quad f(\mathbf{r}) = \int \frac{d^3 k}{(2\pi)^3} e^{i\mathbf{k}\cdot\mathbf{r}} \hat{f}(\mathbf{k}).$$

For notational symmetry, we use the opposite sign convention for the Fourier transform of the conjugate field $\bar{\psi}$. In so doing, $\bar{\psi}(\mathbf{r})\psi(\mathbf{r})$ transforms to $\bar{\psi}_{\mathbf{k}}\psi_{\mathbf{k}}$ and not $\bar{\psi}_{-\mathbf{k}}\psi_{\mathbf{k}}$.

In dimension $d < 2$, the integral in Eq. (1.77) converges, and a non-trivial solution $m \neq 0$ exists for all $g \neq 0$: the spontaneous quantum fluctuations are large enough to break the chiral or parity symmetry for arbitrarily weak coupling strength. The marginal dimension below which fluctuations always destroy the symmetric phase is called *lower critical dimension*. Therefore, the lower critical dimension equals $d_\ell = 2$ in the Gross-Neveu model. In dimension $d \geq 2$, the integral in Eq. (1.77) diverges, which entails that the right-hand side is infinite for non-zero g . This singularity signals that, as expected, the interacting theory should be renormalised, which we have not done yet. Let us therefore introduce a momentum cut-off Λ . In three dimensions, the regularised integral diverges linearly with Λ and leads to

$$1 = g\Lambda K_d \left[1 - \frac{m}{\Lambda} \arctan\left(\frac{\Lambda}{m}\right) \right]. \quad (1.78)$$

For the sake of generality, we introduced in Eq. (1.78) the numerical factor $K_d = \Omega_d (2\pi)^{-d}$, where

$$\Omega_d = \frac{2\pi^{d/2}}{\Gamma_E(d/2)} \quad (1.79)$$

represents the surface of the hypersphere in d dimensions, and Γ_E is Euler's Gamma function. Eq. (1.78) admits a solution for m only if the coupling strength exceeds the critical value $g^* = (\Lambda K_d)^{-1}$. Slightly above this critical coupling strength, the mass m , which acts as an the order parameter, increases with g in a power-law fashion:

$$m \sim (g - g^*)^\beta, \quad (1.80)$$

where the so-called order parameter exponent takes the value $\beta = 1$ in mean field. As is standard in critical phenomena, the \sim symbol indicates an equivalence up to some unimportant (possibly dimensionful) factor. This value of β is inexact, however, because the mean-field description neglects quantum fluctuations, which yet dominate near the critical point. The renormalisation group, on the other hand, accounts for critical fluctuations in a well-controlled fashion.

Formalism of the renormalised effective action — To cure the ultraviolet divergences, one must assume that the *bare* variables that enter the free theory (1.69), become ill-defined when adding an interacting potential. Instead, the interacting theory must be expressed in terms of new *renormalised* fields and parameters. To clearly distinguish between bare and renormalised variables, we will henceforth mark bare quantities with an upper circle ($\overset{\circ}{}$). Let us now consider that the theory is temporarily regularised, for instance using a cut-off Λ (but the following discussion remains valid for any regularisation). We also need to introduce an independent mass scale μ in the theory, which plays the same role as the scaling factor $\ell \propto \mu^{-1}$ in the block-spin transformation, to monitor the renormalisation flow from the microscopic ($\mu = \Lambda$) to the macroscopic ($\mu = 0$) level.

It then becomes possible to relate the bare and renormalised fields through a finite constant $Z_\psi(\Lambda/\mu)$, function of the dimensionless parameter Λ/μ , in the following way:

$$\overset{\circ}{\psi} = Z_\psi^{1/2} \psi, \quad \overset{\circ}{\bar{\psi}} = Z_\psi^{1/2} \bar{\psi}. \quad (1.81)$$

By convention, the square root is introduced in Eq. (1.81) because correlation functions of interest usually contain pairs of fermionic fields. In the end, we choose Z_ψ so that

when Λ is set to infinity, the correlation functions of renormalised fields remain finite (we do not worry about how to achieve that for the moment). Similarly, we reparametrise the mass and the coupling strength in terms of their renormalised values $m(\mu)$ and $g(\mu)$, respectively. For the mass, we define the constant $Z_m(\Lambda/\mu)$ such that

$$\mathring{m} = Z_m Z_\psi^{-1} m. \quad (1.82)$$

The canonical mass dimension of the coupling strength is $[g] = 2 - d$; for convenience, one usually defines the renormalised coupling strength as dimensionless, so that the bare and renormalised couplings differ by a factor μ^{2-d} . We need to introduce a constant $Z_g(\Lambda/\mu)$ so that

$$\mathring{g} = \frac{2\mu^{2-d}}{K_d} \frac{Z_g}{Z_\psi^2} g. \quad (1.83)$$

We extracted a factor $K_d/2$ in Eq. (1.83) to absorb the angular factors from the Feynman diagrams and simplify the equations of the renormalisation flow as much as possible.

Note that we conventionally introduced the constant Z_ψ in Eq. (1.82) and Eq. (1.83) to compensate the rescaling of the fields. Indeed, by expressing the original action S of Eq. (1.69) in terms of the renormalised fields and parameters, we obtain the so-called renormalised action

$$S_R = \int d^d x \left[\bar{\psi} (-Z_\psi i\gamma^\mu \partial_\mu + Z_m m) \psi + \frac{\mu^{2-d}}{K_d} Z_g g (\bar{\psi} \psi)^2 \right]. \quad (1.84)$$

Of course, the two actions $S_R[\bar{\psi}, \psi; \mu] = S[\mathring{\bar{\psi}}, \mathring{\psi}]$ describe the same theory, except that the renormalised action S_R is viewed as a functional of the renormalised fields, while the original action S is viewed as a functional of the bare fields. The Legendre transform of the bare and renormalised actions defines the effective action at a given mass scale μ (the counterpart of the effective macroscopic Hamiltonian for quantum field theories)

$$\Gamma_R[\bar{\chi}, \chi; \mu] = \Gamma[\mathring{\bar{\chi}}, \mathring{\chi}], \quad (1.85)$$

which depends on the macroscopic fields $\bar{\chi} = \langle \bar{\psi} \rangle$ and $\chi = \langle \psi \rangle$. For simplicity, we will nonetheless use the same symbols $\bar{\psi}$ and ψ for the arguments of the effective action. At the microscopic scale $\mu = \Lambda$, one recovers the original action $\Gamma_R[\Lambda] = S_R$. On the contrary, at the macroscopic scale $\mu = 0$, the effective action captures the large-scale physics, or the physics in the thermodynamic limit in statistical theories.

In general, the effective action Γ assumes a complicated functional dependence, with infinitely many high-order operators. We write the functional Taylor expansion of the renormalised effective action as (ZINN-JUSTIN 2002)

$$\Gamma_R = \sum_{n=1}^{\infty} \frac{1}{n!} \int d^d x_1 \dots d^d x_n \Gamma_{i_1, \dots, i_n}^{(2n)}(x_1, \dots, x_n) \bar{\psi}_{i_1}(x_1) \psi_{i_2}(x_2) \dots \bar{\psi}_{i_{2n-1}}(x_{2n-1}) \psi_{i_{2n}}(x_{2n}), \quad (1.86)$$

where the integers i_1, \dots, i_{2n} index both the flavour a and the components of each fermionic field ψ_a or $\bar{\psi}_a$. Hence, The renormalised $2n$ -point *vertex* functions $\Gamma^{(2n)}$ have a tensorial structure, which we will not spell out except when necessary for the exposition. The equality between the bare and renormalised quantum action of Eq. (1.85) leads to the relations for the $2n$ -point vertices (here in Fourier space)

$$\Gamma^{(2n)}(\{\mathbf{k}_i\}; m, g, \mu) = Z_\psi^n \mathring{\Gamma}^{(2n)}(\{\mathbf{k}_i\}; \mathring{m}, \mathring{g}). \quad (1.87)$$

The Gross-Neveu model is multiplicatively renormalisable in two dimensions⁶. This means that to completely renormalise the theory, it is sufficient to determine the renormalisation constants Z_m , Z_ψ and Z_g so as to render the two-point and four-point vertices finite at special sets of momenta. In agreement with the functional form of the action S , we impose on the two-point functions the conditions

$$\begin{cases} \Gamma^{(2)}(\mathbf{k} = \mathbf{0}; m, g, \mu) = \text{finite} \cdot m, & (1.88a) \\ \frac{\partial \Gamma^{(2)}}{\partial k_\mu}(\mathbf{k} = \mathbf{0}; m, g, \mu) = \text{finite} \cdot \gamma^\mu, & (1.88b) \end{cases}$$

where the two finite constants depend on the dimensionless factor Λ/μ . Eq. (1.88a) determines Z_ψ , while Eq. (1.88b) determines Z_m . We find similarly the constant Z_g by enforcing

$$\Gamma^{(4)}(\{\mathbf{k}_i = 0\}; \mu, g, \mu) = \text{finite} \cdot g \quad (1.89)$$

for the four-point vertex function.

Renormalisation flow — Once the renormalised constants are determined, the flow of the coupling constant g is encoded in the so-called beta function (ZINN-JUSTIN 2002)

$$\beta(g) = -\frac{\partial g}{\partial \log \mu}, \quad (1.90)$$

which quantifies how the coupling strength scales with μ near a fixed length scale. The scenario $\beta(g) > 0$ indicates that the coupling strength increases in the infrared limit $\mu \rightarrow 0$. Importantly, the partial derivative of Eq. (1.90) is evaluated with all bare parameters fixed, since only the effective theory depends on the mass scale. The initial condition of the flow at $\mu = \Lambda$ corresponds to the (dimensionless) microscopic coupling $g(\Lambda) = \frac{1}{2}\Lambda^{d-2}\dot{g}$. A naive dimensional analysis suggests that slightly above the microscopic scale, $g(\mu) \propto \mu^{d-2}$, from which we expect $\beta(g) \simeq -(d-2)g$. Obviously, the quantum corrections encoded in the constants Z_g and Z_ψ alter this scaling law, especially at large coupling strengths. Using the prescription (1.83), we find the exact expression for the beta function

$$\beta(g) = -(d-2)g \left(1 + g \frac{\partial \log Z}{\partial g} \right), \quad (1.91)$$

where $Z = Z_g/Z_\psi^2$. For concreteness, let us assume that the first quantum corrections to the beta function are of order two in the coupling strength. Then, there exists some constant A such that

$$\beta(g) \simeq -(d-2)g + Ag^2. \quad (1.92)$$

If furthermore $A > 0$ and we place ourselves in dimension $d > 2$, two large-scale behaviours may arise according to the value of the microscopic coupling strength, as shown in Fig. 1.15.

- If $g(\Lambda)$ is smaller than the critical coupling strength $g^* = (d-2)/A$, the beta function is always negative and the coupling strength decreases under the renormalisation flow. This situation corresponds to the symmetric phase, with zero fermion mass.

⁶We refer the reader to (ZINN-JUSTIN 2002) for inductive proofs of renormalisability

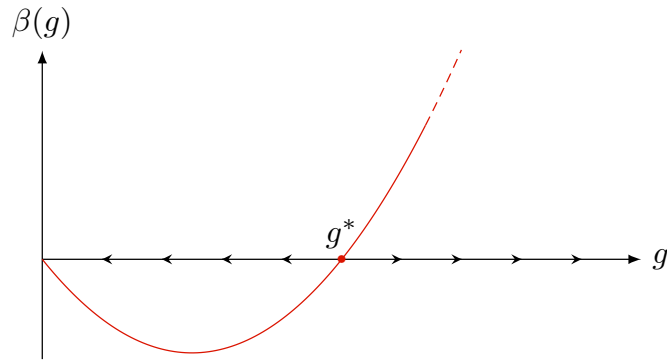


Figure 1.15 | Beta function $\beta(g)$ of the Gross-Neveu model against the quartic coupling strength g , for $N > 1$ flavours of fermions. The beta function is negative below a critical value g^* : the coupling strength decreases in the infrared limit towards the Gaussian fixed point $g = 0$. This asymptotic freedom is a peculiarity of the Gross-Neveu model and more realistic theories like quantum chromodynamics. The beta function is positive above g^* , where the coupling strength increases to infinity: in this strongly interacting regime, quantum fluctuations break the chiral symmetry and spontaneously generate a fermion mass.

- If $g(\Lambda) > g^*$, the beta function becomes positive and the flow enhances the coupling strength. This property is specific to asymptotically free theories, for which the coupling weakens as the energy scale increases. The model then describes a symmetry-broken phase, where the fermions acquire a mass $m \neq 0$.

Similarly, we define the scaling functions for the field and mass

$$\eta_\psi(g) = \frac{\partial \log Z_\psi}{\partial \log \mu} = -\beta(g) \frac{\partial Z_\psi}{\partial g}, \quad \eta_m(g) = \frac{\partial \log Z_m}{\partial \log \mu} = -\beta(g) \frac{\partial Z_m}{\partial g}. \quad (1.93)$$

These functions represent the power-law dependence of the Z constants with the mass scale. Close to the critical point, the theory becomes scale-invariant and the scaling functions tend to constants, from which we deduce the scaling law $Z_m \sim \mu^{\eta_m - \eta_\psi}$ and $Z_\psi \sim \mu^{\eta_\psi}$. The scaling functions thus give the *anomalous* contribution to the critical exponents induced by quantum fluctuations, which correct the predication of the naive dimensional analysis $m \sim \mu$. For instance, upon defining the correlation length exponent ν such that $\mu \sim (g - g^*)^\nu$, we predict that the mass scales according to Eq. (1.80) with a power-law exponent $\beta = \nu(1 + \eta_m - \eta_\psi)$.

1.5.2 Perturbative expansion

The stage is all set to determine the critical properties of the model. Yet, when putting the renormalisation group in action, the computation of renormalisation constants stumbles over a huge obstacle: finding the exact expression of the vertex functions often proves an impossible task. As a result, it is often necessary to resort to a perturbative approach to compute the renormalisation constants and determine the flow of the coupling strength.

Perturbative scheme — Several approximation methods exist, according to which parameter is considered small. In the so-called large fermion number expansion, correlation functions are expanded in the parameter gN^{-1} , with N the number of fermions. The most

natural and common perturbative scheme, though, consists in expanding in the coupling strength g . To do so, let us split the action $S = S_0 + S_{\text{int}}$ into its Gaussian part S_0 and its interacting part S_{int} , proportional to g . We can then expand the partition function as

$$\begin{aligned} \mathcal{Z} &= \int \mathcal{D}\bar{\psi} \mathcal{D}\psi e^{-S} = \int \mathcal{D}\bar{\psi} \mathcal{D}\psi e^{-S_0} \exp \left[-\frac{\dot{g}}{2} \int d^d r (\bar{\psi}\psi)^2 \right] \\ &= \int \mathcal{D}\bar{\psi} \mathcal{D}\psi e^{-S_0} \sum_{L=0}^{\infty} \frac{\dot{g}^L}{2^L L!} \left[- \int d^d r (\bar{\psi}\psi)^2 \right]^L. \end{aligned} \quad (1.94)$$

At this point, the series in Eq. (1.94) behaves well. But to organise the perturbative expansion of correlation functions order by order in the coupling strength, one must, in a leap of faith, swap the path integral and the sum, which gives

$$\mathcal{Z} = \sum_{L=0}^{\infty} \dot{g}^L \mathcal{Z}_L, \quad \mathcal{Z}_L = \frac{(-1)^L}{2^L L!} \left\langle \left[\int d^d r (\bar{\psi}\psi)^2 \right]^L \right\rangle_0, \quad (1.95)$$

where $\langle \dots \rangle_0$ denotes a statistical average over the Gaussian action S_0 . Due to this illegitimate mathematical trick, the coefficients \mathcal{Z}_L of the series in Eq. (1.95) diverge in absence of any regularisation: there lies the mathematical origin of the infinities. Since Gaussian integrals are easy to perform, it is now possible to compute observables from the partition function order by order in the coupling strength. The famous Wick theorem, which we recall in Appendix A, enables to cast the averages of operators of the form $(\bar{\psi}\psi)^{2L}$ into a sum of all possible contractions between the fields ψ and $\bar{\psi}$, each factor giving the propagators of the free theory $\langle \bar{\psi}\psi \rangle_0 = G_0$. In addition, the pictorial method developed by R. Feynman enables to keep track of all those contractions by grouping them into classes of graphs with similar topology. The Feynman rules for the Gross-Neveu model are the following.

- A propagator is depicted as a solid line

$$G_0(\mathbf{k}) = (\gamma^\mu k_\mu + m)^{-1} = \longrightarrow \quad (1.96)$$

While in quantum electrodynamics, the middle arrow conventionally indicate whether the particle or antiparticle propagates, we will use the same arrow to label to direction of the momentum carried by the propagator.

- An interaction vertex is depicted as a node with four legs. It decomposes into two subvertices with different topologies, depending on the way the component indices of the fermionic fields $\bar{\psi}_i$ and ψ_i contract one another. A vertex carries a factor

$$\frac{(-1)^L}{2^L L!} \dot{g}^L = \bullet \times = \begin{array}{c} \diagup \text{---} \diagdown \\ \diagdown \text{---} \diagup \end{array} + \begin{array}{c} \diagup \\ \text{---} \\ \diagdown \end{array} \quad (1.97)$$

- A Feynman diagram carries a combinatorial factor, or *multiplicity*, which can be found by counting all possible Wick contractions that lead to diagrams with the same topology.

Loopwise expansion and counterterms method — As illustrated on the partition function in Eq. (1.95), the bare coupling strength \mathring{g} represents a natural expansion parameter. The *loopwise* expansion consists in organising the series of a bare correlation function order by order in the bare coupling strength \mathring{g} . The terminology refers to the pictorial interpretation of this expansion, which amounts to collect Feynman graphs dressed with the same number of loops. As an example, the perturbative expansion of the bare two-point vertex function reads

$$\begin{aligned}
 \mathring{\Gamma}^{(2)}(\mathring{m}, \mathring{g}) &= \left[\text{---} \right]^{-1} - \text{---} \bigcirc \text{---} - \text{---} \bigcirc \bigcirc \text{---} \\
 &\quad - \text{---} \bigcirc \text{---} + \dots \\
 &= \mathring{\Gamma}_0^{(2)}(\mathring{m}) + \mathring{g} \mathring{\Gamma}_1^{(2)}(\mathring{m}) + \mathring{g}^2 \mathring{\Gamma}_2^{(2)}(\mathring{m}) + \dots
 \end{aligned} \tag{1.98}$$

where the indices $L = 0, 1, 2$, etc. represent the tree level, the one-loop order, the two-loop order, etc. The tree-level vertex function is simply the inverse of the propagator, i.e.

$$\mathring{\Gamma}_0^{(2)}(\mathring{m}) = \gamma^\mu k_\mu + \mathring{m}. \tag{1.99}$$

Yet, the renormalised coupling strength g provides a more adequate expansion parameter, to the extent that we must express the correlation functions in terms of the renormalised parameters to render them finite. The expansion of a renormalised correlation function order by order in the renormalised coupling strength g comprises graphs which are absent from the loopwise expansion, known as *counterterms*. As an example, the renormalised two-point vertex function can be written as

$$\Gamma^{(2)}(m, g, \mu) = \Gamma_0^{(2)}(m, \mu) + g \Gamma_1^{(2)}(m, \mu) + g^2 \Gamma_2^{(2)}(m, \mu) + \dots \tag{1.100}$$

To make contact with Eq. (1.98), we use the prescription of Eq. (1.81) to Eq. (1.83) to express \mathring{g} and \mathring{m} in terms of g and m respectively. In addition, the bare and renormalised vertex functions differ themselves by a factor Z_ψ , as per Eq. (1.87). For instance, the bare vertex function at tree level is of the form

$$Z_\psi \mathring{\Gamma}_0^{(2)}(\mathring{m}) = Z_\psi \gamma^\mu k_\mu + Z_m m = \Gamma_0^{(2)}(m, \mu) + g \left(z_\psi^{(1)} \gamma^\mu k_\mu + z_m^{(1)} m \right) + O(g^2), \tag{1.101}$$

where $z_\psi^{(1)}$ and $z_m^{(1)}$ stand for the first-order coefficients of the constants Z_ψ and Z_m , respectively. The bare vertex function at tree level thus includes a term of order g , which contributes to the first-order renormalised vertex function $\Gamma_1^{(2)}$. The renormalised vertex function at tree level $\Gamma_0^{(2)}(m, \mu) = \gamma^\mu k_\mu + m$ takes the same forms as its bare counterpart, except that it naturally depends on the renormalised mass m . Higher-order vertices in the loopwise expansion can be similarly cast into a first term of order g^L , which coincides with the renormalised vertex at the same order, and corrections of order g^M with $M > L$

coming from the Z constants. These counterterms also admit a graphical representation. Comparing Eq. (1.98) and Eq. (1.100), we write the renormalised vertex at first order as

$$\begin{aligned} \Gamma_1^{(2)}(m, \mu) &= - \text{---} \bigcirc \text{---} + \text{---} \otimes \text{---} \\ &= 2\mu^{-\varepsilon} K_d^{-1} \Gamma_1^{\circ(2)}(m) + \left(z_\psi^{(1)} \gamma^\mu k_\mu + z_m^{(1)} m \right) \end{aligned} \quad (1.102)$$

Alternately, we may view the counterterms as contributions from an extra part δS added to the original action S , such that $S_R[\bar{\psi}, \psi; \mu] = S[\bar{\psi}, \psi; \mu] + \delta S[\bar{\psi}, \psi; \mu]$ with

$$\begin{aligned} \delta S &= (Z_\psi - 1) \int d^d x \bar{\psi} (-i\gamma^\mu \partial_\mu) \psi + (Z_m - 1) m \int d^d x \bar{\psi} \psi \\ &\quad + \frac{\mu^{2-d}}{K_d} (Z_g - 1) g \int d^d x (\bar{\psi} \psi)^2. \end{aligned} \quad (1.103)$$

The Z constants implicitly depend on the coupling strength via $Z_\psi - 1 = gz_\psi^{(1)} + O(g^2)$, $Z_m - 1 = gz_m^{(1)} + O(g^2)$ and $Z_g - 1 = gz_g^{(1)} + O(g^2)$.

Dimensional regularisation — To cure the divergences that arise in correlation functions beyond the tree approximation, the Feynman integrals must be regularised beforehand. Several regularisation schemes exist (KLEINERT 2001; ZINN-JUSTIN 2002).

- The hard *cut-off* regularisation operates by limiting the range of integration to a maximal momentum Λ . In condensed matter, this is the most natural regularisation, since the lattice introduces a short wave length lower bound through the lattice constant $a = \Lambda^{-1}$. But cutting abruptly the integrals destroys most of the original symmetries of the theories (translation, gauge).
- The *Pauli-Villars* regularisation is similar to the cut-off regularisation in spirit but preserve all symmetries. It boosts the convergence of the propagator at high momenta so as to reduce the degree of divergence by introducing a soft cut-off. Unfortunately, this method is ambiguous. For instance, it leads to inconsistent results in quantum electrodynamics without careful analysis of the renormalisation conditions (KLEISS 2015). This scheme seems inappropriate to treat the Gross-Neveu model.
- The *dimensional* regularisation extends the definition of isotropic integrals to arbitrary dimensions. It preserves all symmetries, greatly simplifies the computation of Feynman integrals, and enables to subtract the poles effectively. Importantly, this plays a double role: not only does it regularise divergent integrals, but it also enables to perform the perturbative expansion Eq. (1.95) in a controlled way. We devote ourselves to explaining this scheme in the rest of this section (’T HOOFT 1972).

The mean-field analysis of Sec. 1.5.1 showed that in three dimensions, the dimensionless critical coupling Λg^* is everything but small. How to make sense of a perturbative expansion in small g and then investigate the phase transition, which occurs at coupling strengths of order unity? Dimensional regularisation solves this problem by offering a natural small parameter, which is the distance to the lower or upper critical dimension.

- The *upper* critical dimension d_u denotes the dimension above which the fluctuations are small enough for the Gaussian approximation to predict the universal properties of the system correctly. In the Ising model and its field-theoretical peer the φ^4 theory, the relative fluctuations of the magnetisation vanish at the critical point above $d_u = 4$. This entails that mean-field theory predicts the correct critical exponents above four dimensions. Statistical field theories are renormalisable below d_u . Thus the theory can be advantageously extended to arbitrary dimension $d = d_u - \varepsilon$ slightly below the upper critical dimension, and the position of the critical point controlled via the small parameter ε . The upper critical dimension of the Gross-Neveu model is ill-defined, since the Gaussian theory is not critical (it describes free fermions) unlike the φ^4 theory.
- The *lower* critical dimension d_ℓ denotes the dimension below which the fluctuations are large enough to break the symmetry of the free theory however weak the coupling strength. According to the Mermin-Wagner theorem, the lower critical dimension of models with a continuous symmetry is $d_\ell = 2$. The Gross-Neveu undergoes the breaking of a discrete rather than continuous symmetry, but as per the mean-field analysis of Sec. the lower critical dimension is also $d_\ell = 2$. This is reflected in the canonical dimension of the bare coupling $[\mathring{g}] = 2 - d$ vanishing in two dimensions, and from there in the dominant term of the beta function. According to Eq. (1.92), the critical point $g^* = \varepsilon/A$ is indeed small when $\varepsilon \ll 1$, which justifies the perturbative expansion.

Subtraction scheme — Let us now see how to subtract divergences in the $d = 2 + \varepsilon$ expansion. For concreteness, consider the one-loop 2-point vertex function. Evaluating the corresponding diagram shown in Eq. (1.98), we find that the one-loop contribution is independent of the external momentum \mathbf{k} , and thus renormalises only the mass,

$$\mathring{g} \mathring{\Gamma}_1^{(2)}(\mathring{m}) = 2 \left(-\frac{\mathring{g}}{2} \right) (1 - \text{Tr}) \int_{\mathbf{q}} G(\mathbf{q}) = (n - 1) \mathring{g} \int \frac{d^d q}{(2\pi)^d} \frac{\mathring{m}}{q^2 + \mathring{m}^2}, \quad (1.104)$$

where $n = N \text{Tr} \mathbb{1}$ denotes the total number of fermionic degrees of freedom and the factor 2 accounts for the multiplicity of the diagram. Using the analytical tricks of Appendix A, the d -dimensional integral of Eq. (1.104) gives

$$\mathring{\Gamma}_1^{(2)}(\mathring{m}) = \frac{1}{2} \mathring{m}^{1+\varepsilon} (n - 1) K_d \Gamma_E(-\varepsilon/2) \Gamma_E(1 + \varepsilon/2), \quad (1.105)$$

The Gamma function possesses a pole at the origin, $\Gamma_E(x) = 1/x - \gamma_E + O(x)$ where γ_E is Euler-Mascheroni's constant. We thus can expand in the small parameter ε . To enhance the analogy with the renormalised vertex of Eq. (1.98), we also plug spell out the bare coupling as a function of the renormalised one, and now use the renormalised mass as the argument. Hence

$$\mathring{\Gamma}_1^{(2)}(m) = -m(n - 1) K_d \left[\frac{1}{\varepsilon} + \log(m) + O(\varepsilon) \right], \quad (1.106)$$

In dimensional regularisation, ultraviolet divergences appear in correlation functions as poles in ε . We can now render the corresponding renormalised vertex finite, since according

to Eq. (1.98), we finally get

$$\Gamma_1^{(2)}(\mathbf{k}; m, \mu) = z_\psi^{(1)} \gamma^\mu k_\mu + m \left[z_m^{(1)} - \frac{2(n-1)}{\varepsilon} - 2 \log \left(\frac{m}{\mu} \right) + O(\varepsilon) \right]. \quad (1.107)$$

Two strategies exist to render $\Gamma^{(2)}$ finite at one-loop order by choosing suitable Z constants.

- On one hand, we may enforce that the parameter m represents the actual mass of the fermions, and thus impose $\Gamma_1^{(2)}(\mathbf{k} = \mathbf{0}; m, \mu) = m$ and $\partial_{k_\mu} \Gamma_1^{(2)}(\mathbf{k} = \mathbf{k}; m, \mu) = \gamma^\mu$, in the limit $\varepsilon \rightarrow 0$. This corresponds to the *on-shell* subtraction scheme, widely used in quantum field theories of the standard model to compare the theoretical predictions with observations. In this scheme, the renormalisation constants absorb not only the pole but also finite constants,

$$z_\psi^{(1)} = 0, \quad z_m^{(1)} = \frac{2(n-1)}{\varepsilon} + 2 \log \left(\frac{m}{\mu} \right). \quad (1.108)$$

- On the other hand, we may require that the Z constants absorb only the pole. In this scheme, the renormalisation constants at first order read

$$z_\psi^{(1)} = 0, \quad z_m^{(1)} = \frac{2(n-1)}{\varepsilon}. \quad (1.109)$$

This *minimal* subtraction scheme suffices to renormalise the theory, and leads to simpler expression of the renormalisation constants, at the expense of fermions being off-shell. This is the common procedure in statistical field theories.

Beta functions — Pushing the expansion to order four in the coupling constant, one finds the following expression for the beta functions (GRACEY 2016),

$$\begin{aligned} \beta(g) = & -\varepsilon g + 2(n-2)g^2 - 4(n-2)g^3 - 2(n-2)(n-7)g^4 \\ & - \frac{4}{3}(n-2)[-n^2 - 19n + 48 - 3\zeta(3)(11n-34)]g^5 + O(g^6), \end{aligned} \quad (1.110)$$

where here ζ is Riemann's function, and we recall that $n = N \text{Tr} 1$. The beta function vanishes identically if $n = 2$, which corresponds to a single Dirac fermion in dimension $d \leq 3$. It is of the form of Eq. (1.92) and leads to a (positive) critical fixed point when $n > 2$. At dominant order, the critical coupling strength is $g^* = \varepsilon/2(n-2)$. The reason is that the Gross-Neveu model is equivalent to the so-called abelian Thirring model in this case, due to the Fierz identity $(\bar{\psi}\psi)^2 = -\frac{1}{2}(\bar{\psi}\gamma_\mu\psi)(\bar{\psi}\gamma^\mu\psi)$. The Thirring model is exactly soluble near two dimensions, which explains why the coupling strength is not renormalised. Similarly, the scaling functions read

$$\eta_\psi(g) = -2(n-1)g^2 + 2(n-1)(n-2)g^3 - 2(n-1)(n^2 - 8n + 7)g^4 + O(g^5) \quad (1.111)$$

for the field anomalous dimension, and

$$\begin{aligned} \eta_m(g) = & 2(n-1)g - 2(n-1)g^2 - 2(n-1)(2n-3)g^3 \\ & - 2(n-1)[-5n^2 - 23n + 57 + 6(n-2) + (n-13)\zeta_3]g^4 + O(g^5) \end{aligned} \quad (1.112)$$

for the mass anomalous dimension. Both Eq. (1.111) and Eq. (1.112) vanish identically for $n = 1$, since quartic interactions are zero for Majorana fermions. By evaluating $\eta_\psi(g)$ and $\eta_m(g)$ at the critical coupling strength, we finally obtain the critical exponents. At dominant order, they are

$$\eta_\psi(g^*) = -\frac{n-1}{2(n-2)^2}\varepsilon^2 + O(\varepsilon^3), \quad \eta_m(g^*) = \frac{n-1}{n-2}\varepsilon + O(\varepsilon^2). \quad (1.113)$$

Evanescent operators — When generalising Feynman integrals to arbitrary dimension, we glossed over an important detail: the extension of the Clifford algebra. The Pauli matrices $(\sigma_x, \sigma_y, \sigma_z)$ define indeed a three-dimensional Clifford algebra in Euclidean metric, denoted as $\text{Cl}_3(\mathbb{R})$. In even dimension, the basis of the Clifford algebra $\text{Cl}_d(\mathbb{R})$ is made of d anticommuting elements γ_i with $\{\gamma_i, \gamma_j\} = 2\delta_{ij}\mathbb{1}$ for $i, j = 1, \dots, d$, which admit faithful representations as $2^{d/2}$ -times- $2^{d/2}$ matrices. This algebra can be extended to odd dimensions, though the definition of the elements becomes less straightforward (KENNEDY 1981). But in non-integer dimensions, the products $\gamma_i\gamma_j$ cannot be written as linear combinations of Dirac matrices, which entails that the Clifford algebra becomes infinite dimensional. Beyond three-loop order, the renormalisation flow of the Gross-Neveu model generates new couplings, which we can collect in the antisymmetric channels (VASIL'EV 1997; GRACEY 2008)

$$\Gamma_{\mu_1\mu_2\dots\mu_p} = \gamma_{[\mu_1}\gamma_{\mu_2}\dots\gamma_{\mu_p]} = \frac{1}{p!} \sum_{P \in \mathfrak{S}_p} \epsilon(P) \gamma_{P(\mu_1)} \gamma_{P(\mu_2)} \dots \gamma_{P(\mu_p)}, \quad (1.114)$$

where P are permutations of p elements and $\epsilon(P)$ is the signature of P . Each index μ_i can take an infinite number of integer values. In particular, the quadrilaterals in the fields of the form $(\bar{\psi} \Gamma_{\mu_1\mu_2\dots\mu_p} \psi)^2$ with $p > d$ disappear when the dimension $d = 2$. These *evanescent* operators then collapse on the few physical operators in integer dimension, and therefore contributes to the beta function of the coupling strength g .

Part I

Disorder in three-dimensional relativistic semimetals

The disorder-driven semimetal-metal transition

Real materials always contain some amount of disorder. And disorder can have drastic consequences: for example, the amplitudes of wave packets scattered by random defects can interfere destructively, which results in the localisation of the wave function. In three-dimensional relativistic semimetals, the DoS vanishes at the band crossing, and there are no wave functions to localise; but a strong enough random potential can drive semimetals to a diffusive metal with a sizeable density of states, through a quantum continuous phase transition, distinct from that of Anderson.

This chapter paints a cohesive but concise picture of the properties of the semimetal-metal transition. We first show that this transition occurs in relativistic semimetals when the (effective) dimension exceeds two. The next section is devoted to the phenomenology of this transition: we present the phase diagram and the critical scaling laws for the conductivity and the density of states, this latter quantity playing the role of an order parameter. We then show the existence of a critical point and estimate the critical exponents using a simple analytical technique: the self-consistent Born approximation. Finally, we discuss the geometrical properties of the wave function density, which displays a multifractal behaviour, and relate the scaling laws of average and typical observables.

2.1	Quantum phase transitions in disordered electronic systems	60
2.1.1	A historical example: Anderson's localisation	60
2.1.2	Modelling disorder in relativistic semimetals	63
2.1.3	Relevance of weak disorder	65
2.2	Phenomenology of the semimetal-metal transition	67
2.2.1	Phase diagram	67
2.2.2	Conventional scaling laws	70
2.2.3	Effect of various types of disorder	74
2.3	The self-consistent Born approximation	75
2.3.1	Approximation schemes of the self-energy	76
2.3.2	Solution to the self-consistent equation	78

2.4 Wave function statistics	80
2.4.1 Multifractality	81
2.4.2 Typical versus average densities of states	86
Conclusion	88

2.1 Quantum phase transitions in disordered electronic systems

The effect of disorder on relativistic particles is a rather novel topic. In conventional phases of matter, which usually host massive elementary excitations, disorder can induce phase transitions. Prominent examples include many-body localisation, which currently attracts a lot of attention, but also older topics such as percolation, spin glasses, and the celebrated Anderson’s localisation (THOULESS 1984). This latter transition is a perfect benchmark to introduce the physics of disordered localisation phenomena. With this basic understanding at hand, we then explore the phenomenology of disordered relativistic semimetals.

2.1.1 A historical example: Anderson’s localisation

Scaling theory — Localisation phenomena are ubiquitous in disordered electronic systems: from amorphous semiconductors and their celebrated Mott’s law, to thin metallic films, quantum Hall states; and even manifest themselves beyond condensed matter physics, in electromagnetic or water waves (KRAMER 1993). The archetype remains Anderson’s localisation (ANDERSON 1958). Under strong enough disorder, a three-dimensional metal transits to an insulating phase, as a result of wave functions becoming exponentially localised by multiple destructive scatterings. The same phenomenon can happen to any conducting phase with a large DoS at the Fermi level, provided no other mechanism prevents localisation. In general, lower-dimensional metals are unstable to an arbitrarily weak disorder, and are always insulating. The role of dimensionality can be clearly seen on the scaling with the system size L of the DC conductance $G(L)$ (measured in units of e^2/h and at zero temperature), given by the beta function (ABRAHAMS 1979)

$$\beta(G) = \frac{d \log G}{d \log L}. \quad (2.1)$$

In the one-parameter scaling hypothesis, the beta function depends only on G (and not on temperature or system size independently). Let us find its asymptotic behaviour. In the metallic region (large G), dimensional analysis gives the classical Ohm’s law $\beta(G) = d - 2$; the beta function is negative below dimension $d = 2$. In the localised region (small G), the conductance vanishes exponentially with the system size, so that $\beta(G) = \log G$. This explains why one- and two-dimensional disordered solids behave as insulators in the thermodynamic limit; only three-dimensional metals undergo a second-order phase transition, in agreement with the Mermin-Wagner theorem. Fig. 2.1(a) shows this classical behaviour of the conductance’s scaling. At intermediate values of the conductance, however, quantum corrections alter this prediction, as discussed below.

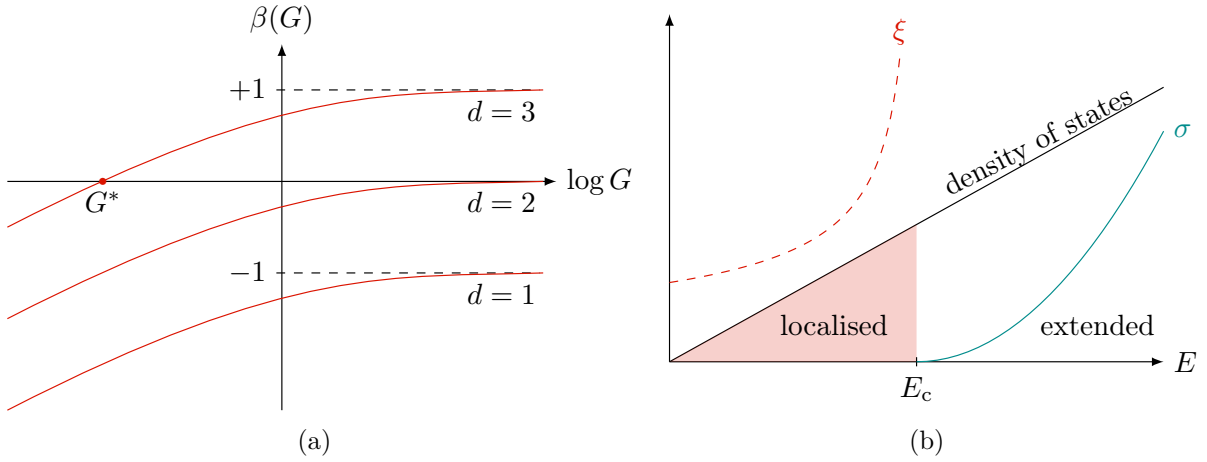


Figure 2.1 | (a) The beta function $\beta(G) = d \log G / d \log L$ encodes the scaling behaviour of the conductance G in Anderson’s localisation. When the beta function is positive, the conductance increases in the thermodynamic limit; when it is negative, the conductance decreases instead. In the classical limit sketched here, the beta function interpolates between the localised (small G) and metallic (large G) behaviours in three dimensions, leading to a second-order (continuous) phase transition at a critical conductance G^* . One- and two-dimensional disordered metals do not undergo such localisation-delocalisation transition in the absence of quantum corrections. (b) Below the mobility edge E_c , all states are localised; above it, all states are extended. On the insulating side, the localisation length diverges as $\xi \propto (E_c - E)^\nu$, while on the metallic side, the DC conductivity at absolute zero vanishes as $\sigma \propto (E - E_c)^s$ with $s = \nu(d - 2)$.

Disorder affects electronic states differently. While extended waves survive in regions of the energy landscape with a high DoS, they become easily localised in lowly populated parts of the spectrum. The *mobility edge* E_c delimits these regions of extended states (above in energy) and localised states (below in energy), as shown in Fig. 2.1(b). On each side of the mobility edge, the localisation length ξ (in the insulating phase) and the DC conductivity σ (in the metallic phase), behave as critical power laws, as expected in continuous transitions (WEGNER 1976):

$$\xi \sim (E_c - E)^\nu, \quad \sigma \sim (E - E_c)^s, \quad (2.2)$$

where the \sim symbol indicates an equivalence up to some unimportant factor. Dimensional analysis predicts that the conductivity scales as $\sigma \sim \xi^{2-d}$, so that $s = \nu(d - 2)$. The correlation length exponent ν takes different values according to the universality class of the transition. From a phenomenological viewpoint, the conductivity offers a good order parameter for the transition. A renormalisation group can determine its precise flow – or usually, the flow of the conductance – near the critical point, including quantum corrections, which were ignored up to now.

Universality classes and quantum corrections — Some models for Anderson’s localisation fall into the conventional Wigner-Dyson symmetry classes inherited from random matrix theory (WIGNER 1951; DYSON 1962). Consider a Bloch Hamiltonian \mathcal{H} with random entries (EVERS 2008). These could be random on-site energies or hopping amplitudes within a tight-binding formulation, for instance. The behaviour under time reversal \mathcal{T} leads to three cases.

- When time-reversal symmetry is absent, the only constraint on the Hamiltonian is its hermiticity, $\mathcal{H}^\dagger = \mathcal{H}$. Such Hamiltonians are invariant under conjugation by any unitary matrix; they belong to the unitary class.
- When time-reversal symmetry is present and the particles carry an integer spin ($\mathcal{T}^2 = \mathbb{1}$), the Hamiltonian is further symmetric, $\mathcal{H}^t = \mathcal{H}$. Such Hamiltonians are invariant under conjugation by any orthogonal matrix; they belong to the orthogonal class.
- When time-reversal symmetry is present and the particles carry a half-integer spin ($\mathcal{T}^2 = -\mathbb{1}$), a natural representation is $\mathcal{T} = i\sigma_y\mathcal{K}$, where \mathcal{K} denotes complex conjugation and the Pauli matrix σ_y lives in the spin sector. The Hamiltonian satisfies $\sigma_y\mathcal{H}^t\sigma_y = \mathcal{H}$. It is invariant under the symplectic group, and thus belongs to the symplectic class.

Yet, additional discrete symmetries are needed to cover all universality classes encountered in nature. Including the chiral symmetry leads to three chiral ensembles (GADE 1991). Including the particle-hole symmetry, on the other hand, leads to four Bogoliubov-De Gennes ensembles (ALTLAND 1997). The latter classification applies notably to disordered superconductors.

A definitive field-theoretical approach for Anderson's localisation remains elusive; the first theoretical breakthroughs relied on self-consistent techniques, lattice models, or numerical simulations. Several authors later developed a field-theoretical approach to study Anderson transitions, known as the non-linear sigma model (WEGNER 1979). This theory is amenable to a renormalisation group analysis in dimension $d = 2 + \varepsilon$, from which flow equations can be extracted for the disorder-averaged conductance (written again as G for simplicity). This is far from the end of the story, however, because much information is lost through the mapping to the non-linear sigma model, in particular about the cumulants of the conductance's distribution. Moreover, the small parameter ε does not control a perturbative fixed point of the theory. In the orthogonal symmetry class, which describes metals with scalar disorder, the ε -expansion leads to the beta function

$$\beta_{\text{O}}(G) = \varepsilon - \frac{1}{\pi G} + O(G^{-3}). \quad (2.3)$$

The critical exponents at leading order in ε follow from the critical conductance $G^* = (\pi\varepsilon)^{-1}$ through $\nu^{-1} = -(G\beta)'(G^*) = \varepsilon$ and $s = \nu\varepsilon = 1$. Likewise, the unitary class yields the exponents $\nu^{-1} = 2\varepsilon$ and $s = 1/2$. In these two classes, quantum corrections enhance backscattering in two dimensions ($\varepsilon = 0$), thereby localising all electronic states: metallic films are always insulating. On the contrary, the beta function for the symplectic class

$$\beta_{\text{Sp}}(G) = \varepsilon + \frac{1}{2\pi G} + O(G^{-3}), \quad (2.4)$$

is positive in two dimensions, at least for weak disorder. This signals the existence of a phase transition, as in three dimensions, and contrasts with the classical picture of Fig. 2.1(a). As often in disorder-induced transitions, long-range correlations also affect criticality (CROY 2012). One-dimensional systems, which are always localised in presence of short-range correlations, can undergo a delocalisation transition in presence of long-range hopping (CAO 2017).

2.1.2 Modelling disorder in relativistic semimetals

A key feature of metals is their large DoS at the Fermi level. In contrast, the DoS vanishes at the band crossing point of relativistic semimetals. In undoped semimetals, the Fermi level lies precisely at the point of zero DoS: Anderson's localisation cannot occur here. Then, how may disorder affect relativistic phases?

Random potential — Let us consider for concreteness a single Weyl node in a three-dimensional semimetal which contains defects; for instance, impurities located randomly at some lattice sites, or extended defects with random orientations. Whatever the nature of disorder, we model its effect on the low-energy physics by a random perturbation that couples linearly to bilinears in the fields, i.e. a background random potential. The effective Hamiltonian is then given in full generality by

$$\mathcal{H} = -i\boldsymbol{\sigma} \cdot \boldsymbol{\partial} + \sum_{\mu=0}^3 \sigma_{\mu} V_{\mu}(\mathbf{r}, t), \quad (2.5)$$

where $V_{\mu}(\mathbf{r}, t)$ for $\mu = 0, 1, 2, 3$, represent four possible couplings to the pseudospin. These four potentials are functions of position \mathbf{r} and in general of time t , which adds further difficulties. Depending on how fast disorder reaches thermodynamic equilibrium, we may consider two limit cases for the time dependence (CARDY 1996).

If the relaxation time of the defects is much less than the typical time of quantum fluctuations, the random degrees of freedom (i.e the positions or orientations of the defects) follow the same dynamics as the intrinsic degrees of freedom of the pure system. Statistical and disorder averages are equivalent. This situation corresponds to *annealed* disorder (BELITZ 2002). In crystalline solids, the defects' relaxation time far exceeds the typical time of quantum fluctuations. The defects are thus frozen at fixed positions or orientations, so that the potential $V_{\mu}(\mathbf{r})$ is no longer a function of time. This regime of *quenched* disorder is of much more practical interest. As a trade-off, statistical averages now depend on a particular realisation of the random variable V_{μ} , and performing averages over disorder configurations becomes notoriously difficult. We will always assume that disorder is quenched in relativistic semimetals.

In addition, the random potential couples to the pseudospin in two possible ways. On one hand, the component V_0 breaks the (emergent) chiral symmetry \mathcal{C} . This perturbation is ubiquitous, and can originate from any type of disorder: impurity-electron Coulomb interaction, alteration of the electron's kinetics by crystalline defects, etc. On the other hand, the components V_i for $i = 1, 2, 3$ break not only \mathcal{C} , but also the (emergent) time-reversal symmetry \mathcal{T} . The impurity-electron Coulomb interaction may break a spinless \mathcal{T} symmetry when the pseudospin represents orbital degrees of freedom, and different orbitals have different charge distributions. Magnetic impurities can also lift the spinful \mathcal{T} symmetry when the pseudospin stems from the actual electronic spin.

Let us compare Eq. (2.5) with equivalent models in two space dimensions, such as disordered graphene. There, the Pauli matrices represent the sublattice degree of freedom. Any local perturbation of the length and direction of the carbon-carbon bonds, or of the coordination number, leads to a random potential that couples asymmetrically to the A and B sublattices. And such deformations inevitably exist as a result of corrugation (the formation of ripples). Graphene thus harbours massless Dirac fermions which propagate in the background of a random non-Abelian gauge field (VOZMEDIANO 2008; VOZMEDIANO

2010). This offers fascinating parallels with gravity and cosmology, since the graphene sheet induces a two-dimensional curved metric. Note in passing that the kinetic part of the Hamiltonian (2.5) reduces to $-i(\sigma_x \partial_x + \sigma_y \partial_y)$ in two dimensions, while the third Pauli matrix σ_z acts as a chiral operator. This allows for an extra type of disorder in graphene: the random mass.

Statistical properties of the random potential — In presence of quenched disorder, we can describe the random potential within a statistical approach. If all components $\mu = 0, \dots, 3$ are independent, we may assign a probability distribution $P_\mu[V_\mu]$ to each separately. These distributions are normalised:

$$\int DV_\mu P_\mu[V_\mu] = 1. \quad (2.6)$$

Since $V_\mu(\mathbf{r})$ depends on position, P_μ is a functional, and Eq. (2.6) stands for a path integral. The functional form of the probability distribution depends on the defects' nature or concentration. But in the limit of a high concentration of weak defects, the central limit theorem ensures that the probability distribution assumes a Gaussian shape,

$$P_\mu[V_\mu] \propto \exp \left[-\frac{1}{2} \int d^d r d^d r' V_\mu(\mathbf{r}) h_\mu(\mathbf{r} - \mathbf{r}') V_\mu(\mathbf{r}') \right], \quad (2.7)$$

Let us show how the central limit theorem applies for point defects, using the so-called Edwards model (EDWARDS 1958; AKKERMANS 2007). Suppose indeed that N_i identical impurities are distributed randomly on lattice sites at positions $\{\mathbf{r}_i, i = 1, \dots, N_i\}$. Each impurity generates a potential $v(\mathbf{r})$, so that the total potential felt by conduction electrons is

$$V(\mathbf{r}) = \sum_{i=1}^{N_i} v(\mathbf{r}). \quad (2.8)$$

Denoting by $n_i = N_i/V$ the impurity density, the cumulants of order q have the following expressions at the thermodynamic limit:

$$\left(\overline{V(\mathbf{r}_1) \cdots V(\mathbf{r}_q)} \right)_c = n_i \int d^d r v(\mathbf{r} - \mathbf{r}_1) \cdots v(\mathbf{r} - \mathbf{r}_q). \quad (2.9)$$

In the limit of a high density $n_i \rightarrow \infty$ but weak potential $v \rightarrow 0$, all cumulants vanish except the variance ($q = 2$): the distribution becomes Gaussian. Advanced techniques can nonetheless extend the study of disordered semimetals to generic probability distributions. One of them is the functional renormalisation group, which we will mention again in the next chapter.

A Gaussian distribution is entirely defined by its mean and variance. The average of the potential over disorder configurations,

$$\overline{V_\mu(\mathbf{r})} = \int DV_\mu P_\mu[V_\mu] V_\mu(\mathbf{r}), \quad (2.10)$$

locally shifts the band crossing point in energy ($\mu = 0$) or momentum ($\mu = 1, 2, 3$). It is induced, in most cases, by charged impurities. Admittedly, doping completely alters electronic properties; but since we wish to probe the stability of the nodal level in Weyl

semimetals, we may as well fix the energy and momentum shift (2.10) to zero. The next order in disorder average is the variance. Assuming translational invariance the variance depends only on the distance between two points,

$$\overline{V_\mu(\mathbf{r})V_\nu(\mathbf{r}')} = \delta_{\mu\nu}g_\mu(\mathbf{r} - \mathbf{r}'). \quad (2.11)$$

The disorder variance $g_\mu > 0$ is nothing more than the inverse distribution h_μ of Eq. (2.7),

$$\int d^d r h_\mu(\mathbf{r}_1 - \mathbf{r})g_\mu(\mathbf{r} - \mathbf{r}_2) = \delta(\mathbf{r}_1 - \mathbf{r}_2). \quad (2.12)$$

Range of disorder correlations — Though real systems might exhibit arbitrary functions for the disorder variance, two main qualitative behaviours stand out. The first family of functions rapidly dies out beyond a finite distance ξ_d , the disorder correlation length. The archetype of such short-range correlation is a Gaussian function, which on virtue of isotropy depends only on the distance r as

$$g_{\mu,S}(\mathbf{r}) \propto e^{-r^2/\xi_d^2}. \quad (2.13)$$

Note that the Gaussian nature of the disorder variance $g_\mu(\mathbf{r})$ has nothing to do with the Gaussian nature of the probability distribution $P_\mu[V_\mu]$; one property does not imply the other. Since the wave length λ diverges at the band crossing point, whereas the range of disorder correlation ξ_d remains finite, the variance essentially reduces to a Dirac peak $g_{\mu,S}(\mathbf{r}) \propto \delta(\mathbf{r})$. Such short-range correlations typically occur with uncharged or screened impurities, vacancies, or insertion atoms. One caveat: numerical simulations on a lattice usually reproduce at least one pair of nodes, separated by a typical momentum b . Hence, ξ_d must be very large compared to b^{-1} in order to suppress internode scattering.

On the opposite side of the spectrum, the disorder variance may decay slowly on distance. Linear dislocations and grain boundaries generate such long-range correlations, provided they orient themselves randomly, with a power-law decay

$$g_{\mu,L}(\mathbf{r}) \propto r^{-a}. \quad (2.14)$$

The parameter a physically represents the codimension of the defects ($a = 2$ for lines, $a = 1$ for planes). Yet for our purposes, a could take on any real value. Another situation where the disorder variance looks similar to Eq. (2.14) is in presence of charged impurities. Indeed, in absence of screening the Coulomb repulsion between ionic impurities forces their relative positions to be correlated over long distances. Long-range correlations can dramatically modify criticality in phase transitions, as is well known in the Ising model (WEINRIB 1983).

2.1.3 Relevance of weak disorder

Does randomness modify qualitatively the system's properties? In systems where the Gaussian theory is critical, like the Ising model, we can ask ourselves whether weak disorder drives the phase transition to a new universality class. And the presence of either short- or long-range correlations of disorder is key input to this problem (WEINRIB 1983). In systems whose pure phase is described by a Gaussian theory, such as relativistic semimetals, the issue to address is whether disorder affects the properties of the clean

system so much as to induce a transition towards a new phase of matter. A simple scaling argument answers this question by comparing the energy of the pure system E to the energy broadening ΔE induced by disorder (IMRY 1975). In the spirit of the Imry-Ma criterion, we devise below a scaling argument adapted to relativistic phases to investigate the crossing point's stability.

For the sake of completeness, consider any gapless semiconductor with generic power-law dispersion $E \propto \lambda^{-\alpha}$, where the wave length λ of the Bloch state diverges at the nodal level. This also represents the mean (kinetic) energy in a weakly disordered system. After averaging over a box of size equal to the wave length λ , the variance of the energy reads

$$(\Delta E)^2 = \lambda^{-d} \int_{\lambda} d^d r \overline{V(\mathbf{0})V(\mathbf{r})} \propto \begin{cases} \lambda^{-d} & (\text{short range}) \\ \lambda^{-a} & (\text{long range}) \end{cases}. \quad (2.15)$$

The smaller the power-law exponent of ΔE in the long-wave length regime, the more relevant the disorder. Yet, both the kinetic energy and the disorder-induced broadening vanish, and so we must compare them near the nodal level. In presence of either short- or long-range correlations, the relative strength of disorder $(\Delta E/E)^2$ scales with the diverging wave length as λ^{-y} , where

$$y = \min(d, a) - 2\alpha. \quad (2.16)$$

The sign of the scaling exponent (2.16) dictates whether weak disorder is relevant or irrelevant. Remarkably, this sign criterion involves not directly the dimension d , but the effective dimension $d_{\text{eff}} = \min(d, a)$. As far as the nodal stability is concerned, disorder correlations matter as much as dimensionality; dimension acts as the default correlation exponent when neighbouring defects disregard one another at long distances.

- When $y < 0$, the relative strength of disorder diverges near the nodal level, which means the weak disorder hypothesis breaks down and impurities smear the properties of the pure system. Such instability occurs in low-dimensional systems with short-range correlations ($d < 2\alpha$) or in systems with sufficiently long-range correlations ($a < 2\alpha$). This criterion says nothing about the nature of the disordered phase, though. Usually a DoS emerges at the Fermi level, and the disordered material acquires a diffusive metallic character.
- When $y > 0$, the relative strength of disorder vanishes near the nodal level, thus preserving the pure crossing point. The relativistic semimetallic phase is immune to a low amount of disorder. This robustness holds in high-dimensional systems or systems with sufficiently short-range correlations ($d < a$ and $d > 2\alpha$, or $a < d$ and $a > 2\alpha$). However, this stability cannot survive in the strong disorder regime. Due to this limited immunity to disorder, Weyl and Dirac semimetals ($d = 3$, $\alpha = 1$) turn into a diffusive metal beyond a non-zero critical disorder strength through a second-order phase transition. E. Fradkin first discovered this semimetal-metal transition (FRADKIN 1986a; FRADKIN 1986b). It was later shown that all degenerate semiconductors undergo non-Anderson disorder-induced transitions (SYZРАНOV 2018; SYZРАНOV 2019). Here again, this simple scaling argument remains powerless to determine the nature of this transition or to explore the vicinity of the critical point. More advanced techniques are needed (mean-field approximation, renormalisation group).

- When $y = 0$, the disorder-induced broadening and the kinetic energy are comparable, showing that the non-Anderson transition in gapless semiconductors have lower critical dimension $d_\ell = 2\alpha$. For relativistic phases, $d_\ell = 2$. This *marginal* situation occurs notably in graphene for short-range correlations ($\alpha = 1$, $a > d$ and $d = 2$). The DoS acquires in graphene a small yet non-zero exponential contribution, however weak the disorder strength (FRADKIN 1986a; FRADKIN 1986b).

In the following section, we discuss the semimetal-metal transition phenomenologically.

2.2 Phenomenology of the semimetal-metal transition

Relativistic semimetals undergo a second-order phase transition, where the critical point is located at zero energy (the nodal level) and non-zero disorder strength. As in all continuous transitions, the physical observable obey universal scaling laws when approaching the critical point. The nodal level acquires an average DoS on the disordered metallic side, and provides a good order parameter for the transition. The mean free path, on the other hand, diverges at the critical point, but is finite in metallic phase and diminishes as disorder strengthens and electronic transport becomes more and more diffusive.

2.2.1 Phase diagram

The density of states as order parameter — The scaling argument of Sec. 2.1.3 predicts that three-dimensional relativistic semimetals are immune to weak disorder. But in the limit of infinitely strong disorder, the electron’s free kinetics becomes irrelevant: the material’s properties should change drastically. A transition must take place at an intermediate disorder strength. E. Fradkin first studied this transition in the simplest case a single Weyl cone affected by short-range correlated disorder which couples symmetrically with the pseudospin (FRADKIN 1986a; FRADKIN 1986b). The restriction to a single Weyl cone is reasonable whenever intravalley scattering dominates over intervalley scattering, which is all the more likely that the typical separation between Weyl cones is large, and the random potential smooth at the microscopic scale. This corresponds to a (time-reversal) \mathcal{T} -preserving perturbation $\sigma_0 V(\mathbf{r})$ with delta-peaked variance

$$g(\mathbf{r}) = \gamma \delta(\mathbf{r} - \mathbf{r}'), \quad (2.17)$$

as defined in Eq. (2.11) and discussed in Sec. 2.1.2.

The *disorder strength* $\gamma > 0$ drives the crossing through the quantum critical point, similarly than temperature drives classical phase transitions. Let γ^* be the critical disorder strength. We wish to find an order parameter for the transition, i.e. a physical observable whose behaviour differs qualitatively in the phases of low and high disorder strengths. As for most second-order phase transitions, a symmetry of the pure Hamiltonian is spontaneously broken under disorder. One natural candidate is the emergent chiral symmetry of a single Weyl node, which associates eigenstates of opposite energies. An energy asymmetry should therefore affect the distribution of eigenstates near the nodal level. And indeed, the disorder-averaged DoS $\bar{\rho}(E)$ acts as an order parameter at zero energy, up to possible small corrections due to rare-region effects. For subcritical disorder ($\gamma < \gamma^*$), it vanishes and the semimetallic phase survives; for supercritical disorder ($\gamma > \gamma^*$), the Fermi level acquires a non-zero DoS, which is characteristic of a metallic phase.

We sketch in Fig. 2.2(a) the typical behaviour of the mean DoS at the Fermi level $\bar{\rho}(0)$ as a function of disorder strength. On the metallic side, the mean free path ξ of zero-energy electronic waves is well defined. (The mean-free path plays the role of the correlation length in spin systems). It diverges at the critical point, and decreases progressively with disorder strength as electronic waves scatter more and more frequently. Both $\bar{\rho}(0)$ and ξ scale in a power-law fashion near the critical point. Sec. 2.2.2 addresses these power laws and their exponents. The critical point is located exactly at $E = 0$ and $\gamma = \gamma^*$, but a critical-like behaviour spreads at finite energy over a small window of disorder strength, which grows as we move away from the nodal level. The crossover region traces out a critical fan in the energy-disorder plane, as in Fig. 2.2(b).

Note that a strong enough disorder can localise semimetallic states if allowed by symmetry, as long as the material passes through an intermediate metallic phase. In fact, some numerical simulations observed a semimetal-metal transition followed by Anderson's localisation on the same lattice model (PIXLEY 2015). For this reason, and to offer a point of comparison, we stretched the axis of schematic 2.2(a) to larger disorder strength to include the metal-insulator transition.

Rare-region effects — Self-consistent and renormalisation group techniques establish that the mean DoS vanishes exactly for subcritical disorder (SYZРАНОВ 2018). Yet perturbative techniques disregard rare disorder fluctuations which could in principle

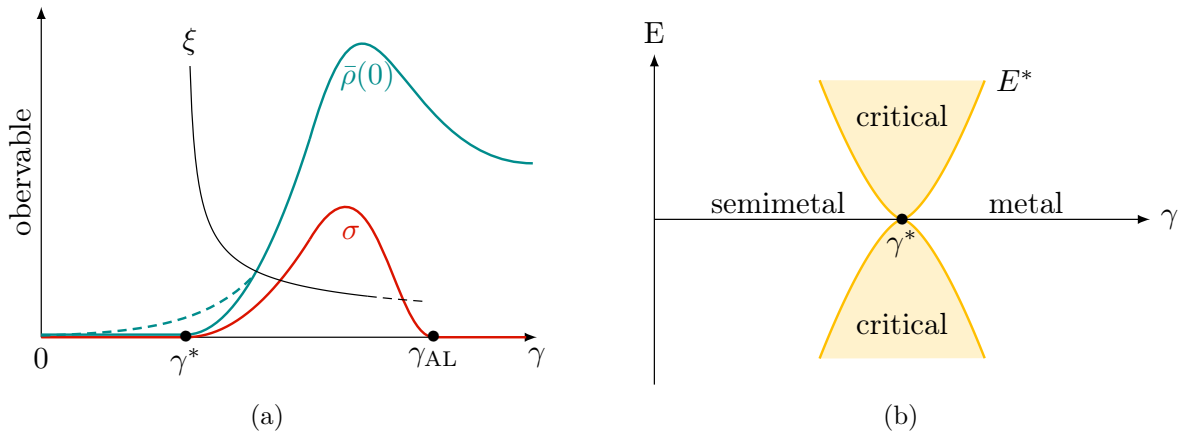


Figure 2.2 | (a) Qualitative behaviour of the mean density of states at the nodal level $\bar{\rho}(0)$ (the solid blue curve) and the mean DC conductivity σ (the solid red curve) against disorder strength γ . Both quantities vanish on the semimetallic side $\gamma < \gamma^*$, where γ^* is the critical disorder strength, notwithstanding exponentially small corrections to the density due to rare-region effects (the dashed blue curve). The density $\bar{\rho}(0) \sim (\gamma - \gamma^*)^\beta$ and the conductivity $\sigma \sim (\gamma - \gamma^*)^s$ increase in a power-law fashion on the diffusive metallic side $\gamma > \gamma^*$. The correlation length, which is also the mean free path (the solid black curve), diverges as $\xi \sim (\gamma - \gamma^*)^{-\nu}$ at the critical point. If allowed by symmetry, a strong enough disorder localises the electronic waves of the metallic phase through the critical point γ_{AL} of an Anderson transition. (b) The critical fan (the yellow solid curve) delineates the crossover region $E^* \sim (\gamma - \gamma^*)^{\nu z}$ for the energy E between a critical behaviour (inside the pale yellow region), and an analytical behaviour (on either side of the fan). Within the fan, the larger the energy, the less sharp the transition.

contribute to the subcritical DoS. The theoretical picture of this phenomenon is still controversial.

Two scenarios have been proposed. In the first scenario, non-perturbative solutions to the classical equation of motion generate small corrections to the mean density, known as Lifshitz tails (NANDKISHORE 2014; YAIDA 2016). These corrections are non-universal; they depend on the microscopic details. They are exponentially suppressed for weak disorder,

$$\bar{\rho}_{\text{tail}}(E = 0, \gamma) \sim e^{-\xi/\gamma} \quad (2.18)$$

where here the equivalence \sim is valid up to some numerical power. Yet (BUCHHOLD 2018b) showed by expanding and integrating out the Gaussian fluctuations around instantonic solutions that the prefactor in Eq. (2.18) vanishes at zero energy. In the second scenario, resonances between two different rare regions with strong disorder generate a non-zero DoS (ZIEGLER 2018), but as was argued in (BUCHHOLD 2018a), these resonances cannot create states exactly at zero energy.

If one of these scenarios is true, either the DoS is no suitable order parameter strictly speaking, which does not preclude other observables to be so, or the system avoids the critical point, leading to a sharp crossover instead of a genuine phase transition. Interestingly, a few numerical simulations found a small nodal density in the semimetallic side compatible with Lifshitz tails, but whether these come from the physics or the method is hard to decide (PIXLEY 2016b; PIXLEY 2016a). At any rate, these thin corrections cannot hide the critical point entirely.

Particle-hole symmetry breaking — Here we link the emergence of a DoS for supercritical disorder to the breaking of chiral symmetry (FRADKIN 1986a; FRADKIN 1986b). Let $\mathcal{H}_0 = -i\boldsymbol{\sigma} \cdot \boldsymbol{\partial}$ be the Hamiltonian of a clean Weyl node. In this model, the chiral symmetry acts by multiplication (conjugation) on eigenstates (the Hamiltonian) by a Pauli matrix σ_i , provided the corresponding coordinate x_i is reversed (this extra requirement is specific to three dimensions). Choosing the z direction,

$$\mathcal{C} : \mathcal{H}_0(x, y, z) \mapsto \sigma_z \mathcal{H}_0(x, y, -z) \sigma_z = -\mathcal{H}_0(x, y, z). \quad (2.19)$$

Since σ_z anticommutes with the Hamiltonian up to a harmless spatial inversion, \mathcal{C} refers strictly speaking to an *antisymmetry*, rather than a symmetry¹. We will also use this loose but widespread terminology unless this lack of rigour threatens the clarity of the exposition.

In presence of disorder, the retarded Green's function G is defined by

$$(\mathcal{H}(\mathbf{r}) - E - i\Gamma)G(\mathbf{r}, \mathbf{r}', E; V(\mathbf{r})) = \delta(\mathbf{r} - \mathbf{r}'), \quad (2.20)$$

where $\Gamma = 0^+$ denotes some infinitesimal broadening, which avoids on-shell divergences. At this stage, G depends on disorder through the random potential $V(\mathbf{r})$. Investigating the system's properties in a particular disorder configuration, which depend on a tremendous number of microscopic parameters, would be a formidable task. Mean observables depend instead on a few macroscopic variables. Fortunately, the particle-hole symmetry of the pure

¹Note also that a chiral (anti)symmetry is unitary, as opposed to its close cousin the particle-hole (anti)symmetry, which is antiunitary.

Hamiltonian enables to build a mean observable as order parameter. Indeed, Eq. (2.19) entails

$$\sigma_z G(\mathbf{r}_-, \mathbf{r}, E; V(\mathbf{r}_-)) \sigma_z = -G(\mathbf{r}, \mathbf{r}, -E; -V(\mathbf{r})), \quad (2.21)$$

where $\mathbf{r} = (x, y, z)$ and $\mathbf{r}_- = (x, y, -z)$. By averaging Eq. (2.21) over the potential, and using that the probability distribution is even in V , we find the anticommutation relation

$$\{\sigma_z, \bar{G}(\mathbf{r}_0, \mathbf{r}_0, 0)\} = 0, \quad (2.22)$$

where $\mathbf{r}_0 = (x, y, 0)$ and \bar{G} denotes the mean Green's function. Also, the well-known expression for the DoS (AKKERMANS 2007)

$$\bar{\rho}(E) = \frac{1}{\pi} \text{Im Tr } \overline{G(\mathbf{r}, \mathbf{r}, E)}, \quad (2.23)$$

applies to any position \mathbf{r} because the disorder average restores homogeneity. Setting $E = 0$ in Eq. (2.23), using Eq. (2.22) and the cyclicity of the trace, we conclude that the DoS should vanish at zero energy, unless a strong enough disorder spontaneously breaks the particle-hole symmetry.

Contrast with Anderson's localisation — Even though the same ingredient, namely disorder, triggers Anderson and non-Anderson transitions, and that both transitions have lower critical dimensions $d_\ell = 2$ in accord with the scaling arguments of Sec. 2.1.1 and Sec. 2.1.3, they differ in many respects.

Anderson's localisation appears in metallic phases, i.e. in electronic phases with a large DoS at the Fermi level. Non-Anderson transitions appear on the contrary in phases where the Fermi level lies near a band edge or crossing point, where the DoS vanishes. Crucially, the origins of the two transitions differ radically. In Anderson's localisation, electronic waves stop propagating when they get trapped by random scatterers; in gapless semiconductors such as relativistic semimetals, there are no propagating waves because of the vanishing DoS, unless disorder is strong enough for nearby energy states to overlap with the nodal level.

As a corollary, the critical manifolds in the energy-disorder strength diagram look dissimilar. Localisation occurs typically when tuning the disorder strength γ at fixed energy, or by tuning the energy below the mobility edge E_c at fixed supercritical disorder strength, as in Fig. 2.1(b). Non-Anderson transitions occur only at a fixed energy (not over an energy window), which is pinned to zero in relativistic semimetals, as in Fig. 2.2. Hence, only the disorder strength controls the proximity to the critical point. Consequently, different order parameters capture the two transitions. In Anderson's localisation, the mean DoS behaves smoothly at the critical point, while the DC conductivity vanishes. In relativistic semimetals, both the mean DoS and the DC conductivity are zero on the semimetallic side, and non-zero on the metallic side. Yet, as we will see in Sec. 2.4, the so-called typical DoS – or any higher-order average – vanishes on the localised and semimetallic side, but not on the metallic side, and thus provides an extra order parameter for Anderson and non-Anderson transitions alike (JANSSEN 2001).

2.2.2 Conventional scaling laws

We now define the conventional critical exponents of the semimetal-metal transition (correlation length exponent ν , dynamical exponent z) and discuss how they dictate the scaling laws of the DoS and other observables.

The one-parameter scaling hypothesis — Experiments and numerical simulations show that in almost all continuous phase transitions, whether classical or quantum, observables behave in a power-law fashion near the critical point as a function of the transition parameter (temperature in the first case, parameter of the Hamiltonian which monitors the ground state in the second case). Many theoretical arguments explain this observation (GOLDENFELD 2018). The singular behaviour of the free energy at the critical point results from the divergence of the correlation length ξ , which quantifies the typical distance over which fluctuations of the order parameter correlate. This length blows up near the critical point as $\xi \sim (\gamma - \gamma^*)^{-\nu}$, and this power law defines the so-called correlation length exponent ν . In the metallic side of the semimetal-metal transition, the mean free path is proportional to the correlation length, and follows the same scaling law (ROY 2016).

Let us now consider how the Green's function scales at the nodal level with the separation r . Widom's one-parameter scaling hypothesis states that there exists a dimensionless function f such that

$$G(\mathbf{0}, \mathbf{r}) = r^{1-d} f(r/\xi). \quad (2.24)$$

Eq. (2.24) represents the probability amplitude that a particle created at the origin propagates to the position \mathbf{r} . Mean-field theory shows that $f(r/\xi) \propto e^{-r/\xi}$ up to some numerical factor. At the critical point, ξ diverges, $f(0)$ is finite, and the Green's function scales as r^{1-d} . In reality, the scaling exponent deviates from the prediction of naive dimensional analysis, because an extra microscopic length scale ℓ interferes. The critical Green's function actually scales as

$$G(\mathbf{0}, \mathbf{r}) \sim r^{1-d} (\ell/r)^\eta, \quad (2.25)$$

where η is the so-called anomalous field exponent. Similarly, the naive dimensional analysis for the energy $|E| = k$ breaks down at the critical point. Instead, the critical dispersion relation is of the form $|E| \sim \ell^{z-1} k^z$, where the dynamical exponent z differs from unity. This implies that defects break the effective Lorentz invariance of the disorder-averaged physics at criticality.

Density of states — From these basic critical exponents, we can find the scaling laws for more complex observables, such as the DoS, which plays the role of an order parameter. The DoS can be found by counting the number of modes in a shell of energy E and infinitesimal width dE . At the critical disorder strength, we have $\bar{\rho}(E) \sim k^{d-1} dk/dE \sim E^{d/z-1}$. Slightly away from criticality, a more general relation holds (KOBAYASHI 2014)

$$\bar{\rho}(E, \gamma) = |E|^{d/z-1} f_1[(\gamma - \gamma^*)|E|^{-1/z\nu}]. \quad (2.26)$$

In Eq. (2.26), the argument of the scaling function f_1 is indeed scale invariant, in accord with the scaling of the crossover region of the critical fan. The scaling law at the critical disorder strength imposes $f_1(0) \sim 1$ to recover the correct energy dependence. On the contrary, at zero energy, we must cancel out the energy dependence in Eq. (2.26) to get the density-disorder strength relation. We thus set $f_1(-\infty) = 0$ to recover the vanishing DoS for subcritical disorder, and $f_1(x) \sim x^{\nu(d-z)}$ in the limit $x \rightarrow +\infty$ for supercritical disorder. All in all, the supercritical DoS at the nodal level scales as $\bar{\rho}(\gamma) \sim (\gamma - \gamma^*)^\beta$ where the density exponent satisfies the hyperscaling relation (SBIERSKI 2016; ROY 2016; GOSWAMI 2011)

$$\beta = \nu(d - z). \quad (2.27)$$

Conductivity — An observable of particular interest in experiments is the DC electrical conductivity. Except for the DoS, we will always deal with disorder-averaged quantities, and so we will neglect the overline when writing the symbol for those observables. Slightly above the critical disorder strength the conductivity at zero doping scales as $\sigma(\gamma) \sim (\gamma - \gamma^*)^s$, where $s = \nu(d - 2)$ as in Anderson’s localisation. Slightly below, however, numerical and analytical results differ. To understand why, we must recall that numerical simulations deal with finite-sized samples exactly at the nodal level (SBIERSKI 2014). Since the DoS vanishes at the nodal level for subcritical disorder, there are no charge carriers, and $\sigma = 0$. Analytical approaches are insensitive to finite-size effects. The vanishing of the DoS $\bar{\rho}$ near the nodal level is compensated by the divergence of the scattering time τ , which leads to a finite conductivity $\sigma = v_F^2 \bar{\rho} \tau$ at zero energy. For very weak disorder $\gamma \ll \gamma^*$ in particular, the conductivity scales as $\sigma(\gamma) \sim \gamma^{-1}$, provided the thermodynamic limit is taken before the zero energy limit. When the material is doped to the energy E , the conductivity satisfies the more general scaling relation (SYZANOV 2015)

$$\sigma(E, \gamma) = (\gamma - \gamma^*)^{\nu(d-2)} f_2 \left[(\gamma - \gamma^*) |E|^{-1/z\nu} \right], \quad (2.28)$$

where f_2 denotes a scaling function, as in Eq. (2.26). At low but non-zero temperatures, we can integrate Eq. (2.28) over the Fermi-Dirac distribution $n_F(E, T) = [1 + \exp(E/k_B T)]^{-1}$

Exponent	Short-range				Long-range
	Numeric	Mean-field	One-loop	Two-loop	Two-loop
ν	1.47 ± 0.03^a 1.01 ± 0.06^f	1^b	1^c	0.67^d	1.60^e
z	1.49 ± 0.02^a 1.50 ± 0.04^f	2^b	1.5^c	1.32^d	1.25^e
η	inaccessible	0^b	0^c	-0.18^e	-0.09^e
β	1.51 ± 0.09^f	1^b	1.5	1.13	2.80

^a(SBIERSKI 2015) ^b(KOBAYASHI 2014) ^c(GOSWAMI 2011) ^d(ROY 2014) ^e(LOUVET 2017) ^f(PIXLEY 2016c)

Table 2.1 | Conventional critical exponents (correlation length exponent ν , dynamical exponent z , anomalous field exponent η , density of states exponent β) at the semimetal-metal transition in three dimensions in the universality classes of short-range (first columns) or long-range (last column) correlated disorder. First column: finite-size scaling analyses of the conductance (quantum transport) or the mean density of states. The correlation length exponent ν ranges from 0.6 to 1.5 according to the details of the simulation. Despite the sensitivity of numerical estimates to the critical point’s location, this inconsistency cannot originate from the method alone, but may signal the non-universality of ν . The issue is still unresolved. Second column: one-loop renormalisation group exponents in dimension $d = 2 + \varepsilon$, with direct substitution $\varepsilon = 1$. Third and fourth column: two-loop results. The estimate of ν , and to a lesser extent of z , worsens with the order of the ε -expansion. Last column: two-loop results in the universality class controlled by long-range correlations. For concreteness, the disorder correlation exponent is set to $a = 2.5$.

to find the T -dependent conductivity,

$$\sigma_{\text{th}}(T, \gamma) = \int_{-\infty}^{\infty} n_{\text{F}}(E, T) \bar{\rho}(E) \sigma(E, \gamma). \quad (2.29)$$

In particular, the critical conductivity scales as $\sigma_{\text{th}}(T, \gamma^*) \sim T^{(d-2)/z}$ (SYZRANOV 2015). The scaling laws of the conductance prove to be useful to determine both the correlation length exponent ν and the dynamical exponent z from numerical simulations, in conjunction with finite-size effects.

Specific heat — Numerical simulations can also extract the dynamical exponent through the scaling of thermodynamic observables. Those are of less interest for our purposes, since we will focus on the pure quantum critical point and disregard any crossover at non-zero temperatures. An example is the specific heat at constant volume $C_V = \partial \langle E \rangle / \partial T$, whose integral expression reads (GOSWAMI 2011)

$$C_V = \int_{-\infty}^{\infty} \frac{\partial n_{\text{F}}}{\partial T}(E, T) \bar{\rho}(E) E = \frac{1}{4k_{\text{B}}T^2} \int_{-\infty}^{\infty} \frac{\bar{\rho}(E) E^2}{\cosh(E/2k_{\text{B}}T)^2}. \quad (2.30)$$

In the semimetallic and metallic phases, the scaling laws read $C_V \sim T^3$ and $C_V \sim T$ respectively. At the critical disorder strength, $C_V \sim T^{d/z}$.

Estimate of the critical exponents — In numerical simulations, the finite-size scaling analysis of the distribution of the mean DoS (2.26) and the conductance (2.28) gives access to the correlation length exponent ν (SBIERSKI 2015; PIXLEY 2016a). The scaling of the critical conductance or the mean critical DoS with doping level, or the temperature dependence of the specific heat, gives access to the dynamical exponent z . The scaling of the mean DoS at the Fermi level gives directly the order parameter exponent β (PIXLEY 2016c; PIXLEY 2015). The anomalous field exponent η , on the other hand, is hard to determine in numerical simulations, because it enters only correlations of operators. The first column of Tab. 2.1 shows independent numerical estimates for ν , z and β . As a general rule, the values of ν are less precise than z , because of the location of the critical point is hard to find. This does not explain, though, the huge discrepancies observed between different studies, and even different methods used in one study. Estimates of ν fall within a range as wide as $[0.6, 1.5]$. No clear answer has been proposed to this issue yet. The correlation length exponent may be non-universal, and sensitive to microscopic details.

Analytical approaches can predict these exponents. The simplest technique, mean-field theory, gives only crude estimates; the renormalisation group leads in principle to better and better estimates as higher-order corrections in disorder strength are included. On one hand, the dynamical exponent $z \simeq 1.5$ agrees well with numerical estimates, especially at one-loop order. The estimate deviates at higher order, but the two-loop and three-loop expansions yield credible results. On the other hand, the determination of the correlation length exponent suffers again from serious flaws. The estimate worsens dramatically with the order of the expansion, so much so that the four-loop result is totally unrealistic (GRACEY 2008a; GRACEY 2008b). The sensitivity of ν to the presence of evanescent operators (operators generated by quantum corrections initially absent from the theory) may explain this unreliability. Anderson's localisation faces the same issue.

2.2.3 Effect of various types of disorder

In the simple picture presented in Sec. 2.2.1, a scalar uncorrelated random potential drives the semimetal to a diffusive metallic phase. When multiple types of disorder interplay, each associated with its own strength parameter, the phase diagram gains in complexity, but the same qualitative features hold. The DoS, conductivity, and other observables obey the scaling laws of Sec. 2.2.2, but the critical exponents depend on the nature of disorder. We consider the effect of correlations and of the symmetries of the random potential separately.

Interplay between disorder correlations — Assume that the scalar potential correlate over distances of the order of the system size, for instance due to the presence of randomly oriented line or plane defects. The disorder variance $g(\mathbf{r}) = \gamma_S \delta(\mathbf{r}) + \gamma_L r^{-a}$ acquires short-range (strength parameter γ_S) and long-range (strength parameter γ_L) contributions, the latter monitored by the disorder correlation exponent a . The phase diagram of a Weyl semimetal in the (γ_S, γ_L) plane is sketched in Fig. 2.3(a) for moderate disorder correlations (the disorder correlation exponent a exceeds the lower critical dimension $d_\ell = 2$) (LOUVET

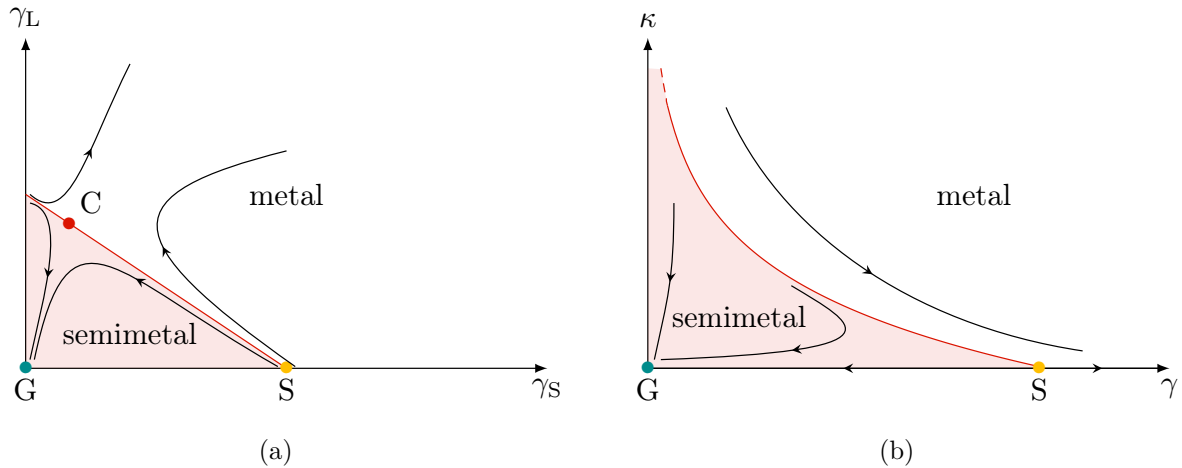


Figure 2.3 | (a) Phase diagram for a random scalar potential with both short-range correlations (coupling strength γ_S) and long-range correlations (coupling strength γ_L). The disorder correlation exponent a lies in the ‘critical’ domain $2 < a \lesssim d$ (with d the space dimension) where long-range correlations control criticality. The black arrows represent several flow lines of the couplings. The Gaussian fixed point G (blue dot \bullet) attracts all coupling strengths inside the light red region; the corresponding basin of attraction delineates the semimetallic phase. Outside coupling strengths flow to infinity, possibly to a remote strong disorder fixed point not accessible by the perturbative renormalisation group; the blank area delimits the metallic phase. The short-range fixed point S (yellow dot \bullet), which controls criticality for white noise disorder, becomes trivial for $a < d$, to the benefit of the critical fixed point C (red dot \bullet): long-range correlations modify the universality class of the semimetal-metal transition. Adapted from (LOUVET 2017). (b) Same phase diagram for a short-range correlated potential with both a time-reversal- (\mathcal{T}) preserving component (coupling strength γ) and a \mathcal{T} -breaking component (coupling strength κ). The critical \mathcal{T} -breaking strength κ^* is rejected to infinity at first order, but should actually be finite to agree with numerical simulations, which observe κ -induced transitions (SBIERSKI 2016). At any rate, the usual short-range fixed point controls criticality.

2017). Instead of a critical point γ^* , a critical line $\gamma_L^*(\gamma_S)$ develops where the mean free path diverges, and the mean DoS emerges at the Fermi level, thereby reproducing the singular behaviour depicted in Fig. 2.2(a). The same line delimits the semimetallic phase (near the origin of the graph) from the metallic phase (in the strong disorder region). Remarkably, long-range correlations generate short-range correlations, even when absent in the microscopic theory, while the reverse is untrue. The white noise perturbation thus plays a special role for the transition.

The power laws discussed in Sec. 2.2.2 still apply near the critical line – the same phenomenology holds –, but the exponents differ in presence of long-range correlations for which $2 < a < d$, which means that in this case the semimetal-metal transition belongs to a distinct universality class parametrised by the disorder correlation exponent a . This new universality class is determined by the critical fixed point C of Fig. 2.3(a). We determine the exponents of this new universality class in Sec. 3.2. The last column of Tab. 2.1 lists the corresponding exponents ν , z , η and β in terms of the small expansion parameter $\delta = a - 2$.

Interplay between \mathcal{T} -preserving and \mathcal{T} -breaking disorder — Suppose now the random potential to be uncorrelated, but to couple to the pseudospin of the Weyl fermions in all possible ways. By virtue of isotropy, we write $g_0(\mathbf{r}) = \gamma \delta(\mathbf{r})$ for the variance of the scalar (time-reversal preserving) perturbation, and $g_i(\mathbf{r}) = \kappa r^{-a}$ with the same disorder strength κ for the three components $i = 1, 2, 3$ of the vectorial (time-reversal breaking) perturbation. As we will see in Sec. 3.2.3, the phase diagram resembles the one previously discussed, except that the critical line crosses the κ -axis at a point beyond the reach of one-loop computations. The exact location of this end point must be finite, because a lone vector potential suffices to induce a transition to the metallic phase in numerical simulations (SBIERSKI 2016). Crucially, a random vector potential *preserves* the universality class of the semimetal-metal transition, however strong (κ large) and long ranged correlated (a small).

The generalisation to a band crossing point with higher degeneracy, such as a Dirac cone or several Weyl nodes connected by intervalley scattering, allows for even more couplings of random scatterers to the electronic degrees of freedom (GOSWAMI 2017). The phase diagram retains, here again, the same features, with a semimetallic region at weak disorder, and a metallic region at strong disorder. We show in Sec. 3.2.3 that the universality class of the transition is unaffected, unless long-range correlations strengthen intervalley scattering so much that they control criticality.

2.3 The self-consistent Born approximation

A simple theoretical approach to the semimetal-metal transition – beyond a phenomenological description – relies on the so-called self-consistent Born approximation (SCBA). This technique implements a microscopic version of the mean-field theory, and follows from a saddle-point approximation of the path integral. The SCBA yields satisfactory results in the weak disorder regime, predicts the existence of the critical point, reproduces the qualitative features of the transition, but misses the anomalous contribution in critical exponents. By carrying out a large N expansion (with N the fermion number) of the path integral, corrections to the SCBA can be found systematically. We also apply the SCBA

in Chapter 4 to probe surface effects. For now, let us see how the Born approximation applies to disordered phases.

2.3.1 Approximation schemes of the self-energy

Self-energy in disordered systems — Though first introduced to solve quantum scattering problems, the SCBA proves useful in statistical field theory to check the existence of a critical point and determine approximately the critical exponents. It advantageously preserves conservation laws – especially the continuity equation. In the original formulation, the Born approximation relates outgoing and incoming energy eigenstates (BORN 1926), but it can do without reference to fields and use Green’s functions instead. The latter perspective better suits our purposes.

The Green’s function G was defined in Eq. (2.20) as the inverse of the full Hamiltonian $\mathcal{H} = \mathcal{H}_0 + V$, where \mathcal{H}_0 is the Weyl Hamiltonian and V the random scalar potential; it represents the response of the Schrödinger equation to a pulse in real space. The amplitude of presence at point \mathbf{r}' in response to a pulse at point \mathbf{r} is given in the pure system by the clean Green’s function $G_0(\mathbf{r} - \mathbf{r}_1)$, which depends only on the distance between positions \mathbf{r} and \mathbf{r}' thanks to translational invariance. In presence of disorder, we can massage the expression of G into the formal self-consistent equation (AKKERMANS 2007)

$$G = G_0 - G_0 V G, \quad (2.31)$$

where the product represents a spatial convolution of some sort,

$$(G_0 V G)(\mathbf{r}, \mathbf{r}') = \int d^d r_1 G_0(\mathbf{r}, \mathbf{r}_1) V(\mathbf{r}_1) G(\mathbf{r}_1, \mathbf{r}'). \quad (2.32)$$

As shown pictorially in Fig. 2.4(a), a particle moving from the origin to point \mathbf{r} either moves freely (this is the first term), or scatter at least once with the interacting potential V before reaching the end point (this is the second term with an impurity line). It is judicious, however, to pursue the self-injection of G to achieve a non-perturbative expansion at second order in V . We arrive at the relation $G = G_0 - G_0 V G_0 + G_0 V G_0 V G$, represented graphically in Fig. 2.4(b). Without pushing the self-substitution ad infinitum, we now average this equation. This kills the first-order term, and any odd power in V that would appear further in the expansion. The reappearance of translational invariance allows to Fourier-transform the disorder-averaged Green’s function \bar{G} . Introducing the momentum \mathbf{k} , which is the conserved quantity associated to translation symmetry, we get the non-perturbative expansion known as the Schwinger-Dyson equation,

$$\bar{G}(\mathbf{k}) = G_0(\mathbf{k}) + G_0(\mathbf{k}) \Sigma(\mathbf{k}) \bar{G}(\mathbf{k}), \quad \Sigma(\mathbf{k}) = \overline{V G_0 V \bar{G}(\mathbf{k})} \bar{G}(\mathbf{k})^{-1}. \quad (2.33)$$

This equation describes how quasiparticles propagate in the background of static random scatterers, which induce an infinite number of elastic scattering processes. Eq. (2.33) conveniently collects a geometric series $\bar{G} = G_0 + G_0 \Sigma G_0 + G_0 \Sigma G_0 \Sigma G_0 + \dots$, depicted as the chain of reducible diagrams of Fig. 2.4(c), into a neat formula. The *self-energy* Σ encodes the average effect of disorder on the quasiparticles’ energy (real part) and lifetime (imaginary part).

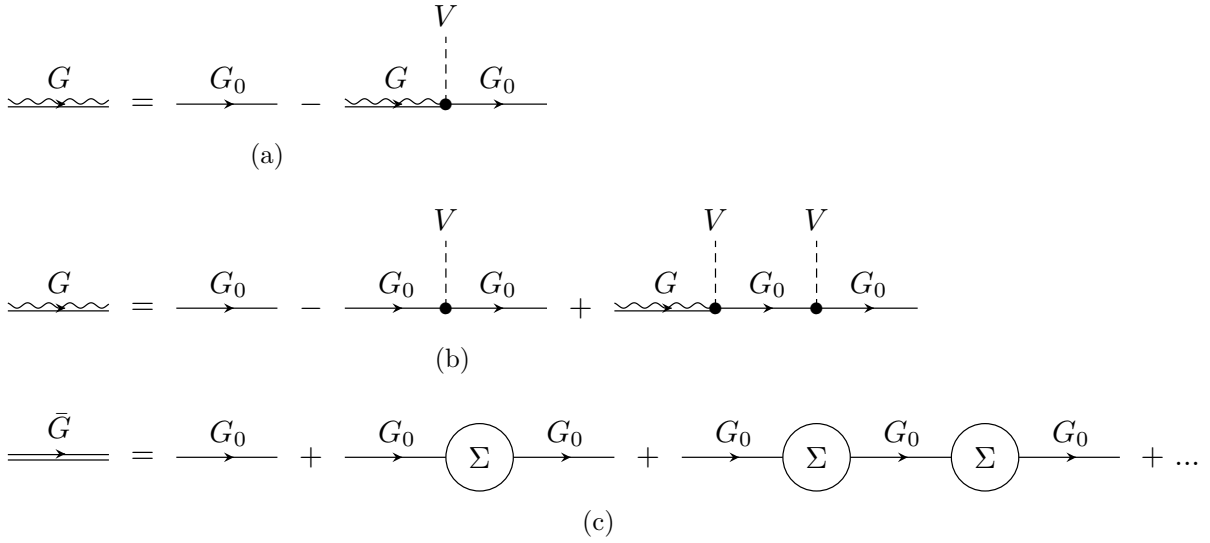


Figure 2.4 | (a) Quasiparticle motion dressed by scattering processes with the background defects. Among all probability amplitudes which contribute to the full Green's function G (wiggly-solid line) in a particular disorder realisation, we can collect those where the particle moves freely (clean Green's function G_0 , simple line), and those where the particle scatters with the interaction potential V , depicted as an impurity line (second term). (b) We can also collect diagrams more thoroughly, with those where the particle moves freely, those where the particle scatters once with the interaction potential V , and those where the particle scatters at least twice (third term). This non-perturbative expansion can be continued indefinitely. (c) The disorder-averaged Green's function \bar{G} (double line) follows from a geometric series in $G_0\Sigma$, with Σ the self-energy, given by all one-particle irreducible two-point diagrams with external legs removed. This expansion is known as the Schwinger-Dyson equation (DYSON 1949).

The Born approximation — At this point, Eq. (2.33) is exact, but we cannot proceed as long as we have no workable expression for the self-energy. An approximation scheme is needed. A first possibility is to ignore scattering processes hidden in the factors G and \bar{G} of the self-energy (2.33), and replace them by the clean Green's function G_0 . This amounts to expand the self-energy perturbatively to second order in the random potential, or equivalently to first order in disorder strength γ . With uncorrelated disorder, the self-energy becomes \mathbf{k} -independent,

$$\Sigma \simeq \int d^d r_1 d^d r_2 e^{-i\mathbf{k}\cdot\mathbf{r}_1} \overline{V(\mathbf{r}_1)V(\mathbf{r}_2)} G_0(\mathbf{r}_2 - \mathbf{r}_1) G_0(\mathbf{r}_2) G_0(\mathbf{k})^{-1} = \gamma \int \frac{d^d q}{(2\pi)^d} G_0(\mathbf{q}). \quad (2.34)$$

Due to the Gaussian nature of the potential's distribution, impurity lines associate by pairs in multiple scattering. The graphical representation of Eq. (2.34) shown in Fig. 2.5(b) thus harbours one pair of scattering processes, depicted like a curved impurity line. This so-called Born approximation treats the background particles as non-interacting. It gives faithful results for $\gamma \ll \gamma^*$ but cannot be trusted in the strong disorder regime, where multiple-scattering processes dominate. In addition, it does not predict the existence of a critical point.

To remedy these shortcomings, we replace the clean Green's function G_0 of Eq. (2.34) by its disorder-averaged counterpart \bar{G} , which in turn depends on Σ through Eq. (2.33). This improvement leads to the self-consistent version of the Born approximation, which

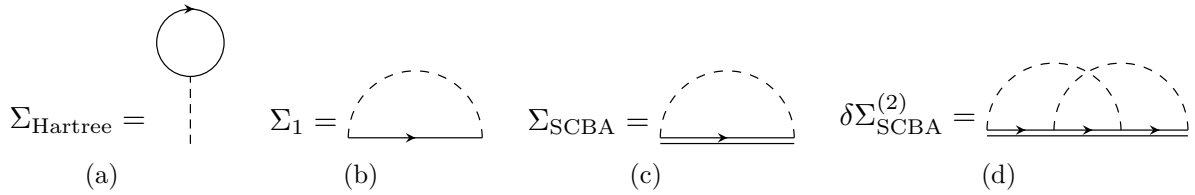


Figure 2.5 | The Hartree diagram (a) describes the classical coupling to the effective potential created by the Fermi sea; it does not intervene when the potential averages to zero, because the positively and negatively charged backgrounds compensate. In such forward scattering process, the momentum and energy of the incident particle are conserved (MATTUCK 1992). We will see in Chapter 3 that graphs with closed fermionic loops (including the Hartree diagram) vanish similarly in the low-energy theory for disordered Weyl semimetals due to the zero-replica limit. The Fock diagram (b) accounts for double scattering processes where particles self-interact at different points in space-time; it corrects the self-energy at first order in disorder strength. In the self-consistent Born approximation (SCBA), infinitely many scattering processes contribute to the self-energy (c), which are hidden in the disorder-averaged Green’s function (double line). Only diagrams with nested particle-particle interactions contribute. Graph (c) corrects the self-consistent Born approximation at second order in disorder strength, by including intertwined exchange scatterings (SINNER 2017). One can neglect this diagram for very dense electron gases, where hole-mediated scattering dominates (SBIERSKI 2014).

reads (restoring the energy dependence)

$$\Sigma(E) \simeq \gamma \int \frac{d^d q}{(2\pi)^d} \bar{G}(E, \mathbf{q}). \quad (2.35)$$

The SCBA accounts for, not only one, but an infinite number of scatterings which host nested particle-hole pair creation-annihilation processes, hidden in the Fock diagram of Fig. 2.5(c). This equation is still approximate, since it ignores diagrams with more complex topology, such as the intertwined exchange processes of Fig. 2.5(d). For uncorrelated disorder, the self-energy depends on the energy E but not on the external momentum \mathbf{k} (correlations weight impurity lines with a \mathbf{q} -dependent factor, in which case virtual modes depend on \mathbf{k}). We can write a more explicit equation using an ansatz for the pseudospin structure of the self-energy. It seems indeed reasonable that the self-energy is proportional to the identity matrix, as the random potential itself. Using Eq. (2.33), we find

$$\Sigma(E) = \gamma \int \frac{d^3 q}{(2\pi)^3} \frac{E + \Sigma}{q^2 - (E + \Sigma)^2}. \quad (2.36)$$

2.3.2 Solution to the self-consistent equation

Scattering rate — The SCBA approach has already been proposed to compute equilibrium and transport properties at the semimetal-metal transition (FRADKIN 1986a; FRADKIN 1986b; OMINATO 2014; KLIER 2019). We will go through the line of reasoning of these papers and present their main results. For simplicity, we place ourselves at the nodal level $E = 0$. The self-energy possesses a real and imaginary part in general. The former induces a shift of the chemical potential away from the nodal energy, which one can show to vanish at zero energy; the latter indicates a broadening of the energy levels

due to random scattering, which should be present. We assume that the nodal self-energy is purely imaginary: $\Sigma = i\Gamma$, where Γ is the so-called scattering rate. Eq. (2.36) then integrates to

$$i\Gamma = \gamma \int \frac{d^3q}{(2\pi)^3} \frac{i\Gamma}{q^2 + \Gamma^2} = \frac{i\Gamma\gamma}{2\pi^2} \left[\Lambda - \Gamma \arctan\left(\frac{\Lambda}{\Gamma}\right) \right], \quad (2.37)$$

upon introducing the ultraviolet cut-off Λ , which represents the momentum above which the linear approximation for the band crossing breaks down. It typically covers a sizeable fraction of the Brillouin zone: $\Lambda \simeq a^{-1}$ is of the order of the inverse lattice constant. Let us analyse Eq. (2.37) as a function of the dimensionless disorder strength $\Delta = \gamma\Lambda/2\pi^2$.

For $\Delta < 1$, the right-hand side is always larger than Γ , and Eq. (2.37) has no solution except the trivial one $\Gamma = 0$. In this low disorder regime, the system is semimetallic. For $\Delta > 1$, Eq. (2.38) has an extra non-trivial solution shown, which satisfies (Klier 2019)

$$\frac{\Gamma}{\Lambda} \arctan\left(\frac{\Lambda}{\Gamma}\right) = \frac{\Delta - 1}{\Delta}. \quad (2.38)$$

This self-consistent equation poses no problem for numerical solving. In this strong disorder regime, quasiparticles have finite a lifetime $\tau \sim \Gamma^{-1}$, and the energy levels broaden by acquiring a Lorentzian width $\delta E = \Gamma$: the system is diffusive metallic. Fig. 2.6 shows the behaviour of the DoS for several energies on the weak and strong disorder sides. A semimetal-metal transition takes place at the critical disorder strength $\Delta^* = 1$.

Mean density of states — The scattering rate gives precious information about various equilibrium or transport observables – the DC conductivity, notably. Here we focus on the

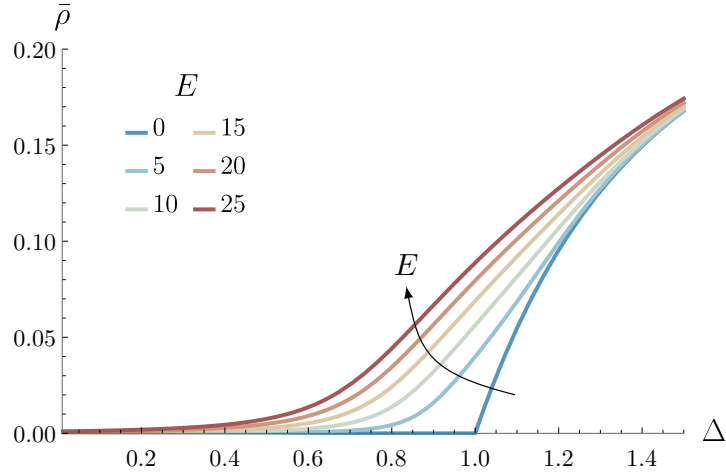


Figure 2.6 | Dimensionless mean density of states $\bar{\rho}$ against disorder strength $\Delta = \gamma\Lambda/2\pi^2$ for an uncorrelated scalar potential, obtained by solving Eq. (2.36) numerically. The momentum Λ , of the order of the inverse lattice constant, serves as an ultraviolet cut-off. The scattering rate $\Gamma = \bar{\rho}\Lambda\Delta = \text{Im}\Sigma$ follows from the imaginary part of the self-energy Σ , which satisfies the self-consistent Born approximation. Each curve corresponds to a given energy $E \ll \Lambda$, in units of $10^{-3}\Lambda$. At the nodal level $E = 0$, the density of states vanishes on the metallic side and develops beyond the critical disorder strength $\Delta^* = 1$. when the Weyl node is doped at an energy $E \neq 0$, the density of states bypasses the critical point, so that the transition is avoided.

order parameter of the semimetal-metal transition: the mean DoS. From Eq. (2.23), we find

$$\bar{\rho} = \frac{1}{\pi} \text{Im Tr} \int \frac{d^d q}{(2\pi)^d} \bar{G}(E, \mathbf{q}) = \frac{2\Gamma}{\pi\gamma}, \quad (2.39)$$

where the factor 2 comes from the trace, which counts the number of degrees of freedom (here, two fermionic components). At the nodal level and slightly above the critical disorder strength, the arctangent of Eq. (2.38) tends to $\pi/2$, and the mean DoS behaves as

$$\bar{\rho}(E = 0, \Delta) \simeq \frac{4\Lambda}{\pi} (\Delta - \Delta^*). \quad (2.40)$$

According to the scaling laws of Sec. 2.2.2, we deduce that $\beta = \nu(d - z) = 1$ in the SCBA. Similarly, at the critical disorder strength but slightly away from the nodal level, the density behaves as

$$\bar{\rho}(E, \Delta = 1) \simeq \frac{2\Lambda^{3/2}}{\pi^{7/2}} |E|^{1/2}. \quad (2.41)$$

Hence $d/z - 1 = 1/2$ and the dynamical exponent is $z = 2$: the critical dispersion relation is quadratic in the SCBA. Combined with the value of β , we further find $\nu = 1$, as expected within mean-field theory. These are the mean-field critical exponents advertised in Tab. 2.1. The table also shows that these exponents deviate from those found with other analytical methods. Why is the SCBA less accurate?

From a physical viewpoint, the SCBA inevitably fails because it neglects fluctuations of the DoS induced by maximally crossed exchange scatterings, which modifies drastically the approach to the critical point. From a mathematical viewpoint, the SCBA is bound to give crude estimates of the exponents, because a self-consistent equation relates two analytic functions on either side of the equal sign. The exponents follow by expanding these functions near the critical point in powers of the order parameter, and so are doomed to take integer values – or simple fractions at best – where the actual exponents can be any real number. To get better estimates, we can either expand the self-energy in disorder strength, whose first order contribution was given in Eq. (2.34), or improve the self-consistent expression of Σ order by order in $1/N$, where N is the fermion number (SINNER 2017). The leading correction to the saddle-point equation appears at order N^{-2} , and enhances (reduces) the self-energy in the weak (strong) disorder regime. These field-theoretical techniques extend to any observable (not only the self-energy) within the renormalisation group formalism. This improvement comes at the cost of a dramatic increase of computational complexity with the order of the expansion.

2.4 Wave function statistics

The conventional scaling laws involve apply to disorder-averaged observables, thereby hiding valuable information about the probability distribution of the DoS, conductivity, or any observable. Yet higher moments of the DoS exhibit scaling behaviours of their own at criticality. The associated *multifractal* exponents encode the geometric properties and statistics of the wave function density.

2.4.1 Multifractality

The concept of multifractality, first introduced by mathematician B. Mandelbrot (MANDELBROT 1974), has proved fruitful in infinitely various topics. From the velocity field in hydrodynamic turbulence (PARISI 1988) to time series in financial markets (MANDELBROT 1999), or the dynamics of human heartbeat (IVANOV 1999), the list of problems subjected to a multifractal analysis is booming. Including in condensed matter physics: disordered classical spin models (DUPLANTIER 1991), disordered elastic systems (FEDORENKO 2014), but also – closest to our interest – Anderson’s localisation (WEGNER 1980). Recently, S. Syzranov et al. showed that the critical wave functions at the semimetal-metal transition exhibit multifractality as well (SYZRANOV 2016). Unlike the few conventional exponents (dynamical, field or correlation length), the multifractal spectrum consists of a continuous set of exponents, and therefore contains all information about the probability distribution of the wave function density; in particular, it dictates the scaling behaviour for the most probable value of the DoS (the *typical* DoS), which serves as an alternative order parameter for both Anderson and non-Anderson transitions. We hereafter transpose key notions about wave function statistics (participation ratios, multifractal exponents, typical DoS), which are now well-established tools for Anderson’s localisation, to the semimetal-metal transition (BRILLAUX 2019).

Geometrical interpretation of multifractality — In metallic phases, the Bloch waves vary periodically at the atomic scale, while at larger scale, these sharp modulations average out and the wave function spreads evenly over the sample, as shown in Fig. 2.7(a). Wave functions satisfy this property in a clean metal, or in the diffusive metallic side phase of a dirty Weyl semimetal. In a localised phase, the wave function density displays instead a few peaks, and vanishes everywhere else, as in Fig. 2.7(c). How do these drastically different behaviours connect at a localisation-delocalisation point? In absence of any typical length

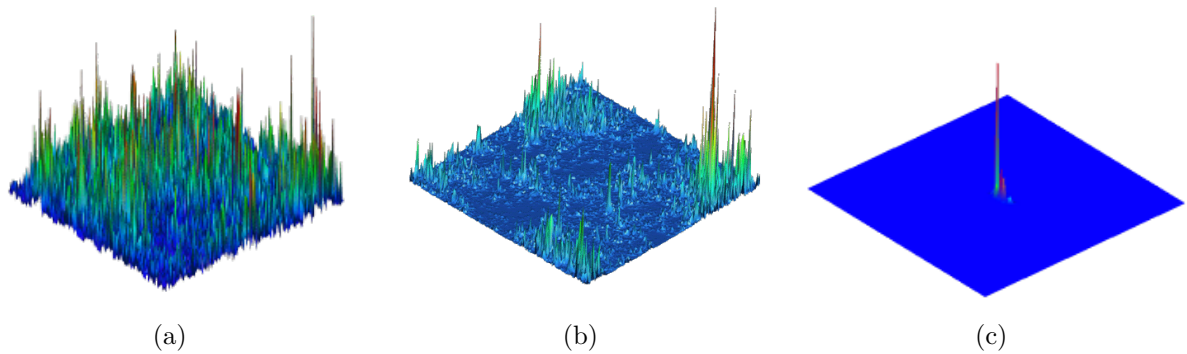


Figure 2.7 | Maps of the electronic wave function density $|\psi|^2$ near the Anderson localisation point of a two-dimensional system. The colour code is blue for a low density, and red for a high density. Extracted from (GRUZBERG 2009). (a) A metallic phase is populated by extended states, which despite atomic-scale modulations have a globally flat density $|\psi|^2 \simeq V^{-1}$ where V is the system volume. (b) At the localisation-delocalisation point, critical wave functions fluctuate wildly and display complex patterns which roughly repeat themselves at all length scales, but with different scaling dimensions. The probability distribution of the wave function is multifractal. The multifractal nature manifests itself in non-integer scaling exponents of the moments $|\psi|^{2q}$. (c) A localised state spreads over a finite distance ξ from a localisation centre.

in the system, we expect to find patterns that repeat themselves at all scales. Fig. 2.7(b) shows such critical wave function density at the Anderson transition. When averaged over many disorder realisations, the moments of the wave function density scale with the system size L with non-integer dimensions. When these moments scale with independent exponents, the distribution of the wave function density is said to be *multifractal*.

The same features develop at the semimetal-metal transition. Consider a Weyl semimetal subject to disorder of strength γ . The multifractal behaviour can be seen on the (generalised) inverse participation ratio (EVERS 2008)

$$P_q(E, \gamma) = \int d^d r |\psi(\mathbf{r})|^{2q}, \quad (2.42)$$

which represents the moments of the inverse volume spanned by the wave function at energy E . We typically choose integer powers q , but nothing forbids it to take real values from a theoretical viewpoint (even negative ones, provided the wave functions are smooth enough at the microscopic scale). For a finite system near criticality (within an energy window $\propto L^{-z}$ and a disorder strength window $\propto L^{-\nu}$), the inverse participation ratio scales on average as $\bar{P}_q(E=0, \gamma^*) \sim L^{-\tau_q}$. This scaling law defines a continuous set of exponents τ_q known as the *multifractal spectrum*.

To see more clearly the geometrical interpretation of multifractality, let us also define the *Renyi dimension* D_q such that (HUCKESTEIN 1995)

$$\tau_q = D_q(q - 1), \quad (2.43)$$

where a limit is implicit for $q \rightarrow 1$. The Renyi dimension represents the fractal dimension of the measure induced by the moments of the wave function density. First envisage two limit cases: extended states on one hand; localised states on the other hand. As shown in Fig. 2.7(a), extended waves covers a sizeable fraction of the system volume, if not all of it. For normalised plane waves, $|\psi|^2 \sim L^{-d}$, the inverse participation ratio scales as $P_q \sim L^{-d(q-1)}$ and thus $D_q = d$ for all q . The localised states of Fig. 2.7(c), on the contrary, span a small constant volume. For an exponentially localised state $|\psi|^2 \sim \xi^{-d} e^{-2r/\xi}$, with ξ the localisation length, the inverse participation ratio $P_q \sim \xi^{-d(q-1)}$ becomes volume-independent, and the Renyi dimension is trivial: $D_q = 0$ for all q .

By contrast, critical wave functions scale with intermediate non-integer dimensions (hence the *fractal* nature), which differ for all moments of the wave function density (hence the *multi*-fractality), as shown in Fig. 2.7(b). The Renyi dimension still satisfies the following properties. By definition, the inverse participation ratio at $q = 0$ equals the volume of the system. Thus $D_0 = d$ is the geometrical dimension. The information dimension D_1 describes the fractality of the measure $d\mu = d^d r |\psi|^2$ induced by the electronic probability of presence. For a normalised state, $P_1 = 1$ and $D_1 = 0$. Intuitively, the larger q , the more the participation ratio (2.42) should be dominated by points where the wave function density exceeds its average value. In the limit $q \rightarrow +\infty$, the maxima of the wave function control the scaling law, which fixes an upper bound $D_{+\infty}$ for the Renyi dimension. This argument applies symmetrically in the limit $q \rightarrow -\infty$, where the minima control the scaling law and fixes a lower bound $D_{-\infty}$.

Anomalous part of the multifractal scaling — Interestingly, we can also observe multifractality in the scaling of the local DoS through the so-called participation ratio.

Consider a finite lattice model of a Weyl semimetal. Let us provide the Hilbert space with a basis of normalised eigenstates $\{\psi_i(\mathbf{r})\}$ of discrete energies E_i . Inspired by the integral expression (2.42) for the inverse participation ratio, we first build a spatially resolved equivalent of the DoS,

$$\rho(\mathbf{r}, E) = \sum_i |\psi_i(\mathbf{r})|^2 \delta(E - E_i), \quad (2.44)$$

This *local* DoS counts the number of states at energy E and weights this number by the electron's probability of presence. The usual DoS derives from Eq. (2.44) by a spatial average,

$$\rho(E) = \frac{1}{V} \int d^d r \rho(\mathbf{r}, E) = \frac{1}{V} \sum_i \delta(E - E_i), \quad (2.45)$$

with $V = L^d$ the system volume. The (generalised) participation ratio p_q extends Eq. (2.45) to higher moments of the DoS. It is defined by (WEGNER 1980)

$$p_q(E, \gamma)^{-1} = \frac{1}{V} \int d^d r \rho(\mathbf{r}, E)^q \bar{\rho}(E)^{-q}, \quad (2.46)$$

and represents the moments of the fraction of sites occupied by the wave function. Note that integrating out the random defect's positions restores homogeneity, so that the spatial integrals of Eq. (2.42) and Eq. (2.46) are actually optional. In lattice simulations, though, the spatial average is kept to reduce fluctuations and improve convergence. Near criticality, the mean participation ratio scales with system size as $\bar{p}_q(E=0, \gamma^*) \sim L^{\Delta_q}$, where Δ_q are the *anomalous multifractal exponents*.

The scaling laws of the inverse participation ratio and participation ratio are not independent; they satisfy the hyperscaling relation (EVERS 2008),

$$\tau_q = d(q-1) + \Delta_q. \quad (2.47)$$

This exponent Δ_q captures the anomalous part of τ_q , while the contribution $d(q-1)$ follows from naive dimensional analysis of a plane wave. For extended states, the anomalous multifractal exponents formally vanish off criticality: $\Delta_q = 0$. For localised states, the anomalous exponents formally take the value $\Delta_q = -q(d-1)$ and $\tau_q = 0$. But Δ_q depends linearly on q , which shows that the distribution of localised wave functions is not multifractal. The moments of a multifractal distribution scale indeed with different Renyi dimensions, which entails that Δ_q varies non-linearly with q at criticality. Since the participation ratio for $q > 1$ is at best intensive, Δ_q is negative in this condition. Also, the anomalous exponents vanish for $q = 0$ and $q = 1$ to agree with the geometrical and information dimensions $D_0 = d$ and $D_1 = 0$. Besides, in non-linear sigma models formulations of Anderson's localisation, the anomalous multifractal exponent is symmetric around the index $q = 1/2$, i.e. $\Delta_q = \Delta_{1-q}$ (MIRLIN 2006). This relation holds in all Wigner-Dyson classes. Whether the same symmetry applies to the semimetal-metal transition is undecided, but the results currently available (two-loop order expansion in dimension $d = 2 + \varepsilon$) meet this requirement

The anomalous multifractal exponents also govern the scaling of the moments $\bar{\rho}^q \sim L^{\Delta_q}$ of the normalised DoS $\varrho = \rho/\bar{\rho}$. A renormalisation group analysis gives easy access to the scaling dimension η_q of the moments $\bar{\rho}^q \sim L^{-\eta_q}$, from which we can determine

$$\Delta_q = \eta_q - q\eta_1. \quad (2.48)$$

Note that $\eta_1 = d - z$ is related to the familiar dynamical exponent.

Multifractal scaling laws in a relativistic semimetal — A Weyl semimetal becomes metallic at moderate disorder strengths. If allowed by symmetry, a strong enough disorder can then suppress backscattering in the metallic phase and lead to Anderson localisation (ALTLAND 2016). A dirty Weyl semimetal can thus explore three phases (semimetallic, metallic, localised). We discuss below the scaling laws of \bar{P}_q and \bar{p}_q slightly off the critical point in an infinite system, and prove that the inverse participation ratio plays the role of an order parameter for the semimetal-metal transition. Since the constant disorder strength path $\gamma = \gamma^*$ lies inside the critical fan, we define the multifractal exponents of an infinite system as a function of γ instead of the energy E , in compliance with Sec. 2.2.2, but unlike the usual conventions for Anderson’s localisation (HUCKESTEIN 1995).

- In the *semimetallic* phase, the Fermi level is empty of states. Both P_q and p_q vanish in the thermodynamic limit for $q > 1$.
- In the *metallic* phase, extended states exist at the Fermi level. In the thermodynamic limit, P_q still vanishes for $q > 1$ while p_q remains sizeable in the same condition. The inverse participation ratio $P_q = V^{1-q}$ dies out for $q > 1$, while the participation ratio $p_q = 1$ is intensive. Near the critical point of the semimetal-metal transition, the mean participation ratio decays in a power-law fashion on the metallic side as

$$\bar{p}_q(E = 0, \gamma) \sim (\gamma - \gamma^*)^{\mu_q}. \quad (2.49)$$

The exponent $\mu_q = -\nu\Delta_q$ is positive for $q > 1$, which is consistent with \bar{p}_q vanishing on the semimetallic side. The inverse participation ratio, on the other hand, plays no role at the semimetal-metal transition.

- In the *localised* phase, on the contrary, p_q vanishes while P_q remains sizeable. For a localised state, the inverse participation ratio $P_q \propto V^0$ is intensive, while the participation ratio $p_q \propto V^{-d(q-1)}$ dies out in an infinite system for $q > 1$. Near the localisation-delocalisation point, the mean inverse participation ratio behaves on the insulating side as

$$\bar{P}_q(E, \gamma) \sim (\gamma - \gamma^*)^{\pi_q}, \quad (2.50)$$

where the exponent $\pi_q = \nu\tau_q$ is positive for $q > 1$. The participation ratio vanishes as in Eq. (2.49) with a different exponent μ_q .

Fig. 2.8(a) summarises the behaviour of \bar{P}_q and \bar{p}_q in the three phases of a disordered Weyl semimetal. The previous examples on purely extended and purely localised waves suggest that the participation and inverse participation ratios satisfy $\bar{P}_q \bar{p}_q = V^{1-q}$ (WEGNER 1980). This relation actually holds for all electronic waves, in particular for critical ones. This enforces the hyperscaling relation

$$\pi_q + \mu_q = d\nu(q - 1), \quad (2.51)$$

which is the counterpart of Eq. (2.47) for the scaling laws at the thermodynamic limit.

Singularity spectrum — Rather than focussing on how the wave function density itself is distributed, one might instead wish to know how the scaling dimension of the wave function density is distributed. This change of perspective brings information which is easier to grasp than the multifractal spectrum: how many states scale with an exponent

smaller than the geometrical dimension d , how many scale with an exponent larger than d , what is the most probable scaling dimension, etc. These questions find their answer in the *singularity spectrum* (EVERS 2008). The singularity spectrum follows from a Legendre transformation of the function $q \mapsto \tau_q$, namely

$$f_\tau(x) = xq - \tau_q, \quad \text{where } x(q) = \frac{d\tau_q}{dq} \quad (2.52)$$

represents the scaling dimension of the wave function density. The reason for the Legendre transformation will become clearer when introducing the typical DoS in Sec. 2.4.2. For now, let us discuss the main properties of f_τ . The singularity spectrum gives the fractal dimension of the manifold composed of points \mathbf{r} where the wave function density scales as $|\psi(\mathbf{r})|^2 \sim L^{-x}$; in other words, the volume of this manifold scales as $L^{f_\tau(x)}$ (HALSEY 1987). Since the function $q \mapsto \tau_q$ is increasing concave (at least for small enough values of q), f_τ is a well-defined concave function on the semi-axis $x \geq 0$. It peaks at a certain value x_0 , with a maximum $f_\tau(x_0) = d$. Hence x_0 gives the most probable scaling dimension for the wave function density, and the volume of the corresponding manifold scales like the volume of the whole sample, as L^d .

The counterpart of Eq. (2.52) for the anomalous multifractal exponents is the *anomalous singular exponents*. It is defined as the Legendre transform of the function $q \mapsto \Delta_q$,

$$f_\Delta(y) = yq - \Delta_q, \quad \text{where } y(q) = \frac{d\Delta_q}{dq} \quad (2.53)$$

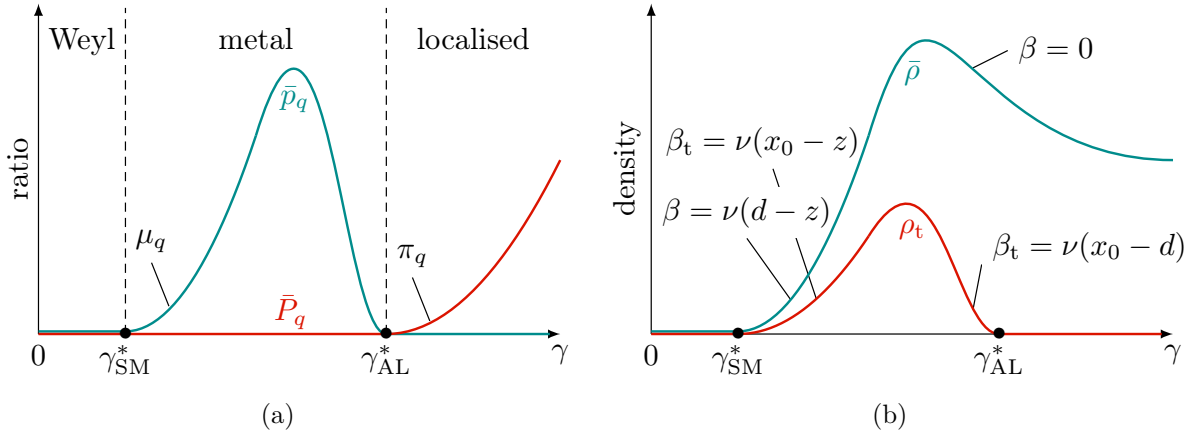


Figure 2.8 | (a) Mean participation ratios \bar{p}_q (in blue) and inverse participation ratios \bar{P}_q (in red) at the semimetal-metal transition (weak disorder strength γ_{SM}^*) and Anderson’s localisation (strong disorder strength γ_{AL}^*), for $q > 1$. The participation ratio \bar{P}_q vanishes on the metallic with an exponent μ_q , and stays zero on the weak disorder side. The inverse participation ratio vanishes on the localised and semimetallic side with a generic exponent π_q (different for each transition). Both ratios vanish in the semimetallic phase, due to the absence of zero energy eigenstates. (b) The average $\bar{\rho}$ and typical ρ_t densities of states at the Fermi level are both non-zero in the metallic region, but only the latter vanishes at the localisation point. The hyperscaling relations for the corresponding exponents β and β_t are given at the Anderson transition (JANSSEN 1998) and the semimetal-metal transition (BRILLAUX 2019).

represents the scaling dimension of the normalised wave function density ϱ . From Eq. (2.47) follows the plain relation $f_\Delta(x) = f_\tau(x + d) - d$ between the singularity spectrum and the anomalous singular exponents. In particular, the anomalous singular exponent peaks at $y_0 = x_0 - d$, with a maximum $f_\Delta(y_0) = 0$.

When d approaches the lower critical dimension $d_\ell = 2$, the critical fluctuations diminish as the wave functions progressively shape into extended states. In this regime of weak multifractality, the anomalous multifractal spectrum becomes parabolic, $\Delta_q = -y_0 q(q - 1)$, as well as the singularity spectrum and the anomalous singular exponents

$$f_\tau(x) = d - \frac{(x - x_0)^2}{4(x_0 - d)}, \quad f_\Delta(y) = -\frac{(y - y_0)^2}{4y_0}. \quad (2.54)$$

The spectrum is exactly quadratic in some systems, as for a random vector potential in two dimensions (FOSTER 2009; FOSTER 2012).

2.4.2 Typical versus average densities of states

Here, we relate multifractality to the scaling laws of the typical and mean DoS (BRILLAUX 2019).

Universal scaling law — We emphasised that the average DoS $\bar{\rho}(E, \gamma)$ varies smoothly around the critical point of Anderson’s localisation, and thus cannot pinpoint this transition. By contrast, the *typical* DoS, defined as the geometric mean

$$\rho_t(E, \gamma) = \exp \left[\overline{\ln \rho(\mathbf{r}, E)} \right], \quad (2.55)$$

remains finite for extended states, decreases when approaching the critical point, and vanishes in the localised phase. Indeed upon localisation the local spectrum changes from continuous to discrete. The typical DoS acts as an order parameter for Anderson’s localisation in addition to the DC conductivity (JANSSEN 1998). That the typical and average DoS so strongly differ should not surprise, because the broad distribution of the local DoS at criticality leads to rare realisations of wave functions with high amplitudes, which dominate the average density. By contrast, the typical DoS is less sensitive to these rare fluctuations. A similar observation applies to the semimetal-metal transition, except that both typical and average DoS vanish at the nodal level of the semimetallic phase. They do so, however, with different power-law exponents: in the metallic phase

$$\rho_t(E = 0, \gamma) \sim (\gamma - \gamma^*)^{\beta_t}, \quad (2.56)$$

where $\beta_t \neq \beta$. Remarkably, a universal scaling law completely determines β_t .

This universal scaling law is an intrinsic property of the probability distribution for the DoS. It applies to any non-self-averaging spectrum, which includes some disordered phases, and the critical point of disorder-induced transitions. Let us consider the distribution $P(\varrho, L)$ of the normalised density ϱ in a system of a finite size L . The moments of the normalised density read

$$\overline{\varrho^q} = \int_0^\infty d\varrho P(\varrho, L) \varrho^q. \quad (2.57)$$

Guided by the physical interpretation of the singularity spectrum, we now change the variable from ϱ to y such that $\varrho = L^{-y}$. We introduce the associated distribution by setting $d\varrho P(\varrho, L) = dy P'(y, L)$, which we set in an exponential form as well, $P'(y, L) = L^{f_\Delta(y)}$. At this stage, nothing links y or f_Δ to the power q . We arrive at

$$\bar{\varrho}^q = \int_0^\infty dy P'(y, L) L^{-y} = \int_0^\infty dy \exp[-(yq - f_\Delta(y)) \log L]. \quad (2.58)$$

Applying the steepest descent method, we get $\bar{\varrho}^q \simeq \exp[-(yq - f_\Delta(y)) \log L]$, where now the function $q \mapsto y(q)$ satisfies $f'_\Delta(y) = q$. We recognise the argument in the exponential as the Legendre transform of f_Δ , which is nothing other than the anomalous multifractal exponent $\Delta_q = yq - f_\Delta(y)$. As expected, we recover the scaling law $\bar{\varrho}^q \sim L^{-\Delta_q}$. Most importantly, we may now determine the scaling of the typical DoS, since

$$\varrho_t = \frac{\rho_t}{\bar{\rho}} = \exp\left[\int_0^\infty d\varrho P(\varrho, L) \log \varrho\right] = \exp\left[-\log L \int_0^\infty dy y L^{f_\Delta(y)}\right] \simeq L^{-y_0}, \quad (2.59)$$

where the last equality stems again from the steepest descent method. Let us discuss the implications of Eq. (2.59) on the scaling laws in Anderson's localisation on one hand, and in the semimetal-metal transition on the other hand.

The typical density exponent — For Anderson's localisation, the mean DoS behaves smoothly near the critical point, so that $\beta = 0$ formally. Eq. (2.59) predicts that the corresponding exponent for the typical DoS is $\beta_t = \nu(x_0 - d)$, in agreement with well-established results (JANSSEN 1998). By directly tracking the typical DoS through the Anderson critical point, numerical studies are able to estimate x_0 . In the orthogonal class, (PIXLEY 2015) finds $x_0 = 4.0 \pm 0.3$, in agreement with the four-loop result $\alpha_0 = 4.043$.

For the semimetal-metal transition, $\beta = \nu(d - z)$, and Eq. (2.59) entails $\beta_t = \nu(x_0 - z)$. Despite much effort, numerical simulations have trouble finding precise or consistent values for the correlation length exponent ν ; it is therefore more useful to deduce a scaling relation wherein ν is absent, as in

$$\frac{\beta_t}{\beta} = \frac{x_0 - z}{d - z}. \quad (2.60)$$

By combining the numerical estimates of (PIXLEY 2015; SBIERSKI 2015; PIXLEY 2016b; PIXLEY 2016c; ROY 2016), we find a dynamical exponent $z = 1.485 \pm 0.015$ and a mean density exponent $\beta = 1.50 \pm 0.04$ for the semimetal-metal transition in the universality class of uncorrelated disorder. (PIXLEY 2015; ROY 2016) find the typical density exponents $\beta_t = 2.0 \pm 0.3$ and $\beta_t = 1.8 \pm 0.2$ respectively. Using Eq. (2.60), we predict $x_0 = 3.4 \pm 0.2$. (PIXLEY 2015) also estimates the second Renyi dimension $D_2 = 1.2 \pm 0.3$. Under the assumption of weak multifractality, $D_2 = 3d - 2x_0$, which yields $x_0 \simeq 3.90 \pm 0.15$. But due to the poor control over this approximation, the uncertainty on the last estimate should be taken with a grain of salt.

Smearing by rare-region effects — Some authors recently argued that the presence of rare large regions with strong disorder potential creates a non-zero nodal DoS even for weak disorder (NANDKISHORE 2014; PIXLEY 2016b). This would introduce a new length scale above which the wave function is not multifractal, or at least not with the same multifractal spectrum. However, Eq. (2.59) still applies below this crossover length scale, which is accessible numerically (PIXLEY 2016b; PIXLEY 2016a).

Conclusion

Summary — We have seen that disorder can dramatically affect the properties of electronic phases. In systems with a high density of states, defects can localise electrons due to destructive scattering processes. Three-dimensional relativistic semimetals, whose density of states vanishes at the Fermi level, can transit towards a metallic phase under strong enough disorder through a quantum critical point. A small set of exponents – dynamical exponent z , anomalous field exponent η , correlation length exponent ν – encodes most scaling laws at this semimetal-metal transition, especially the critical behaviour of the average density of states, which acts as an order parameter. A simple analytical approach, the self-consistent Born approximation, predicts the existence of the transition and the values of these critical exponents within mean-field theory. These conventional exponents do not capture the scaling behaviour of higher moments of the density of states, which is described by the so-called multifractal spectrum. The multifractal spectrum has often proved a useful concept, notably in Anderson’s localisation; we have extended this notion to the semimetal-metal transition, where we have determined the scaling law of the typical density of states.

Outlook — The universality class of the semimetal-metal transition, and thus the values of the conventional and multifractal exponents, depend on the range of disorder correlations. We have distinguished two regimes of disorder corrections: when defects correlate over a finite distance, the variance of the random potential essentially reduces to a delta peak in real space; otherwise, the variance of the random potential decays algebraically with distance. All these exponents can be determined within a field-theoretical framework. In particular the perturbative renormalisation group predicts analytical estimates of these exponents order by order in the small parameter $\varepsilon = d - 2$, the ‘distance’ to the lower critical dimension $d_\ell = 2$. By comparing estimates of the conventional exponents from different numerical and analytical techniques, it appears that the values of the correlation length exponent ν vary tremendously between different numerical simulations. Besides bringing valuable information about the geometrical properties of the wave function, the multifractal spectrum manifests itself in the scaling exponent of the typical density of states, for which numerical simulations find consistent estimates. It thus provides a robust set of exponents to characterise the semimetal-metal transition, and in principle to discriminate between the two universality classes (with short-range or long-range disorder correlations). The stage is now set to determine the multifractal exponents within a field-theoretical approach.

Field-theoretical description of the semimetal-metal transition

In the previous chapter, we reviewed the phenomenology of the semimetal-metal transition, and got crude estimates of the critical exponents using the self-consistent Born approximation. We briefly discussed numerical methods to determine the exponents. The multifractal exponents, notably, bring valuable information about the distribution of the wave function density and density of states. This chapter puts the spotlight on a powerful analytical technique: the renormalisation group. We first map the physics of disordered Weyl semimetals to an effective low-energy field theory closely related to the Gross-Neveu model, thanks to the so-called replica trick. We then renormalise this theory in presence of short- and long-range correlations of disorder to determine the flow of the disorder strengths, along with the phase diagram. Finally, we renormalise the composite operator associated to the moments of the wave function density, whose scaling dimension gives the multifractal exponents.

3.1	Effective field theory	90
3.1.1	From clean to dirty Weyl semimetals	90
3.1.2	Replicated action	93
3.2	Renormalisation group in presence of correlated disorder	95
3.2.1	Renormalisation group procedure	95
3.2.2	Beta functions and flow diagram	97
3.2.3	Time-reversal- and valley-symmetry breaking disorder	100
3.3	Multifractality within the replicated field theory	103
3.3.1	Multifractal spectrum to two-loop order	103
3.3.2	Comparison with other transitions	106
	Conclusion	108

3.1 Effective field theory

3.1.1 From clean to dirty Weyl semimetals

Theory of a clean Weyl semimetal — The low-energy excitations of a Weyl semimetal are described by a set of two conjugate Weyl spinors $\{\Psi^\dagger, \Psi\}$ and the Weyl Hamiltonian $\mathcal{H}_0 = i\boldsymbol{\sigma} \cdot \boldsymbol{\partial}$. To map standard quantum mechanics to quantum field theory, we interpret the quantity $\Psi^\dagger \mathcal{H}_0 \Psi$ as a Hamiltonian density and promote the conjugate Weyl spinors to Grassmann fields, which we denote as $\bar{\psi} = (\bar{\psi}_1, \bar{\psi}_2)$ and $\psi = (\psi_1, \psi_2)$ to emphasise their independence¹ (ZINN-JUSTIN 2002). The Hamiltonian of the effective field theory is

$$H_0 = \int d^d r \bar{\psi} (i\boldsymbol{\sigma} \cdot \boldsymbol{\partial}) \psi, \quad (3.1)$$

where the fields $\bar{\psi}(\mathbf{r}, t)$ and $\psi(\mathbf{r}, t)$ implicitly depend on the space-time arguments. The Hamiltonian $H_0(\pi, \psi)$ depends naturally on the generalised coordinates ψ and their canonical momenta $\pi = i\bar{\psi}$. The Lagrangian ensues from the Legendre transformation of Eq. (3.1),

$$L_0 = \int d^d r \pi \partial_t \psi - H_0 = \int d^d r \bar{\psi} (i\sigma^\mu \partial_\mu) \psi, \quad (3.2)$$

where in the Minkowskian metric $\sigma^\mu \partial_\mu = \partial_t - \boldsymbol{\sigma} \cdot \boldsymbol{\partial}$. Thanks to a Wick rotation from real time t to imaginary time $\tau = -it$, the Hamiltonian, Lagrangian and action can be expressed in the Euclidean (trivial) metric instead, at the cost of losing the explicit Lorentz-invariant form of these functionals. This also enables to cast the Feynman weight e^{iS} to the more statistical-friendly Boltzmann weight e^{-S} . The corresponding Euclidean action reads

$$S_0[\bar{\psi}, \psi] = \int_{-\infty}^{+\infty} d\tau L_0 = \int d^d r d\tau \bar{\psi} (\partial_\tau - i\boldsymbol{\sigma} \cdot \boldsymbol{\partial}) \psi. \quad (3.3)$$

Since the low-energy theory of a clean Weyl node is associated with a Gaussian fermionic theory, we will refer to the action S_0 of (3.3) as the *free* action. We can determine expectation values of the free fields using a path integral representation. The partition function

$$\mathcal{Z}[J] = \int D\bar{\psi} D\psi e^{-S_0 - S_J}, \quad (3.4)$$

generates insertions of the fields by functional derivation with respect to a source current J incorporated in the extra term S_J . To get correlations of $\bar{\psi}$ and ψ at different points in space-time, the source current consists of two external Grassmann fields $\bar{\eta}$ and η that couple linearly to the Weyl fields, i.e. $S_J = -\int \bar{\eta} \psi + \bar{\psi} \eta$ in symbolic notations.

Treatment of disorder — In presence of disorder, the Bloch Hamiltonian $\mathcal{H} = \mathcal{H}_0 + V$ includes the random potential $V(\mathbf{r})$. For the moment, we need not specify its pseudospin structure. Going through the same line of reasoning as before, the full action of the disordered Weyl semimetal reads

$$S[\bar{\psi}, \psi, V] = \int d^d r d\tau \bar{\psi} (\partial_\tau - i\boldsymbol{\sigma} \cdot \boldsymbol{\partial} - V) \psi. \quad (3.5)$$

¹For Dirac spinors, the usual convention is to assimilate $\bar{\psi}$ with the adjoint $\bar{\Psi} = \Psi^\dagger \gamma_0$ instead of Ψ^\dagger , but the two choices are equivalent and related by a harmless change of variable in the path integral.

The partition function for a given disorder configuration follows from Eq. (3.4),

$$\mathcal{Z}[\bar{\eta}, \eta, V] = \int D\bar{\psi} D\psi e^{-S-S_J}. \quad (3.6)$$

The statistically averaged observable X of a system affected by quenched disorder depends on a particular realisation of the random potential; it is not accessible experimentally, and is, by definition, a random variable itself. What is measurable and in principle predictable, though, is the probability distribution of X . Rather than determining the whole distribution, which is a formidable task, we can instead focus on a few representative values, such as its mean \bar{X} . This information completely determine the equilibrium properties of non-critical systems, where the free energy W is a self-averaging quantity. An observable X is said to be self-averaging when its relative variance

$$v_X = \frac{\overline{X^2}}{\bar{X}^2} - 1 \quad (3.7)$$

vanishes in the thermodynamic limit $L \rightarrow \infty$, as does any higher-order moment of the distribution, which essentially reduces to a single peak centred at \bar{X} . To understand why, consider the free energy of a large system, of size $L \gg \xi$ much greater than the correlation length. By virtue of additivity, it can be decomposed into the sum $W = \sum_i W_i$ of the free energies W_i of smaller, independent subsystems of size ξ . Each such subsystem sees its own disorder configuration. Computing the total free energy per site, which is nothing other than a spatial average of the free energy, amounts to average over all realisations of the random potential. Thus, a non-critical free energy W tends to its disorder average \bar{W} in the thermodynamic limit.

At criticality, ξ diverges and the above argument breaks down. Fluctuations prevail and broaden the probability distribution; additive quantities, such as the free energy, no longer satisfies the self-averaging property. And multifractality attests this failure: as per the scaling of the participation ratio (2.46), the critical relative variance of the DoS scales as

$$v_\rho = (\bar{p}_2)^{-1} - 1 \sim L^{-\Delta_2}, \quad (3.8)$$

which diverges in the thermodynamic limit since $\Delta_2 < 0$. The breakdown of the self-averaging property applies to any critical observable. Multifractality precisely encodes the scaling of the variance and all higher-order cumulants, which the large fluctuations generate at criticality.

For quenched disorder, the random degrees of freedom follow their own statistics, which means that in the mean free energy, they are summed over not in the partition function \mathcal{Z} , but after taking the logarithm. Consider a source field J which couples linearly to a field operator \mathcal{O} . Let $\langle \mathcal{O} \rangle$ be its statistical average in a given disorder configuration, which follows from the free energy by functional derivation. The disorder average of $\langle \mathcal{O} \rangle$ then reads

$$\overline{\langle \mathcal{O} \rangle} = \frac{\delta \bar{W}}{\delta J}, \quad \bar{W} = \int DV P[V] \ln \mathcal{Z}[J, V], \quad (3.9)$$

where we recall that $P[V]$ is assumed Gaussian. Unfortunately, taking the Gaussian integral of a logarithm is far from straightforward. Three procedures overcome this obstacle. They all amount in some way or another to normalise the partition function (3.6) to unity in absence of source fields.

- The *Keldysh* method considers the time evolution from $t = -\infty$ to $t = +\infty$, then back to $t = -\infty$ again through a closed contour in the complex time plane. Originally introduced to study non-equilibrium systems, this technique has proved useful in disordered equilibrium systems too (CHAMON 1999). Indeed, the partition function computed along a closed contour has value 1 by construction in absence of source fields.
- The *supersymmetric* method consists in introducing bosonic fields in the partition function with the same kinetics and coupling to the random potential as the fermionic fields (EFETOV 1996). The statistical average of an observable \mathcal{O} for a given realisation of the potential reads

$$\langle \mathcal{O} \rangle = \frac{1}{\mathcal{Z}_F} \frac{\delta \mathcal{Z}_F}{\delta J}, \quad (3.10)$$

where the right-hand side is evaluated at zero source field, and we renamed the partition function \mathcal{Z}_F to highlight the fermionic nature of the theory. The rule of Gaussian integration over Grassmann fields gives $\mathcal{Z}_F[J = 0] = \det(\partial_\tau - i\boldsymbol{\sigma} \cdot \boldsymbol{\partial} - V)$. The zero-field partition function depends on the random potential, which forbids to directly average Eq. (3.10) over disorder. To solve this issue, we add to the fermionic action S_F the bosonic action

$$S_B[\bar{\varphi}, \varphi, V] = \int d^d r d\tau \bar{\varphi} (\partial_\tau - i\boldsymbol{\sigma} \cdot \boldsymbol{\partial} - V) \varphi, \quad (3.11)$$

where $\{\bar{\varphi}, \varphi\}$ are two-component commuting fields. The zero-field partition function associated to this action is $\mathcal{Z}_B[J = 0] = \det(\partial_\tau - i\boldsymbol{\sigma} \cdot \boldsymbol{\partial} - V)^{-1}$, i.e the reciprocal of the fermionic partition function. The supersymmetric action $S = S_F + S_B$ leads to an effective partition function $\mathcal{Z} = \mathcal{Z}_F \mathcal{Z}_B = 1$ in absence of source fields. Averaging Eq. (3.10) over disorder now becomes feasible by using the supersymmetric partition function. This results in an effective coupling between fermionic and bosonic fields.

- The *replica* method was first introduced for the problem of spin glasses (EDWARDS 1975; PARISI 1979; MEZARD 1987). It rests on the following trick. First compute the replicated partition function \mathcal{Z}^N for integer N , which represents the partition function of N copies (replicas) of the fermionic fields, all with the same free dynamics and in the same disorder configuration. Each replica is thus described by the action (3.5). Then average the replicated partition function over disorder. Finally, use the mathematical identity

$$\ln \mathcal{Z} = \lim_{N \rightarrow 0} \frac{\mathcal{Z}^N - 1}{N}, \quad (3.12)$$

and send N to zero. This limit assumes that the analytical continuation for arbitrary small N exists. The continuation breaks down when the probability distribution of the partition function is too broad, especially in the strong disorder regime. By contrast, the replica trick maps the physics of weakly disordered Weyl semimetals to an effective replicated theory amenable to perturbative treatments; the correlation functions of the effective theory, when expanded order by order in disorder strength, have a polynomial dependence on N , and the zero-replica limit is well defined.

The multifractal spectrum at the semimetal-metal transition has been determined for uncorrelated disorder in the supersymmetric approach (SYZРАНOV 2016). In the weak disorder regime, it is believed that these three methods – Keldysh, supersymmetric, and replica – leads to the same critical exponents order by order in the perturbative expansion. To test this insensitivity to the disorder-averaging technique, we will use a different approach: the replica method. The replica method will also enable us to map the theory of disordered Weyl semimetals to the well-known Gross-Neveu model, which was discussed at length in Sec. 1.5.

3.1.2 Replicated action

We now use the replica method to map the low-energy theory of Weyl semimetals either to the Gross-Neveu model (for uncorrelated scalar potential) or to the Thirring model (for uncorrelated vectorial potential). We then extend the replicated theory to include long-range disorder correlations, \mathcal{T} -breaking random potentials and intervalley scattering.

Theory of a disordered Weyl semimetal — Let us introduce a replica index $\alpha = 1, \dots, N$ to label the N copies of the Weyl fermionic fields. Each of them has two components. We collect all these degrees of freedom into $2N$ -component Grassman fields $\bar{\psi} = (\bar{\psi}_1, \dots, \bar{\psi}_N)$ and $\psi = (\psi_1, \dots, \psi_N)$. The first step of the trick consists in replicating the partition function,

$$\mathcal{Z}^N = \int D\bar{\psi} D\psi \exp\left(-\sum_{\alpha=1}^N S[\bar{\psi}_\alpha, \psi_\alpha, V]\right), \quad (3.13)$$

where the functional S is the action (3.5). For the sake of completeness, we now consider both the \mathcal{T} -preserving and \mathcal{T} -breaking parts of the random potential, and write $V = \sum_\mu \sigma_\mu V_\mu$. By averaging Eq. (3.13) over disorder, we find

$$\begin{aligned} \overline{\mathcal{Z}^N} \propto & \int D\bar{\psi} D\psi DV \exp\left(-\sum_{\alpha=1}^N \int d^d r d\tau \bar{\psi}_\alpha (\partial_\tau - i\boldsymbol{\sigma} \cdot \boldsymbol{\partial}) \psi_\alpha \right. \\ & \left. - \sum_\mu \int d^d r d\tau V_\mu(\mathbf{r}) \sum_{\alpha=1}^N \bar{\psi}_\alpha \sigma_\mu \psi_\alpha - \frac{1}{2} \sum_\mu \int d^d r_1 d^d r_2 V_\mu(\mathbf{r}_1) h_\mu(\mathbf{r}_1 - \mathbf{r}_2) V_\mu(\mathbf{r}_2)\right). \end{aligned} \quad (3.14)$$

where the functions h_μ were defined in Eq. (2.12); their inverse is the disorder variance g_μ . The Gaussian integral over the random potential leads to the replicated partition function

$$\begin{aligned} \overline{\mathcal{Z}^N} \propto & \int D\bar{\psi} D\psi \exp\left(-\sum_{\alpha=1}^N \int d^d r d\tau \bar{\psi}_\alpha (\partial_\tau - i\boldsymbol{\sigma} \cdot \boldsymbol{\partial}) \psi_\alpha \right. \\ & \left. + \frac{1}{2} \sum_\mu \sum_{\alpha, \beta=1}^N \int d^d r_1 d^d r_2 d\tau_1 d\tau_2 g_\mu(\mathbf{r}_1 - \mathbf{r}_2) (\bar{\psi}_\alpha \sigma_\mu \psi_\alpha)(\mathbf{r}_1, \tau_1) (\bar{\psi}_\beta \sigma_\mu \psi_\beta)(\mathbf{r}_2, \tau_2)\right). \end{aligned} \quad (3.15)$$

Hence, the average properties of disordered Weyl semimetals derive from fermionic fields described by the effective action $S_{\text{eff}} = S_0 + S_{\text{int}}$. The terms S_0 and S_{int} correspond to the Gaussian and quartic parts of Eq. (3.15), respectively (LOUVET 2016). In order to diagonalise the Gaussian part, let us Fourier transform the fermionic fields, as we did in Sec. 1.5. The Fourier parameter conjugate to imaginary time is the so-called Matsubara

frequency ω . We write the Fourier-transformed fields in compact forms $\{\bar{\psi}_{\mathbf{k},\omega}, \psi_{\mathbf{k},\omega}\}$. On one hand, the Gaussian action coincides with the original free action (3.3),

$$S_0[\bar{\psi}, \psi] = \int_{\mathbf{k},\omega} \bar{\psi}_{\mathbf{k},\omega} (\boldsymbol{\sigma} \cdot \mathbf{k} - i\omega) \psi_{\mathbf{k},\omega}, \quad (3.16)$$

except that $\bar{\psi}\psi = \sum_{\alpha} \bar{\psi}_{\alpha} \psi_{\alpha}$ now stands for a scalar product over the $2N$ components of the replicated field². We recall the notation shorthand

$$\int_{\mathbf{k},\omega} = \int \frac{d^d k d\omega}{(2\pi)^{d+1}}. \quad (3.17)$$

On the other hand, the quartic action

$$S_{\text{int}}[\bar{\psi}, \psi] = -\frac{1}{2} \sum_{\mu} \int_{\mathbf{k}_i, \mathbf{q}, \omega_i} g_{\mu}(\mathbf{q}) \bar{\psi}_{\mathbf{k}_1, \omega_1} \sigma_{\mu} \psi_{\mathbf{k}_1 + \mathbf{q}, \omega_1} \bar{\psi}_{\mathbf{k}_2, \omega_2} \sigma_{\mu} \psi_{\mathbf{k}_2 - \mathbf{q}, \omega_2}, \quad (3.18)$$

describes an effective attraction between replicas, mediated by scatterings on the average background of random defects. The coupling strength in Eq. (3.18) is precisely the variance g_{μ} of the random potential: the stronger the disorder correlation, the stronger the quasiparticles attraction. As the Gaussian action S_0 , the interacting part of the action S_{int} is blind to the replica index, since the random potential couples to the total current $\bar{\psi} \sigma_{\mu} \psi$. All replicated theories in the weak disorder limit enjoy a discrete replica symmetry encoded in the permutation group \mathfrak{S}_N (MEZARD 1987). In fermionic theories, this invariance extends to a continuous $U(N)$ symmetry.

In addition, the quartic interactions of Eq. (3.18) preserve the frequency. Incoming quasiparticles keep the same frequencies ω_1 or ω_2 after scattering, unlike the exchanged momentum \mathbf{q} . This disparity between space and time variables can be traced back to the quenched nature of disorder: because the defects are frozen in place at microscopic time scales, defect-electron interactions lead only to elastic scattering, which preserves the particle's energy (LUDWIG 1994). An important consequence is that both Gaussian and interacting actions can be computed at a fixed frequency ω , the same for all fermionic fields. This viewpoint demotes the frequency to a simple parameter of the theory, so that for brevity we will drop all frequency indices in the fields and integrals.

Scalar potential: the Gross-Neveu model — The actions (3.16) and (3.18) reduce to well-known theories for uncorrelated disorder, where the variance of the random potential is flat in Fourier space. Let us first consider a scalar potential with momentum-independent disorder strength $g_0(\mathbf{q}) = \gamma$. The quartic action simplifies to a density-density interaction

$$S_{\text{int}}[\bar{\psi}, \psi] = -\frac{\gamma}{2} \int_{\mathbf{k}_i, \mathbf{q}} \bar{\psi}_{\mathbf{k}_1} \psi_{\mathbf{k}_1 + \mathbf{q}} \bar{\psi}_{\mathbf{k}_2} \psi_{\mathbf{k}_2 - \mathbf{q}} = -\frac{\gamma}{2} \int d^d r (\bar{\psi}\psi)^2. \quad (3.19)$$

The full effective action

$$S_{\text{GN}}[\bar{\psi}, \psi] = \int d^d r \left[\bar{\psi} (-i\boldsymbol{\sigma} \cdot \boldsymbol{\partial} - i\omega) \psi - \frac{\gamma}{2} (\bar{\psi}\psi)^2 \right] \quad (3.20)$$

describes the Gross-Neveu model in d dimensions with fermion mass $m = -i\omega$ and coupling strength $g = -\gamma$, according to the conventions of Sec. 1.5 (GROSS 1974; ZINN-JUSTIN

²We will always omit the implicit identity matrix in the replica sector.

2002). Luckily, the beta function is known to four-loop order in dimension $d = 2 + \varepsilon$, and was given in Eq. (1.110) (GRACEY 2016). The flow of the disorder strength of the replicated theory γ follows from the beta function of the Gross-Neveu model in the limit $N \rightarrow 0$ and $\varepsilon \rightarrow 1$.

The replicated theory with long-range correlations does not share the same fame as the Gross-Neveu model, but was investigated recently by (LOUVET 2017). The variance splits into a flat part and an algebraic part in Fourier space, $g_0(\mathbf{q}) = \gamma_S + \gamma_L q^{a-d}$. The beta functions for the disorder strengths γ_S and γ_L are known to two-loop order, which is enough to determine the leading term of the multifractal exponents.

Vectorial potential: the Thirring model — For a vectorial uncorrelated potential, the variances are $g_i(\mathbf{q}) = \kappa$ for $i = 1, 2, 3$, where we assumed the same disorder strength κ for the three spatial directions. The full effective action simplifies to

$$S_{\text{Th}}[\bar{\psi}, \psi] = \int d^d r \left[\bar{\psi}(-i\boldsymbol{\sigma} \cdot \boldsymbol{\partial} - i\omega)\psi - \frac{\kappa}{2} (\bar{\psi}\boldsymbol{\sigma}\psi)^2 \right], \quad (3.21)$$

where particles now interact through the current-current channel. Eq. (3.21) describes the Thirring model, with fermion mass $m = -i\omega$ and coupling strength $g = -\kappa$ (THIRRING 1958). It is exactly soluble in two dimensions, and is renormalisable in the large N expansion between two and four dimensions. The three-dimensional model is not amenable to a $d = 2 + \varepsilon$ expansion, however, because evanescent operators appear at one-loop order. Admittedly, the Thirring and Gross-Neveu models are related by Fierz identities, but only for $N = 1$ (BONDI 1990). Another expansion scheme should be used, compatible with the zero-replica limit.

In Sec. 3.2.3, we adapt the so-called ε_m -expansion developed by (ROY 2018), which consists in expanding, not near the lower critical dimension, but near the critical disorder correlation r^{-2} , thus avoiding the emergence of evanescent operators. The variance splits again into a flat and an algebraic part in Fourier space, $g_i(\mathbf{q}) = \kappa_S + \kappa_L q^{a-d}$, where now $\delta = a - 2$, like $\varepsilon = d - 2$, is seen as a small expansion parameter. Furthermore, this scheme fits perfectly the replicated theory with generic disorder, since it naturally accounts for long-range correlations.

3.2 Renormalisation group in presence of correlated disorder

In this section we renormalise the replicated theory with both short- and long-range correlations (whether of the Gross-Neveu or Thirring type) directly in the zero-replica limit $N \rightarrow 0$. We set the renormalisation group approach and present the phase diagram for a scalar potential only, and discuss the effects of a vectorial potential in Sec. 3.2.3.

3.2.1 Renormalisation group procedure

Renormalisation constants — The renormalisation procedure consists in reparametrising the action so that the correlation functions of the interacting theory converge in the large momentum limit. This amounts to rescale the bare fields, parameters, and couplings in terms of renormalised ones, from which are defined the new, finite correlation functions.

The relation between bare and renormalised quantities is made through the so-called Z constants:

$$\mathring{\psi} = Z_\psi^{1/2} \psi, \quad \mathring{\bar{\psi}} = Z_\psi^{1/2} \bar{\psi}, \quad \mathring{\omega} = Z_\omega Z_\psi^{-1} \omega, \quad (3.22)$$

for the fields and frequency, and

$$\mathring{\gamma}_S = \frac{2\mu^{-\varepsilon} Z_S}{K_d Z_\psi^2} \gamma_S, \quad \mathring{\gamma}_L = \frac{2\mu^{-\delta} Z_L}{K_d Z_\psi^2} \gamma_L, \quad (3.23)$$

for the coupling strengths. Since the two coupling strengths are associated to distinct operators, the flow differently under the renormalisation procedure, which explains why two constants $Z_{S,L}$ are needed. The factor K_d was introduced in Eq. (1.79), and compensates the annoying angular factors appearing in Feynman integrals to ease the computations of the beta functions. The canonical dimensions of the disorder strengths are $[\gamma_S] = -\varepsilon$ and $[\gamma_L] = -\delta$, where $\varepsilon = d - 2$ and $\delta = a - 2$. Here we adopt the double expansion in the small parameters ε and δ developed in (WEINRIB 1983; FEDORENKO 2006; DUDKA 2016). The two expansion parameters ε and δ are treated as independent. The parameter μ is the mass scale of the renormalised theory. The renormalised Gaussian action reads

$$S_0 = \int_{\mathbf{k}} \bar{\psi}_{\mathbf{k}} (Z_\psi \boldsymbol{\sigma} \cdot \mathbf{k} - i Z_\omega \omega) \psi_{\mathbf{k}} \quad (3.24)$$

while the renormalised quartic interaction reads

$$S_{\text{int}} = -K_d^{-1} \int_{\mathbf{k}_i} \left(\mu^{-\varepsilon} Z_S \gamma_S + \mu^{-\delta} Z_L \gamma_L q^{\delta-\varepsilon} \right) \bar{\psi}_{\mathbf{k}_1} \psi_{\mathbf{k}_1+\mathbf{q}} \bar{\psi}_{\mathbf{k}_2} \psi_{\mathbf{k}_2-\mathbf{q}}. \quad (3.25)$$

Expansion and subtraction scheme — We cure the divergences of the Feynman diagrams using the minimal subtraction scheme: the Z constants absorb only the poles in inverse powers of ε and δ but no constant terms. The Z constants at order L in the loopwise expansion take the form of a finite Laurent series

$$Z(\gamma) = 1 + \frac{A(\gamma)}{\varepsilon} + \frac{B(\gamma, \varepsilon/\delta)}{\delta} + \dots, \quad (3.26)$$

where A and B are polynomials of order L in the coupling strengths $\gamma = \{\gamma_S, \gamma_L\}$. The function $x \mapsto B(\gamma, x)$ is analytic at $x = 0$ because the theory is renormalisable in two dimensions in presence of long-range correlations only. The ellipsis stands for higher order terms of the Laurent series, which originates from diagrams of order larger than two. In the standard ε -expansion, these terms compensate one another in the scaling functions, and thus play no role in the determination of the critical exponents. We will assume that the same happens in Eq. (3.26), which also contains poles in δ .

For each coupling strength γ_i , for $i = S, L$, we define the beta function

$$\beta_i(\gamma) = -\frac{\partial \gamma_i}{\partial \log \mu} \quad (3.27)$$

where all bare quantities are fixed in the derivative. From the renormalisation constants for the couplings and the field, we extract the beta functions using Eq. (3.23),

$$\begin{pmatrix} \beta_S \\ \beta_L \end{pmatrix} = Y^{-1} \begin{pmatrix} -\varepsilon \gamma_S \\ -\delta \gamma_L \end{pmatrix}, \quad Y_{ij} = \delta_{ij} + \gamma_i \frac{\partial \log(Z_i/Z_\psi^2)}{\partial \gamma_j}, \quad (3.28)$$

where here again all bare quantities are fixed in the derivative. The beta functions at order L follow by expanding the matrix Y^{-1} in the coupling strengths up to the power L . The scaling functions for the field and frequency then read

$$\eta_\psi = \frac{\partial \log Z_\psi}{\partial \log \mu} = - \sum_i \beta_i \frac{\partial Z_\psi}{\partial \gamma_i}, \quad \eta_\omega = \frac{\partial \log Z_\omega}{\partial \log \mu} = - \sum_i \beta_i \frac{\partial Z_\omega}{\partial \gamma_i}. \quad (3.29)$$

The critical exponents η and z are given by the suitable scaling functions evaluated at the critical point, $\eta = \eta_\psi(\gamma^*)$ for the anomalous field exponent and $z = 1 + \eta_\omega(\gamma^*) - \eta_\psi(\gamma^*)$ for the dynamical critical exponent. We will restrict the expansion to two-loop order.

Renormalisation of the vertex functions — To determine the renormalisation constants for the fields and frequency on one hand, and for the coupling strengths on the other hand, it is sufficient to render respectively the two-point and four-point vertices finite at special sets of momenta. Guided by the form of the vertex in the tree approximation, we impose on the two-point vertex function the renormalisation condition

$$\Gamma^{(2)}(\mathbf{k} = \mathbf{0}; \omega, \gamma, \mu) = \text{finite}, \quad \frac{\partial \Gamma^{(2)}}{\partial \mathbf{k}}(\mathbf{k} = \mathbf{0}; \omega, \gamma, \mu) = \text{finite}. \quad (3.30)$$

We also decompose the four-point vertex function into the contact and long-range components

$$\Gamma^{(4)}(\mathbf{k}_1, \mathbf{k}_1 + \mathbf{q}, \mathbf{k}_2, \mathbf{k}_2 - \mathbf{q}; \omega, \gamma, \mu) = \Gamma_S^{(4)}(\{\mathbf{k}_i\}; \omega, \gamma, \mu) + \Gamma_L^{(4)}(\{\mathbf{k}_i\}; \omega, \gamma, \mu) q^{a-d} \quad (3.31)$$

and enforce similar finiteness conditions,

$$\Gamma_S^{(4)}(\{\mathbf{k}_i = \mathbf{0}\}; \mu, \gamma, \mu) = \text{finite}, \quad \Gamma_L^{(4)}(\{\mathbf{k}_i = \mathbf{0}\}; \mu, \gamma, \mu) = \text{finite}. \quad (3.32)$$

The self-energy Σ is linked to the two-point function by the relation $\Gamma^{(2)} = G_0^{-1} - \Sigma$. Fig. 3.1 gives the one-particle irreducible diagrams that contribute to the self-energy at one- and two-loop orders. The four-point vertex is given in Appendix B by the diagrams of Fig. B.2 at one-loop order, and of Fig. B.2 to Fig. B.4 at two-loop order. The Feynman rules are akin to that of the Gross-Neveu model. However, an interaction line now represents the scattering of two particles mediated by an intermediate random defect, averaged over all disorder configurations, i.e an impurity line. Each impurity line carries either a factor $K_d^{-1} \mu^{-\varepsilon} Z_S \gamma_S$ for a contact interaction, or a factor $K_d^{-1} \mu^{-\delta} Z_L \gamma_L q^{\delta-\varepsilon}$ for a long-range interaction.

3.2.2 Beta functions and flow diagram

The results of this section come from the works of T. Louvet et al. on the effect of long-range correlations on the semimetal-metal transition (LOUVET 2017).

Beta functions — The beta functions for scalar random potentials to two-loop order in the disorder strengths γ_S and γ_L are

$$\begin{cases} \beta_S = -\varepsilon \gamma_S + 4\gamma_S^2 + 4\gamma_S \gamma_L + 8\gamma_S^3 + 20\gamma_S^2 \gamma_L + 16\gamma_S \gamma_L^2 + 4\gamma_L^3, & (3.33a) \\ \beta_L = -\delta \gamma_L + 4\gamma_L^2 + 4\gamma_S \gamma_L + 4\gamma_L^3 + 4\gamma_S^2 \gamma_L + 8\gamma_S \gamma_L^2. & (3.33b) \end{cases}$$

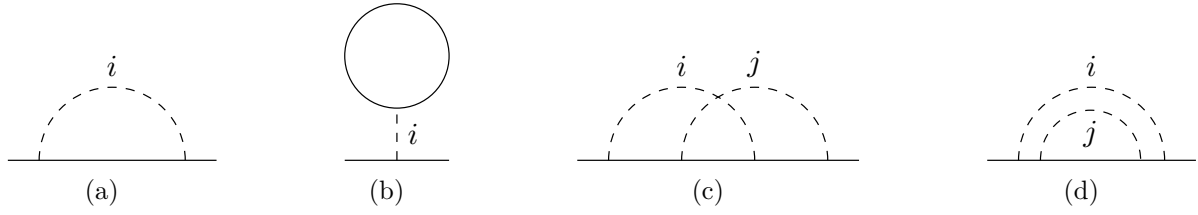


Figure 3.1 | The corrections to the two-point vertex function beyond the tree level coincide (up to a sign) with the self-energy $\Sigma = G_0^{-1} - \Gamma^{(2)}$. Each index i, j refers to either short- or long-range interactions. (a) Self-energy at one-loop order. (b) In a closed fermionic loop, the two indices of the free Green's function are contracted. The trace brings out a factor N in the graph's multiplicity (the number of replicas), which vanishes in the zero-replica limit. Those diagrams that contain closed fermionic loops do not enter the effective theory of disordered relativistic semimetals. (c)-(d) Self-energy at two-loop order. These graphs correct the anomalous field η_ψ and frequency η_ω exponents at order ε^2 in the small parameter $\varepsilon = d - 2$. The counterterms are not shown.

In absence of long-range correlations ($\gamma_L = 0$), the beta function (3.33a) agrees with that of the Gross-Neveu model given in Eq. (1.110) in the limit $N \rightarrow 0$, up to the sign flip $g = -\gamma_S$. Remarkably, long-range correlations generate a contact interaction at two-loop order even when the latter is absent at tree level, but not vice versa, the beta function (3.33b) being proportional to γ_L at all orders. The $4\gamma_L^3$ contribution to Eq. (3.33a) comes from the three-barred ladder diagrams of Fig. B.4, where a particle-hole pair self-interacts sequentially, and diagrams with a loop and a two-barred ladder intertwined. The scaling functions for the field and frequency read,

$$\eta_\psi = -2\gamma_S^2 + 2\gamma_L^2 - \frac{4\varepsilon}{\delta}\gamma_L(\gamma_S + \gamma_L), \quad z = 1 + 2(\gamma_S + \gamma_L) + 2(\gamma_S + \gamma_L)^2. \quad (3.34)$$

The beta functions possess three fixed points, whose stability depends on the values of ε and δ . The stability regions are summarised in Fig. 3.2.

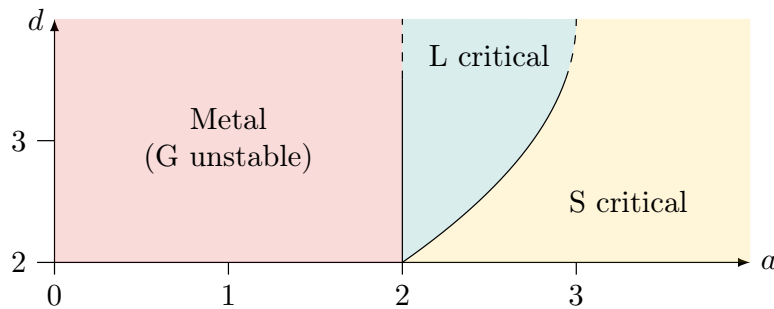


Figure 3.2 | Stability regions of the Gaussian G, short-range S and long-range L fixed points, in the (a, d) plane, where $a = 2 + \delta$ represents the disorder correlation exponent and $d = 2 + \varepsilon$ the space dimension (LOUVET 2017). Only the area above the lower critical dimension $d_\ell = 2$ is shown, where the semimetallic phase may survive moderate disorder. For $a < 2$, G is unstable and the flow exhibits a runaway behaviour, reflecting the instability of the semimetal with respect to very long-range correlations. A diffusive metallic phase then settles at arbitrarily weak disorder. The line $\delta^*(\varepsilon) = \varepsilon - \frac{1}{4}\varepsilon^2 + O(\varepsilon^3)$ separates the regions where the S (below) or L (above) fixed point controls criticality.

- The Gaussian fixed point G has coordinates $\gamma_S = \gamma_L = 0$; its basin of attraction covers the semimetallic phase. This fixed point – and thus the semimetallic phase – is unstable for $\delta < 0$, i.e. when the disorder correlation exponent a is less than the lower critical dimension $d_\ell = 2$.
- The short-range fixed point S has coordinates

$$\gamma_S = \frac{\varepsilon}{4} - \frac{\varepsilon^2}{8} + O(\varepsilon^3), \quad \gamma_L = 0. \quad (3.35)$$

Since uncorrelated disorder cannot generate long-range correlations under the renormalisation flow, the vanishing of γ_L at this fixed point holds at any order of the expansion. S has a single unstable direction for $\delta > \delta^*(\varepsilon) = \varepsilon - \frac{1}{4}\varepsilon^2 + O(\varepsilon^3)$, and thus controls the universality class of the semimetal-metal transition for $a \gtrsim d$. The critical exponents are

$$\nu^{-1} = \varepsilon + \frac{\varepsilon^2}{2} + O(\varepsilon^3), \quad z = 1 + \frac{\varepsilon}{2} - \frac{\varepsilon^2}{8} + O(\varepsilon^3). \quad (3.36)$$

- The short-range fixed point L has coordinates

$$\gamma_S = \frac{\delta^3}{16(\varepsilon - \delta)} + O(\varepsilon^3), \quad \gamma_L = \frac{\delta}{4} - \frac{\delta^2 \varepsilon}{16(\varepsilon - \delta)} + O(\varepsilon^3). \quad (3.37)$$

It has a single unstable direction for $0 < \delta < \delta^*$ where it drives the transition to a new universality class with critical exponents

$$\nu^{-1} = \delta + \frac{\delta^2(2\delta + \varepsilon)}{4\varepsilon} + O(\varepsilon^3), \quad z = 1 + \frac{\delta}{2}. \quad (3.38)$$

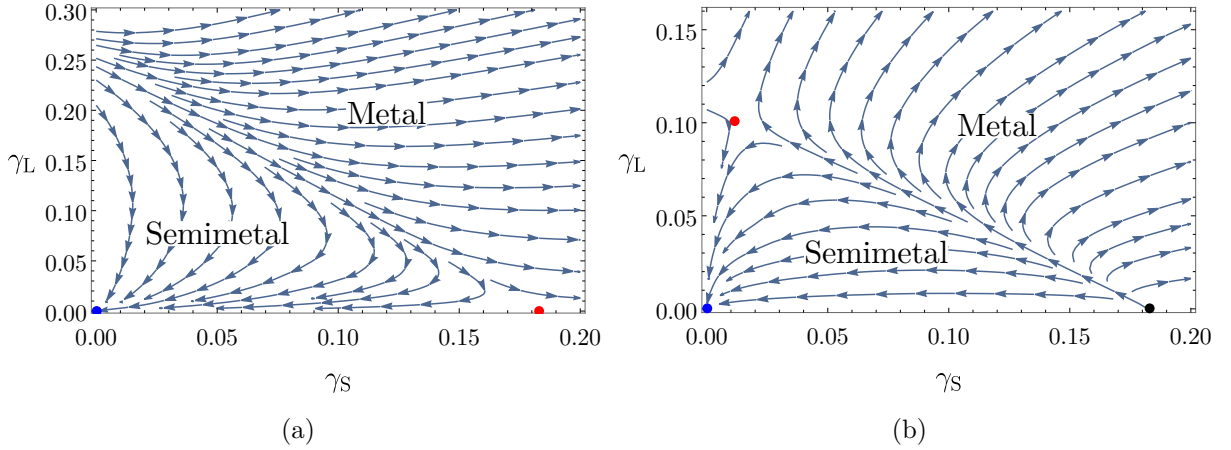


Figure 3.3 | Flow diagram of a Weyl semimetal in three dimensions under a scalar random potential. The coupling constant γ_S (γ_L) quantifies the strength of short-range (long-range) disorder correlations. The Gaussian fixed point (blue dot \bullet) attracts all coupling strengths initially in the semimetallic region. In the strong disorder regime, both coupling strengths exhibit a runaway behaviour. (a) For a disorder correlation exponent $a = 3.5$, the short-range fixed point (red dot \bullet) is critical and determines the universality class. (b) For a disorder correlation exponent $a = 2.5$, the long-range fixed point (red dot \bullet) is critical and the short-range fixed point (black dot \bullet) becomes trivial. Long-range correlations determine the universality class. Adapted from (LOUVET 2017).

The two-loop correction to the dynamical exponent magically vanishes. The expression $z = a/2$ is actually exact. The scaling function (3.34) for the dynamical exponent coincides indeed with that of the reduced temperature in the two-dimensional Ising model with correlated random bond disorder, for which $\nu_{\text{Ising}}^{-1} = 2/a$ exactly (DUDKA 2016).

Phase diagram — Fig. 3.3 represents the phase diagram of a dirty Weyl semimetal along with the renormalisation flow of the disorder strengths. For $\delta > \delta^*$, long-range correlations can induce a phase transition even in absence of uncorrelated disorder, but play no role in the critical behaviour. The short-range fixed point S determines the universality class. The long-range fixed point, on the other hand, is located in the unphysical region $\gamma_L < 0$ of the phase diagram. For $\delta < \delta^*$, the long-range fixed point L determines the universality class.

3.2.3 Time-reversal- and valley-symmetry breaking disorder

Vector potential disorder — The effect of vector potential disorder on the semimetal-metal transition is not settled. Numerical simulations show that an uncorrelated random vector potential drives the system to a diffusive metal phase if more than two components out of three are included (SBIERSKI 2016). Though the one-loop correlation length exponent $\nu = 1$ agrees with that of the ‘scalar’ fixed point, nothing rules out the possibility that the two transitions belong to different universality classes (SBIERSKI 2016; LEE 2017). we hereby demonstrate that vector potential disorder is less relevant than scalar disorder at one-loop order, to the extent that it preserves the universality class controlled by the scalar fixed point (BRILLAUX 2019).

Unfortunately, the one-loop ladder diagrams generate an infinite number of evanescent operators in dimensional regularisation. As discussed previously, projecting these unphysical operators onto the physical ones is a difficult task in three dimensions. To bypass this problem, another regularisation scheme must be used. Here we use the ε_m -expansion of (ROY 2018) to investigate the interplay between scalar and vectorial random potentials, with independent and arbitrary correlations. Instead of lowering the degree of divergence near the lower critical dimension $d_\ell = 2$, the ε_m expansion regularises Feynman integrals near the critical disorder correlation r^{-2} . We thus fix the dimension $d = 3$, and assume an algebraic form for both scalar correlations $g_0(\mathbf{q}) = \gamma q^{\varepsilon-1}$ and vectorial correlations $g_i(\mathbf{q}) = \kappa q^{\delta-1}$ for $i = 1, 2, 3$. The renormalisation flow preserves the isotropy of the current-current interaction $(\bar{\psi} \boldsymbol{\sigma} \psi)^2$, so that a single coupling strength κ is needed. Note, however, that this scheme works properly in the zero-replica limit $N \rightarrow 0$ at one-loop order. For arbitrary N , diagrams with closed loop contribute and produce new couplings with higher power correlations. Similarly, two-loop diagrams create contact interactions, which cannot be included without dimensional regularisation.

The renormalised interacting action reads (in compact form)

$$S_{\text{int}} = -\frac{\mu^{-\varepsilon} Z_\gamma \gamma}{K_d} \int_{\mathbf{k}_i} q^{\varepsilon-1} (\bar{\psi} \psi)^2 - \frac{\mu^{-\delta} Z_\kappa \kappa}{K_d} \int_{\mathbf{k}_i} q^{\delta-1} (\bar{\psi} \boldsymbol{\sigma} \psi)^2. \quad (3.39)$$

The subspace of quartic interactions spanned by S_{int} is invariant under the renormalisation flow; the couplings beyond the tree level are all included in Eq. (3.39). The relations

between bare and renormalised couplings are similar to Eq. (3.23),

$$\dot{\gamma} = \frac{2\mu^{-\varepsilon}}{K_d} \frac{Z_\gamma}{Z_\psi^2} \gamma, \quad \dot{\kappa} = \frac{2\mu^{-\delta}}{K_d} \frac{Z_\kappa}{Z_\psi^2} \kappa. \quad (3.40)$$

The 4-point vertex function split again into the contact and long-range components, but they now possess a non-trivial tensorial structure

$$\Gamma^{(4)} = \Gamma_\gamma^{(4)} \mathbb{1} \otimes \mathbb{1} + \Gamma_\kappa^{(4)} q^{a-d} \boldsymbol{\sigma} \otimes \boldsymbol{\sigma}, \quad (3.41)$$

where \otimes stands for the Kronecker product and $\boldsymbol{\sigma} \otimes \boldsymbol{\sigma} = \sigma_x \otimes \sigma_x + \sigma_y \otimes \sigma_y + \sigma_z \otimes \sigma_z$. The renormalisation conditions on $\Gamma_\gamma^{(4)}$ and $\Gamma_\kappa^{(4)}$ are similar to Eq. (3.32). Besides the Feynman rules already presented in Sec. 1.5.2, each vertex now carries either σ_0 or $\boldsymbol{\sigma}$ matrices. At the critical power-law correlations ($\varepsilon = \delta = 0$), the ladder diagrams are finite, and thus do not contribute to the beta functions. By omitting them, we are left with Yukawa-like couplings, where internal impurity lines affect only two of the four external legs.

Unlike dimensional regularisation, the ε_m -expansion generates one-loop anomalous dimensions for the field and frequency. The renormalisation constants read

$$Z_\psi = 1 - \frac{2}{3} \left(\frac{\gamma}{\varepsilon} - \frac{\kappa}{\delta} \right), \quad Z_\omega = 1 + 2 \left(\frac{\gamma}{\varepsilon} + \frac{3\kappa}{\delta} \right) \quad (3.42)$$

for the field and frequency, and

$$Z_\gamma = 1 + 4 \left(\frac{\gamma}{\varepsilon} + \frac{3\kappa}{\delta} \right), \quad Z_\kappa = 1 + \frac{4}{3} \left(-\frac{\gamma}{\varepsilon} + \frac{\kappa}{\delta} \right) \quad (3.43)$$

for the coupling strengths. we deduce the anomalous dimensions $\eta_\psi = -\frac{2}{3}(\gamma - \kappa)$ and $\eta_\omega = 2(\gamma + 3\kappa)$, along with the beta functions

$$\beta_\gamma = -\varepsilon\gamma + \frac{32}{3}\gamma\kappa + \frac{16}{3}\gamma^2, \quad \beta_\kappa = -\delta\kappa. \quad (3.44)$$

Fig 3.4(a) shows the renormalisation flow generated by the beta functions (3.44) in three dimensions, and for uncorrelated disorder ($\varepsilon = \delta = 1$). Due to the trivial flow of κ even in presence of a scalar potential, we recover the Gaussian $G = (0, 0)$ and the ‘scalar’ $S = (3\varepsilon/16, 0)$ fixed points. For moderately long-range correlations of the vector potential ($\delta > 0$), the scalar fixed point controls criticality and the transition lies in the universality class of the three-dimensional Gross-Neveu model. Otherwise, the Gaussian fixed point is unstable and an infinitesimal amount of disorder drives the system to a metallic phase, as was the case for a scalar potential. The one-loop anomalous exponents are $\eta_\psi = -\varepsilon/8$ and $\eta_\omega = 3\varepsilon/8$. Remarkably, the dynamical exponent $z = 1 + \varepsilon/2$ agrees in both ε - and ε_m -expansion schemes, which demonstrates once more the robustness of this exponent.

Extension to binodal systems — When random scattering mixes the valleys, whether they represent two remote Weyl nodes or a single Dirac node, a minimal Hamiltonian must be binodal. The insensitivity of the single-node system to vector potential disorder suggests some kind of *super-universality* of the semimetal-metal transition, which falls into the same universality class whatever the symmetry of the perturbation. A natural inquiry is whether this super-universality survives the presence of intervalley scattering. We now extend the work of (ROY 2018) to study the interplay between intervalley and

Intravalley		\mathcal{T}	\mathcal{I}	\mathcal{P}		Intervalley		\mathcal{T}	\mathcal{I}	\mathcal{P}	
potential	$\Psi^\dagger \Psi$	✓	✓		γ	temporal tensor	$\Psi^\dagger \gamma_0 \sigma_{0j} \Psi$				λ
axial potential	$\Psi^\dagger \gamma_5 \Psi$	✓		✓		spatial tensor	$\Psi^\dagger \gamma_0 \sigma_{jk} \Psi$	✓	✓		
current	$\Psi^\dagger \gamma_0 \gamma_j \Psi$				κ	mass	$\Psi^\dagger \gamma_0 \Psi$				✓
axial current	$\Psi^\dagger \gamma_0 \gamma_5 \gamma_j \Psi$		✓	✓		pseudomass	$\Psi^\dagger i \gamma_0 \gamma_5 \Psi$	✓			✓

Table 3.1 | Random bilinear perturbations of a binodal Weyl system split into eight classes, four of which preserve the emergent U(1) valley symmetry (intravalley scattering), while the other four break it (intervalley scattering). They are specified by the emergent time-reversal \mathcal{T} , inversion \mathcal{I} , and particle-hole \mathcal{P} symmetries. The chemical potential and current perturbations respectively match the scalar and vector potential disorders of the single-node system. Axial potential disorder is inevitable in \mathcal{I} -breaking materials, because of asymmetries in the position of each valley’s nodal level. Magnetic impurities create axial current disorder when the pseudospin stands for the actual electronic spin. The spin tensor $\sigma_{\mu\nu} = \frac{i}{2}[\gamma_\mu, \gamma_\nu]$ completes the basis of the so(4) algebra, besides the gamma matrices γ_μ and γ_5 . Adapted from (ROY 2018).

intravalley scatterings in presence of long-range correlations. Tab. 3.1 reports all possible perturbations in binodal Weyl or Dirac materials. Since the axial their corresponding non-axial perturbations flow identically, we will focus on scalar (or chemical potential) and vector (or current) perturbations on one hand (intravalley scattering), and the temporal tensor and mass perturbations on the other hand (intervalley scattering). In addition, disorder correlations which decay slower than r^{-2} always drive the system to a metallic phase, whatever the symmetry of the perturbation; we will restrict myself to the effect of moderately long-range intervalley scatterings on the ‘scalar’ critical point.

Intervalley scatterings split into tensorial and mass-like perturbations. A lone random tensor acquires no corrections at one-loop order, like in Eq. (3.44) for the vectorial potential; a lone random mass is even renormalised downwards. Neither induces a transition at this order. Let us now consider the competition with scalar disorder. Mass-like perturbations leave the universality class of the semimetal-metal transition unchanged. But a new critical point appears in presence of sufficiently long-range correlated tensorial perturbations. Let λ be the coupling strength of a random temporal tensor. The coupled flow has the form

$$\beta_\gamma = -\varepsilon\gamma + \frac{40}{3}\gamma\lambda + \frac{16}{3}\gamma^2, \quad \beta_\lambda = -\delta\lambda + \frac{8}{3}\lambda\gamma. \quad (3.45)$$

As Fig. 3.4(b) shows, the ‘scalar’ fixed point becomes unstable for $0 < \delta < \varepsilon/2$, in which case a new ‘tensorial’ fixed point $T = (3\delta/8, 3(\varepsilon - 2\delta)/40)$ controls criticality. In this universality class, the anomalous exponents are $\eta_\psi = -(3\delta + \varepsilon)/20$ and $\eta_\omega = 3(3\varepsilon - \delta)/20$, but the dynamical exponent $z = 1 + \varepsilon/2$ assumes once again the same value as for scalar disorder.

All in all, super-universality does not extend to binodal Weyl systems, although intervalley scattering preserves the dynamical exponent, which assumes the same expression as for scalar uncorrelated disorder. This ‘weak’ form of super-universality leads us to postulate – though without proof at present – that intervalley scattering plays no role in the determination of the multifractal exponents defined in Sec. 3.3. Under thus assumption, only scalar disorder requires scrutiny, though short-range and long-range contributions must both be considered.

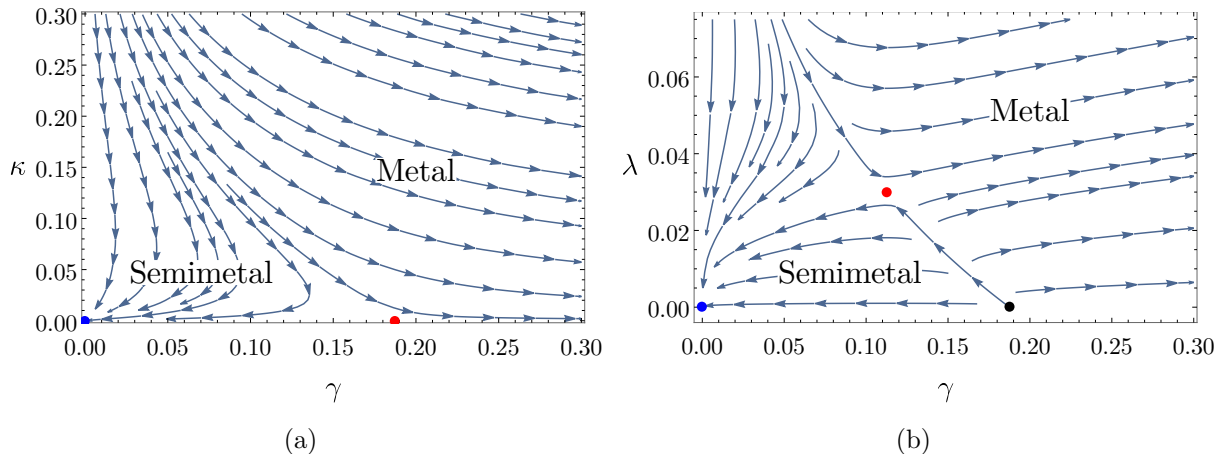


Figure 3.4 | Phase diagram of Weyl or Dirac semimetals in three dimensions under an uncorrelated scalar potential, with disorder strength γ , in presence of (a) a random vector potential in a single-node system, with disorder strength κ ; (b) a random spinorial tensor in a binodal system. The variance of the random vector or tensor decays as r^{-a} with distance r . The Gaussian fixed point (blue dot \bullet) attracts all disorder strengths initially in the semimetallic region. In the strong disorder regime, both strengths run away in the metallic region. (a) With a random vector, the ‘scalar’ fixed point (red dot \bullet) remains critical and determines the universality class (here $a = 3$). (b) With a sufficiently long-range correlated random tensor (here $2 < \delta = 2.3 < 2.5$), a new critical fixed point emerges (red dot \bullet), and the scalar fixed point (black dot \bullet) becomes unstable. The universality class changes, but the dynamical exponent coincides with that determined by scalar disorder.

3.3 Multifractality within the replicated field theory

In this section, we compute the multifractal spectrum at the semimetal-metal transition for both a short-range and a long-range correlated scalar potential. As shown in the previous section, time-reversal-breaking disorder and intervalley scattering should not affect the multifractality of critical wave functions in absence of very long-range correlations. Before this work, these exponents were known for uncorrelated disorder in the supersymmetric method (SYZRANOV 2016). Here, we use instead the replica method (BRILLAUX 2019).

3.3.1 Multifractal spectrum to two-loop order

Suitable composite operator — We now wish to build a suitable composite operator to represent the moments of the local DoS within the effective theory. The operator canonically associated to the wave function density is the local operator $\bar{\psi}\psi$, where the two fields $\bar{\psi}$ and ψ are evaluated at the same point. As is standard in field theories, the corresponding scaling dimension differs from that of $\bar{\psi}(\mathbf{r}_1)\psi(\mathbf{r}_2)$, where \mathbf{r}_1 and \mathbf{r}_2 are distinct points, because of short-distance singularities. Let us add to the original action S the source term

$$S_J = - \int d^d r J \bar{\psi}\psi. \quad (3.46)$$

This source term enables to insert $\bar{\psi}\psi$ in correlation functions, by deriving the partition function with respect to J as many times as the number of insertions (ZINN-JUSTIN 2002).

I now apply the replica trick to cast the expectation value of $\bar{\psi}\psi$ into a form suitable for disorder averaging. Let q be an integer that divides the replica number N . We now use the replica trick in the following way:

$$\langle \bar{\psi}\psi \rangle = \frac{\delta \ln Z}{\delta J} \propto \lim_{N \rightarrow 0} Z^{N/q-1} \frac{\delta Z}{\delta J}, \quad (3.47)$$

where the functional derivative is evaluated at $J = 0$. Keeping the zero-replica limit in mind, we raise Eq. (3.47) to the power q , so as to insert q distinct replicated operators $\bar{\psi}_\alpha \psi_\alpha$. In other words,

$$\langle \bar{\psi}\psi \rangle^q \propto Z^{N-q} \left(\frac{\delta Z}{\delta J} \right)^q = \int \mathcal{D}\bar{\psi} \mathcal{D}\psi \left(\prod_{\alpha=1}^q \bar{\psi}_\alpha \psi_\alpha \right) \exp \left(- \sum_{\alpha=1}^N S[\bar{\psi}_\alpha, \psi_\alpha, V] \right) \quad (3.48)$$

Averaging over disorder is now straightforward. we get

$$\overline{\langle \bar{\psi}\psi \rangle^q} = \int \mathcal{D}\bar{\psi} \mathcal{D}\psi \left(\prod_{\alpha=1}^q \bar{\psi}_\alpha \psi_\alpha \right) \exp(-S_{\text{eff}}[\bar{\psi}, \psi]). \quad (3.49)$$

The moments of the local DoS are thus represented in the replicated theory by an expectation value of the composite operator

$$\mathcal{O}_q = \prod_{\alpha=1}^q \bar{\psi}_\alpha \psi_\alpha. \quad (3.50)$$

Note that in Eq. (3.50) the product is done over *distinct* replicas. Were it performed over the same replicas, or equivalently over the sum of all replicas, the scaling dimension would be different. The similar-looking operator

$$\tilde{\mathcal{O}}_q = \left(\sum_{\alpha=1}^n \bar{\psi}_\alpha \psi_\alpha \right)^q \quad (3.51)$$

captures deviations of the random potential from a Gaussian distribution due to the generation of higher-order vertices under the renormalisation flow. While \mathcal{O}_q represents the disorder average of $\langle \bar{\psi}\psi \rangle^q$, the operator $\tilde{\mathcal{O}}_q$ represents the disorder average of $\langle (\bar{\psi}\psi)^q \rangle$, and gets already corrected at one-loop order. At first order in $\varepsilon = d - 2$, its scaling dimension reads $\tilde{d}_q = (d - 1)q - 2\gamma = (1 + \varepsilon)q - \frac{1}{2}q^2\varepsilon$ (LOUVET 2016). The critical fluctuations of the density is a more subtle effect, and manifest themselves in the scaling dimension of \mathcal{O}_q only beyond two-loop order.

Renormalisation at two-loop order — The renormalisation of \mathcal{O}_q requires to introduce a new constant Z_q . The renormalised proper vertex $\Gamma_{\mathcal{O}}^{(q)}$, which follows from the ensemble average of \mathcal{O}_q over the quantum action Γ , is rendered finite by setting

$$\Gamma_{\mathcal{O}}^{(q)}(\{\mathbf{k}_i\}; \dot{\gamma}, \dot{\omega}) = Z_q Z_\psi^{-q} \Gamma_{\mathcal{O}}^{(q)}(\{\mathbf{k}_i\}; \gamma, \omega, \mu), \quad (3.52)$$

Dimensional analysis indicates that the scaling dimension of \mathcal{O}_q is $d_q = (d - 1 + \eta_\psi)q - \eta_q$. The anomalous scaling dimension which stems from the Z_q constant is

$$\eta_q = - \sum_i \beta_i \frac{\partial \ln Z_q}{\partial \gamma_i}. \quad (3.53)$$

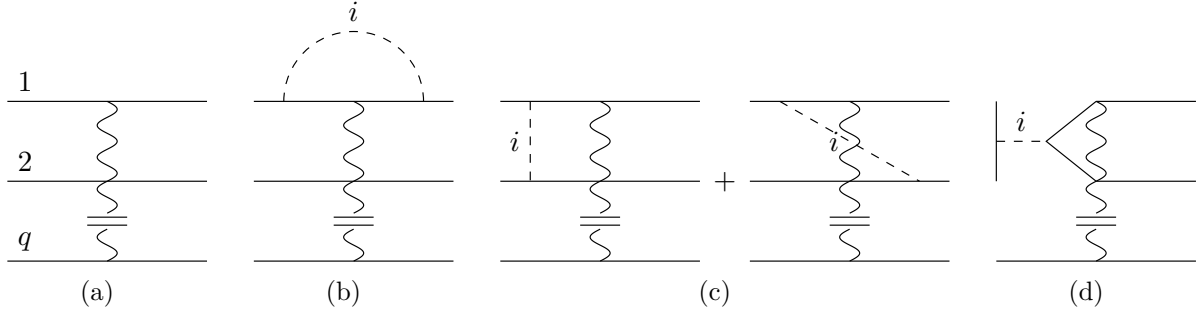


Figure 3.5 | One-loop corrections to the vertex function with a single insertion of the multifractal operator \mathcal{O}_q . We employ the graphical conventions of (SYZРАНОВ 2016), with the difference that impurity lines carry either short-range ($i = \text{S}$, coupling strength γ_{S}) or long-range ($i = \text{L}$, coupling strength γ_{L}) disorder correlations. (a) Vertex at tree level. Solid lines stand for the free Green’s functions in distinct replica sectors $\alpha = 1, \dots, q$. The wavy line indicates the insertion of \mathcal{O}_q . Diagram (b) has multiplicity $2q$ and pole $\gamma_{\text{S}}/\varepsilon + \gamma_{\text{L}}/\delta$, where $\varepsilon = d - 2$ is the distance to the lower critical dimension and $\delta = a - 2$ the distance to the critical disorder correlation exponent. The two ladder diagrams (c) cancel one another. Diagram (d) vanishes because fields from different replicas are contracted. It contributes, however, to the analogous operator $\tilde{\mathcal{O}}_q$ defined in Eq. (3.51), and which captures how much the distribution of the density of states deviates from a Gaussian law.

From there, the multifractal anomalous exponents $\Delta_q = d_q - qd_1 = q\eta_1 - \eta_q$ can be easily computed. The anomalous field dimension plays no role since it enters only the linear part of d_q .

The one- and two-loop diagrams for this vertex function are shown in Fig. 3.5, and B.5 in Appendix B, respectively. Tab. B.1 summarises the poles of the corresponding diagrams with their multiplicities. As for the four-point vertex, the ladder diagrams of Fig. 3.5(c) vanish. Only the loop diagram of Fig. 3.5(b) contributes. The tree-level vertex is depicted as q solid lines connected by a wavy line, which stands for the source of \mathcal{O}_q . We find the anomalous dimension η_q at second order in the coupling strengths to be

$$\eta_q = q \left[2(\gamma_{\text{S}} + \gamma_{\text{L}}) - 6\gamma_{\text{S}}^2 + \left(1 - \frac{7\varepsilon}{\delta}\right) \gamma_{\text{L}}^2 - \gamma_{\text{S}}\gamma_{\text{L}} \left(11 + \frac{4\varepsilon}{\delta} - \frac{3\delta}{\varepsilon}\right) \right] + q^2 \left[6\gamma_{\text{S}}^2 + 3 \left(5 - \frac{\delta}{\varepsilon}\right) \gamma_{\text{S}}\gamma_{\text{L}} + 3 \left(1 + \frac{\varepsilon}{\delta}\right) \gamma_{\text{L}}^2 \right]. \quad (3.54)$$

We can check that Eq. (3.54) gives the correct exponent for $q = 1$. And indeed $\eta_1 = 2(\gamma_{\text{S}} + \gamma_{\text{L}}) + 4\gamma_{\text{L}}^2 + 4(1 - \frac{\varepsilon}{\delta})\gamma_{\text{L}}(\gamma_{\text{S}} + \gamma_{\text{L}})$ agrees with the frequency exponent η_ω of Eq. (3.34). Eventually,

$$\Delta_q = q(1 - q) \left[6\gamma_{\text{S}}^2 + 3 \left(5 - \frac{\delta}{\varepsilon}\right) \gamma_{\text{S}}\gamma_{\text{L}} + 3 \left(1 + \frac{\varepsilon}{\delta}\right) \gamma_{\text{L}}^2 \right]. \quad (3.55)$$

Anomalous multifractal exponents — To determine the anomalous multifractal exponents at the semimetal-metal transition we evaluate Eq. (3.55) at the relevant critical fixed point.

- For $\delta > \delta^*$, the short-range fixed point controls criticality. Substituting Eq. (3.35)

into Eq. (3.55) we recover the result of S. V. Syzranov (SYZRANOV 2016),

$$\Delta_q = \frac{3}{8}q(1-q)\varepsilon^2 + O(\varepsilon^3). \quad (3.56)$$

- For $0 < \delta < \delta^*$, the long-range fixed point controls criticality. Injecting Eq. (3.37) we find the anomalous multifractal exponents of the new universality class (BRILLAUX 2019)

$$\Delta_q = \frac{3}{16}q(1-q)\delta(\delta + \varepsilon) + O(\varepsilon^3). \quad (3.57)$$

As a consistency check, the two expressions (3.56) and (3.57) match on the line $\delta = \delta^*$, which separates the regions of stability of the short- and long-range fixed points. The expression of Eq. (3.57) also vanishes at $\delta = 0$, in agreement with the disappearance of the transition at the lower critical dimension.

Singularity spectrum — The singularity spectrum f_τ corresponding to the multifractal spectra (3.56) and (3.57) is quadratic, and peaks at x_0 with a maximum $f_\tau(x_0) = d$. This leads to a log-normal distribution $P(\varrho, L)$ for the local DoS. The location of the maximum depends, here again, on the universality class.

- For short-range correlated disorder ($\delta > \delta^*$),

$$x_0 = 2 + \varepsilon + \frac{3}{8}\varepsilon^2 + O(\varepsilon^3). \quad (3.58)$$

The [1/1] Padé approximant of Eq. (3.58) gives $x_0 = 3.6$ in three dimensions, while direct substitution gives $x_0 = 3.375$. We found in Sec. 2.4.2 the numerical estimate $x_0 = 3.4 \pm 0.2$, which agrees with the theoretical prediction. Unfortunately, the large uncertainties prevent any conclusive remark on whether the multifractal exponents behave well under the ε expansion, like the dynamical exponent, or are not Borel summable, like the correlation length exponent.

- For long-range correlated disorder ($0 < \delta < \delta^*$),

$$x_0 = 2 + \varepsilon + \frac{3}{16}\delta(\varepsilon + \delta) + O(\varepsilon^3). \quad (3.59)$$

In this case x_0 is smaller and the DoS distribution thinner. To the best of my knowledge, the effect of long-range correlations on the typical DoS have not been probed in numerical simulations. Hopefully, future research may provide a point of comparison to test the validity of Eq. (3.59).

3.3.2 Comparison with other transitions

Non-Anderson transition in gapless semiconductors — We can compare multifractality at the semimetal-metal in presence of uncorrelated disorder to that in other non-Anderson transitions, which occur in all gapless semiconductors with algebraic dispersion relation $E \propto k^\alpha$ where $d > 2\alpha$. Due to the inversion symmetry, the ladder diagrams add up instead of cancelling out, so that multifractality appears at one-loop order in this

case, instead of two-loop order. Expanding in dimension $d = 2\alpha + \varepsilon$, the multifractal exponents read (SYZANOV 2016)

$$\Delta_q = -\frac{\varepsilon}{2}q(q-1). \quad (3.60)$$

The probability distribution of the local DoS is thus broader in inversion-symmetric systems that undergo a non-Anderson transition when compared to the semimetal-metal transition. To first order in $\varepsilon = d - 2\alpha$, the exponents read $\nu^{-1} = \varepsilon$ and $z = \alpha + \frac{\varepsilon}{4}$. The peak of the singularity spectrum is located at

$$x_0 = 2\alpha + \frac{3}{2}\varepsilon + O(\varepsilon^2). \quad (3.61)$$

The average and typical DoS decay algebraically near the critical disorder strength with the exponents $\beta = \nu(d - z)$ and $\beta_t = \nu(x_0 - z)$ respectively, whose one-loop values are

$$\beta = \frac{3}{4} + \frac{\alpha}{\varepsilon}, \quad \beta_t = \frac{5}{4} + \frac{\alpha}{\varepsilon}. \quad (3.62)$$

In the conventional case of a quadratic dispersion ($\alpha = 2$), criticality is observed only in higher dimension, e.g. in $d = 5$, which kicked quantum rotors can emulate (MOORE 1994). In this situation, $\varepsilon = 1$, and the critical exponents read $\nu = 1$, $z = 2.25$, $\beta = 2.75$ and $\beta_t = 3.25$.

We can also carry out similar computations in presence of long-range correlations, using again an $\delta = a - 2$ expansion. The renormalisation constant is $Z_q = 1 + 2q^2(\frac{\gamma_S}{\varepsilon} + \frac{\gamma_L}{\delta})$, from which we find $\eta_q = 2q^2(\gamma_S + \gamma_L)$. Plugging in the coordinates of the long-range fixed point, we get without surprise the same expression as Eq. (3.60) with δ substituting ε ,

$$\Delta_q = -\frac{\delta}{2}q(q-1). \quad (3.63)$$

The critical exponents ν , z , β and β_t follow immediately.

Anderson's localisation — The anomalous multifractal exponents were determined at four-loop order in the orthogonal and unitary classes (WEGNER 1987). In $d = 2 + \varepsilon$ dimension, they read

$$\Delta_q^{(O)} = q(1-q)\varepsilon + \frac{\zeta(3)}{4}q(q-1)(q^2-q+1)\varepsilon^4 + O(\varepsilon^5) \quad (3.64)$$

for the orthogonal class, and

$$\Delta_q^{(U)} = q(1-q)\sqrt{\frac{\varepsilon}{2}} - \frac{3\zeta(3)}{8}q^2(q-1)^2\varepsilon^2 + O(\varepsilon^{5/2}) \quad (3.65)$$

for the unitary class. In particular the orthogonal class in $d = 3$ has $x_0 = 4$ at leading order, in excellent agreement with the numerical result $\alpha_0 = 4.03 \pm 0.05$ (MILDENBERGER 2002). In conclusion, multifractality is 'stronger' at Anderson's localisation than at the semimetal-metal transition, to the extent that the distribution of the local DoS is broader. In semimetals, this distribution is itself broader when driven by uncorrelated disorder, than by long-range correlated disorder. The exact origin of this hierarchy remains unclear; yet it seems reasonable that the wave function density is more broadly distributed when particles localise, and the extension of the wave function is restricted dramatically, than when extended waves roughly keep the same shape while spreading over an energy region (the nodal level) which was unavailable in absence of random scatterers.

Conclusion

Summary — Among other techniques, the replica trick enables to cast the low-energy theory of disordered relativistic semimetals to a relativistic field theory with an effective interaction, whose strength is given by the variance of the random potential. When particles move in the background of a Gaussian, spatially uncorrelated random potential, the replicated theory follows from either the Gross-Neveu model for a scalar potential, or the Thirring model for a vectorial potential, in the limit of a vanishing number of fermions. We have presented the flow diagram when the random scalar potential comprises both short-range and long-range correlations, and estimated the conventional exponents at two-loop order for the two corresponding universality classes. Importantly, we have shown how to represent the moments of the density of states as a composite operator of the replicated theory, and have determined the multifractal spectrum for the two universality classes. In the former case, the exponents agree with those found in a supersymmetric approach at the same order, and leads to a scaling exponent of the typical density of states consistent with numerical estimates. We have also compared our results for the multifractal spectrum to similar non-Anderson transitions and to Anderson’s localisation.

Outlook — We know that at Anderson’s localisation the four-loop corrections to the multifractal exponents dominate at large moments, which puts into question the validity of the ε -expansion. The same issue is likely to occur at the semimetal-metal transition, since the Gross-Neveu model is not multiplicatively renormalisable in three dimensions. Two main alternative theories exist. One resorts to the functional renormalisation group; the other rests on the equivalence between the Gross-Neveu and the Gross-Neveu-Yukawa models. First, the functional renormalisation group includes fluctuations of the random potential beyond the Gaussian approximation (WIESE 2006). The fermions interact in the replicated theory via a generic potential W function of the total density (BALOG 2018). Instead of following the flow of a single coupling strength, this method keeps track of the whole functional dependence of W in the infrared limit. Second, the Gross-Neveu-Yukawa model proceeds from the Gross-Neveu model by decoupling the action using a Hubbard-Stratonovitch transformation with ancillary scalar field, and endow it with a kinetic term and a quartic potential (LOUVET 2016). A large N expansion in $d = 4 - \varepsilon$ dimensions enables to compute the correlation length exponent ν in the zero-replica limit.

Multifractality at the semimetal-metal transition still reserves many open questions. First, we know from Anderson’s localisation that the ensemble averaging plays a crucial role in the inverse participation ratios (EVERS 2000). The mean ratio \bar{p}_q , which we have considered so far, and the typical ratio $p_q^t = \exp(\overline{\log p_q})$, carry the same information for the most probable realisations of the wave function, but differ significantly in the region of strong multifractality, i.e. for large moments where the mean singularity spectrum terminates (when $f_\tau(0) < 0$) or freezes (when $f_\tau(0) = 0$). In this region, extremely sparse eigenfunctions with diverging peaks dominate the scaling of the average singularity spectrum in the thermodynamic limit. Second, the wave functions fluctuate more at the surface than in the bulk when crossing the localisation-delocalisation point (SUBRAMANIAM 2006). Surface effects thus dominate the large moments of the wave function’s distribution. These topics, which have been explored at Anderson’s localisation but not at the semimetal-metal transition, promise an exciting future research on multifractality.

Surface criticality in disordered semimetals

Disordered relativistic semimetals undergo a quantum phase transition towards a metallic phase, which we covered in the previous chapters. The signatures of this semimetal-metal transition (behaviour of the density of state and other mean observables, critical exponents) reflect the properties of the bulk excitations. Yet, relativistic semimetals harbour peculiar surface states on their boundary, whose dispersion relation differs entirely from their bulk counterpart. The effect of disorder on these surface states (Fermi rays, arcs and Dirac surface states) has started to attract attention, and motivated a few analytical (SHTANKO 2018) and numerical (SLAGER 2017; WILSON 2018) studies.

In this chapter we study the effect of weak disorder on the surface states produced by generic boundary conditions in a minimal model for Weyl and Dirac semimetals. We develop a local version of the self-consistent Born approximation (KLIER 2019) to compute the density of states profile and the surface group velocity as a function of disorder strength. While the self-consistent Born approximation is poorly controlled close to the transition and fails to produce the correct critical exponents, it still captures the qualitative behaviour of the system (SINNER 2017). In particular, we investigate the phase diagram of Dirac semimetals in presence of a surface, and show that it bears similarities with that of semi-infinite magnetic systems, which exhibit ordinary, surface and extraordinary phase transitions (LUBENSKY 1975a; LUBENSKY 1975b). The boundary of a semimetal that hosts Dirac surface states turns into a metallic state at a critical disorder strength lower than that in the bulk. Upon further increasing disorder, the bulk becomes metallic in presence of the metallic surface, thereby experiencing an extraordinary transition. In Weyl semimetals, the extension of Fermi arcs in momentum space smooths out the surface criticality observed in Dirac surface states.

4.1	Surface states in clean semimetals	110
4.1.1	Boundary conditions	110
4.1.2	Surface states	114
4.2	Spatially resolved properties with disorder	119
4.2.1	Qualitative effect of disorder	119
4.2.2	Self-consistent approach	121
4.2.3	Profile of the local density of states	123

4.2.4 Beyond the local self-consistent approximation	125
4.3 Surface states of disordered semimetals	127
4.3.1 Criticality of Dirac surface states	127
4.3.2 Robustness of Fermi arcs	129
Conclusion	131

4.1 Surface states in clean semimetals

The presence of a boundary leads to new states in Weyl and Dirac semimetals that were absent in the infinite material. These surface states can be classified according to whether the reflection of incoming particles on the boundary preserves chirality. Taking account of the distinction between Weyl and Dirac semimetals, this classification results in three types of surface states: the celebrated Fermi arcs, along with Dirac surface states, when chirality is broken; and the Fermi rays, when chirality is preserved. In this section we discuss the properties of these surface states in clean relativistic semimetals, and show how they arise from the boundary condition. Some of the following results are original (BRILLAUX 2021b).

4.1.1 Boundary conditions

Bulk Hamiltonian — Surface states in Weyl and Dirac semimetals originate from the topological nature of Weyl nodes. The Nielsen-Ninomiya theorem constrains relativistic semimetals to host pairs of nodes with opposite Berry charges (NIELSEN 1981). A minimal low-energy theory for the surface of semimetals thus comprises two Weyl nodes of opposite chiralities. Let $2\mathbf{b}$ be their separation in momentum space. The electron dynamics follows from the binodal Weyl Hamiltonian (ALTLAND 2016; FARAEEI 2018)

$$\mathcal{H}_0 = -i\tau_z\boldsymbol{\sigma} \cdot \boldsymbol{\partial} + \tau_0\boldsymbol{\sigma} \cdot \mathbf{b}. \quad (4.1)$$

We defined two sets of Pauli matrices. The set $\boldsymbol{\sigma} = (\sigma_x, \sigma_y, \sigma_z)$ represents the pseudospin. The other set (τ_x, τ_y, τ_z) represents instead the valley – or chiral in this case – degree of freedom. We denote by σ_0 and τ_0 the corresponding identity matrices. The Hamiltonian of Eq. (4.1) describes two Weyl nodes related by time reversal; it could typically represent a magnetic Weyl semimetal.

The chief advantage of the Hamiltonian (4.1) is that we can formally tune \mathbf{b} to describe either a pair of Weyl cones (for \mathbf{b} arbitrary) or a single Dirac cone (for $\mathbf{b} = \mathbf{0}$). Note that the two Weyl cones could originate from the crossing of the *same* energy bands at distinct points of the Brillouin zone. Merging the nodes opens a gap in this case, which does not correspond to what happens when setting $\mathbf{b} = \mathbf{0}$ in Eq. (4.1). A Dirac node forms only when spatial symmetries prevent the nodes from hybridising. In addition, the minimal model of Eq. (4.1) cannot reproduce double Fermi arcs connecting a pair of Dirac nodes (twice more bands would be required to do so). We will consider only single Fermi arcs.

Boundary condition — Since large wave length fluctuations governs the approach to criticality, large-scale properties of a finite sample can play an essential role in phase

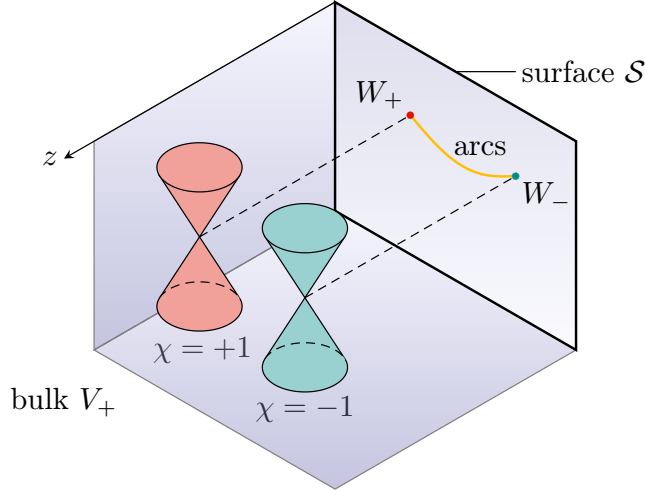


Figure 4.1 | A minimal model for a semi-infinite Weyl semimetal comprises two Weyl cones (in red and blue) in the bulk $V_+ : \{z > 0\}$. The surface $\mathcal{S} : \{z = 0\}$ faces the vacuum, which particles are forbidden to explore. Boundary scattering then gives rise to evanescent waves localised at the surface. These topological excitations disperse at the Fermi level along a line which connects to the bulk Weyl nodes W_{\pm} of chiralities $\chi = \pm 1$ at both ends. When boundary scattering breaks chirality, and that the Weyl nodes do not overlap when projected to the surface Brillouin zone, the surface hosts Fermi arcs (shown here).

transitions (CARDY 1996). The related phenomena – rounding of the transition, influence of geometry, surface criticality – are collectively known as finite-size effects. The local degrees of freedom couple to the critical fluctuations differently near a boundary than inside the bulk. To investigate the effect of a surface without introducing a new length scale (the system size L), we model the material as a d -dimensional semi-infinite system with a single planar $(d - 1)$ -dimensional boundary. Whenever the correlation length exceeds the typical size of the surface irregularities, the boundary can be viewed as smooth. Let us consider then a semi-infinite Weyl or Dirac semimetal filling the half-space $V_+ : \{z \geq 0\}$ (Fig. 4.1). The vector $\mathbf{b} = \mathbf{b}_{\parallel} + b_z \mathbf{e}_z$ splits into components respectively parallel and normal to the surface $\mathcal{S} : \{z = 0\}$. The Weyl nodes project to the momenta $\pm \mathbf{b}_{\parallel}$ on the surface Brillouin zone; as far as surface properties are concerned, only this parallel separation matters. If the material were cleaved in the direction normal to \mathbf{b} , the projected nodes would indeed overlap and be indistinguishable from a single Dirac cone.

We must now supplement the bulk Hamiltonian (4.1) with proper boundary conditions. Let $\Psi_S = \Psi(z = 0)$ be the surface Dirac spinor. A generic relativistic boundary condition involves a dimensionless unitary matrix M such that

$$M\Psi_S = \Psi_S. \quad (4.2)$$

Though M could depend on momentum, we will regard it as constant in the low-energy limit. This boundary condition is of Dirichlet-type, in contrast to bosonic theories, where the field's first derivative appears (LUBENSKY 1975a; LUBENSKY 1975b). Not any boundary matrix is suitable, of course. Because the sample faces vacuum, no particles exit the boundary, and the boundary condition must ensure that the cross current $J_z = \Psi^\dagger \gamma_0 \gamma_z \Psi$ vanishes at the surface (where $\gamma_0 \gamma_z = \sigma_z \tau_z$ in the chosen representation). Besides, Eq. (4.2) amounts to add a surface term $\mathcal{H}_S = i\gamma_0 \gamma_z M \delta(z)$ to the Hamiltonian. The full Hamiltonian

$\mathcal{H} = \mathcal{H}_0 + \mathcal{H}_S$ should be hermitician: for all Dirac spinors Ψ , we have (WITTEN 2016)

$$\langle \Psi | \mathcal{H} \Psi \rangle = \langle \mathcal{H} \Psi | \Psi \rangle. \quad (4.3)$$

Writing the scalar products in terms of spatial integrals, we find

$$\int_0^\infty dz \Psi^\dagger (-i\gamma_0\gamma_z) \partial_z \Psi + \Psi_S^\dagger (i\gamma_0\gamma_z M) \Psi_S = \int_0^\infty dz \partial_z \Psi^\dagger (i\gamma_0\gamma_z) \Psi + \Psi_S^\dagger (-iM^\dagger \gamma_0\gamma_z) \Psi_S. \quad (4.4)$$

An integration by parts then leads to

$$\left[\Psi^\dagger \gamma_0 \gamma_z \Psi \right]_0^\infty = \Psi_S^\dagger (\gamma_0 \gamma_z M + M^\dagger \gamma_0 \gamma_z) \Psi_S. \quad (4.5)$$

The conservation of J_z enforces the left-hand side of Eq. (4.5) to vanish. Let us assume further that M itself is hermitian. Eq. (4.5) then entails that the boundary matrix anticommutes with the cross current operator (HASHIMOTO 2017; FARAEI 2018)

$$\{M, \gamma_0 \gamma_z\} = 0, \quad M^2 = M^\dagger M = \mathbb{1}. \quad (4.6)$$

The two conditions of Eq. (4.6) ensure that the cross current vanishes at the surface, as required.

The boundary matrix — We will give the most general solution of Eq. (4.6) at the end of this paragraph for the four-times-four matrix M . Two classes of suitable matrices naturally come to mind: one that decouples left- and right-handed Weyl fermions, thus preserving chirality, the other that couples them, and applies only to Dirac fermions (FARAEI 2018).

Let us consider the first class, denoted generically as M_1 . In each chiral sector, M_1 anticommutes with the pseudospin σ_z , which is only possible for σ_x or σ_y . A superposition of these two matrices is of the form $\boldsymbol{\sigma} \cdot \mathbf{e}$ where $\mathbf{e} \in \mathcal{S}$ is a unitary vector of the surface. Combining the two sectors together in a block diagonal form, we get

$$M_1 = \sum_{\chi=\pm} \hat{\tau}_\chi (\boldsymbol{\sigma} \cdot \mathbf{e}_\chi) = \begin{pmatrix} 0 & e^{-i\theta_+} & 0 & 0 \\ e^{i\theta_+} & 0 & 0 & 0 \\ 0 & 0 & 0 & e^{-i\theta_-} \\ 0 & 0 & e^{i\theta_-} & 0 \end{pmatrix} \quad (4.7)$$

where $\chi = \pm$ is the chiral index, $\mathbf{e}_\pm = (\cos \theta_\pm, \sin \theta_\pm)$ are two unitary surface vectors, and $\hat{\tau}_\pm = \frac{1}{2}(\tau_0 \pm \tau_z)$ are the chiral projectors. The two angles θ_\pm are independent and arbitrary. We will see in Sec. 4.1.2 that the constant-energy contours at the surface take the form of (Fermi) rays, and that the angles θ_\pm select the orientation of the rays. A basis-independent expression is $M_1 = -\gamma_0 \boldsymbol{\gamma} \cdot \mathbf{m}$ with the surface (matrix) vector

$$\mathbf{m} = (\gamma_5 \cos \varphi_+ \cos \varphi_- + \sin \varphi_+ \sin \varphi_-, \gamma_5 \sin \varphi_+ \cos \varphi_- - \cos \varphi_+ \cos \varphi_-), \quad (4.8)$$

where $\varphi_\pm = \frac{1}{2}(\theta_+ \pm \theta_-)$. This boundary condition clearly breaks the rotational symmetry in the (x, y) plane; it even breaks all discrete space groups of the crystal, except for special values of the angles (WITTEN 2016). It also mixes neighbouring Landau levels in a background magnetic field, making Landau quantisation ill-defined (FARAEI 2018).

We now consider the second class, denoted generically as M_2 . A plain example is γ_z . In general, such chirality-breaking boundary matrix is of the form

$$M_2 = \sum_{\chi=\pm} (\boldsymbol{\tau} \cdot \mathbf{e}_\chi) \hat{\sigma}_\chi = \begin{pmatrix} 0 & 0 & e^{-i\theta_+} & 0 \\ 0 & 0 & 0 & e^{-i\theta_-} \\ e^{i\theta_+} & 0 & 0 & 0 \\ 0 & e^{i\theta_-} & 0 & 0 \end{pmatrix} \quad (4.9)$$

where here again $\mathbf{e}_\pm = (\cos \theta_\pm, \sin \theta_\pm)$, and $\hat{\sigma}_\pm = \frac{1}{2}(\sigma_0 \pm \sigma_z)$ are the pseudospin projectors. An alternate expression is $M_2 = \gamma_0(\cos \varphi_+ \cos \varphi_- + i\gamma_5 \sin \varphi_+ \sin \varphi_-) + \gamma_z(\sin \varphi_+ \cos \varphi_- - i\gamma_5 \cos \varphi_+ \cos \varphi_-)$, where $\varphi_\pm = \frac{1}{2}(\theta_+ \pm \theta_-)$. Unlike for M_1 , the relative position of the Weyl nodes constrains the angles θ_\pm in the M_2 boundary condition. This further requirement stems from the arc-shaped line which connects the nodes at the Fermi level, known as a Fermi arc, as we will see in Sec. 4.1.2. In particular, the parameter

$$\theta = \frac{1}{2}(\theta_+ - \theta_- + \pi) \quad (4.10)$$

dictates the curvature of the Fermi arc. This boundary condition conserves most of the spatial symmetries of the bulk Hamiltonian. When the nodes project to the same point on the surface, the original $O(2)$ symmetry is preserved. When the two projected nodes are separated, the original mirror symmetries $M_x : x \mapsto -x$ and $M_y : y \mapsto -y$ are both preserved for a straight arc ($\theta = 0$); otherwise, M_y is also broken. Tab. 4.1 recaps which symmetries are preserved or broken for each boundary condition.

The linear superposition of two matrices of the form (4.7) and (4.9) automatically anticommutes with $\gamma_0\gamma_z$, but the coefficients should be tuned to preserve the unitary. One can also check that such linear superpositions span all possible solutions. We find the most general boundary matrix to be

$$M(\varphi, \theta_{1\pm}, \theta_{2\pm}) = M_1(\theta_{1\pm}) \cos \varphi + M_2(\theta_{2\pm}) \sin \varphi, \quad (4.11)$$

with the extra condition that $(\theta_{1+} - \theta_{1-}) - (\theta_{2+} - \theta_{2-}) = \pi$ (BRILLAUX 2021b). For a non-zero mixing angle φ , this boundary condition breaks all symmetries, spatial and chiral.

Parallel separation	Bulk	Surface M_1	Surface M_2	
$\mathbf{b}_\parallel = \mathbf{0}$	$O(2) \times U(1)$	$\{\mathbb{1}\} \times U(1)$	$O(2)$	$O(2)$
$\mathbf{b}_\parallel \propto \mathbf{e}_x$	$D_2 \times U(1)$	$\{\mathbb{1}\} \times U(1)$	D_2	$\{\mathbb{1}, M_x\}$
			$\theta = 0$	$\theta \neq 0$

Table 4.1 | When the projected nodes overlap ($\mathbf{b}_\parallel = 0$), any parallel plane deep in the bulk enjoys an $O(2)$ symmetry. Otherwise, the symmetry group is restricted to $D_2 = \{\mathbb{1}, M_x, M_y, M_x M_y\}$, where M_x and M_y denotes the mirror symmetries which respectively exchange the nodes and leave them in place. The elements of the group act by matrix multiplication on the Dirac spinor. In the corresponding linear representation Υ , a rotation $R_\phi \in SO(2)$ is represented by $\Upsilon(R_\phi) = \exp(-\frac{i}{2}\phi\tau_0\sigma_z)$. The boundary condition M_2 breaks the $U(1)$ chiral symmetry but preserves most of the bulk spatial symmetries, according to the Fermi arc's curvature θ , in total opposition with M_1 .

For simplicity, we will disregard this type of boundary condition, and focus on M_1 and M_2 separately. We now move on to determine the surface states from the Green's function.

4.1.2 Surface states

Green's function of the clean system — The Green's function G_0 of a clean semi-infinite system can be Fourier-transformed in the two directions (x, y) parallel to the surface, but not in the normal direction z due to the absence of translational invariance (FARAEI 2018). We can thus express G_0 in a mixed momentum-real space, as a function of the parallel momentum $\mathbf{k} = (k_x, k_y)$, and two distances z and z' to the boundary. To simplify the notation we will omit the dependence on \mathbf{k} . The Green's function satisfies the equation

$$(\mathcal{H}_0 - E)G_0(E, z, z') = \delta(z - z'), \quad (4.12)$$

where the bulk Hamiltonian $\mathcal{H}_0 = \tau_z \boldsymbol{\sigma} \cdot \mathbf{k} - i\tau_z \sigma_z \partial_z + \boldsymbol{\sigma} \cdot \mathbf{b}$ is expressed in the mixed position-momentum space, and identity matrices are omitted. As per Eq. (4.2), the Green's function also fulfils the boundary condition

$$MG_0(E, 0, z') = G_0(E, 0, z'). \quad (4.13)$$

A general solution to the linear differential equation (4.12) is written as a sum of two terms: a particular solution for the infinite system, which by virtue of translational invariance depends only on $|z - z'|$; a solution of the homogeneous equation, which depends on z and z' separately. The particular solution is easily found by a Fourier transform of the bulk Green's function. For instance, for $\mathbf{b} = \mathbf{0}$, we find

$$G_b(E, z - z') = [\tau_z \boldsymbol{\sigma} \cdot \mathbf{k} + E + i\kappa \operatorname{sgn}(z - z')] \frac{e^{-\kappa|z-z'|}}{2\kappa}, \quad (4.14)$$

where $\kappa = \sqrt{k^2 - E^2}$, and $\operatorname{sgn}(x)$ is the sign function. Particles that propagate in the bulk satisfy $\kappa = 0$. On the contrary, surface states are off-shell excitations, whose amplitude decays exponentially in the bulk over a distance of the order of the penetration length $\xi = \kappa^{-1}$. Thanks to the method of images, we know that the solution of the homogeneous equation must be a function of $|z + z'|$, but its matrix structure is far from trivial (FARAEI 2018). Combining the bulk part (particular solution) and excess part (solution of the homogeneous equation), which enable the full Green's function to satisfy Eq. (4.13), we write

$$G_0(E, z, z') = G_b(E, z - z') + G_e(E, z + z'). \quad (4.15)$$

The off-diagonal components of the bulk part in the pseudospin sector are

$$(G_b)_{\chi\chi'}^{\bar{\sigma}\sigma}(E, z - z') = \frac{\chi k_x^{\chi} + i\sigma k_y^{\chi}}{2 \kappa_{\chi} + i\chi b_z} \delta_{\chi\chi'} e^{-(\kappa_{\chi} + i\chi b_z)|z-z'|}. \quad (4.16)$$

where $\sigma = \pm 1$ is the pseudospin index, $\bar{\sigma} = -\sigma$, and $\{\chi, \chi'\}$ are two independent chiral indices. The vector $\mathbf{k}^{\chi} = \mathbf{k} - \chi \mathbf{b}_{\parallel}$ represents the momentum measured from the surface-projected node of chirality χ . As for the case of zero separation, the decay rates are given by $\kappa_{\chi}^2 = (\mathbf{k}^{\chi})^2 - E^2$. The excess part, on the other hand, reads

$$(G_e)_{\chi\chi'}^{\bar{\sigma}\sigma}(E, z + z') = -\frac{\chi k_x^{\chi} + i\sigma k_y^{\chi}}{2 \kappa_{\chi} + i\chi b_z} (A_0)_{\chi\chi'}^{\bar{\sigma}\sigma}(E) e^{-(\kappa_{\chi} + i\chi b_z)|z+z'|}, \quad (4.17)$$

The coefficient $A_0(E)$ represents the reflectivity of the boundary, and always differs from unity for off-shell excitations. It depends on the boundary condition. For M_1 , the off-diagonal chiral components vanish, as for the bulk part,

$$(A_0)_{\chi\chi'}^{\bar{\sigma}\sigma}(E) = \frac{E - i\chi\sigma\kappa_\chi + 2\sigma b_z - \chi e^{-i\sigma\theta_\chi}(k_x^\chi + i\sigma k_y^\chi)}{E + i\chi\sigma\kappa_\chi - \chi e^{-i\sigma\theta_\chi}(k_x^\chi + i\sigma k_y^\chi)} \delta_{\chi\chi'}. \quad (4.18)$$

The M_2 boundary condition, on the other hand, couples the chiral indices, and $A_0(E)$ takes a more involved form,

$$(A_0)_{\chi\chi'}^{\bar{\sigma}\sigma}(E) = 1 - \frac{2i\chi\sigma\kappa_\chi e^{i\chi\theta_\sigma}}{D_{\chi\chi'}^{\bar{\sigma}\sigma}(E)} (k_x^{\bar{\chi}} + i\sigma k_y^{\bar{\chi}}), \quad (4.19)$$

where the denominator reads

$$D_{\chi\chi'}^{\bar{\sigma}\sigma}(E) = e^{i\chi\theta_\sigma} (E + i\chi\sigma\kappa_\chi)(k_x^{\bar{\chi}} + i\sigma k_y^{\bar{\chi}}) + e^{i\chi\theta_\sigma} (E + i\bar{\chi}\sigma\kappa_{\bar{\chi}})(k_x^\chi + i\sigma k_y^\chi). \quad (4.20)$$

The components which are diagonal in pseudospin follow from the relation

$$(G_0)_{\chi\chi'}^{\sigma\sigma}(E, z, z') = \chi \frac{E - i\chi\sigma\partial_z + \sigma b_z}{k_x^\chi + i\sigma k_y^\chi} (G_0)_{\chi\chi'}^{\bar{\sigma}\sigma}(E, z, z'). \quad (4.21)$$

The dispersion relation of the bulk states $E(\mathbf{k})$ corresponds to the pole of the bulk part of the Green's function G_b . Likewise, the surface dispersion relation $E_s(\mathbf{k})$ corresponds to the pole of the excess part G_e . In other words, the denominator of $A_0(E_s)$ vanishes. Following (FARAEI 2018), we determine below the surface dispersion relation for both boundary conditions (BRILLAUX 2021b).

Chirality-preserving boundary condition — For M_1 , the coefficient $A_0(E)$ is given by Eq. (4.18). Unsurprisingly, we find two independent dispersion relations in this case, one for each node,

$$E_s^X = \chi k_\chi \cos(\phi_\chi - \theta_\chi), \quad \kappa_\chi = k_\chi \sin(\phi_\chi - \theta_\chi), \quad (4.22)$$

where k_χ and ϕ_χ are respectively the norm and the angle of the \mathbf{k}^χ in the basis $(\mathbf{e}_x, \mathbf{e}_y)$ chosen to define the angles θ_\pm . The requirement that κ_χ be positive, which ensures that surface wave functions are normalisable, selects the half-plane $\phi_\chi - \theta_\chi \in [0, \pi]$. Since the pseudospin index does not enter the dispersion relation, each surface energy band is two-fold degenerate, contrary to the bulk Weyl cones where particles and holes have opposite pseudospins. At the nodal level, E_s^X vanishes, so that $\phi_\chi = \theta_\chi + \frac{\pi}{2}$. The zero-energy surface states disperse along two independent Fermi rays pointing in the directions orthogonal to \mathbf{e}_χ , and stemming from the nodes of chiralities $\chi = \pm 1$ respectively, as sketched in Fig. 4.2(a). Fermi rays are semi-infinite straight lines in the low-energy theory, but we expect their large-momentum behaviour to be modified at energy scales of the order of the ultraviolet cut-off.

Let us now find the eigenstates associated to this boundary condition. The eigenvalue equation reads $\mathcal{H}_0\Psi_1(\mathbf{r}, z) = E\Psi_1(\mathbf{r}, z)$, where the Dirac spinor satisfies $M_1\Psi_1(\mathbf{r}, 0) = \Psi_1(\mathbf{r}, 0)$ and \mathbf{r} marks the position the (x, y) pane. Since chirality is a good quantum

number, we write the Dirac spinor as a linear superposition of the two chiral eigenstates, and factor out the boundary plane wave,

$$\Psi_1(\mathbf{r}, z) = e^{-i\mathbf{r}\cdot\mathbf{k}} \sum_{\chi=\pm} c_\chi \Psi_\chi(z), \quad (4.23)$$

where c_\pm are two complex constants. The chiral eigenstates take the form of evanescent plane waves. Up to an arbitrary phase factor, they are

$$\Psi_+(z) = \sqrt{\varkappa_+} e^{-z\varkappa_+} \begin{pmatrix} 1 \\ e^{i\theta_+} \\ 0 \\ 0 \end{pmatrix}, \quad \Psi_-(z) = \sqrt{\varkappa_-} e^{-z\varkappa_-} \begin{pmatrix} 0 \\ 0 \\ 1 \\ e^{i\theta_-} \end{pmatrix}. \quad (4.24)$$

They are indeed normalisable provided that $\varkappa_\chi > 0$. Would \varkappa_χ be negative, the amplitude would increase exponentially in the inside of the material; these solutions are unphysical.

The M_1 boundary condition breaks the rotational symmetry. It forces the Fermi rays' orientations, which must be determined by microscopic details of the boundary, and thus should be very sensitive to surface roughness (WITTEN 2016). Yet, no analogous features have been observed in real materials. In the context of condensed matter, we expect these seemingly infinite Fermi rays to be low-energy truncations of Fermi arcs that terminate at another remote pair of Weyl nodes. This is all the more likely that at higher energies, the boundary matrix depends on momentum. The Fermi lines, with parametric equation $\phi_\chi(k) = \theta_\chi(k) + \frac{\pi}{2}$ in polar coordinates, would then deviate from straight rays. In the context of quantum field theory, however, the M_1 boundary condition has no reason to be unphysical and could describe the scattering of Weyl fermions on an infinite potential barrier.

Chirality-breaking boundary condition — For M_2 , the coefficient $A_0(E)$ is given by Eq. (4.19), and the denominator D by Eq. (4.20). The poles couple the parameters

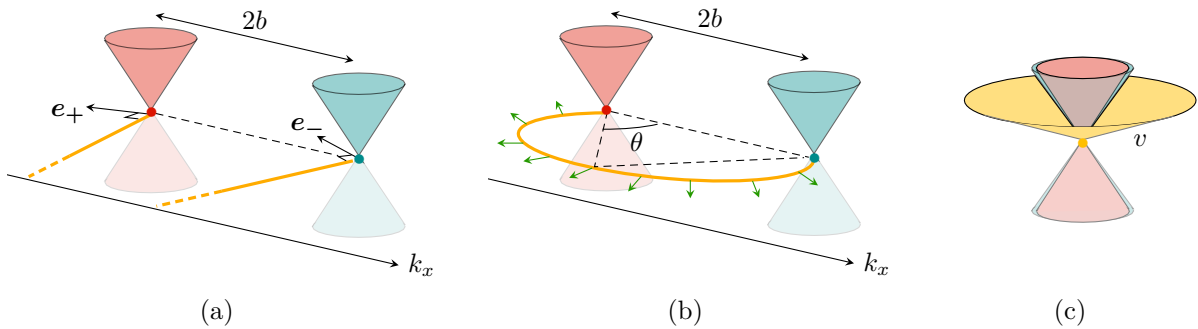


Figure 4.2 | (a) Chirality-preserving boundary conditions lead to one disconnected Fermi ray at each node (in orange), parametrised by a normal surface vector \mathbf{e}_\pm . (b) Pairs of Weyl nodes of opposite chiralities host Fermi arcs at the nodal level (in orange), parametrised by an aperture angle θ . The group velocity of the surface states (in green) is locally normal to the arc. (c) The same chirality-breaking boundary condition leads to Dirac surface states in Dirac nodes, which disperse along a single-nappe cone of positive energy on one surface (in orange) and negative energy on the other. The slope of the cone corresponds to a lessened Fermi velocity $v = \cos \theta$.

associated to the two Weyl nodes, e.g. the momenta k_+ and k_- . We expect, therefore, that a continuous band structure emerges from one node and terminates on the other. Solving $D_{\chi\chi'}^{\sigma\sigma'}(E_s) = 0$ for all possible values of the pseudospin and chiral indices, we find indeed a single dispersion relation,

$$E_s = k_\chi \cos \beta_\chi, \quad \varkappa_\chi = k_\chi \sin \beta_\chi, \quad (4.25)$$

where the angles β_χ are completely determined by the relation $\beta_+ + \beta_- = 2\theta + \phi_+ - \phi_-$, along with the tacit condition $k_+ \cos \beta_+ = k_- \cos \beta_-$ of Eq. (4.25) (BRILLAUX 2021b). Shifting the angle θ by π leads to the same surface properties: we will thus restrict its domain of definition to the interval $[0, \pi]$. As for Fermi rays, the pseudospin leads to a two-fold degeneracy of the energy levels. Unlike rays, though, the band structure depends on the parallel separation of the nodes. We must distinguish the cases for which this separation is non-zero, from those for which it vanishes.

Fermi arcs — We already introduced the angle θ in Eq. (4.10), which dictates the curvature of the Fermi arc. We expect that the parameters of the M_2 boundary condition in general, and θ in particular, depend on the microscopic details of the surface. Lattice models show that the chemical composition of the first boundary layer also determines which Weyl nodes pair up to form Fermi arcs (OKUGAWA 2014). Even away from the nodal level, surface termination affects the surface energy contours dramatically. On the other hand, the parameter $\vartheta = \frac{1}{2}(\theta_+ + \theta_- - \pi)$ fixes the direction of the arc, which is constrained by the position of the Weyl nodes. The half-separation $\mathbf{b}_\parallel = b \mathbf{n}$, with norm b , has for orientation vector $\mathbf{n} = (\cos \vartheta, \sin \vartheta)$. Assume for clarity that the nodes are aligned along the x axis. Then $\vartheta = 0$ and $\theta = \theta_+$ remains the only free variable. For non-zero b , the parametric equation (4.25) is hard to study analytically at arbitrary energy. But at the Fermi level, the polar coordinates satisfy

$$\phi_+ - \phi_- = \pi - 2\theta. \quad (4.26)$$

Eq. (4.26) describes a circular arc of diameter $d_A = b/\sin(2\theta)$ and centre $\mathbf{k}_A = -2b \cot(2\theta) \mathbf{e}_y$. The perimeter is $L_A = 4\theta d_A$. For $\theta = 0$, the arc reduces to a straight line that joins the nodes on either end. As θ goes up, the arc bends itself, until it becomes infinitely large at $\theta = \pi/2$. This angle thus quantifies the curvature of the Fermi arc; we will call it *aperture angle*. For $\theta < \pi/2$, the normalisability of the surface states restricts the arc to the half-plane $\phi_\pm \in [0, \pi]$. The other half-plane can be explored for $\theta > \pi/2$, but leads to the same physics, so that we will further restrict θ to the domain $[0, \pi/2]$. Fig. 4.2(b) depicts a schematic Fermi arc in a binodal Weyl semimetal.

A compelling way to picture the band structure is through the spectral density

$$A(\mathbf{k}, E, z) = \frac{1}{\pi} \text{Im}[\text{Tr} G_0(\mathbf{k}, E, z, z)], \quad (4.27)$$

which represents the momentum-resolved DoS. By varying the photon's momentum, ARPES experiments give access to the spectral density as a function of the parallel \mathbf{k} and normal k_z momentum components, from which the local, surface and bulk band structures can be reconstructed. In the mixed position-momentum space, the spectral density becomes a function of the parallel momentum \mathbf{k} in a two-dimensional Brillouin zone projected on a slab at distance z from the surface. Since the elementary excitations

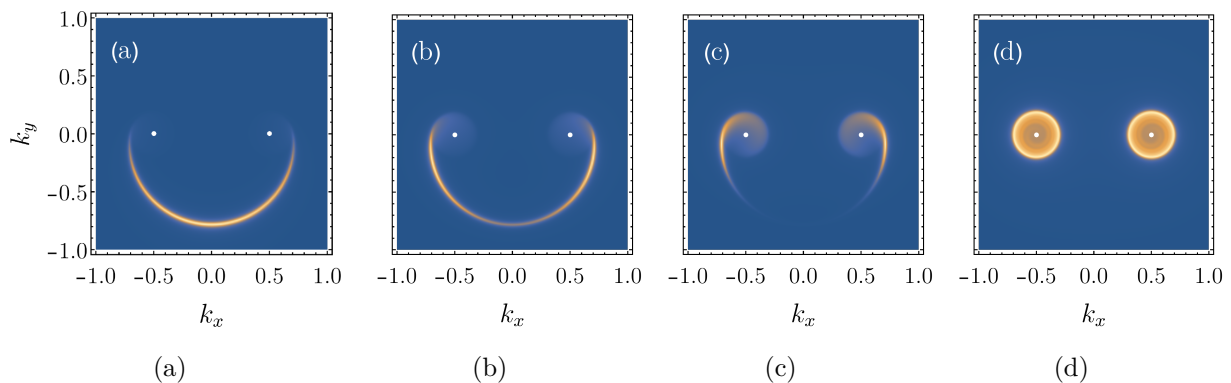


Figure 4.3 | Calculated spatially resolved spectral density map of a Fermi arc in a slightly doped Weyl semimetal. The two-dimensional reciprocal spaces (k_x, k_y) are projections of the three-dimensional Brillouin zone over slabs at fixed distance z from the surface. The energy $E = 0.2$, the momenta k , and the distance z are all measured in the same natural units, determined by a fixed cut-off. (a) $z = 0$, the surface supports a Fermi arc with aperture angle $\theta = \pi/4$. (b) $z = 2$, (c) $z = 5$, the surface states amplitude decays exponentially in the bulk, where the penetration length is smallest at the middle of the arc, and infinite at the tips in contact with the nodes. (d) $z = \infty$, the Fermi level cuts circular blobs through the bulk band structure, centred at the Weyl nodes.

are poles of the Green's function, the local band structure appears as a singularity of the spectral map. In real materials, the elementary excitations develop a finite lifetime τ in presence of arbitrarily weak disorder, which smooths out the singularities of the spectral density. In a first approximation, the spectrum acquires a Lorentzian broadening of width equal to the scattering rate $\Gamma = \tau^{-1}$. Even though impurities are evenly distributed in the bulk, surface states feel their presence because they extend in the bulk over some penetration length, which diverges at the contact with the Weyl points (GORBAR 2016).

We show spectral density maps in Fig. 4.3 in a binodal Weyl semimetal with Fermi arcs positively doped. The surface states are confined exponentially at the surface, some more loosely than others: the further apart the momentum is from the Weyl nodes, the quicker the arc dissolves in the bulk. This leads to high-density spectral features that touch the Weyl cones in a spiralling fashion. In experiments, Fermi arcs are usually distorted because of higher-order corrections to the linear dispersion relation (XU 2015; LV 2015; INOUE 2016). They can join two Weyl nodes (our model) but also two Dirac nodes or surface-projected nodes with higher topological charges, in which case multiple arcs are attached to the pair.

Dirac surface states — When $b = 0$, the two valleys merge and Eq. (4.25) reduces to

$$E_s = k \cos \theta, \quad \varkappa = k \sin \theta. \quad (4.28)$$

Although the eigenstates associated to the band structure of Eq. (4.28) are not specific to Dirac semimetals but also emerge whenever two Weyl nodes are projected to the same point in the surface Brillouin zone, we will refer to them as *Dirac surface states*. These surface states spread out along a single-branched cone, which extends in either the electron or hole side depending on the orientation of the surface. In our case, this corresponds to the positive energies, as shown in Fig. 4.2(c). The slope of the cone gives corresponds to a

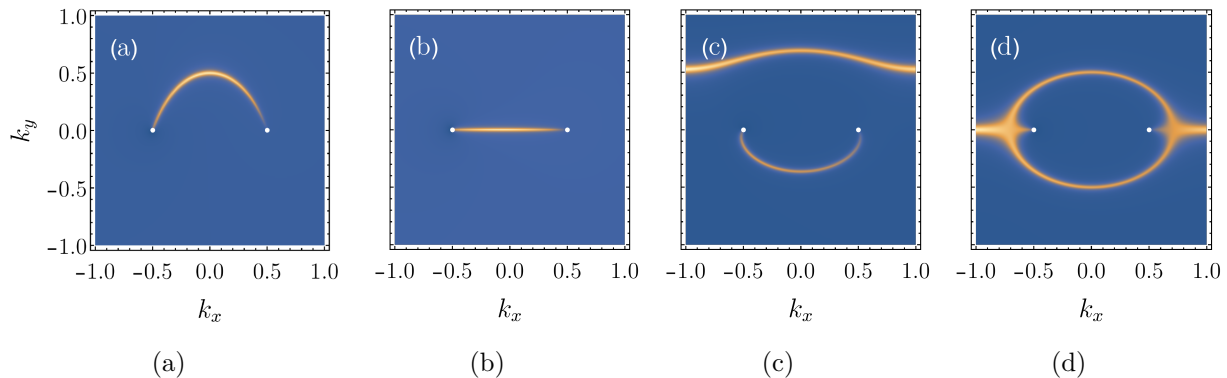


Figure 4.4 | Calculated surface spectral density map at the Fermi level for a mixing of the boundary conditions M_1 and M_2 with equal weight ($\varphi = \pi/4$) and preserving the mirror symmetry $x \mapsto -x$ ($\vartheta = 0$). The scattering rate is set to $\Gamma = 0.05\Lambda$. The parameter θ takes the values (a) $\theta = 0$, (b) $\theta = \pi/4$, (c) $\theta = 9\pi/20$, and (d) $\theta = \pi/2$. A curved Fermi arc still extends between the pair of the Weyl nodes, while the Fermi rays deform themselves into a trivial Fermi line with infinite extension in momentum space.

diminished Fermi velocity $v = \cos\theta$. This electron-hole surface asymmetry persists in the presence of a magnetic field or a gap, where the dispersion relation also depends on the parameter ϑ (SHTANKO 2018). As opposed to Fermi rays and arcs, which give rise to a non-zero surface DoS at all energies, the density of the Dirac surface states vanishes at the nodal level, like for the bulk states.

General surface states — Mixing the boundary conditions M_1 and M_2 lead to complex surface states. The Fermi arcs keep their integrity, but deviate from a circular shape, as can be seen in Fig. 4.4. The three independent parameters θ_{1+} , θ_{1-} and ϑ enable to play not only on the curvature of the arc, but also its distortion towards one node or the other, thus breaking the $M_x : x \mapsto -x$ mirror symmetry. Besides, the material hosts trivial surface states with infinite extension in momentum space, reminiscent of the Fermi rays.

4.2 Spatially resolved properties with disorder

The boundary breaks translational symmetry in the normal direction: physical observables are no longer homogeneous but depend on the distance z to the boundary. This remains true in presence of disorder. For this reason, the determination of disorder-averaged observables poses a greater challenge than in the infinite system. In this section we analytically probe the mean local DoS for the two classes of boundary conditions M_1 and M_2 . The SCBA seems a natural option for a first approach (KLIER 2019). The self-consistent equation is solvable, provided we resort to a further *local* approximation to get a closed equation for the self-energy at a given z (BRILLAUX 2021b).

4.2.1 Qualitative effect of disorder

The stability of surface states under weak perturbations varies considerably according to the nature of the boundary condition, the degeneracy of the band crossing, and the spatial

distribution of disorder. In discussion below, and throughout this chapter, we restrict ourselves a scalar and uncorrelated random potential.

Bulk disorder — The surface of clean Dirac semimetals supports double Fermi arcs. Yet, experiments detect instead closed Fermi pockets in Cd_3As_2 , Na_3Bi , or PtBi_2 (WU 2019). Though perturbations cannot fully remove double Fermi arcs in presence of time-reversal symmetry, topology offers no protection either to the bulk Dirac nodes or to the surface states. Within a simple four-band model, small perturbations destroy Fermi arcs in Dirac semimetals, even when preserving all symmetries (KARGARIAN 2016; KARGARIAN 2018). When adding an extra mass term to the two-dimensional effective Hamiltonian, the tips of the arcs detach from the nodes and merge to form a single Fermi pocket. Strangely enough, transport experiments in Cd_3As_2 show Shubnikov-de Haas oscillations similar to those observed in Weyl semimetals, which arise from ‘Weyl orbits’, i.e. the intertwined cyclotron motion of chiral bulk and surface states, which seems inconsistent with ARPES measurements of the surface band structure (MOLL 2016). This discrepancy probably comes from doping. Dirac nodes in real materials are usually close to, but not exactly at the Fermi level; Fermi arcs may well be connected with the bulk band structure at the Fermi energy, and lead to Weyl orbits, and yet form a closed Fermi contour at the nodal energy.

By contrast, Fermi arcs in Weyl semimetals share the immunity of the bulk crossing point under a weak disorder, according to numerical simulations (SLAGER 2017). They do not survive a strong enough disorder, though. At the semimetal-metal critical point, they dissolve in the bulk, because the Weyl nodes no longer protect them due to the loss of the topological charge in the metallic phase. There, the surface Fermi surface broadens dramatically, the hitherto-localised states merge with non-perturbative bulk states due to rare realisations of disorder, and lose their support on the boundary. The presence of a near surface at the opposite side of the material boosts the hybridisation and dissolution of surface states (WILSON 2018). In Sec. 4.2.2, we compare these numerical findings with the results of an analytical self-consistent approach. Our study is not restricted to Fermi arcs, but also investigate the fate of Fermi rays and Dirac surface states.

Surface disorder — The previous observations apply for random scatterers that are evenly distributed in the bulk. Yet, disorder can also affect the surface alone. Surface defects consist chiefly of quenched vacancies, which are known to be plentiful in real samples. Unlike the surface states of topological insulators, Fermi arcs resist better surface disorder than bulk disorder, because evanescent waves leak through the bulk over a large distance (compared to the microscopic scale) and are thus likely to avoid surface scatterers. Though the conductivity is highly suppressed in both relativistic semimetals and topological insulators, they differ by one to two orders of magnitude, to the benefit of the semimetal (RESTA 2018). Other works have addressed the properties of Dirac surface states under surface disorder (SHTANKO 2018). Dirac surface states are largely insensitive to surface disorder, and propagate quasi-ballistically. The suppression of random scattering due to the small overlap of Dirac surface states with boundary impurities enhances the mean free path, which can be a hundred times larger than the carrier wave length. These also apply to two-dimensional Dirac materials, where ballistic edge transport extend to an anomalously long range.

Surface impurities require a treatment of their own; we will no longer address this type

of disorder in the following, and focus instead on the effect of bulk disorder. If defects are evenly distributed in the bulk, their mean number per unit of area vanishes in the limit of an infinitely thin boundary. This hypothesis ensures that the boundary condition remains the same in presence of disorder: the Green's function still satisfies Eq. (4.13).

4.2.2 Self-consistent approach

In the following sections, we assume the random potential scalar and uncorrelated, and aim at determining the disorder-averaged DoS.

Disorder-averaged Green's function — For brevity, let us simplify the notations and denote by G the disorder-averaged Green's function. In the mixed position-momentum representation, the self-energy Σ depends a priori on z and z' separately. Yet, in the SCBA, the bulk self-energy is independent of the transferred momentum. We thus search for self-consistent solutions for Σ that depend only on one distance z . In addition, we postulate that the self-energy $\Sigma(E, z, z') = \Sigma(E, z)\tau_0\sigma_0$ shares the same matrix structure as the potential, so that it is proportional to the identity. The defining equation of the self-energy then reads

$$[\mathcal{H}_0 - E - \Sigma(E, z)]G(E, z, z') = \delta(z - z'). \quad (4.29)$$

Performing the similar calculations that led to the free Green's function in Sec. 4.1.2, we arrive at the following form for the off-diagonal pseudospin components:

$$G_{\chi\chi'}^{\bar{\sigma}\sigma}(E, z, z') = \frac{\chi}{2} \frac{k_x^\chi + i\sigma k_y^\chi}{h'_{\chi\sigma}(z') + i\chi b_z} \left[\delta_{\chi\chi'} e^{-|h_{\chi\sigma}(z) - h_{\chi\sigma}(z')| - i\chi b_z |z - z'|} - A_{\chi\chi'}^{\bar{\sigma}\sigma}(E, z') e^{-[h_{\chi\sigma}(z) + h_{\chi\sigma}(z') + i\chi b_z(z + z')]} \right]. \quad (4.30)$$

The diagonal components are

$$G_{\chi\chi}^{\sigma\sigma}(E, z, z') = \chi \frac{E + \Sigma(E, z) - i\chi\sigma\partial_z + \sigma b_z}{k_x^\chi + i\sigma k_y^\chi} G_{\chi\chi}^{\bar{\sigma}\sigma}(E, z, z'). \quad (4.31)$$

The matrix function $A(E, z')$ now depends on z' besides the energy E . For the M_1 boundary condition, only the diagonal chiral components are non-zero,

$$\left[A_{\chi\chi'}^{\bar{\sigma}\sigma} \right]_1(E, z') = \frac{E + \Sigma_s(E) - i\chi\sigma h'_{\chi\sigma}(z') + 2\sigma b_z - \chi e^{-i\sigma\theta_\chi} (k_x^\chi + i\sigma k_y^\chi)}{E + \Sigma_s(E) + i\chi\sigma h'_{\chi\sigma}(z') - \chi e^{-i\sigma\theta_\chi} (k_x^\chi + i\sigma k_y^\chi)} \delta_{\chi\chi'}, \quad (4.32)$$

where $\Sigma_s(E) = \Sigma(E, 0)$ is the surface self-energy. For the M_2 boundary condition, the chiral components are coupled, and $A_{\chi\chi'}^{\bar{\sigma}\sigma}(z')$ takes a more complex form,

$$\left[A_{\chi\chi'}^{\bar{\sigma}\sigma} \right]_2(E, z') = 1 - \frac{2i\chi\sigma h'_{\chi\sigma}(z') e^{i\chi\theta_\sigma}}{D_{\chi\chi'}^{\bar{\sigma}\sigma}(E, z')} (k_x^{\bar{\chi}} + i\sigma k_y^{\bar{\chi}}), \quad (4.33)$$

where the denominator reads

$$D_{\chi\chi'}^{\bar{\sigma}\sigma}(E, z') = e^{i\chi\theta_\sigma} \left[E + \Sigma_s(E) + i\chi\sigma h'_{\chi\sigma}(z') \right] (k_x^{\bar{\chi}} + i\sigma k_y^{\bar{\chi}}) + e^{i\chi\theta_\sigma} \left[E + \Sigma_s(E) + i\bar{\chi}\sigma h'_{\bar{\chi}\sigma}(z') \right] (k_x^\chi + i\sigma k_y^\chi). \quad (4.34)$$

The four functions $h_{\chi\sigma}(z)$, indexed by chirality χ and pseudospin σ , implicitly depends on the energy, and satisfy the non-linear differential equation

$$(\mathbf{k}^\chi)^2 - (E + \Sigma)^2 - i\chi\sigma\Sigma' + h_{\chi\sigma}'' - (h_{\chi\sigma}')^2 = 0, \quad (4.35)$$

where the $'$ represents a derivative with respect to z . For a zero self-energy (in the clean system), we recover $h_{\chi\sigma}(z) = \varkappa_\chi z$. Eq. (4.35) still admits a simple solution for a constant self-energy, but is extremely hard to solve for a general function $\Sigma(z)$. We now turn to a simplified self-consistent approach to obtain analytical results, and propose later an algorithm to solve the ‘exact’ SCBA in Sec. 4.2.4.

The local self-consistent Born approximation — In the SCBA, the self-energy fulfils the condition

$$\Sigma(E, z) = \frac{\gamma}{4} \int_{k < \Lambda} \frac{d^2k}{(2\pi)^2} \text{Tr} G(E, z, z), \quad (4.36)$$

where the factor $4 = \text{Tr} \mathbb{1}$ compensates the trace, and Λ is an ultraviolet cut-off. Eq. (4.29) and Eq. (4.36) provides a closed set of equations from which the self-energy can be determined in principle. In particular, the latter equation relates the self-energy on the left-hand side to the Green’s function on the right-hand side, which depends itself implicitly on the whole function $z \mapsto \Sigma(E, z)$ via Eq. (4.35). The scheme we refer to as the local SCBA rests upon the following observation: assuming Σ constant only in the integrand of Eq. (4.36), the disorder-averaged Green’s function reduces to the free Green’s function, up to the substitution $E \mapsto E + \Sigma$, i.e. $G(E, z, z') = G_0(E + \Sigma(E, z), z, z')$. The self-consistency now concerns only the scalar $\Sigma(E, z)$ at fixed E and z , instead of a function,

$$\Sigma(E, z) = \frac{\gamma}{4} \int_{k < \Lambda} \frac{d^2k}{(2\pi)^2} \text{Tr} G_0(E + \Sigma(E, z), z, z). \quad (4.37)$$

Within this approximation, the self-consistent approach is amenable to a numerical resolution.

Solution for the minimum of the self-energy — Since the random potential averages to zero, the defects cannot dope the bulk Weyl nodes away from the Fermi energy $E = 0$. However, it is quite common in interface phenomena that the chemical potential varies close to a surface, as numerical studies have found in analogous Dirac materials (PAPAJ 2019). The local self-energy then acquires a real part at the bulk nodal level, which complicates the analysis. Two approaches are possible. Either the self-energy profile is determined at $E = 0$, but we then compare slices of the band structure with very different DoS (zero in the bulk, but large at the surface). Or the self-energy profile is determined at the local energy $\epsilon(z)$ such that

$$\epsilon(z) + \text{Re} \Sigma(\epsilon(z), z) = 0. \quad (4.38)$$

In the second option, $E + \text{Re} \Sigma(E, z) = i\Gamma(z)$ is purely imaginary, which means that disorder only broadens the spectral function, while preserving the shape of the band structure. This provides a less faithful picture of real three-dimensional materials, where chemical doping affects the Fermi level uniformly. Yet, this approach alone can reveal the critical nature of disordered Dirac surface states, which would otherwise be hidden by the

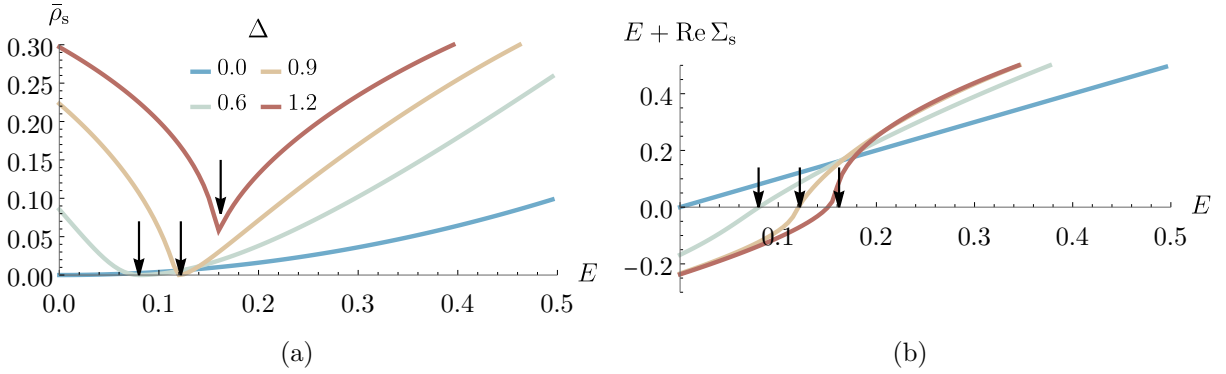


Figure 4.5 | Surface self-energy of Dirac surface states Σ_s against energy E , for subcritical (0.0, 0.6, 0.9) and supercritical (1.2) disorder strengths Δ . The bulk critical disorder strength is $\Delta^* = 1$. We set the angular parameter of the boundary matrix to $\theta = \pi/12$, which corresponds to a surface Fermi velocity $v_0 = \cos \theta \simeq 0.97$. (a) The minimum of the mean density of states $\bar{\rho} \propto \text{Im}\Sigma/\Delta$, marked by the three arrows, moves in the energy landscape as the disorder strength increases. (b) This minimum coincides with the vanishing of $E + \text{Re}\Sigma$ for subcritical disorder strength. The two energies remain close for reasonable supercritical disorder strength.

non-zero DoS which develops at zero energy at all disorder strengths. The vanishing of $E + \text{Re}\Sigma$ matches indeed the minimum of the scattering rate Γ as a function of energy E , at least for subcritical disorder (when Γ vanishes smoothly). The energy shift $\epsilon(z)$ remains close to but not exactly at this minimum for moderate supercritical disorder, as the Kramers-Krönig relations break down when the scattering rate becomes non-analytic, as shown in Fig. 4.5. At this energy the local SCBA takes the dimensionless form

$$\frac{s}{\Delta} = g(s, u) = s \left(\sqrt{1 + s^2} - s \right) + f(s, u) \quad (4.39)$$

where $s = \Gamma(z)\Lambda^{-1}$ and $u = \Lambda z$. The first part of the function $g(s, u)$ comes from the bulk part of the Green's function, see Eq. (C.3). The second part $f(s, u)$ is the excess contribution.

For the M_1 boundary condition, we find that the energy which cancels the real part of the self-energy vanishes, $\epsilon_1(z) = 0$. In Fermi rays the minimum of the local scattering rate in the energy landscape is located at the bulk nodal level. The excess contribution of Eq. (4.39) reads

$$f_1(s, u) = \frac{1}{4u^2} \left\{ e^{-2us} - e^{-2u\sqrt{1+s^2}} \left[1 + 2u \left(\sqrt{1+s^2} - s \right) \right] \right\}. \quad (4.40)$$

Unfortunately, the excess contribution for the M_2 boundary condition admits no simple expression. We resort to numerical integration to estimate the excess contribution f_2 in this case. The local energy shift $\epsilon_2(z)$ is non-zero, and can be found from the zeroes of the function $E \mapsto E + \Sigma(E, z)$, which is plotted in Fig. 4.5(b) in the case $z = 0$.

4.2.3 Profile of the local density of states

Using the relation between the DoS and the Green's function, we extract the minimum of the mean local DoS, which in natural units reads

$$\bar{\rho}(z) = \frac{4\pi}{\gamma\Lambda^2} \text{Im} \Sigma[\epsilon(z), z] = \frac{\Gamma(z)}{\Delta\Lambda}. \quad (4.41)$$

We now apply Eq. (4.41) to the case $b = 0$ for the two boundary conditions, which describes either a single Dirac node when b_z is also zero, or Weyl nodes whose projections overlap on the surface otherwise. We mention the effects of a non-zero b_z in the last paragraph, and focus now the case of a single Dirac node. The surface states are then either Fermi rays (M_1) or Dirac surface states (M_2).

Bulk properties and Fermi rays — Fig. 4.6(a) depicts the DoS profiles for various disorder strengths, while Fig. 4.6(b) shows the same profiles for Dirac surface states with $\theta = \pi/4$, for which the surface Fermi velocity is reduced to $v = 1/\sqrt{2}$. For both boundary conditions, we recover the bulk transition in the limit $z \rightarrow +\infty$, with the (bulk) critical disorder strength $\Delta_b^* = 1$. For larger Δ , the DoS scales as

$$\bar{\rho}_b = \frac{1}{2} (1 - \Delta^{-2}) \sim (\Delta - \Delta_b^*)^{\beta_b}, \quad (4.42)$$

where as anticipated $\beta_b = 1$ in mean field. Combined with the mean field value $\nu = 1$ for the correlation length exponent, and using the hyperscaling relation $\beta_b = \nu(d - z_b)$, we also recover the mean-field dynamical exponent $z_b = 2$. Below this critical disorder strength, the density vanishes, in agreement with the results established in Sec. 2.3 for infinite systems (Klier 2019). Exactly at the critical point, the DoS profile falls off algebraically as z^{-1} . These results confirm the validity of the local SCBA in the bulk, where the self-energy tends towards a constant.

Near the surface, the DoS behaves very differently depending on the boundary condition. For Fermi rays, disorder hardly affects the DoS close to the surface, which saturates to $\bar{\rho}_s = 1/2$. The existence of infinite Fermi rays is inconsistent with a low-energy theory, which is only defined below the ultraviolet momentum Λ . In agreement with the discussion of Sec. 4.2.1, the surface modes populating the Fermi rays propagate diffusively. The mean free path $l = 2/\Delta$ decreases as more random scatterers invade the material.

At intermediate distances from the surface, disorder always enhances the local DoS. In

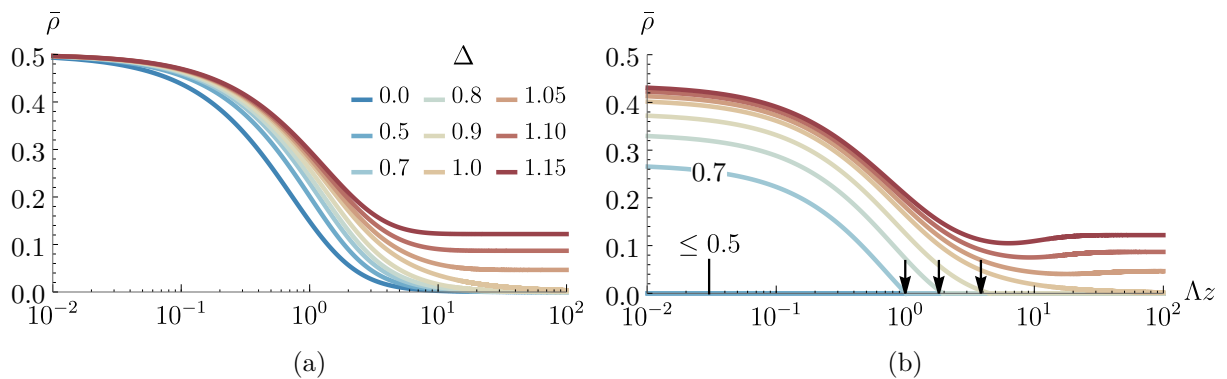


Figure 4.6 | Profile of the density of states $\bar{\rho}$ for various disorder strengths Δ , as a function of the dimensionless distance Λz to the surface. The bulk density of states emerges above the critical value $\Delta_b^* = 1$, and vanishes below. (a) For Fermi rays (M_1 boundary condition), the profile tends to a universal function in the clean limit. The surface density is pinned to $1/2$ due to the infinite extension of the rays. (b) For Dirac surface states (M_2 boundary condition, here with $\theta = \pi/4$), the profile vanishes identically below a critical strength $\Delta_s^* = \cos^2(\theta)$.

the clean limit, the DoS profile tends to a universal curve which decays asymptotically as z^{-2} . Above the bulk critical point, Fermi rays dissolve into the metallic bulk.

Dirac surface states — As seen in Fig. 4.6(b), the local density of Dirac surface states vanishes above a distance $\Lambda z = \xi$ from the boundary (the penetration length), such that

$$\frac{1 - e^{-2\xi}}{2\xi} = \frac{\Delta^{-1} - 1}{\tan^2(\theta)}. \quad (4.43)$$

we expect the exact vanishing of the DoS beyond the penetration length to be an artefact of the local SCBA. The local SCBA is indeed justified when the derivative of Γ is small compared to Γ^2 , which is satisfied close to the surface and deep in the bulk, but breaks down at intermediate distances. In all likelihood, the real density profile in the limits $\Lambda z = 0$ and for $\Lambda z \gg 1$ match smoothly between. Dirac surface states spread maximally at the bulk critical point where the penetration length diverges as $\xi \sim (\Delta_b^* - \Delta)^{-\nu}$ with $\nu = 1$. This power can be identified with the correlation length exponent, though the actual correlation length (the bulk mean free path), is well defined for supercritical, not subcritical, disorder. In addition, both ξ and $\bar{\rho}$ vanish identically at the critical disorder strength $\Delta_s^* = v^2$, where $v = \cos \theta$. The expression of Δ_s^* is consistent with dimensional analysis for a Dirac cone (whether with one or two nappes) of Fermi velocity v . The vanishing of the surface order parameter $\bar{\rho}_s$ indicates that a surface transition takes place at $\Delta_s^* \leq \Delta_b^*$. We will explore the properties of this transition in Sec. 4.3.

Effect of a longitudinal separation — When two distinct Weyl nodes are projected to the same point of the surface, they are separated in the three-dimensional Brillouin zone by a purely longitudinal momentum $\mathbf{b} = \Lambda b_z \mathbf{e}_z$. First, this separation induces quantum interferences between chiral eigenstates, which modulates the density profile with a period $u_0 = \pi/b_z$. Second, the introduction of an extra length scale modifies the bulk critical disorder strength, which moves to a higher value $\Delta_b^* = [1 - b_z \arctan(1/b_z)]^{-1}$. This shift has no consequence on the properties of disordered Dirac surface states.

4.2.4 Beyond the local self-consistent approximation

Throughout Sec. 4.2.2, we pointed out some deficiencies of the local SCBA. We now propose an algorithm to improve it. For concreteness, let us consider the equation for $b = 0$ for the M_1 boundary condition, where the self-energy is imaginary at zero energy. Eq. (4.35) reduces in this case to a pair of equations for two functions $h_\zeta(z)$ indexed by the product $\zeta = \chi\sigma = \pm$, which read

$$k^2 + \Gamma^2 + \zeta\Gamma' + y'_\zeta - y_\zeta^2 = 0, \quad (4.44)$$

where $y_\zeta = h'_\zeta$ is the spatial derivative of h_ζ . Usually, such a first-order differential non-linear equation is supplemented by one initial condition $y_\zeta(0) = a_\zeta$. However, our physical problem enforces more naturally one *asymptotic* condition, with the long-distance behaviour $y_\zeta(+\infty) = \varkappa_b$ where $\varkappa_b^2 = k^2 + \Gamma_b^2$ and Γ_b denotes the bulk scattering rate. Another constraint deals with the short-distance behaviour $h_\zeta(0) = 0$, which fixes the constant of integration.

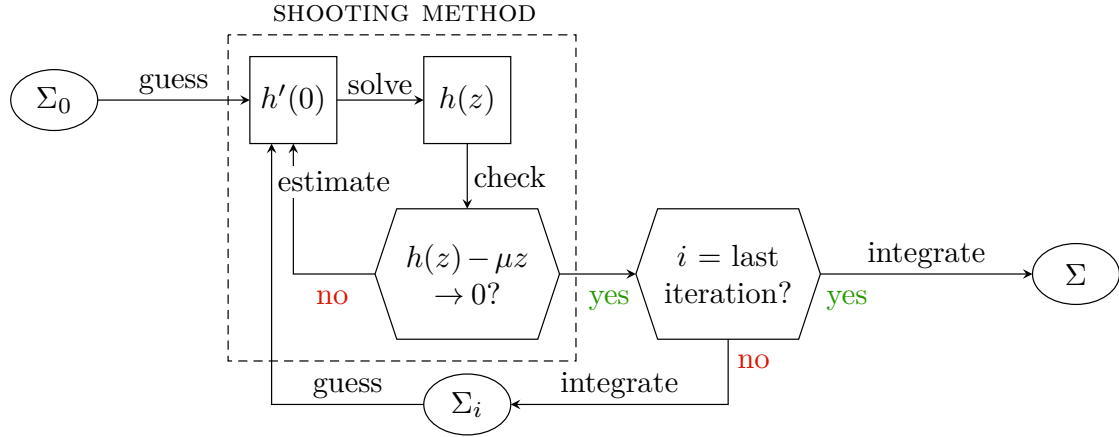


Figure 4.7 | This algorithm solves the spatially resolved self-consistent Born equation numerically, without resorting to a local approximation. The input $\Sigma_0(z)$ is the first-order self-energy, function of the distance z to the boundary. Through a shooting procedure, we determine the auxiliary function $h(z)$, which enters the exponential dependence of the Green's function, in compliance with the large-distance limit $h(z) \simeq \varkappa_b z$ where $\varkappa_b^2 = \mathbf{k}^2 + \Gamma_b^2$, with \mathbf{k} the in-plane momentum and Γ_b the bulk scattering rate. Then the Green's function is integrated numerically over \mathbf{k} , which leads finally to the self-energy $\Sigma(z)$. Multiple iterations allow to improve the result, by using the output self-energy as the input for the next iteration.

The resolution of differential equations constrained by such boundary conditions relies on the so-called shooting method. First guess a value for the initial condition a_ζ , solve the equation and compare the actual long-distance limit $y_\zeta(+\infty)$ with the target \varkappa_b . Then choose a better guess, e.g. iterate this procedure until the long-distance limit approaches the target with a suitable accuracy. To solve the 'exact' SCBA, we propose the iterative algorithm schematised by the flowchart of Fig. 4.7, which presents the following steps.

- (i) Guess a function $\Sigma_0(z) = i\Gamma_0(z)$ for the self-energy as the input. A natural candidate is the self-energy at first order of the disorder strength γ .
- (ii) Pick a value of the in-plane momentum k , guess an initial condition for a_ζ , and solve Eq. (4.44) numerically with $\Gamma_0(z)$ as the scattering rate. Let $y_\zeta(\mathbf{k}, z; a_\zeta)$ be the output function.
- (iii) Estimate the discrepancy in the long-distance limit by computing the error $\text{Err}(a_\zeta) = |y_\zeta(\mathbf{k}, +\infty; a_\zeta) - \varkappa_b|$. Search for the zero of $\text{Err}(a_\zeta)$, for instance using a Newton algorithm. The final output is $y_\zeta^{(1)}(\mathbf{k}, z)$. Sets the integration constant to zero to determine the function $h_\zeta^{(1)}(\mathbf{k}, z)$.
- (iv) Express the Green's function $G_1(\mathbf{k}, z, z)$ using $h_\zeta^{(1)}(\mathbf{k}, z)$, and integrate the SCBA Eq. (4.36) over momentum \mathbf{k} numerically. This gives the first output for the self-energy $\Sigma_1(z)$, which provides a new guess for step (i). Iterate steps (i) to (iv) as many times as wished. The final iteration gives the estimated solution $\Sigma(z)$ of the SCBA.

4.3 Surface states of disordered semimetals

The local DoS also gives information about the surface properties. We show below that Dirac surface states undergo a phase transition analogous to the bulk semimetal-metal transition, but at a smaller critical disorder strength. Fermi arcs avoid this surface critical point because of their extension in momentum space even in absence of disorder. We disregard Fermi rays in this section, whose key properties were already discussed in Sec. 4.2.3.

4.3.1 Criticality of Dirac surface states

Density of states — The analytical resolution of the local SCBA can be pushed further for the M_2 boundary condition if we restrict to the surface properties. First, the energy shift is non-zero, including at the surface, where it reads

$$\epsilon_s = \frac{\Delta \tan \theta}{2} \left[1 - \frac{s^2}{v} \log \left(1 + \frac{v}{s^2} \right) \right], \quad (4.45)$$

where we recall that $v = \cos^2(\theta)$. Below the critical disorder strength, the surface DoS vanishes identically at the energy $\epsilon_s = \frac{1}{2}\Delta \tan \theta$. Above, the minimum of the DoS and the energy ϵ_s diverge, because the scattering rate suppresses ϵ_s . Now the excess contribution to the local SCBA, defined in Eq. (4.39), is

$$f_2(s, 0) = \tan^2(\theta) \left\{ s \left(\sqrt{1 + s^2} - s \right) + \frac{2s^2}{\sin(2\theta)} \left[\arctan(\cot \theta) - \arctan \left(\frac{s \tan \theta}{\sqrt{1 + s^2}} \right) \right] \right\}. \quad (4.46)$$

The local SCBA leads to the surface density of Dirac surface states shown in Fig. 4.8(a). Except for the pathological case of a non-dispersing flat band ($\theta = \pi/2$), eigenstates populate the surface projection of the Weyl node only above a non-zero critical disorder strength. However, this surface critical strength $\Delta_s^* = v^2$ is smaller than the bulk critical strength $\Delta_b^* = 1$. In the opposite case of $\theta = 0$, the surface Weyl cone merges with the bulk band structure, and the difference between surface and bulk states fades out.

This contrasts with Dirac fermions in two dimensions, as in graphene, where a non-zero DoS develops at the nodal level under arbitrary weak disorder (OSTROVSKY 2006). At the lower critical dimension, disorder is indeed marginal, and induces an exponentially small density $\bar{\rho} \sim e^{-1/\Delta}$. The difference comes from the ability of Dirac surface states to overcome disorder by leaking through the bulk: carrier transport at the boundary of a three-dimensional disordered material does not compare to the two-dimensional case. Since evanescent waves explore the volume within a distance ξ from the surface, the problem is effectively three-dimensional. We expect an even more pronounced stability of Dirac surface states when the impurities are confined to the boundary.

Group velocity — The group velocity of the Dirac surface states also reveals a critical behaviour at the surface transition. By definition, the group velocity is $\mathbf{v}_g = \partial_{\mathbf{k}} E_s$, where $E_s(\mathbf{k})$ is the surface dispersion relation (WILSON 2018). Let us consider first the clean material. By differentiating the equation $D(E_s, \mathbf{k}) = 0$, where D is the pole of the excess Green's function, the group velocity can be cast into $\mathbf{v} = -\partial_{\mathbf{k}} D / \partial_E D$, expression which depends only on the functional dependence of the pole. In presence of impurities,

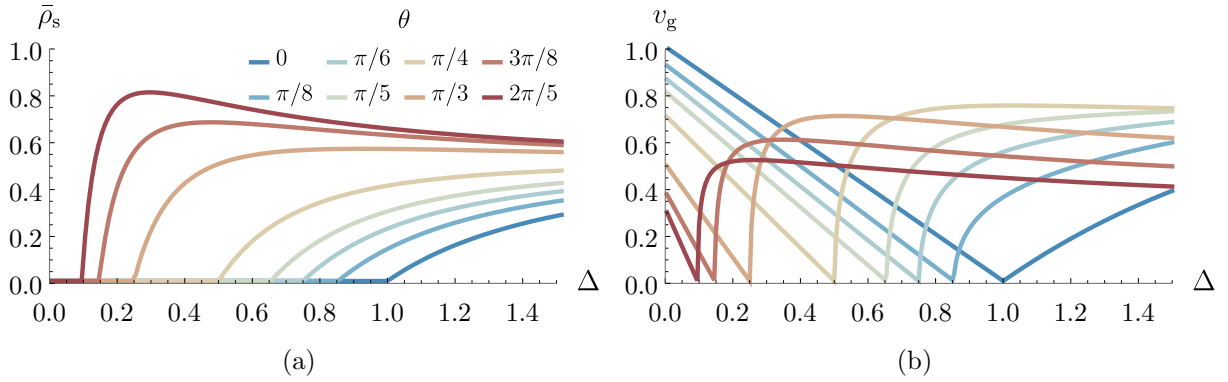


Figure 4.8 | (a) Surface density of Dirac surface states $\bar{\rho}_s$ against disorder strength Δ , for several angles $\theta \in [0, \pi/2]$. The Dirac surface states become metallic above the critical value $\Delta_s^* = \cos^2(\theta)$. (b) The group velocity v_g vanishes at the same surface critical point.

the defining equation of the dispersion relation becomes $D(E_s + \text{Re } \Sigma(E_s, z=0), \mathbf{k}) = 0$. At the surface energy shift ϵ_s , we thus find

$$\mathbf{v}_g = \mathbf{v}[1 + \partial_E(\text{Re } \Sigma)(\epsilon_s, 0)]^{-1} \quad (4.47)$$

The derivative of the self-energy follows by solving Eq. (2.36) numerically for energies E around ϵ_s . Fig. 4.8(b) shows the norm of the group velocity as a function of disorder strength. Below the surface critical point, the group velocity admits the analytical expression $v_g = v(1 - \Delta v^{-2})$, where we recall that $v = \cos \theta$. On both sides, the group velocity vanishes linearly near the critical disorder strength. The power-law behaviour $v_g \propto |\Delta - \Delta_s^*|^{\nu(z_s-1)}$ is consistent with the mean-field value of the dynamical exponent $z_s = 2$.

Phase diagram of the semi-infinite system — We found that when Dirac semimetals host Dirac surface states, the semimetal-metal transition occurs not only in the volume, but also at the boundary, though at a smaller different disorder strength. The properties of the semi-infinite system at the energies $E = 0$ in the bulk and $E = \epsilon_s$ at the surface can be summarised as the phase diagram in the (Δ, θ) plane shown in Fig. 4.9(a). This diagram features two critical lines. The so-called *extraordinary* transition occurs at the critical line E : $\{\Delta = 1\}$, and is reminiscent of the usual semimetal-metal transition of infinite systems. It separates the region $\Delta > 1$, where the bulk and the surface are metallic, and the region $\Delta < 1$, where the bulk keep its semimetallic properties. At the critical point, the penetration length ξ diverges. The *surface* transition, with critical line S : $\{\Delta = \cos^2(\theta)\}$, runs through the subcritical region $\Delta < 1$, and determines when the surface becomes metallic, in presence of the semimetallic bulk. At the surface critical point, the penetration depth ξ vanishes, in agreement with the surface and bulk states merging at the Dirac node in the clean material. Surface and extraordinary critical lines meet at the special point $(\Delta = 1, \theta = 0)$.

This phase diagram resembles the one found in semi-infinite spin systems, from which we borrow the terminology (LUBENSKY 1975a; LUBENSKY 1975b). As we discuss in more detail in Appendix C, the equivalent of the angle θ which parametrises the boundary matrix is the surface nearest-neighbour interaction strength J_s , which usually differs from

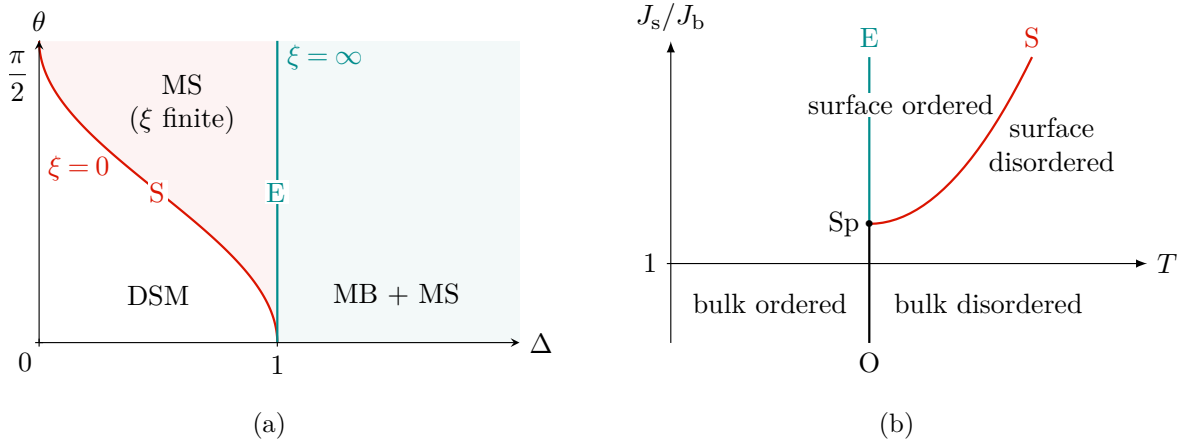


Figure 4.9 | (a) Phase diagram of a semi-infinite semimetal hosting Dirac surface states, typically a Dirac semimetal (DSM), or a Weyl semimetal where two nodes of opposite chiralities overlap when projected to the surface. The parameter Δ represents the disorder strength; the angle θ parametrises the chirality-breaking boundary matrix. The surface transition occurs on the critical line $S : \{\Delta = \cos^2(\theta)\}$. At a larger disorder strength, metallic eigenstates populate the surface, and penetrate in the bulk over a finite length ξ (MS). Beyond the extraordinary line $E : \{\Delta = 1\}$, the bulk becomes metallic as well (MS + MB). (b) Semi-infinite spin systems exhibit a similar diagram in the temperature T - surface neighbour coupling J_s plane. Here the vertical axis represents the relative surface strength, i.e. the ratio J_s/J_b of surface and bulk coupling strength. When the bulk coupling J_b exceeds the surface coupling J_s , the system undergoes an extraordinary transition, where the bulk and surface become magnetic simultaneously.

the bulk strength J_b . For J_s above the special point, the surface becomes magnetised at a temperature higher than for the bulk, but for J_s below the special point, bulk and surface order at the same temperature, as shown in Fig. 4.9(b). This *ordinary* transition is absent in semi-infinite semimetals. Another key difference between spin systems and relativistic phases lies in the universality class of the surface transition. In spin systems, the surface transition in d dimensions shows the same critical behaviour as the bulk transition in $d - 1$ dimensions. This cannot be the case in the semimetal-metal transition, in two dimensions, disorder is marginal.

4.3.2 Robustness of Fermi arcs

The separation of the surface-projected Weyl nodes generates a sizeable surface density in the clean system, phenomenon which is observed in numerical works as well (WILSON 2018). The two-dimensional density of the arc coincides with its length in momentum space, $\rho_A = 4\theta b / \cos(2\theta)$. The surface density ρ_s plotted in Fig. 4.10(a), on the other hand, represents the three-dimensional density of states taken at $z = 0$. It differs from ρ_A to the extent that the arc extends in the bulk over a distance of order b , so that $\rho_s \propto \rho_A b \propto b^2$. The θ -dependence of ρ_s is harder to find. At any rate, the extension of the surface Fermi surface smooths out the sharp transition observed at the boundary of Dirac semimetals. Fermi arcs are indeed diffusive metallic for arbitrarily weak disorder. With increasing disorder strength, the Fermi arc broadens. The effect of disorder on the surface density of states is less clear, and depends on the original extension of the clean arc. For close Weyl nodes, as in Fig. 4.10(a) where $b = 0.1\Lambda$ and the aperture is moderate, more random

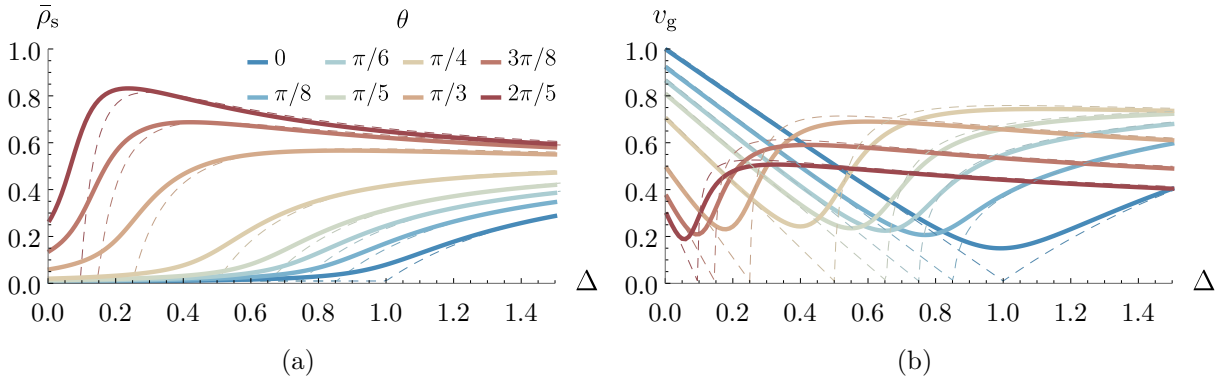


Figure 4.10 | (a) Surface density of states $\bar{\rho}_s$ and (b) group velocity v_g of Fermi arcs (solid curves) against disorder strength Δ , for several aperture angles $\theta \in [0, \pi/2]$. The half-separation between the Weyl nodes is set to $b = 0.1\Lambda$ in units of the ultraviolet cut-off Λ , and the dashed curves is for comparison with Dirac surface states ($b = 0$). Both observables show that the Fermi arcs avoid the surface critical point.

scatterers entails more surface eigenstates at the Fermi level, in agreement with (WILSON 2018). This enhancement of the density of states is less apparent in straight Fermi arcs due to their reduced size.

The group velocity of the Fermi arc states similarly avoids the surface transition observed in Dirac semimetals. The group velocity at the contact points with the nodes, where it is maximal, is shown in Fig. 4.10(b). The significant drop near the critical disorder strength $\Delta_s^* = \cos^2(\theta)$ reflects the proximity of Fermi arcs to the avoided critical point, which is not utterly hidden for ‘small’ arcs. In numerical simulations on lattice models, where Weyl nodes can be separated by momenta of the order of the Brillouin zone’s size, the group velocity decreases monotonically and vanishes at strong disorder strengths where localisation takes place (WILSON 2018). This localisation point is inaccessible in our analytical study. The behaviour of both the density of states and the group velocity indicates that the surface of Weyl semimetals lies in the crossover region of a surface transition. The dimensionless quantity ξb compares the penetration length ξ with the typical length scale over which intervalley scattering occurs at the boundary, of the order b^{-1} . The larger ξb , the more rounded the transition is.

Conclusion

Summary — We have seen that three-dimensional relativistic semimetals harbour exotic states on their surface. Experimentalists have observed these surface states since the first material realisations of the three-dimensional relativistic semimetals, in the form of curved Fermi arcs which connect to a Weyl or Dirac node on either end. While topologically protected in Weyl semimetals, Fermi arcs do not survive moderate disorder in Dirac semimetals, where they detach from the nodes to form closed loops of trivial states. The low-energy physics of Weyl and Dirac semimetals allows for a wider range of surface modes: besides the Fermi arcs, Dirac surface states and Fermi rays are valid solutions of the boundary condition for Dirac fermions; the first two arise from chirality-breaking reflection processes, characterised by a boundary matrix M_1 , the last one from chirality-preserving reflection processes, characterised by a boundary matrix M_2 . We have extracted the dispersion relation of the surface elementary excitations from the pole of the Green's function.

We have then included disorder. Using a spatially resolved version of the self-consistent Born approximation, and resorting to a ‘local’ approximation of our own design, we have determined the spatial profile of the average density of states for the two types of boundary conditions. In particular, Dirac surface states, which disperse along a single-branch cone, display their own critical behaviour at a lowest disorder strength. The full phase diagram in the (Δ, θ) plane, where Δ represents the disorder strength and θ determines the Fermi velocity of Dirac surface states, shares many similarities with that found in spin systems, which displays an extraordinary (bulk) and a surface transition. These results offer a new perspective on how disorder affect Fermi arcs, since they appear to avoid the critical point of the surface transition because of their finite extension, of the order of the momentum separation b between the paired Weyl nodes.

Outlook — A natural extension of this work would be to determine the critical properties of the extraordinary and surface transitions in a field-theoretic framework. Such an approach has given fruitful results in spin systems. The correlation functions acquire additional divergences when one point belongs to the surface, which must be subtracted to make the theory finite. In the context of disordered relativistic phases, these surface singularities encode the power-law scaling of the surface dispersion relation, field amplitude and density of states at the extraordinary transition (work in progress) (BRILLAUX 2021a). A crucial difference between the two systems lies in the nature of the surface transition. While the surface transition of a d -dimensional spin system belongs to the universality class of the $(d - 1)$ -dimensional bulk transition, the surface transition observed in Dirac surface states bears no similarity with its bulk counterpart. Therefore, it requires its own treatment within the field theory.

Part II

Electronic interactions in twisted bilayer graphene

Overview of magic angle twisted bilayer graphene

The fascinating properties of graphene change substantially when several layers bond together through Van der Waals attractions. The energy bands of bilayer graphene depend heavily on the stacking arrangement. Bernal-stacked bilayer graphene, for instance, hosts massive chiral excitations, in contrast to monolayer graphene. Even these commensurate bilayer systems carry their share of exotic features, many-body effects do not completely alter their qualitative properties. On the contrary, when two graphene flakes are overlaid with a twist at special ‘magic’ angles, a plethora of correlated phases appears: superconductivity, Mott insulation, nematic ordering, etc., which suggests the presence of strong electronic interactions. Twisted and untwisted bilayers differ essentially by the magnitude of their characteristic length scale: while the atomic distance fixes the energy scale of commensurate packings of crystalline membranes, incommensurate packings obtained by a small twist develop a moiré pattern with a period hundreds of times larger than the atomic distance. At special values of the twist angle, known as ‘magic’ angles, the energy bands flatten out dramatically, so that the kinetic and interaction energies become comparable, even though interactions have essentially the same absolute strength than in monolayer graphene.

The phase diagram of twisted bilayer graphene bears striking similarities with that of high-temperature cuprates, while being much easier to explore, thanks to the experimental expertise gained on graphene: by using electrical gate doping, researchers can evidence all phases of the doping-temperature plane in a single sample, which would require to grow many samples with various compositions in cuprates. In this chapter we introduce twisted bilayer graphene and the ‘magic’ angle physics that manifests itself at special twist configurations, and review the major experimental findings in twisted bilayer graphene, with a primary focus on the insulating phase at charge neutrality.

5.1	Bilayer graphene systems	136
5.1.1	Commensurate stacking arrangements	136
5.1.2	Twisted bilayer graphene	139
5.2	Band structure	143

5.2.1	Effect of interlayer hopping	143
5.2.2	The magic angle physics	144
5.3	Experimental findings	147
5.3.1	Experimental setup	147
5.3.2	Global phase diagram	149
5.3.3	Nematic phases	151
Conclusion	154

5.1 Bilayer graphene systems

The properties of multilayer graphene systems differ substantially from their monolayer counterpart. Of particular interest is bilayer graphene, whose electronic spectrum depends on the stacking arrangement. The commensurate AA and especially AB packings, which formally correspond to a 0° and 60° twist, represent the most common arrangements in graphite. At intermediate twist angles, the stacking becomes incommensurate, and the bilayer forms wide moiré patterns with a period as large as several hundred lattice spacings. Although twisting the bilayer breaks translational invariance at the microscopic scale, the standard tools of crystalline state physics apply exceptionally well as far as the single-particle physics is concerned.

5.1.1 Commensurate stacking arrangements

Introduction — Bilayer graphene consists of two graphene flakes overlaid and weakly bound by Van der Waals interactions (MCCANN 2013). Multilayer graphene systems are useful to understand the properties of graphite; but they are also noteworthy in themselves. The study of Van der Waals heterostructures has become a booming research area: few-layer atomic compounds can be assembled sheet by sheet to design versatile materials with a high degree of controllability (GEIM 2013). Among the building bricks of Van der Waals heterostructures feature graphene and graphene-like two-dimensional crystals such as fluorographene, hexagonal boron nitride (hBN), dichalcogenides such as molybdenum disulphide (MoS_2) and tungsten diselenide (WSe_2), or layered oxides. Notably, graphene-based heterostructures represent promising platforms to study unconventional superconductivity, where the growth techniques of high-temperature superconducting cuprates offer limited tunability.

The interlayer spacing of bilayer graphene $c \simeq 3.3 \text{ \AA}$ represents a few times the length of the carbon-carbon covalent bond $a_0 = 1.42 \text{ \AA}$, as shown in Fig. 5.1(a). Each crystalline layer hosts two interpenetrating triangular sublattices A and B, which we will index as A1 or B1 for the bottom layer, and A2 or B2 for the top layer. Two possible stacking arrangements of the bilayer exist which preserve the crystalline periodicity of the monolayer.

- In the AA stacking, the layers are exactly superimposed, so that each atom of the top layer matches a neighbour below. Since AA stacking is rarely found in nature, this structure is believed to be weakly stable. AA-stacked bilayer graphene can be semimetallic, metallic, or insulating, depending on interlayer spacing (ANDRES 2008).

- In the AB or *Bernal* stacking, half the atoms of the top layer lie directly above another atom of the bottom layer. Graphitic layers usually stack in this way, and the corresponding -ABABAB- sequence forms the hexagonal allotrope of graphite.

Band structure of Bernal-stacked bilayer graphene — We consider here the most common, Bernal stacking. Like in monolayer graphene, the band structure depends strongly on the intensity and symmetry of hopping processes. The electron motion on a bilayer differs significantly from that on a monolayer due to interlayer tunnelling mechanisms. Following Sec. 1.2.3 on monolayer graphene, we determine the electronic spectrum of bilayer graphene from a tight-binding model.

The bilayer crystal combines the three-fold and in-plane reflection symmetry, already present in monolayer graphene, with spatial inversion; it is therefore centrosymmetric. Since the top and bottom layers are merely shifted in Bernal stacking, the bilayer and the monolayer have identical Brillouin zones, shown in Fig. 1.4(c). In particular, two time-reversal partner points K and K' lie at the corners of the Brillouin zone of the bilayer. Let $A2$ and $B1$ be the sublattices that match vertically. The atoms on $A1$ and $B2$ sites then bond with their three remote neighbours on the opposite layer. The unit cell of the bilayer contains four sites: $A1$, $B1$, $A2$ and $B2$, each with filled sp^2 orbitals and half of which host a vacant $2p_z$ orbital responsible for electrical conduction.

What fate does interlayer tunnelling reserve for the Dirac points at the K and K' points? For a faithful representation of the band structure, four types of bonds must be considered, as shown in Fig 5.1(a). The intralayer bonds between neighbour A and B atoms have energies $t_0 \simeq -3.16$ eV, determined by infrared spectroscopy (KUZMENKO 2009). This value agrees with experiments on graphite, and slightly deviates from the valence bond amplitude $t \simeq -2.60$ eV in monolayer graphene. At least three interlayer hopping processes have a sizeable amplitude. The $A2$ - $B1$ and bonds $A1$ - $B2$ have a similar energy $t_1 \simeq t_2 \simeq 0.38$ eV respectively; the $A1$ and $A2$ atoms bond more weakly, with an energy $t_4 \simeq 0.14$ eV. As in 1.4(c), we ignore overlap integrals and on-site energies. In a basis $\{\psi_{A1}, \psi_{B1}, \psi_{A2}, \psi_{B2}\}$ made of linear superpositions of on-site orbitals, the Bloch Hamiltonian reads (GUINEA 2006)

$$\mathcal{H} = \begin{pmatrix} 0 & t_0 f(\mathbf{k}) & t_4 f(\mathbf{k}) & t_3 f(\mathbf{k})^* \\ t_0 f(\mathbf{k})^* & 0 & t_1 & t_4 f(\mathbf{k}) \\ t_4 f(\mathbf{k})^* & t_1 & 0 & t_0 f(\mathbf{k}) \\ t_3 f(\mathbf{k}) & t_4 f(\mathbf{k})^* & t_0 f(\mathbf{k})^* & 0 \end{pmatrix}, \quad (5.1)$$

where $f(\mathbf{k})$ is still given by Eq. (1.26). Note that only the $A2$ - $B1$ pairs of sites couple vertically, so that in-plane spatial modulations do not affect $A2$ - $B1$ hopping processes: the function $f(\mathbf{k})$ is absent from these terms. The diagonalisation of Hamiltonian (5.1) gives the four energy bands represented in Fig. 5.1(b).

Near the K and K' points, the bands organise in two sets: one pair of bands touch quadratically at the Fermi level, while the other pair is separated by an energy gap $2t_1$. Let $s = \pm 1$ be the valley index, with a plus sign for the valley K and a minus sign for the valley K' . At low energies $E \ll t_1$, the effective Hamiltonian for the two bands closest to the Fermi level,

$$\mathcal{H}(s\mathbf{K} + \mathbf{q}) \simeq \frac{q^2}{2m} \boldsymbol{\sigma} \cdot \mathbf{n}, \quad (5.2)$$

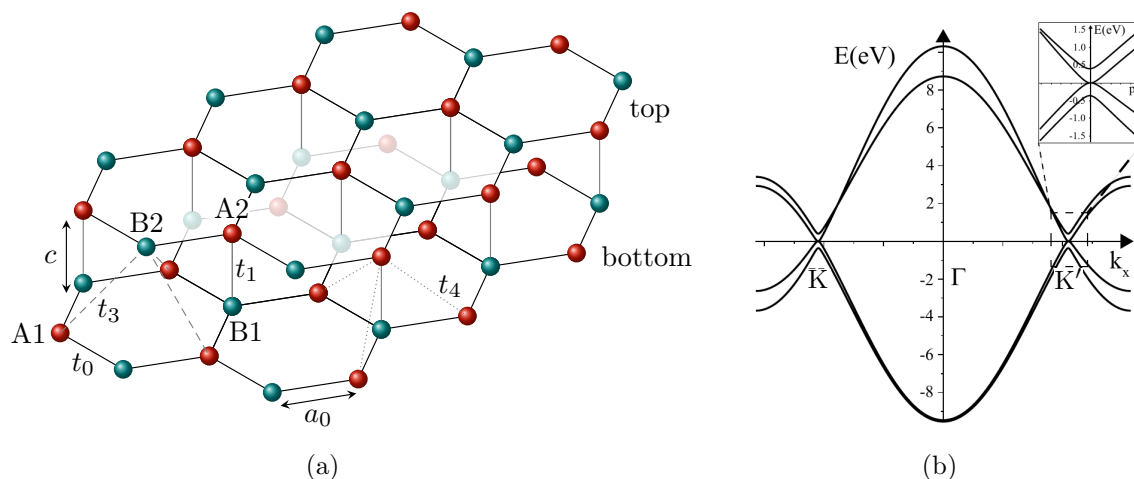


Figure 5.1 | (a) In Bernal-stacked bilayer graphene, the A2 atoms of the top layer face the B1 atoms on the bottom layer, while the B2 atoms lie at the vertical of hexagons' centres. The carbon-carbon bonds have length $a_0 = 1.42 \text{ \AA}$ within a layer, which is more than twice shorter than the interlayer spacing $c \simeq 3.35 \text{ \AA}$. Besides the intralayer hopping of amplitude t_0 , three interlayer hopping processes dominate, with amplitudes t_1 , t_3 and t_4 . (b) The $2p_z$ orbitals of the carbon atoms leads to four energy bands (one per sublattice and layer); two valence π bands (full), and two conduction π^* bands (empty). On this plot the Fermi level lies at zero energy. Two particle-hole symmetric bands out of the four touch quadratically near the K and K' points, where chiral massive fermions emerge as low-energy excitations. The other bands are gapped by an energy $2t_1$. Adapted from (MCCANN 2013).

leads to non-relativistic chiral excitations of mass $m = t_1/2v_F^2$, where v_F is the Fermi velocity of monolayer graphene, and momentum $\mathbf{q} = q(\cos \phi, \sin \phi)$. As in graphene, the energy eigenstates have fixed helicity $\boldsymbol{\sigma} \cdot \mathbf{n} = \pm 1$, where the in-plane axis of quantisation $\mathbf{n} = -(\cos(2\phi), s \sin(2\phi))$ winds twice around the origin under a closed Berry loop. Bilayer graphene exhibits an integer quantum Hall effect similar to that found in conventional semiconductors, where the transverse conductivity per spin and valley jumps by units of e^2/h . A difference appears at low densities, where the conductivity curve displays instead a step of $2e^2/h$ at zero magnetic field, due to the eight-fold degeneracy of the zero-energy Landau levels (NOVOSELOV 2006).

Robustness to perturbations — The predictions of electronic band theory for bilayer graphene usually tally with experimental results. Disorder suppresses the DC conductivity, but leads to no qualitative change (KOSHINO 2006). Furthermore, the non-zero DoS at the Fermi level survives weak electron-electron interactions; many-body effects affect transport properties only at low carrier density and in the presence of a magnetic field, even though experimental and theoretical studies often find conflicting results because of the sensitivity of the correlated phase to microscopic details. Among them feature spin ferromagnetism, layer anti-ferromagnetism, a charge density wave state, or a quantum spin Hall state. But the absence of superconductivity, along with the stringent conditions for many-body effects to manifest themselves, pushed research to look for new materials. One of these, which is closely linked to graphene, exceeded all expectations: twisted bilayer graphene.

5.1.2 Twisted bilayer graphene

When two-dimensional meshes are overlaid, their interference forms exotic pseudo-periodic structures known as moiré patterns. Beyond their aesthetic interest in textiles and art, such patterns affect the electronic motion in planar crystals and may lead to new phases of matter (ANDREI 2020). Moiré patterns arise in particular when the symmetry axes of the two layers are oriented along different directions, as was already observed in graphite under scanning tunnelling microscopy (XHIE 1993). However, researchers only recently achieved a high degree of control over the twist angle (CAO 2018a). Misalignment abounds naturally in few-layer graphene, especially in epitaxially grown samples on silicon carbide.

Geometry — Let us pack two layers of graphene with an AA stacking order. We then apply a relative twist of angle θ around an arbitrary origin where two atoms A1 (of the bottom layer) and A2 (of the top layer) overlap, and translate the top layer by a vector \mathbf{d} . Let a_0 be the in-plane carbon-carbon distance, and $a = \sqrt{3}a_0$ graphene’s lattice spacing. A basis for the triangular Bravais lattice of an untwisted layer is

$$\mathbf{a}_1 = \frac{a_0}{2} (3, \sqrt{3}), \quad \mathbf{a}_2 = \frac{a_0}{2} (3, -\sqrt{3}). \quad (5.3)$$

For convenience, we choose the x -axis such that the top and bottom layers are rotated by $+\theta/2$ and $-\theta/2$ respectively, as in Fig. 5.2. In a twisted bilayer, the A sites of the bottom and top layers are located at positions

$$\mathbf{r}_{\mathbf{A1}}(m, n) = R_{-\theta/2}(m\mathbf{a}_1 + n\mathbf{a}_2), \quad \mathbf{r}_{\mathbf{A2}}(k, l) = R_{+\theta/2}(k\mathbf{a}_1 + l\mathbf{a}_2) + \mathbf{d}, \quad (5.4)$$

respectively, where R_φ operates an in-plane rotation of angle φ , and $m, n, k, l \in \mathbb{Z}$. The B sites are located at $\mathbf{r}_{\mathbf{B}} = \mathbf{r}_{\mathbf{A}} + R_{\pm\theta/2}\boldsymbol{\delta}$, where $\boldsymbol{\delta} = a_0(1, 0)$ is the vector that joins the A and B sites within the unit cell of an untwisted layer.

The beauty of moiré patterns — The twisted bilayer is not crystalline in general, because nowhere do the A1 and A2 sublattices match for arbitrary twists. Yet, there exists a discrete set of twist angles for which some sites A1 and A2 stack perfectly on one another repeatedly, which restores periodicity, albeit on a larger scale. To fulfil this commensuration condition, there must exist a tuple (m, n, k, l) such that $\mathbf{r}_{\mathbf{A1}}(m, n) = \mathbf{r}_{\mathbf{A2}}(k, l)$. Crucially, commensuration depends only on the basis vectors of the Bravais lattice and on the relative twist, but not on the structure of the layers’ unit cell. Neither the presence of two carbon atoms per unit cell nor the stacking arrangement before twist matter in the end. Similarly, the translation vector \mathbf{d} shifts the commensurate structure, but does not change either its shape or size. The corresponding commensurate angles $\theta(r, s)$ are parametrised by two coprime integers r and s according to (SHALLCROSS 2010; LOPES DOS SANTOS 2012)

$$\cos \theta = \frac{3r^2 - s^2}{3r^2 + s^2}. \quad (5.5)$$

The set of commensurate structures is thus isomorphic to the set of rational numbers \mathbb{Q} , which is dense in the set of real numbers \mathbb{R} . Hence, for any angle θ , there exists a commensurate structure corresponding to a twist angle $\theta(r, s)$ given by Eq. (5.5) as close to θ as desired. We can distinguish two large-scale structures emerging from the twisted bilayer.

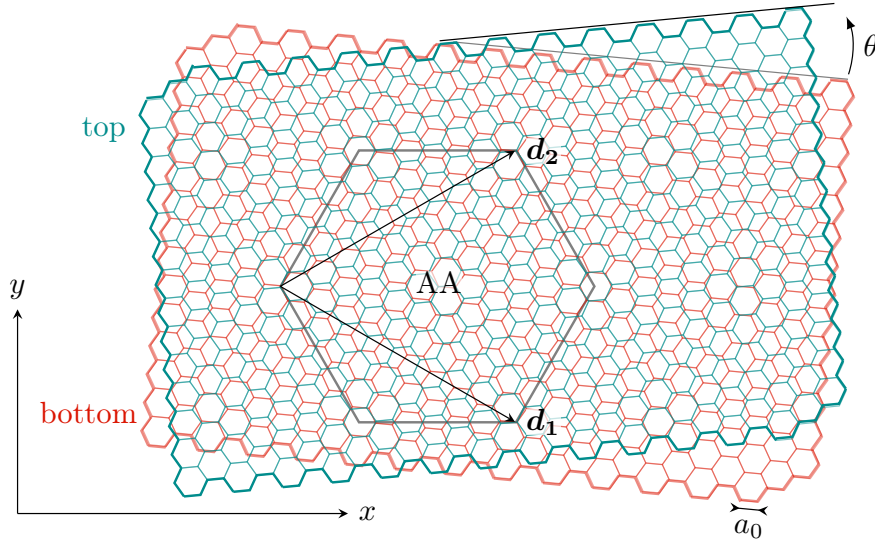


Figure 5.2 | When two graphene layers are overlaid with a relative twist, a six-fold symmetric moiré pattern emerges due to the interference of the mismatched lattices. This so-called moiré pattern does not arise from an underlying periodic structure for a generic twist angle θ , except for a discrete subset of commensurate values where it coincides with a superlattice of basis $(\mathbf{d}_1, \mathbf{d}_2)$. The conventional supercell is made of a hexagon with AA stacking regions at the centre and the corners. On this schematic, the twist corresponds to a commensurate angle $\theta(r, s) \simeq 11^\circ$ with $r = 6$ and $s = 1$, and the superlattice spacing is about $10a_0$, where a_0 is the carbon-carbon distance. For $\theta \simeq 1^\circ$ and below, the supercell encompasses tens of thousands of atoms.

- At a generic commensurate twist (for arbitrary r and s), the bilayer forms a *superlattice* of basis vectors given by smallest coincident lattice vectors,

$$\mathbf{d}_1 = \mathbf{r}_{A1}(m, n) = \mathbf{r}_{A2}(k, l), \quad \mathbf{d}_2 = R_{\pi/3}\mathbf{d}_1, \quad (5.6)$$

where the pairs (m, n) and (k, l) are minimal and entirely determined by the integers r and s , up to a three-fold rotation of the basis. As for the monolayer, the Wigner-Seitz cell of the superlattice is triangular. The superlattice is extremely sensitive to the precise twist angle $\theta(r, s)$, since infinitely small variations of the twist angle always lead to sizeable translations far enough from the origin, and can dramatically alter the commensuration condition. Fig. 5.3 shows how crucially the number of atoms per commensuration cell N depends on the twist.

- At a generic angle, whether commensurate or incommensurate, a large *moiré* pattern, with six-fold rotational symmetry, strikes the eye. This periodic pattern originates from the interference between the mismatched sublattices of the bilayer, where alternate local AA and AB stacking regions, as visible in Fig. 5.2. The moiré period L , which separates two adjacent AA stacking regions, corresponds to the distance between the origin and the point where two rotated straight lines deviate exactly by the microscopic lattice spacing a . Choosing a basis of unit vectors $(\mathbf{e}_x, \mathbf{e}_y)$ in the plane, we see that to meet this condition, we must have

$$L(R_{+\theta/2}\mathbf{e}_x - R_{-\theta/2}\mathbf{e}_x) = a\mathbf{e}_y, \quad (5.7)$$

which gives $L = a/2 \sin(\theta/2)$.

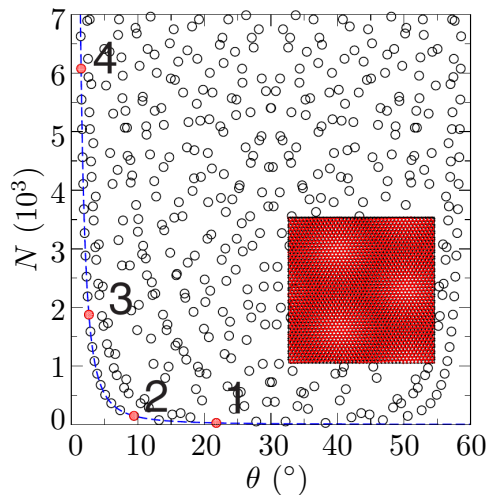


Figure 5.3 | Number of atoms N per commensuration cell of twisted bilayer graphene against relative twist angle θ . The set of commensurate structures (circles) is parametrised by a rational number r/s . The moiré period $L \propto \theta^{-1}$, which is the structural length scale that stands out to the eye, fixes a lower bound for the size of the commensuration cell, and thus the number of atoms per supercell $N \propto \theta^{-2}$ (blue dashed line). The associated moiré pattern coincides with a superlattice, where the bilayer recovers strict periodicity, on a subset $\theta(r, s = 1)$ of the commensurate twist angles. The inset shows the moiré pattern for the commensurate structure labelled ‘4’ on the upper left. Adapted from (SHALLCROSS 2010).

The moiré pattern coincides with the superlattice in the special case of a commensurate angle $\theta(r, s)$ with $s = 1$. At a generic commensurate twist, the moiré period L fixes a lower bound for the superlattice spacing $|\mathbf{d}_1|$. Similarly, since there are four atoms per graphene unit cell (one for each sublattice and layer), the number of atoms per moiré cell $N_m = 4(L/a)^2 = \sin(\theta/2)^{-2}$ sets a lower bound for the number of atoms per commensuration cell N , as shown in 5.3. For $\theta \simeq 1^\circ$, the moiré unit cell encompasses a tremendous number of 10 000 atoms.

We will see below that the moiré pattern represents the structural building block from which we can build a continuum description of TBG, where the standard tools of crystalline matter physics apply at all twist angles.

Continuum description — For incommensurate angles, hexagonal tiles roughly repeat themselves when wandering along the twisted bilayer, so that long-range crystalline order remains. But strict periodicity is lost. In such materials, known as quasi-crystals, electron diffraction patterns lead nonetheless to sharp Bragg peaks similar to that found in perfect crystals, as in aluminium-manganese metallic alloys, the first representative of the family (SHECHTMAN 1984). Quasi-crystalline electronic phases resemble disordered phases in some respects: a random tiling can be viewed as geometric disorder. It seems, however, that the non-periodicity of TBG is not an essential input to understand its properties; treating the moiré pattern as a superlattice for all small θ appears to describe the single-particle band structure correctly when compared to numerical tight-binding studies, and offers a workable – though unusual – free theory to which one may incorporate many-body effects. To justify this approach a priori, we could also argue that the set of commensurate twist angles for which the moiré pattern corresponds to a superlattice

becomes denser as θ decreases, as appears on Fig. 5.3; an approximate periodicity should thus be recovered in the low twist angle limit with increasing accuracy. At zero twist, the electronic band structure should match that of the AA-stacked bilayer.

Under this assumption, we can build a *continuum* model for TBG, where the standard tools of crystalline matter physics – the real and reciprocal lattices, the Brillouin zone, Bloch’s theorem, etc. – apply (LOPES DOS SANTOS 2007; SHALLCROSS 2010; BISTRITZER 2011). We review below the basic ingredients of the continuum model of the decoupled bilayer, and discuss in Sec. 5.2 the fascinating ‘magic angle’ physics that emerges when turning on the interlayer tunnelling.

As any Bravais lattice in real space, the triangular moiré pattern comes with its reciprocal superlattice and a corresponding Brillouin zone. The microscopic structure of graphene and the emerging moiré pattern share the same six-fold symmetry, except that the moiré period L exceeds the microscopic lattice spacing a by a factor $\simeq \theta^{-1}$. We thus expect the moiré, or *mini* Brillouin zone to be hexagonal, and smaller than graphene’s Brillouin zone by a factor $\simeq \theta$. Unlike the Bernal-stacked bilayer, where the Brillouin zone coincides with that of the single layer, the mini Brillouin zone of TBG differs in orientation and in size.

The simple geometric construction of Fig. 5.4 enables to trace the mini Brillouin zone. Let \mathbf{K} be the Dirac momentum of the valley K of graphene before the twist, and $K = 4\pi/3a$ its norm. After the twist, the corresponding Dirac points of the top and bottom layers are located at $\mathbf{K}_t = R_{+\theta/2}\mathbf{K}$ and $\mathbf{K}_b = R_{-\theta/2}\mathbf{K}$, respectively. The vector $\mathbf{q}_1 = \mathbf{K}_b - \mathbf{K}_t$ which joins the top and bottom Dirac nodes, of length $k_\theta = 2K \sin(\theta/2) = 4\pi/3L$, delimits one segment of the hexagonal mini Brillouin zone for the valley K. In the (x, y) basis of Fig. 5.4, its coordinates are $\mathbf{q}_1 = k_\theta(0, -1)$. The other sides of the mini Brillouin zone are found by the three-fold rotational symmetry, i.e. by moving along the vectors $\mathbf{q}_2 = R_{2\pi/3}\mathbf{q}_1$ and $\mathbf{q}_3 = R_{4\pi/3}\mathbf{q}_1$. The basis vectors $\mathbf{Q}_1 = \mathbf{q}_2 - \mathbf{q}_1$ and $\mathbf{Q}_2 = \mathbf{q}_3 - \mathbf{q}_1$ generate the reciprocal superlattice of the moiré pattern.

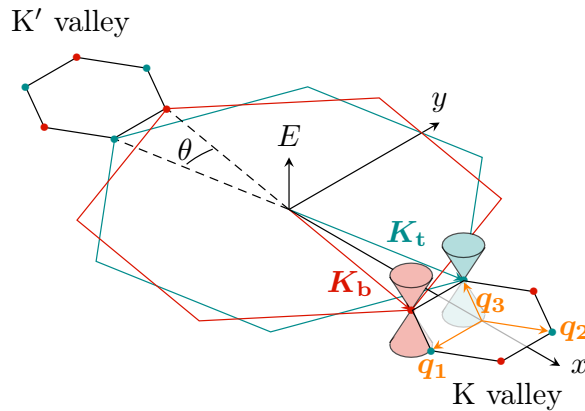


Figure 5.4 | For most purposes one can treat twisted bilayer graphene by a triangular Bravais lattice of spacing $L = a/2 \sin(\theta/2)$ for all twist angles, with a being graphene’s lattice constant. As any lattice in real space, the moiré pattern admits a Brillouin zone in momentum space, of size $k_\theta = 4\pi/3L = 2K \sin(\theta/2)$, where $K = 4\pi/3a$ is the Dirac momentum of graphene. The tilted Dirac points \mathbf{K}_b and \mathbf{K}_t of the bottom and top layers respectively delimit the corners of the moiré (or mini) Brillouin zone. There are actually two mini Brillouin zones related by time reversal and six-fold rotation: one for the valley K, the other for the valley K’.

The valley K' hosts a similar mini Brillouin zone as a result of the time-reversal or six-fold symmetry. Confusingly, what could be called the valley degree of freedom of the mini Brillouin zone corresponds in fact to the layer degree of freedom of graphene, while the two valleys K and K' of graphene lead to yet another degree of freedom. To avoid any ambiguity, we will always associate the non-equivalent Dirac cones of the mini Brillouin zone to the ‘layer’ degree of freedom, and the non-equivalent Dirac cones of the Brillouin zone of monolayer graphene to the ‘valley’. Note also that two Dirac cones of the top and bottom layers, located at K_t and K_b respectively, are described by the *same* copy of the Dirac Hamiltonian, in contrast to the valleys K and K' in graphene which are related by time reversal. In particular, the Dirac cones located at K_t and K_b have the same winding number: the topology of the bilayer differs from that of the single layer.

5.2 Band structure

We now explore how interlayer tunnelling affects the band structure of TBG. We denote by w the interlayer hopping strength, which is assumed independent of the twist. As seen in Sec. 5.1.2, the twist angle affects the characteristic momentum $k_\theta \simeq K\theta$ of the mini Brillouin zone. Because of the relativistic dispersion relation, this momentum scale of the mini Brillouin zone is naturally associated to a characteristic energy scale of the mini bands $E_K \simeq \hbar v_F k_\theta$, which vanishes in the low twist angle limit. We first discuss the effect of interlayer tunnelling on the single-particle band structure as a function of the twist, and show notably that interlayer hopping strongly suppresses the Fermi velocity at the Dirac points. We then explain this quenching of the kinetic energy with a qualitative argument, and define ‘magic’ values of the twist angle, for which the Fermi velocity vanishes and the mini bands closest to the Fermi level flatten out.

5.2.1 Effect of interlayer hopping

Band structure calculations can incorporate interlayer tunnelling in the electron dynamics. In *ab initio* (first-principle) calculations, the Schrödinger equation is solved over a workable set of basis functions. A popular implementation of this approach is density functional theory, where the band structure is found by minimising the energy as a functional of the electronic density, from which ground-state observables can be determined. These numerical techniques demand a huge computational effort when the unit cell contains many atoms, and are doable at large twists only (typically $\theta > 10^\circ$). To explore smaller twists, one can fit the *ab initio* band structures found at large twists with that obtained in Bernal stacking to build an effective tight-binding Hamiltonian, from which band structures at small twists can be extrapolated (SUÁREZ MORELL 2010). Fig. 5.5 shows band structures computed numerically for several twisted configurations near 2° . As the twist angle decreases, interlayer tunnelling prevails over the kinetic energy, which dampens the Fermi velocity at the Dirac points. At the same time, the bandwidth measured at the Γ point goes down. The same conclusions apply to other bilayer systems, such as graphene on hexagonal boron nitride (FANG 2016).

The above qualitative picture holds whatever the numerical approach used, even though the details of the band structure may differ. For instance, when diagonalising the tight-binding Hamiltonian with the Lanczos algorithm for large sparse matrices, a gap develops above 1.9° in the energy spectrum, which disappears below (SBOYCHAKOV 2015). In this

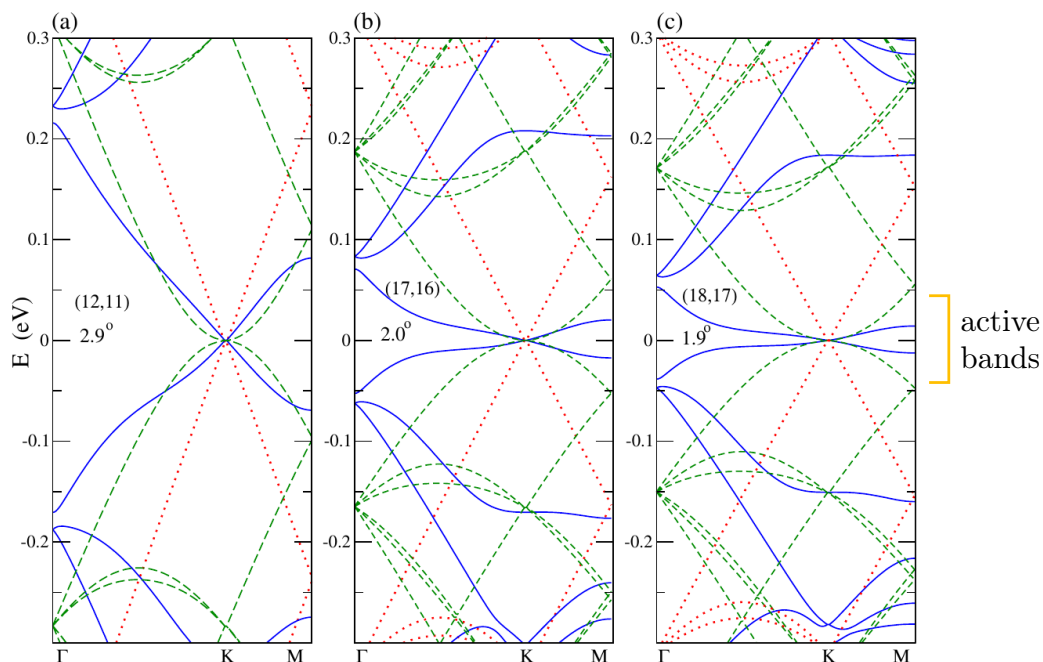


Figure 5.5 | Calculated band structure of twisted bilayer graphene at small twist angles (in blue), Bernal-stacked bilayer graphene (in dashed green), and monolayer graphene (in dotted red). The three panels correspond to decreasing twist angles (a) $\theta = 2.9^\circ$, (b) $\theta = 2.0^\circ$, and (c) $\theta = 1.9^\circ$. As the relative twist is reduced, the kinetic energy of the mini bands closest to the neutrality point – the *active* bands – decreases. Interlayer hopping suppresses both the Fermi velocity at the Dirac points (K point) and the bandwidth at the centre of the moiré Brillouin zone (Γ point). By contrast, the band structures of Bernal-stacked graphene and monolayer graphene are respectively parabolic, and linear with a fixed Fermi velocity $v_F \simeq 10^6 \text{ m} \cdot \text{s}^{-1}$. Adapted from (SUÁREZ MORELL 2010).

regime of low twist, the Dirac points seem to be pushed slightly off the charge neutrality point, and TBG may be metallic. This contrasts with the results of (SUÁREZ MORELL 2010), but in both cases, interlayer tunnelling reduces the bandwidth and dampens the Fermi velocity. Let us try to understand why interlayer hopping tends to shrink the lowest energy bands.

5.2.2 The magic angle physics

The first magic angle — The *first magic angle* θ_0 is defined as the twist angle where interlayer hopping dampens the Fermi velocity so much that it vanishes. By comparing the energy scales at play – the intralayer kinetic energy and the interlayer tunnelling amplitude –, we can easily estimate this magic value. In the limit of decoupled layers, the top and bottom Dirac cones cross at opposite points split by an energy $\Delta E \simeq \hbar v_F k_\theta$, which is roughly proportional to the twist angle θ . Due to interlayer hopping, these two bands hybridise over an energy region w , leading to two symmetric saddle points separated by a smaller energy $\Delta E \simeq \hbar v_F k_\theta - 2w$ (ANDREI 2020). Upon decreasing the twist angle, the saddle point ultimately reaches the Dirac nodes, and destroys the linear dispersion dispersion, as shown in Fig. 5.6. The energy split ΔE vanishes at the first magic angle $\theta_0 \simeq aw/\pi\hbar v_F$. With $w \simeq 0.1 \text{ eV}$ (KUZMENKO 2009; BISTRITZER 2011), $v_F \simeq 10^6 \text{ m} \cdot \text{s}^{-1}$

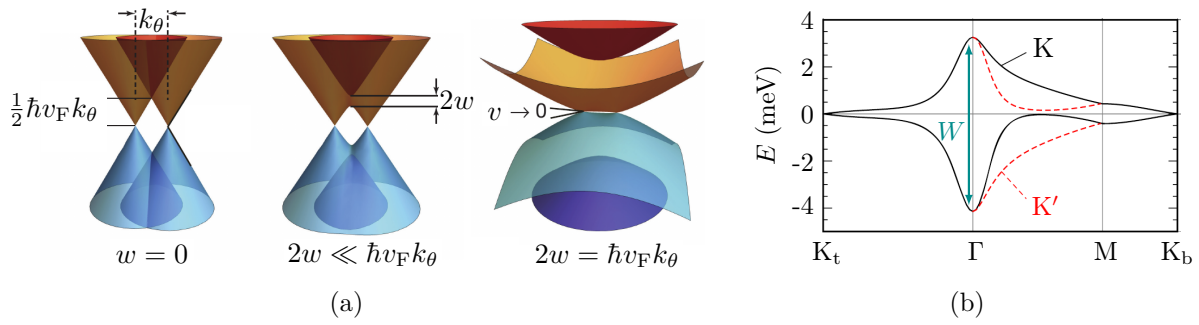


Figure 5.6 | (a) In a decoupled bilayer of graphene, the typical energy split between the particle and hole crossing points of the tilted Dirac cones is $\Delta E = \hbar v_F k_\theta$, where $v_F \simeq 10^6 \text{ m} \cdot \text{s}^{-1}$ is graphene's Fermi velocity. The momentum $k_\theta \propto K\theta$ represents the size of the moiré Brillouin zone; it is smaller than the Dirac momentum K by a factor θ , which is the low twist angle of the bilayer. After interlayer hopping is switched on, the top and bottom layer hybridise over an energy window $2w$, where w denotes the hopping amplitude. The energy split diminishes to $\Delta E = \hbar v_F k_\theta - 2w$. Reducing the twist angle suppresses utterly this energy split – and thus the typical kinetic energy – at the first magic angle $\theta_0 \simeq 1^\circ$. The Fermi velocity vanishes at the same time. Adapted from (CAO 2018a). (b) At the first magic angle $\theta_0 = 1.05^\circ$, the calculated band structure harbours two mini flat bands on either side of the neutrality point (zero energy). The K and K' valleys of graphene are conjugate under time reversal or six-fold rotation. Three properties characterise the magic angle physics: the Fermi velocity vanishes, leading to a quadratic low-energy dispersion; the bandwidth $W \simeq 8 \text{ meV}$ is minimal, which signals that the bands flatten out significantly; the gap with surrounding bands (beyond this panel) is maximal. Adapted from (KOSHINO 2018).

and $a \simeq 2.5 \text{ \AA}$, we estimate $\theta_0 \simeq 1^\circ$. This simple argument leads to a good quantitative agreement with analytical and numerical results, in particular with the band structure of Fig. 5.5. Close to the first magic angle, three phenomena happen.

- The Fermi velocity v vanishes at the Dirac points. This is observed in numerical (SUÁREZ MORELL 2010) and analytical studies (BISTRITZER 2011). In experiments, the slow-down of the quasi-particle motion manifests itself as a high effective mass in quantum oscillations (LUICAN 2011; CAO 2018a). As a result of the vanishing velocity, the dispersion relation becomes quadratic near the Dirac points, and the lowest mini bands flatten locally. The vanishing of the velocity results from charge carriers propagating with opposite velocities on the top and bottom layer, thus compensating with one another and leading to a zero net flow (BISTRITZER 2011).
- The bandwidth measured at the Γ point is minimal near the first magic angle. interlayer hopping reduces the bandwidth to values as low as $W \simeq 8 \text{ meV}$ (KOSHINO 2018), and thus enhances the DoS dramatically, which diverges at two energy levels that flank the neutrality point. These so-called Van-Hove singularities are seen in scanning tunnelling microscopy (LUICAN 2011).
- The energy gap between the flat mini (or active) bands and the passive bands immediately above and below, is maximal, about 14 meV (KOSHINO 2018). The active bands are well separated from the passive ones at the first magic angle.

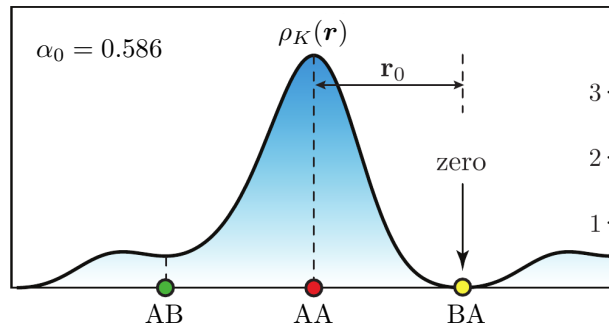


Figure 5.7 | Wave function density $\rho_K(\mathbf{r})$ (arbitrary units) of the zero energy mode of twisted bilayer graphene at the first magic angle. The electronic density peaks near AA stacking regions, while interlayer tunnelling tends to deplete AB and BA regions. In the special model presented here, where interlayer tunnelling preserves the chiral symmetry of graphene, the density vanishes exactly at B1A2 regions, where the label 1 (2) refers to the bottom (top) layer respectively. In passing, this difference between AB-BA regions illustrates the three-fold (instead of six-fold) symmetry of the single-valley continuum model. Adapted from (TARNOPOLSKY 2019).

The minimal bandwidth and maximal band gap occur close to, but not exactly at the first magic angle θ_0 . The slight discrepancies between the three criteria that characterise the magic angle physics come from unimportant details of how the layers couple to one another. In a simplified model which preserves the original chiral symmetry of graphene, these criteria all agree on the location of the magic angle: they all occur concomitantly at the exact value θ_0 (TARNOPOLSKY 2019). This chirally symmetric model delivers a unified and cohesive picture of the magic angle physics, and shows that the key ingredient is the tunnelling between the A and B sublattices of neighbour moiré cells. Tunnelling processes at smaller wave lengths or which operate on the same sublattice only add refinements. In particular, in the presence of chiral symmetry, the flat mini bands are pinned at zero energy. Besides, the wave function density condenses in islets centred at AA stacking regions, while it vanishes at BA regions, as in Fig. 5.7. These topographic features indicate that electrons are confined near the AA sites of the moiré pattern. In more realistic models, a small DoS appears on BA regions, and the flat bands acquire a weak dispersion in momentum space, which leads to a bandwidth $W \simeq 8 \text{ meV}$.

Comparison between kinetic and interaction energies — Details of the interlayer tunnelling aside, the quenching of the kinetic energy bears huge consequences for magic angle TBG. Flat bands and van Hove singularities are known to favour many-body effects (VOZMEDIANO 2002); electron-electron interactions, notably. We may estimate the Coulomb on-site energy as

$$U = \frac{e^2}{4\pi\epsilon d}, \quad (5.8)$$

where d is the effective size of the superlattice sites and ϵ the dielectric constant. Using the estimates $\epsilon = 10\epsilon_0$, and d about half the moiré period, we get $U \simeq 25 \text{ meV}$, which is several times larger than the bandwidth $W \simeq 8 \text{ meV}$ (CAO 2018a). Scanning tunnelling microscopy confirms this estimate of the Coulomb repulsion (XIE 2019; WONG 2020). We clearly see that interactions should dominate the electron dynamics, and dramatically alter the electronic properties predicted by band theory.

Higher-order magic angles — These phenomena are not restricted to the single magic value θ_0 , but appear repeatedly at smaller discrete magic angles θ_n , with n a positive integer, where the Fermi velocity vanishes exactly. The hierarchy of the magic angles is complex, but they seem to recur with a period $\Delta(\theta^{-1}) = 3/\theta_0$ in the chirally symmetric model (TARNOPOLSKY 2019). Chirality breaking should completely modify this quantitative prediction, however (BISTRITZER 2011). These extra magic configurations appear because the Fermi velocity changes signs beyond the first magic angle, and then oscillates back and forth as higher-order tunnelling processes dominate interlayer tunnelling. Because of this sign change, TBG undergoes a quantum phase transition from a semimetal to another semimetallic phase where the Dirac cones have reversed their helicity (FU 2018). Across this magic-angle critical point, TBG explores a narrow intermediate metallic phase with multifractal wave functions.

5.3 Experimental findings

Near the first magic angle, where the mini bands flatten out, many-body effects should control the electron’s dynamics. In 2018, the team led by P. Jarillo-Herrero first evidenced correlated phases in TBG, and thereby confirmed that the physics beyond the single-particle level is central to understanding moiré materials (CAO 2018a; CAO 2018b). These extraordinary discoveries spurred tremendous activity on the subject. After three years of intense research, much remains to understand. The phase diagram of TBG bears apparent similarities with that of high-temperature cuprates, with insulators at integer fillings of the mini bands surrounded by superconducting domes. Some correlated states, and in particular the insulator at the neutrality point, break the three-fold symmetry in the cleanest samples (LU 2019; JIANG 2019; CAO 2020b). The appearance of rotational symmetry breaking, but also most characteristics of the superconducting and insulating regions, depend strongly on the sample details. A strange metallic behaviour (CAO 2020a) and anti-ferromagnetism (SHARPE 2019; LU 2019), which is accompanied by an anomalous Hall effect, were also reported.

The microscopic mechanisms at play remain mysterious. While the insulating and superconducting orders were first thought to share a common origin, recent experiments suggest instead that they compete (STEPANOV 2020). Without aiming exhaustivity, this section outlines a selection of major experimental findings in the present state of knowledge. We will quickly narrow our focus to the nematic insulating behaviour found at charge neutrality, which we study theoretically in Chapter 7. For a pedagogical review on the topic, see (MACDONALD 2019). For more specialised expositions, see (ANDREI 2020; MOGERA 2020; BALENTS 2020).

5.3.1 Experimental setup

Sample preparation — Chemical synthesis has progressively superseded the historic method for graphene production, based on mechanical exfoliation. The so-called chemical vapour deposition technique enables to grow clean and large crystals of graphene with a high degree of tunability (GUAN 2020). By depositing methane on copper or nickel substrates, seeds of graphene grow by precipitation or adsorption, and ultimately form a continuous film. This technique extends to multilayer systems in several ways. Either the sample is exposed to a fresh copper foil placed upstream of the methane flow, so as to

grow new seeds on top of the first graphene flake; or hydrogen passivates the graphene edges to force methane to diffuse underneath the first flake. By tuning the methane concentration and pressure or the growth time, experimentalists precisely control the number of layers (LIU 2019). Unfortunately, chemical vapour deposition offers no control over the stacking arrangement. To form twisted bilayers, two graphene flakes must be overlaid by hand.

The tear-and-stack method enables to superimpose two layers with well-controlled twist angle (CAO 2016). Rather than using two distinct flakes, a single flake is torn apart and the lower piece rotated with the desired twist angle, before stacking the two layers. The initial graphene flake can be either exfoliated from graphite or grown chemically, but the first option is preferred over the second one, because chemically grown samples are highly polycrystalline, which offers no guarantee the two graphene pieces to be aligned before rotation. A precision of 0.1° over the twist angle can be achieved. Other techniques of synthesis rely on the delamination and folding of a graphene sheet on hydrophilic-hydrophobic substrates (WANG 2017), or Joule heating on a nickel foil (NI 2009). Using a polymer stamp, the twisted bilayer is then encapsulated between flakes of hexagonal boron nitride, and the stack deposited on SiO_2/Si substrate, as shown in Fig. 5.8(a). The polymer is finally removed using acetone or thermal annealing. To carry out transport measurements, the stack is sandwiched between metallic gates, on which two or more contacts are carved, as in the device of Fig. 5.8(b). The success of the procedure can be checked by optical imagery, as in Fig. 5.8(c), or Raman spectroscopy (MOGERA 2020), and the twist angle accurately measured by selected area electron diffraction (GUAN 2020).

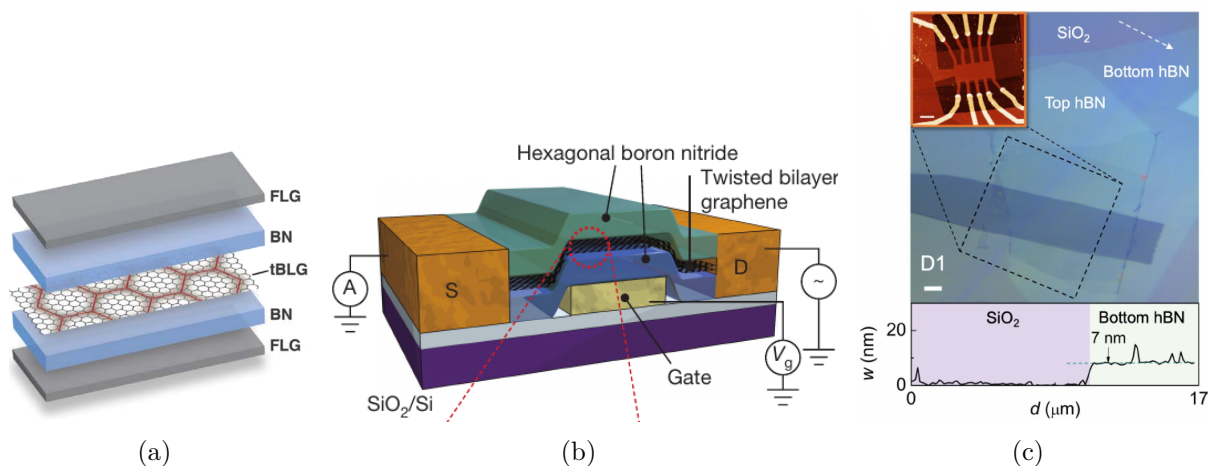


Figure 5.8 | (a) In transport experiments, twisted bilayer graphene (tBLG) is encapsulated in hexagonal boron nitride (BN). The whole stack is sandwiched between two metallic, graphitic, or here multilayer-graphene gates. Extracted from (YANKOWITZ 2019). (b) To measure the transport properties of twisted bilayer graphene, the bilayer edges are put into contact with a source (S) and drain (D), which impose the voltage and current. The gate below the bilayer is biased at a voltage V_g and controls the doping level. Extracted from (CAO 2018a). (c) The twisted bilayer, of width $w \simeq 7$ nm, is visible in optical microscopy (the dark patch). Exfoliated graphene flakes have a typical size of $10 \mu\text{m}$. To perform transport measurements, the bilayer graphene – hexagonal boron nitride (hBN) stack is deposited on a silicate (SiO_2) substrate, and eight contacts are connected to the gates. Extracted from (STEPANOV 2020).

Measurements techniques — Two techniques of measurement can probe the electronic properties of TBG: scanning tunnelling microscopy and transport. Scanning tunnelling microscopy enables to visualise the local electronic DoS. A metallic tip biased at a voltage $V_b \simeq 200$ mV with respect to the contact spans the sample’s surface. The microscope works either at fixed tunnelling current $I \simeq 10$ pA (where the height encodes the topography), or at fixed height (where the current encodes the topography) (JIANG 2019). The gate voltage V_g between the contact and the gate controls the doping of the sample. The tunnelling resistance $R = dI/dV_b$ gives a faithful map of the local DoS. Transport studies, on the other hand, gives access to the electrical conductance. The standard setups rely on a four-probe or eight-probe geometry, as in Fig. 5.8(c). The longitudinal conductance reveals insulating and superconducting regions in the phase diagram of TBG at low temperature, and gives access to thermal activation gaps. A magnetic field suppresses the resistive and superconducting behaviours, and the dependence of the conductance on its orientation reflects the spin or orbital nature of Zeeman splitting.

With the recent progress in photoemission spectroscopic technology at the submicrometric scale, ARPES has also been proposed to measure the twist angle, the interlayer hopping amplitude, and the spectral redistribution induced by electron-electron correlations (ZHU 2020).

5.3.2 Global phase diagram

Insulating and superconducting states — In 2018, the team led by P. Jarillo-Herrero at MIT reported the existence of correlated phases in magic angle TBG. Upon varying the doping level through the electrical gating method discussed in Sec. 5.3.1, the authors found insulating and superconducting phases (CAO 2018a; CAO 2018b). In the carrier density n – temperature T phase diagram alternate thin regions of insulating behaviour (with a large longitudinal resistance) and large superconducting domes (with a zero longitudinal resistance). Owing to the large gap that separates the active from the passive bands, conventional band insulators flank this collection of correlated states at empty or full filling of the moiré unit cell. Due to the spin and valley degeneracy, filling the active bands require four electrons per moiré cell, which corresponds to a filling factor $\nu = +4$, or equivalently to a carrier density $n_s = 4/A$, with A the surface of the moiré cell. The experimental value varies from sample to sample, but revolves around $n_s \simeq 3 \times 10^{-12}$ cm⁻². The measured charge gap of these band insulators, about 40 meV, is of the same order of magnitude as the one predicted by electronic band theory (Sec. 5.2.2).

The insulating phases which appear at intermediate filling factors ν are compatible with Mott insulators, in which electronic correlations open gaps within the degenerate active bands. These gaps induce a drop in the conductance measured in transport measurements at zero magnetic field, but also manifest themselves in quantum oscillations (CAO 2018b). The first experiments observed insulators only at half-filling of the active bands ($\nu = \pm 2$), but others were then found at all integer filling factors, on both the hole ($\nu = -3, -2, -1$) and particle ($\nu = 1, 2, 3$) sides of the active bands (YANKOWITZ 2019). In all cases, the charge gaps are of the order of 0.3 meV. Interestingly, in highly angle-homogeneous samples, an extra Mott insulator appears at charge neutrality ($\nu = 0$) (LU 2019). At all filling factors, the insulating character disappears above a temperature of the order of 4 K, where the sample becomes diffusive metallic. The insensitivity of the conductance to the field’s orientation points towards a spin-singlet insulator, i.e. the active bands

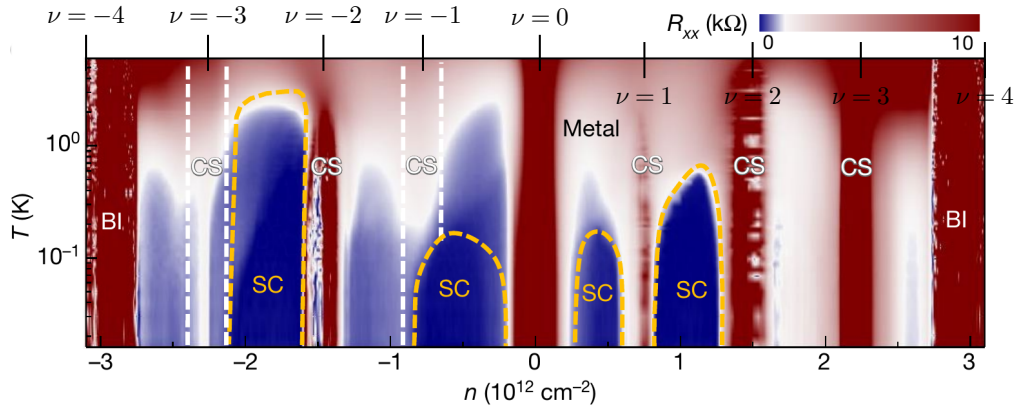


Figure 5.9 | Temperature T versus carrier density n phase diagram of twisted bilayer graphene at magic twist angle. The diagram spans all intermediate fillings of the active mini bands, and is centred around the charge neutrality point $n = 0$; two band insulators (BI) flank the diagram at full fillings, which corresponds to carrier densities $\pm n_s$ with $n_s \simeq 3 \times 10^{12} \text{ cm}^{-2}$, according to the hole (negative n) or particle (positive n) doping, as predicted by the single-particle physics. However, the longitudinal resistance R_{xx} peaks at integer filling factors $\nu = 0, \pm 1, \pm 2, \pm 3$ of the spin-valley degenerate mini bands, and signals correlated Mott-like insulators (CS). By contrast, it drops to zero within superconducting domes (SC) that surround some of the insulating regions. The critical temperature of a few Kelvin is enormous given the very low carrier density. Extracted from (LU 2019).

retain their spin degeneracy. In this scenario, the sample starts conducting when the Zeeman energy fills the charge gap. The existence of these insulating states is confirmed independently by capacitance measurements. In addition, the insulators at three-quarter fillings ($\nu = \pm 3$) exhibit a hysteretic anomalous Hall effect: a magnetic field generates a transverse conductivity, which persists when the field is switched off (SHARPE 2019). The insulators at three-quarter fillings also display ferromagnetism. Since the weak spin-orbit coupling cannot explain such a large susceptibility, the magnetisation probably originates from the orbital angular momentum of electrons. If these results were to be confirmed, TBG would be the first example of an orbital ferromagnet.

Though correlated phases were expected, the discovery of unconventional superconductivity in TBG stroke as a great surprise. Indeed, the emergence of nearby insulating states cannot be explained by the Bardeen-Cooper-Schrieffer theory, which relies on a weak electron-phonon coupling mechanism. From the current state of knowledge, superconductivity could equally well be mediated by phonon scattering (SHARMA 2020; CHOI 2018) or by pure electron-electron interactions. A perpendicular magnetic field $B_{\perp} \simeq 0.1 \text{ T}$ destroys the superconductivity, in agreement with a vortex-induced dissipation mechanism. Owing to the atomic thickness of TBG, an in-plane magnetic field $B_{\parallel} \simeq 1 \text{ T}$ also suppresses superconductivity, but through a different mechanism, probably through the Zeeman splitting of the Cooper pairs (CAO 2018b). As seen in Fig. 5.9, the critical superconducting temperature reaches values up to $T_c \simeq 2 \text{ K}$. This value is impressively high given the low carrier concentration: the critical to Fermi temperature ratio $T_c/T_F \simeq 0.08$ even exceeds that of cuprates by an order of magnitude (CAO 2018b). In addition, like in high-temperature cuprates, a strange metallic state surmounts the superconducting domes, which exhibits a linear T -dependence of the resistivity inconsistent with the Fermi liquid theory (CAO 2020a). Whether this anomalous metallic behaviour stems from the proximity

to quantum criticality or phonon scattering remains an open question (ANDREI 2020).

It is not known whether the insulating and superconducting phases arise from the same microscopic mechanism. In spite of the resemblance of the phase diagram of TBG with that of cuprates, where insulation and superconductivity are believed to share a common origin, some experiments showed that, unlike the superconducting domes, the insulating regions die out under moderate screening (STEPANOV 2020). This difference in robustness may indicate that two orders compete near the same filling factors.

Mott insulation at charge neutrality — The sample preparation and device geometry deeply affect the experimental results near the magic angle, because the band structure is extremely sensitive to strain and lattice relaxation. The tear-and-stack method introduces a significant amount of twist-angle heterogeneity, as a result of variations in local strain or the presence of substrate defects. Yet, even small modulations of the twist angle lead to a sizeable smearing of the electronic properties. Fortunately, several groups have devised a mechanical cleaning process which relaxes local strains and reach a high angle homogeneity (LU 2019; STEPANOV 2020). These clean samples revealed the existence of an strong insulator at charge neutrality, which was absent in earlier experiments, with a charge gap $\Delta = 0.86$ meV larger than at any other integer filling, as shown in Fig. 5.9.

Scanning tunnelling microscopy does not offer the precision necessary to observe a charge gap. Nevertheless, some authors reported pseudo-gaps at charge neutrality, i.e. large doping region where the local DoS near AA stacking sites is highly suppressed, but where band theory predicts a DoS peak instead, as large as 30 meV (JIANG 2019; KERELSKY 2019; CHOI 2019; XIE 2019). The pseudo-gap manifests itself in the tunnel conductance dI/dV , which shows a clear dip at charge neutrality surrounded by two peaks on the hole and electron sides.

5.3.3 Nematic phases

Several regions of the phase diagram of TBG break the three-fold symmetry of the moiré pattern. This is the case of the insulator at charge neutrality, which we discuss first. The physics at charge neutrality represents a natural starting point for an interacting theory of TBG, since this corresponds to the doping level where the single-particle low-energy theory is relativistic. For this reason, we will study the strong nematic insulator at the neutrality point. For completeness, we also discuss in this section other regions of the phase diagram which display nematicity.

Nematicity at charge neutrality — The insulator at charge neutrality also destroys the three-fold symmetry of TBG in favour of a preferred axis (JIANG 2019). Such electronic phase which breaks the lattice point group down to a two-fold symmetric group is termed nematic, in analogy with their classical equivalents, the liquid crystals (FRADKIN 2010). The origins of the orientational order differ entirely in quantum and classical phases, however. While molecules in liquid crystals have rod-like shapes, electrons are intrinsically isotropic entities. In Landau’s theory of Fermi liquids (which does not apply in TBG, unfortunately), the standard mechanism that leads to nematicity is a Pomeranchuk instability: when a Landau parameter becomes negative, the Fermi surface is distorted in a channel of possibly non-zero angular momentum ℓ , in which case a rotational order with lower symmetry settles. For a quadrupolar distortion ($\ell = 2$), the

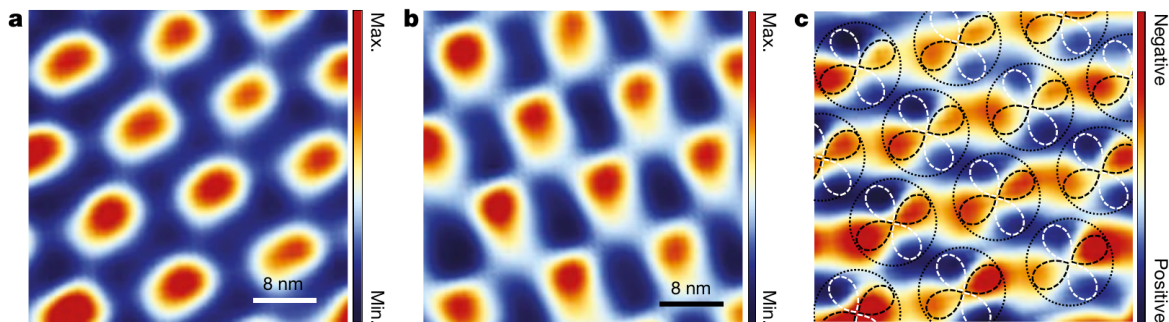


Figure 5.10 | The topography of the moiré superlattice, obtained by scanning tunnelling microscopy, reveals a stripe order in the charge distribution of undoped twisted bilayer graphene at the magic angle. The AA regions are electron doped (in red), while the neighbouring AB and BA regions are hole-doped (in blue). The lower band (a) and upper band (b) near charge neutrality display asymmetric charge distributions in orthogonal directions. The net charge distribution (c) displays a quadrupolar distortion, with two opposite lobes doped in holes, the other two doped in electrons. This nematic order generates stripes that break the six-fold rotational symmetry of the moiré pattern. Extracted from (JIANG 2019).

Fermi surface becomes elliptic and the order is nematic. Apart from TBG and cuprate superconductors, nematic electronic phases were found in the quantum Hall state of GaAs/GaAlAs heterostructures (LILLY 1999).

Evidencing nematicity in experiments can prove a subtle task (KIVELSON 2003). The nematic order manifests itself as anisotropies in transport measurements, diffraction patterns, or scanning tunnelling spectroscopic maps. A possible order parameter is the resistivity anisotropy defined by $\delta\rho = \rho_{xx} - \rho_{yy}$, where ρ_{ab} denotes the resistivity tensor, and where the x and y directions coincide with inequivalent crystalline axes. Similarly, electronic diffraction patterns reveal a nematic order as peaks of the form factors at unexpected wave vectors. Scanning tunnelling microscopy remains the optimal tool, since this technique probes a spatially resolved quantity (the local DoS) instead of spatially averaged quantities, as in transport measurements. As seen in Fig. 5.10, the insulator at charge neutrality displays a nematic order in the form of charge-ordered *stripes* in the DoS maps. The six-fold symmetry of the moiré pattern is clearly visible in the DoS maps, but the large hexagonal structure is accompanied by small spatial modulations near AA regions, where the DoS is maximal. We saw in Sec. 5.3.2 that the spectral weight is transferred from the charge neutrality point to the hole (lower band) and electron (upper band) sides. However, the orientation of the charge transfer differs in the lower (Fig. 5.10(a)) and (Fig. 5.10(b)) bands. As a result, the net charge distribution exhibits quadrupolar distortions and form ordered stripes separated by the moiré lattice constant (Fig. 5.10(c)).

Nematic superconductivity — A nematic ordering was also reported in a resistive patch shown in Fig. 5.11, which spread between the Mott insulator at half-negative filling ($\nu = -2$) and the nearby superconducting dome on the hole side of the spectrum (CAO 2020b). Using transport measurements, the authors observed a transverse resistivity ρ_{xy} at zero magnetic field, which can only stem from an anisotropy in the longitudinal resistivity, i.e. $\rho_{xy} \propto \rho_{xx} - \rho_{yy} \neq 0$. When a strong magnetic field destroys the superconducting phase, the nematic patch, which has a well-defined nematic axis, spread in the region

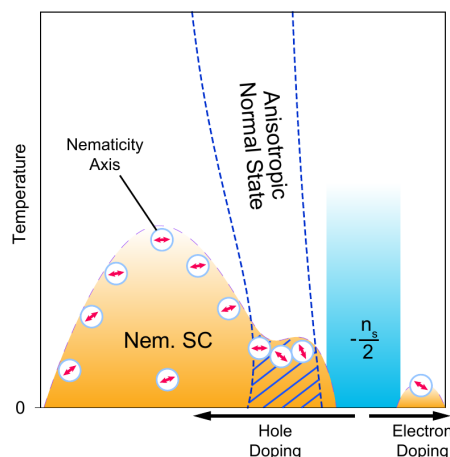


Figure 5.11 | Anisotropies in longitudinal transport measurements reveal a nematic order in TBG near half-hole filling, i.e for a number $-\nu = 2$ of active mini bands entirely empty. An anisotropic normal state develops between the correlated insulator at half-filling (blue region) and the left superconducting dome (yellow region). Both this resistive state and the nearby superconductor display a nematic order, but with different preferred direction. Since the nematic order of the resistive state spreads over the yellow region under a strong magnetic field that suppresses superconductivity, these two orders compete, and probably comes from distinct microscopic mechanisms. Extracted from (CAO 2020b).

initially occupied by the superconducting dome at zero field. On the other hand, both the longitudinal resistivity ρ_{xx} (along the drain-gate line) and the critical current respond anisotropically to a in-plane magnetic field in the superconductor. The field's orientation for which the resistivity drops, which is the direction favoured by the nematic order, varies continuously with carrier density across the dome. At the crossing with the resistive patch, it rotates quickly and align along the nematic axis of the resistive region, which is an entirely different direction. This observation tallies with the hypothesis of two nematic orderings competing; one intrinsic to the superconducting dome but with no preferred axis, the other pinned in a specific direction within the resistive patch. The nematic ordering of the superconducting region favours p -wave or d -wave Cooper pairings over of an isotropic, s -wave pairing, as found in conventional superconductors.

Several mechanisms could explain the appearance of a joint nematic-superconducting order. The suppression of superconductivity under in-plane magnetic fields (CAO 2018b) points towards a spin-singlet pairing (WU 2019). Some authors theorised from atomistic modelling that superconductivity develops through d -wave pairing as a result of strong on-site repulsion (as in cuprates) (LÖTHMAN 2021). In stark contrast to cuprates, though, the spectrum for Cooper pairs is fully gapped and the gap function highly inhomogeneous, which explains the moiré-scale nematicity. Other authors claimed using a Ginzburg-Landau phenomenology that the nematic order develops only under a magnetic field, but that the zero-magnetic field phase is chiral instead of nematic (YU 2021). A superconductor is chiral when the gap function acquires a non-zero phase when the momentum winds around a closed path of the Fermi surface (KALLIN 2016). Under an in-plane magnetic fields, two chiral superconducting orders with $p \pm ip$ pairings, which are both isotropic, could overlap and thus lead to an anisotropic transport response.

Conclusion

Summary — When two layers of graphene overlap with a relative twist, the interference of the two mismatched lattices form large-scale moiré patterns. Although the atomic sites of the bilayers organise into a periodic superlattice only at commensurate twist angles, the moiré pattern defines an effective Bravais lattice from which we can build a continuum description of the low-energy physics of twisted bilayer graphene. The corresponding mini Brillouin zone, which is a hundred times smaller than the Brillouin zone of graphene for twist angles $\simeq 1^\circ$, host two non-equivalent Dirac points at its corners associated to the two layers, but originating from the same valley of graphene. Yet, interlayer tunnelling in TBG strongly renormalises the spectrum by flattening the energy bands. At special ‘magic’ angles, the Fermi velocity of the Dirac cones vanish. Other phenomena accompany the magic angle physics, since the bandwidth of the flat bands becomes minimal and the gap with passive bands above and below maximal.

This dramatic quench of the kinetic energy leaves the door open for electron-electron interactions. Experiments confirmed the importance of many-body effects; twisted bilayer graphene displays indeed a rich and complex phase diagram, whose prominent features are the presence of insulators at integer fillings of the flat bands surrounded by superconducting domes. In particular, transport measurements and scanning tunnelling microscopy evidence the breaking of the three-fold rotational symmetry in several regions of the phase diagram, and notably in the strong insulator found at charge neutrality in the most angle-homogeneous devices. Twisted bilayer graphene offers unprecedented tunability. The tear-and-stack method allows for the high degree of control necessary to tune the twist angle precisely at the magic values and observe correlated phases. A low carrier density $n_s \simeq 3 \times 10^{12} \text{ cm}^{-2}$ suffices to explore the whole phase diagram, and can be easily achieved by voltage gating. On the contrary, changing the carrier density in cuprates (LEE 2006) or layered organic materials (POWELL 2011) requires to synthesis several samples each with different chemical doping. This takes time, and is less precise.

In the next chapters, we focus on the low-energy physics of twisted bilayer graphene near charge neutrality. After proposing a single-valley continuum model for the single-particle physics, we identify all insulating interaction channels allowed by symmetry, and study the emergence of a gap and a nematic order through a renormalisation group approach. This project was done in collaboration with L. Savary at the Laboratoire de Physique, and led to the preprint (BRILLAUX 2020).

Outlook — We will restrict our study to twisted bilayer graphene at the first magic angle $\theta_0 \simeq 1.1^\circ$. It is worth mentioning that correlated phases were also observed in twisted bilayer graphene at lower magic angles, in particular at the second magic angle $\theta_1 \simeq 0.5^\circ$ (LU 2020). Achieving such higher-order magic twists is challenging, because the lower the twist angle, the higher the relative sensitivity of the magic angle condition. Thicker Van der Waals heterostructures also develop moiré patterns under a twist, and were similarly theorised to host flat mini bands (KHALAF 2019; CHEBROLU 2019; MORA 2019). Experiments have evidenced correlated phases in trilayer graphene (CHEN 2019; CHEN 2020), twisted double-bilayer graphene (SAMAJDAR 2021), and 30° -twisted bilayer graphene (YAO 2018).

Low-energy theory near charge neutrality

In the previous chapter, we explained with a simple energetic argument the origin of band flattening in magic angle twisted bilayer graphene. When the twist angle becomes small enough that the kinetic energy is comparable to the interlayer tunnelling amplitude, the Fermi velocity of the Dirac cones vanishes, and the overall bandwidth is minimal. To demonstrate the exact vanishing of the Fermi velocity, we need a low-energy effective theory. This effective relativistic theory also provides a basis to incorporate many-body effects and study the nematic insulator observed at charge neutrality. The sublattice and layer degrees of freedom play a key role in the electron dynamics at the magic angle, while in a first approximation, the spin and valley degrees of freedom can be ignored.

In the present chapter, we thus propose a single-valley low-energy description of twisted bilayer graphene, close in spirit to the seminal continuum model introduced by R. Bistritzer and A. MacDonald, but where the ratio of intra- over inter-sublattice hopping amplitudes is kept as a free parameter. After presenting the single-particle description, we identify all contact quartic interactions allowed by the symmetries of the model: the three-fold out-of-plane rotation, a mirror symmetry, a particle-hole symmetry, and an antiunitary symmetry stemming from the combination of time reversal and spatial inversion. We restrict this classification to particle-hole channels, which are commonly at the origin of correlated insulating phases.

6.1	Single-particle description	156
6.1.1	The single-valley continuum model	156
6.1.2	Hopping strength expansion	159
6.2	Algebraic classification of interaction channels	163
6.2.1	Symmetry analysis of the model	164
6.2.2	Symmetry-preserving contact interactions	167
	Conclusion	172

6.1 Single-particle description

Experiments find correlated states at partial fillings of the two flat bands (per spin and valley) closest to charge neutrality. Because of the large band gap that separates these flat bands from the rest of the spectrum, a minimal low-energy theory can be restricted to the Hilbert space composed of those flat bands. In a first approximation, the degrees of freedom of sublattice and layer dictate the dynamics, while the electronic spin and the presence of two valleys can be ignored. This single-valley continuum model leads to a low-energy theory which is already far from standard at the single-particle level, because of the spatial modulation of the interlayer tunnelling amplitude over the moiré period. To diagonalise the Hamiltonian, we thus resort to an approximation scheme: we assimilate the hopping term as a perturbation of the kinetic term, and expand the Hamiltonian accordingly.

6.1.1 The single-valley continuum model

Physical ingredients — The low-energy theory of twisted bilayer graphene comprises four degrees of freedom, each associated to a spin one-half fermion: the valley of graphene, the electronic spin, the sublattice, and the layer. Yet, intervalley scattering involves the transfer of momenta of the order of the Dirac momentum K , which exceeds the size of the mini Brillouin zone $k_\theta \simeq K\theta$ by several orders of magnitude in the low twist angle limit, where typically $\theta \simeq 1^\circ$. Hence, the valley degree of freedom can be ignored. Similarly, spin-orbit coupling plays a minor role in graphene, so that we can neglect the electronic spin in a first approximation. As we did for Bernal-stacked bilayer graphene in Sec. 5.1.1, we now build a simple tight-binding model for the low-energy excitations of the twisted bilayer, using the sublattice and layer as inputs. Three ingredients of the model are the geometry, the intralayer dynamics, and the interlayer coupling (BALENTS 2019).

First, the layer twist results in a change of coordinates, which shifts the Dirac point of the valley K from \mathbf{K} to $\mathbf{K}_{\mathbf{t},\mathbf{b}}$ for the top and bottom layers respectively. The twist also implements a rotation of the pseudospin $\boldsymbol{\sigma}$, which is tied to the orientation of the sublattices within each layer. The interplay between these geometrical effects and intralayer dynamics leads to the following Hamiltonian of the decoupled twisted layers:

$$\hat{\mathcal{H}}_s = iv_F \left(R_{s\theta/2} \boldsymbol{\sigma} \right) \cdot \boldsymbol{\partial} + \frac{s}{2} v_F \boldsymbol{\sigma} \cdot \mathbf{q}_1, \quad (6.1)$$

where v_F is the Fermi velocity of graphene, $s = +1$ (-1) for the top (bottom) layer, and the momentum $\mathbf{q}_1 = \mathbf{K}_{\mathbf{t}} - \mathbf{K}_{\mathbf{b}}$ is represented in Fig. 5.4. The rotation of the pseudospin implemented by the operators $R_{s\theta/2}$ has no qualitative consequences, and can be safely ignored in Eq. (6.1); besides, it corrects the dynamics at order θ only. On a strained layer, the Hamiltonian acquires an artificial gauge field due to the local in-plane deformation of the bonds (MAÑES 2013) and the out-of-plane relaxation of the bilayer (GUINEA 2008). Assuming that the layers undergo a perfectly rigid rotation, the change of coordinates preserves the dynamics of the Dirac fermions in the frame of reference of the twisted layers, and Eq. (6.1) captures all aspects of the intralayer dynamics.

Last but not least, the proximity of the two graphene sheets leads electronic orbitals on both sides to overlap significantly, which allow for Dirac fermions to hop between layers.

The Hamiltonian for the coupled bilayer thus contains hopping terms that are off diagonal in layer, which we write generically as

$$\hat{\mathcal{H}} = \begin{pmatrix} \hat{\mathcal{H}}_+ & \hat{T}(\mathbf{r}) \\ \hat{T}^\dagger(\mathbf{r}) & \hat{\mathcal{H}}_- \end{pmatrix} = \begin{pmatrix} v_F \boldsymbol{\sigma} \cdot \left(i \boldsymbol{\partial} + \frac{\mathbf{q}_1}{2} \right) & \hat{T}(\mathbf{r}) \\ \hat{T}^\dagger(\mathbf{r}) & v_F \boldsymbol{\sigma} \cdot \left(i \boldsymbol{\partial} - \frac{\mathbf{q}_1}{2} \right) \end{pmatrix}. \quad (6.2)$$

An uncommon feature of Hamiltonian (6.2) is that the tunnelling matrix $T(\mathbf{r})$ depends explicitly on position \mathbf{r} , as a result of the twist destroying translational symmetry at the atomic scale. This tunnelling matrix obeys the translational invariance of the large-scale moiré pattern, however; we decompose it as a Fourier series over the reciprocal superlattice generated by the vectors $\mathbf{Q}_1 = \mathbf{q}_2 - \mathbf{q}_1$ and $\mathbf{Q}_2 = \mathbf{q}_3 - \mathbf{q}_1$, where \mathbf{q}_3 and \mathbf{q}_2 are defined in Fig. 5.4. As was proven analytically and numerically, the hopping amplitude falls off rapidly with momentum, so that a few first Fourier components dominate the series (BISTRITZER 2010; BERNEVIG 2020a). To ensure the three-fold rotational symmetry of the Hamiltonian, we keep the three coefficients

$$\hat{T}(\mathbf{r}) = \hat{T}_0 + e^{-i\mathbf{Q}_1 \cdot \mathbf{r}} \hat{T}_1 + e^{-i\mathbf{Q}_2 \cdot \mathbf{r}} \hat{T}_2, \quad (6.3)$$

where the constant hopping matrices for $j = 0, 1, 2$ read

$$\hat{T}_j = u \sigma_0 + w \left(\zeta^j \sigma_+ + \zeta^{-j} \sigma_- \right), \quad (6.4)$$

where $\zeta = e^{2i\pi/3}$. The pseudospin ladder operators $\sigma_\pm = \frac{1}{2}(\sigma_x \pm i\sigma_y)$ present in the second term of Eq. (6.4) implement the hopping of Dirac fermions between sites A and B of distinct layers. The parameter $w \simeq 110$ meV, which we introduced phenomenologically in Sec. 5.2, thus quantifies the inter-sublattice hopping strength (BISTRITZER 2011). The first term of Eq. (6.4), proportional to the identity in the sublattice sector, describes intra-sublattice hopping processes with strength u . We will keep u and w as free independent parameters, because lattice relaxation suppresses the on-diagonal hopping amplitude u with respect to the off-diagonal one w . Lattice relaxation tends indeed to pull the layers away near AA-stacked regions – a mechanism known as corrugation –, resulting in spatial modulations of the interlayer distance (KOSHINO 2018). Numerical calculations find $u \simeq 90$ meV (LUCIGNANO 2019).

Change of basis and limit models — To simplify the form of the Hamiltonian (6.2), it is judicious to relocate the two Dirac cones at the same crystal momentum. We achieve this change of basis through the unitary transformation

$$\mathcal{H} = A(\mathbf{r})^\dagger \hat{\mathcal{H}} A(\mathbf{r}), \quad A(\mathbf{r}) = \exp \left(-\frac{i\mathbf{q}_1 \cdot \mathbf{r}}{2} \tau_z \right), \quad (6.5)$$

where (τ_x, τ_y, τ_z) denote the Pauli matrices in the layer sector. Furthermore, we remove all dimensions by measuring momenta in units of the size of the mini Brillouin zone k_θ , and energies in units of the kinetic energy $E_K = v_F k_\theta$. The resulting Hamiltonian is

$$\mathcal{H} = i\tau_0 \boldsymbol{\sigma} \cdot \boldsymbol{\partial} + \alpha \sum_{j=1}^3 \sum_{\eta=\pm} e^{-i\eta \mathbf{q}_j \cdot \mathbf{r}} T_j^\eta, \quad (6.6)$$

where $\alpha = w/E_K$ represents the dimensionless strength of inter-sublattice hopping. Note that the index j now runs from 1 to 3, unlike in Eq. (6.4). The index $\eta = \pm$ indicates a hopping from the bottom to the top layer for the plus sign, and vice versa for the minus sign. The four-times-four hopping matrices T_j^η present in the second term of Eq. (6.6) split into two conjugate blocks in the layer sector. The upper right block

$$T_j^+ = \tau_+ \left(\beta \sigma_0 + \zeta^{j-1} \sigma_+ + \zeta^{1-j} \sigma_- \right) \quad (6.7)$$

describes bottom-to-top tunnelling, while the lower left block $T_j^- = (T_j^+)^\dagger$ describes top-to-bottom tunnelling. The parameter $\beta = u/w$ is the relative intra- versus inter-sublattice hopping strength. As for the pseudospin, τ_\pm denote the ladder operators in the layer sector. Three limit cases can be considered according to the value of β .

- The isotropic limit $\beta = 1$ ($u = w$) corresponds to the seminal Bistritzer-MacDonald model (BISTRITZER 2011). This model explains well the vanishing Dirac velocity and finds a good estimate for the first magic angle. Still, it misses some qualitative features of the band structure, in particular, the existence of a gap between the active flat bands and the excited bands.
- The first chiral limit $\beta = 0$ ($u = 0$ with w non-zero) restores the original chiral symmetry of monolayer graphene, implemented by the operator σ_z . This model has a remarkable mathematical structure, since the eigenvalue equation can be solved exactly using complex analysis. The local DoS vanishes exactly at the B1-A2 regions, and a perfectly flat band develops at zero energy (TARNOPOLSKY 2019). This model captures correctly the phenomenology of the magic angles, and unifies the different notions of band flatness (maximal band gap, minimal bandwidth, zero Fermi velocity) under a single definition, because these three phenomena happen precisely at the same twist angle. Moreover, a simple law relates the magic angles that also appear in multilayer extensions of the model to the first magic angle of TBG (KHALAF 2019).
- The second chiral limit $\beta = \infty$ with $\alpha = 0$ ($w = 0$ with u non-zero) has interesting properties as well (BERNEVIG 2020b). This model enjoys a hidden chiral symmetry implemented by the operator $\tau_z \sigma_z$. This extra symmetry forces the energy spectrum to be fully connected, leaving no gaps between active and passive bands. Such band structure leads to a ‘perfect’ metallic behaviour, to the extent that the DoS remains sizeable at all energies. Yet, this second chiral limit corresponds to an unphysical configuration where the two layers are closer to one another in AA regions than in AB/BA regions, which is incompatible with lattice relaxation. In addition, intra-sublattice hopping enhances the Fermi velocity instead of suppressing it, so that the magic angle physics does not apply in this model.

In practice, numerical studies find $\beta \simeq 0.8$ (LUCIGNANO 2019). Given the uncertainty on this estimate, and the sensitivity of the band structure to intra-sublattice hopping, we will keep β as a free parameter.

Gauge potential formulation — Interestingly, the spatial modulation of interlayer tunnelling acts for the Dirac fermions as a background non-Abelian potential $A_\mu = (\Phi, \mathbf{A})$, with Hamiltonian (SAN-JOSE 2012)

$$\mathcal{H} = \boldsymbol{\sigma} \cdot [i\boldsymbol{\partial}\tau_0 + \alpha\mathbf{A}(\mathbf{r})] + \alpha\beta\Phi(\mathbf{r}). \quad (6.8)$$

This non-Abelian potential lives in the layer $\mathfrak{su}(2)$ algebra, being a linear superposition of the generators τ_x and τ_y . The vectorial part \mathbf{A} accounts for inter-sublattice hopping, and couples to the fermions with a strength α . The scalar part Φ accounts for intra-sublattice hopping, and couples to the fermions with a strength $\alpha\beta$. Such potentials are known to induce intriguing interference phenomena, which are absent in conventional $U(1)$ gauges (of the Aharonov-Bohm type). These interferences tend to confine zero-energy electronic waves near the AA stacking regions, which explains the enhancement of the local DoS observed in Fig. 5.7. This reformulation in terms of gauge potential brings to light interesting parallels between the interlayer coupling dynamics in moiré materials and quantum field theories.

Diagonalisation of the Hamiltonian — To determine the interlayer hopping corrections to the Fermi velocity, we diagonalise Hamiltonian (6.6). The kinetic term poses no problem (it is diagonal in momentum space), but the hopping term depends explicitly on position, and renders an exact diagonalisation extremely difficult. Instead, we treat interlayer hopping as a perturbation of the kinetic term, and expand the Hamiltonian order by order in α . This method provides analytical results for the corrected Fermi velocity, and therefore, the values of the magic angles. Unfortunately, it applies only to a small domain of twist angles. On one hand, the continuum description requires the twist angle θ to be small. On the other hand, the smaller θ , the larger the dimensionless hopping strength $\alpha \propto \theta^{-1}$, and the less accurate the perturbative expansion. We will see that the first magic angle $\theta_0 \simeq 1.1^\circ$ corresponds to a magic value α_0 of order unity, so that the perturbative approach offers less control over smaller magic angles, which appear as higher order zeros of the Fermi velocity.

6.1.2 Hopping strength expansion

Following the idea of (BISTRITZER 2011; TARNOPOLSKY 2019), we expand the Hamiltonian in the dimensionless hopping strength α , while treating β non-perturbatively (BRILLAUX 2020). To deal with the highly non-standard low-energy theory of TBG, where the lattice mismatch leads to large spatial modulations of the hopping amplitude, we develop a diagrammatic technique to organise the perturbative expansion. The Feynman rules we introduce here will also be useful for the interacting theory studied in Chapter 7. The self-energy encodes the correction to the wave function amplitude and the band structure induced by interlayer hopping.

Perturbative approach — The Green's function associated to the Hamiltonian of the decoupled bilayer $\mathcal{H}_0 = i\boldsymbol{\sigma} \cdot \boldsymbol{\partial}$ is

$$G_0(\mathbf{k}, \Omega) = (\boldsymbol{\sigma} \cdot \mathbf{k} - i\Omega)^{-1} \quad (6.9)$$

in Fourier space, where \mathbf{k} is the momentum, Ω the Mastubara frequency¹, and we omitted the identity matrices σ_0 and τ_0 for brevity. We set $v_F = 1$, so that the Fermi velocity corrected by interlayer hopping is measured in units of the Fermi velocity of graphene.

¹As a general rule, we distinguish between external momentum \mathbf{k} and frequency Ω , and internal momentum \mathbf{q} and frequency ω , which appear as integration variables in the interacting theory.

In analogy with quantum field theories, we will refer to Eq. (6.9) as the free propagator. Other correlation functions are generated by the free action

$$S_0 = \int d^2r d\tau \bar{\psi}(\mathcal{H}_0 - \partial_\tau)\psi = \int_{\mathbf{k}, \Omega} \bar{\psi}_{\mathbf{k}}(\boldsymbol{\sigma} \cdot \mathbf{k} - i\Omega)\psi_{\mathbf{k}}, \quad (6.10)$$

where $\{\bar{\psi}, \psi\}$ are two Grassman fields, and we assimilate $\bar{\psi}$ to the conjugate Dirac field Ψ^\dagger instead of the adjoint $\bar{\Psi}$.

Similarly, the hopping term of the Hamiltonian (6.6) can be represented by the action

$$S_\alpha = \alpha \sum_{j=1}^3 \sum_{\eta=\pm} \int d^2r d\tau (\bar{\psi} T_j^\eta \psi) e^{-i\eta \mathbf{q}_j \cdot \mathbf{r}} = \alpha \sum_{j=1}^3 \sum_{\eta=\pm} \int_{\mathbf{k}, \Omega} \bar{\psi}_{\mathbf{k}} T_j^\eta \psi_{\mathbf{k} + \eta \mathbf{q}_j}. \quad (6.11)$$

This hopping action S_α breaks the continuous translational invariance of the kinetic action S_0 down to a discrete translational invariance on the moiré lattice $\mathbf{d}_1\mathbb{Z} + \mathbf{d}_2\mathbb{Z}$, where \mathbf{d}_1 and \mathbf{d}_2 are the superlattice vectors of Fig. 5.2. As a result, the Fourier space representation of the action (6.11) couples conjugate fields at *different* momenta \mathbf{k} and $\mathbf{k} + \eta \mathbf{q}_j$. The low-energy description described by the full action $S'_0 = S_0 + S_\alpha$ is highly unusual: unlike most free field theories, it does not conserve momentum. Because of this non-conservation, the quantum action contains an infinite number of two-point vertices where the total momentum is preserved only up to a vector \mathbf{Q} of the reciprocal superlattice, which is generated by the (linearly dependent) family of vectors $\{\mathbf{q}_j, j = 1, 2, 3\}$. The two-point connected correlation functions thus take the form of the infinite sum

$$\langle \psi_{\mathbf{k}, \Omega} \bar{\psi}_{\mathbf{k} + \mathbf{q}, \Omega} \rangle'_0 = \sum_{\mathbf{Q} \in \mathcal{R}} G'_0(\mathbf{Q}, \mathbf{k}, \Omega) \delta(\mathbf{Q} - \mathbf{q}). \quad (6.12)$$

The term of Eq. (6.12) with zero momentum transfer $\mathbf{Q} = \mathbf{0}$, abbreviated as $G'_0(\mathbf{k}, \Omega) = G'_0(\mathbf{0}, \mathbf{k}, \Omega)$, indicates how interlayer hopping renormalises the dispersion relation. We introduce the translational-invariant part Σ' of the self-energy such that

$$G'_0(\mathbf{k}, \Omega)^{-1} = G_0(\mathbf{k}, \Omega)^{-1} - \Sigma'(\mathbf{k}, \Omega). \quad (6.13)$$

In the low-energy limit $k, \Omega \ll 1$, we expect the self-energy to take the same form as the kinetic term of the decoupled bilayer. At lowest order in \mathbf{k} and Ω , we can write

$$\Sigma'(\mathbf{k}, \Omega) \simeq (1 - N_\psi)(\boldsymbol{\sigma} \cdot \mathbf{k} - i\Omega) + N_\psi \delta v \boldsymbol{\sigma} \cdot \mathbf{k}. \quad (6.14)$$

The parameter $N_\psi(\alpha, \beta)$ diminishes the amplitude of the wave function, while $\delta v(\alpha, \beta)$ reduces the Fermi velocity from unity to $v = 1 - \delta v$. The series of magic angles and their corresponding magic hopping strengths α_n are those which fulfil $v(\alpha_n, \beta) = 0$.

Diagrammatic expansion of the self-energy — In standard field theories, the self-energy, being a two-point vertex function, can be represented as one-particle irreducible graphs. As a natural extension of this property, the contributions to Σ' come from the connected two-point diagrams that conserve total momentum and that cannot be cut by one stroke into two subdiagrams that conserve themselves total momentum. We can define the following Feynman rules.

- A free propagator is depicted as a solid line

$$G_0(\mathbf{k}, \Omega) = (\boldsymbol{\sigma} \cdot \mathbf{k} - i\Omega)^{-1} = \longrightarrow \quad (6.15)$$

For pedagogical reasons, we keep the arrow that indicates the direction of momentum in the following Feynman rules, but will soon drop it to ease the reading of graphs with more complex topology.

- The corrected propagator is depicted as a double line

$$G'_0(\mathbf{k}, \Omega) = \Longrightarrow \quad (6.16)$$

- The insertion of a hopping matrix T_j^η inside a correlation function is accompanied with the transfer of a momentum $\eta\mathbf{q}_j$. We represent this insertion with a wavy line. Each insertion contributes a factor α to the correlation function.

$$\alpha T_j^\eta = \begin{array}{c} \eta, j \\ \text{wavy line} \\ \longrightarrow \mathbf{k} \quad \longrightarrow \mathbf{k} + \eta\mathbf{q}_j \end{array} \quad (6.17)$$

- The algebra of the hopping matrices, along with Σ' satisfying translational invariance, impose stringent conditions on which graphs actually contribute. Let us consider successive hopping processes with momentum transfers $\{\eta_1\mathbf{q}_{j_1}, \dots, \eta_m\mathbf{q}_{j_m}\}$ in this precise order. The corresponding two-point diagram vanishes unless

(i) total momentum is conserved, i.e. $\sum_{r=1}^m \eta_r \mathbf{q}_{j_r} = \mathbf{0}$;

(ii) consecutive hopping processes affect distinct layers, i.e. $\eta_{2r} = -\eta_{2r-1}$ for all $r = 1, 2, \dots, m/2$ with m even.

Condition (ii) forbids odd numbers of insertions, so that all correlation functions can be expanded in α^2 instead of α . It also implies that a hopping sequence is entirely determined by the sign of the first hopping process $\eta = \eta_1$ and the channels j_1, j_2, \dots, j_m of the subsequent transfers. Combined with condition (i), it further yields that the transfer of a momentum at one point of the diagram must be followed by the transfer of the opposite momentum at another point. Thus we can join insertions of opposite momenta by a single wavy line, as in Fig. 6.1(a). Furthermore, the total count of wavy line crossings must be even. Hence the sixth order diagram 6.1(e) contributes, whereas the analogue of diagram 6.1(b) where the two wavy lines cross vanishes.

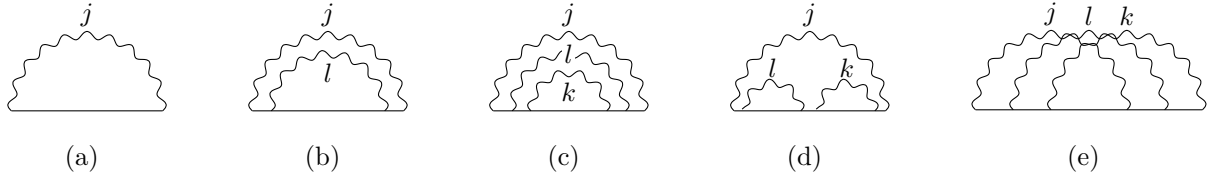


Figure 6.1 | Diagrammatic expansion of the self-energy to order six in the dimensionless hopping strength $\alpha = w/E_K$, where w is the AA hopping amplitude and E_K the typical kinetic energy of the decoupled twisted layers. A wavy line stands for a pair of hopping processes; it bears an index j (or l, k at higher orders) and carries a momentum \mathbf{q}_j , summed over the channels $j = 1, 2, 3$ arising from the three-fold rotational symmetry. Each graph is summed over the sign $\eta = \pm$ of the first momentum transfer, which corresponds to bottom-to-top ($\eta = +$) or top-to-bottom hopping ($\eta = -$). We show here the graphs at order (a) two (b) four, and (c-e) six in α . At order six, the hopping lines can be (c) nested, (d) in a row, or (e) crossed.

Determination of the magic angles — We are now able to expand the self-energy to an arbitrary order in α . In the following, we restrict ourselves to the sixth order. The interested reader may find the details of the computation in Appendix E. Within the low-energy limit $k, \Omega \ll 1$, we can further expand at lowest order in momentum \mathbf{k} and frequency Ω . Then, the translational-invariant part of the corrected propagator can be massaged into

$$G'_0(\mathbf{k}, \Omega) \simeq N_\psi^{-1} (v\boldsymbol{\sigma} \cdot \mathbf{k} - i\Omega)^{-1}, \quad (6.18)$$

where the normalisation of the wave function reads

$$N_\psi = 1 + 3\alpha^2(1 + \beta^2) + 2\alpha^4(1 + 7\beta^2 + 4\beta^4) + \frac{3}{28}\alpha^6(8 + 16\beta^2 + 376\beta^4 + 187\beta^6) + O(\alpha^8). \quad (6.19)$$

In addition, the Fermi velocity corrected by interlayer hopping v follows from the relation

$$N_\psi v = 1 - 3\alpha^2 + \alpha^4(1 - \beta^2)^2 - \frac{3}{49}\alpha^6(37 - 112\beta^2 + 119\beta^4 - 70\beta^6) + O(\alpha^8). \quad (6.20)$$

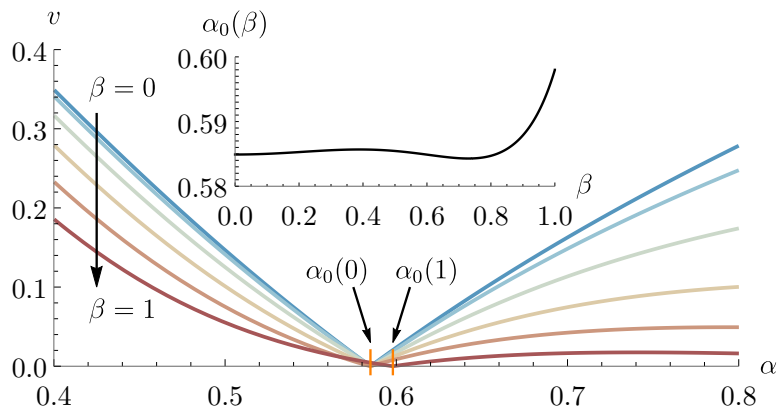


Figure 6.2 | Fermi velocity corrected by interlayer hopping $v(\alpha, \beta)$ at order α^6 , as a function of the dimensionless hopping strength α in units of the kinetic energy. As the twist angle increases, so does α , and the velocity vanishes at the first magic manifold $\alpha_0(\beta)$, which corresponds to the first magic angle $\theta_0 \simeq 1.1^\circ$. The parameter β quantifies the asymmetry between intra- and inter-sublattice hopping, which originates from lattice relaxation. Inset: the first magic angle $\alpha_0(\beta)$ depends weakly on β , and thus on corrugation effects.

The first magic angle corresponds to the lowest α for which Eq. (6.20) vanishes. A quick estimate gives $\alpha_0 \simeq 1/\sqrt{3}$, as was originally found in the seminal works (LOPES DOS SANTOS 2007; SHALLCROSS 2010; BISTRITZER 2011); this sets the first magic angle about $\theta_0 \simeq 1.1^\circ$, in excellent agreement with experiments. Due to lattice relaxation, the vanishing of v defines in fact a magic manifold $\alpha_0(\beta)$ in parameter space. As shown in Fig. 6.2, the above estimate of the first magic angle is trustworthy, because the first magic hopping strength depends weakly on β . It ranges from $\alpha_0(1) = 0.598$ in the isotropic limit to $\alpha_0(0) = 0.585$ in the first chiral limit (these limits were defined in Sec. 6.1.1). This robustness with respect to the precise strength of intra-sublattice hopping breaks down for the higher-order magic manifolds $\alpha_n(\beta)$ with $n > 0$, where the perturbative expansion is less controlled. In the second chiral limit, where $\alpha\beta \propto u$ remains finite and $\alpha \propto w$ is set to zero, hopping corrections to the Fermi velocity are weaker, of the order $N_\psi v - 1 \simeq (\alpha\beta)^4$, as originally noted by (MELE 2011).

Many numerical studies report that the vanishing of the Dirac velocity, the maximal band gap and the minimal bandwidth occur almost at the same magic value α_0 , thereby showing the universality of the magic angle physics. Apart from the chirally symmetric model, where the flat bands appear at exactly zero energy due to the mathematical structure of the eigenvalue equation, the reason why these phenomena happen simultaneously is obscure. A. Bernevig et al. showed in an approximate two-band model that the bandwidth vanishes exactly on a *different* magic manifold (BERNEVIG 2020a)

$$\alpha'_0(\beta) = 2\sqrt{1 + \beta^2} - \sqrt{2 + 3\beta^2}. \quad (6.21)$$

Yet, these two manifolds stay extremely close for moderate amplitudes of intra-sublattice hopping (for β between 0 and 1), which explains why tuning the model away from the chiral limit preserves the band flatness with an excellent accuracy.

Exactly at the first magic angle, the dominant correction to the relation dispersion is quadratic. To order two in momentum, we find indeed

$$\Sigma'(\mathbf{k}, \Omega) \simeq \frac{\tau_z}{2m} \begin{pmatrix} 0 & ik^2 \\ -i\mathbf{k}^{*2} & 0 \end{pmatrix} + (N_\psi - 1)i\Omega\tau_0\sigma_0, \quad (6.22)$$

where $\mathbf{k} = k_x + ik_y$, and the fermion mass m is such that $m^{-1} = 6(\alpha\beta)^2 [1 - 3\alpha^2(1 - \beta^2)]$. The low-energy band structure becomes similar to that of the Bernal-stacked bilayer, where massive chiral fermions emerge as elementary excitations. This parabolic dispersion is fully consistent with numerical findings.

6.2 Algebraic classification of interaction channels

We now use the symmetries of the single-valley model developed in Sec. 6.1 to identify all allowed contact interactions near charge neutrality. We will consider only particle-hole repulsive channels (the ones relevant for an insulating ground state), such as those that arise from electron-electron Coulomb interaction. We base our analysis on the theory of the linear representations of groups. Appendix D reviews the definitions and theorems needed to perform this group-theoretical analysis. For specialised papers and books on group theory, see (DIXON 1970; GAO 2002; MA 2007; MA 2004; DRESSELHAUS 2007).

6.2.1 Symmetry analysis of the model

Generators of the symmetry group — Interlayer hopping strongly restricts the symmetries of the single-particle Hamiltonian $\mathcal{H} = \mathcal{H}_0 + \mathcal{H}_\alpha$ given in Eq. (6.6). Indeed, the Hamiltonian of the decoupled bilayer $\mathcal{H}_0 = i\tau_0 \boldsymbol{\sigma} \cdot \boldsymbol{\partial}$ is invariant under the combination of inversion and time reversal $\Theta = \mathcal{IT}$, an accidental particle-hole symmetry \mathcal{P} , which we will soon define, space-time translations \mathbb{R}^{1+2} , and the Lorentz transformations $O(1, 2)$. The two former sets form the Poincaré group $\mathbb{R}^{1+2} \rtimes O(1, 2)$, where \rtimes indicates a semi-direct product.

The hopping Hamiltonian \mathcal{H}_α breaks Lorentz invariance, continuous space translations and layer rotational symmetry. The symmetry group in the space-time sector thus reduces to the symmorphic group $\mathbb{R} \times T \rtimes D_3$, composed of time translations \mathbb{R} , discrete translations on the moiré lattice $T = \mathbf{d}_1 \mathbb{Z} + \mathbf{d}_2 \mathbb{Z}$, and the point group D_3 . The latter is generated by the rotation \mathcal{C}_3 which rotates the bilayer by an angle $2\pi/3$ around the out-of-plane z -axis, and the rotation \mathcal{C}_2 which rotates the bilayer by an angle π around the in-plane x axis which passes through the bilayer at mid-distance (see Fig. 5.2). It consists of the six elements

$$D_3 = \{\mathbb{1}, \mathcal{C}_3, \mathcal{C}_3^2, \mathcal{C}_2, \mathcal{C}_2\mathcal{C}_3, \mathcal{C}_2\mathcal{C}_3^2\}. \quad (6.23)$$

We now focus on the magnetic group generated by \mathcal{C}_3 , \mathcal{C}_2 , and the two special symmetries Θ and \mathcal{P} . These four operations act by conjugation on the single-particle Hamiltonian \mathcal{H} in a four-dimensional representation, denoted as Υ . The three-fold rotation \mathcal{C}_3 affects the sublattice but leaves the layer degree of freedom untouched. Its matrix representation reads

$$\Upsilon(\mathcal{C}_3) = e^{2i\pi/3\sigma_z} \tau_0. \quad (6.24)$$

Though often viewed as a mirror symmetry, the operation \mathcal{C}_2 flips both sublattices and layers, which means that it acts as a proper rotation in three dimensions. It is represented by

$$\Upsilon(\mathcal{C}_2) = \sigma_x \tau_x. \quad (6.25)$$

These two operations $R = \mathcal{C}_3, \mathcal{C}_2$ define unitary spatial symmetries of the Hamiltonian; they act as

$$\Upsilon(R)^{-1} \mathcal{H}(R\mathbf{r}, t) \Upsilon(R) = \mathcal{H}(\mathbf{r}, t). \quad (6.26)$$

Let us consider now the two special symmetries. The composition $\Theta = \mathcal{IT}$ of spatial inversion \mathcal{I} and time reversal \mathcal{T} is represented by

$$\Upsilon(\Theta) = \sigma_x \tau_0 \mathcal{K}, \quad (6.27)$$

where \mathcal{K} denotes complex conjugation. Since the electron spin does not enter our low-energy model, Θ squares to identity. As an antiunitary symmetry, it acts on the Hamiltonian as

$$\Upsilon(\Theta)^{-1} \mathcal{H}(-\mathbf{r}, -t)^* \Upsilon(\Theta) = \mathcal{H}(\mathbf{r}, t). \quad (6.28)$$

Note that time reversal here is spinless, so that $\Theta^2 = \mathbb{1}$. The Θ symmetry protects a \mathbb{Z} topology of the active flat bands, characterised by a winding number (SONG 2019; AHN 2019). This protection manifests itself in an obstruction to build Wannier (atomically localised) wave functions which are invariant under Θ out of eigenstates of the active flat bands. The topology is fragile, which means that including higher-energy bands trivialise the flat bands. However, this fragile topology becomes robust type when including a

particle-hole symmetry \mathcal{P} . This latter operation relates eigenstates of opposite energies, and acts in real space as the reflection $x \mapsto -x$. Its matrix representation reads

$$\Upsilon(\mathcal{P}) = \sigma_x \tau_z. \quad (6.29)$$

Following (HEJAZI 2019), we define \mathcal{P} as a unitary operation² in order to have a single antiunitary generator Θ , unlike the conventions of (SONG 2019). This operation actually corresponds to an *antisymmetry*, since it anticommutes with the Hamiltonian,

$$\Upsilon(\mathcal{P})^{-1} \mathcal{H}(\mathcal{P}\mathbf{r}, t) \Upsilon(\mathcal{P}) = -\mathcal{H}(\mathbf{r}, t). \quad (6.30)$$

Because the operators \mathcal{P} and \mathcal{C}_2 anticommute, the combined antisymmetry $\mathcal{P}\mathcal{C}_2$ leads to a Kramers degeneracy through the relation $(\mathcal{P}\mathcal{C}_2)^2 = -\mathbb{1}$. This degeneracy has important consequences on the linear representation theory of the symmetry group of TBG, as we will see shortly. Unlike the three other symmetries, the particle-hole antisymmetry is accidental, and indeed appears to be broken in experiments. From the perspective of our low-energy theory, the \mathcal{P} symmetry is lost when the angular dependence of the kinetic terms $(R_{\pm\theta/2} \boldsymbol{\sigma}) \cdot \mathbf{k}$ is kept, when the single-particle Hamiltonian includes quadratic terms in momentum, or when intervalley scattering affects the dynamics (SONG 2019). As a result, the topological constraints, which forbids lattice models to preserve both Θ and \mathcal{P} (BERNEVIG 2020b; SONG 2020), seem to be specific to microscopic details. For this reason, we disregard the topological aspects of the low-energy theory of TBG in this work. Besides, we believe that topology plays a minor role in identifying interaction channels and in a renormalisation group framework.

Since Υ is a faithful representation, the multiplication table of the symmetry group follows from that of the matrix representations of the four generators. In the following paragraphs, we determine the classes of conjugation and irreducible representations, first of the symmetry group generated by D_3 and \mathcal{P} (the unitary group), then when including the antiunitary operation Θ (the magnetic group).

Representations of the unitary group — We define the *unitary* group \tilde{D}_3 as the subgroup which contains all unitary operators, whether symmetries or antisymmetries. In other words, for all $R \in \tilde{D}_3$,

$$\Upsilon(R)^{-1} \mathcal{H}(R\mathbf{r}, t) \Upsilon(R) = \pm \mathcal{H}(\mathbf{r}, t). \quad (6.31)$$

Eq. (6.31) shows that the set \tilde{D}_3 has indeed the structure of a group. It is generated by the point group D_3 and \mathcal{P} as the semi-direct product

$$\tilde{D}_3 = \{\mathbb{1}, \mathcal{P}, \bar{\mathbb{1}}, \bar{\mathcal{P}}\} \rtimes D_3, \quad (6.32)$$

where the ‘anti-identity’ $\bar{\mathbb{1}} = (\mathcal{P}\mathcal{C}_2)^2$ is represented by the matrix $\Gamma(\bar{\mathbb{1}}) = -\tau_0 \sigma_0$ and a barred operator stands for the product of this operator with $\bar{\mathbb{1}}$. This new element can be seen as a 2π rotation in the double covering of D_3 , or *double group*

$$D_3^{(2)} = D_3 \times \{\mathbb{1}, \bar{\mathbb{1}}\}, \quad (6.33)$$

²Strictly speaking, this operation is a chiral rather than a particle-hole symmetry, but to avoid any confusion with the chiral symmetry of monolayer graphene implemented by the operator σ_z , we will nonetheless refer to \mathcal{P} as a particle-hole symmetry.

where the identity $\mathbb{1}$ is assimilated to a 4π rotation. Double groups often show up in models where the excitations have a half-integer spin. This example shows that unitary antisymmetries can also generate a double group, due to the anticommutation of \mathcal{P} and \mathcal{C}_2 . The double group is a normal subgroup of \tilde{D}_3 . Hence the structure of the quotient set $\tilde{D}_3/D_3^{(2)} \sim \{\mathbb{1}, \mathcal{P}\}$ is also that of a group, which simplifies the determination of the irreducible representations (irrep.) of \tilde{D}_3 . We can indeed find the irrep. of \tilde{D}_3 from the composite operator method (CHEN 2002), or build them by induction from that of D_3 . We illustrate the second method in Appendix D. The table of characters of the unitary group is shown in Tab. 6.1.

Corepresentations of the magnetic group — A group generated by a crystallographic point group and an antiunitary operator is *magnetic*, or Shubnikov group (BUERGER 1964). In general, this antiunitary operator is time reversal, under which the electron spin is odd. Magnetic groups give clues about the magnetic properties of a crystal, hence its name. The group generated by \tilde{D}_3 and Θ is a grey magnetic group, i.e. the direct product

$$\mathcal{M} = \tilde{D}_3 \times \{\mathbb{1}, \Theta\}. \quad (6.34)$$

The ‘representations’ of a magnetic group do not share all the defining properties of the standard representations of finite groups. To stress the difference, the term corepresentation is used instead, but for simplicity, we will refer to irreducible corepresentations as irrep. We determine the irrep. in Appendix D. All irrep. ϖ of \tilde{D}_3 generate two irrep. of \mathcal{M} , denoted as ϖ^\pm , except E_1 and E_5 . In the former case $\varpi^\pm(\Theta) = \pm 1$ for the one-dimensional irrep., and $\varpi^\pm(\Theta) = \pm\mu_x$ for the two-dimensional irrep., where μ_x represents here a generic x

Irrep.	$\mathbb{1}$	$\bar{\mathbb{1}}$	$2\mathcal{C}_3$	$2\bar{\mathcal{C}}_3$	$2\mathcal{P}\mathcal{C}_2$	$2\mathcal{P}\mathcal{C}_2\mathcal{C}_3$	$2\mathcal{P}\mathcal{C}_2\mathcal{C}_3^2$	$6\mathcal{P}$	$6\mathcal{C}_2$
A_1	1	1	1	1	1	1	1	1	1
A_2	1	1	1	1	-1	-1	-1	1	-1
a_1	1	1	1	1	-1	-1	-1	-1	1
a_2	1	1	1	1	1	1	1	-1	-1
E_1	2	-2	-1	1	0	$\sqrt{3}$	$-\sqrt{3}$	0	0
E_2	2	2	-1	-1	2	-1	-1	0	0
E_3	2	-2	2	-2	0	0	0	0	0
E_4	2	2	-1	-1	-2	1	1	0	0
E_5	2	-2	-1	1	0	$-\sqrt{3}$	$\sqrt{3}$	0	0

Table 6.1 | Table of characters of the unitary group \tilde{D}_3 , generated by the three-fold out-of-plane rotation \mathcal{C}_3 , the bilayer flip \mathcal{C}_2 , and the particle-hole (anti)symmetry \mathcal{P} . Each column corresponds to a class of conjugation, and each line to an irreducible representation. For the one-dimensional representations already present in the point group D_3 , we use the symbol A prescribed by Mulliken’s notation (MULLIKEN 2004). The symbol a denotes a one-dimensional representation whose character takes opposite signs on antisymmetric operators, and is specific to the full unitary group. The symbol E denotes a two-dimensional representation.

Pauli matrix (unrelated to any degree of freedom). In the latter case, E_1 and E_5 generate a single four-dimensional on \mathcal{M} , which is equivalent to Υ .

Extended symmetries in the spin-valley sector — The four generators discussed above describe entirely the single-valley model with spinless fermions, within which we identify the allowed interactions in Sec. 6.2.2. When both valleys are considered, e.g. when accounting for intervalley scattering, the low-energy theory of TBG acquires two extra discrete symmetries, which are time reversal \mathcal{T} and the six-fold rotation C_6 about the out-of-plane axis z . Both operations map the valleys K and K' to one another, and each valley enjoys an internal $U(2)$ spin symmetry. This leads to a global $U(2)_K \times U(2)_{K'}$ spin-valley symmetry (BERNEVIG 2020b).

6.2.2 Symmetry-preserving contact interactions

Principle of the method — The fermionic Grassmann fields $\{\psi, \bar{\psi}\}$ define two conjugate representations of the magnetic group \mathcal{M} , one which we denoted as Υ , the conjugate representation being Υ^\dagger . The action of the free decoupled bilayer reads

$$S_0 = \int d^d r d\tau \bar{\psi}(\mathcal{H}_0 - \partial_\tau)\psi, \quad (6.35)$$

where $d = 2$ is the space dimension. Eq. (6.35) describes two copies of $(2 + 1)$ -dimensional massless Dirac fermions, each associated to one layer of TBG. Importantly, these copies correspond to the same representation of the Dirac matrices, unlike the two valleys of monolayer graphene, which are time-reversal partners. The behaviour under the Θ symmetry is modified accordingly. The representation Υ is four-dimensional, unitary, and reducible; we decomposed it into the direct sum

$$\Upsilon \sim E_1 \oplus E_5. \quad (6.36)$$

The elements $R \in \mathcal{M}$ act by matrix multiplication on the fields, $R \cdot \psi(x) = \Upsilon(R)\psi(R^{-1}x)$ and $R \cdot \bar{\psi}(x) = \bar{\psi}(R^{-1}x)\Upsilon^\dagger(R)$, where $x = (\mathbf{r}, t)$ is the space-time variable, and $\Upsilon^\dagger(R) = \Upsilon(R)^{-1}$ by unitarity. Let us consider now the action of the free coupled bilayer

$$S'_0 = \int d^d r d\tau \bar{\psi}(\mathcal{H} - \partial_\tau)\psi, \quad (6.37)$$

where \mathcal{H} is given by Eq. (6.6). The bilinear form $\bar{\psi}\psi$ transforms in the direct product of representations $\Upsilon^\dagger \otimes \Upsilon$, which, of course, leads to the invariance of the action. Indeed,

$$R \cdot \bar{\psi}(x)\mathcal{H}(x)\psi(x) = \bar{\psi}(R^{-1}x)\Upsilon^\dagger(R)\mathcal{H}(x)\Upsilon(R)\psi(R^{-1}x) = \bar{\psi}(R^{-1}x)\mathcal{H}(R^{-1}x)\psi(R^{-1}x). \quad (6.38)$$

Upon changing the integration variable from x to $R^{-1}x$, the action (6.37) remains unaffected. From the perspective of the matrix representation of the bilinear form, among all irrep. that enter the decomposition of $\Upsilon^\dagger \otimes \Upsilon$, the Bloch Hamiltonian \mathcal{H} transforms according to the trivial representation A_1^+ of \mathcal{M} .

We now add a contact quartic interaction. The interaction is thus independent of the space-time variable, but only in the original basis of eigenvectors $(\hat{\psi}, \hat{\bar{\psi}})$ where the two

Dirac nodes are separated, and the origin of momentum coincides with the centre of the mini Brillouin zone. We look for interaction actions of the form

$$S_{\text{int}} \propto \int d^d r d\tau (\hat{\psi} \hat{M} \hat{\psi})(\hat{\psi} \hat{N} \hat{\psi}), \quad (6.39)$$

where \hat{M} and \hat{N} are constant four-dimensional matrices. Each bilinear $\hat{\psi} \hat{M} \hat{\psi}$ and $\hat{\psi} \hat{N} \hat{\psi}$ belongs to a representation that enters the decomposition of $\Upsilon^\dagger \otimes \Upsilon$. To ensure that Eq. (6.39) is also invariant under the symmetry group \mathcal{M} , we must find the suitable matrices (\hat{M}, \hat{N}) such that $(\hat{\psi} \hat{M} \hat{\psi})(\hat{\psi} \hat{N} \hat{\psi})$ belongs to the trivial representation of the direct product $(\Upsilon^\dagger \otimes \Upsilon) \otimes (\Upsilon^\dagger \otimes \Upsilon)$. The entries of the interaction matrices \hat{M} and \hat{N} are given by the so-called Clebsch-Gordan coefficients.

Interaction matrices in the unrotated basis — The decomposition of the direct product $\Upsilon^\dagger \otimes \Upsilon$ into irrep. of \mathcal{M} (the Clebsch-Gordan series) reads

$$X(\Upsilon^\dagger \otimes \Upsilon)X^{-1} = A_1^+ \oplus a_1^+ \oplus A_2^+ \oplus a_2^+ \oplus A_1^- \oplus a_1^- \oplus A_2^- \oplus a_2^- \oplus E_2^+ \oplus E_4^+ \oplus E_2^- \oplus E_4^-, \quad (6.40)$$

where the sixteen-times-sixteen transformation matrix X contains the Clebsch-Gordan coefficients, which are given in Appendix D.

To find the quartic interactions that preserve \mathcal{M} we must find all copies of the trivial irrep. A_1^+ in the product $(\Upsilon^\dagger \otimes \Upsilon) \otimes (\Upsilon^\dagger \otimes \Upsilon)$. By inspecting the characters, it is clear that only products of the same irrep. decompose themselves into a copy of A_1^+ . For the one-dimensional irrep. $\varpi = A_1^+, a_1^+, A_2^+, a_2^+, A_1^-, a_1^-, A_2^-$ and a_2^- , the decomposition is simply

$$\varpi \otimes \varpi = A_1^+. \quad (6.41)$$

The quartic interaction corresponding to one of these irrep. is of the form $\hat{M} \otimes \hat{M}$, where $\hat{M} = \hat{N}$ follows from Eq. (6.40). The interaction matrices for these eight one-dimensional irrep. are listed in Tab. 6.2. For the two-dimensional irrep., we have

$$E_2^\pm \otimes E_2^\pm \sim A_1^\pm \oplus A_2^\pm \oplus E_4^\pm, \quad E_4^\pm \otimes E_4^\pm \sim A_1^\pm \oplus A_2^\pm \oplus E_2^\pm. \quad (6.42)$$

irrep.	A_1^+	a_1^+	A_2^+	a_2^+	A_1^-	a_1^-	A_2^-	a_2^-
\hat{M}	$\sigma_0 \tau_0$	$\sigma_0 \tau_x$	$\sigma_0 \tau_z$	$\sigma_0 \tau_y$	$\sigma_z \tau_y$	$\sigma_z \tau_z$	$\sigma_z \tau_x$	$\sigma_z \tau_0$
Θ	+1 (✓)	+1 (✓)	+1 (✓)	+1 (✓)	-1	-1	-1	-1
\mathcal{C}_2	+1 (✓)	+1 (✓)	-1	-1	+1 (✓)	+1 (✓)	-1	-1
\mathcal{P}	+1	-1 (✓)	+1	-1 (✓)	+1	-1 (✓)	+1	-1 (✓)

Table 6.2 | One-dimensional irreducible corepresentations (irrep.) of the magnetic symmetry group of the continuum model, with their associated coupling matrices \hat{M} , expressed in sublattice (Pauli matrices σ) and layer (Pauli matrices τ) sectors. The basis $\hat{\psi}$ is chosen at the centre of the mini Brillouin zone, for which the coupling matrices are space-independent. The matrices are normalised such that $\text{Tr}(\hat{M}\hat{M}^\dagger) = 4$. The entries are the eigenvalues with respect to the symmetries $\Theta = \mathcal{IT}$ (product of space inversion and time reversal), \mathcal{C}_2 (flip of the bilayer), and \mathcal{P} (particle-hole antisymmetry). The irrep. can either break or preserve (✓) those symmetries, in which case the eigenvalues are +1 for symmetries, -1 for antisymmetries that act on a field bilinear. They all preserve the three-fold rotational symmetry \mathcal{C}_3 .

irrep.	E_2^+	E_4^+	E_2^-	E_4^-
$\sqrt{2} \hat{M}$	$\sigma\tau_0$	$\sigma\tau_x$	$\sigma\tau_y$	$\sigma\tau_z$
Θ	+1	+1	-1	+1

Table 6.3 | Two-dimensional irreducible corepresentations (simplified as irrep.) of the magnetic symmetry group of the continuum model, with their associated coupling matrices \hat{M} , expressed in sublattice (Pauli matrices σ) and layer (Pauli matrices τ) sectors. The hat indicates that the basis is chosen at the centre of the mini Brillouin zone, for which the coupling matrices are space-independent. These coupling matrices are normalised such that $\text{Tr}(\hat{M} \cdot \hat{M}^\dagger) = 4$, hence the factor $\sqrt{2}$. These two-dimensional irrep. all break the three-fold rotational symmetry \mathcal{C}_3 , but in the chosen basis where the quadrilinear form is written as a square of bilinears $\hat{M} \otimes \hat{M}$, all matrix vectors are eigenvectors of the antiunitary symmetry $\Theta = \mathcal{IT}$. The last line indicates the eigenvalue with respect to Θ . The presence of the reflection \mathcal{C}_2 symmetry or the particle-hole antisymmetry \mathcal{P} depends on the spatial direction in which the order develop.

For each of these irrep., the invariant combination transforming as A_1^+ is $\hat{M} \otimes \hat{N}$, where (\hat{M}, \hat{N}) forms an orthonormal basis of the two-dimensional space on which the irrep. acts. A natural choice for this basis is $\hat{M} = \sigma_+ \tau_\mu$ and $\hat{N} = \sigma_- \tau_\mu$ where σ_\pm are the pseudospin ladder operators, for $\mu = 0, \dots, 3$. However the quadrilinear form can be cast into a perfect square $\hat{M} \otimes \hat{M}$ where $\hat{M} = \sigma \tau_\mu$ in the new basis. Tab. 6.2 lists the interaction matrices for these four two-dimensional irrep.

Interaction matrices in the rotated basis — The interaction matrices in the rotated basis $M(\mathbf{r})$ follow by conjugation with the transformation matrix $A(\mathbf{r})$ of Eq. (6.5),

$$M(\mathbf{r}) = A^\dagger(\mathbf{r}) \hat{M} A(\mathbf{r}). \quad (6.43)$$

Though both \hat{M} and $M(\mathbf{r})$ describe contact interactions, \hat{M} is space-independent, while $M(\mathbf{r})$ depends in general on position. However, the transformed matrix $M(\mathbf{r})$ remains space-independent if the channel affects the two layers separately. Indeed, if \hat{M} is diagonal in layer, i.e. proportional to $\tau_{0/z}$, it commutes with $A(\mathbf{r})$, so that $M(\mathbf{r}) = \hat{M}$. This class of scattering processes leads to no momentum transfer between interacting particles.

If instead \hat{M} is off diagonal in layer, i.e. proportional to $\tau_{x/y}$, $M(\mathbf{r})$ differs from \hat{M} , and is modulated periodically over a distance of the order of the moiré lattice constant. The off-diagonal Pauli matrices $\tau_{x/y}$ are indeed transformed into

$$\begin{cases} A^\dagger(\mathbf{r}) \tau_x A(\mathbf{r}) = e^{-i\mathbf{q}_1 \cdot \mathbf{r}} \tau_- + e^{i\mathbf{q}_1 \cdot \mathbf{r}} \tau_+, \\ A^\dagger(\mathbf{r}) \tau_y A(\mathbf{r}) = -ie^{-i\mathbf{q}_1 \cdot \mathbf{r}} \tau_+ + ie^{i\mathbf{q}_1 \cdot \mathbf{r}} \tau_-. \end{cases} \quad (6.44)$$

Due to the momentum transfer in Eq. (6.44), these couplings will turn out to be irrelevant in the renormalisation group approach. We will clarify this point in Chapter 7. The same conclusions apply to two-dimensional irrep., where a vector of matrices \hat{M} replaces the single matrix \hat{M} .

Interaction channels — All in all, we find the allowed couplings to be: eight channels originating from one-dimensional irrep., four of which involve intralayer scatterings; and

four channels originating from two-dimensional irrep., two of which involve intralayer scatterings. The one- versus two-dimensional nature of the irrep. transpires in the field theory as quartic couplings between either density or current operators. The one-dimensional channels describes couplings between density operators $\rho_i(\mathbf{r}) = \bar{\psi} M_i(\mathbf{r}) \psi$, which are diagonal in sublattice and preserve \mathcal{C}_3 . The two-dimensional channels describe couplings between current operators $\mathbf{J}_l(\mathbf{r}) = \bar{\psi} \mathbf{M}_l(\mathbf{r}) \psi$, which are off diagonal in sublattice and break \mathcal{C}_3 . The complete interaction action has the form

$$S_{\text{int}} = - \sum_{i=1}^8 g_i \int d^2r d\tau \rho_i(\mathbf{r}) \rho_i(\mathbf{r}) - \sum_{l=1}^4 \lambda_l \int d^2r d\tau \mathbf{J}_l(\mathbf{r}) \cdot \mathbf{J}_l(\mathbf{r}). \quad (6.45)$$

The parameters g_i and λ_l of Eq. (6.45) denote the coupling strengths of the density-density and current-current interactions, respectively. We collect the density couplings into two sets, represented in Tab. 6.2; the vectors of couplings matrices of Tab. 6.3 constitute a third set.

- Out of the eight density-density couplings, the four interactions associated to irrep. which preserve Θ are those symmetric in the A/B sublattices. The corresponding channels are of the form $\hat{\psi} \sigma_0 \tau_\mu \hat{\psi}$ for $\mu = 0, x, y, z$, in the original unrotated basis. They differ by their breaking of \mathcal{C}_2 or \mathcal{P} . Setting aside the layer degree of freedom, this corresponds to a ‘pure’ density-density interaction, of the form $(\hat{\psi} \hat{\psi})^2$. This instability renormalises the chemical potential, which is not associated to a correlated phase.
- The four density channels which break Θ are those antisymmetric in the A/B

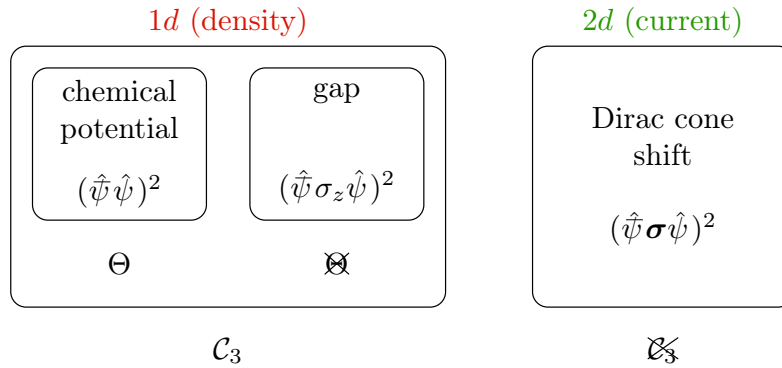


Figure 6.3 | Among the twelve contact interaction channels at charge neutrality in twisted bilayer graphene, eight correspond to one-dimensional (1d) irreducible representations (irrep.), and lead to density-density couplings; four correspond to 2d irrep., and lead to current-current couplings. The current channels break the three-fold \mathcal{C}_3 symmetry, and have a structure $\sigma = (\sigma_x, \sigma_y)$ in the sublattice sector, as a result of the relativistic dispersion relation and the sublattice acting as a pseudospin. The corresponding instability tends to shift the Dirac cones from the corners of the hexagonal mini Brillouin zone. Among the eight density channels, four preserve the product of time reversal and spatial inversion $\Theta = \mathcal{IT}$, and develop a (possibly staggered) chemical potential; four break Θ , and develop a gap. These four latter channels have a structure σ_z in the sublattice sector, which corresponds to a mass term in graphene. The shape of the quadrilinear form presented is valid in the basis $(\hat{\psi}, \hat{\psi})$ where the origin of momentum is taken at the centre of the mini Brillouin zone.

sublattices, of the form $\hat{\psi}\sigma_z\tau_\mu\hat{\psi}$. Similarly to the first set, they can break \mathcal{C}_2 or \mathcal{P} . Those which preserve the particle-hole symmetry lead to on-diagonal in layer instabilities. These four couplings corresponds to a chiral interaction, of the form $(\hat{\psi}\gamma_5\hat{\psi})^2$, where $\gamma_5 = \sigma_z$ in $(2+1)$ dimensions. This instability is reminiscent of the spontaneous mass generation of the Gross-Neveu model.

- Finally, the four current channels assume the form $\hat{\psi}\boldsymbol{\sigma}\tau_\mu\hat{\psi}$. They break most of the symmetries of the free model in general (and always the three-fold rotational symmetry \mathcal{C}_3) except the anti-unitary symmetry Θ (see Tab. 6.3). Depending on the direction selected by $\hat{\psi}\boldsymbol{\sigma}\tau_\mu\hat{\psi}$, these couplings can preserve \mathcal{C}_2 and \mathcal{P} .

We summarise all these channels in Fig. 6.3. We will discuss the nature of the correlated phase associated to the dominant instabilities in Sec. 7.1.

Conclusion

Summary — The low-energy physics of twisted bilayer graphene can be described near charge neutrality by a pair of Dirac cones, each originating from the same valley of graphene, and pulled apart by the twist. In a first approximation, only the sublattice and layer degrees of freedom control the dynamics. Particles can tunnel between the layers, with an amplitude that is spatially modulated by the moiré pattern. To diagonalise the Hamiltonian of this highly non-standard free theory, we have expanded it order by order in the dimensionless hopping strength α . Remarkably, the kinetic energy becomes so small at low twist angles that interlayer hopping completely suppresses the Fermi velocity at a discrete set of ‘magic’ angles. We have calculated the correction to the Fermi velocity and the wave function amplitude at order six in α , and have shown that corrugation of the graphene layers weakly alters the first magic angle.

Focusing then on many-body effects, we have identified the contact quartic interactions that preserve the symmetries of the model: the three-fold in-plane rotation, a mirror symmetry, an accidental particle-hole antisymmetry, and the antiunitary product of time reversal and spatial inversion. In the basis where the Dirac cones of each layer are superimposed to the same momentum, half the allowed particle-hole channels display interlayer coherence, meaning that the coupling matrix has off-diagonal entries in the layer sector and is associated with momentum transfers of the order of the moiré momentum. Because such channels require the quasiparticles to scatter with a wave length of the order of the moiré period, they will not compete as dominant instabilities in the infrared limit, as we will see in Chapter 7. The remaining instabilities correspond either to density-density couplings, which preserves the three-fold rotational symmetry, or current-current couplings, which break it. The relevant density instabilities will turn out to be those which open gaps in the energy spectrum. The current instabilities, on the other hand, shift the Dirac cones from the corners of the Brillouin zone.

Outlook — To go beyond the low-energy theory proposed in this chapter, we could include the valley degree of freedom. Neglecting the valley is a good approximation, because intervalley scattering occurs at atomic length scales, which are several orders of magnitude smaller than the moiré period at low twist angles. We thus expect that ground states which differ only in their ordering in the valley sector have close energies. The valley degeneracy of the channels we considered in our single-valley model, which is protected by time-reversal symmetry, could be split by tenuous effects such as strain or substrate alignment. The hierarchy of the possible ground states also depends strongly on corrugation and lattice relaxation, which affect the amplitude of intra-sublattice hopping processes. Besides, the single-particle band structure displays a valley asymmetry along the Γ – M lines of the mini Brillouin zone: the interplay between dispersion and Coulomb repulsion could also explain why the valley degree of freedom plays a small but non-negligible role in magic angle twisted bilayer graphene. We will ignore these refinements, and treat only the competition between instabilities at the lowest energy scale, where only the band structure near the Dirac cones matter.

Nematic insulator at charge neutrality

The continuum single-valley model proposed in the previous chapter captures the magic angle physics near charge neutrality. At certain twist angles, interlayer hopping decreases the energy bandwidth so much that the kinetic and interaction energy scales become comparable. To account for many-body effects, we include in the model all contact interactions channels allowed by symmetry, which we identified using a formal group-theoretical approach. These channels split into three sets: two sets correspond to density-density couplings and preserve the three-fold rotational symmetry; the last set corresponds to current-current couplings, and break the rotational symmetry.

We now study the competition between these instabilities and identify the dominant one, responsible for the correlated phase observed at charge neutrality. We look for the dominant instabilities using mean-field and renormalisation group methods. In the mean-field description, we determine the order parameters associated to the relevant instabilities (gap and momentum shift) in a self-consistent way. Doing so, we take into account their reduction by interlayer hopping, in a similar way as we did for the Fermi velocity. We then resort to the renormalisation group to discard irrelevant instabilities, and study the competition between the four remaining instabilities. We find that the asymptotic behaviour of the renormalisation flow selects a nematic insulator with layer-polarised gap and momentum shift as the correlated phase observed at charge neutrality. Finally, we put our results in perspective with other effects, such as twist angle disorder, long-range components of the electron-electron interaction, and the valley or spin degrees of freedom.

7.1	Mean-field approach	174
7.1.1	Nature of the correlated phases	174
7.1.2	Solutions of the self-consistent equations	176
7.2	Renormalisation group approach	179
7.2.1	Renormalisation procedure	179
7.2.2	Loopwise and hopping strength expansions	184
7.2.3	Flow diagram	185
7.3	Perspective	187
7.3.1	Twist angle disorder	187

7.3.2 Coulomb interaction	188
7.3.3 Valley and spin degrees of freedom	189
Conclusion	191

7.1 Mean-field approach

We perform here a mean-field analysis to prove the emergence of a correlated phase near the first magic angle (BRILLAUX 2020). To gain some intuition on the correlated phases at play, we first identify the order parameters associated to the four relevant interacting channels, which leads to a gap or a momentum shift of the Dirac cones. We then solve the self-consistent equation for each of these order parameters separately, where we include the effect of interlayer hopping, which tends to reduce the gaps and momentum shifts. To do so, we diagonalise and expand the mean-field Hamiltonian at order six in the dimensionless hopping strength α , as we have done in Sec. 6.1.2 for the Fermi velocity.

7.1.1 Nature of the correlated phases

As we will see in the renormalisation group study of Sec. 7.2 below, only four interactions turn out to dominate the long wave length physics. We consider only these in this section. These interactions are associated to the coupling matrices $\sigma_z\tau_{0/z}$ and $\boldsymbol{\sigma}\tau_{0/z}$ and the coupling constants $g_{0/z}$ and $\lambda_{0/z}$, respectively. The first set of channels breaks the product of time reversal and spatial inversion $\Theta = \mathcal{IT}$, and generates a phase with a gap $\Delta_\mu \propto g_\mu \langle \bar{\psi} \sigma_z \tau_\mu \psi \rangle$, with $\mu = 0, z$. The second set of channels breaks the three-fold rotational symmetry \mathcal{C}_3 , and generates a phase where the Dirac cones are shifted by a momentum $\mathcal{G}_\mu \propto \lambda_\mu \langle \bar{\psi} \boldsymbol{\sigma} \tau_\mu \psi \rangle$. We account for these couplings by introducing four order parameters, which enter the mean-field Hamiltonian

$$\mathcal{H}_{\text{MF}} = \mathcal{H}_0 + \sigma_z(\Delta_0\tau_0 + \Delta_z\tau_z) + \boldsymbol{\sigma} \cdot (\mathcal{G}_0\tau_0 + \mathcal{G}_z\tau_z), \quad (7.1)$$

where $\mathcal{H}_0 = \tau_0 \boldsymbol{\sigma} \cdot \mathbf{k}$ is the single-particle Hamiltonian of the decoupled bilayer. At this stage, we ignore the corrections induced by interlayer hopping. We also treat each order parameter individually, and reconstruct schematically the band structure near the corners of the mini Brillouin zone as in Fig. 7.1.

The two terms in the first parenthesis of Eq. (7.1), being proportional to σ_z , open gaps of energy $2\Delta_{0/z}$ at the Dirac points of the mini Brillouin zone. The sublattice polarisation leads to two topological bands (per spin and valley) with Chern numbers $C = \sigma_z\tau_z$ (BULTINCK 2020b). These two insulating phases have identical band structures, but differ by the spatial charge redistribution, since the first one breaks the mirror symmetry \mathcal{C}_2 , while the other preserves it. In the $\sigma_z\tau_z$ channel, and assuming Δ_z to be positive, particle excitations are localised on the A1 (bottom layer) and B2 (top layer) sublattices near the band edges, and vice versa for the holes, as shown in Fig. 7.1(a). In the $\sigma_z\tau_0$ channel, particles localise on the A sublattice and holes on the B sublattice, irrespectively of the layer, as in Fig. 7.1(b).

The two terms in the second parenthesis of Eq. (7.1), being proportional to $\sigma_{x,y}$, shift the bottom and top Dirac points away from the corners of the mini Brillouin zone. The perturbation $\boldsymbol{\sigma} \cdot \mathcal{G}_z\tau_z$ pushes the top and bottom Dirac nodes asymmetrically by an

amount $\pm\mathcal{G}_z$, as in Fig. 7.1(c). The charge distribution organises into stripes. When the direction of this shift coincides with the high-symmetry line K-M, these stripes are oriented along the direction normal to \mathcal{G}_z (along the x -axis), as shown in Fig. 7.2. We dub this state a *nematic* phase by analogy with similar states discussed in (FRADKIN 2010). The $\tau_0\sigma \cdot \mathcal{G}_0$ perturbation pushes the top and bottom Dirac nodes symmetrically, as in Fig. 7.1(d), which modulates the phase of the wave function identically in the top and bottom layers. This perturbation leaves no signatures in scanning tunnelling microscopy or transport measurements, and does not lead to a correlated phase per se.

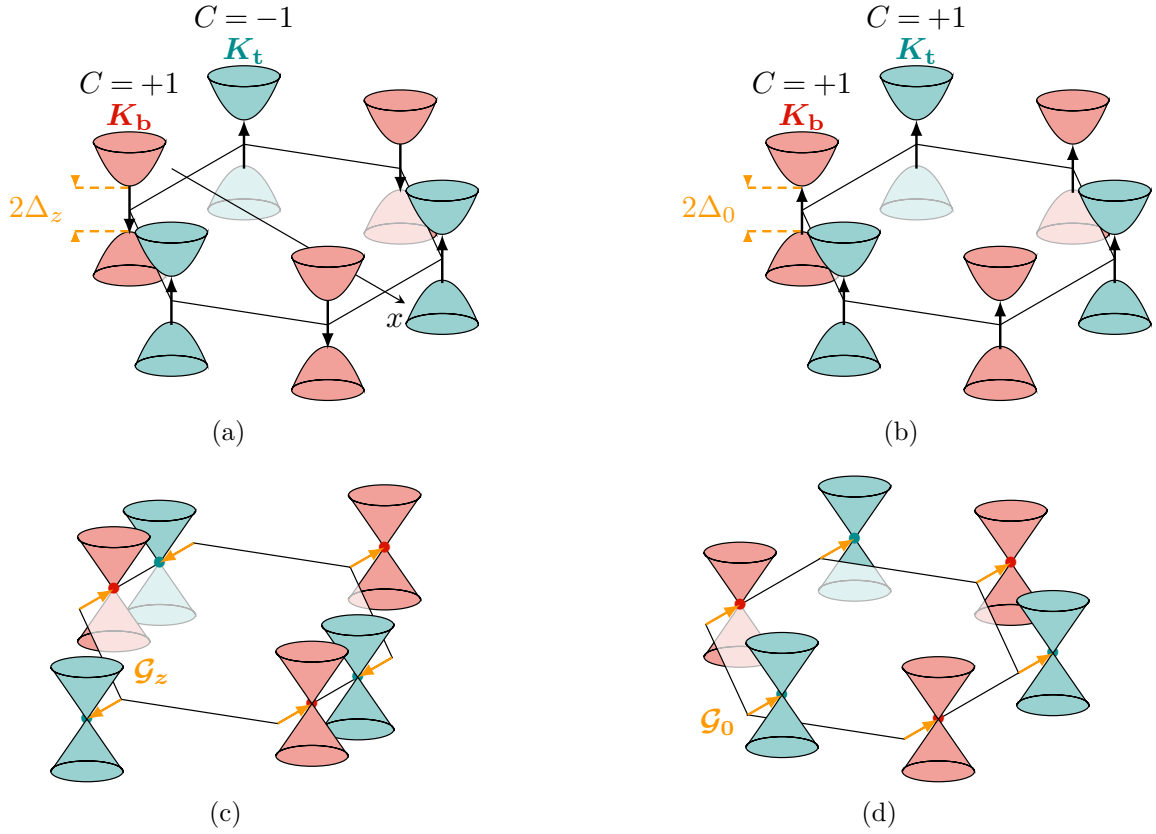


Figure 7.1 | Schematic low-energy dispersion relation over the mini Brillouin zone and corresponding correlated phases of twisted bilayer graphene, in the single-valley continuum model. (a)-(b) represent gapped phases, while (c)-(d) represent density-modulated phases. (a) A term $\Delta_z\tau_z\sigma_z$ in the mean-field Hamiltonian opens a gap at the \mathbf{K}_t (blue dots \bullet) and \mathbf{K}_b (red dots \bullet) Dirac points of the top and bottom layers respectively. Near the band edges, the A sublattice (black dots \bullet) harbours particles on the top layer, and holes on the bottom layer. (b) A term $\Delta_0\tau_0\sigma_z$ opens a gap as well, but the spatial distribution near the band edges is symmetric: the particle states are localised on the A sublattice on both the top and bottom layers. (c) A term $\tau_z\sigma \cdot \mathcal{G}_z$ (yellow arrow) detaches the Dirac points asymmetrically from the corners of the Brillouin zone, leading to a nematic phase. (d) A term $\tau_0\sigma \cdot \mathcal{G}_0$ instability (yellow arrow) shifts all Dirac points by the same vector, and merely modulates the global phase of the wave function.

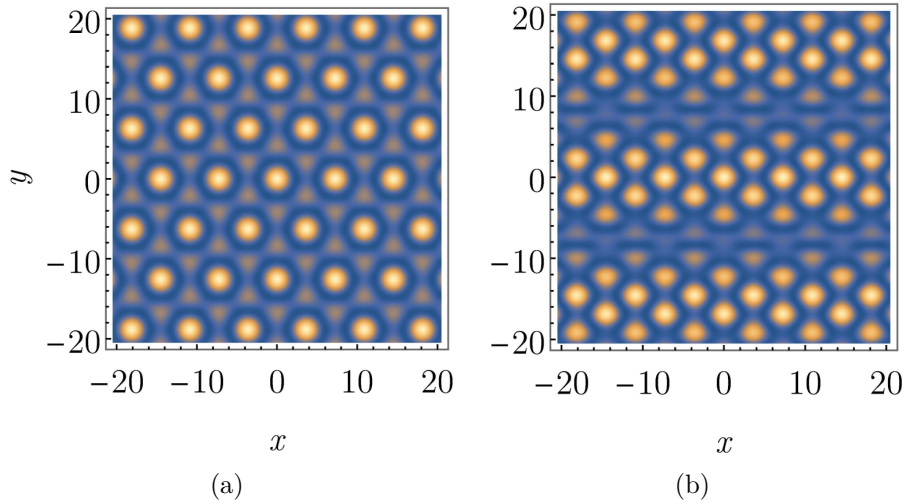


Figure 7.2 | Theoretical map of the local density of states of twisted bilayer graphene, in absence of correlations (a), and in the nematic phase (b). These colour plots represent the imbalanced density $|\psi_t + r\psi_b|^2$ probed e.g. by a scanning tunnelling microscopy tip located on the top layer, where for concreteness we set the relative amplitude of tunnelling through the bottom layer to $r = 0.5$. The coordinates (x, y) are measured in units of the moiré period. (a) In absence of correlation, the wave function density peaks at AA stacking regions (in orange), which form a hexagonal pattern. (b) The nematic phase is characterised by an asymmetric shift $\pm \mathcal{G}_z$ of the top and bottom Dirac cones from the corners of the mini Brillouin zone. Here, $\mathcal{G}_z = 0.3 \mathbf{e}_y$ in units of the moiré momentum k_θ , where \mathbf{e}_y denotes the unit vector in the y direction. The three-fold symmetry breaking appears as charge stripes perpendicular to \mathcal{G}_z , and separated by a distance \mathcal{G}_z^{-1} .

7.1.2 Solutions of the self-consistent equations

Correction of order parameters by interlayer hopping — We found in Eq. (6.18) that the propagator corrected by interlayer hopping has the form $G_0'^{-1} \simeq N_\psi(v\boldsymbol{\sigma} \cdot \mathbf{k} - i\Omega)$ in the low-energy limit $k, \Omega \ll 1$. Interlayer hopping enhances the wave function amplitude by a factor N_ψ , while reducing the Fermi velocity to $|v| < 1$. The expressions of N_ψ and v at order six in the dimensionless hopping strength α were given in Eq. (6.19) and Eq. (6.20), respectively. Similarly, we can determine the correction to the four order parameters introduced in Sec. 7.1.1 by expanding the mean-field Hamiltonian of the coupled bilayer order by order in α . By adding the hopping term to Eq. (7.1), we arrive at the full mean-field Hamiltonian

$$\mathcal{H}'_{\text{MF}} = \mathcal{H}_{\text{MF}} + \mathcal{H}_\alpha = \mathcal{H} + \sigma_z(\Delta_0\tau_0 + \Delta_z\tau_z) + \boldsymbol{\sigma} \cdot (\mathcal{G}_0\tau_0 + \mathcal{G}_z\tau_z), \quad (7.2)$$

where the Hamiltonian of the free theory \mathcal{H} is given by Eq. (6.6). Diagonalising Eq. (7.2) in the low-energy limit, we find a mean-field propagator of the form

$$G_{\text{MF}}'^{-1} \simeq N_\psi \left\{ v \boldsymbol{\sigma} \cdot \left[(\mathbf{k} + N_0^{(\mathcal{G})} \mathcal{G}_0) \tau_0 + N_z^{(\mathcal{G})} \mathcal{G}_z \tau_z \right] + \sigma_z \left(N_0^{(\Delta)} \Delta_0 \tau_0 + N_z^{(\Delta)} \Delta_z \tau_z \right) - i\Omega \right\}. \quad (7.3)$$

The factors $N_{0/z}^{(\mathcal{G}/\Delta)}(\alpha, \beta)$ encode the renormalisation of the order parameters by interlayer hopping; they are the counterparts of the corrected Fermi velocity for the matrix structures

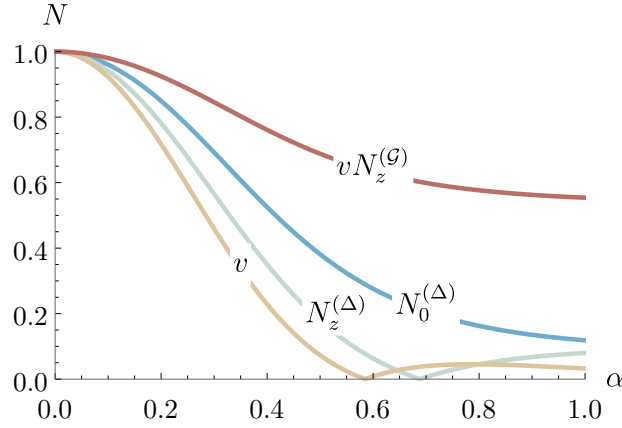


Figure 7.3 | Interlayer hopping correction of the order parameter against dimensionless hopping strength α , for the four relevant instabilities of twisted bilayer graphene: layer-symmetric gap (channel $\Delta_0\sigma_z\tau_0$, factor $N_0^{(\Delta)}$), layer-polarised gap (channel $\Delta_z\sigma_z\tau_z$, factor $N_z^{(\Delta)}$), momentum shift (channel $\tau_0\sigma \cdot \mathcal{G}_0$, factor v equal to the corrected Fermi velocity), and layer-polarised momentum shift (channel $\tau_z\sigma \cdot \mathcal{G}_z$, factor $vN_z^{(\mathcal{G})}$). The first pair of instabilities generates a gapped phase, while the layer-polarised shift leads to a nematic phase. The ratio of intra-sublattice over inter-sublattice hopping amplitudes is set to $\beta = 0.82$ (LUCIGNANO 2019). The corrected Fermi velocity $v(\alpha, \beta)$ vanishes at the first magic value $\alpha_0 \simeq 0.59$. Strikingly, the layer-polarised gap corrected by hopping vanishes at a hopping strength $\tilde{\alpha}_0 \simeq 0.69$ slightly larger than the first magic value. At the mean-field level, the layer-polarised gap is more suppressed in the vicinity of the magic angle than the layer-symmetric gap, which is itself more suppressed than the layer-polarised momentum shift.

$\sigma_z\tau_{0/z}$ and $\sigma\tau_{0/z}$. By definition of the Fermi velocity, we have $N_0^{(\mathcal{G})} = 1$. We calculate the other non-trivial factors diagrammatically to sixth order in α , and plot their dependence on α in Fig. 7.3. Their expressions are given in Appendix E.

Strikingly, we find that the correction to the layer-polarised gap $N_z^{(\Delta)}$ vanishes at a dimensionless hopping strength $\tilde{\alpha}_0(\beta)$ slightly larger than the first magic value $\alpha_0(\beta)$. Though this particular value of the hopping strength plays no role in the magic angle physics (the bandwidth is not especially small at $\tilde{\alpha}_0$), the strong reduction of the layer-polarised gap in the vicinity of the first magic angle entails that at the mean-field level, a gap instability should preferably develop in the channel $\sigma_z\tau_0$ rather than $\sigma_z\tau_z$. In addition, the factor $vN_z^{(\mathcal{G})}$ which renormalises the asymmetric momentum shift \mathcal{G}_z stays non-zero at the first magic angle, which entails that the local DoS in the nematic phase becomes modulated over a distance of the order of the moiré period L . Since the momentum shift becomes of the order of the mini Brillouin zone’s size k_θ , the Dirac cones can overlap. This rotational-symmetry-breaking instability cannot form a gap by itself, though, because the non-equivalent Dirac cones of the mini Brillouin zone originate from the same valley of graphene, and therefore have the same winding number. We now confirm these conclusions by solving the mean-field self-consistent equations.

Solution to the self-consistent equations — For the sake of simplicity, we write the mean-field self-consistent equations for each order parameter separately. Upon introducing an ultraviolet cut-off Λ , these equations read

$$\begin{cases} \Delta_\mu = -2g_\mu \int d\omega \int_\Lambda \frac{d^2q}{(2\pi)^3} \langle \bar{\psi}_{q,\omega} \sigma_z \tau_\mu \psi_{q,\omega} \rangle, & (7.4a) \\ \mathcal{G}_\mu = -2\lambda_\mu \int d\omega \int_\Lambda \frac{d^2q}{(2\pi)^3} \langle \bar{\psi}_{q,\omega} \boldsymbol{\sigma} \tau_\mu \psi_{q,\omega} \rangle, & (7.4b) \end{cases}$$

for $\mu = 0, z$, where the momentum integral runs over a sphere of radius Λ in Eq. (7.4a) and a square of side Λ in Eq. (7.4b), and $\{\psi_{q,\omega}, \bar{\psi}_{q,\omega}\}$ denote the Fourier-transformed fields. The correlators in Eq. (7.4) represent the translational-invariant parts of statistical averages computed over the mean-field Hamiltonian \mathcal{H}'_{MF} defined in Eq. (7.2). By expanding the correlators in powers of α , we automatically correct the order parameters by the factors $N_{0/z}^{(\mathcal{G}/\Delta)}$ introduced in Eq. (7.3). Details can be found in Appendix E. Fig. 7.4 shows the

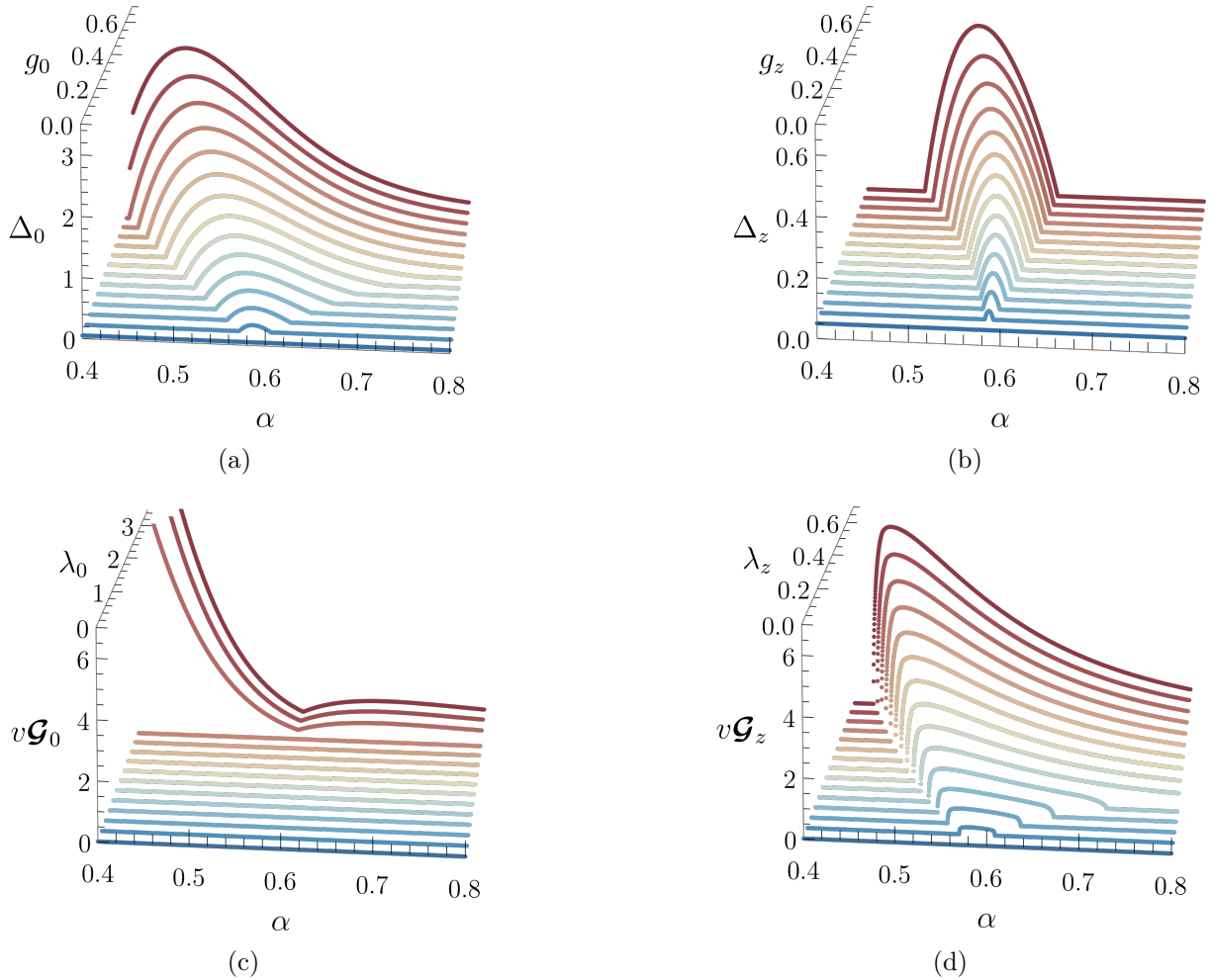


Figure 7.4 | Mean-field order parameters of the leading instabilities as a function of the dimensionless hopping strength α , for various coupling constants $g_{0/z}, \lambda_{0/z}$. (a) Layer-polarised gap Δ_z and (b) layer-symmetric gap Δ_0 . Energies (c) $v\mathcal{G}_z$ and (d) $v\mathcal{G}_0$ associated to the layer-polarised shift \mathcal{G}_z and layer-symmetric shift \mathcal{G}_0 of the Dirac cones (here the shifts are oriented along the y -axis). The ratio of intra- versus inter-sublattice hopping amplitudes is set to $\beta = 0.82$, and the order parameters are measured in units of $10^{-2}\Lambda$, where Λ is an ultraviolet energy cut-off.

solutions to the self-consistent equations (7.4). For simplicity we assume the shift momenta $\mathcal{G}_{0/z}$ to be aligned along a crystallographic axis of the moiré pattern, here along the y -axis. The Dirac points then move along the high-symmetry line K-M of the mini Brillouin zone.

As expected, we see on Fig. 7.4(a), Fig. 7.4(b), and Fig. 7.4(d) that the gaps $\Delta_{0/z}$ and the asymmetric momentum shift \mathcal{G}_z develop at arbitrary small coupling constants $g_{0/z}$ and λ_z near the first magic angle, as a result of the kinetic energy vanishing. Only the layer-symmetric momentum shift \mathcal{G}_0 requires a non-zero coupling constant λ_0 to develop, as shown in Fig. 7.4(c). We can therefore exclude this instability from the competing orders at the first magic angle. The layer-polarised gap Δ_z emerges over a thinner region near the magic angle than the layer-symmetry gap Δ_0 . Within the mean-field description, the insulating phase at charge neutrality likely originates from a layer-symmetric gap, which corresponds to the dominant gapping channel. We will see in the next section, however, that including fluctuations completely reverses this hierarchy.

7.2 Renormalisation group approach

The conclusions drawn from the mean-field description should be compared with a renormalisation group approach, since we expect fluctuations near the first magic angle to play a crucial role in the competition between instabilities. To do so, we decouple the interacting action using a Hubbard-Stratonovitch transformation, and analyse the scaling behaviour of all allowed contact interactions at first order in the coupling strengths and second order in α . By studying the renormalisation flow, we rule out all one-dimensional channels that preserve Θ , and all channels that are off diagonal in layer sector, which are irrelevant instabilities. The renormalisation flow of the four relevant instabilities shows that the two dominant ones lead to a nematic phase with a layer-polarised gap. Aside from being responsible for the magic angle physics, interlayer hopping plays a crucial role in the nematic-gap competition, since the nematic order develops over a region of the phase diagram that grows with the hopping strength.

7.2.1 Renormalisation procedure

Hubbard-Stratonovitch decoupling — We aim at finding the insulating order near charge neutrality. We therefore restrict ourselves to particle-hole channels, with order parameters of the form $\langle \bar{\psi} M \psi \rangle$ for $M \in \{M_i, \mathbf{M}_l\}$, where now the bracket $\langle \dots \rangle$ denotes the ensemble average over the complete action $S = S'_0 + S_{\text{int}}$. This contrasts with superconducting channels, where the Cooper pairing of electrons spontaneously generate correlations of the form $\langle \psi M \psi \rangle$ and $\langle \bar{\psi} M \bar{\psi} \rangle$. Albeit not obvious in Eq. (6.45), it is possible to rewrite the interactions in terms of superconducting channels using Fierz identities, but we will not address superconductivity in this thesis. Using Hubbard-Stratonovitch transformations, we can introduce auxiliary bosonic fields to decouple the quartic interactions into Yukawa couplings. We must distinguish between the one-dimensional irrep., for which a scalar field ϕ_i for $i = 1, \dots, 8$, is sufficient, and the two-dimensional irrep., for which a two-component field $\varphi_l = (\varphi_{l1}, \varphi_{l2})$ must be introduced, for $l = 1, \dots, 4$. All these bosonic fields can be chosen real. Such transformation enables to

recast the action for quartic fermion interactions (6.45) into

$$S_{\text{int}}[\bar{\psi}, \psi] \mapsto S_{\text{Hub}}[\bar{\psi}, \psi, \phi_i, \boldsymbol{\varphi}_l] = \sum_{i=1}^8 \int d^2r d\tau \left(\phi_i^2 + 2\sqrt{g_i} \phi_i \bar{\psi} M_i \psi \right) + \sum_{l=1}^4 \int d^2r d\tau \left(\boldsymbol{\varphi}_l^2 + 2\sqrt{\lambda_l} \boldsymbol{\varphi}_l \cdot \bar{\psi} \mathbf{M}_l \psi \right), \quad (7.5)$$

where the sum runs over both one-dimensional (first sum) and two-dimensional (second sum) irrep. The original four-fermion vertex thus splits into a bosonic Gaussian part (the first term in the parentheses), and a Yukawa vertex (the second term in the parentheses). Our choice of modelling many-body effects by instantaneous contact interactions, which obviously violate Lorentz covariance, lead to a peculiar property: the boson of Eq. (7.5) have no kinetics, they are only characterised by their mass (set to unity).

Regularisation scheme — A noteworthy consequence of the Hubbard-Stratonovitch decoupling is the absence of ladder diagrams. Indeed, the ladder diagrams generate a four-fermion vertex at two-loop order, but do not correct the Yukawa coupling at one-loop order. This solves one issue of dimensional regularisation, since ladder diagrams create evanescent operators in presence of current-current interactions. Thanks to the absence of these diagrams, each coupling defines an invariant subspace of the renormalisation flow. Another issue with dimensional regularisation deals with the analytic continuation of the chiral matrix $\gamma_5 = \sigma_z \tau_0$. In arbitrary dimension, the trace rule $\gamma_\mu \gamma_5 \gamma^\mu = (d-2)\gamma_5$ and the anticommutation rule $\{\gamma_\mu, \gamma_5\} = 0$ cannot be both valid, except when $d = 1$, where these two conditions become accidentally compatible. For this reason, and because the Matsubara frequency ω plays a different role than space variables, a natural regularisation scheme consists in isolating the frequency variable, over which Feynman diagrams are integrated from $-\infty$ to $+\infty$, from the momentum variables, which we continue analytically in $d = 1 + \varepsilon$ space dimensions.

Renormalised action — To renormalise the field theory described by the action $S = S'_0 + S_{\text{Hub}}$, we relate the bare fields $\overset{\circ}{\phi}$ for $\phi \in \{\phi_i, \boldsymbol{\varphi}_l\}$ and the bare couplings $\overset{\circ}{g}$ for $g \in \{g_i, \lambda_l\}$ to their renormalised counterparts. The Z constants for the bosonic fields are such that

$$\overset{\circ}{\phi} = Z_\phi^{1/2} \phi. \quad (7.6)$$

We work in an isotropic space dimension $d = 1 + \epsilon$, and introduce a dummy mass scale μ to render the regularised coupling constants dimensionless. Note that at one-loop order, the fermionic fields are not renormalised, so that the constant $Z_\psi = 1$ is trivial here. A generic coupling constant g is defined from its bare value $\overset{\circ}{g}$ by

$$\overset{\circ}{g} = \mu^{-\epsilon} N_\psi^2 Z_g^2 Z_\phi^{-1} g. \quad (7.7)$$

The hopping correction to the wave function amplitude N_ψ compensate those same factors that appear at all loop orders from the corrected fermionic propagator G'_0 . We also assume the interlayer hopping amplitudes α and β to be scale-invariant, i.e. constant under the renormalisation flow so that, like for the fermionic fields, there is no need to add extra Z constants for translational-breaking part of the fermionic two-point function. This assumption is valid at all orders, but for contact interactions only. Using Eq. (7.6) and Eq. (7.7), we find the renormalised action $S_R = S_{R,0} + S_{R,\alpha} + S_{R,\phi} + S_{R,\text{Yuk}}$. In order to

cure infrared divergences, we add a mass regulator $\mu \sigma_z$ to the quadratic action of the decoupled bilayer

$$S_{R,0} = \int_{\mathbf{k},\Omega} \bar{\psi}_{\mathbf{k}} (\boldsymbol{\sigma} \cdot \mathbf{k} - i\Omega + \mu \sigma_z) \psi_{\mathbf{k}}, \quad (7.8)$$

where the mass scale μ vanishes in the infrared limit. The quadratic hopping action reads

$$S_{R,\alpha} = \alpha \sum_{j=1}^3 \sum_{\eta=\pm} \int_{\mathbf{k},\Omega} \bar{\psi}_{\mathbf{k}} T_j^\eta \psi_{\mathbf{k}+\eta\mathbf{q}_j}. \quad (7.9)$$

The quadratic bosonic part of the action is given by

$$S_{R,\phi} = \sum_{i=1}^8 Z_{\phi_i} \int_{\mathbf{k},\Omega} (\phi_i^2)_{\mathbf{k}} + \sum_{l=1}^4 Z_{\varphi_l} \int_{\mathbf{k},\Omega} (\varphi_l^2)_{\mathbf{k}}. \quad (7.10)$$

Finally, the Yukawa coupling is

$$S_{R,\text{Yuk}} = 2\mu^{-\varepsilon/2} N_\psi \left[\sum_{i=1}^8 Z_{g_i} \sqrt{g_i} \int_{\mathbf{k},\Omega_k, \mathbf{q}, \Omega_p} \bar{\psi}_{\mathbf{k}} (\phi_i M_i)_{\mathbf{k}-\mathbf{q}} \psi_{\mathbf{q}} + \sum_{l=1}^4 Z_{\lambda_l} \sqrt{\lambda_l} \int_{\mathbf{k},\Omega_k, \mathbf{q}, \Omega_p} \bar{\psi}_{\mathbf{k}} (\boldsymbol{\varphi}_l \cdot \mathbf{M}_l)_{\mathbf{k}-\mathbf{q}} \psi_{\mathbf{q}} \right]. \quad (7.11)$$

Among the Yukawa couplings of Eq. (7.11), the layer off-diagonal vertices break translational invariance: the bosonic field transfer the momenta $\pm\mathbf{q}_j$ for $j = 1, 2, 3$, because of the spatial dependence of the coupling matrix (see Eq. (6.44)). For brevity we omitted the dependence of the fields on frequency and used the notation shorthand

$$\int_{\mathbf{k},\Omega} = \int_{-\infty}^{+\infty} \frac{d\Omega}{2\pi} \int_{\mathbb{R}^d} \frac{d^d k}{(2\pi)^d}. \quad (7.12)$$

Unlike the low-energy theory of relativistic semimetals in presence of quenched disorder, here the frequency is also transferred in the Yukawa coupling, and loops contain both a dummy frequency, integrated from $-\infty$ to ∞ , and a dummy momentum, integrated in space dimension $d = 1 + \varepsilon$. To fix the Z constants, we use again the minimal subtraction scheme: we absorb only the divergent parts of the Feynman diagrams. Inspecting Eq. (7.10) and (7.11), we see that the constants Z_ϕ can be found by absorbing the divergences of the polarisation, i.e. the bosonic self-energy, while the constants Z_g can be found from the divergences of the three-point Yukawa vertices. Before computing these diagrams, let us outline the general strategy.

The theory acquires two extra Feynman rules when including interactions.

- The free bosonic propagators are depicted as dashed lines,

$$\Delta_0^{(i)}(\mathbf{k}, \Omega) = Z_{\phi_i}^{-1} = \text{---} \overset{i}{\text{---}} \text{---} \quad (7.13)$$

for the one-dimensional channels, and similarly for the two-dimensional channels.

- In the tree-level Yukawa vertex, two fermionic lines join with a bosonic one. For layer-diagonal channels, the vertex with zero bosonic momentum is weighted by the matrix factor

$$2\mu^{-\varepsilon/2} N_\psi Z_{g_i} \sqrt{g_i} M_i = \text{---} \overset{i}{\text{---}} \begin{array}{l} \nearrow \mathbf{k} \\ \searrow \mathbf{k} \end{array} \quad (7.14)$$

for the one-dimensional channels, and similarly for the two-dimensional channels. For layer off-diagonal channels, translational invariance is broken and the vertex with zero bosonic momentum is weighted by the matrix factor

$$2\mu^{-\varepsilon/2} N_\psi Z_{g_i} \sqrt{g_i} M_i^{(\eta j)} = \text{---} \overset{i}{\text{---}} \begin{array}{l} \nearrow \mathbf{k} + \eta \mathbf{q}_j \\ \searrow \mathbf{k} \end{array} \quad (7.15)$$

where the coupling matrix is decomposed into $M_i(\mathbf{r}) = \sum_{\eta=\pm} \sum_{j=1}^3 M_i^{(\eta j)} e^{-i\eta \mathbf{q}_j \cdot \mathbf{r}}$.

Treatment of the hopping term — This theory is highly non-standard already at the single-particle level, as we have seen in Sec. 6.1. There, we diagonalised the Hamiltonian perturbatively order by order in the hopping strength α . In the same spirit, we expand the correlation functions of the interacting theory not only in the coupling constants but also in the hopping strength. The insertion of hopping matrices leads to two classes of diagrams.

- When all hopping matrices affect a subgraph which has two external legs and contains no three-point vertex, the diagram is topologically equivalent to those of the theory without interlayer hopping. Such subgraphs can be resummed at all order in α to bring out the corrected propagator of Eq. (6.18). This method captures efficiently the vanishing energy scale at the magic angle by extracting a factor v^{-L} at order L of the loopwise expansion. Hence, the proper expansion parameter is not the coupling constant g , but the ratio g/v .
- In other cases, hopping matrices meddle with three-point vertices and the diagram is not topologically equivalent to those of the theory without interlayer hopping. Such diagrams contribute a term of order $\alpha^n g^{L+1}$ in the beta function, where n is the (even) number of non-resummable insertions. As in the first case, we extract a factor v^{-L} by resumming insertions over single fermionic lines.

The loopwise expansion comprises two steps. We first draw the standard diagrams with Yukawa vertices, and replace all solid lines by double lines, like in the polarisation of Fig. 7.5(a), or the three-point vertex of Fig. 7.5(c). We then include wavy lines connecting distinct fermionic lines in all possible ways, as in Fig. 7.5(b) for the polarisation, or Fig. 7.5(d) to Fig. 7.5(g) for the three-point vertex. We restrict the computation to the first non-trivial order α^2 .

Importantly, the graphs affected by hopping carry fermionic propagators evaluated at the momenta $\mathbf{q} + \eta \mathbf{q}_j$, where \mathbf{q} is the loop momentum and \mathbf{q}_j , for $j = 1, 2, 3$ are the leading

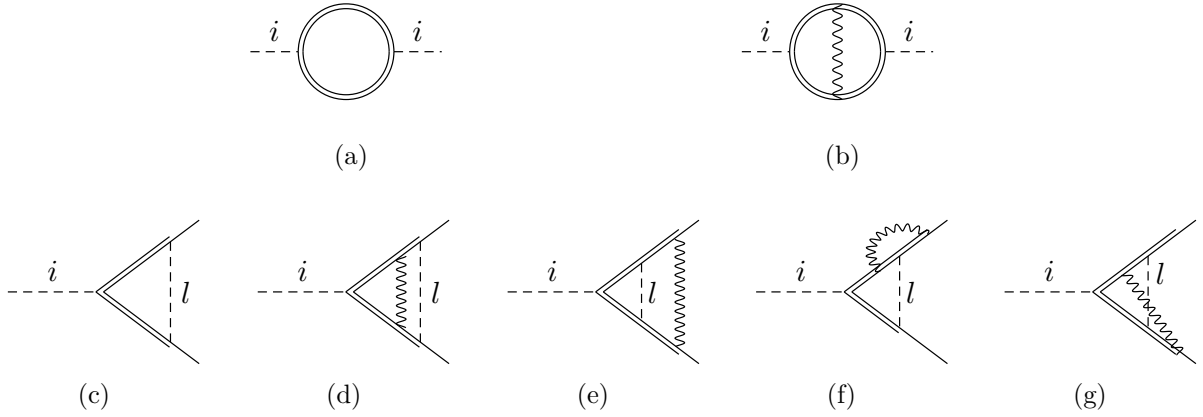


Figure 7.5 | One-particle irreducible diagrams at first order in the loopwise expansion and second order in the dimensionless hopping strength α . The double line stands for the fermionic propagator corrected by interlayer hopping, the dashed line for a bosonic propagator, and the wavy line for the sum of all interlayer hopping channels with momenta $\eta\mathbf{q}_j$, for $\eta = \pm$ and $j = 1, 2, 3$. The polarisation Π_i , i.e. the corrections to the bosonic propagator of type i , is taken at zero external momentum and frequency and given by (a) at order α^0 and (b) at order α^2 . The three-point Yukawa vertex V_{il} , also at zero external momenta and frequencies, is drawn in (c) at order α^0 , and in (d)-(g) at order α^2 . The hopping line can be (d) internal, (e) external, (f) isolated and (g) crossed with respect to the internal vertex of type l .

Fourier momenta of the tunnelling amplitude. The norm of the \mathbf{q}_j is unity – the size of the mini Brillouin zone. Yet, the instabilities develop at wave lengths much larger than the moiré period, so that the loop momentum \mathbf{q} and the loop frequency ω are negligible with respect to the momenta \mathbf{q}_j transferred by interlayer hopping. We can therefore simplify

$$G_0(\mathbf{q} + \eta\mathbf{q}_j, \omega) \simeq G_0(\eta\mathbf{q}_j, 0) = \eta\boldsymbol{\sigma} \cdot \mathbf{q}_j, \quad (7.16)$$

in Feynman integrals.

Reduction to the four relevant instabilities — As advertised in Sec. 7.1, only four interactions out of twelve are relevant. The four instabilities which develop in density-like channels $\bar{\psi}\sigma_0\tau_\mu\psi$ have no poles near $(1+1)$ dimensions, because the spatial and temporal divergences compensate. The vanishing of the corrections to the vertex seems to persist at all order in perturbation theory. The four remaining instabilities which develop in layer off-diagonal channels $\bar{\psi}\tau_{x/y}\psi$ lead to order parameters with fast spatial modulations (of the order of the moiré pattern’s size) because of the spatial dependence of the coupling matrix. Due to the net separation of energy scales, captured by Eq. (7.16), the corrections to these interactions vanish. We are left with a four-dimensional subspace of the flow corresponding to the four irrep. a_2^- (layer-symmetric gap), a_1^- (layer-polarised gap) of Tab. 6.2, and E_2^+ (layer-symmetric momentum shift), E_4^- (layer-polarised momentum shift) of Tab. 6.3. Each of them is associated with a phase transition towards a correlated phase, and the renormalisation group flow captures the competition between these phases.

7.2.2 Loopwise and hopping strength expansions

We compute the polarisation and the three-point vertices, the two diagrams necessary to determine the flow of the coupling constants. We relegate the details of the calculation to Appendix E. Fig. 7.5 presents all one-loop diagrams up to order α^2 .

Polarisation — The polarisations Π_i are the self-energy of the bosonic fields ϕ_i , for $i = 1, \dots, 8$, and similarly for the vector fields φ_l , for $l = 1, \dots, 4$. If $\Delta_i(\mathbf{k}, \Omega)$ denotes the (renormalised) propagator of the bosonic field, we have $\Delta_i^{-1}(\mathbf{k}, \Omega) = Z_{\phi_i} - \Pi_i(\mathbf{k}, \Omega)$. The one-loop diagrams contributing to the polarisation are drawn in Fig. 7.5(a) at order α^0 and Fig. 7.5(b) at order α^2 . The finiteness of $\Delta_i(\mathbf{k} = \mathbf{0}, \Omega = 0)$ leads to the following expression of the Z_{ϕ_i} constants,

$$Z_{\phi_i} = 1 - \frac{4ng_i I_i [1 + 3\alpha^2 \chi_i h_i(\beta)]}{v\epsilon}, \quad (7.17)$$

where $n = 4$ stands for the number of degrees of freedom. The quantity χ_i equals either $+1$ for the interaction matrices $\sigma_z \tau_0$ and $\sigma \tau_z$, or -1 for the interaction matrices $\sigma_z \tau_z$ and $\sigma \tau_0$; the function $h_i(\beta)$ equals either $1 - \beta^2$ or 1 if the interaction matrix matches σ_0 or σ_z in the sublattice sector, respectively. The integrals I_i are numerical constants listed in Appendix E.

Yukawa vertices — We enforce the finiteness of $V_i(\{\mathbf{k} = \mathbf{0}\}, \{\Omega = 0\})$. The diagram of order α^0 is drawn in Fig. 7.5(c), while the diagram of order α^2 is given by Fig. 7.5(d) to Fig. 7.5(g). All internal vertices contribute to the vertex function i if the external vertex is of type i . The Z constants for the couplings read

$$Z_{g_i} = 1 - \frac{4}{v\epsilon} \sum_{l=1}^{12} g_l \left\{ [1 + 6\alpha^2 h_i(\beta) \chi_i] J_{il} + 2\alpha^2 K_{il}(\beta) \right\}, \quad (7.18)$$

where by definition $g_l = \lambda_{l-8}$ for $l = 9, \dots, 12$. The sum of Eq. (7.18) runs over all channels for generality, but we will focus only on the four relevant ones. One-dimensional and two-dimensional channels alike contribute to the sum. The integrals J_{il} are numerical constants listed in Appendix E, while K_{il} depend on β .

Beta functions — We express the renormalisation constant $Z_i = Z_{g_i}^2 Z_{\phi_i}^{-1}$ at first order in the coupling constants as

$$Z_i = 1 + \sum_{l=1}^{12} \frac{f_{il}(\alpha, \beta) g_l}{v\epsilon}, \quad (7.19)$$

where v is the corrected Fermi velocity of Eq. (6.20) and the explicit expressions of the functions f_{il} are given in Tab. 7.1 for the four relevant instabilities. The hopping-independent correction vanishes for the one-dimensional channels in the case of a single Dirac fermion ($n = 2$), in agreement with the absence of any flow in the (1+1)-dimensional Thirring model (GRACEY 2016). The beta functions follow from Eq. (7.19) from the relation

$$\beta_i = -\frac{\partial g_i}{\partial \log \mu} = -\epsilon g_i + \frac{g_i}{v} \sum_{l=1}^{12} f_{il}(\alpha, \beta) g_l. \quad (7.20)$$

The physical (2+1)-dimensional model is recovered for $\epsilon = 1$.

7.2.3 Flow diagram

Dominant instabilities — We now discuss the key features of this four-dimensional flow as a function of α . The Gaussian fixed point at the origin is always stable in $(2 + 1)$ dimensions, and attracts all flowing coupling strengths whose microscopic value lies within the semimetallic region. Besides, we identify four critical points for non-special values of α , one for each non-trivial coupling, at locations $g_i^* = \varepsilon v / f_{ii}$, with v the corrected Fermi velocity. These fixed points control phase transitions towards the four correlated phases discussed in the mean-field analysis of Sec. 7.1. As α approaches the first magic value α_0 , all critical fixed points collapse on the Gaussian fixed point: all non-trivial perturbations become relevant, and the semimetallic region shrinks to the Gaussian fixed point and disappears entirely. Hence the correlated phases correspond to runaway flows in specific directions, and are not described by a perturbative stable fixed point. A natural way to identify the dominant instabilities among those four is to select those couplings whose critical fixed point collapse the fastest near the magic angle. We see from Tab. 7.1 that this criterion elects the layer-polarised channels $\sigma_z \tau_z$ and $\sigma \tau_z$, with coupling constants g_z and λ_z , at the expense of the layer-symmetric channels $\sigma_z \tau_0$ and $\sigma \tau_0$, with coupling constants g_0 and λ_0 .

This hierarchy of the four relevant instabilities seems at odds with the mean-field results of Sec. 7.1. The mean-field analysis predicted the layer-symmetric gap Δ_0 to be less suppressed by interlayer hopping than the layer-polarised gap Δ_z . Admittedly, the two approaches treat interlayer hopping differently: in the mean-field analysis of Sec. 7.1, we diagonalised the correlators of the mean-field self-consistent equations, whereas in the present renormalisation group analysis, we study how interlayer hopping processes affect the flow of the coupling strengths. But this discrepancy shows above all the importance of fluctuations of the order parameters near the first magic angle, and proves that a renormalisation group analysis is necessary to study the competition of instabilities.

$\pi f_{il}/2$	$\sigma_z \tau_0$	$\sigma_z \tau_z$	$\sigma \tau_0$	$\sigma \tau_z$
$\sigma_z \tau_0$	$2[1 - 12\alpha^2(1 - \beta^2)]$	$-2[1 - 6\alpha^2(1 - \beta^2)]$	$2[1 - 6\alpha^2(1 + \beta^2)]$	$2[1 + 6\alpha^2(3 - \beta^2)]$
$\sigma_z \tau_z$	$-2[1 - 6\alpha^2(1 - \beta^2)]$	2	$2[1 - 6\alpha^2(1 - \beta^2)]$	$2[1 - 6\alpha^2(1 - \beta^2)]$
$\sigma \tau_0$	$1 - 6\alpha^2(1 + \beta^2)$	$1 - 6\alpha^2(1 - \beta^2)$	$2[1 - 3\alpha^2(1 - \beta^2)]$	$-6\alpha^2\beta^2$
$\sigma \tau_z$	$1 + 6\alpha^2(3 - \beta^2)$	$1 - 6\alpha^2(1 - \beta^2)$	$-6\alpha^2\beta^2$	$2[1 + 3\alpha^2(1 + \beta^2)]$

Table 7.1 | List of the one-loop coefficients $f_{il}(\alpha, \beta)$ of the beta functions defined in Eq. (7.20), at second order in the dimensionless hopping strength α , and function of the relative AA/AB hopping strength β . Only the four non-trivial channels are presented, with matrix structures $\sigma_z \tau_0$ (layer-symmetric gap), $\sigma_z \tau_z$ (layer-polarised gap), $\sigma \tau_0$ (layer-symmetric momentum shift), and $\sigma \tau_z$ (layer-polarised momentum shift).

Layer-polarised gap versus nematic competition — Discarding the coupling constants g_0 and λ_0 , we are left with a two-dimensional flow diagram for the coupling constants g_z and λ_z , which is easier to study. While the gapped phase, induced by g_z , is reminiscent of the dynamical mass generation in the Gross-Neveu model (GROSS 1974; ROSENSTEIN 1991), the \mathcal{C}_3 -breaking phase is specific to TBG. The competition between these two dominant instabilities follows from the coupled flow equations

$$\left\{ \begin{array}{l} \beta_{g_z} = -\epsilon g_z + \frac{4g_z^2}{\pi v} + \frac{4g_z\lambda_z}{\pi v} [1 - 6\alpha^2(1 - \beta^2)], \end{array} \right. \quad (7.21a)$$

$$\left\{ \begin{array}{l} \beta_{\lambda_z} = -\epsilon\lambda_z + \frac{4\lambda_z^2}{\pi v} [1 + 3\alpha^2(1 + \beta^2)] + \frac{2\lambda_z g_z}{\pi v} [1 - 6\alpha^2(1 - \beta^2)]. \end{array} \right. \quad (7.21b)$$

To explore the competition between the phases in vicinity of the magic angle, we plot the renormalisation flow of the coupling constants rescaled by the vanishing velocity v in Fig. 7.6. Only the $g_z > 0$ and $\lambda_z > 0$ region corresponds to repulsive interactions, which are the only physical insulating mechanisms. The comparison between the flows for highly suppressed interlayer hopping (Fig. 7.6(a)) and close to the first magic angle (Fig. 7.6(b)) reveals that the proximity to the magic angle favours the nematic phase by enlarging the corresponding region of the phase diagram. This behaviour parallels the Mott multicriticality found in monolayer graphene in the limit of a large fermion number, though the competition involves slightly different phases (CLASSEN 2015). The fastest diverging coupling commands the large-scale behaviour; this selects two regions with runaway g_z (a purely gapped phase) or λ_z (a purely nematic phase). Within the one-loop analysis, a crossover line separates these regions, with parametric equation

$$\lambda_z = \frac{1 + 6\alpha^2(1 - \beta^2)}{6\alpha^2(3 - \beta^2)} g_z. \quad (7.22)$$

Next to the crossover line, both order parameters coexist over a large range of length scales, so that neither phase prevails. This mixed state develops a gap with periodic modulations of the density, and breaking the rotational \mathcal{C}_3 and antiunitary Θ symmetries. We call this phase a *nematic insulator*.

Similar nematic orderings were reported in recent works. The starting point and strategy of these works differ entirely from our approach, and rely on effective tight-binding models built from exponentially localised Wannier orbitals and analysed in mean field. (KLUG 2020) finds a stripe order at filling factors $|\nu| < 2$, including at charge neutrality $\nu = 0$, with a few possible ordering vectors of the order of superlattice reciprocal vectors \mathbf{Q}_1 and \mathbf{Q}_2 . The emergence of a gap is not explored in this work. On the other hand, (LIU 2021) studied a momentum-space continuum model where they break the three-fold symmetry by hand by distorting one of the three tunnelling matrices T_j^\pm . By minimising the energy of possible correlated states through a Hartree-Fock analysis, they find a gapped nematic ground state at all values of the symmetry-breaking parameter. As in our renormalisation group approach, they noticed the interplay between the gapped and nematic instabilities. But unlike in previous studies, in our renormalisation group analysis we clearly identify a nematic order parameter through the correlation function $\langle \bar{\psi} \boldsymbol{\sigma} \tau_z \psi \rangle$, and prove that quantum fluctuations favour the spontaneous emergence of a combined insulating and stripe order.

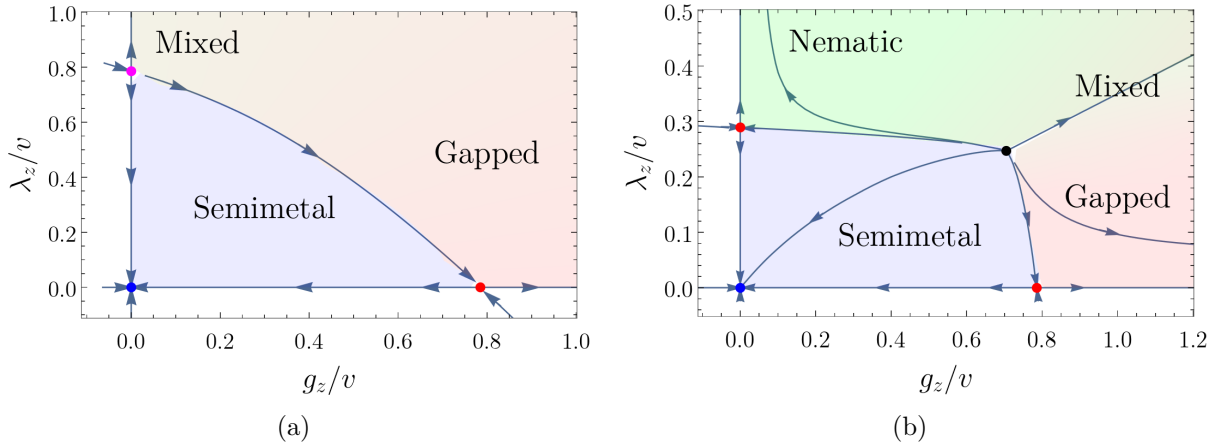


Figure 7.6 | Renormalisation flow of the coupling constants g_z , associated to a layer-polarised gap, and λ_z , associated to a layer-polarised momentum shift. Due to the vanishing of the kinetic energy at the magic angle, the coupling constants are rescaled by the Fermi velocity corrected by interlayer hopping $v \rightarrow 0$. All interactions corrected at one-loop order are thus relevant perturbations in magic twisted bilayer graphene. The ratio of intra- over inter-sublattice hopping amplitudes is set to $\beta = 0.82$. (a) In the absence of hopping ($\alpha = 0$), a critical fixed point (red dot \bullet) on the g_z -axis controls the transition towards a correlated insulator (gapped phase, reddish region). The Gaussian sink point (blue dot \bullet) defines the semimetallic phase (blueish region). The fixed point on the λ_z -axis is marginal (pink dot \bullet). (b) Near the first magic angle ($\alpha \simeq \alpha_0$), the semimetallic region shrinks to the origin in the (g_z, λ_z) plane. When rescaled by v , a second critical fixed point appears on the λ_z -axis, which controls the transition towards a \mathcal{C}_3 -breaking (nematic) phase (greenish region). A source fixed point (black dot \bullet) gives rise to a crossover region (mixed state). It migrates away from the vertical axis as α increases, thus expanding the region with nematic order.

7.3 Perspective

Before concluding, we wish to put our results in perspective in the context of the very active field of TBG. We first discuss the effect of twist angle disorder, which completely suppresses the gap at charge neutrality in experiments. We also compare our results with a different renormalisation group approach in presence of Coulomb interactions. Finally, we discuss the ordering of the nematic insulator at charge neutrality in the valley and spin sectors.

7.3.1 Twist angle disorder

Several sources of disorder can smear the properties of pristine TBG samples. An obvious one is charge disorder, but it appears to be fairly low, with deviations of carrier density about $\delta n \simeq 10^{10}$ meV (CAO 2018a). Another comes from the alignment of TBG with the hBN substrate, which breaks the Θ symmetry and opens a gap. These types of defects do not explain why devices with disordered samples fail to see a large gap at charge neutrality, which yet appears clearly in clean samples (LU 2019). The most important source of disorder thus appears to be angular heterogeneity.

It was not until experimentalists managed to devise angle-homogeneous samples that the strong insulator at charge neutrality was observed (LU 2019). This suggests that

at the charge neutrality point, more than at any other band filling, TBG is sensitive to the heterogeneity of the twist angle. This heterogeneity results from local strains on the bilayer, whose relaxation towards the energetically favoured Bernal stacking is impeded by the substrate. This new type of *angular* disorder was studied numerically (WILSON 2019). The authors consider a real-space microscopic model with a sample made of several patches with uniform twist angles randomly chosen from a box distribution. They point out two main effects of disorder. On one hand, the Fermi velocity seems extremely robust to angular disorder, apart from a small rounding near the magic angle. On the other hand, electronic states tend to fill the gap between the active bands and passive bands under increasing disorder, which even vanishes when fluctuations in twist angle exceed a few percents. This sensitivity explains why the carrier density required to reach full filling of the active bands varies strongly from sample to sample (YANKOWITZ 2019).

The interplay between angular disorder and many-body effects, however, remains an open field of research. The low-energy interacting theory studied in this chapter provides a valid basis to tackle this problem. Indeed, a heterogeneity in twist angle θ entails a heterogeneity in the dimensionless hopping strength $\alpha \propto \theta^{-1}$. Instead of treating α as a fixed parameter, we could assume the position-dependent $\alpha(\mathbf{r})$ to be a random variable, e.g. of Gaussian distribution

$$P[\alpha] \propto \exp \left[-\frac{1}{2\sigma_\alpha} \int d^d r (\alpha(\mathbf{r}) - \bar{\alpha})^2 \right], \quad (7.23)$$

with mean $\bar{\alpha}$ and variance σ_α . We thus recover a problem similar to that of disordered Weyl semimetals, as we have seen in Chapter 3. In principle, the renormalisation group study of Sec. 7.2 could be extended to a replicated theory of disordered TBG by substituting α for $\bar{\alpha}$, incorporating the action

$$S_{\sigma_\alpha} = -\frac{\sigma_\alpha}{2} \sum_{j,l=1}^3 \sum_{\eta,\mu=\pm} \int_{\mathbf{k}_i, \mathbf{q}} \bar{\psi}_{\mathbf{k}_1} T_j^\eta \psi_{\mathbf{k}_1 + \mathbf{q} + \eta \mathbf{q}_j} \bar{\psi}_{\mathbf{k}_2} T_l^\mu \psi_{\mathbf{k}_2 - \mathbf{q} + \mu \mathbf{q}_l}, \quad (7.24)$$

and expanding order by order in σ_α . At this stage, it seems unclear which physical mechanism could explain that the gap of the nematic insulator at charge neutrality is so effectively suppressed by angular disorder.

7.3.2 Coulomb interaction

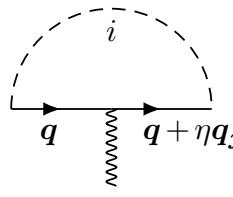
We modelled many-body effects in TBG as contact interactions at the scale of the moiré wave length. Recently, O. Vafeek et al. independently developed a renormalisation group approach for the generalised continuum model (continuum model with arbitrary AA and AB/BA hopping amplitudes) in presence of unscreened Coulomb repulsion, instead of contact interaction (VAFEK 2020).

In the first stage of their renormalisation procedure, both interaction and interlayer hopping are treated perturbatively. Using momentum-shell integration, the authors find that the Coulomb repulsion enhances the dimensionless Fermi velocity v and the AB/BA hopping strength w in the infrared limit, while the AA hopping strength u remains fixed:

$$-\mu \frac{dv}{d\mu} = \frac{e^2}{4\epsilon}, \quad -\mu \frac{dw}{d\mu} = w \frac{e^2}{4\epsilon v}, \quad -\mu \frac{du}{d\mu} = 0, \quad (7.25)$$

where μ denotes the mass scale, and ϵ is the dielectric constant. The scaling behaviour of the Fermi velocity agrees with that in monolayer graphene. The low-energy theory of graphene flows indeed to the fixed point of $(2 + 1)$ -dimensional quantum electrodynamics, where v equals the speed of light (VOZMEDIANO 2011). The generalised continuum model thus flows towards the fixed point $\beta = 0$, which corresponds to the first chiral limit discussed in Sec. 6.1.1.

The flow of w described by Eq. (7.25) contrasts with our results of Sec. 7.2 for contact interactions, where we kept $\alpha \propto w$ and $\beta = u/w$ as fixed parameters; the two-point vertices which break momentum conservation all converge at one-loop order, so that we needed not introduce renormalisation constants $Z_{\alpha,\beta}$ in the renormalised hopping action of Eq. (7.9). An example of diagram that contributes to the vertex function $\langle \bar{\psi}_{\mathbf{k}} T_j^\eta \psi_{\mathbf{k}+\eta\mathbf{q}_j} \rangle_{\text{1PI}}$ is the one-loop correction



$$= \alpha N_\psi^2 (4g_i) \int_{\mathbf{q}, \omega} M_i G'_0(\mathbf{q} + \eta\mathbf{q}_j, \omega) T_j^\eta G'_0(\mathbf{q}, \omega) M_i \Delta_{0,i}(\mathbf{q}, \omega), \quad (7.26)$$

where $\Delta_{0,i}(\mathbf{q}, \omega)$ is the free bosonic propagator, and the external momentum and frequency are set to $\mathbf{k} = \mathbf{0}$ and $\Omega = 0$, respectively. Due to the net separation of energy scales, $q, \omega \ll |\mathbf{q}_j|$ and Eq. (7.26) has no pole whatever the bosonic propagator $\Delta_{0,i}(\mathbf{q}, \omega)$, which is an even function of \mathbf{q} and ω . This holds for contact interactions, where $\Delta_{0,i}(\mathbf{q}, \omega) = 1$, but also for Coulomb repulsion, for which $\Delta_{0,i}(\mathbf{q}, \omega) = e^2/\epsilon q^2$. Screening cannot bring corrections to the hopping strengths either, and higher order diagrams in the loopwise expansion appear to converge as well. Hence, we cannot predict any renormalisation of the hopping strengths in our scheme.

7.3.3 Valley and spin degrees of freedom

The Landau levels emerging from the Mott insulators at integer fillings $\nu = \pm 1, \pm 2, \pm 3$ follow a two-fold degenerate sequence (LU 2019). This observation holds at charge neutrality $\nu = 0$ for the two lowest Landau levels, although the Landau fan recovers a four-fold degeneracy at larger quantisation indices. These results suggest that the spin-valley degeneracy is partially lifted, and that the order parameters of the insulating phases have a non-trivial structure in the spin or valley sectors. Besides, quantum oscillations point towards a trivial spin order but non-trivial valley order (YANKOWITZ 2019). Let us discuss the structure of the gap order parameter in the valley sector.

Starting from the layer-polarised order parameter $\Delta_z \propto \langle \bar{\psi} \sigma_z \tau_z \psi \rangle$, which we found to be the order favoured at charge neutrality, the inclusion of the valley degree of freedom leads to three structures for Δ_z . Either the charge neutrality point develops a valley-symmetric gap, which corresponds to a trivial μ_0 identity matrix in the valley sector. Or, correlations break time-reversal symmetry, leading to a valley polarisation μ_z . Or, correlations break the valley U(1) charge, which induces an intervalley coherent order $\mu_x \cos \theta + \mu_y \sin \theta$ and lifts the valley degeneracy. In the following, we discuss the probable valley orders at non-zero filling factors and at charge neutrality, in light of recent numerical studies.

Non-zero filling factors — Numerical studies usually rely on a tight-binding description. The Wannier functions of the flat bands, which provide a basis of orbitals localised at the AA sites of the moiré pattern, strongly overlap with their neighbours through their three lobes, which leads to an unusual interaction Hamiltonian (KANG 2019). Within a mean-field approach, the ground states at half filling ($\nu = \pm 2$) and quarter filling ($\nu = \pm 1$) develop a mixed spin-valley order. These SU(4) ‘ferromagnets’ are not necessarily spin magnetic, unless an unknown mechanism further lift the spin-valley degeneracy. In particular, the two valleys K and K’ carry opposite spins at half filling. The insulator at three-quarter filling ($\nu = \pm 3$) could be an anomalous Hall state, which exhibits both valley and spin polarisations (BULTINCK 2020a).

Charge neutrality — The hierarchy of the energy scales associated to the possible instabilities at charge neutrality depends strongly on interlayer hopping amplitude, twist angle, and to a lesser extent on the dielectric permittivity, so that theoretical studies do not agree as to the nature of the ground state (XIE 2020; CHOI 2019). Most probably, the insulator at charge neutrality develop an intervalley-coherent order, which unlike the SU(4) ferromagnet breaks time-reversal symmetry to the benefit of an effective Kramers symmetry, and leads to a band structure with trivial topology. (PO 2018; BULTINCK 2020b; LIU 2021). The mean-field analysis results in the following classification: the semimetallic phase is the most energetic, followed by a valley Hall phase, a valley-polarised phase, and finally the presumed ground state with Kramers intervalley coherence (BULTINCK 2020b). Intervalley coherence cannot induce Mott insulation by itself. The authors propose the breaking of \mathcal{C}_3 as the gapping mechanism, instead of the independent Θ -breaking mechanism that we proposed in Sec. 7.1.

Conclusion

Summary — By applying a mean-field analysis supplemented by a renormalisation group approach, we have shown that the proximity to the first magic angle in twisted bilayer graphene favours a gapped nematic state at charge neutrality. Within the mean-field analysis, the dominant insulating instability emerges from a layer-symmetric gap. By including quantum fluctuations, the renormalisation group analysis favours instead a layer-polarised gap. The discrepancy between the mean-field and renormalisation group analyses illustrates the limits of the former, and justifies the necessity of a renormalisation group description. Due to the non-standard nature of the free theory, we have renormalised the interacting theory in a unusual way by expanding correlation functions at leading order in both the dimensionless hopping strength α and the coupling constants g , so as to capture vanishing Fermi velocity v . The competition between the gap and the three-fold symmetry breaking instability leads to a so-called nematic insulator, which develops spatial modulations of the local density of states in the form of stripes. Remarkably, the increase in interlayer hopping favours nematicity, since it enlarges the runaway region of the coupling constant associated to the three-fold symmetry breaking.

Our results agree with the observation of a large gap at charge neutrality in scanning tunnelling spectroscopy (JIANG 2019; CHOI 2019; KERELSKY 2019; XIE 2019) and four-terminal transport measurements (LU 2019). Other studies reported a nematic order at charge neutrality (JIANG 2019; KERELSKY 2019). These experimental findings strongly support the emergence of a nematic insulator at charge neutrality in twisted bilayer graphene, which we have identified in this chapter. This nematic gapped phase was predicted numerically by explicitly breaking the rotational symmetry (LIU 2021), but we have proven that quantum fluctuations within the renormalisation group formalism spontaneously generate a nematic ordering.

Outlook — Our renormalisation group approach does not rule out other correlations to develop conjointly with the nematic order. This includes intervalley coherence and generalised (spin or valley) ferromagnetism (OCHI 2018; BULTINCK 2020b; CHICHINADZE 2020; ZHANG 2020). Some theoretical works suggest that the energies scales of these correlated states are close to one another, resulting in a strong sensitivity to microscopic details (ZHANG 2020). In addition, the observation of a distinct type of nematicity in the superconducting domes raises the questions of the relation between different nematic orders in the phase diagram of magic angle twisted bilayer graphene (CAO 2020b).

General conclusion

In relativistic semimetals, the dynamics of the low-energy excitations follows the massless Dirac equation, thereby bridging a gap between condensed matter and high-energy physics. This is all the more remarkable that these two domains belong to fundamentally distinct research traditions, and deal with the physical properties at wildly different energy scales. Two-dimensional (graphene) and three-dimensional (Weyl and Dirac) relativistic semimetals provide a wonderful playground to experimentally realise exotic equilibrium, transport, topological or surface properties. We have shown in this project that we cannot overlook perturbations of these materials, which can destabilise the linear crossing points and utterly change the nature of the phase, leading to a diffusive metal in disordered Weyl semimetals or strongly correlated states in twisted bilayer graphene. A field-theoretical formalism stands out as the natural framework to analyse the low-energy physics of perturbed relativistic semimetals. Besides, the renormalisation group appears as a strikingly powerful tool to investigate the large-scale behaviour of such diverse physical systems.

In the first part of this thesis, we have mapped the low-energy theory of Weyl semimetals in presence of uncorrelated disorder to the Gross-Neveu model. To account for the various types of disorder, we have extended this theory to include long-range correlations. Disordered Weyl and Dirac semimetals undergo a continuous phase transition towards a metallic phase; the average density of states at the Fermi level acts as an order parameter, since it vanishes in the semimetallic side, while being non-zero above the critical disorder strength. A few critical exponents – the anomalous field, dynamical and correlation length exponents – determine the scaling behaviour of many observables, in particular the average density of states. We have also found signatures of criticality in the geometrical properties of the electronic wave function, in the form of multifractality. The multifractal nature of the critical wave functions originates from the presence of multiple length scales in the spatial distribution of electrons; multifractals thus obey multiple scaling rules instead of a global one. The celebrated renormalisation group technique provides a systematic way to compute the critical exponents at this semimetal-metal transition: within a two-loop ε -expansion, we have computed the scaling exponents of the moments of the wave function density, which give direct access to the multifractal spectrum, for the two universality classes of the Weyl semimetal-metal transition controlled by either short-range or long-range disorder correlations. By relating the multifractal spectrum to the distribution width of critical observables, we have predicted the scaling exponent of the typical density of states at the semimetal-metal transition, in agreement with numerical estimates.

We have seen that disorder impacts not only the bulk electronic properties, but also the surface ones. Three-dimensional relativistic semimetals harbour exotic states on their

surface, in the form of curved Fermi arcs, Dirac surface states and Fermi rays. We have modelled these surface states by considering appropriate boundary conditions for Dirac fermions confined in a semi-infinite space. The symmetries of the boundary condition and of the bulk low-energy theory determine the nature of the surface states. We have then included disorder and probed the spatially resolved density of states using a ‘local’ version of the self-consistent Born approximation. We have seen that Dirac surface states, like the bulk excitations, undergo a phase transition towards a metallic state, but at a lower disorder strength, whereas Fermi arcs avoid this critical point because of their extension in momentum space. Surprisingly, the phase diagram of semi-infinite Dirac semimetals shares some similarities with that found in spin systems, which also display a so-called extraordinary transition, reminiscent of the bulk transition, and a surface transition.

To go beyond this work on disordered relativistic semimetals, we could endeavour to better understand the origin of multifractality in disorder-induced phase transitions. Strangely enough, the Anderson and semimetal-metal transitions both display multifractality, even though the nature of these two transitions differ substantially. At the Anderson transition, critical wave functions are intermediate between extended and localised; in contrast, at the semimetal-metal transition, the Fermi level hosts extended states on the strong disorder side, and . . . no states on the weak disorder side. In addition, multifractality not only characterises equilibrium properties, such as the density of states, but also dictates the long-time behaviour of transport properties. Density fluctuations often induce anomalous diffusion in localisation phenomena, but much about the critical transport properties of the semimetal-metal transition remains to explore. More generally, multifractality has become a widely used tool to study disorder-driven phase transitions: Anderson’s localisation and the semimetal-metal transition, but also many-body localisation, the ferromagnetic ordering in spin systems, etc. This concept has even reached a great – and probably greater – popularity beyond condensed matter physics, and scientists apply multifractal analyses in a growing number of mathematical, physical, biological or financial problems. This ubiquity perhaps testifies that the scientific community appreciates better and better the full complexity of random phenomena, which carry essential information beyond the average properties.

We could also envision to draw experimental predictions from the surface properties of disordered relativistic semimetals. Interestingly, the band dispersion of Dirac surface states could be tuned by voltage gating or by controlling the microscopic details of the boundary (surface termination, presence of adatoms, etc.). It would thus be of practical utility to better understand the effect of disorder on edge and surface modes in Dirac materials. From a theoretical viewpoint, the quantitative study of criticality in Dirac surface states could benefit from a renormalisation group analysis, since the renormalisation of fermionic theories in semi-infinite space remains an uncharted territory. By comparison, the field-theoretical description of surface criticality in spin systems has a decades-long history of research activity. The renormalisation of fermionic theories in semi-infinite space poses a great challenge; technically, because the lack of translational invariance increases the computational complexity, and fundamentally, because the perturbative expansion leads to extra surface singularities. We hope that these obstacles will be overcome eventually.

As another outlook, we could investigate alternative field-theoretical descriptions of disordered relativistic semimetals. Indeed, the perturbative renormalisation group gives much information about the weak disorder regime, but disregards non-perturbative phenomena such as rare-region effects, which possibly turn the semimetal-metal transition

into a sharp cross-over. It is also unclear whether we can extract reliable estimates of the critical exponents from the ε -expansion. Alternative approaches include the functional renormalisation group, the Gross-Neveu-Yukawa model, or the non-linear sigma model.

In the second part of this thesis, we have addressed the effect of electron correlations in twisted bilayer graphene, and the emergence of a joint insulating and nematic order at charge neutrality. By overlaying two layers of graphene with a twist, the interference of the two mismatched lattices form large-scale moiré patterns, which spatially modulates interlayer tunnelling. As a result, the Fermi velocity of the Dirac cones vanish at special ‘magic’ angles, where interactions dominate the electron dynamics. We have reviewed major experimental results of twisted bilayer graphene, whose phase diagram features insulating regions at integer fillings of the flat bands surrounded by superconducting domes. Transport measurements and scanning tunnelling microscopy have proved that the strong insulator at charge neutrality breaks the three-fold rotational symmetry. We have built a continuum model for twisted bilayer graphene, and diagonalised the single-particle Hamiltonian perturbatively in the tunnelling strength to determine the correction to the Fermi velocity and explain the origin of the magic angle physics. Focusing then on many-body effects, we have identified the contact quartic interactions that preserve the symmetries of the model. By applying both a mean-field analysis and a renormalisation group approach, we have shown that quantum fluctuations spontaneously break the three-fold symmetry near the first magic angle. Due to the highly non-standard nature of the free theory, we have treated the interacting theory perturbatively in both the tunnelling strength and the coupling constants associated to the relevant interactions. The competition between the gap and the three-fold symmetry breaking instabilities leads to a so-called nematic insulator compatible with experimental findings.

Although our works have focussed on twisted bilayer graphene, the magic angle physics comes into play in a variety of Van der Waals heterostructures (twisted double-bilayer graphene, trilayer graphene, dichalcogenides-based bilayers), where similar correlated phases were found. Thanks to their incredible versatility, these moiré materials represent a wonderful platform to explore the richness of many-body effects. We have indeed identified the nature of the correlated phase which appears at charge neutrality in twisted bilayer graphene, but this phase remains to be characterised. In particular, the unusual emergence of a combined insulating and nematic order should lead to anisotropies in physical observables. What are the electrical, magnetic, optical or thermal properties of such a nematic insulator? Answering these questions will probably leverage much theoretical research effort in the future. In addition, despite the expertise gained on cuprates and pnictides, the microscopic mechanisms at play in unconventional superconductors hold a part of mystery, which twisted bilayer graphene could partially solve. Understanding the origin of superconductivity in twisted bilayer graphene, which exhibits remarkably large critical temperatures close to the limit of Bose-Einstein condensation, may represent a step forward in the on-going race towards high-temperature superconductivity.

Standard field-theoretic tools

A.I Grassmann algebra

Being operators, the quantised Dirac fields satisfy an anticommutating algebra, as required by the spin-statistics theorem. In contrast, usual integration variables are real- or complex-valued and therefore commute with one another. To preserve the algebra of fermions when writing the partition function

$$\mathcal{Z} = \int D\bar{\psi} D\psi e^{-S}, \quad (\text{A.1})$$

we must replace the classical fields $\bar{\psi}$ and ψ by a continuous set of scalar but anticommuting variables, known as Grassmann variables (EFETOV 1996; ZINN-JUSTIN 2002). Acquiring an intuition about what Grassmann variables represent physically is hard, if not hopeless. The best to do is accept them as handy mathematical tools, and go through their formal definition and properties.

A complex Grassmann algebra is an associative algebra generated by the identity and a set of conjugate generators $\{\theta_i, \bar{\theta}_i\}$ which satisfy the anticommuting relations

$$\{\chi_i, \chi_j\} = 0, \quad \text{for } \chi = \theta, \bar{\theta}. \quad (\text{A.2})$$

As a result, any function f defined on the Grassmann algebra reduces to sum of monomials of the form $\chi_{i_1} \dots \chi_{i_p}$. Consider a particular generator χ_i . Any such function can be written $f = f_1 + \chi_i f_2$ after appropriate commutations. We define the derivation and integration with respect to χ_i as the nilpotent operation

$$\int d\chi_i f(\chi_i) = \frac{\partial f}{\partial \chi_i} = f_2. \quad (\text{A.3})$$

Though surprising at first, the definition (A.3) of the so-called Berezin integration is consistent with the usual properties of definite integrals (linearity, Leibniz formula, a total derivative integrates to zero). The use of two different symbols for the same operation seems redundant, but enables to strengthen the similarity with bosonic path integrals. The crucial difference with bosons lies in changes of variables. Indeed the Jacobian of the transformation $\chi'_i \mapsto \chi_i(\chi')$ becomes

$$J(\chi') = \det^{-1} \left(\frac{\partial \chi_i}{\partial \chi'_j} \right), \quad (\text{A.4})$$

with an inverse determinant where we would expect the determinant itself for bosonic variables. A corollary is that the fermionic Gaussian integral

$$I = \int \prod_i d\bar{\theta}_i d\theta_i \exp \left(\sum_{ij} \bar{\theta}_i M_{ij} \theta_j \right) \quad (\text{A.5})$$

gives the inverse $I = \det(M)$ of its bosonic counterpart. Similarly, Wick's theorem applies to Grassmann variables with the correct sign,

$$\langle \bar{\theta}_{i_1} \theta_{i_1} \dots \bar{\theta}_{i_p} \theta_{i_p} \rangle = \sum_{P \in \mathfrak{S}_p} \epsilon(P) \langle \bar{\theta}_{i_1} \theta_{i_{P(1)}} \rangle \dots \langle \bar{\theta}_{i_p} \theta_{i_{P(p)}} \rangle, \quad (\text{A.6})$$

where \mathfrak{S}_p denotes the set of permutations of p elements and ϵ is the signature.

A.II Dimensional regularisation

A.II.1 Basic properties

Definition — Let d be an integer dimension. Let f be an analytic function of a single variable (typically a rational fraction). We consider the following isotropic integral over this function

$$I_d[f] = \int_{\mathbf{q}} f(q) = \int \frac{d^d q}{(2\pi)^d} f(\mathbf{q}), \quad (\text{A.7})$$

where $\mathbf{q} = (q_1, q_2, \dots, q_d)$ is a d -dimensional vector and q is its norm. For values of d where this integral converges, Eq. (A.7) is well defined. Thanks to rotational invariance, we can change from Cartesian to angular coordinates. The angular integral is trivial and only the integral over the norm q remains,

$$I_d[f] = K_d \int_0^\infty dq q^{d-1} f(q), \quad (\text{A.8})$$

Eq. (A.8) defines a one-dimensional Riemann integral. The conventional factor in front is

$$K_d = \frac{\Omega_d}{(2\pi)^d}, \quad \text{where } \Omega_d = \frac{2\pi^{d/2}}{\Gamma(d/2)} \quad (\text{A.9})$$

stands for the area of the hypersphere in d dimensions. The function Γ is Euler's Gamma function, whose properties we shall soon discuss. Now, for all values of d in the complex plane, except possibly at isolated points, we define the dimensional continuation of the integral (A.7) by Eq. (A.8). One of these singularity point typically corresponds to the lower critical dimension of the theory. This d -dimensional integral meets the following requirements (ZINN-JUSTIN 2002).

(i) Translation: for any d -dimensional vector \mathbf{p} ,

$$\int_{\mathbf{q}} f(|\mathbf{q} + \mathbf{p}|) = \int_{\mathbf{q}} f(q). \quad (\text{A.10})$$

(ii) Dilatation: for any positive scalar λ ,

$$\int_{\mathbf{q}} f(\lambda q) = \lambda^{-d} \int_{\mathbf{q}} f(q). \quad (\text{A.11})$$

(iii) Factorisation: for any analytical functions f and g ,

$$\int_{\mathbf{q}} \int_{\mathbf{p}} f(\mathbf{q})g(\mathbf{p}) = \int_{\mathbf{q}} f(\mathbf{q}) \int_{\mathbf{p}} g(\mathbf{p}). \quad (\text{A.12})$$

Remark — Property (ii) implies that the integral of a power of q vanishes, i.e.

$$\int_{\mathbf{q}} q^{-\alpha} = 0, \quad (\text{A.13})$$

for any real α , a result known as Veltman's formula. The vanishing of Eq. (A.13) hides in fact a cancellation between ultraviolet and infrared divergences. For example, Feynman diagrams require to integrate products of propagators, whose leading large momentum behaviour is frequently q^{-2} . The Feynman integral can be split into

$$\int_{\mathbf{q}} q^{-2} = K_d \left(\int_1^\infty dq q^{d-3} + \int_0^1 dq q^{d-3} \right). \quad (\text{A.14})$$

The first term of Eq. (A.14) leads to an ultraviolet pole, which contributes to the renormalisation flow of the field amplitude, frequency, coupling strength, or any operator of the theory. The second term of Eq. (A.14) appears only in massless theories, where infrared divergences mix with ultraviolet ones. This mixing happens in the Gross-Neveu model. To prevent infrared singularities, we can attach a dummy mass m to the fields, which ultimately vanishes at the end of the calculations, but serves as an intermediate regulariser. Eq. (A.14) becomes

$$\int_{\mathbf{q}} \frac{1}{q^2 + m^2} = 2K_d \Gamma_{\text{E}}(1 - d/2) \Gamma_{\text{E}}(d/2) m^{d-2}, \quad (\text{A.15})$$

by virtue of Eq. (A.20). The integral (A.15) displays a pole in $\varepsilon = d - 2$ as expected.

A.II.2 Explicit calculation

Several analytical tricks ease the explicit computation of the d -dimensional integrals found in Feynman diagrams (SREDNICKI 2007; KLEINERT 2001; ZINN-JUSTIN 2002).

Feynman's trick and Schwinger's representation — One is Feynman's trick,

$$\frac{1}{AB} = \int_0^1 \frac{dx}{Ax + B(1-x)}, \quad (\text{A.16})$$

valid for any expressions A and B , which permits to linearise a product of two denominators. Typically, A and B are quadratic polynomials in the norm of loop momenta q , p , etc. The generalisation to higher powers of denominators reads

$$\frac{1}{A^a B^b} = \frac{\Gamma_{\text{E}}(a+b)}{\Gamma_{\text{E}}(a)\Gamma_{\text{E}}(b)} \int_0^1 dx \frac{x^{a-1}(1-x)^{b-1}}{[Ax + B(1-x)]^{a+b}}, \quad (\text{A.17})$$

for positive reals a and b , and where Γ_{E} denotes Euler's Gamma function. Similarly, the trick can be extended to products of more than two denominators, such that

$$\frac{1}{A_1 \cdots A_n} = \Gamma_{\text{E}}(n) \int_0^1 dx_1 \cdots dx_n \frac{\delta(1 - x_1 + \cdots + x_n)}{(A_1 x_1 + \cdots + A_n x_n)^{a_1 + \cdots + a_n}}. \quad (\text{A.18})$$

Alternately, Schwinger's proper time representation can prove helpful:

$$\frac{1}{A^a} = \frac{1}{\Gamma_{\mathbb{E}}(a)} \int_0^\infty d\tau \tau^{a-1} e^{-\tau A}. \quad (\text{A.19})$$

This trick enable to cast complicated rational fractions into Gaussian integrals. When Feynman integrals simplify themselves to isotropic integrals in arbitrary dimension d , one often encounters one-loop integrals of the form

$$\int_{\mathbf{q}} \frac{q^{2a}}{(q^2 + m^2)^b} = \frac{\Gamma_{\mathbb{E}}(b - a - d/2) \Gamma_{\mathbb{E}}(a + d/2)}{(4\pi)^{d/2} \Gamma_{\mathbb{E}}(b) \Gamma_{\mathbb{E}}(d/2)} m^{-2(b-a-d/2)}, \quad (\text{A.20})$$

for positive reals a and b . The mass $m \rightarrow 0$ plays the role either of an infrared regulator in massless theories, or of the fixed Matsubara frequency. When one-loop Feynman diagrams include an external momentum \mathbf{k} , we can use the formula

$$\int_{\mathbf{q}} \frac{1}{(q^2 + m^2)^a [(q + \mathbf{k})^2 + m^2]^b} = \frac{\Gamma_{\mathbb{E}}(a + b)}{(4\pi)^{d/2} \Gamma_{\mathbb{E}}(a) \Gamma_{\mathbb{E}}(b)} \int_0^1 dx \frac{(1-x)^{a-1} x^{b-1}}{[k^2 x(1-x) + m^2]^{a+b-d/2}}. \quad (\text{A.21})$$

Generalisations exist for at two-loop order, where more denominators come into play.

Tensor structure — In fermionic theories, the integrand may carry a non-trivial tensorial structure. The integral may be parametric and depend on an external momentum \mathbf{k} . The two symmetric tensors with two indices that we can build from \mathbf{k} are $k_\mu k_\nu$ and $\delta_{\mu\nu}$. Hence (ZINN-JUSTIN 2002),

$$\int_{\mathbf{q}} q_\mu q_\nu f(q, p, \mathbf{q} \cdot \mathbf{k}) = A(k) k_\mu k_\nu + B(k) \delta_{\mu\nu}. \quad (\text{A.22})$$

The functions A and B depend only on the norm k and can be found by tracing or multiplying Eq. (A.22) with k_μ ,

$$\begin{cases} (d-1)A(k)k^2 = \int_{\mathbf{q}} [d(\hat{\mathbf{k}} \cdot \mathbf{q})^2 - q^2] f(q, p, \mathbf{q} \cdot \mathbf{k}) & (\text{A.23}) \\ (d-1)B(k) = \int_{\mathbf{q}} [q^2 - (\hat{\mathbf{k}} \cdot \mathbf{q})^2] f(q, p, \mathbf{q} \cdot \mathbf{k}), & (\text{A.24}) \end{cases}$$

where $\hat{\mathbf{k}} = \mathbf{k}/k$.

Euler's Gamma function — Euler's Gamma function $\Gamma_{\mathbb{E}}$ generalises the factorial to the complex plane; it is defined by

$$\Gamma_{\mathbb{E}}(z) = \int_0^\infty dt t^{z-1} e^{-t}. \quad (\text{A.25})$$

The Gamma function satisfies the recursive relation $\Gamma_{\mathbb{E}}(z+1) = z\Gamma_{\mathbb{E}}(z)$. It is holomorphic except at all negative integer values $z = 0, -1, -2$, etc. Near one of these poles, it satisfies

$$\Gamma_{\mathbb{E}}(-n+x) = \frac{(-1)^n}{n!} \left[\frac{1}{x} + \psi(n+1) + O(x) \right] \quad (\text{A.26})$$

for all real x and integer n ; this relation is usually used with $x = \varepsilon$ in dimension $d = 2 + \varepsilon$ (close to the lower critical dimension) or $d = 4 - \varepsilon$ (close to the upper critical dimension). In Eq. (A.26), $\psi = (\ln \Gamma)'$ is Euler's Digamma function. One particular value is $\psi(1) = -\gamma_E$, where $\gamma_E \simeq 0.58$ is Euler-Mascheroni's constant. The constant term of Eq. (A.26) contributes in counterterms beyond two-loop order, but plays no role at one-loop order in the minimal subtraction scheme.

A.II.3 Feynman integrals with long-range correlation

We reproduce below the list of two-loop integrals presented in (DUDKA 2016), which enter the second-order corrections to the beta functions and the leading contribution to the multifractal exponents. At this order, the Feynman diagrams involve integrals over two internal momenta \mathbf{q} and \mathbf{p} . The graphs are depicted in the following Appendix B; they host three impurity lines labelled each by a symbol a , b or c , which can take the value S for short-range correlations, or L for long-range correlations. We use the shorthand notations $[1] = q^2 + \omega^2$, $[2] = p^2 + \omega^2$, $[3] = (\mathbf{q} + \mathbf{p})^2 + \omega^2$ for the integrands, and

$$\int = K_d^{-2} \int \frac{d^d q}{(2\pi)^d} \int \frac{d^d p}{(2\pi)^d}, \quad (\text{A.27})$$

where K_d is defined in Eq. (A.9). Only the poles are given, unless the leading contribution of the integral is a constant. We collect the Feynman integrals according to the nature of impurity lines.

Case $a = b = c = \text{S}$ —

$$\int \frac{1}{[1][2]} = \int \frac{1}{[1][3]} = \omega^{-2\varepsilon} \left[\frac{4}{\varepsilon^2} \right], \quad (\text{A.28})$$

$$\int \frac{1}{[1][3]^2} = \int \frac{1}{[1][2]^2} = \omega^{-2\varepsilon-2} \left[\frac{2}{\varepsilon} \right]. \quad (\text{A.29})$$

Case $a = \text{L}$ —

$$\int \frac{q^{a-d}}{[1][2]} = \int \frac{q^{a-d}}{[1][3]} = \omega^{-\varepsilon-\delta} \left[\frac{4}{\varepsilon\delta} \right], \quad (\text{A.30})$$

$$\int \frac{q^{a-d}}{[2][3]} = \omega^{-\varepsilon-\delta} \left[\frac{8}{\delta(\delta + \varepsilon)} \right], \quad (\text{A.31})$$

$$\int \frac{q^{a-d}}{[1][2]^2} = \int \frac{q^{a-d}}{[1][3]^2} = \omega^{-\varepsilon-\delta-2} \left[\frac{2}{\delta} \right], \quad (\text{A.32})$$

$$\int \frac{q^{a-d}}{[2]^2[3]} = \int \frac{q^{a-d}}{[2][3]^2} = \omega^{-\varepsilon-\delta-2} \left[\frac{2}{\delta} \right], \quad (\text{A.33})$$

$$\int \frac{q^2 q^{a-d}}{[2]^2[3]^2} = \omega^{-\varepsilon-\delta-2} \left[\frac{4}{\delta} \right], \quad (\text{A.34})$$

$$\int \frac{q^{a-d}}{[1]^2[2]} = \omega^{-\varepsilon-\delta-2} \left[\frac{2}{\varepsilon} \right], \quad (\text{A.35})$$

$$\int \frac{q^2 q^{a-d}}{[2]^3 [3]} = \omega^{-\varepsilon-\delta-2} [-1], \quad (\text{A.36})$$

$$\int \frac{q^{a-d}}{[2]^3 [3]} = \omega^{-\varepsilon-\delta-4} \left[\frac{1}{\delta} \right]. \quad (\text{A.37})$$

Case $a = \mathbf{L}$ and $b = \mathbf{L}$ —

$$\int \frac{q^{a-d} p^{a-d}}{[1][2]} = \omega^{-2\delta} \left[\frac{4}{\delta^2} \right], \quad (\text{A.38})$$

$$\int \frac{q^{a-d} p^{a-d}}{[1][3]} = \int \frac{q^{a-d} p^{a-d}}{[2][3]} = \omega^{-2\delta} \left[\frac{2(3\delta-\varepsilon)}{\delta^2(2\delta-\varepsilon)} \right], \quad (\text{A.39})$$

$$\int \frac{q^{a-d} p^{a-d}}{[1][3]^2} = \int \frac{q^{a-d} p^{a-d}}{[2][3]^2} = \omega^{-2\delta-2} \left[\frac{2}{2\delta-\varepsilon} \right], \quad (\text{A.40})$$

$$\int \frac{q^{a-d} p^{a-d}}{[2]^2 [3]} = \int \frac{q^{a-d} p^{a-d}}{[1][2]^2} = \omega^{-2\delta-2} \left[\frac{2}{\delta} \right], \quad (\text{A.41})$$

$$\int \frac{p^2 q^{a-d} p^{a-d}}{[1]^2 [3]} = \omega^{-2\delta} \left[\frac{2(3\delta-\varepsilon)}{\delta^2(2\delta-\varepsilon)} - \frac{2(3\delta-\varepsilon)}{\delta^2} \right], \quad (\text{A.42})$$

$$\int \frac{[2] q^{a-d} p^{a-d}}{[1]^2 [3]^2} = \omega^{-2\delta-2} \left[\frac{2(3\delta-\varepsilon)}{\delta(2\delta-\varepsilon)} \right], \quad (\text{A.43})$$

$$\int \frac{[2] q^{a-d} p^{a-d}}{[1][3]^2} = \omega^{-2\delta} \left[\frac{2(3\delta-\varepsilon)}{\delta^2(2\delta-\varepsilon)} - \frac{2}{\delta} \right], \quad (\text{A.44})$$

$$\int \frac{[2] q^{a-d} p^{a-d}}{[1]^2 [3]} = \omega^{-2\delta} \left[\frac{2(3\delta-\varepsilon)}{\delta^2(2\delta-\varepsilon)} - \frac{2(2\delta-\varepsilon)}{\delta^2} \right], \quad (\text{A.45})$$

$$\int \frac{p^4 q^{a-d} p^{a-d}}{[1]^2 [3]^2} = \omega^{-2\delta} \left[\frac{8(3\delta-\varepsilon)}{\delta^2(2\delta-\varepsilon)} - \frac{2(8\delta-3\varepsilon)(3\delta-\varepsilon)}{\delta^2(2\delta-\varepsilon)} \right]. \quad (\text{A.46})$$

Case $b = \mathbf{L}$ and $c = \mathbf{L}$ —

$$\int \frac{p^{2(a-d)}}{[1][2]} = \int \frac{p^{2(a-d)}}{[2][3]} = \omega^{-2\delta} \left[\frac{4}{\varepsilon(2\delta-\varepsilon)} \right], \quad (\text{A.47})$$

$$\int \frac{p^{2(a-d)}}{[1][3]} = \omega^{-2\delta} \left[\frac{4}{\delta(2\delta-\varepsilon)} \right], \quad (\text{A.48})$$

$$\int \frac{p^{2(a-d)}}{[1][2]^2} = \int \frac{p^{2(a-d)}}{[2]^2[3]} = \omega^{-2\delta-2} \left[\frac{2}{\varepsilon} \right]. \quad (\text{A.49})$$

Case $a = \mathbf{L}$, $b = \mathbf{L}$, and $c = \mathbf{L}$ —

$$\int \frac{q^{a-d} p^{2(a-d)}}{[1][2]} = \omega^{-3\delta+\varepsilon} \left[\frac{4}{\delta(2\delta-\varepsilon)} \right], \quad (\text{A.50})$$

$$\int \frac{q^{a-d} p^{2(a-d)}}{[1][3]} = \omega^{-3\delta+\varepsilon} \left[\frac{4(5\delta-3\varepsilon)}{(3\delta-2\varepsilon)(2\delta-\varepsilon)(3\delta-\varepsilon)} \right], \quad (\text{A.51})$$

$$\int \frac{q^{a-d} p^{2(a-d)}}{[2][3]} = \omega^{-3\delta+\varepsilon} \left[\frac{8(2\delta-\varepsilon)}{\delta(3\delta-2\varepsilon)(3\delta-\varepsilon)} \right], \quad (\text{A.52})$$

$$\int \frac{q^{a-d} p^{2(a-d)}}{[2]^2[3]} = \omega^{-3\delta+\varepsilon-2} \left[\frac{2}{\delta} \right], \quad (\text{A.53})$$

$$\int \frac{q^{a-d} p^{a-d} |\mathbf{q}+\mathbf{p}|^{a-d}}{[1][2]} = \omega^{-3\delta+\varepsilon} \left[\frac{8}{(2\delta-\varepsilon)(3\delta-\varepsilon)} \right]. \quad (\text{A.54})$$

Feynman graphs of the replicated theory

B.I Four-point vertex functions

We introduce the renormalisation constants Z_ψ , Z_ω such that the renormalised Gaussian action reads

$$S_0 = \int_{\mathbf{k}} \bar{\psi}_{\mathbf{k}} (Z_\psi \boldsymbol{\sigma} \cdot \mathbf{k} - iZ_\omega \omega) \psi_{\mathbf{k}}. \quad (\text{B.1})$$

These constants are found by rendering the two-point vertex function $\Gamma^{(2)}$ finite. The renormalisation constants Z_S , Z_L are such that the renormalised quartic interaction reads

$$S_{\text{int}} = -K_d^{-1} \int_{\mathbf{k}_i} (\mu^{-\varepsilon} Z_S \gamma_S + \mu^{-\delta} Z_L \gamma_L q^{\delta-\varepsilon}) \bar{\psi}_{\mathbf{k}_1} \psi_{\mathbf{k}_1+\mathbf{q}} \bar{\psi}_{\mathbf{k}_2} \psi_{\mathbf{k}_2-\mathbf{q}}. \quad (\text{B.2})$$

The constants make the link between bare and renormalised coupling strengths,

$$\dot{\gamma}_S = \frac{2\mu^{-\varepsilon}}{K_d} \frac{Z_S}{Z_\psi^2} \gamma_S, \quad \dot{\gamma}_L = \frac{2\mu^{-\delta}}{K_d} \frac{Z_L}{Z_\psi^2} \gamma_L, \quad (\text{B.3})$$

They can be found by rendering the four-point vertex function $\Gamma^{(4)}$ finite. Because of disorder correlations, the four-point vertex function splits into contact and long-range components,

$$\Gamma^{(4)}(\mathbf{k}_1, \mathbf{k}_1 + \mathbf{q}, \mathbf{k}_2, \mathbf{k}_2 - \mathbf{q}; \omega, \gamma, \mu) = \Gamma_S^{(4)}(\{\mathbf{k}_i\}; \omega, \gamma, \mu) + \Gamma_L^{(4)}(\{\mathbf{k}_i\}; \omega, \gamma, \mu) q^{a-d}, \quad (\text{B.4})$$

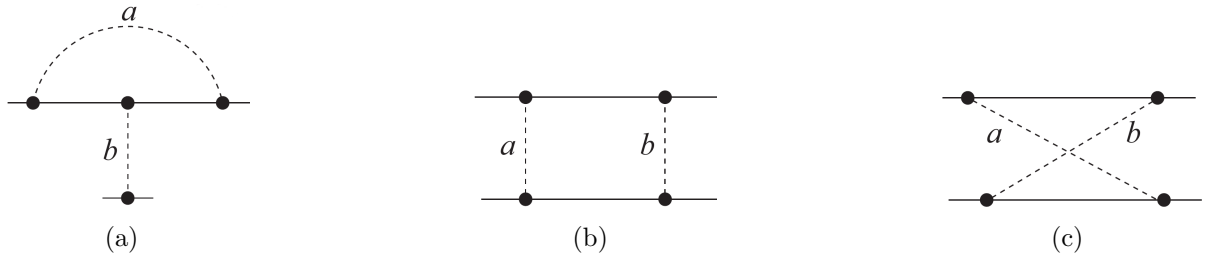


Figure B.1 | Four-point vertex functions of the replicated theory at one-loop order. A solid line stands for a fermionic propagator; a dashed line for an impurity scattering. The symbols a and b each label either short- (strength γ_S) or long-range (strength γ_L) correlations of disorder. Diagram (a) contributes to the flow of γ_b , while the poles of the ladder diagrams (b) and (c) compensate one another as a result of particle-hole symmetry. The counterterms are not shown. Extracted from (DUDKA 2016).

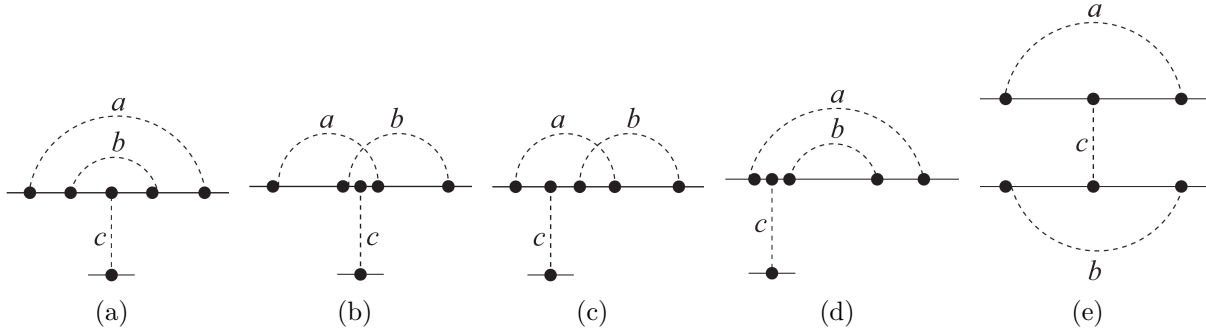


Figure B.2 | Four-point vertex functions of the replicated theory at two-loop order. A solid line stands for a fermionic propagator; a dashed line for an impurity scattering. The symbols a , b , c each label either short- (strength γ_S) or long-range (strength γ_L) correlations of disorder. Shown here are the single-barred graphs, the only ones to contribute to the flow of γ_L , when $c = L$. They also contribute to the flow of γ_S when $c = S$. The counterterms are not shown. Extracted from (DUDKA 2016).

which differ in their dependence on the transferred momentum \mathbf{q} . Each component depends on the set of the two coupling strengths $\gamma = \{\gamma_S, \gamma_L\}$. The finiteness conditions apply to the short- and long-range components separately,

$$\Gamma_S^{(4)}(\{\mathbf{k}_i = \mathbf{0}\}; \mu, \gamma, \mu) = \text{finite}, \quad \Gamma_L^{(4)}(\{\mathbf{k}_i = \mathbf{0}\}; \mu, \gamma, \mu) = \text{finite}. \quad (\text{B.5})$$

At two-loop order, the loopwise expansion of the bare four-point vertex of type $a = S, L$ takes the form

$$\mathring{\Gamma}_a^{(4)}(\dot{\omega}, \dot{\gamma}) = -\frac{\dot{\gamma}_a}{2} \left[1 + \sum_b \dot{\gamma}_b \mathring{\Gamma}_{1,ab}^{(4)}(\dot{\omega}) + \sum_{b,c} \dot{\gamma}_b \dot{\gamma}_c \mathring{\Gamma}_{2,abc}^{(4)}(\dot{\omega}) \right] - \frac{\dot{\gamma}_{\bar{a}}}{2} \sum_{b,c} \dot{\gamma}_b \dot{\gamma}_c \mathring{\Gamma}_{2,\bar{a}bc}^{(4)}(\dot{\omega}), \quad (\text{B.6})$$

where $\bar{a} = S$ if $a = L$ and vice versa. A similar expansion can be written down for the renormalised vertex, which then includes counterterms as separate graphs. The one-loop graphs, which contribute to the vertices $\mathring{\Gamma}_{1,ab}^{(4)}$ are listed in Fig. B.1. The vertices $\mathring{\Gamma}_{2,abc}^{(4)}(\dot{\omega})$ are given by the two-loop graphs of Fig. B.2, Fig. B.3 and Fig. B.4, according to the presence of one, two or three forward scattering processes respectively. The two-loop vertices $\mathring{\Gamma}_{2,\bar{a}bc}^{(4)}(\dot{\omega})$ contribute to short-range correlations only ($a = S$ and $\bar{a} = L$), and are given by the three-barred diagrams of Fig. B.4. They originate from graphs with long-range correlations only, when $b = L$ and $c = L$. We refer the reader to Sec. A.II.3 for the poles of the Feynman integrals.

Replacing the bare coupling strengths $\dot{\gamma}_a$ by their renormalised counterpart as per Eq. (B.3), and relating the bare and renormalised vertex through

$$\Gamma_a^{(4)}(\omega, \gamma, \mu) = Z_\psi^2 \mathring{\Gamma}_a^{(4)}(\dot{\omega}, \dot{\gamma}), \quad (\text{B.7})$$

we can cure the divergences of the Feynman diagrams using the minimal subtraction scheme: the Z constants absorb only the poles in inverse powers of ε and δ , so as to ensure the finiteness conditions (B.5). The constants at order two in the loopwise expansion take the form of a finite Laurent series

$$Z_a(\gamma) = 1 + \frac{A_a(\gamma)}{\varepsilon} + \frac{B_a(\gamma, \varepsilon/\delta)}{\delta} + \dots, \quad (\text{B.8})$$

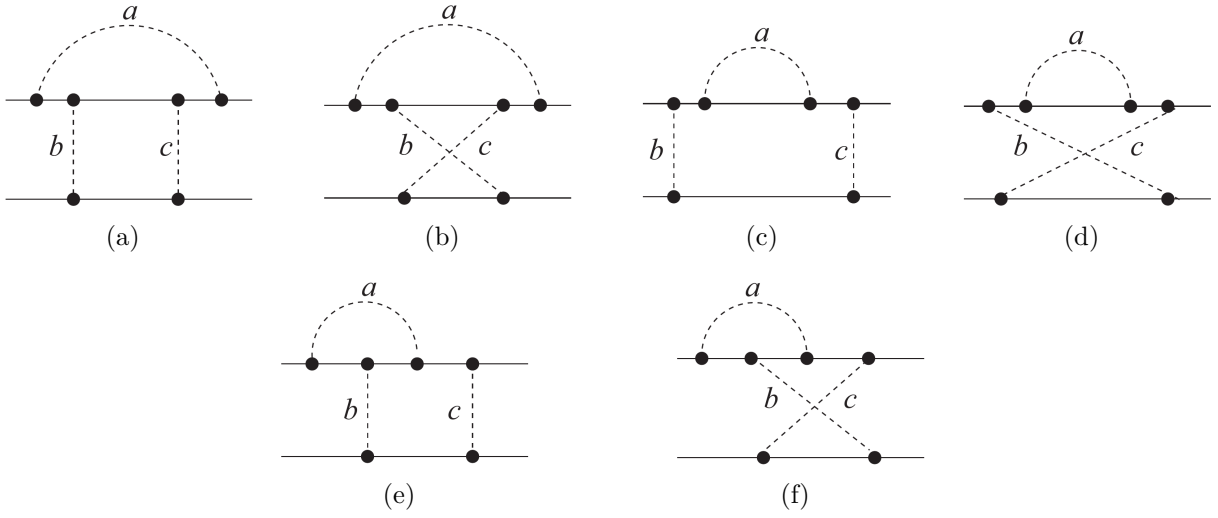


Figure B.3 | Four-point vertex functions at two-loop order for the replicated theory. A solid line stands for a fermionic propagator; a dashed line for an impurity scattering. The symbols a , b and c label each either short-range (strength γ_S) or long-range (strength γ_L) correlations of disorder. Shown here are all the double-barred diagrams. Diagrams (a) compensates with (b), and diagram (c) with (d). Diagram (e) and (f) contribute to the flow of γ_S only. Remarkably, they are responsible for the spontaneous generation of short-range correlations by long-range correlations, when a , b and c all carry long-range impurity lines. All these graphs are topologically identical to those considered in (DUDKA 2016). The counterterms are not shown.

Due to the spontaneous generation of a contact interaction by long-range correlations, the functions $A_S(\gamma)$ and $B_S(\gamma, x)$ for the contact interaction comprise a second-order polynomial in the coupling strengths, plus an extra term of order γ_L^3/γ_S . The function $x \mapsto B_a(\gamma, x)$ is analytic at $x = 0$ because the theory is renormalisable in two dimensions in presence of long-range correlations only. The ellipsis stands for higher order terms of the Laurent series, which originates from diagrams of order larger than two. In the standard ε -expansion, these terms compensate one another in the scaling functions, and thus play no role in the determination of the critical exponents. We will assume that the

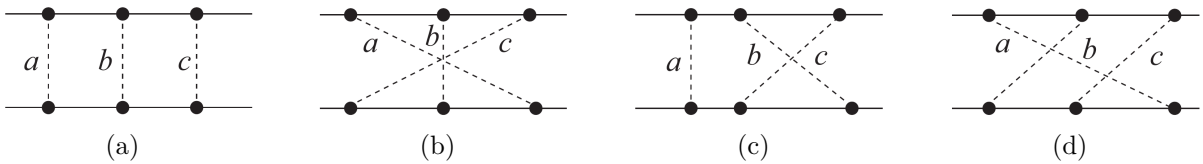


Figure B.4 | Four-point vertex functions at two-loop order for the replicated theory. A solid line stands for a fermionic propagator; a dashed line for an impurity scattering. The symbols a , b and c label each either short-range (strength γ_S) or long-range (strength γ_L) correlations of disorder. Shown here are all the triple-barred diagrams, which contribute to the flow of γ_S only. Remarkably, they are responsible for the spontaneous generation of short-range correlations by long-range correlations, when a , b and c all carry long-range impurity lines. All these graphs are topologically identical to those considered in (DUDKA 2016). The counterterms are not shown.

same happens in Eq. (B.8), which also contains poles in δ .

B.II Two-loop multifractal vertex

We now consider the renormalisation of the composite operator

$$\mathcal{O}_q = \prod_{\alpha=1}^q \bar{\psi}_\alpha \psi_\alpha. \quad (\text{B.9})$$

The standard procedure consists in adding a source $J(r, \tau)$ to the renormalised action which couples linearly to the operator (B.9) (ZINN-JUSTIN 2002)

$$S_{\text{R}}[\bar{\psi}, \psi] \rightarrow S_{\text{R}}[\bar{\psi}, \psi, J] = S_{\text{R}}[\bar{\psi}, \psi] + Z_q \int d^d r d\tau J(r, \tau) \mathcal{O}_q(r, \tau). \quad (\text{B.10})$$

To insert the operator \mathcal{O}_q into a correlation function (vertex function), one has to derive the action (quantum action) with respect to the source J . In particular, the renormalised vertex function with a single insertion of \mathcal{O}_q reads

$$\Gamma_{\mathcal{O}}^{(q)}(r, \tau) = \left. \frac{\delta \Gamma[\bar{\psi}, \psi, J]}{\delta J(r, \tau)} \right|_{J=0}. \quad (\text{B.11})$$

Since the vertex functions represent the one-particle diagrams without the external legs, the vertex function (B.11) can also be written as an ensemble average $\Gamma_{\mathcal{O}}^{(q)}(r, \tau) = \langle \mathcal{O}_q(r, \tau) \rangle_{\text{1PI}}$ restricted over one-particle irreducible (1PI) diagrams.

The bare and renormalised vertex functions are linked in the usual way; in Fourier space, we have

$$\mathring{\Gamma}_{\mathcal{O}}^{(q)}(\{\mathbf{k}_i = \mathbf{0}\}, \hat{\omega}, \hat{\gamma}) = Z_q Z_\psi^{-q} \Gamma_{\mathcal{O}}^{(q)}(\{\mathbf{k}_i = \mathbf{0}\}, \omega, \gamma, \mu), \quad (\text{B.12})$$

where $\{\mathbf{k}_i\}$ represents a set of $2q$ external momenta with zero sum. The renormalisation constant Z_q is chosen to render $\Gamma_{\mathcal{O}}^{(q)}$ finite when ε and δ vanish. From Eq. (B.12), it is easy to find the corresponding Callan-Symanzik equation by deriving with respect to the mass scale μ ,

$$\left[\mu \frac{\partial}{\partial \mu} + (1-z)\omega \frac{\partial}{\partial \omega} + \sum_{i=\text{S,L}} \beta_i \frac{\partial}{\partial \Delta_i} + \eta_q - q\eta_\psi \right] \Gamma_{\mathcal{O}}^{(q)}(\{\mathbf{k}_i\}, \omega, \gamma, \mu) = 0, \quad (\text{B.13})$$

The functions β_i are the beta functions for the coupling constant γ_i , for $i = \text{S, L}$, while z is the dynamical exponent and η_ψ the anomalous field exponent. Similarly, the renormalisation constant Z_q is associated to its own scaling function

$$\eta_q = - \sum_{i=\text{S,L}} \beta_i \frac{\partial \log Z_q}{\partial \gamma_i}. \quad (\text{B.14})$$

The anomalous multifractal exponents at a fixed point γ^* follow from the relation $\Delta_q = \eta_q(\gamma^*) - q\eta_1(\gamma^*)$. The renormalisation constant Z_q at two-loop order is given by the graphs

of Fig. B.5, whose poles are summarised in Tab. B.1. It reads

$$\begin{aligned}
 Z_q = & 1 + 2q \left[\frac{\gamma_S}{\varepsilon} + \frac{\gamma_L}{\delta} \right] + \gamma_S^2 \left[\frac{1}{\varepsilon} (3q - 3q^2) + \frac{1}{\varepsilon^2} (-4q - 2q^2) \right] \\
 & + \gamma_S \gamma_L \left[\frac{1}{\varepsilon} (-3q + 3q^2) + \frac{4q}{\delta} + \frac{1}{\varepsilon + \delta} (10q - 18q^2) + \frac{1}{\varepsilon \delta} (-22q + 2q^2) + \frac{1}{\delta(\varepsilon + \delta)} (28q - 12q^2) \right] \\
 & + \gamma_L^2 \left[\frac{\varepsilon}{\delta^2} \left(\frac{7q}{2} - \frac{3q^2}{2} \right) + \frac{1}{\delta} \left(-\frac{q}{2} - \frac{3q^2}{2} \right) + \frac{1}{\delta^2} (-7q + q^2) + \frac{1}{\delta(\varepsilon + \delta)} (3q - 3q^2) \right].
 \end{aligned} \tag{B.15}$$

As in Eq. (B.8) for the renormalisation constants of the coupling strengths, we isolate the residues of Z_q as

$$Z_q(\gamma) = 1 + \frac{A_q(\gamma)}{\varepsilon} + \frac{B_q(\gamma, \varepsilon/\delta)}{\delta} + \dots, \tag{B.16}$$

where A_q and B_q are the following second-order polynomials in $\gamma = \{\gamma_S, \gamma_L\}$,

$$\left\{ \begin{array}{l} A_q(\gamma) = 2q\gamma_S + 3\gamma_S^2 q(1-q) - 3\gamma_S \gamma_L q(1-q), \\ B_q(\gamma, x) = 2q\gamma_L + 4q\gamma_S \gamma_L + 2q\gamma_S \gamma_L \frac{5-9q}{1+x} + \frac{\gamma_L^2}{2} q [(7-3q)x - (1+3q)]. \end{array} \right. \tag{B.17a}$$

$$\left\{ \begin{array}{l} A_q(\gamma) = 2q\gamma_S + 3\gamma_S^2 q(1-q) - 3\gamma_S \gamma_L q(1-q), \\ B_q(\gamma, x) = 2q\gamma_L + 4q\gamma_S \gamma_L + 2q\gamma_S \gamma_L \frac{5-9q}{1+x} + \frac{\gamma_L^2}{2} q [(7-3q)x - (1+3q)]. \end{array} \right. \tag{B.17b}$$

Using the first order approximation for the beta functions $\beta_S(\gamma) = -\varepsilon\gamma_S + 4\gamma_S^2 + 4\gamma_S\gamma_L + O(\gamma^3)$ and $\beta_L(\gamma) = -\delta\gamma_L + 4\gamma_L^2 + 4\gamma_S\gamma_L + O(\gamma^3)$ of Eq. (3.33), we deduce the following expression for the anomalous scaling exponent,

$$\eta_q = \gamma_S \frac{\partial A_q(\gamma)}{\partial \gamma_S} + \gamma_L \frac{\delta}{\varepsilon} \frac{\partial A_q(\gamma)}{\partial \gamma_L} + \gamma_S \frac{\varepsilon}{\delta} \frac{\partial B_q(\gamma, \varepsilon/\delta)}{\partial \gamma_S} + \gamma_L \frac{\partial B_q(\gamma, \varepsilon/\delta)}{\partial \gamma_L}, \tag{B.18}$$

while the poles cancel one another. This leads to the expression of η_q given in Eq. (3.54) in the main text.

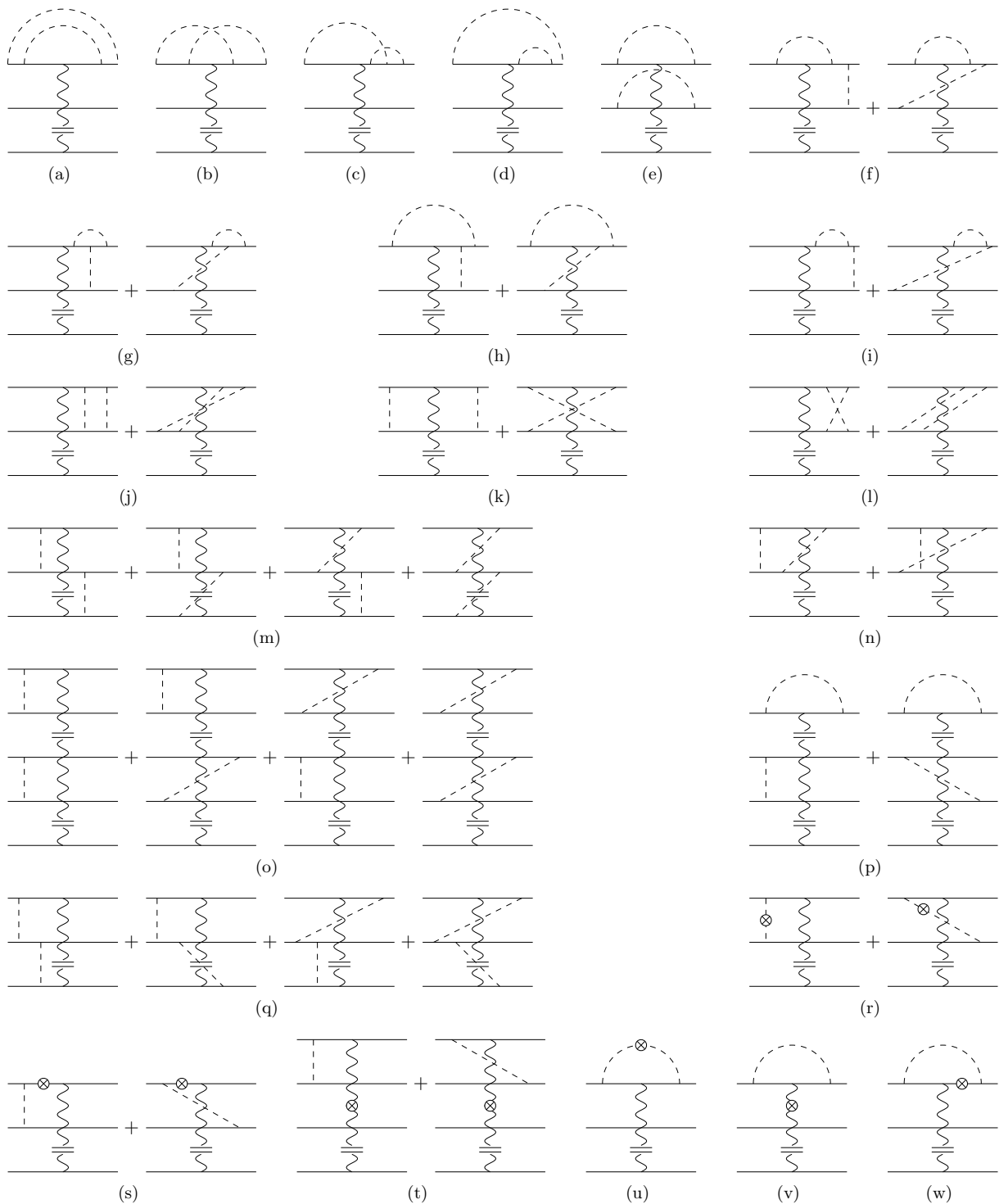


Figure B.5 | (a)-(q) One-particle irreducible diagrams contributing to the renormalisation of the multifractal operator \mathcal{O}_q to two-loop order. These diagrams are topologically identical to those considered in (SYZANOV 2016), but here each dashed line corresponds to either short-range (γ_S) or long-range (γ_L) disorder vertices. (r)-(w) Counterterms. The cross represents the one-loop correction to the quartic interaction (dashed line), to the free Green's function (solid line), or to the source of the multifractal operator (wavy line).

Diagram	Multiplicity	γ_S^2	$\gamma_S\gamma_L$	γ_L^2
(a)	$4q$	$\frac{1}{\varepsilon^2} + \frac{2}{\varepsilon}$	$\frac{1}{\varepsilon\delta} + \frac{2}{\delta(\delta+\varepsilon)} + \frac{3}{\delta} + \frac{1}{\varepsilon}$	$\frac{3\delta-\varepsilon}{\delta(2\delta-\varepsilon)} + \frac{3\delta-\varepsilon}{2\delta^2(2\delta-\varepsilon)}$
(b)	$4q$	$-\frac{1}{2\varepsilon^2} - \frac{1}{\varepsilon}$	$-\frac{2}{\delta(\delta+\varepsilon)} - \frac{2}{\delta}$	$-\frac{1}{2\delta(2\delta-\varepsilon)} - \frac{1}{2\delta-\varepsilon}$
(c)	$8q$	$\frac{1}{2\varepsilon^2} + \frac{1}{\varepsilon}$	$\frac{2}{\delta(\varepsilon+\delta)} + \frac{1}{\varepsilon} + \frac{1}{\delta}$	$\frac{1}{2\delta^2} + \frac{1}{\delta}$
(d)	$8q$	$\frac{1}{2\varepsilon}$	$\frac{1}{2\varepsilon} + \frac{1}{2\delta} - \frac{\delta-\varepsilon}{2\delta(\varepsilon+\delta)}$	$\frac{1}{2\delta} - \frac{\delta-\varepsilon}{4\delta^2}$
(e)	$2q(q-1)$	$\frac{1}{\varepsilon^2} + \frac{2}{\varepsilon}$	$\frac{2}{\varepsilon\delta} + \frac{2}{\varepsilon} + \frac{2}{\delta}$	$\frac{1}{\delta^2} + \frac{2}{\delta}$
(f)	$8q(q-1)$	$\frac{1}{\varepsilon}$	$\frac{1}{\varepsilon} + \frac{1}{\delta}$	$\frac{1}{\delta}$
(g)	$8q(q-1)$	$\frac{1}{\varepsilon}$	$\frac{1}{\varepsilon} + \frac{1}{\delta}$	$\frac{1}{\delta}$
(j)	$4q(q-1)$	$\frac{1}{\varepsilon^2} + \frac{1}{2\varepsilon}$	$\frac{1}{\varepsilon\delta} + \frac{2}{\delta(\delta+\varepsilon)} + \frac{1}{2\varepsilon} + \frac{1}{\delta+\varepsilon}$	$\frac{3\delta-\varepsilon}{2\delta^2(2\delta-\varepsilon)} + \frac{3\delta-\varepsilon}{4\delta^2}$
(k)	$2q(q-1)$	$\frac{1}{\varepsilon^2} + \frac{1}{2\varepsilon}$	$\frac{1}{\varepsilon\delta} + \frac{2}{\delta(\delta+\varepsilon)} + \frac{1}{2\varepsilon} + \frac{1}{\delta+\varepsilon}$	$\frac{3\delta-\varepsilon}{2\delta^2(2\delta-\varepsilon)} + \frac{3\delta-\varepsilon}{4\delta^2}$
(l)	$4q(q-1)$	$-\frac{1}{2\varepsilon^2} - \frac{1}{2\varepsilon}$	$-\frac{2}{\delta(\delta+\varepsilon)} - \frac{2}{\varepsilon+\delta}$	$-\frac{1}{2\delta(2\delta-\varepsilon)} - \frac{1}{2\delta}$
(n)	$8q(q-1)$	$-\frac{1}{2\varepsilon^2} - \frac{1}{2\varepsilon}$	$-\frac{2}{\delta(\delta+\varepsilon)} - \frac{2}{\varepsilon+\delta}$	$-\frac{1}{2\delta(2\delta-\varepsilon)} - \frac{1}{2\delta}$
(p)	$4q(q-1)(q-2)$	$\frac{1}{\varepsilon}$	$\frac{1}{\varepsilon} + \frac{1}{\delta}$	$\frac{1}{\delta}$
(r)	$2q(q-1)$	$-\frac{4}{\varepsilon}$	$-\frac{4}{\varepsilon} - \frac{4}{\delta}$	$-\frac{4}{\delta}$
(t)	$2q(q-1)$	$-\frac{2q}{\varepsilon}$	$-\frac{2q}{\varepsilon} - \frac{2q}{\delta}$	$-\frac{2q}{\delta}$
(u)	$2q$	$-\frac{4}{\varepsilon^2} - \frac{4}{\varepsilon}$	$-\frac{8}{\varepsilon\delta} - \frac{4}{\varepsilon} - \frac{4}{\delta}$	$-\frac{4}{\delta^2} - \frac{4}{\delta}$
(v)	$2q$	$-\frac{2q}{\varepsilon^2} - \frac{2q}{\varepsilon}$	$-\frac{4q}{\varepsilon\delta} - \frac{2q}{\varepsilon} - \frac{2q}{\delta}$	$-\frac{2q}{\delta^2} - \frac{2q}{\delta}$
(w)	$4q$	$-\frac{1}{\varepsilon}$	$-\frac{1}{\varepsilon} - \frac{1}{\delta}$	$-\frac{1}{\delta}$

Table B.1 | Poles of the diagrams depicted in Fig. B.5. The first column gives the diagram's label as per the conventions of Fig. B.5. The second column indicates the multiplicity. The last three columns give the terms proportional to γ_S^2 , $\gamma_S\gamma_L$ and γ_L^2 , respectively, where γ_S denotes the short-range correlated disorder strength and γ_L the long-range correlated disorder strength. Diagrams (h), (i), (m), (o), (q) and (s) cancel each other. In computing these diagrams one encounters many different types of integrals which can be found in Appendix B of (DUDKA 2016). Diagrams (r) – (w) are counterterms.

Surface properties of disordered relativistic semimetals

C.I Solution to the self-consistent equation

C.I.1 Bulk contribution

We recall the local SCBA for the spatially resolved self-energy $\Sigma(E, z)$,

$$\Sigma(E, z) = \frac{\gamma}{4} \int_{k < \Lambda} \frac{d^2 k}{(2\pi)^2} \text{Tr} G_0(E + \Sigma(E, z), z, z). \quad (\text{C.1})$$

Although Eq. (C.1) can be solved numerically, we can further simplify it analytically in the case $b = 0$, which corresponds to either a single Dirac cone, or two Weyl nodes whose surface projections overlap. We will also set b_z to zero for simplicity. To avoid any ambiguity we explicitly indicate the dependence of the Green's function on the momentum, which in polar coordinates reads $\mathbf{k} = k(\cos \phi, \sin \phi)$. For convenience, we introduce the dimensionless disorder strength $\Delta = \gamma\Lambda/4\pi$. The integrand of Eq. (C.1) naturally splits into two parts, one involving the bulk part of the Green's function, given by Eq. (4.14), the other involving the excess part of the Green's function. Thus, we can cast Eq. (C.1) into

$$\begin{aligned} \frac{\Sigma}{\Delta} &= \frac{\pi}{\Lambda} \int_{k < \Lambda} \frac{d^2 k}{(2\pi)^2} \text{Tr} G_0(E + \Sigma, z, z, k, \phi) \\ &= \frac{1}{4\pi\Lambda} \int_0^\Lambda k dk d\phi \text{Tr} \left[G_b(E + \Sigma, k, \phi) + e^{-2\kappa z} G_e(E + \Sigma, k, \phi) \right], \end{aligned} \quad (\text{C.2})$$

where $\kappa^2 = k^2 - (E + \Sigma)^2$. The quantities G_b and G_e represent the bulk and excess Green's functions deprived from the z -dependent exponential factor.

The first term of Eq. (C.2) is common to both boundary conditions M_1 and M_2 , and does not depend on distance z . It can be integrated to

$$\frac{1}{4\pi\Lambda} \int_0^\Lambda k dk d\phi \text{Tr} G_b(E + \Sigma, k, \phi) = \frac{E + \Sigma}{\Lambda} \left(\sqrt{-(E + \Sigma)^2} - \sqrt{\Lambda^2 - (E + \Sigma)^2} \right). \quad (\text{C.3})$$

The self-consistent equation derived from Eq. (C.3) is exact in the limit $z \rightarrow +\infty$, where it leads to the bulk self-energy Σ_b . At zero energy, it takes the dimensionless form

$$\frac{s}{\Delta} = s \left(\sqrt{1 + s^2} - s \right) \quad (\text{C.4})$$

where $s = \Gamma_b \Lambda^{-1}$ with $\Gamma_b = \text{Im } \Sigma_b$. The solution of this equation has been discussed in Sec. 2.3.2.

C.I.2 Chirality-preserving boundary condition

The spatial dependence originates from the second term of Eq. (C.2) only. For the M_1 boundary condition, the excess propagator G_e is diagonal in the chiral sector. Thus the trace of G_e splits into two partial traces wherein the integration variable \mathbf{k} can be rotated by an arbitrary angle to absorb the parameters θ_{\pm} defined in Eq. (4.7). As a result, we choose pleasant values of these angles to simplify the calculus, namely $\theta_+ = 0$ and $\theta_- = \pi$. We then have

$$\frac{1}{2} \text{Tr } G_e(E + \Sigma, k, \phi) = \frac{E + \Sigma}{\sqrt{k^2 - (E + \Sigma)^2}} + \frac{\sqrt{k^2 - (E + \Sigma)^2}}{E + \Sigma - k \cos \phi}. \quad (\text{C.5})$$

The excess contribution to the local SCBA reads

$$\begin{aligned} & \frac{1}{4\pi\Lambda} \int_0^\Lambda k \, dk \, d\phi \, e^{-2zz} \text{Tr } G_e(E + \Sigma, k, \phi) \\ &= \frac{1}{4\Lambda z^2} \left[e^{-2z\sqrt{\Lambda^2 - (E + \Sigma)^2}} \left(2iz\sqrt{\Lambda^2 - (E + \Sigma)^2} + i - 2z(E + \Sigma) \right) \right. \\ & \quad \left. - e^{2z\sqrt{-(E + \Sigma)^2}} \left(2iz\sqrt{-(E + \Sigma)^2} + i - 2z(E + \Sigma) \right) \right]. \quad (\text{C.6}) \end{aligned}$$

At zero energy the local SCBA takes the dimensionless form

$$\frac{s}{\Delta} = s \left(\sqrt{1 + s^2} - s \right) + f_1(s, u) \quad (\text{C.7})$$

where $s = \Gamma(z)\Lambda^{-1}$ with $\Gamma(z) = \text{Im } \Sigma(E = 0, z)$, $u = \Lambda z$, and

$$f_1(s, u) = \frac{1}{4u^2} \left\{ e^{-2us} - e^{-2u\sqrt{1+s^2}} \left[1 + 2u \left(\sqrt{1 + s^2} - s \right) \right] \right\}. \quad (\text{C.8})$$

This proves Eq. (4.40) in the main text.

C.I.3 Chirality-breaking boundary condition

When $b = 0$, the self-consistent equation depends solely on the parameter θ of the M_2 boundary matrix, which dictates the Fermi velocity of the Dirac surface states $v = \cos^2(\theta)$. The integrand of the excess contribution looks like Eq. (C.5), except that θ replaces the integration variable ϕ ,

$$\frac{1}{2} \text{Tr } G_e(E + \Sigma, k, \phi) = \frac{E + \Sigma}{\sqrt{k^2 - (E + \Sigma)^2}} + \frac{\sqrt{k^2 - (E + \Sigma)^2}}{E + \Sigma - k \cos \theta}. \quad (\text{C.9})$$

The excess contribution to the local SCBA can be written as

$$\begin{aligned} & \frac{1}{4\pi\Lambda} \int_0^\Lambda k \, dk \, d\phi \, e^{-2zz} \text{Tr } G_e(E + \Sigma, k, \phi) = \frac{(E + \Sigma) \left(e^{-2z\sqrt{-(E + \Sigma)^2}} - e^{-2z\sqrt{\Lambda^2 - (E + \Sigma)^2}} \right)}{2\Lambda z} \\ & \quad - \frac{1}{2\Lambda} \frac{\partial}{\partial z} \int_0^\Lambda k \, dk \, \frac{e^{-2z\sqrt{k^2 - (E + \Sigma)^2}}}{E + \Sigma - k \cos \theta}. \quad (\text{C.10}) \end{aligned}$$

The integral of Eq. (C.10) does not admit a simple expression for general z . Focussing on surface properties, and setting $z = 0$, the local SCBA further simplifies to

$$\frac{\Sigma_s}{\Delta} = \frac{E + \Sigma_s}{\Lambda} \left(\sqrt{\Lambda^2 - (E + \Sigma_s)^2} - \sqrt{-(E + \Sigma_s)^2} \right) - \Lambda \sec \theta - \sec^2(\theta)(E + \Sigma_s) \log \left(1 - \frac{\Lambda \cos \theta}{E + \Sigma_s} \right), \quad (\text{C.11})$$

where $\Sigma_s = \Sigma(z = 0)$ denotes the surface self-energy. Eq. (C.11) can be solved numerically to plot the surface DoS $\rho_s(E) = \text{Im} \Sigma_s(E)/\pi$ as a function of the energy, as in Fig. 4.5. The local energy shift $\epsilon(z)$ is non-zero, and can be found from the zeroes of the function $E \mapsto E + \text{Re} \Sigma(E, z)$, which is plotted in Fig. 4.5(b) in the case $z = 0$. Setting $\Sigma_s = -\epsilon_s + i\Lambda s$ with $\epsilon_s = \epsilon(z = 0)$ and $s > 0$, and taking the real part of Eq. (C.11), we find

$$\epsilon_s = \frac{\Delta \tan \theta}{2} \left[1 - \frac{s^2}{v} \log \left(1 + \frac{v}{s^2} \right) \right], \quad (\text{C.12})$$

as was advertised in Eq. (4.45). Taking the imaginary part, we find the self-consistent equation

$$\frac{s}{\Delta} = s \sec^2(\theta) \left(\sqrt{1 + s^2} - s \right) + \frac{s^2 \sin \theta}{\cos^3(\theta)} \left[\arctan(\cot \theta) - \arctan \left(\frac{s \tan \theta}{\sqrt{1 + s^2}} \right) \right], \quad (\text{C.13})$$

in agreement with Eq. (4.46).

C.II The semi-infinite Ising ferromagnet

In this section, we review the phase diagram of semi-infinite Ising ferromagnets, from which we borrow the terminology to characterise the phase diagram of semi-infinite Dirac semimetals. For a pedagogical introduction to the topic, see (CARDY 1996). For a textbook introduction to the renormalisation of the semi-infinite φ^4 theory, see (DOMB 2000).

C.II.1 Mean-field approach

A seminal example for phase transitions is the ferromagnetic Ising model. The first theoretical works on spin models on a semi-infinite lattice leveraged most of the techniques already available for infinite systems: mean-field theory (LUBENSKY 1975b), high- and low-temperature expansions, Monte Carlo analyses, renormalisation group approach with an ε -expansion (LUBENSKY 1975a) or large N expansion (OHNO 1983), and even exact solutions (BRAY 1977). The advantage of the semi-infinite geometry is that surface properties become apparent without bothering with finiteness smearing the sharp critical behaviour. We thus decouple strict finite-size effects from surface effects.

We treat here the effect of a surface at the mean-field level. Let $J(z)$ be the space-dependent ferromagnetic coupling, and R its range (of microscopic size). Near the boundary at $z = 0$, the deficit of neighbour spins makes the coupling to drop from its bulk value J_b , so that at first approximation $J(z) = J_b[1 - (R^2/2\lambda)\delta(z)]$ with $\lambda \gg R > 0$. From this local coupling strength, we define the surface coupling strength

$$J_s = \frac{1}{R} \int_0^R dz J(z) = J_b(1 - R/2\lambda) \quad (\text{C.14})$$

In special cases, this surface coupling could be enhanced rather than diminished; we will thus allow ourselves to consider $\lambda < 0$. We now write down the self-consistent equation for the magnetisation $M(z)$ obtained by minimising the free energy:

$$\int dz' J(z - z') M(z') = J(z) M + \frac{J(z)}{2R^2} \frac{d^2 M}{dz^2} = k_B T \operatorname{argth}(M) \simeq k_B T \left(M + \frac{1}{3} M^3 \right). \quad (\text{C.15})$$

where the last equality holds for small M and hence in vicinity of the critical point, i.e. for a reduced temperature $t \simeq 0$. Expanding the left-hand side, one arrives at (CARDY 1996)

$$\frac{1}{2R^2} \frac{d^2 M}{dz^2} = tM + \frac{1}{3} M^3, \quad (\text{C.16})$$

along with a Robin boundary condition at $z = 0^+$

$$\frac{dM}{dz} = cM, \quad (\text{C.17})$$

with $c = 1/\lambda$. The magnetisation profile slightly below the critical point is sketched in Fig. C.1(a). Let us analyse separately the cases $c > 0$ and $c < 0$.

For $c > 0$, the magnetisation vanishes at a distance of approximately λ outside the material; for this reason, λ is referred to as the extrapolation length (though this reading breaks down beyond mean-field). Also, the surface magnetisation $M_s = M(0)$ and the bulk magnetisation $M_b = M(+\infty)$ vanish conjointly. For $c = 0$, the profile is constant. For $c < 0$, the surface orders at a higher temperatures than the bulk. Yet the differences between bulk and surface criticality does not stop to the magnetisation being weakened or enhanced. The critical exponents also differ. Indeed the usual scaling argument states the existence of a scaling function f such that $M(z) = (-t)^{1/2} f[(z + \lambda)R^{-1}|t|^{1/2}]$ and $f(+\infty) \sim 1$. By contrast, $f(0) = 0$ by definition of the extrapolation length. Since f is analytic near the origin, it must vanish as $f(x) \sim x$. Thus $M_s \sim (-t)^{1/2} f(\lambda R^{-1}|t|^{1/2}) \sim (-t)^{\beta_s}$ with the mean-field surface exponent $\beta_s = 1$, which differs from the corresponding bulk exponent $\beta = 1/2$ (LUBENSKY 1975b).

C.II.2 Phase diagram

As a summary, the phase diagram, depicted in Fig. C.1(b), presents the following features.

- Provided the surface coupling is small enough, the surface orders at the same temperature as the bulk. This common bulk-surface transition resembles the one encountered in the infinite system, and so is termed *ordinary*. The ordinary transition survives up until a *special*, tricritical point, usually placed above the point of equal couplings $J_s = J_b$ due to renormalisation effects. At the ordinary transition, the surface magnetisation increases in a power-law fashion $M_s \sim (-t)^{\beta_o}$, with a critical exponent β_o which differs from the bulk exponent. The latter follows from the exponents of the transition in the infinite system.
- Above the special point c_s , the large surface coupling enhances the magnetisation so much as to order the surface in presence of the disordered bulk. A critical line separates the two regions, with a power-law behaviour $t_s \sim (c_{sp} - c)^{1/\Phi}$ in vicinity of the special point; this defines the crossover exponent Φ . The magnetisation increases

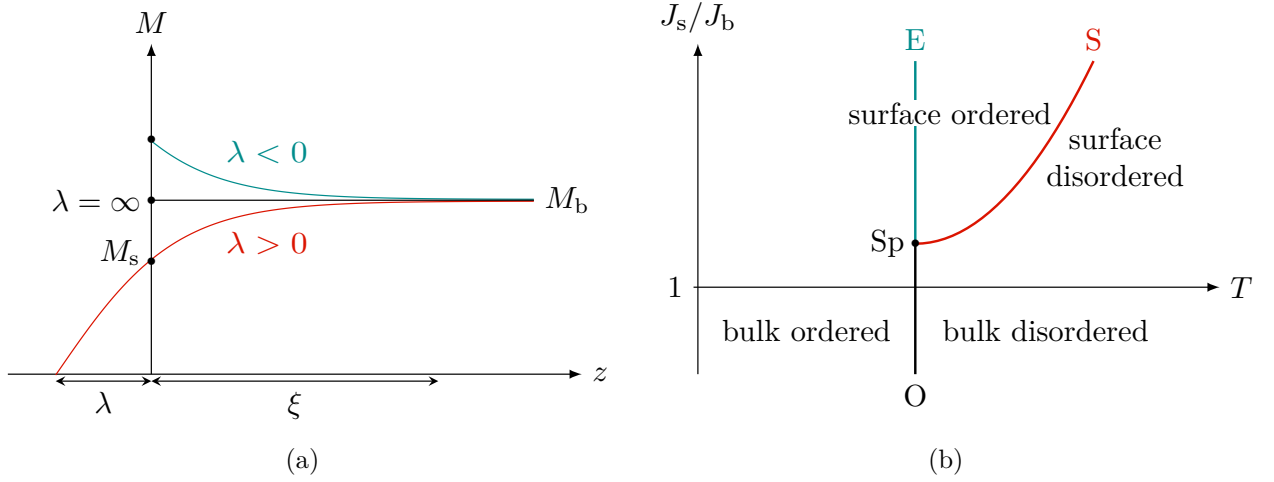


Figure C.1 | (a) Magnetisation profile as a function of the distance z from the surface. For $\lambda > 0$ and near the critical point, the magnetisation vanishes at a distance $\lambda \ll \xi$ outside the material, with ξ the correlation length; for this reason, λ is referred to as the extrapolation length (though this reading breaks down beyond mean-field). Also, the surface (M_s) and bulk (M_b) magnetisations vanish conjointly. For $\lambda = \infty$, the profile is constant. For $\lambda < 0$, the surface orders at a higher temperatures than the bulk. (b) For small surface coupling J_s with respect to the bulk coupling J_b , both bulk and surface order at the bulk critical point $T = T_c$. For large surface coupling, the surface orders at a higher temperature. The bulk critical lines for diminished (in black) and enhanced (in red) surface coupling are known as the ordinary and extraordinary transition, respectively. The surface transition (in blue) meets the two bulk critical lines at a tricritical point, the special transition.

in a power-law fashion $M_s \sim (t_s - t)^{\beta_s}$ with a surface critical exponent β_s . This *surface* transition belongs in the universality class of the $(d - 1)$ -bulk transition of Ising ferromagnets, but this property does not extend to the semimetal-metal transition.

- Above the special point again, the bulk orders at the usual bulk critical point $t = 0$, but in presence of the surface. This *extraordinary* transition leads to identical bulk critical properties as the ordinary one. The surface magnetisation acquires a singular part on top of a smooth background. The scaling behaviour at the extraordinary transition $M_s = M_0 + A(-t)^{\beta_e}$ involves yet another surface critical exponent β_e , different than that at the surface transition β_s , and of course than the analogous bulk exponent β .

Linear representation of point groups

D.I Representations and group actions

For introductions to the group theory and linear representations from the physicist’s viewpoint, see (ATKINS 1970; DRESSELHAUS 2007; WOIT 2017; MA 2004; MA 2007; CHEN 2002b). We restrict the discussion to finite groups, such as crystalline point groups. This excludes the orthogonal $O(N)$ and unitary groups $U(N)$, among others. The results will be given without proof. Throughout the exposition, we will use the dihedral group D_3 as an example. In Sec. D.III we extend D_3 to the symmetry group of twisted bilayer graphene, which includes additional antiunitary and particle-hole symmetries.

D.I.1 Definitions

Let G be a finite group of cardinal g , V_n an n -dimensional vectorial space (typically \mathbb{C}) and $M_n(\mathbb{C})$ the set of $n \times n$ matrices with complex coefficients.

A *linear representation* Υ of the group G is a homomorphism from G to the set of linear operators acting on V_n , i.e. the set of matrices $M_n(\mathbb{C})$ up to a choice of basis:

$$\begin{aligned} \Upsilon : G &\rightarrow M_n(\mathbb{C}) \\ R &\mapsto \Upsilon(R). \end{aligned} \tag{D.1}$$

Hence for all $R, S \in G$, $\Upsilon(R^{-1}) = \Upsilon(R)^{-1}$ and $\Upsilon(RS) = \Upsilon(R)\Upsilon(S)$. The representation is *faithful* when there is a one-to-one correspondence between G and $\Upsilon(G)$.

Example — The dihedral group $D_3 = \{\mathbb{1}, \mathcal{C}_3, \mathcal{C}_3^2, \mathcal{C}_2, \mathcal{C}_2', \mathcal{C}_2''\}$ is a finite group of $g = 6$ elements. The trivial representation is the one-dimensional representation defined via $\Upsilon(R) = 1$ for all elements $R \in D_3$. One gets another representation by tracking how the summits 1, 2, 3 of a triangle are swapped under the rotations of D_3 . The three-fold rotation \mathcal{C}_3 sends 1 to 2, 2 to 3 and 3 to 1. The reflexion \mathcal{C}_2 whose axis goes through the summit number 1 exchanges 2 and 3. Hence D_3 is isomorphic to the permutation group of three

elements \mathfrak{S}_3 . This latter representation acts in the following way:

$$\Upsilon(\mathbb{1}) = \begin{pmatrix} 1 & 0 & 0 \\ 0 & 1 & 0 \\ 0 & 0 & 1 \end{pmatrix}, \quad \Upsilon(\mathcal{C}_3) = \begin{pmatrix} 0 & 0 & 1 \\ 1 & 0 & 0 \\ 0 & 1 & 0 \end{pmatrix}, \quad \Upsilon(\mathcal{C}_2) = \begin{pmatrix} 1 & 0 & 0 \\ 0 & 0 & 1 \\ 0 & 1 & 0 \end{pmatrix}. \quad (\text{D.2})$$

Two representations Υ and Υ' are *equivalent* if and only if there exists a similarity transformation that maps one to the other:

$$\Upsilon' \sim \Upsilon \Leftrightarrow \exists X \in \text{GL}_n(\mathbb{C}), \Upsilon' = X^{-1}\Upsilon X. \quad (\text{D.3})$$

A representation is *irreducible* if it is not equivalent to a representation with block-diagonal matrices. On the contrary, a reducible representation Υ can be decomposed as a direct sum $\Upsilon = \bigoplus_{i=1}^m \Upsilon_i$, such that for all $R \in G$,

$$\Upsilon(R) \sim \begin{pmatrix} \Upsilon_1(R) & 0 & 0 & 0 \\ 0 & \Upsilon_2(R) & 0 & 0 \\ 0 & 0 & \dots & 0 \\ 0 & 0 & 0 & \Upsilon_m(R) \end{pmatrix} \quad (\text{D.4})$$

The conjugation by an element $X \in G$, $R \sim S \Leftrightarrow R = X^{-1}SX$ for all $R, S \in G$, defines an equivalence on G . The *class of conjugation* of an element R is defined as

$$C(R) = \{X^{-1}RX, X \in G\}. \quad (\text{D.5})$$

An important theorem enables to easily determine the number of irrep. of a group. The number n of irrep. Υ_i of a group G equals the number n_C of conjugation classes of G ,

$$n = n_C. \quad (\text{D.6})$$

Furthermore, let $[G, G]$ be the commutator subgroup of G , i.e. the normal subgroup generated by all possible commutators of elements in G . The quotient set $G/[G, G]$, which is also a group thanks to the commutator subgroup being normal, is called the abelianisation of G . Then the number n_1 of one-dimensional irrep. of G equals the index of $[G, G]$ (the cardinal of the quotient group),

$$n_1 = |G/[G, G]|. \quad (\text{D.7})$$

D.I.2 Characters

Definition — The *character* χ of a representation Υ is defined as the trace of any matrix representation of the elements of G , i.e. for all $R \in G$,

$$\chi(R) = \text{Tr } \Upsilon(R). \quad (\text{D.8})$$

It is well-defined (independent of the choice of the matrix representation), since the cyclicity of the trace ensures that equivalent representations have the same character. For all $X \in \text{GL}_n(\mathbb{C})$, $\chi_{\Upsilon'} = \text{Tr } \Upsilon' = \text{Tr } (X^{-1}\Upsilon X) = \text{Tr } (X X^{-1}\Upsilon) = \text{Tr } \Upsilon = \chi_{\Upsilon}$. For the same reason, all elements R that belong the same class of G have identical characters,

$$\chi(R) = \chi(C(R)). \quad (\text{D.9})$$

A character is a natural function of the classes of G , rather than the elements themselves.

The character of a reducible representation $\Upsilon = \oplus_{i=1}^m \Upsilon_i$ split into the sum of the corresponding characters, also called *primary* characters χ_i . Hence,

$$\chi = \sum_{i=1}^m \chi_i. \tag{D.10}$$

Orthonormality theorem — A character is primary if and only if it is of norm one for the scalar product $\langle \chi_1, \chi_2 \rangle = g^{-1} \sum_{R \in G} \chi_1^*(R) \chi_2(R)$, namely if

$$\frac{1}{g} \sum_{R \in G} \chi^*(R) \chi(R) = 1 \tag{D.11}$$

The sum may also be written as a sum over classes,

$$\sum_{R \in G} \chi^*(R) \chi(R) = \sum_{C(R)} c \chi^*(R) \chi(R), \tag{D.12}$$

where c is the number of elements in class $C(R)$. In addition, the primary characters of a group are orthogonal, i.e. for all $i \neq j$,

$$\sum_{R \in G} \chi_i^*(R) \chi_j(R) = 0 \tag{D.13}$$

Hence, they form an orthonormal basis for the vectorial space composed of all characters of a group G . The dimension d of an irrep. denotes the size of all its matrix representations, and is given by $d = \chi(\mathbb{1})$. The set of dimensions d_i of the irrep. Υ_i of a group G of cardinal g satisfies the completeness relation

$$\tag{D.14}$$

Example — The dihedral group D_3 has three classes, $\{\mathbb{1}\}$ written as $\mathbb{1}$, $\{\mathcal{C}_3, \mathcal{C}_3^2\}$ written as $2\mathcal{C}_3$, and $\{\mathcal{C}_2, \mathcal{C}_2\mathcal{C}_3, \mathcal{C}_2\mathcal{C}_3^2\}$ written as $3\mathcal{C}_2$. The irreducible characters of D_3 are the following

D_3	$\mathbb{1}$	$2\mathcal{C}_3$	$3\mathcal{C}_2$
A_1	1	1	1
A_2	1	1	-1
E	2	-1	0

Among the irrep. of a group features always the trivial representation A_1 for which $\chi = 1$. According to Mulliken's notation, one-dimensional representations are represented with the symbols A or B , the two-dimensional ones with the symbol E , and the three-dimensional ones (less common), with T . The completeness relation is satisfied for D_3 since $1^2 + 1^2 + 2^2 = 6$, as are the orthonormality relations.

Mullikens' notation — Mulliken's notation is widespread among theoretical chemists. Group theory is indeed a powerful method to predict which vibrational or rotational radiations molecules can emit. The conventions to represent irrep. of groups are the following. A denotes a singly degenerate state (one-dimensional irrep.) which is symmetric with respect to rotation about the principal C_n axis. B denotes singly degenerate state which is antisymmetric with respect to rotation about the principal C_n axis. E is used for doubly degenerate states and T for triply degenerate states. Let X be any of these four previous symbols. X_g (for 'gerade', symmetric) is used when the sign of the wavefunction is invariant under spatial inversion through the center of the atom, while X_u ('ungerade', antisymmetric) is used when spatial inversion reverses the sign of the wavefunction. Similarly, we use X_1 when the sign of the wavefunction is invariant under rotation about the center of the atom, and X_2 otherwise. Finally, ' indicates that the representation is symmetric with respect to a horizontal symmetry plane σ_h , and " that it is antisymmetric.

Class operator method — Even though the above theorems bring a lot of useful information about the primary characters of a group, they are often insufficient to find all of them from scratch. The class operator method enables to compute all the irrep. of a group G systematically knowing its multiplication table and its classes of conjugation (CHEN 2002b). The algorithm is the following. First endow the group G with an addition (an associative, commutative operation $+$ between elements), thereby promoting G to an algebra. For each class, define the class operator as the sum of all elements in the class. If $R \in G$ is a representative of the class, the class operator of $C(R)$ reads

$$[R] = \sum_{S \in C(R)} S. \quad (\text{D.15})$$

Then look at the action of a class operator $[R]$ under a multiplication in the vectorial space of all class operators $\text{Vect}([R_1], [R_2], \dots, [R_n])$. Since the product is an internal operation, all multiplications of class operators can be decomposed into a linear combination

$$[R] \cdot [R_i] = \sum_j a_{ij} [R_j]. \quad (\text{D.16})$$

The $n \times n$ matrix $D([R])_{ij} = a_{ij}$ is diagonalisable; its n eigenvectors Q_i are each associated with an irrep Υ_i of G . More precisely, the component $(Q_i)_j$ is equal (modulo a normalisation factor) to the character χ_i of the irrep Υ_i evaluated on the class $C(R_j)$. When an eigenvalue of $D([R])$ is m -degenerate, several eigenvectors Q_1, \dots, Q_m are associated to the same eigenvalue. To find which linear combination gives the character $\chi_i(R_j)$, one has to compute the matrix representation of another class operator $[S]$, and diagonalise both $D([R])$ and $D([S])$ simultaneously. Continue to add class operators until the set of matrices $D([R]), D([S]), \dots$ is mutually diagonalisable with non-degenerate eigenvalues.

D.II Key properties of irreducible representations

D.II.1 Direct product

Definition — The *direct product* of two representations Υ_1 and Υ_2 , of dimensions d_1 and d_2 , is defined as the representation of G on V_n which acts as

$$\Upsilon_1 \otimes \Upsilon_2 : G \rightarrow M_{n_1 n_2}(\mathbb{C}) \quad (\text{D.17})$$

$$R \longmapsto \Upsilon_1(R) \otimes \Upsilon_2(R) \quad (\text{D.18})$$

where the Kronecker product of matrices $\Upsilon_1(R) \otimes \Upsilon_2(R)$ has entries $\Upsilon_1 \otimes \Upsilon_2(R)_{i_1 i_2, j_1 j_2} = \Upsilon_1(R)_{i_1 j_1} \Upsilon_2(R)_{i_2 j_2}$. Even if Υ_1 and Υ_2 are irreducible of G , $\Upsilon_1 \otimes \Upsilon_2$ is in general reducible. The character of a direct product representation is the product of the characters, i.e.

$$\chi_{\Upsilon_1 \otimes \Upsilon_2} = \chi_{\Upsilon_1} \chi_{\Upsilon_2}. \quad (\text{D.19})$$

Let Υ be a reducible representation of G and $\Upsilon_1, \Upsilon_2, \dots, \Upsilon_m$ be the list of irrep. of G , whose number m equals the number of classes in the group. The decomposition of Υ reads

$$\Upsilon \sim \bigoplus_{i=1}^m a_i \Upsilon_i \quad (\text{D.20})$$

where a_i is the multiplicity of Υ_i in the decomposition of Υ and the list $\{a_i, i = 1, \dots, m\}$ is called the *Clebsch-Gordan series*. The character χ of Υ enables to easily determine the coefficient a_i using the scalar product

$$a_i = \frac{1}{g} \sum_{C(R)} c \chi(R) \chi_i^*(R), \quad (\text{D.21})$$

where c is the cardinal of the class $C(R)$. Applying Eq. (D.20) to a direct product $\Upsilon = \Upsilon_a \otimes \Upsilon_b$, we find

$$a_i = \frac{1}{g} \sum_{C(R)} c \chi_a(R) \chi_b(R) \chi_i^*(R). \quad (\text{D.22})$$

Example — The three-dimensional (3d) representation Υ of D_3 defined in the first example has the following character table:

D_3	$\mathbb{1}$	$2C_3$	$3C_2$
Υ	3	0	1

Hence $a(A_1) = \frac{1}{6}(1 \cdot 3 \cdot 1 + 2 \cdot 0 \cdot 1 + 3 \cdot 1 \cdot 1) = 1$, $a(A_2) = \frac{1}{6}(1 \cdot 3 \cdot 1 + 2 \cdot 0 \cdot 1 + 3 \cdot 1 \cdot (-1)) = 0$ and $a(E) = \frac{1}{6}(1 \cdot 3 \cdot 2 + 2 \cdot 0 \cdot (-1) + 3 \cdot 1 \cdot 0) = 1$. We conclude that

$$\Upsilon \sim A_1 \oplus E.$$

The product table of irrep. lists all possible direct products between the irrep. of G . This table is symmetric since $\Upsilon_a \otimes \Upsilon_b \sim \Upsilon_b \otimes \Upsilon_a$. For the dihedral group D_3 we have

D_3	A_1	A_2	E
A_1	A_1	A_2	E
A_2	A_2	A_1	E
E	E	E	$A_1 \oplus A_2 \oplus E$

In general a reducible representation Υ is not already in a block-diagonal form. To bring to light the block decomposition in a direct sum of irrep., we must perform a similarity transformation first,

$$X^{-1}\Upsilon X = \bigoplus_{i=1}^m a_i \Upsilon_i. \quad (\text{D.23})$$

The entries of the invertible matrix X are the *Clebsch-Gordan coefficients*. Let us assume again that $\Upsilon = \Upsilon_a \otimes \Upsilon_b$ where a and b index two irrep. of G . The irrep Υ_a is expressed in matrix form by choosing a basis $|ai\rangle$ composed of n_a vectors, and similarly we choose a basis $|bj\rangle$ composed of n_b vectors suitable for Υ_b . The matrix X transforms the product basis $|ai; bj\rangle$ into the block-diagonal basis $|ckr\rangle$ where c is the irrep, k is the index of the vector in irrep c and r is the index to distinguish from the a_c different copies of Υ_c . Then the Clebsch-Gordan coefficients squared, $|\langle ai; bj|ckr\rangle|^2$, satisfy the following identity:

$$\sum_r |\langle ai; bj|ckr\rangle|^2 = \frac{n_c}{g} \sum_R \Upsilon_a(R)_{ij} \Upsilon_b(R)_{ij} \Upsilon_c^*(R)_{kk}. \quad (\text{D.24})$$

Example — The non-trivial coefficients for D_3 are listed below.

$$A_2 \otimes E$$

E	$ E1\rangle$	E	$ E2\rangle$
$ A_2; E1\rangle$	i	$ A_2; E1\rangle$	0
$ A_2; E2\rangle$	0	$ A_2; E2\rangle$	$-i$

$$E \otimes E$$

A_1	$ A_1\rangle$	A_2	$ A_2\rangle$	E	$ E1\rangle$	E	$ E2\rangle$
$ E1; E1\rangle$	0	$ E1; E1\rangle$	0	$ E1; E1\rangle$	0	$ E1; E1\rangle$	1
$ E1; E2\rangle$	$1/\sqrt{2}$	$ E1; E2\rangle$	$i/\sqrt{2}$	$ E1; E2\rangle$	0	$ E1; E2\rangle$	0
$ E2; E1\rangle$	$1/\sqrt{2}$	$ E2; E1\rangle$	$-i/\sqrt{2}$	$ E2; E1\rangle$	0	$ E2; E1\rangle$	0
$ E2; E2\rangle$	0	$ E2; E2\rangle$	0	$ E2; E2\rangle$	1	$ E2; E2\rangle$	0

D.II.2 Reality

Definition — We introduced representations on a complex vectorial space. Some representations however, can be 'real' in a sense which we define more precisely below. We will distinguish real, pseudo-real and complex representations as follows.

- (i) A representation is *real* when it is *self-conjugate*,

$$\Upsilon \sim \Upsilon^\dagger, \quad (\text{D.25})$$

and when it is equivalent to a representation with real coefficients.

- (ii) A representation is *pseudo-real* when it is *self-conjugate*,

$$\Upsilon \sim \Upsilon^\dagger, \quad (\text{D.26})$$

and when it is *not* equivalent to a representation with real coefficients.

- (iii) A representation is *complex* when it is *not self-conjugate*.

Properties — An irrep. Υ is self-conjugate if and only if its character χ is real. For every self-conjugate irrep. Υ , there exists a transformation matrix X such that $X^{-1}\Upsilon X = \Upsilon^\dagger$. This matrix X is antisymmetric if Υ is pseudo-real and symmetric if Υ is real. A pseudo-real irrep. is necessarily of even dimension. Finally, the following criterion holds.

$$\frac{1}{g} \sum_R \chi(R^2) = \begin{cases} +1 & \text{if } \Upsilon \text{ real} \\ 0 & \text{if } \Upsilon \text{ complex} \\ -1 & \text{if } \Upsilon \text{ pseudo-real} \end{cases} \quad (\text{D.27})$$

Example — All irrep. of D_3 are real.

D.II.3 Magnetic point groups

Anti-unitary symmetries — Consider a group G that contains unitary (and thus linear) operators R , but also anti-unitary (and thus anti-linear) operators S . A famous example of an anti-linear operator is time reversal \mathcal{T} , whose spinful version for a single fermion is represented by

$$\mathcal{T} = i\sigma_y \mathcal{K}, \quad (\text{D.28})$$

where σ_y denotes the second Pauli matrix in the spin sector and \mathcal{K} is complex conjugation. The action of time reversal on time t , position \mathbf{r} , wavevector \mathbf{k} , angular momentum \mathbf{L} (orbital or spin) and energy E is

$$\mathcal{T} : t \rightarrow -t, \quad \mathbf{r} \rightarrow \mathbf{r}, \quad \mathbf{r} \rightarrow -\mathbf{r}, \quad \mathbf{L} \rightarrow -\mathbf{L}, \quad E \rightarrow E. \quad (\text{D.29})$$

For a system of n spins one-half, we have the fundamental property that

$$\mathcal{T}^2 = (-1)^n \mathbb{1} = \begin{cases} \mathbb{1} & \text{if } n \text{ even} \\ \bar{\mathbb{1}} & \text{if } n \text{ odd} \end{cases}$$

where $\mathbb{1}$ is the identity operator (the rotation by 4π) and $\bar{\mathbb{1}} = -\mathbb{1}$ (the rotation by 2π). In the following we will consider only spinless ($n = 0$) or spin one-half ($n = 1$) particles.

Decomposition of a magnetic group — Assume for concreteness that the group G contains time reversal \mathcal{T} (the discussion below applies with any anti-unitary generator). Let us call H the subgroup of G composed of linear operators only. For a spin one-half particle, H is a *double* group, meaning that it also includes all the product of the spinless linear operators with $\bar{\mathbb{1}}$. Since linear operators leave time t and angular momentum \mathbf{L} unchanged, they commute with \mathcal{T} . As a result, H is a *normal* subgroup of G , and any anti-unitary element S of G can be decomposed as $S = \mathcal{T}R$ where the operator $R \in H$ is linear. We refer to G as a *magnetic* point group and write

$$G = H + \mathcal{T}H. \quad (\text{D.30})$$

We would like to find the irrep. D of G (the so-called irreducible corepresentations) from the irrep. Υ of H . A corepresentation D satisfies the following properties

$$\begin{aligned} D(R_1)D(R_2) &= D(R_1R_2), & D(S)D(R)^* &= D(SR), \\ D(R)D(S) &= D(RS), & D(S_1)D(S_2)^* &= D(S_1S_2), \end{aligned} \quad (\text{D.31})$$

for any linear operators $R_{1,2}$ and anti-linear operators $S_{1,2}$. The symbol $*$ designates the complex conjugation of the matrix entries (and not Hermitian conjugation). Depending on the properties of a representation Υ of H , the presence of anti-unitary operators may or may not double the dimension of the representation. Three cases must be distinguished.

- (i) There exists an anti-unitary operator $S_0 = U_0 T$ such that the representations $R \mapsto \Upsilon(R)$ and $R \mapsto \Upsilon(S_0^{-1} R S_0)^*$ are *inequivalent*. Then the associated corepresentation D of G has twice the dimension of Υ and reads

$$D(R) = \begin{pmatrix} \Upsilon(R) & 0 \\ 0 & \Upsilon(S_0^{-1} R S_0)^* \end{pmatrix} \quad (\text{D.32})$$

for unitary operators $R \in H$, and

$$D(S) = \begin{pmatrix} 0 & \Upsilon(S S_0) \\ \Upsilon(S_0^{-1} S)^* & 0 \end{pmatrix} \quad (\text{D.33})$$

for anti-unitary operators $S \in \mathcal{T}H$.

- (ii) For all elements $S \in \mathcal{T}H$, the representation $R \mapsto \Upsilon(R)$ and $R \mapsto \Upsilon(S^{-1} R S)^*$ are *equivalent*. Let us choose one particular element S_0 . There exists an invertible matrix U such that for all $R \in H$, $\Upsilon(S_0^{-1} R S_0)^* = U^{-1} \Upsilon(R) U$.

- Case (ii-a). If $U U^* = \Upsilon(S_0^2)$, there is no degeneracy and

$$D(R) = \Upsilon(R) \quad \text{and} \quad D(S_0) = U. \quad (\text{D.34})$$

- Case (ii-b). If $U U^* = -\Upsilon(S_0^2)$, the degeneracy is doubled and

$$D(R) = \begin{pmatrix} \Upsilon(R) & 0 \\ 0 & \Upsilon(R) \end{pmatrix} \quad (\text{D.35})$$

for unitary operators $R \in H$, and

$$D(S) = \begin{pmatrix} 0 & \Upsilon(S S_0^{-1}) U \\ -\Upsilon(S S_0^{-1}) U & 0 \end{pmatrix} \quad (\text{D.36})$$

for anti-unitary operators $S \in \mathcal{T}H$.

Finding which case describes the group H becomes straightforward by using generalised Frobenius-Schur criterion, which states that

$$\frac{(-1)^n \chi(\mathbb{1})}{\chi(S_0^2) h} \sum_{R \in H} \chi(S_0^{-1} R S_0 R) = \begin{cases} +1 & \text{for case (ii-a)} \\ -1 & \text{for case (ii-b)} \\ 0 & \text{for case (i)} \end{cases}, \quad (\text{D.37})$$

where $h = |H|$ denotes the cardinal of H .

Regular vs non-regular — The irrep. of the double covering $G^{(2)}$ of a group G (the double group) have the following properties. Since $\bar{1}$ commutes with all elements of $G^{(2)}$, the irrep. can be classified into two sets: the ones that coincide on barred elements $\bar{R} = \bar{1}R$ and unbarred elements R :

$$\Upsilon_+(\bar{R}) = \Upsilon_+(R) \quad (\text{D.38})$$

and the ones where a minus sign appears:

$$\Upsilon_-(\bar{R}) = -\Upsilon_-(R). \quad (\text{D.39})$$

The first ones (Υ_+) correspond to inductions of the irrep. Υ of G onto the double group $G^{(2)}$. The others (Υ_-) have nothing to do with the irrep. of G . The number of extra irrep. equals the number of extra classes that appear when we add barred operators to D_3 . In this regard, certain general rules enable to find the classes of $G^{(2)}$. The Opechowski rule dictates the fate of the two following types of conjugation classes.

- The *regular* classes C of the group G form two separates classes C and \bar{C} of the double group $G^{(2)}$. A set of proper or improper rotations by the same angle $2\pi/n$ forms a regular class, except for $n = 2$ when there exists a π rotation around a perpendicular axis.
- The *non-regular* classes C of the group G form a single class $\{C, \bar{C}\}$ of the double group $G^{(2)}$. The characters of the extra irrep. of the double group vanish on a non-regular class since $\chi_-(C) = -\chi_-(\bar{C}) = -\chi_-(C)$.

Example — The class $3\mathcal{C}_2$ of D_3 is regular according to Opechowski's rule, so that $3\mathcal{C}_2$ and $3\bar{\mathcal{C}}_2$ form separate classes. The rule says nothing for $2\mathcal{C}_3$, but this class turns out to be also regular. The character table for $D_3^{(2)}$ reads

D_3	$\bar{1}$	$2\mathcal{C}_3$	$3\mathcal{C}_2$	$\bar{1}$	$2\bar{\mathcal{C}}_3$	$3\bar{\mathcal{C}}_2$
A_1	1	1	1	1	1	1
A_2	1	1	-1	1	1	-1
E	2	-1	0	2	-1	0
$\Upsilon_{1/2}$	2	1	0	-2	-1	0
ϖ	1	-1	i	-1	1	$-i$
ϖ^\dagger	1	-1	$-i$	-1	1	i

The irrep. denoted as $\Upsilon_{1/2}$ represents the spin one-half representation of the rotation group $SO(3)$ subduced onto D_3 . Thus if a spinless fermion is an state $\psi(x)$ which transforms in, say, the irrep. E , the spinful fermion is in a state $\psi(x)s$ of the product $E \otimes \Upsilon_{1/2}$, where s is the spin state, i.e. a linear combination of $|\uparrow\rangle$ and $|\downarrow\rangle$. The representations ρ and ρ^\dagger are two complex conjugate irrep.

Suppose that we consider the group generated by D_3 and the operator $\Theta = \mathcal{IT}$, which is the product of inversion \mathcal{I} with time reversal \mathcal{T} . The magnetic point group D_3^M has 24 elements and can be decomposed as

$$D_3^M = D_3^{(2)} + \Theta D_3^{(2)} = D_3 + \bar{1}D_3 + \Theta D_3 + \bar{1}\Theta D_3. \quad (\text{D.40})$$

The irrep. A_1 , A_2 and E of D_3 belong to case (ii-a) of Eq. (D.34), because they are real. Moreover, the corresponding matrix $U = D(\Theta)$ reduces to the identity for all three irrep. Hence the characters of A_1 , A_2 and E coincide on $D_3^{(2)}$ and $\Theta D_3^{(2)}$.

D.II.4 Induction

Quotient map — Let H be a normal subgroup of G . The quotient set G/H also has the structure of a group. Let

$$\begin{aligned} \pi : G &\rightarrow G/H \\ g &\mapsto gH \end{aligned} \quad (\text{D.41})$$

be the associated quotient map. Let $\varpi_1, \varpi_2, \dots, \varpi_n$ be the irrep. of the quotient group G/H . Each irrep. ϖ_i of G/H generates an irrep. of G , as

$$\begin{aligned} \Upsilon_i = \varpi_i \circ \pi : G &\rightarrow \text{GL}(\mathbb{R}^{d_i}) \\ g &\mapsto \varpi_i(gH) \end{aligned} \quad (\text{D.42})$$

where d_i is the dimension of ϖ_i .

Example — The cyclic group $C_3 = \{\mathbb{1}, C_3, C_3^2\}$ is a normal subgroup of D_3 , with quotient group $D_3/C_3 = C_2 = \{\mathbb{1}, C_2\}$. The irrep. of C_2 are

$$\begin{array}{c|cc} C_2 & \mathbb{1} & C_2 \\ \hline A_1 & 1 & 1 \\ A_2 & 1 & -1 \end{array}$$

Thus D_3 has at least two one-dimensional irrep., which are the well-known representations A_1 and A_2 ,

$$\begin{array}{c|ccc} D_3 & \mathbb{1} & 2C_3 & 3C_2 \\ \hline A_1 & 1 & 1 & 1 \\ A_2 & 1 & 1 & -1 \end{array}$$

Induction — Let Υ be an irrep. of a subgroup H of a group G , whose character is χ . We can extend the irrep. Υ onto G by a procedure called *induction*. The induced irrep, denoted as $\Upsilon_{\uparrow G}$, is a (a priori) reducible rep of G acting on a vectorial space with dimension $I \cdot d$ where $d = \chi(\mathbb{1})$ is the dimension of Υ and $I = |G/H|$ the index of H . The character of $\Upsilon_{\uparrow G}$ is given by the Schur-Fröbenius formula,

$$\chi_{\uparrow G}(g) = \sum_{x \in G/H} \hat{\chi}(x^{-1}gx), \quad (\text{D.43})$$

where $\hat{\chi}(y) = \chi(y)$ if $y \in H$ and 0 otherwise.

Example — The induction enables for instance to find the irrep. of a *chiral* group, a group of the Hamiltonian containing anti-commuting operators. Let G be the generalised symmetry group of a d -times- d Hamiltonian \mathcal{H} belonging to a representation D of dimension d , i.e. the set $G = \{R, D(R)^{-1}\mathcal{H}D(R) = \pm\mathcal{H}\}$. Let us define the mapping

$$\begin{aligned} \epsilon : G &\rightarrow \mathbb{Z}_2 \\ g &\mapsto \epsilon(g) \end{aligned} \quad (\text{D.44})$$

where $\epsilon(g) = 1$ if g is a symmetry and -1 if it is an anti-symmetry. $\text{Ker}(\epsilon) = G_+$ is a normal subgroup of G , called the symmetry group of H . Let C be a chiral generator of \mathcal{H} . The quotient $G/\text{Ker}(\epsilon) := \{e, C\}$ is a group, whose irrep. are

$G/\text{Ker}(\epsilon)$	$\mathbb{1}$	C
A	1	1
a	1	-1

Saying that \mathcal{H} is invariant under G means that \mathcal{H} belongs to the representation $a \circ \epsilon$ under (the group action of) conjugation. Besides the trivial irrep. $A \circ \epsilon$ and the irrep. $b \circ \epsilon$, the other irrep. of G can be found by decomposing the representations induced from irrep. of G_+ .

D.III Symmetry-preserving interactions in twisted bilayer graphene

Principle of the method — The fermionic Grassmann fields $\{\psi, \bar{\psi}\}$ define two conjugate representations of the symmetry group \mathcal{M} , which we denoted as Υ , the conjugate being Υ^\dagger . Here we define the Grassmann fields such that the action of the free decoupled bilayer reads

$$S_0 = \int d^d r d\tau \bar{\psi}(\mathcal{H}_0 - \partial_\tau)\psi, \quad (\text{D.45})$$

where $d = 2$ is the space dimension. We thus assimilate $\bar{\psi}$ to the conjugate Dirac field Ψ^\dagger instead of the adjoint $\bar{\Psi}$. Eq. (6.35) describes two copies of $(2 + 1)$ -dimensional massless Dirac fermions. Importantly, these copies correspond to the same exact representation of the Dirac matrices, and are not related by time reversal as the two valleys of monolayer graphene. The behaviour under the Θ symmetry is modified accordingly. The representation Υ is four-dimensional, unitary, and reducible; we decomposed it into the direct sum

$$\Upsilon \sim E_1 \oplus E_5. \quad (\text{D.46})$$

The elements $R \in G$ act by matrix multiplication on the fields, $R \cdot \psi(x) = \Upsilon(R)\psi(R^{-1}x)$ and $R \cdot \bar{\psi}(x) = \bar{\psi}(R^{-1}x)\Upsilon^\dagger(R)$, where $x = (\mathbf{r}, t)$ is the space-time variable, and $\Upsilon^\dagger(R) = \Upsilon(R)^{-1}$ by unitarity. Consider now the action of the free coupled bilayer

$$S'_0 = \int d^d r d\tau \bar{\psi}(\mathcal{H} - \partial_\tau)\psi. \quad (\text{D.47})$$

The field bilinear transforms in the direct product of representations $\Upsilon^\dagger \otimes \Upsilon$, which of course leads to the invariance of the action. Indeed,

$$R \cdot \bar{\psi}(x)\mathcal{H}(x)\psi(x) = \bar{\psi}(R^{-1}x)\Upsilon^\dagger(R)\mathcal{H}(x)\Upsilon(R)\psi(R^{-1}x) = \bar{\psi}(R^{-1}x)\mathcal{H}(R^{-1}x)\psi(R^{-1}x). \quad (\text{D.48})$$

Upon changing the integration variable from x to $R^{-1}x$, the action (D.47) remains unaffected. From the perspective of the matrix representation of the field bilinear, among all irrep. that enter the decomposition of $\Upsilon^\dagger \otimes \Upsilon$, the Bloch Hamiltonian \mathcal{H} transforms according to the trivial representation A_1^+ of \mathcal{M} .

We now add a contact quartic interaction. The interaction is thus independent of the space-time variable, but only in the original basis of eigenvectors $(\hat{\psi}, \hat{\bar{\psi}})$ where the two Dirac nodes are separated, and the origin of momentum coincides with the center of the mini Brillouin zone. We look for interaction actions of the form

$$S_{\text{int}} \propto \int d^d r d\tau (\hat{\bar{\psi}} \hat{M} \hat{\psi})(\hat{\psi} \hat{N} \hat{\bar{\psi}}), \quad (\text{D.49})$$

where \hat{M} and \hat{N} are two constant four-dimensional matrices. Each bilinear $\hat{\bar{\psi}} \hat{M} \hat{\psi}$ and $\hat{\psi} \hat{N} \hat{\bar{\psi}}$ belongs to a representation that enters the decomposition of $\Upsilon^\dagger \otimes \Upsilon$. To ensure that Eq. (D.49) is also invariant under the symmetry group \mathcal{M} , we must find the suitable matrices (\hat{M}, \hat{N}) such that $(\hat{\bar{\psi}} \hat{M} \hat{\psi})(\hat{\psi} \hat{N} \hat{\bar{\psi}})$ belongs to the trivial representation of the direct product $(\Upsilon^\dagger \otimes \Upsilon) \otimes (\Upsilon^\dagger \otimes \Upsilon)$. The components of the interaction matrices \hat{M} and \hat{N} are given by the so-called Clebsch-Gordan coefficients

Representations of the unitary group — We define the *unitary* group \tilde{D}_3 as the subgroup which contains all unitary operators including the pure symmetries and antisymmetries. In other words, for all $R \in \tilde{D}_3$,

$$\Upsilon(R)^{-1} \mathcal{H}(R\mathbf{r}, t) \Upsilon(R) = \pm \mathcal{H}(\mathbf{r}, t). \quad (\text{D.50})$$

Eq. (D.50) shows that it has indeed the structure of a group. It is generated by the point group D_3 and \mathcal{P} as the semi-direct product

$$\tilde{D}_3 = \{\mathbb{1}, \mathcal{P}, \bar{\mathbb{1}}, \bar{\mathcal{P}}\} \rtimes D_3, \quad (\text{D.51})$$

where the ‘anti-identity’ $\bar{\mathbb{1}} = (\mathcal{P}\mathcal{C}_2)^2$ is represented by the matrix $\Gamma(\bar{\mathbb{1}}) = -\tau_0\sigma_0$ and a barred operator stands for the product of this operator by $\bar{\mathbb{1}}$. This new element can be seen as a 2π rotation of the double covering of D_3 , or double group

$$D_3^{(2)} = D_3 \times \{\mathbb{1}, \bar{\mathbb{1}}\}, \quad (\text{D.52})$$

the identity $\mathbb{1}$ being assimilated to a 4π rotation. Double groups are known to arise when including time-reversal symmetry in models that include the electron spin. This example shows that unitary antisymmetries can also generate a double group. The main interest in considering the double group is that it is a normal subgroup of \tilde{D}_3 , unlike the simple group D_3 . The structure of the quotient set $\tilde{D}_3/D_3^{(2)} \sim \{\mathbb{1}, \mathcal{P}\}$ is also that of a group,

Name	$\mathbb{1}$	$\bar{\mathbb{1}}$	$2\mathcal{C}_3$	$2\bar{\mathcal{C}}_3$	$2\mathcal{P}\mathcal{C}_2$	$2\mathcal{P}\mathcal{C}_2\mathcal{C}_3$
Set	$\{\mathbb{1}\}$	$\{\bar{\mathbb{1}}\}$	$\{\mathcal{C}_3, \mathcal{C}_3^2\}$	$\{\bar{\mathcal{C}}_3, \bar{\mathcal{C}}_3^2\}$	$\{\mathcal{P}\mathcal{C}_2, \bar{\mathcal{P}}\mathcal{C}_2\}$	$\{\mathcal{P}\mathcal{C}_2\mathcal{C}_3, \bar{\mathcal{P}}\mathcal{C}_2\mathcal{C}_3^2\}$
Name	$2\mathcal{P}\mathcal{C}_2\mathcal{C}_3^2$		$6\mathcal{P}$		$6\mathcal{C}_2$	
Set	$\{\bar{\mathcal{P}}\mathcal{C}_2\mathcal{C}_3, \mathcal{P}\mathcal{C}_2\mathcal{C}_3^2\}$		$\{\mathcal{P}, \mathcal{P}\mathcal{C}_3, \mathcal{P}\mathcal{C}_3^2, \bar{\mathcal{P}}, \bar{\mathcal{P}}\mathcal{C}_3, \bar{\mathcal{P}}\mathcal{C}_3^2\}$		$\{\mathcal{C}_2, \mathcal{C}_2\mathcal{C}_3, \mathcal{C}_2\mathcal{C}_3^2, \bar{\mathcal{C}}_2, \bar{\mathcal{C}}_2\mathcal{C}_3, \bar{\mathcal{C}}_2\mathcal{C}_3^2\}$	

Table D.1 | Classes of conjugation of the unitary group \tilde{D}_3 , with their names (first line) and their elements (second line). $\mathbb{1}$ is the identity operator, $\bar{\mathbb{1}}$ the 2π rotation of a spin one half, and \bar{R} denotes the product $\bar{\mathbb{1}}R$.

which simplifies the determination of the irrep. of \tilde{D}_3 from that of D_3 . To find the irrep. of \tilde{D}_3 we can indeed find them from scratch using the composite operator method (CHEN 2002a), or build them by induction and other tricks from that of D_3 . Let us illustrate the second method.

We start with the one-dimensional irrep. The quotient group $\{\mathbb{1}, \mathcal{P}\}$ possesses two one-dimensional irrep., which we denote as A_1 for the trivial one, and a_1 for the non-trivial one. Of course A_1 also corresponds to the trivial irrep. of D_3 (and to any group in general), by putting ones for all conjugacy classes. The one-dimensional irrep. of D_3 , named A_1 and A_2 , induce over the unitary group the representations $A_1 \uparrow \tilde{D}_3 \sim A_1 \oplus a_1 \oplus E_3$ and $A_2 \uparrow \tilde{D}_3 \sim A_2 \oplus a_2 \oplus E_3$ respectively, where \oplus denotes a direct sum. This defines and determines completely the irrep. E_3 and a_2 . We have found four one-dimensional irrep. (A_2 , a_1 , A_2 and a_2). The commutator subgroup $[\tilde{D}_3, \tilde{D}_3]$ is isomorphic to D_3 , whose index $|\tilde{D}_3/D_3| = 4$ gives the number of one-dimensional irrep. Hence we have found all of them.

The cardinal of the group being $|\tilde{D}_3| = 24$, the remaining irrep. must be two-dimensional, of which there are five, including E_3 . We can decompose the four-dimensional (reducible) representation Υ as a sum of two representations $\Upsilon \sim E_1 \oplus E_5$. In addition, the two-dimensional irrep. E of D_3 induces the representations $E \uparrow \tilde{D}_3 \sim E_1 \oplus E_2 \oplus E_4 \oplus E_5$, where the remaining irrep. E_2 and E_4 can be found by orthonormality of the characters. We have found all the irrep., whose characters are given in Tab. D.2. Tab. D.1 summarises the classes of conjugation of \tilde{D}_3 , which are invariant subsets (and thus the natural argument) of the characters.

Corepresentations of the magnetic group — A group generated by a crystallographic point group and an antiunitary operator is *magnetic*, or Shubnikov group. In general, this antiunitary operator is time reversal, under which the electron spin is odd. Magnetic groups give clues about the magnetic properties of a crystal, hence its name. The group

Irrep.	$\mathbb{1}$	$\bar{\mathbb{1}}$	$2C_3$	$2\bar{C}_3$	$2PC_2$	$2PC_2C_3$	$2PC_2C_3^2$	$6P$	$6C_2$
A_1	1	1	1	1	1	1	1	1	1
A_2	1	1	1	1	-1	-1	-1	1	-1
a_1	1	1	1	1	-1	-1	-1	-1	1
a_2	1	1	1	1	1	1	1	-1	-1
E_1	2	-2	-1	1	0	$\sqrt{3}$	$-\sqrt{3}$	0	0
E_2	2	2	-1	-1	2	-1	-1	0	0
E_3	2	-2	2	-2	0	0	0	0	0
E_4	2	2	-1	-1	-2	1	1	0	0
E_5	2	-2	-1	1	0	$-\sqrt{3}$	$\sqrt{3}$	0	0

Table D.2 | Table of characters of the unitary group \tilde{D}_3 . Each column corresponds to a class of conjugation, and each line to an irrep. We use the symbols A and E prescribed by Mulliken's notation; the symbol a denotes a one-dimensional irrep. whose character have opposite signs on the antisymmetric operators.

generated by \tilde{D}_3 and Θ is a grey magnetic group, i.e. the direct product

$$\mathcal{M} = \tilde{D}_3 \times \{\mathbb{1}, \Theta\}. \quad (\text{D.53})$$

The ‘representations’ of a magnetic group do not share all the defining properties of the standard representations of finite groups. To stress the difference, the term corepresentation is used instead, but for simplicity, we will refer to irreducible corepresentations as irrep.. To find the irrep. of \mathcal{M} from that of \tilde{D}_3 , we apply the Schur-Frobenius criterion (MA 2007; ATKINS 1970; DRESSELHAUS 2007; WOIT 2017; MA 2004). This criterion states the following. For all irrep. ϖ of \tilde{D}_3 , we define another representation of \tilde{D}_3 as with the same dimension,

$$\varpi' : \tilde{D}_3 \rightarrow M_n(\mathbb{C}), \quad (\text{D.54})$$

$$R \mapsto \varpi(\Theta \cdot R \cdot \Theta^{-1})^*. \quad (\text{D.55})$$

This representation falls into either one of the three following categories. (i,ii) Either ϖ' is equivalent to ϖ , in which case there exists an invertible matrix U such that $\varpi' = U\varpi U^{-1}$. (i) If $UU^* = \varpi(\Theta^2)$, then ϖ canonically generates two irrep. of \mathcal{M} , ϖ_+ and ϖ_- , upon defining $\varpi_{\pm}(\Theta) = \pm U$, and which coincide with ϖ on \tilde{D}_3 , $\varpi_{\pm}(R) = \varpi(R)$. There is no Kramer degeneracy. (ii) If $UU^* = -\varpi(\Theta^2)$, the irrep. ϖ_M issued from ϖ has twice its dimension. On \tilde{D}_3 it coincides with $\varpi_M = \varpi \oplus \varpi$, but it has off-diagonal form on all antiunitary operators, with $\varpi_M(\Theta) = i\sigma_y U$. (iii) Or ϖ' is not equivalent to ϖ , in which case it is necessarily equivalent to another irrep. of \tilde{D}_3 . Again, ϖ_M has twice the dimension of ϖ , and coincides with $\varpi_M = \varpi \oplus \varpi'$ on \tilde{D}_3 , while $\varpi_M(\Theta) = \sigma_x \mathbb{1}$.

All irrep. of \tilde{D}_3 fall into category (i), except E_1 and $E_5 = E'_1$, which fall into category (iii). In the former case, each irrep. leads to two irrep., with $\varpi(\Theta) = \pm 1$ for the 1d irrep. or $\varpi(\Theta) = \pm \sigma_x$ for the 2d irrep., where σ_x represents here a generic Pauli matrix, but has nothing to do with the pseudospin. In the latter case, the one irrep. formed by E_1 and E_5 is equivalent to the four-dimensional representation Υ . In the following, we write each irrep. with an exponent \pm to indicate whether the eigenvalues of $\varpi(\Theta)$ are $+1$ or -1 .

Interaction matrices in the unrotated basis — The decomposition of the direct product $\Upsilon^\dagger \otimes \Upsilon$ into irrep. of \mathcal{M} (the Clebsch-Gordan series) reads

$$X(\Upsilon^\dagger \otimes \Upsilon)X^{-1} = A_1^+ \oplus a_1^+ \oplus A_2^+ \oplus a_2^+ \oplus A_1^- \oplus a_1^- \oplus A_2^- \oplus a_2^- \oplus E_2^+ \oplus E_4^+ \oplus E_2^- \oplus E_4^-, \quad (\text{D.56})$$

where the sixteen-times-sixteen transformation matrix X contains the Clebsch-Gordan coefficients. It can be found using the projection formula (MA 2007)

$$X_{ik,\gamma m} X_{jl,\gamma n}^* = \frac{n_\gamma}{|\mathcal{M}|} \sum_{R \in \mathcal{M}} \varpi_\gamma(R)_{mn}^* \Upsilon^\dagger(R)_{ij} \Upsilon(R)_{kl}, \quad (\text{D.57})$$

where ϖ_γ is the γ^{th} irrep. in the series (6.40), with dimension n_γ , and $|\mathcal{M}| = 48$ is the cardinal of the group. The indices i, j, k and l run from 1 to 4, while m and n run from 1 to n_γ . Some irrep. of Eq. (6.40) are one-dimensional; only one matrix M is associated to the Clebsch-Gordan coefficients. Others are two-dimensional; two matrices $M^{(1)}$ and $M^{(2)}$ are associated to the Clebsch-Gordan coefficients. The components of the matrices $\mathbf{M}_\gamma = (M_\gamma^{(1)}, M_\gamma^{(2)})$, which belong to the irrep. ϖ_γ , are listed in the γ^{th} column of X , i.e. for $a, b = 1, \dots, 4$,

$$\left(M_\gamma^{(1)}\right)_{ab} = X_{ab,\gamma 1}, \quad \left(M_\gamma^{(2)}\right)_{ab} = X_{ab,\gamma 2}. \quad (\text{D.58})$$

Diagrammatic expansion in twisted bilayer graphene

E.I Free theory

E.I.1 Correction of the Fermi velocity by interlayer hopping

We consider here the low-energy Hamiltonian of the coupled bilayer

$$\mathcal{H} = i\tau_0 \boldsymbol{\sigma} \cdot \boldsymbol{\partial} + \alpha \sum_{j=1}^3 \sum_{\eta=\pm} e^{-i\eta \mathbf{q}_j \cdot \mathbf{r}} T_j^\eta, \quad (\text{E.1})$$

where α represents the dimensionless strength of inter-sublattice hopping, and the hopping matrices have the form

$$T_j^\pm = \tau_\pm \left(\beta \sigma_0 + \zeta^{j-1} \sigma_+ + \zeta^{1-j} \sigma_- \right), \quad (\text{E.2})$$

where τ_\pm denote the ladder operators in the layer sector. The parameter $\beta = u/w$ is the relative intra- versus inter-sublattice hopping strength. From the translational-invariant part of the two-point connected correlation functions $G'_0(\mathbf{k}, \Omega)$, we introduce the translational-invariant part Σ' of the self-energy such that

$$G'_0(\mathbf{k}, \Omega)^{-1} = G_0(\mathbf{k}, \Omega)^{-1} - \Sigma'(\mathbf{k}, \Omega) \simeq N_\psi (v \boldsymbol{\sigma} \cdot \mathbf{k} - i\Omega), \quad (\text{E.3})$$

where the last equality holds in the low-energy limit $k, \Omega \ll 1$.

We now expand the self-energy to sixth order to determine the corrected Fermi velocity v and the normalisation of the wave function amplitude N_ψ . For brevity, we omit to write the Ω -dependence, and split the self-energy into the five contributions represented by the graphs of Fig. E.1,

$$\Sigma'(\mathbf{k}) = \alpha^2 \Sigma'_2(\mathbf{k}) + \alpha^4 \Sigma'_4(\mathbf{k}) + \alpha^6 \left[\Sigma'_{6,\text{nes}}(\mathbf{k}) + \Sigma'_{6,\text{row}}(\mathbf{k}) + \Sigma'_{6,\text{cro}}(\mathbf{k}) \right] + O(\alpha^8). \quad (\text{E.4})$$

We also introduce the shorthand notation $\bar{\eta} = -\eta$ with $\eta = \pm$. The second order contribution (Fig. E.1(a)) reads

$$\Sigma'_2(\mathbf{k}) = \sum_{\eta=\pm} \sum_j T_j^{\bar{\eta}} G_0(\mathbf{k} + \eta \mathbf{q}_j) T_j^\eta. \quad (\text{E.5})$$

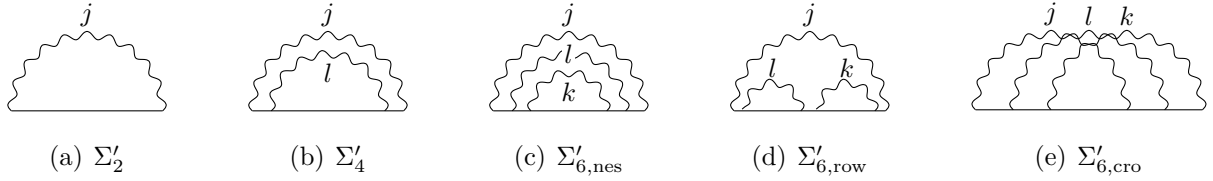


Figure E.1 | Diagrammatic expansion of the self-energy to order six in the dimensionless hopping strength $\alpha = w/E_K$. Each hopping (wavy) line bears an index j (or l, k at higher orders) and carries a corresponding momentum \mathbf{q}_j . The graphs are summed over all channels $j = 1, 2, 3$ (similarly for l, k) and the sign $\eta = \pm$ of the first momentum transfer. The graphs are of order (a) two (b) four, and (c-e) six in α . At order six, the hopping lines can be (c) nested, (d) in a row, or (e) crossed. For these diagrams to be one-particle irreducible, the consecutive hopping induces must be different. Hence, $j \neq l$ in diagram (b), $l \neq j$ and $l \neq k$ in diagrams (c) and (d), and the indices j, l, k differ two by two in diagram (e).

The fourth order contribution (Fig. E.1(b)) reads

$$\Sigma'_4(\mathbf{k}) = \sum_{\eta=\pm} \sum_{j \neq l} T_j^{\bar{\eta}} G_0(\mathbf{k} + \eta \mathbf{q}_j) T_l^{\eta} G_0(\mathbf{k} + \eta \mathbf{q}_j - \eta \mathbf{q}_l) T_l^{\bar{\eta}} G_0(\mathbf{k} + \eta \mathbf{q}_j) T_j^{\eta}. \quad (\text{E.6})$$

The sixth order contribution breaks up into three terms. The first diagram hosts three nested hopping lines (Fig. E.1(c)),

$$\Sigma'_{6,\text{nes}}(\mathbf{k}) = \sum_{\eta=\pm} \sum_{\substack{l \neq j \\ l \neq k}} T_j^{\bar{\eta}} G_0(\mathbf{k} + \eta \mathbf{q}_j) T_l^{\eta} G_0(\mathbf{k} + \eta \mathbf{q}_j - \eta \mathbf{q}_l) T_k^{\bar{\eta}} G_0(\mathbf{k} + \eta \mathbf{q}_j + \eta \mathbf{q}_k - \eta \mathbf{q}_l) T_k^{\eta} G_0(\mathbf{k} + \eta \mathbf{q}_j - \eta \mathbf{q}_l) T_l^{\bar{\eta}} G_0(\mathbf{k} + \eta \mathbf{q}_j) T_j^{\eta}. \quad (\text{E.7})$$

The second diagram hosts two hopping lines in a row, embedded in a third one (Fig. E.1(d)),

$$\Sigma'_{6,\text{row}}(\mathbf{k}) = \sum_{\eta=\pm} \sum_{\substack{l \neq j \\ l \neq k}} G_0(\mathbf{k} + \eta \mathbf{q}_j) T_l^{\eta} G_0(\mathbf{k} + \eta \mathbf{q}_j - \eta \mathbf{q}_l) T_l^{\bar{\eta}} G_0(\mathbf{k} + \eta \mathbf{q}_j) T_k^{\eta} G_0(\mathbf{k} + \eta \mathbf{q}_j - \eta \mathbf{q}_k) T_k^{\bar{\eta}} G_0(\mathbf{k} + \eta \mathbf{q}_j) T_j^{\eta}. \quad (\text{E.8})$$

The third diagram consists in three crossing hopping lines (Fig. E.1(e)),

$$\Sigma'_{6,\text{cro}}(\mathbf{k}) = \sum_{\eta=\pm} \sum_{j \neq l \neq k} T_k^{\bar{\eta}} G_0(\mathbf{k} + \eta \mathbf{q}_k) T_l^{\eta} G_0(\mathbf{k} + \eta \mathbf{q}_k - \eta \mathbf{q}_l) T_j^{\bar{\eta}} G_0(\mathbf{k} + \eta \mathbf{q}_j + \eta \mathbf{q}_k - \eta \mathbf{q}_l) T_k^{\eta} G_0(\mathbf{k} + \eta \mathbf{q}_j - \eta \mathbf{q}_l) T_l^{\bar{\eta}} G_0(\mathbf{k} + \eta \mathbf{q}_j) T_j^{\eta}. \quad (\text{E.9})$$

By expanding Eq. (E.4) at order one in \mathbf{k} and Ω , we get the expressions (6.19) and (6.20) for the wave function amplitude and Fermi velocity, respectively. By keeping the order two in momentum, we get the quadratic dispersion relation of Eq. (6.22).

E.I.2 Correction of the order parameters by interlayer hopping

We now consider the mean-field Hamiltonian of the decoupled bilayer

$$\mathcal{H}_{\text{MF}} = \mathcal{H}_0 + \sigma_z (\Delta_0 \tau_0 + \Delta_z \tau_z) + \boldsymbol{\sigma} \cdot (\mathcal{G}_0 \tau_0 + \mathcal{G}_z \tau_z), \quad (\text{E.10})$$

where $\mathcal{H}_0 = \tau_0 \boldsymbol{\sigma} \cdot \mathbf{k}$ is the single-particle Hamiltonian of the decoupled bilayer. Including the hopping term, we find

$$\mathcal{H}'_{\text{MF}} = \mathcal{H} + \sigma_z (\Delta_0 \tau_0 + \Delta_z \tau_z) + \boldsymbol{\sigma} \cdot (\mathcal{G}_0 \tau_0 + \mathcal{G}_z \tau_z), \quad (\text{E.11})$$

where the Hamiltonian of the coupled bilayer \mathcal{H} is given by Eq. (6.6). The scalar order parameters $\Delta_{0/z}$ gap out the energy spectrum, while the vectorial order parameters $\mathcal{G}_{0/z}$ shift the Dirac cones from the corners of the mini Brillouin zone. We proceed as in Sec. E.I.1 to diagonalise the Hamiltonian (E.11) in the low-energy limit. Let G_{MF} be the translation-invariant part of the propagator corresponding to Hamiltonian (E.10), and G'^{-1}_{MF} be the similar function for Hamiltonian (E.11). We can write the latter as

$$G'^{-1}_{\text{MF}}(\mathbf{k}, \Omega) = G_{\text{MF}}(\mathbf{k}, \Omega)^{-1} - \Sigma'(\mathbf{k}, \Omega) \simeq N_\psi \left\{ v \boldsymbol{\sigma} \cdot \left[(\mathbf{k} + N_0^{(\mathcal{G})} \mathcal{G}_0) \tau_0 + N_z^{(\mathcal{G})} \mathcal{G}_z \tau_z \right] + \sigma_z \left(N_0^{(\Delta)} \Delta_0 \tau_0 + N_z^{(\Delta)} \Delta_z \tau_z \right) - i\Omega \right\}. \quad (\text{E.12})$$

The factors $N_{0/z}^{(\mathcal{G}/\Delta)}(\alpha, \beta)$ encode the renormalisation of the order parameters by interlayer hopping; they are the counterparts of the corrected Fermi velocity for the matrix structures $\sigma_z \tau_{0/z}$ and $\boldsymbol{\sigma} \tau_{0/z}$. By definition of the corrected Fermi velocity, we have $N_0^{(\mathcal{G})} = 1$. We calculate the other non-trivial factors diagrammatically to sixth order in α , by replacing the free propagator G_0 by the mean-field propagator G_{MF} in the second, fourth and sixth order contributions to the self-energy given by Eq. (E.5) to Eq. (E.9). The results are

$$N_\psi N_0^{(\Delta)} = 1 + 3\alpha^2 (1 - \beta^2) + 2\alpha^4 (1 - \beta^2) (1 + 2\beta^2) + \frac{1}{28} \alpha^6 (24 - 80\beta^2 + 352\beta^4 - 233\beta^6) + O(\alpha^8), \quad (\text{E.13})$$

$$N_\psi N_z^{(\Delta)} = 1 - 3\alpha^2 (1 - \beta^2) + 2\alpha^4 (1 - \beta^2) (1 - 4\beta^2) - \frac{1}{28} \alpha^6 (56 - 304\beta^2 + 872\beta^4 - 561\beta^6) + O(\alpha^8), \quad (\text{E.14})$$

and

$$v N_\psi N_z^{(\mathcal{G})} = 1 + 3\alpha^2 + \alpha^4 (1 + 10\beta^2 + \beta^4) + \frac{3}{49} \alpha^6 (9 + 441\beta^4 + 70\beta^6) + O(\alpha^8). \quad (\text{E.15})$$

E.I.3 Mean-field self-consistent equations

For the sake of simplicity, we write the mean-field self-consistent equations for each order parameter separately. Upon introducing an ultraviolet cut-off Λ , these equations read

$$\begin{cases} \Delta_\mu = -2g_\mu \int d\omega \int_\Lambda \frac{d^2q}{(2\pi)^3} \langle \bar{\psi}_{q,\omega} \sigma_z \tau_\mu \psi_{q,\omega} \rangle, & (\text{E.16a}) \\ \mathcal{G}_\mu = -2\lambda_\mu \int d\omega \int_\Lambda \frac{d^2q}{(2\pi)^3} \langle \bar{\psi}_{q,\omega} \boldsymbol{\sigma} \tau_\mu \psi_{q,\omega} \rangle, & (\text{E.16b}) \end{cases}$$

for $\mu = 0, z$, where the momentum integral runs over a square of side Λ , and $\{\psi_{q,\omega}, \bar{\psi}_{q,\omega}\}$ denote the Fourier-transformed fields. The correlators in Eq. (E.16) represent the

translational-invariant parts of statistical averages computed over the mean-field Hamiltonian \mathcal{H}'_{MF} defined in Eq. (7.2). By expanding the correlators in powers of α , we automatically correct the order parameters by the factors $N_{0/z}^{(\mathcal{G}/\Delta)}$ introduced in Eq. (E.11). We can express these self-consistent equations analytically. The quantities $\Delta'_{0/z} = N_{0/z}^{(\Delta)} \Delta_{0/z}$ and $\mathcal{G}'_{0/z} = N_{0/z}^{(\mathcal{G})} \mathcal{G}_{0/z}$ satisfy the relations

$$\left\{ \begin{array}{l} \Delta'_{0/z} = \frac{g_{0/z} N_{0/z}^{(\Delta)} \Lambda^2}{v N_\psi} F(\Delta'_{0/z}), \\ \mathcal{G}'_{0/z} = \frac{\lambda_{0/z} N_{0/z}^{(\Delta)} \Lambda^2}{N_\psi} F_{0/z}(\mathcal{G}'_{0/z}), \end{array} \right. \quad (\text{E.17a})$$

$$\left\{ \begin{array}{l} \Delta'_{0/z} = \frac{g_{0/z} N_{0/z}^{(\Delta)} \Lambda^2}{v N_\psi} F(\Delta'_{0/z}), \\ \mathcal{G}'_{0/z} = \frac{\lambda_{0/z} N_{0/z}^{(\Delta)} \Lambda^2}{N_\psi} F_{0/z}(\mathcal{G}'_{0/z}), \end{array} \right. \quad (\text{E.17b})$$

where for simplicity we assume the shift momenta $\mathcal{G}_{0/z} = \mathcal{G}_{0/z} \mathbf{e}_y$ to be aligned along a crystallographic axis of the moire pattern, here along the y axis. The dimensionless functions F and $F_{0/z}$ read

$$F(x) = \frac{2x}{\pi^2} \left[-\log(\sqrt{x^2+2}-1) + \log(\sqrt{x^2+2}+1) - 2x \cot^{-1}(x\sqrt{x^2+2}) + 2 \coth^{-1}(\sqrt{x^2+2}) \right], \quad (\text{E.18})$$

$$F_0(x) = \frac{1}{\pi^2} \left[-\sqrt{y_-} + \sqrt{y_+} + \tanh^{-1}(\sqrt{y_-}) - \tanh^{-1}(\sqrt{y_+}) - y_- \coth^{-1}(\sqrt{y_-}) + y_+ \coth^{-1}(\sqrt{y_+}) \right], \quad (\text{E.19})$$

and

$$F_z(x) = \frac{1}{2\pi^2} \left[x^2 \log\left(\frac{1-x}{1+x}\right) - 2x^2 \tanh^{-1}(x) + (1-2x) \log(\sqrt{y_-}-1) - (1+2x) \log(\sqrt{y_+}-1) + z_+ \log(\sqrt{y_+}+1) - z_- \log(\sqrt{y_-}+1) + 2(\sqrt{y_+}-\sqrt{y_-}) \right], \quad (\text{E.20})$$

where $y_\pm = 2 + x(x \pm 2)$ and $z_\pm = 1 + 2x(x \pm 1)$.

E.II Renormalisation group analysis of the interacting theory

We decompose the renormalised action into $S_{\text{R}} = S_{\text{R},0} + S_{\text{R},\alpha} + S_{\text{R},\phi} + S_{\text{R},\text{Yuk}}$. In order to cure infrared divergences, we add a mass regulator $\mu \sigma_z$ to the quadratic action of the decoupled bilayer

$$S_{\text{R},0} = \int_{\mathbf{k},\Omega} \bar{\psi}_{\mathbf{k}} (\boldsymbol{\sigma} \cdot \mathbf{k} - i\Omega + \mu \sigma_z) \psi_{\mathbf{k}}, \quad (\text{E.21})$$

where the mass scale μ vanishes in the infrared limit. The quadratic hopping action reads

$$S_{\text{R},\alpha} = \alpha \sum_{j=1}^3 \sum_{\eta=\pm} \int_{\mathbf{k},\Omega} \bar{\psi}_{\mathbf{k}} T_j^\eta \psi_{\mathbf{k}+\eta\mathbf{q}_j}. \quad (\text{E.22})$$

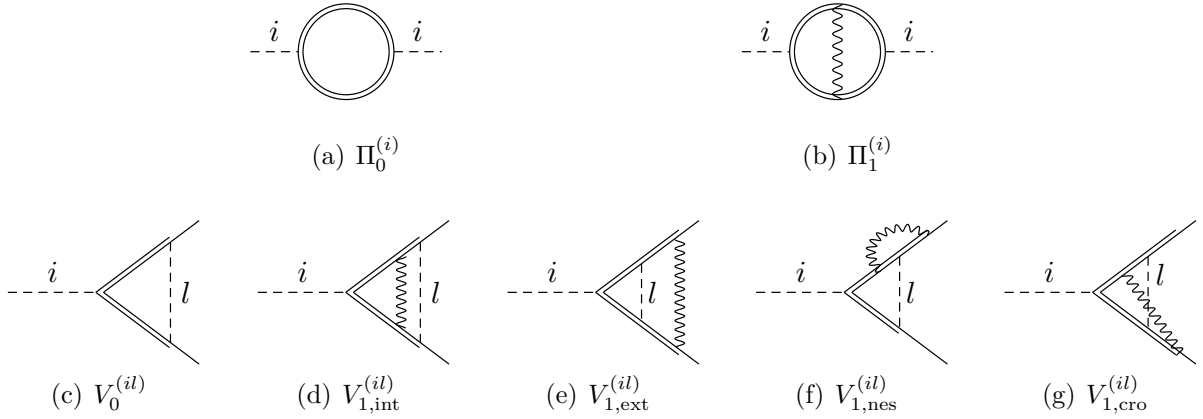


Figure E.2 | One-particle irreducible diagrams at first order in the loopwise expansion and second order in the dimensionless hopping strength α . The double line stands for the fermionic propagator corrected by interlayer hopping, the dashed line for the bosonic propagator, and the wavy line for the sum of all interlayer hopping channels with momenta $\eta\mathbf{q}_j$, for $\eta = \pm$ and $j = 1, 2, 3$. The polarisation Π_i , i.e. the corrections to the bosonic propagator of type i , is taken at zero external momentum and frequency and given by (a) at order α^0 and (b) at order α^2 . The three-point Yukawa vertex $V^{(il)}$, also at zero external momenta and frequencies, is drawn in (c) at order α^0 , and in (d)-(g) at order α^2 . The hopping line can be (d) internal, (e) external, (f) isolated and (g) crossed with respect to the internal vertex of type l .

The bosonic part of the renormalised action is given by

$$S_{\text{R},\phi} = \sum_{i=1}^8 Z_{\phi_i} \int_{\mathbf{k},\Omega} (\phi_i^2)_{\mathbf{k}} + \sum_{l=1}^4 Z_{\varphi_l} \int_{\mathbf{k},\Omega} (\varphi_l^2)_{\mathbf{k}}. \quad (\text{E.23})$$

The renormalised Yukawa coupling is

$$S_{\text{R},\text{Yuk}} = 2\mu^{-\varepsilon/2} N_{\psi} \left[\sum_{i=1}^8 Z_{g_i} \sqrt{g_i} \int_{\mathbf{k},\Omega_k, \mathbf{q}, \Omega_p} \bar{\psi}_{\mathbf{k}} (\phi_i M_i)_{\mathbf{k}-\mathbf{q}} \psi_{\mathbf{q}} + \sum_{l=1}^4 Z_{\lambda_l} \sqrt{\lambda_l} \int_{\mathbf{k},\Omega_k, \mathbf{q}, \Omega_p} \bar{\psi}_{\mathbf{k}} (\varphi_l \cdot \mathbf{M}_l)_{\mathbf{k}-\mathbf{q}} \psi_{\mathbf{q}} \right]. \quad (\text{E.24})$$

The factor N_{ψ} is the field amplitude corrected by interlayer hopping of Eq. (6.20). Here we determine the renormalisation constants Z_{χ} for bosonic fields $\chi \in \{\phi_i, \varphi_l\}$, and Z_u for coupling strengths $u \in \{g_i, \lambda_l\}$. We denote by G'_0 be the fermionic propagator corrected by interlayer hopping of Eq. (6.13). The one-particle irreducible diagrams are listed in Fig. E.2. In the following, the expressions of the Feynman integrals hold for all couplings which are diagonal in the layer sector, but some numerical values are given for the four relevant interactions only, of coupling matrices $M = \sigma_z \tau_{0/z}$ and $\mathbf{M} = \boldsymbol{\sigma} \tau_{0/z}$.

E.II.1 Polarisation

Consider one of the four relevant instabilities labelled i with interaction matrix \mathbf{M}_i (which is a vector of one or two components). The polarisation at order zero in α is given by

diagram E.2(a),

$$\Pi_0^{(i)} = -4u_a N_\psi^2 \int_{\mathbf{q}, \omega} \text{Tr}[\mathbf{M}_i G'_0(\mathbf{q}, \omega) \cdot \mathbf{M}_i G'_0(\mathbf{q}, \omega)], \quad (\text{E.25})$$

where an scalar products over the components of \mathbf{M}_i is performed. The polarisation at order two in α is given by diagram E.2(b),

$$\Pi_1^{(i)} = -4u_i N_\psi^2 \alpha^2 \sum_{j=1}^3 \sum_{\eta=\pm} \int_{\mathbf{q}, \omega} \text{Tr}[\mathbf{M}_i G'_0(\mathbf{q}, \omega) T_j^{\bar{\eta}} G'_0(\mathbf{q} + \eta \mathbf{q}_j, \omega) \cdot \mathbf{M}_i G'_0(\mathbf{q} + \eta \mathbf{q}_j, \omega) T_j^\eta G'_0(\mathbf{q}, \omega)]. \quad (\text{E.26})$$

The pole of the integral in Eq. (E.25) per number of fermion flavours n (equal to four in our case) can be cast into $\Pi_0^{(i)} = -4nu_i I_i / v\varepsilon$ where v is the corrected Fermi velocity and

$$I_i = \lim_{\varepsilon \rightarrow 0} \frac{v\varepsilon N_\psi^2}{n} \int_{\mathbf{q}, \omega} \text{Tr}[\mathbf{M}_i G'_0(\mathbf{q}, \omega) \cdot \mathbf{M}_i G'_0(\mathbf{q}, \omega)] = \begin{cases} \frac{1}{2\pi} & \text{for } \mathbf{M}_i \propto \sigma_z, \\ \frac{1}{4\pi} & \text{for } \mathbf{M}_i \propto \boldsymbol{\sigma}. \end{cases} \quad (\text{E.27})$$

In Eq. (E.26) we can use the separation of energy scales: the theory is meaningful only at length scales much larger than the moiré periodicity, i.e. for $q, \omega \ll 1$, so that $G'_0(\mathbf{q} + \eta \mathbf{q}_j, \omega)$ can be replaced by $G'_0(\eta \mathbf{q}_j, 0)$. This results in $\Pi_1^{(i)} = -3\alpha^2 s_i h_i(\beta) \Pi_0^{(i)}$ where s_i equals either $+1$ for the interaction matrices $\sigma_z \tau_0$ and $\boldsymbol{\sigma} \tau_z$ or -1 for the interaction matrices $\sigma_z \tau_z$ and $\boldsymbol{\sigma} \tau_0$; and the corrugation-dependent function $h_i(\beta)$ equals either $1 - \beta^2$ or 1 if the interaction matrix matches σ_0 or σ_z in the pseudospin sector, respectively. The finiteness of the renormalised polarisation fixes the bosonic field constant to

$$Z_{\chi_i} = 1 - \frac{4nu_i I_i [1 + 3\alpha^2 s_i h_i(\beta)]}{v\varepsilon}. \quad (\text{E.28})$$

E.II.2 Yukawa vertex

Consider now two instabilities labelled a and b , the former appearing in an external Yukawa vertex, the latter entering as an internal vertex. If instability a is two-dimensional, we focus on the a single component M_i of the interaction matrix. The other component gives the same corrections to the vertex. The three-point Yukawa vertex at order zero in α is given by diagram E.2(c),

$$V_0^{(il)} = N_\psi^3 (2\sqrt{u_i}) (4u_l) \int_{\mathbf{q}, \omega} \mathbf{M}_l G'_0(\mathbf{q}, \omega) M_i G'_0(\mathbf{q}, \omega) \mathbf{M}_l. \quad (\text{E.29})$$

The Yukawa vertex at order two in α have either multiplicity one or two. Those with multiplicity one are dressed by either an internal hopping line, as in Fig. E.2(d),

$$V_{1, \text{int}}^{(il)} = N_\psi^3 (2\sqrt{u_i}) (4u_l \alpha^2) \sum_{\eta, j} \int_{\mathbf{q}, \omega} \mathbf{M}_l G'_0(\mathbf{q}, \omega) T_j^{\bar{\eta}} G'_0(\mathbf{q} + \eta \mathbf{q}_j, \omega) M_i G'_0(\mathbf{q} + \eta \mathbf{q}_j, \omega) T_j^\eta G'_0(\mathbf{q}, \omega) \cdot \mathbf{M}_l, \quad (\text{E.30})$$

or an external hopping line, as in Fig. E.2(e),

$$V_{1,\text{ext}}^{(il)} = N_\psi^3 (2\sqrt{u_i}) (4u_l \alpha^2) \sum_{\eta,j} \int_{\mathbf{q},\omega} T_j^{\bar{\eta}} G'_0(\eta\mathbf{q}_j, \omega) \mathbf{M}_l G'_0(\mathbf{q}, \omega) M_i G'_0(\mathbf{q}, \omega) \cdot \mathbf{M}_l G'_0(\eta\mathbf{q}_j, \omega) T_j^\eta. \quad (\text{E.31})$$

The diagrams corrected by interlayer hopping with multiplicity two nest either an isolated hopping line, as in Fig. E.2(f),

$$V_{1,\text{iso}}^{(il)} = 2N_\psi^3 (2\sqrt{u_i}) (4u_l \alpha^2) \sum_{\eta,j} \int_{\mathbf{q},\omega} T_j^{\bar{\eta}} G'_0(\eta\mathbf{q}_j, \omega) \mathbf{M}_l G'_0(\mathbf{q} + \eta\mathbf{q}_j, \omega) T_j^\eta G'_0(\mathbf{q}, \omega) M_i G'_0(\mathbf{q}, \omega) \cdot \mathbf{M}_l, \quad (\text{E.32})$$

or a hopping line that crosses the interaction line, shown in Fig. E.2(g),

$$V_{1,\text{cro}}^{(il)} = 2N_\psi^3 (2\sqrt{u_i}) (4u_l \alpha^2) \sum_{\eta,j} \int_{\mathbf{q},\omega} \mathbf{M}_l G'_0(\bar{\eta}\mathbf{q}_j, \omega) T_j^{\bar{\eta}} G'_0(\mathbf{q}, \omega) M_i G'_0(\mathbf{q}, \omega) \cdot \mathbf{M}_l G'_0(\eta\mathbf{q}_j, \omega) T_j^\eta. \quad (\text{E.33})$$

Similarly, we can define the pole of the integral appearing in Eq. (E.29) as

$$J_{il} = \lim_{\varepsilon \rightarrow 0} \frac{v\varepsilon N_\psi^2}{n} \int_{\mathbf{q},\omega} \text{Tr}[\mathbf{M}_l G'_0(\mathbf{q}, \omega) M_i G'_0(\mathbf{q}, \omega) \cdot \mathbf{M}_l M_i] = \begin{cases} 0 & i = 2d, l = 2d, \\ \frac{-1}{4\pi} & i = 2d, l = 1d, \\ \frac{-1}{2\pi} & i = 1d, l = 2d, \\ \frac{1}{2\pi} & i = 1d, l = 1d, \end{cases} \quad (\text{E.34})$$

where the four possible values of J_{il} depend on the dimension of the irrep. associated to the channels i and l ($1d$ for the matrix structure σ_z , or $2d$ for the matrix structure $\boldsymbol{\sigma}$). Hence $V_{1,\text{in}}^{(il)} = V_{1,\text{ext}}^{(il)} = 3\alpha^2 s_i h_i(\beta) V_0^{(il)}$ with $V_0^{(il)} = N_\psi (2i\sqrt{u_i}) (4u_l J_{il}/v\varepsilon)$. We also define the pole appearing in the sum of the diagrams with multiplicity two as

$$K_{il}(\beta) = \lim_{\varepsilon \rightarrow 0} \frac{v\varepsilon N_\psi^4}{n} \sum_{\eta,j} \int_{\mathbf{q},\omega} \text{Tr} \left\{ \mathbf{M}_l G'_0(\eta\mathbf{q}_j, \omega) T_j^\eta G'_0(\mathbf{q}, \omega) M_i G'_0(\mathbf{q}, \omega) \cdot \mathbf{M}_l \left[M_i T_j^{\bar{\eta}} G'_0(\eta\mathbf{q}_j, \omega) + G'_0(\bar{\eta}\mathbf{q}_j, \omega) T_j^{\bar{\eta}} M_i \right] \right\}, \quad (\text{E.35})$$

such that $V_{1,\text{iso}}^{(il)} + V_{1,\text{cro}}^{(il)} = N_\psi (2i\sqrt{u_i}) [8\alpha^2 u_l K_{il}(\beta)]/v\varepsilon$. The numerical constants J_{il} depend neither on the number of fermion flavours n nor on the parameter β , while $K_{il}(\beta)$ depends on β . Using commutation relations between interaction and hopping matrices, we can express all vertices (E.29) – (E.33) in terms of J_{il} and K_{il} only. We then find the vertex renormalization constant to be

$$Z_{u_i} = 1 - \frac{4}{v\varepsilon} \sum_l u_l [(1 + 6\alpha^2 s_i h_i(\beta)) J_{il} + 2\alpha^2 K_{il}(\beta)]. \quad (\text{E.36})$$

This proves the expressions of the functions $f_{il}(\alpha, \beta)$ given in Tab. 7.1 in the main text.

References

Introduction

- BARDEEN, J. and W. H. BRATTAIN (July 1948). “The Transistor A Semi-Conductor Triode”. *Physical Review* 74.2, pp. 230–231.
- CHEN, G., O. ZILBERBERG, and W. CHEN (Mar. 2020). “Detection of Fermi arcs in Weyl semimetals through surface negative refraction”. *Physical Review B* 101.12, p. 125407.
- KITTEL, C. (1971). *Introduction to solid state physics*. Wiley. ISBN: 9780471490210.
- LIU, Z. K., B. ZHOU, Y. ZHANG, Z. J. WANG, H. M. WENG, D. PRABHAKARAN, S.-K. MO, Z. X. SHEN, Z. FANG, X. DAI, Z. HUSSAIN, and Y. L. CHEN (Feb. 2014). “Discovery of a Three-Dimensional Topological Dirac Semimetal Na₃Bi”. *Science* 343.6173, pp. 864–867.
- LV, B. Q., H. M. WENG, B. B. FU, X. P. WANG, H. MIAO, J. MA, P. RICHARD, X. C. HUANG, L. X. ZHAO, G. F. CHEN, Z. FANG, X. DAI, T. QIAN, and H. DING (July 2015). “Experimental Discovery of Weyl Semimetal TaAs”. *Physical Review X* 5.3, p. 031013.
- NOVOSELOV, K. S., A. K. GEIM, S. V. MOROZOV, D. JIANG, Y. ZHANG, S. V. DUBONOS, I. V. GRIGORIEVA, and A. A. FIRSOV (Oct. 2004). “Electric Field Effect in Atomically Thin Carbon Films”. *Science* 306.5696, pp. 666–669.
- WU, Y., Y.-M. LIN, A. A. BOL, K. A. JENKINS, F. XIA, D. B. FARMER, Y. ZHU, and P. AVOURIS (Apr. 2011). “High-frequency scaled graphene transistors on diamond-like carbon”. *Nature* 472.7341, pp. 74–78.

Relativistic condensed matter

- 'T HOOFT, G. and M. VELTMAN (July 1972). “Regularization and renormalization of gauge fields”. *Nuclear Physics B* 44.1, pp. 189–213.
- ADLER, S. L. (Jan. 1969). “Axial-Vector Vertex in Spinor Electrodynamics”. *Physical Review* 177.5, pp. 2426–2438.
- ANDERSON, P. W. (Mar. 1958). “Absence of Diffusion in Certain Random Lattices”. *Physical Review* 109.5, pp. 1492–1505.
- ARMITAGE, N. P., E. J. MELE, and A. VISHWANATH (Jan. 2018). “Weyl and Dirac semimetals in three-dimensional solids”. *Reviews of Modern Physics* 90.1, p. 015001.
- BELL, J. S. and R. JACKIW (Mar. 1969). “A PCAC puzzle: $\pi_0 \mapsto \gamma\gamma$ in the σ -model”. *Il Nuovo Cimento A* 60.1, pp. 47–61.

- BERNEVIG, B. A. and T. L. HUGHES (2013). *Topological Insulators and Topological Superconductors*. Princeton University Press. ISBN: 9780691151755.
- BJORKEN, J. and S. DRELL (2013). *Relativistic Quantum Fields*. Dover Books on Physics Series. Dover Publications, Incorporated. ISBN: 978-0-486-48588-1.
- BLOCH, F. (July 1929). “Über die Quantenmechanik der Elektronen in Kristallgittern”. *Zeitschrift für Physik* 52.7-8, pp. 555–600.
- BORISENKO, S., Q. GIBSON, D. EVTUSHINSKY, V. ZABOLOTNYY, B. BÜCHNER, and R. J. CAVA (July 2014). “Experimental Realization of a Three-Dimensional Dirac Semimetal”. *Physical Review Letters* 113.2, p. 027603.
- BURDICK, G. A. (Jan. 1963). “Energy Band Structure of Copper”. *Physical Review* 129.1, pp. 138–150.
- BURKOV, A. A. (Feb. 2015). “Chiral anomaly and transport in Weyl metals”. *Journal of Physics: Condensed Matter* 27.11, p. 113201.
- CAO, Y., V. FATEMI, A. DEMIR, S. FANG, S. L. TOMARKEN, J. Y. LUO, J. D. SANCHEZ-YAMAGISHI, K. WATANABE, T. TANIGUCHI, E. KAXIRAS, R. C. ASHOORI, and P. JARILLO-HERRERO (Mar. 2018a). “Correlated insulator behaviour at half-filling in magic-angle graphene superlattices”. *Nature* 556.7699, pp. 80–84.
- CAO, Y., V. FATEMI, S. FANG, K. WATANABE, T. TANIGUCHI, E. KAXIRAS, and P. JARILLO-HERRERO (Mar. 2018b). “Unconventional superconductivity in magic-angle graphene superlattices”. *Nature* 556.7699, pp. 43–50.
- CARDY, J., P. GODDARD, and J. YEOMANS (1996). *Scaling and Renormalization in Statistical Physics*. Cambridge Lecture Notes in Physics. Cambridge University Press. ISBN: 9780521499590.
- CASTRO NETO, A. H., F. GUINEA, N. M. R. PERES, K. S. NOVOSELOV, and A. K. GEIM (Jan. 2009). “The electronic properties of graphene”. *Reviews of Modern Physics* 81.1, pp. 109–162.
- CHEN, G., O. ZILBERBERG, and W. CHEN (Mar. 2020). “Detection of Fermi arcs in Weyl semimetals through surface negative refraction”. *Physical Review B* 101.12, p. 125407.
- CHEN, R. Y., S. J. ZHANG, J. A. SCHNEELOCH, C. ZHANG, Q. LI, G. D. GU, and N. L. WANG (Aug. 2015). “Optical spectroscopy study of the three-dimensional Dirac semimetal ZrTe₅”. *Physical Review B* 92.7, p. 075107.
- CHIU, C.-K., J. C. Y. TEO, A. P. SCHNYDER, and S. RYU (Aug. 2016). “Classification of topological quantum matter with symmetries”. *Reviews of Modern Physics* 88.3, p. 035005.
- DAS SARMA, S., S. ADAM, E. H. HWANG, and E. ROSSI (May 2011). “Electronic transport in two-dimensional graphene”. *Reviews of Modern Physics* 83.2, pp. 407–470.
- DIRAC, P. A. M. and R. H. FOWLER (Feb. 1928). “The quantum theory of the electron”. *Proceedings of the Royal Society of London. Series A, Containing Papers of a Mathematical and Physical Character* 117.778, pp. 610–624.
- DUPLANTIER, B. and A. W. W. LUDWIG (Jan. 1991). “Multifractals operator-product expansion and field theory”. *Physical Review Letters* 66.3, pp. 247–251.
- DYSON, F. J. (June 1949). “The S Matrix in Quantum Electrodynamics”. *Physical Review* 75.11, pp. 1736–1755.
- FARAEI, Z., T. FARAJOLLAHPOUR, and S. A. JAFARI (Nov. 2018). “Greens function of semi-infinite Weyl semimetals”. *Physical Review B* 98.19, p. 195402.
- FEYNMAN, R. P. (Sept. 1949a). “The Theory of Positrons”. *Physical Review* 76.6, pp. 749–759.

- FEYNMAN, R. P. (Sept. 1949b). “Space-Time Approach to Quantum Electrodynamics”. *Physical Review* 76.6, pp. 769–789.
- FEYNMAN, R. P. (Nov. 1950). “Mathematical Formulation of the Quantum Theory of Electromagnetic Interaction”. *Physical Review* 80.3, pp. 440–457.
- FRADKIN, E. (Mar. 1986). “Critical behavior of disordered degenerate semiconductors. II. Spectrum and transport properties in mean-field theory”. *Physical Review B* 33.5, pp. 3263–3268.
- FUCHS, J.-N. and M.-O. GOERBIG (2008). *Introduction to the Physical Properties of Graphene*.
- FUKUDA, Y. (Aug. 1998). “Measurements of the Solar Neutrino Flux from Super-Kamiokandes First 300 Days”. *Physical Review Letters* 81.6, pp. 1158–1162.
- GEIM, A. K. and K. S. NOVOSELOV (Mar. 2007). “The rise of graphene”. *Nature Materials* 6.3, pp. 183–191.
- GIAMARCHI, T. and O. U. PRESS (2004). *Quantum Physics in One Dimension*. International Series of Monogr. Clarendon Press. ISBN: 978-0-19-852500-4.
- GOLDENFELD, N. (2018). *Lectures On Phase Transitions And The Renormalization Group*. CRC Press. ISBN: 978-0-429-97312-3.
- GONZÁLEZ, J., F. GUINEA, and M. VOZMEDIANO (Aug. 1994). “Non-Fermi liquid behavior of electrons in the half-filled honeycomb lattice A renormalization group approach”. *Nuclear Physics B* 424.3, pp. 595–618.
- GORNYI, I. V., V. Y. KACHOROVSKII, and A. D. MIRLIN (Oct. 2015). “Rippling and crumpling in disordered free-standing graphene”. *Physical Review B* 92.15, p. 155428.
- GOUDSMIT, S. and G. E. UHLENBECK (1926). “Over het roteerende electron en de structuur der spectra”. *Physica* 6, pp. 273–290.
- GRACEY, J. A. (Oct. 2008). “Four loop MS mass anomalous dimension in the Gross–Neveu model”. *Nuclear Physics B* 802.3, pp. 330–350.
- GRACEY, J. A., T. LUTHE, and Y. SCHRÖDER (Dec. 2016). “Four loop renormalization of the Gross-Neveu model”. *Physical Review D* 94.12, p. 125028.
- GROSS, D. J. and A. NEVEU (Nov. 1974). “Dynamical symmetry breaking in asymptotically free field theories”. *Physical Review D* 10.10, pp. 3235–3253.
- HASHIMOTO, K., C. SOHRMANN, J. WIEBE, T. INAOKA, F. MEIER, Y. HIRAYAMA, R. A. RÖMER, R. WIESENDANGER, and M. MORGENSTERN (Dec. 2008). “Quantum Hall Transition in Real Space: From Localized to Extended States”. *Physical Review Letters* 101.25, p. 256802.
- HASHIMOTO, K., T. KIMURA, and X. WU (May 2017). “Boundary conditions of Weyl semimetals”. *Progress of Theoretical and Experimental Physics* 2017.5.
- HUCKESTEIN, B. (1995). “Scaling theory of the integer quantum Hall effect”. *Reviews of Modern Physics* 67.2, pp. 357–396.
- KADANOFF, L. P. (June 1966). “Scaling laws for ising models near T_c ”. *Physique Physique Fizika* 2.6, pp. 263–272.
- KARGARIAN, M., M. RANDEIRA, and Y.-M. LU (Aug. 2016). “Are the surface Fermi arcs in Dirac semimetals topologically protected?” *Proceedings of the National Academy of Sciences* 113.31, pp. 8648–8652.
- KENNEDY, A. D. (July 1981). “Clifford algebras in 2ω dimensions”. *Journal of Mathematical Physics* 22.7, pp. 1330–1337.
- KITTEL, C. (1971). *Introduction to solid state physics*. Wiley. ISBN: 9780471490210.

- KLEIN, O. (Mar. 1929). “Die Reflexion von Elektronen an einem Potentialsprung nach der relativistischen Dynamik von Dirac”. *Zeitschrift für Physik* 53.3-4, pp. 157–165.
- KLEINERT, H. and V. SCHULTE-FROHLINDE (2001). *Critical Properties of ϕ^4 -theories*. World Scientific. ISBN: 9789810246594.
- KLEISS, R. H. P. and T. JANSSEN (Feb. 2015). “Ambiguities in Pauli–Villars regularization”. *The European Physical Journal C* 75.2, p. 46.
- KLITZING, K. V., G. DORDA, and M. PEPPER (Aug. 1980). “New Method for High-Accuracy Determination of the Fine-Structure Constant Based on Quantized Hall Resistance”. *Physical Review Letters* 45.6, pp. 494–497.
- LE BELLAC, M. (2002). *Des phénomènes critiques aux champs de jauge*. Savoirs actuels. Série Physique. EDP Sciences. ISBN: 9782868833594.
- LIU, D. F., A. J. LIANG, E. K. LIU, Q. N. XU, Y. W. LI, C. CHEN, D. PEI, W. J. SHI, S. K. MO, P. DUDIN, T. KIM, C. CACHO, G. LI, Y. SUN, L. X. YANG, Z. K. LIU, S. S. P. PARKIN, C. FELSER, and Y. L. CHEN (Sept. 2019). “Magnetic Weyl semimetal phase in a Kagomé crystal”. *Science* 365.6459, pp. 1282–1285.
- LIU, Y., G. BIAN, T. MILLER, and T.-C. CHIANG (Oct. 2011). “Visualizing Electronic Chirality and Berry Phases in Graphene Systems Using Photoemission with Circularly Polarized Light”. *Physical Review Letters* 107.16, p. 166803.
- LIU, Z. K., J. JIANG, B. ZHOU, Z. J. WANG, Y. ZHANG, H. M. WENG, D. PRABHAKARAN, S.-K. MO, H. PENG, P. DUDIN, T. KIM, M. HOESCH, Z. FANG, X. DAI, Z. X. SHEN, D. L. FENG, Z. HUSSAIN, and Y. L. CHEN (July 2014a). “A stable three-dimensional topological Dirac semimetal Cd_3As_2 ”. *Nature Materials* 13.7, pp. 677–681.
- LIU, Z. K., B. ZHOU, Y. ZHANG, Z. J. WANG, H. M. WENG, D. PRABHAKARAN, S.-K. MO, Z. X. SHEN, Z. FANG, X. DAI, Z. HUSSAIN, and Y. L. CHEN (Feb. 2014b). “Discovery of a Three-Dimensional Topological Dirac Semimetal Na_3Bi ”. *Science* 343.6173, pp. 864–867.
- LOUVET, T., P. DELPLACE, A. A. FEDORENKO, and D. CARPENTIER (Oct. 2015). “On the origin of minimal conductivity at a band crossing”. *Physical Review B* 92.15, p. 155116.
- LV, B. Q., H. M. WENG, B. B. FU, X. P. WANG, H. MIAO, J. MA, P. RICHARD, X. C. HUANG, L. X. ZHAO, G. F. CHEN, Z. FANG, X. DAI, T. QIAN, and H. DING (July 2015). “Experimental Discovery of Weyl Semimetal TaAs”. *Physical Review X* 5.3, p. 031013.
- MCCANN, E. and M. KOSHINO (May 2013). “The electronic properties of bilayer graphene”. *Reports on Progress in Physics* 76.5, p. 056503.
- MEYER, J. S. and G. REFAEL (Mar. 2013). “Disordered topological metals”. *Physical Review B* 87.10, p. 104202.
- NIELSEN, H. and M. NINOMIYA (Oct. 1981). “A no-go theorem for regularizing chiral fermions”. *Physics Letters B* 105.2, pp. 219–223.
- NOVOSELOV, K. S., A. K. GEIM, S. V. MOROZOV, D. JIANG, Y. ZHANG, S. V. DUBONOS, I. V. GRIGORIEVA, and A. A. FIRSOV (Oct. 2004). “Electric Field Effect in Atomically Thin Carbon Films”. *Science* 306.5696, pp. 666–669.
- PERES, N. M. R. (Sept. 2010). “The transport properties of graphene: An introduction”. *Reviews of Modern Physics* 82.3, pp. 2673–2700.
- PESKIN, M. E. and D. V. SCHROEDER (1995). *An Introduction to Quantum Field Theory*. Advanced book classics. Avalon Publishing. ISBN: 978-0-201-50397-5.

- ROSENSTEIN, B., B. J. WARR, and S. H. PARK (June 1991). “[Dynamical symmetry breaking in four-fermion interaction models](#)”. *Physics Reports* 205.2, pp. 59–108.
- SASLOW, W., T. K. BERGSTRESSER, and M. L. COHEN (Feb. 1966). “[Band Structure and Optical Properties of Diamond](#)”. *Physical Review Letters* 16.9, pp. 354–356.
- SCHWEBER, S. (2020). *QED and the Men Who Made It: Dyson Feynman Schwinger and Tomonaga*. Princeton Series in Physics. Princeton University Press. ISBN: 978-0-691-21328-6.
- SCHWINGER, J. (Feb. 1948). “[On Quantum-Electrodynamics and the Magnetic Moment of the Electron](#)”. *Physical Review* 73.4, pp. 416–417.
- SHTANKO, O. and L. LEVITOV (June 2018). “[Robustness and universality of surface states in Dirac materials](#)”. *Proceedings of the National Academy of Sciences* 115.23, pp. 5908–5913.
- SOLUYANOV, A. A., D. GRESCH, Z. WANG, Q. WU, M. TROYER, X. DAI, and B. A. BERNEVIG (Nov. 2015). “[Type-II Weyl Semimetals](#)”. *Nature* 527.7579, pp. 495–498.
- SON, D. T. and B. Z. SPIVAK (Sept. 2013). “[Chiral anomaly and classical negative magnetoresistance of Weyl metals](#)”. *Physical Review B* 88.10, p. 104412.
- SREDNICKI, M. (2007). *Quantum Field Theory*. Cambridge University Press. ISBN: 97811-39462761.
- SYZRANOV, S. V. and L. RADZIHOVSKY (Mar. 2018). “[High-Dimensional Disorder-Driven Phenomena in Weyl Semimetals Semiconductors and Related Systems](#)”. *Annual Review of Condensed Matter Physics* 9.1, pp. 35–58.
- TEPPE, F., M. MARCINKIEWICZ, S. S. KRISHTOPENKO, S. RUFFENACH, C. CONSEJO, A. M. KADYKOV, W. DESRAT, D. BUT, W. KNAP, J. LUDWIG, S. MOON, D. SMIRNOV, M. ORLITA, Z. JIANG, S. V. MOROZOV, V. GAVRILENKO, N. N. MIKHAILOV, and S. A. DVORETSKII (Aug. 2016). “[Temperature-driven massless Kane fermions in HgCdTe crystals](#)”. *Nature Communications* 7.
- TOMONAGA, S. (Aug. 1946). “[On a Relativistically Invariant Formulation of the Quantum Theory of Wave Fields](#)”. *Progress of Theoretical Physics* 1.2, pp. 27–42.
- TONG, D. (Sept. 2016). “[Lectures on the Quantum Hall Effect](#)”. *arXiv:1606.06687 [cond-mat, physics:hep-th]*.
- TWORZYDŁO, J., B. TRAUZETTEL, M. TITOV, A. RYCERZ, and C. W. J. BEENAKKER (June 2006). “[Sub-Poissonian Shot Noise in Graphene](#)”. *Physical Review Letters* 96.24.
- VASIL’EV, A. N. and M. I. VYAZOVSKY (Oct. 1997). “[Proof of the absence of multiplicative renormalizability of the Gross-Neveu model in the dimensional regularization \$d = 2 + 2\epsilon\$](#) ”. *Theoretical and Mathematical Physics* 113.1, pp. 1277–1288.
- VOZMEDIANO, M. A. H., F. D. JUAN, and A. CORTIJO (Oct. 2008). “[Gauge fields and curvature in graphene](#)”. *Journal of Physics: Conference Series* 129, p. 012001.
- VOZMEDIANO, M. A. H. (July 2011). “[Renormalization group aspects of graphene](#)”. *Philosophical Transactions of the Royal Society A: Mathematical, Physical and Engineering Sciences* 369.1946, pp. 2625–2642.
- WALLACE, P. R. (May 1947). “[The Band Theory of Graphite](#)”. *Physical Review* 71.9, pp. 622–634.
- WAN, X., A. M. TURNER, A. VISHWANATH, and S. Y. SAVRASOV (May 2011). “[Topological semimetal and Fermi-arc surface states in the electronic structure of pyrochlore iridates](#)”. *Physical Review B* 83.20, p. 205101.
- WEINBERG, S. (1995). *The Quantum Theory of Fields: Volume 1: Foundations*. Vol. 1. Cambridge University Press. ISBN: 978-0-521-67053-1.

- WEYL, H. (May 1929). “Elektron und Gravitation. I”. *Zeitschrift für Physik* 56.5, pp. 330–352.
- WILSON, K. G. (Nov. 1971a). “Renormalization Group and Critical Phenomena. I. Renormalization Group and the Kadanoff Scaling Picture”. *Physical Review B* 4.9, pp. 3174–3183.
- WILSON, K. G. (Nov. 1971b). “Renormalization Group and Critical Phenomena. II. Phase-Space Cell Analysis of Critical Behavior”. *Physical Review B* 4.9, pp. 3184–3205.
- WILSON, K. G. (Aug. 1974). “The renormalization group and the ϵ expansion”. *Physics Reports* 12.2, pp. 75–199.
- WILSON, K. G. and M. E. FISHER (Jan. 1972). “Critical Exponents in 3.99 Dimensions”. *Physical Review Letters* 28.4, pp. 240–243.
- WITTEN, E. (June 2016). “Three Lectures On Topological Phases Of Matter”. *La Rivista del Nuovo Cimento* 39.7, pp. 313–370.
- WU, Y., N. H. JO, L.-L. WANG, C. A. SCHMIDT, K. M. NEILSON, B. SCHRUNK, P. SWATEK, A. EATON, S. L. BUD’KO, P. C. CANFIELD, and A. KAMINSKI (Apr. 2019). “Fragility of Fermi arcs in Dirac semimetals”. *Physical Review B* 99.16, p. 161113.
- XU, G., H. WENG, Z. WANG, X. DAI, and Z. FANG (Oct. 2011). “Chern Semimetal and the Quantized Anomalous Hall Effect in HgCr_2Se_4 ”. *Physical Review Letters* 107.18, p. 186806.
- XU, Q., E. LIU, W. SHI, L. MUECHLER, C. FELSER, and Y. SUN (June 2018). “Topological surface Fermi arcs in magnetic Weyl semimetal $\text{Co}_3\text{Sn}_2\text{S}_2$ ”. *Physical Review B* 97.23, p. 235416.
- XU, S.-Y., N. ALIDOUST, I. BELOPOLSKI, Z. YUAN, G. BIAN, T.-R. CHANG, H. ZHENG, V. N. STROCOV, D. S. SANCHEZ, G. CHANG, C. ZHANG, D. MOU, Y. WU, L. HUANG, C.-C. LEE, S.-M. HUANG, B. WANG, A. BANSIL, H.-T. JENG, T. NEUPERT, A. KAMINSKI, H. LIN, S. JIA, and M. Z. HASAN (Sept. 2015a). “Discovery of a Weyl fermion state with Fermi arcs in niobium arsenide”. *Nature Physics* 11.9, pp. 748–754.
- XU, S.-Y., I. BELOPOLSKI, N. ALIDOUST, M. NEUPANE, G. BIAN, C. ZHANG, R. SANKAR, G. CHANG, Z. YUAN, C.-C. LEE, S.-M. HUANG, H. ZHENG, J. MA, D. S. SANCHEZ, B. WANG, A. BANSIL, F. CHOU, P. P. SHIBAYEV, H. LIN, S. JIA, and M. Z. HASAN (Oct. 2015b). “Discovery of a Weyl fermion semimetal and topological Fermi arcs”. *Science* 349.6248, pp. 613–617.
- YANG, K.-Y., Y.-M. LU, and Y. RAN (Aug. 2011). “Quantum Hall effects in a Weyl semimetal: Possible application in pyrochlore iridates”. *Physical Review B* 84.7, p. 075129.
- ZINN-JUSTIN, J. (2002). *Quantum Field Theory and Critical Phenomena*. International series of monographs on physics. Clarendon Press. ISBN: 9780198509233.
- ZINN-JUSTIN, J. (2012). *Transitions de phase et groupe de renormalisation*. Savoirs actuels. EDP Sciences. ISBN: 978-2-7598-0150-3.

Disorder in three-dimensional relativistic semimetals

- ABRAHAMS, E., P. W. ANDERSON, D. C. LICCIARDELLO, and T. V. RAMAKRISHNAN (Mar. 1979). “Scaling Theory of Localization: Absence of Quantum Diffusion in Two Dimensions”. *Physical Review Letters* 42.10, pp. 673–676.
- AKKERMANS, E. and G. MONTAMBAUX (2007). *Mesoscopic Physics of Electrons and Photons*. Cambridge University Press. ISBN: 978-0-521-85512-9.

- ALTLAND, A. and D. BAGRETS (Feb. 2016). “Theory of the strongly disordered Weyl semimetal”. *Physical Review B* 93.7, p. 075113.
- ALTLAND, A. and M. R. ZIRNBAUER (Jan. 1997). “Nonstandard symmetry classes in mesoscopic normal-superconducting hybrid structures”. *Physical Review B* 55.2, pp. 1142–1161.
- ANDERSON, P. W. (Mar. 1958). “Absence of Diffusion in Certain Random Lattices”. *Physical Review* 109.5, pp. 1492–1505.
- BALOG, I., D. CARPENTIER, and A. A. FEDORENKO (Oct. 2018). “Disorder-Driven Quantum Transition in Relativistic Semimetals: Functional Renormalization via the Porous Medium Equation”. *Physical Review Letters* 121.16, p. 166402.
- BELITZ, D. and T. R. KIRKPATRICK (Oct. 2002). “Electrons in an annealed environment: A special case of the interacting electron problem”. *Physical Review B* 66.15, p. 155101.
- BONDI, A., G. CURCI, G. PAFFUTI, and P. ROSSI (May 1990). “Metric and central charge in the perturbative approach to two dimensional fermionic models”. *Annals of Physics* 199.2, pp. 268–339.
- BORN, M. (Nov. 1926). “Quantenmechanik der Stoßvorgänge”. *Zeitschrift für Physik* 38.11-12, pp. 803–827.
- BRILLAUX, E. and A. A. FEDORENKO (2021a). “The semi-infinite Gross-Neveu model”. *In preparation*.
- BRILLAUX, E., D. CARPENTIER, and A. A. FEDORENKO (Oct. 2019). “Multifractality at the Weyl-semimetal – diffusive-metal transition for generic disorder”. *Physical Review B* 100.13, p. 134204.
- BRILLAUX, E. and A. A. FEDORENKO (Feb. 2021b). “Fermi arcs and surface criticality in dirty Dirac materials”. *Physical Review B* 103.8, p. L081405.
- BUCHHOLD, M., S. DIEHL, and A. ALTLAND (Nov. 2018a). “Nodal points of Weyl semimetals survive the presence of moderate disorder”. *Physical Review B* 98.20, p. 205134.
- BUCHHOLD, M., S. DIEHL, and A. ALTLAND (Nov. 2018b). “Vanishing Density of States in Weakly Disordered Weyl Semimetals”. *Physical Review Letters* 121.21, p. 215301.
- CAO, X., A. ROSSO, J.-P. BOUCHAUD, and P. LE DOUSSAL (June 2017). “Genuine localization transition in a long-range hopping model”. *Physical Review E* 95.6, p. 062118.
- CARDY, J., P. GODDARD, and J. YEOMANS (1996). *Scaling and Renormalization in Statistical Physics*. Cambridge Lecture Notes in Physics. Cambridge University Press. ISBN: 9780521499590.
- CHAMON, C., A. W. W. LUDWIG, and C. NAYAK (July 1999). “Schwinger-Keldysh approach to disordered and interacting electron systems: Derivation of Finkelstein’s renormalization-group equations”. *Physical Review B* 60.4, pp. 2239–2254.
- CROY, A., P. CAIN, and M. SCHREIBER (May 2012). “The role of power-law correlated disorder in the Anderson metal-insulator transition”. *The European Physical Journal B* 85.5, p. 165.
- DUDKA, M., A. A. FEDORENKO, V. BLAVATSKA, and Y. HOLOVATCH (2016). “Critical behavior of the two-dimensional Ising model with long-range correlated disorder”. *Physical Review B* 93.22, p. 224422.
- DUPLANTIER, B. and A. W. W. LUDWIG (Jan. 1991). “Multifractals operator-product expansion and field theory”. *Physical Review Letters* 66.3, pp. 247–251.
- DYSON, F. J. (June 1949). “The S Matrix in Quantum Electrodynamics”. *Physical Review* 75.11, pp. 1736–1755.

- DYSON, F. J. (Nov. 1962). “The Threefold Way. Algebraic Structure of Symmetry Groups and Ensembles in Quantum Mechanics”. *Journal of Mathematical Physics* 3.6, pp. 1199–1215.
- EDWARDS, S. F. and P. W. ANDERSON (May 1975). “Theory of spin glasses”. *Journal of Physics F: Metal Physics* 5.5, pp. 965–974.
- EDWARDS, S. F. (Sept. 1958). “A new method for the evaluation of electric conductivity in metals”. *Philosophical Magazine* 3.33, pp. 1020–1031.
- EFETOV, K. (1996). *Supersymmetry in Disorder and Chaos*. Cambridge University Press.
- EVERS, F. and A. D. MIRLIN (Apr. 2000). “Fluctuations of the Inverse Participation Ratio at the Anderson Transition”. *Physical Review Letters* 84.16, pp. 3690–3693.
- EVERS, F. and A. D. MIRLIN (Oct. 2008). “Anderson transitions”. *Reviews of Modern Physics* 80.4, pp. 1355–1417.
- FARAEI, Z., T. FARAJOLLAHPOUR, and S. A. JAFARI (Nov. 2018). “Greens function of semi-infinite Weyl semimetals”. *Physical Review B* 98.19, p. 195402.
- FEDORENKO, A. A., P. LE DOUSSAL, and K. J. WIESE (Jan. 2014). “Non-Gaussian effects and multifractality in the Bragg glass”. *EPL (Europhysics Letters)* 105.1, p. 16002.
- FEDORENKO, A. A., P. LE DOUSSAL, and K. J. WIESE (Dec. 2006). “Statics and dynamics of elastic manifolds in media with long-range correlated disorder”. *Physical Review E* 74.6, p. 061109.
- FOSTER, M. S. (Feb. 2012). “Multifractal nature of the surface local density of states in three-dimensional topological insulators with magnetic and nonmagnetic disorder”. *Physical Review B* 85.8, p. 085122.
- FOSTER, M. S., S. RYU, and A. W. W. LUDWIG (Aug. 2009). “Termination of typical wave-function multifractal spectra at the Anderson metal-insulator transition: Field theory description using the functional renormalization group”. *Physical Review B* 80.7, p. 075101.
- FRADKIN, E. (Mar. 1986a). “Critical behavior of disordered degenerate semiconductors. I. Models symmetries and formalism”. *Physical Review B* 33.5, pp. 3257–3262.
- FRADKIN, E. (Mar. 1986b). “Critical behavior of disordered degenerate semiconductors. II. Spectrum and transport properties in mean-field theory”. *Physical Review B* 33.5, pp. 3263–3268.
- GADE, R. and F. WEGNER (Aug. 1991). “The $n \rightarrow 0$ replica limit of U_n and models”. *Nuclear Physics B* 360.2-3, pp. 213–218.
- GOLDENFELD, N. (2018). *Lectures On Phase Transitions And The Renormalization Group*. CRC Press. ISBN: 978-0-429-97312-3.
- GORBAR, E. V., V. A. MIRANSKY, I. A. SHOVKOVY, and P. O. SUKHACHOV (June 2016). “Origin of dissipative Fermi arc transport in Weyl semimetals”. *Physical Review B* 93.23, p. 235127.
- GOSWAMI, P. and S. CHAKRAVARTY (Nov. 2011). “Quantum Criticality between Topological and Band Insulators in $3 + 1$ Dimensions”. *Physical Review Letters* 107.19, p. 196803.
- GOSWAMI, P. and S. CHAKRAVARTY (Feb. 2017). “Superuniversality of topological quantum phase transition and global phase diagram of dirty topological systems in three dimensions”. *Physical Review B* 95.7, p. 075131.
- GRACEY, J. A. (Oct. 2008a). “Four loop MS mass anomalous dimension in the Gross–Neveu model”. *Nuclear Physics B* 802.3, pp. 330–350.

- GRACEY, J. A. (Oct. 2008b). “Four loop vacuum bubbles for two-dimensional four-fermi theory renormalization”. *Nuclear Physics B - Proceedings Supplements* 183, pp. 251–255.
- GRACEY, J. A., T. LUTHE, and Y. SCHRÖDER (Dec. 2016). “Four loop renormalization of the Gross-Neveu model”. *Physical Review D* 94.12, p. 125028.
- GROSS, D. J. and A. NEVEU (Nov. 1974). “Dynamical symmetry breaking in asymptotically free field theories”. *Physical Review D* 10.10, pp. 3235–3253.
- GRUZBERG, I. (2009). *Laplacian Eigenvalues and Eigenfunctions: Theory Computation Application*.
- HALSEY, T. C., M. H. JENSEN, L. P. KADANOFF, I. PROCACCIA, and B. I. SHRAIMAN (1987). “Fractal measures and their singularities: The characterization of strange sets”. *Nuclear Physics B (Proceedings Supplements)* 2.C, pp. 501–511.
- HASHIMOTO, K., T. KIMURA, and X. WU (May 2017). “Boundary conditions of Weyl semimetals”. *Progress of Theoretical and Experimental Physics* 2017.5.
- HUCKESTEIN, B. (1995). “Scaling theory of the integer quantum Hall effect”. *Reviews of Modern Physics* 67.2, pp. 357–396.
- IMRY, Y. and S.-K. MA (Nov. 1975). “Random-Field Instability of the Ordered State of Continuous Symmetry”. *Physical Review Letters* 35.21, pp. 1399–1401.
- INOUE, H., A. GYENIS, Z. WANG, J. LI, S. W. OH, S. JIANG, N. NI, B. A. BERNEVIG, and A. YAZDANI (Mar. 2016). “Quasiparticle interference of the Fermi arcs and surface-bulk connectivity of a Weyl semimetal”. *Science* 351.6278, pp. 1184–1187.
- IVANOV, P. C., L. A. N. AMARAL, A. L. GOLDBERGER, S. HAVLIN, M. G. ROSENBLUM, Z. R. STRUZIK, and H. E. STANLEY (June 1999). “Multifractality in human heartbeat dynamics”. *Nature* 399.6735, pp. 461–465.
- JANSSEN, M. (2001). *Fluctuations and Localization in Mesoscopic Electron Systems*. World Scientific lecture notes in physics. World Scientific. ISBN: 978-981-02-4209-1.
- JANSSEN, M. (1998). “Statistics and scaling in disordered mesoscopic electron systems”. *Physica Report* 295.1-2, pp. 1–91.
- KARGARIAN, M., Y.-M. LU, and M. RANDEIRA (Apr. 2018). “Deformation and stability of surface states in Dirac semimetals”. *Physical Review B* 97.16, p. 165129.
- KARGARIAN, M., M. RANDEIRA, and Y.-M. LU (Aug. 2016). “Are the surface Fermi arcs in Dirac semimetals topologically protected?” *Proceedings of the National Academy of Sciences* 113.31, pp. 8648–8652.
- KLIER, J., I. V. GORNYI, and A. D. MIRLIN (Sept. 2019). “From weak to strong disorder in Weyl semimetals: Self-consistent Born approximation”. *Physical Review B* 100.12, p. 125160.
- KOBAYASHI, K., T. OHTSUKI, K.-I. IMURA, and I. F. HERBUT (Jan. 2014). “Density of States Scaling at the Semimetal to Metal Transition in Three Dimensional Topological Insulators”. *Physical Review Letters* 112.1, p. 016402.
- KRAMER, B. and A. MACKINNON (Dec. 1993). “Localization: theory and experiment”. *Reports on Progress in Physics* 56.12, pp. 1469–1564.
- LEE, Y.-L. and Y.-W. LEE (July 2017). “Nature of the magnetic phase transition in a Weyl semimetal”. *Physical Review B* 96.4, p. 045115.
- LOUVET, T., D. CARPENTIER, and A. A. FEDORENKO (Dec. 2016). “On the disorder-driven quantum transition in three-dimensional relativistic metals”. *Physical Review B* 94.22, p. 220201.

- LOUVET, T., D. CARPENTIER, and A. A. FEDORENKO (Jan. 2017). “[New Quantum Transition in Weyl Semimetals with Correlated Disorder](#)”. *Physical Review B* 95.1, p. 014204.
- LUBENSKY, T. C. and M. H. RUBIN (June 1975a). “[Critical phenomena in semi-infinite systems. I. \$\epsilon\$ expansion for positive extrapolation length](#)”. *Physical Review B* 11.11, pp. 4533–4546.
- LUBENSKY, T. C. and M. H. RUBIN (Nov. 1975b). “[Critical phenomena in semi-infinite systems. II. Mean-field theory](#)”. *Physical Review B* 12.9, pp. 3885–3901.
- LUDWIG, A. W. W., M. P. A. FISHER, R. SHANKAR, and G. GRINSTEIN (Sept. 1994). “[Integer quantum Hall transition: An alternative approach and exact results](#)”. *Physical Review B* 50.11, pp. 7526–7552.
- LV, B. Q., H. M. WENG, B. B. FU, X. P. WANG, H. MIAO, J. MA, P. RICHARD, X. C. HUANG, L. X. ZHAO, G. F. CHEN, Z. FANG, X. DAI, T. QIAN, and H. DING (July 2015). “[Experimental Discovery of Weyl Semimetal TaAs](#)”. *Physical Review X* 5.3, p. 031013.
- MANDELBROT, B. B. (1974). “[Intermittent turbulence in self-similar cascades: divergence of high moments and dimension of the carrier](#)”. *Journal of Fluid Mechanics* 62.2, pp. 331–358.
- MANDELBROT, B. B. (Feb. 1999). “[A Multifractal Walk down Wall Street](#)”. *Scientific American* 280.2, pp. 70–73.
- MATTUCK, R. (1992). *A Guide to Feynman Diagrams in the Many-body Problem*. Dover Books on Physics Series. Dover Publications. ISBN: 978-0-486-67047-8.
- MEZARD, M., G. PARISI, and M. VIRASORO (1987). *Spin Glass Theory and Beyond*. Lecture Notes in Physics Series. World Scientific. ISBN: 978-9971-5-0115-0.
- MILDENBERGER, A., F. EVERS, and A. D. MIRLIN (July 2002). “[Dimensionality dependence of the wave-function statistics at the Anderson transition](#)”. *Physical Review B* 66.3, p. 033109.
- MIRLIN, A. D., Y. V. FYODOROV, A. MILDENBERGER, and F. EVERS (July 2006). “[Exact Relations between Multifractal Exponents at the Anderson Transition](#)”. *Physical Review Letters* 97.4, p. 046803.
- MOLL, P. J. W., N. L. NAIR, T. HELM, A. C. POTTER, I. KIMCHI, A. VISHWANATH, and J. G. ANALYTIS (July 2016). “[Transport evidence for Fermi-arc-mediated chirality transfer in the Dirac semimetal Cd₃As₂](#)”. *Nature* 535.7611, pp. 266–270.
- MOORE, F. L., J. C. ROBINSON, C. BHARUCHA, P. E. WILLIAMS, and M. G. RAIZEN (Nov. 1994). “[Observation of Dynamical Localization in Atomic Momentum Transfer: A New Testing Ground for Quantum Chaos](#)”. *Physical Review Letters* 73.22, pp. 2974–2977.
- NANDKISHORE, R., D. A. HUSE, and S. L. SONDHI (June 2014). “[Rare region effects dominate weakly disordered three-dimensional Dirac points](#)”. *Physical Review B* 89.24, p. 245110.
- NIELSEN, H. and M. NINOMIYA (Oct. 1981). “[A no-go theorem for regularizing chiral fermions](#)”. *Physics Letters B* 105.2, pp. 219–223.
- OKUGAWA, R. and S. MURAKAMI (June 2014). “[Dispersion of Fermi arcs in Weyl semimetals and their evolutions to Dirac cones](#)”. *Physical Review B* 89.23, p. 235315.
- OMINATO, Y. and M. KOSHINO (Feb. 2014). “[Quantum transport in a three-dimensional Weyl electron system](#)”. *Physical Review B* 89.5, p. 054202.

- OSTROVSKY, P. M., I. V. GORNYI, and A. D. MIRLIN (Dec. 2006). “[Electron transport in disordered graphene](#)”. *Physical Review B* 74.23, p. 235443.
- PAPAJ, M., H. ISOBE, and L. FU (May 2019). “[Nodal arc of disordered Dirac fermions and non-Hermitian band theory](#)”. *Physical Review B* 99.20, p. 201107.
- PARISI, G. (Dec. 1979). “[Infinite Number of Order Parameters for Spin-Glasses](#)”. *Physical Review Letters* 43.23, pp. 1754–1756.
- PARISI, G. and U. FRISCH (1988). “[Turbulence and predictability of geophysical flows and climatic dynamics](#)”. *Conference Proceedings of International School of Physics "Enrico Fermi"*. Ed. by N. GHIL, R. BENZI, and G. PARISI. Amsterdam: North Holland, pp. 84–87.
- PIXLEY, J. H., P. GOSWAMI, and S. DAS SARMA (Aug. 2015). “[Anderson Localization and the Quantum Phase Diagram of Three Dimensional Disordered Dirac Semimetals](#)”. *Physical Review Letters* 115.7, p. 076601.
- PIXLEY, J. H., P. GOSWAMI, and S. DAS SARMA (Feb. 2016a). “[Disorder-driven itinerant quantum criticality of three-dimensional massless Dirac fermions](#)”. *Physical Review B* 93.8, p. 085103.
- PIXLEY, J. H., D. A. HUSE, and S. DAS SARMA (June 2016b). “[Rare-Region-Induced Avoided Quantum Criticality in Disordered Three-Dimensional Dirac and Weyl Semimetals](#)”. *Physical Review X* 6.2, p. 021042.
- PIXLEY, J. H., D. A. HUSE, and S. D. SARMA (Sept. 2016c). “[Uncovering the hidden quantum critical point in disordered massless Dirac and Weyl semi-metals](#)”. *Physical Review B* 94.12, p. 121107.
- RESTA, G., S.-T. PI, X. WAN, and S. Y. SAVRASOV (Feb. 2018). “[High surface conductivity of Fermi-arc electrons in Weyl semimetals](#)”. *Physical Review B* 97.8, p. 085142.
- ROY, B. and S. DAS SARMA (Dec. 2014). “[Diffusive quantum criticality in three-dimensional disordered Dirac semimetals](#)”. *Physical Review B* 90.24, p. 241112.
- ROY, B., V. JURIČIĆ, and S. DAS SARMA (Oct. 2016). “[Universal optical conductivity of a disordered Weyl semimetal](#)”. *Scientific Reports* 6.1, p. 32446.
- ROY, B., R.-J. SLAGER, and V. JURIČIĆ (Sept. 2018). “[Global Phase Diagram of a Dirty Weyl Liquid and Emergent Superuniversality](#)”. *Physical Review X* 8.3, p. 031076.
- SBIERSKI, B., E. J. BERGHOLTZ, and P. W. BROUWER (Sept. 2015). “[Quantum critical exponents for a disordered three-dimensional Weyl node](#)”. *Physical Review B* 92.11, p. 115145.
- SBIERSKI, B., K. S. C. DECKER, and P. W. BROUWER (Dec. 2016). “[Weyl node with random vector potential](#)”. *Physical Review B* 94.22, p. 220202.
- SBIERSKI, B., G. POHL, E. J. BERGHOLTZ, and P. W. BROUWER (July 2014). “[Quantum Transport of Disordered Weyl Semimetals at the Nodal Point](#)”. *Physical Review Letters* 113.2, p. 026602.
- SHTANKO, O. and L. LEVITOV (June 2018). “[Robustness and universality of surface states in Dirac materials](#)”. *Proceedings of the National Academy of Sciences* 115.23, pp. 5908–5913.
- SINNER, A. and K. ZIEGLER (Oct. 2017). “[Corrections to the self-consistent Born approximation for Weyl fermions](#)”. *Physical Review B* 96.16, p. 165140.
- SLAGER, R.-J., V. JURIČIĆ, and B. ROY (Nov. 2017). “[Dissolution of topological Fermi arcs in a dirty Weyl semimetal](#)”. *Physical Review B* 96.20, p. 201401.

- SUBRAMANIAM, A. R., I. A. GRUZBERG, A. W. W. LUDWIG, F. EVERS, A. MILDENBERGER, and A. D. MIRLIN (2006). “Surface criticality and multifractality at localization transitions”. *Physical Review Letters* 96.12, pp. 2–5.
- SYZRANOV, S. V. and V. GURARIE (Dec. 2019). “Duality between disordered nodal semimetals and systems with power-law hopping”. *Physical Review Research* 1.3, p. 032035.
- SYZRANOV, S. V., V. GURARIE, and L. RADZIHOVSKY (2016). “Multifractality at non-Anderson disorder-driven transitions in Weyl semimetals and other systems”. *Annals of Physics* 373, pp. 694–706.
- SYZRANOV, S. V., L. RADZIHOVSKY, and V. GURARIE (Apr. 2015). “Critical Transport in Weakly Disordered Semiconductors and Semimetals”. *Physical Review Letters* 114.16, p. 166601.
- SYZRANOV, S. V. and L. RADZIHOVSKY (Mar. 2018). “High-Dimensional Disorder-Driven Phenomena in Weyl Semimetals Semiconductors and Related Systems”. *Annual Review of Condensed Matter Physics* 9.1, pp. 35–58.
- THIRRING, W. E. (Jan. 1958). “A soluble relativistic field theory”. *Annals of Physics* 3.1, pp. 91–112.
- THOULESS, D. J. (Mar. 1984). “Percolation and localization”. *Ill-Condensed Matter*. co-published with north-holland publishing co., pp. 1–62. ISBN: 978-9971-950-59-0 978-981-4412-72-8.
- VOZMEDIANO, M. A. H., M. I. KATSNELSON, and F. GUINEA (Nov. 2010). “Gauge fields in graphene”. *Physics Reports* 496.4-5, pp. 109–148.
- VOZMEDIANO, M. A. H., F. D. JUAN, and A. CORTIJO (Oct. 2008). “Gauge fields and curvature in graphene”. *Journal of Physics: Conference Series* 129, p. 012001.
- WEGNER, F. J. (Dec. 1976). “Electrons in disordered systems. Scaling near the mobility edge”. *Zeitschrift für Physik B - Condensed Matter and Quanta* 25.4, pp. 327–337.
- WEGNER, F. J. (Sept. 1979). “The mobility edge problem: Continuous symmetry and a conjecture”. *Zeitschrift für Physik B - Condensed Matter and Quanta* 35.3, pp. 207–210.
- WEGNER, F. J. (Sept. 1980). “Inverse participation ratio in $2 + \epsilon$ dimensions”. *Zeitschrift für Physik B - Condensed Matter and Quanta* 36.3, pp. 209–214.
- WEGNER, F. J. (Jan. 1987). “Anomalous dimensions for the nonlinear sigma-model in $2 + \epsilon$ dimensions I”. *Nuclear Physics B* 280, pp. 193–209.
- WEINRIB, A. and B. I. HALPERIN (Jan. 1983). “Critical phenomena in systems with long-range-correlated quenched disorder”. *Physical Review B* 27.1, pp. 413–427.
- WIESE, K. J. and P. LE DOUSSAL (Nov. 2006). “Functional Renormalization for Disordered Systems Basic Recipes and Gourmet Dishes”. *arXiv:cond-mat/0611346*.
- WIGNER, E. P. (Jan. 1951). “On a Class of Analytic Functions from the Quantum Theory of Collisions”. *The Annals of Mathematics* 53.1, p. 36.
- WILSON, J. H., J. H. PIXLEY, D. A. HUSE, G. REFAEL, and S. DAS SARMA (June 2018). “Do the surface Fermi arcs in Weyl semimetals survive disorder?” *Physical Review B* 97.23, p. 235108.
- WITTEN, E. (June 2016). “Three Lectures On Topological Phases Of Matter”. *La Rivista del Nuovo Cimento* 39.7, pp. 313–370.
- WU, Y., N. H. JO, L.-L. WANG, C. A. SCHMIDT, K. M. NEILSON, B. SCHRUNK, P. SWATEK, A. EATON, S. L. BUD’KO, P. C. CANFIELD, and A. KAMINSKI (Apr. 2019). “Fragility of Fermi arcs in Dirac semimetals”. *Physical Review B* 99.16, p. 161113.

- XU, S.-Y., I. BELOPOLSKI, D. S. SANCHEZ, C. ZHANG, G. CHANG, C. GUO, G. BIAN, Z. YUAN, H. LU, T.-R. CHANG, P. P. SHIBAYEV, M. L. PROKOPOVYCH, N. ALIDOUST, H. ZHENG, C.-C. LEE, S.-M. HUANG, R. SANKAR, F. CHOU, C.-H. HSU, H.-T. JENG, A. BANSIL, T. NEUPERT, V. N. STROCOV, H. LIN, S. JIA, and M. Z. HASAN (Nov. 2015). “[Experimental discovery of a topological Weyl semimetal state in TaP](#)”. *Science Advances* 1.10, e1501092.
- YAIDA, S. (Feb. 2016). “[Instanton calculus of Lifshitz tails](#)”. *Physical Review B* 93.7, p. 075120.
- ZIEGLER, K. and A. SINNER (Oct. 2018). “[Short Note on the Density of States in 3D Weyl Semimetals](#)”. *Physical Review Letters* 121.16, p. 166401.
- ZINN-JUSTIN, J. (2002). *Quantum Field Theory and Critical Phenomena*. International series of monographs on physics. Clarendon Press. ISBN: 9780198509233.

Electronic interactions in twisted bilayer graphene

- AHN, J., S. PARK, and B.-J. YANG (Apr. 2019). “[Failure of Nielsen-Ninomiya Theorem and Fragile Topology in Two-Dimensional Systems with Space-Time Inversion Symmetry: Application to Twisted Bilayer Graphene at Magic Angle](#)”. *Physical Review X* 9.2, p. 021013.
- ANDREI, E. Y. and A. H. MACDONALD (Dec. 2020). “[Graphene bilayers with a twist](#)”. *Nature Materials* 19.12, pp. 1265–1275.
- ANDRES, P. L. DE, R. RAMIREZ, and J. A. VERGES (Jan. 2008). “[Strong covalent bonding between two graphene layers](#)”. *Physical Review B* 77.4, p. 045403.
- BALENTS, L. (2019). “[General continuum model for twisted bilayer graphene and arbitrary smooth deformations](#)”. *SciPost Physics* 7.4, p. 48.
- BALENTS, L., C. R. DEAN, D. K. EFETOV, and A. F. YOUNG (July 2020). “[Superconductivity and strong correlations in moiré flat bands](#)”. *Nature Physics* 16.7, pp. 725–733.
- BERNEVIG, B. A., Z. SONG, N. REGNAULT, and B. LIAN (Sept. 2020a). “[TBG I: Matrix Elements Approximations Perturbation Theory and a \$k \cdot p\$ 2-Band Model for Twisted Bilayer Graphene](#)”. *arXiv:2009.11301*.
- BERNEVIG, B. A., Z. SONG, N. REGNAULT, and B. LIAN (Sept. 2020b). “[TBG III: Interacting Hamiltonian and Exact Symmetries of Twisted Bilayer Graphene](#)”. *arXiv:2009.12376*.
- BISTRITZER, R. and A. H. MACDONALD (June 2010). “[Transport between twisted graphene layers](#)”. *Physical Review B* 81.24, p. 245412.
- BISTRITZER, R. and A. H. MACDONALD (July 2011). “[Moire bands in twisted double-layer graphene](#)”. *Proceedings of the National Academy of Sciences* 108.30, pp. 12233–12237.
- BRILLAUX, E., D. CARPENTIER, A. A. FEDORENKO, and L. SAVARY (Aug. 2020). “[Nematic insulator at charge neutrality in twisted bilayer graphene](#)”. *arXiv:2008.05041*.
- BUERGER, M. J. (1964). “[Colored Symmetry. A series of publications from the Institute of Crystallography Academy of Sciences U.S.S.R. 1951-1958. A. V. Shubnikov N. V. Belov and others. Translated from the Russian by Jack Itzkoff and Jack Gollob.](#)” *Science* 145.3634, pp. 804–805.

- BULTINCK, N., S. CHATTERJEE, and M. P. ZALETEL (Apr. 2020a). “[Mechanism for Anomalous Hall Ferromagnetism in Twisted Bilayer Graphene](#)”. *Physical Review Letters* 124.16, p. 166601.
- BULTINCK, N., E. KHALAF, S. LIU, S. CHATTERJEE, A. VISHWANATH, and M. P. ZALETEL (Aug. 2020b). “[Ground State and Hidden Symmetry of Magic-Angle Graphene at Even Integer Filling](#)”. *Physical Review X* 10.3, p. 031034.
- CAO, Y. (June 2016). “[Electronic Transport in Low-Angle Twisted Bilayer Graphene](#)”. MA thesis. Massachusetts Institute of Technology, p. 48.
- CAO, Y., D. CHOWDHURY, D. RODAN-LEGRAIN, O. RUBIES-BIGORDÀ, K. WATANABE, T. TANIGUCHI, T. SENTHIL, and P. JARILLO-HERRERO (Feb. 2020a). “[Strange metal in magic-angle graphene with near Planckian dissipation](#)”. *Physical Review Letters* 124.7, p. 076801.
- CAO, Y., V. FATEMI, A. DEMIR, S. FANG, S. L. TOMARKEN, J. Y. LUO, J. D. SANCHEZ-YAMAGISHI, K. WATANABE, T. TANIGUCHI, E. KAXIRAS, R. C. ASHOORI, and P. JARILLO-HERRERO (Mar. 2018a). “[Correlated insulator behaviour at half-filling in magic-angle graphene superlattices](#)”. *Nature* 556.7699, pp. 80–84.
- CAO, Y., V. FATEMI, S. FANG, K. WATANABE, T. TANIGUCHI, E. KAXIRAS, and P. JARILLO-HERRERO (Mar. 2018b). “[Unconventional superconductivity in magic-angle graphene superlattices](#)”. *Nature* 556.7699, pp. 43–50.
- CAO, Y., D. RODAN-LEGRAIN, J. M. PARK, F. N. YUAN, K. WATANABE, T. TANIGUCHI, R. M. FERNANDES, L. FU, and P. JARILLO-HERRERO (Apr. 2020b). “[Nematicity and Competing Orders in Superconducting Magic-Angle Graphene](#)”. *arXiv:2004.04148*.
- CHEBROLU, N. R., B. L. CHITTARI, and J. JUNG (Jan. 2019). “[Flatbands in twisted bi-bilayer graphene](#)”. *arXiv:1901.08420*.
- CHEN, G., A. L. SHARPE, E. J. FOX, Y.-H. ZHANG, S. WANG, L. JIANG, B. LYU, H. LI, K. WATANABE, T. TANIGUCHI, Z. SHI, T. SENTHIL, D. GOLDHABER-GORDON, Y. ZHANG, and F. WANG (Mar. 2020). “[Tunable correlated Chern insulator and ferromagnetism in a moiré superlattice](#)”. *Nature* 579.7797, pp. 56–61.
- CHEN, G., A. L. SHARPE, P. GALLAGHER, I. T. ROSEN, E. J. FOX, L. JIANG, B. LYU, H. LI, K. WATANABE, T. TANIGUCHI, J. JUNG, Z. SHI, D. GOLDHABER-GORDON, Y. ZHANG, and F. WANG (Aug. 2019). “[Signatures of tunable superconductivity in a trilayer graphene moiré superlattice](#)”. *Nature* 572.7768, pp. 215–219.
- CHEN, J., J. PING, and F. WANG (2002). *Group Representation Theory for Physicists: Second Edition*. World Scientific Publishing Company. ISBN: 9789813106000.
- CHICHINADZE, D. V., L. CLASSEN, and A. V. CHUBUKOV (Sept. 2020). “[Valley magnetism nematicity and density wave orders in twisted bilayer graphene](#)”. *Physical Review B* 102.12, p. 125120.
- CHOI, Y. W. and H. J. CHOI (Dec. 2018). “[Strong electron-phonon coupling electron-hole asymmetry and nonadiabaticity in magic-angle twisted bilayer graphene](#)”. *Physical Review B* 98.24, p. 241412.
- CHOI, Y., J. KEMMER, Y. PENG, A. THOMSON, H. ARORA, R. POLSKI, Y. ZHANG, H. REN, J. ALICEA, G. REFAEL, F. VON OPPEN, K. WATANABE, T. TANIGUCHI, and S. NADJ-PERGE (Nov. 2019). “[Electronic correlations in twisted bilayer graphene near the magic angle](#)”. *Nature Physics* 15.11, pp. 1174–1180.
- CLASSEN, L., I. F. HERBUT, L. JANSSEN, and M. M. SCHERER (July 2015). “[Mott multicriticality of Dirac electrons in graphene](#)”. *Physical Review B* 92.3, p. 035429.

- DIXON, J. D. (1970). “Computing Irreducible Representations of Groups”. *Mathematics of Computation* 24.111, pp. 707–712.
- DRESSELHAUS, M., G. DRESSELHAUS, and A. JORIO (2007). *Group Theory: Application to the Physics of Condensed Matter*. Springer Berlin Heidelberg. ISBN: 978-3-540-32897-1.
- FANG, S. and E. KAXIRAS (June 2016). “Electronic structure theory of weakly interacting bilayers”. *Physical Review B* 93.23, p. 235153.
- FRADKIN, E., S. A. KIVELSON, M. J. LAWLER, J. P. EISENSTEIN, and A. P. MACKENZIE (Aug. 2010). “Nematic Fermi Fluids in Condensed Matter Physics”. *Annual Review of Condensed Matter Physics* 1.1, pp. 153–178.
- FU, Y., E. J. KÖNIG, J. H. WILSON, Y.-Z. CHOU, and J. H. PIXLEY (Sept. 2018). “Magic-angle semimetals”. *arXiv:1809.04604*.
- GAO, M., J. PING, F. WANG, and J. CHEN (2002). *Group Representation Theory For Physicists 2nd Edition*. World Scientific Publishing Company. ISBN: 978-981-310-600-0.
- GEIM, A. K. and I. V. GRIGORIEVA (July 2013). “Van der Waals heterostructures”. *Nature* 499.7459, pp. 419–425.
- GRACEY, J. A., T. LUTHE, and Y. SCHRÖDER (Dec. 2016). “Four loop renormalization of the Gross-Neveu model”. *Physical Review D* 94.12, p. 125028.
- GROSS, D. J. and A. NEVEU (Nov. 1974). “Dynamical symmetry breaking in asymptotically free field theories”. *Physical Review D* 10.10, pp. 3235–3253.
- GUAN, R., A. YUAN, and B. LUO (2020). “Bilayer Graphene: From Stacking Order to Growth Mechanisms”. *physica status solidi (RRL) – Rapid Research Letters* 14.3, p. 1900605.
- GUINEA, F., A. H. CASTRO NETO, and N. M. R. PERES (June 2006). “Electronic states and Landau levels in graphene stacks”. *Physical Review B* 73.24, p. 245426.
- GUINEA, F., B. HOROVITZ, and P. LE DOUSSAL (May 2008). “Gauge field induced by ripples in graphene”. *Physical Review B* 77.20, p. 205421.
- HEJAZI, K., C. LIU, H. SHAPOURIAN, X. CHEN, and L. BALENTS (Jan. 2019). “Multiple topological transitions in twisted bilayer graphene near the first magic angle”. *Physical Review B* 99.3, p. 035111.
- JIANG, Y., X. LAI, K. WATANABE, T. TANIGUCHI, K. HAULE, J. MAO, and E. Y. ANDREI (Sept. 2019). “Charge order and broken rotational symmetry in magic-angle twisted bilayer graphene”. *Nature* 573.7772, pp. 91–95.
- KALLIN, C. and J. BERLINSKY (May 2016). “Chiral superconductors”. *Reports on Progress in Physics* 79.5, p. 054502.
- KANG, J. and O. VAFEK (June 2019). “Strong Coupling Phases of Partially Filled Twisted Bilayer Graphene Narrow Bands”. *Physical Review Letters* 122.24, p. 246401.
- KERELSKY, A., L. J. MCGILLY, D. M. KENNES, L. XIAN, M. YANKOWITZ, S. CHEN, K. WATANABE, T. TANIGUCHI, J. HONE, C. DEAN, A. RUBIO, and A. N. PASUPATHY (Aug. 2019). “Maximized electron interactions at the magic angle in twisted bilayer graphene”. *Nature* 572.7767, pp. 95–100.
- KHALAF, E., A. J. KRUCHKOV, G. TARNOPOLSKY, and A. VISHWANATH (Aug. 2019). “Magic angle hierarchy in twisted graphene multilayers”. *Physical Review B* 100.8, p. 085109.
- KIVELSON, S. A., I. P. BINDLOSS, E. FRADKIN, V. OGANESYAN, J. M. TRANQUADA, A. KAPITULNIK, and C. HOWALD (Oct. 2003). “How to detect fluctuating stripes in the high-temperature superconductors”. *Reviews of Modern Physics* 75.4, pp. 1201–1241.

- KLUG, M. J. (July 2020). “Charge order and Mott insulating ground states in small-angle twisted bilayer graphene”. *New Journal of Physics* 22.7, p. 073016.
- KOSHINO, M. and T. ANDO (June 2006). “Transport in bilayer graphene: Calculations within a self-consistent Born approximation”. *Physical Review B* 73.24.
- KOSHINO, M., N. F. Q. YUAN, T. KORETSUNE, M. OCHI, K. KUROKI, and L. FU (Sept. 2018). “Maximally Localized Wannier Orbitals and the Extended Hubbard Model for Twisted Bilayer Graphene”. *Physical Review X* 8.3, p. 031087.
- KUZMENKO, A. B., I. CRASSEE, D. VAN DER MAREL, P. BLAKE, and K. S. NOVOSELOV (Oct. 2009). “Determination of the gate-tunable band gap and tight-binding parameters in bilayer graphene using infrared spectroscopy”. *Physical Review B* 80.16, p. 165406.
- LEE, P. A., N. NAGAOSA, and X.-G. WEN (Jan. 2006). “Doping a Mott insulator: Physics of high-temperature superconductivity”. *Reviews of Modern Physics* 78.1, pp. 17–85.
- LILLY, M. P., K. B. COOPER, J. P. EISENSTEIN, L. N. PFEIFFER, and K. W. WEST (Jan. 1999). “Evidence for an Anisotropic State of Two-Dimensional Electrons in High Landau Levels”. *Physical Review Letters* 82.2, pp. 394–397.
- LIU, D. F., A. J. LIANG, E. K. LIU, Q. N. XU, Y. W. LI, C. CHEN, D. PEI, W. J. SHI, S. K. MO, P. DUDIN, T. KIM, C. CACHO, G. LI, Y. SUN, L. X. YANG, Z. K. LIU, S. S. P. PARKIN, C. FELSER, and Y. L. CHEN (Sept. 2019). “Magnetic Weyl semimetal phase in a Kagomé crystal”. *Science* 365.6459, pp. 1282–1285.
- LIU, S., E. KHALAF, J. Y. LEE, and A. VISHWANATH (Jan. 2021). “Nematic topological semimetal and insulator in magic-angle bilayer graphene at charge neutrality”. *Physical Review Research* 3.1, p. 013033.
- LOPES DOS SANTOS, J. M. B., N. M. R. PERES, and A. H. CASTRO NETO (Dec. 2007). “Graphene Bilayer with a Twist: Electronic Structure”. *Physical Review Letters* 99.25, p. 256802.
- LOPES DOS SANTOS, J. M. B., N. M. R. PERES, and A. H. CASTRO NETO (Oct. 2012). “Continuum model of the twisted graphene bilayer”. *Physical Review B* 86.15, p. 155449.
- LÖTHMAN, T., J. SCHMIDT, F. PARHIZGAR, and A. M. BLACK-SCHAFFER (Jan. 2021). “Nematic superconductivity in magic-angle twisted bilayer graphene from atomistic modeling”. *arXiv:2101.11555*.
- LU, X., B. LIAN, G. CHAUDHARY, B. A. PIOT, G. ROMAGNOLI, K. WATANABE, T. TANIGUCHI, M. POGGIO, A. H. MACDONALD, B. A. BERNEVIG, and D. K. EFETOV (Dec. 2020). “Multiple Flat Bands and Topological Hofstadter Butterfly in Twisted Bilayer Graphene Close to the Second Magic Angle”. *arXiv:2006.13963*.
- LU, X., P. STEPANOV, W. YANG, M. XIE, M. A. AAMIR, I. DAS, C. URGELL, K. WATANABE, T. TANIGUCHI, G. ZHANG, A. BACHTOLD, A. H. MACDONALD, and D. K. EFETOV (Oct. 2019). “Superconductors orbital magnets and correlated states in magic-angle bilayer graphene”. *Nature* 574.7780, pp. 653–657.
- LUCIGNANO, P., D. ALFÈ, V. CATAUDELLA, D. NINNO, and G. CANTELE (May 2019). “Crucial role of atomic corrugation on the flat bands and energy gaps of twisted bilayer graphene at the magic angle $\theta \sim 1.08^\circ$ ”. *Physical Review B* 99.19, p. 195419.
- LUICAN, A., G. LI, A. REINA, J. KONG, R. R. NAIR, K. S. NOVOSELOV, A. K. GEIM, and E. Y. ANDREI (Mar. 2011). “Single-Layer Behavior and Its Breakdown in Twisted Graphene Layers”. *Physical Review Letters* 106.12, p. 126802.
- MA, Z.-Q. (2007). *Group Theory for Physicists*. World Scientific Publishing Company. ISBN: 9789813101487.

- MA, Z.-Q. and X.-Y. GU (2004). *Problems And Solutions In Group Theory For Physicists*. World Scientific Publishing Company. ISBN: 9789814482769.
- MACDONALD, A. H. (May 2019). “Bilayer Graphene’s Wicked Twisted Road”. *Physics* 12, p. 12.
- MAÑES, J. L., F. DE JUAN, M. STURLA, and M. A. H. VOZMEDIANO (Oct. 2013). “Generalized effective Hamiltonian for graphene under nonuniform strain”. *Physical Review B* 88.15, p. 155405.
- MCCANN, E. and M. KOSHINO (May 2013). “The electronic properties of bilayer graphene”. *Reports on Progress in Physics* 76.5, p. 056503.
- MELE, E. J. (Dec. 2011). “Band symmetries and singularities in twisted multilayer graphene”. *Physical Review B* 84.23, p. 235439.
- MOGERA, U. and G. U. KULKARNI (Jan. 2020). “A new twist in graphene research: Twisted graphene”. *Carbon* 156, pp. 470–487.
- MORA, C., N. REGNAULT, and B. A. BERNEVIG (Jan. 2019). “Flat bands and perfect metal in trilayer moiré graphene”. *arXiv:1901.05469*.
- MULLIKEN, R. S. (Dec. 2004). “Electronic Population Analysis on LCAO–MO Molecular Wave Functions. I”. *The Journal of Chemical Physics* 23.10, p. 1833.
- NI, Z., L. LIU, Y. WANG, Z. ZHENG, L.-J. LI, T. YU, and Z. SHEN (Sept. 2009). “G-band Raman double resonance in twisted bilayer graphene: Evidence of band splitting and folding”. *Physical Review B* 80.12, p. 125404.
- NOVOSELOV, K. S., E. MCCANN, S. V. MOROZOV, V. I. FAL’KO, M. I. KATSNELSON, U. ZEITLER, D. JIANG, F. SCHEDIN, and A. K. GEIM (Mar. 2006). “Unconventional quantum Hall effect and Berry’s phase of 2π in bilayer graphene”. *Nature Physics* 2.3, pp. 177–180.
- OCHI, M., M. KOSHINO, and K. KUROKI (Aug. 2018). “Possible correlated insulating states in magic-angle twisted bilayer graphene under strongly competing interactions”. *Physical Review B* 98.8, p. 081102.
- PO, H. C., L. ZOU, A. VISHWANATH, and T. SENTHIL (Sept. 2018). “Origin of Mott Insulating Behavior and Superconductivity in Twisted Bilayer Graphene”. *Physical Review X* 8.3, p. 031089.
- POWELL, B. J. and R. H. MCKENZIE (May 2011). “Quantum frustration in organic Mott insulators: from spin liquids to unconventional superconductors”. *Reports on Progress in Physics* 74.5, p. 056501.
- ROSENSTEIN, B., B. J. WARR, and S. H. PARK (June 1991). “Dynamical symmetry breaking in four-fermion interaction models”. *Physics Reports* 205.2, pp. 59–108.
- SAMAJDAR, R., M. S. SCHEURER, S. TURKEL, C. RUBIO-VERDÚ, A. N. PASUPATHY, J. W. F. VENDERBOS, and R. M. FERNANDES (Feb. 2021). “Electric-field-tunable electronic nematic order in twisted double-bilayer graphene”. *arXiv:2102.08385*.
- SAN-JOSE, P., J. GONZÁLEZ, and F. GUINEA (May 2012). “Non-Abelian Gauge Potentials in Graphene Bilayers”. *Physical Review Letters* 108.21.
- SBOYCHAKOV, A. O., A. L. RAKHMANOV, A. V. ROZHKOV, and F. NORI (Aug. 2015). “Electronic spectrum of twisted bilayer graphene”. *Physical Review B* 92.7.
- SHALLCROSS, S., S. SHARMA, E. KANDELAKI, and O. A. PANKRATOV (Apr. 2010). “Electronic structure of turbostratic graphene”. *Physical Review B* 81.16, p. 165105.
- SHARMA, G., M. TRUSHIN, O. P. SUSHKOV, G. VIGNALE, and S. ADAM (May 2020). “Superconductivity from collective excitations in magic-angle twisted bilayer graphene”. *Physical Review Research* 2.2, p. 022040.

- SHARPE, A. L., E. J. FOX, A. W. BARNARD, J. FINNEY, K. WATANABE, T. TANIGUCHI, M. A. KASTNER, and D. GOLDHABER-GORDON (Aug. 2019). “Emergent ferromagnetism near three-quarters filling in twisted bilayer graphene”. *Science* 365.6453, pp. 605–608.
- SHECHTMAN, D., I. BLECH, D. GRATIAS, and J. W. CAHN (Nov. 1984). “Metallic Phase with Long-Range Orientational Order and No Translational Symmetry”. *Physical Review Letters* 53.20, pp. 1951–1953.
- SONG, Z.-D., B. LIAN, N. REGNAULT, and B. A. BERNEVIG (Oct. 2020). “TBG II: Stable Symmetry Anomaly in Twisted Bilayer Graphene”. *arXiv:2009.11872*.
- SONG, Z., Z. WANG, W. SHI, G. LI, C. FANG, and B. A. BERNEVIG (July 2019). “All Magic Angles in Twisted Bilayer Graphene are Topological”. *Physical Review Letters* 123.3, p. 036401.
- STEPANOV, P., I. DAS, X. LU, A. FAHIMNIYA, K. WATANABE, T. TANIGUCHI, F. H. L. KOPPENS, J. LISCHNER, L. LEVITOV, and D. K. EFETOV (July 2020). “Untying the insulating and superconducting orders in magic-angle graphene”. *Nature* 583.7816, pp. 375–378.
- SUÁREZ MORELL, E., J. D. CORREA, P. VARGAS, M. PACHECO, and Z. BARTICEVIC (Sept. 2010). “Flat bands in slightly twisted bilayer graphene: Tight-binding calculations”. *Physical Review B* 82.12, p. 121407.
- TARNOPOLSKY, G., A. J. KRUCHKOV, and A. VISHWANATH (Mar. 2019). “Origin of Magic Angles in Twisted Bilayer Graphene”. *Physical Review Letters* 122.10, p. 106405.
- VAFEK, O. and J. KANG (Dec. 2020). “Renormalization Group Study of Hidden Symmetry in Twisted Bilayer Graphene with Coulomb Interactions”. *Physical Review Letters* 125.25, p. 257602.
- VOZMEDIANO, M., J. GONZÁLEZ, F. GUINEA, J. ALVAREZ, and B. VALENZUELA (Dec. 2002). “Properties of electrons near a Van Hove singularity”. *Journal of Physics and Chemistry of Solids* 63.12, pp. 2295–2297.
- VOZMEDIANO, M. A. H. (July 2011). “Renormalization group aspects of graphene”. *Philosophical Transactions of the Royal Society A: Mathematical, Physical and Engineering Sciences* 369.1946, pp. 2625–2642.
- WANG, B., M. HUANG, N. Y. KIM, B. V. CUNNING, Y. HUANG, D. QU, X. CHEN, S. JIN, M. BISWAL, X. ZHANG, S. H. LEE, H. LIM, W. J. YOO, Z. LEE, and R. S. RUOFF (Mar. 2017). “Controlled Folding of Single Crystal Graphene”. *Nano Letters* 17.3, pp. 1467–1473.
- WILSON, J. H., Y. FU, S. D. SARMA, and J. H. PIXLEY (Aug. 2019). “Disorder in Twisted Bilayer Graphene”. *arXiv:1908.02753*.
- WONG, D., K. P. NUCKOLLS, M. OH, B. LIAN, Y. XIE, S. JEON, K. WATANABE, T. TANIGUCHI, B. A. BERNEVIG, and A. YAZDANI (June 2020). “Cascade of electronic transitions in magic-angle twisted bilayer graphene”. *Nature* 582.7811, pp. 198–202.
- WU, F. and S. DAS SARMA (June 2019). “Identification of superconducting pairing symmetry in twisted bilayer graphene using in-plane magnetic field and strain”. *Physical Review B* 99.22, p. 220507.
- XHIE, J., K. SATTLER, M. GE, and N. VENKATESWARAN (June 1993). “Giant and supergiant lattices on graphite”. *Physical Review B* 47.23, pp. 15835–15841.
- XIE, M. and A. H. MACDONALD (Mar. 2020). “Nature of the Correlated Insulator States in Twisted Bilayer Graphene”. *Physical Review Letters* 124.9, p. 097601.

- XIE, Y., B. LIAN, B. JÄCK, X. LIU, C.-L. CHIU, K. WATANABE, T. TANIGUCHI, B. A. BERNEVIG, and A. YAZDANI (Aug. 2019). “Spectroscopic signatures of many-body correlations in magic-angle twisted bilayer graphene”. *Nature* 572.7767, pp. 101–105.
- YANKOWITZ, M., S. CHEN, H. POLSHYN, Y. ZHANG, K. WATANABE, T. TANIGUCHI, D. GRAF, A. F. YOUNG, and C. R. DEAN (Mar. 2019). “Tuning superconductivity in twisted bilayer graphene”. *Science* 363.6431, pp. 1059–1064.
- YAO, W., E. WANG, C. BAO, Y. ZHANG, K. ZHANG, K. BAO, C. K. CHAN, C. CHEN, J. AVILA, M. C. ASENSIO, J. ZHU, and S. ZHOU (July 2018). “Quasicrystalline 30° twisted bilayer graphene as an incommensurate superlattice with strong interlayer coupling”. *Proceedings of the National Academy of Sciences* 115.27, pp. 6928–6933.
- YU, T., D. M. KENNES, A. RUBIO, and M. A. SENTEF (Jan. 2021). “Nematicity Arising from a Chiral Superconducting Ground State in Magic-Angle Twisted Bilayer Graphene under In-Plane Magnetic Fields”. *arXiv:2101.01426*.
- ZHANG, Y., K. JIANG, Z. WANG, and F. ZHANG (July 2020). “Correlated insulating phases of twisted bilayer graphene at commensurate filling fractions: A Hartree-Fock study”. *Physical Review B* 102.3, p. 035136.
- ZHU, J., J. SHI, and A. H. MACDONALD (Aug. 2020). “Theory of ARPES in Graphene-Based Moiré Superlattices”. *arXiv:2006.08908*.

Appendices

- ATKINS, P. W., M. CHILD, and C. PHILLIPS (1970). *Tables for group theory*. Oxford U.P.
- BRAY, A. J. and M. A. MOORE (Nov. 1977). “Critical behaviour of semi-infinite systems”. *Journal of Physics A: Mathematical and General* 10.11, pp. 1927–1962.
- CARDY, J., P. GODDARD, and J. YEOMANS (1996). *Scaling and Renormalization in Statistical Physics*. Cambridge Lecture Notes in Physics. Cambridge University Press. ISBN: 9780521499590.
- CHEN, J., J. PING, and F. WANG (2002a). *Group Representation Theory for Physicists: Second Edition*. World Scientific Publishing Company. ISBN: 9789813106000.
- CHEN, J.-Q., J. PING, and F. WANG (Jan. 2002b). *Group Representation Theory for Physicists*. World Scientific. ISBN: 978-981-238-065-4.
- DOMB, C. (2000). *Phase Transitions and Critical Phenomena*. ISSN. Elsevier Science. ISBN: 978-0-08-053876-1.
- DRESSELHAUS, M. S., G. DRESSELHAUS, and A. JORIO (2007). *Group Theory: Application to the Physics of Condensed Matter*. SpringerLink: Springer e-Books. Springer Berlin Heidelberg. ISBN: 9783540328971.
- DUDKA, M., A. A. FEDORENKO, V. BLAVATSKA, and Y. HOLOVATCH (2016). “Critical behavior of the two-dimensional Ising model with long-range correlated disorder”. *Physical Review B* 93.22, p. 224422.
- EFETOV, K. (1996). *Supersymmetry in Disorder and Chaos*. Cambridge University Press.
- KLEINERT, H. and V. SCHULTE-FROHLINDE (2001). *Critical Properties of ϕ^4 -theories*. World Scientific. ISBN: 9789810246594.
- LUBENSKY, T. C. and M. H. RUBIN (June 1975a). “Critical phenomena in semi-infinite systems. I. ϵ expansion for positive extrapolation length”. *Physical Review B* 11.11, pp. 4533–4546.

- LUBENSKY, T. C. and M. H. RUBIN (Nov. 1975b). “Critical phenomena in semi-infinite systems. II. Mean-field theory”. *Physical Review B* 12.9, pp. 3885–3901.
- MA, Z.-Q. (2007). *Group Theory for Physicists*. World Scientific Publishing Company. ISBN: 9789813101487.
- MA, Z.-Q. and X.-Y. GU (2004). *Problems And Solutions In Group Theory For Physicists*. World Scientific Publishing Company. ISBN: 9789814482769.
- OHNO, K. and Y. OKABE (1983). “Three-dimensional surface critical exponents in $1/n$ expansion”. *Journal of Magnetism and Magnetic Materials* 31-34, pp. 1261–1262.
- SREDNICKI, M. (2007). *Quantum Field Theory*. Cambridge University Press. ISBN: 97811-39462761.
- SYZRANOV, S. V., V. GURARIE, and L. RADZIHOVSKY (2016). “Multifractality at non-Anderson disorder-driven transitions in Weyl semimetals and other systems ”. *Annals of Physics* 373, pp. 694–706.
- WOIT, P. (2017). *Quantum Theory Groups and Representations: An Introduction*. Springer International Publishing. ISBN: 9783319646121.
- ZINN-JUSTIN, J. (2002). *Quantum Field Theory and Critical Phenomena*. International series of monographs on physics. Clarendon Press. ISBN: 9780198509233.